Fusion Materials
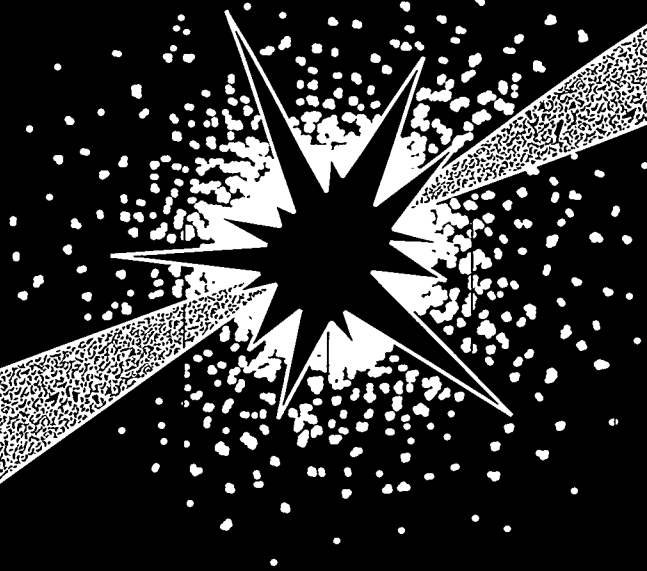
**Semiannual Progress Report
for Period Ending
December 31, 1998**

U. S. Department of Energy
Office of Fusion Energy Sciences

DISCLAIMER

Portions of this document may be illegible in electronic image products. Images are produced from the best available original document.

FUSION MATERIALS

SEMIANNUAL PROGRESS REPORT

FOR THE PERIOD ENDING

December 31, 1998

Prepared for

DOE Office of Fusion Energy Sciences

(AT 60 20 00 0)

DATE PUBLISHED: APRIL 1999

FOREWORD

This is the tweny-fifth in a series of semiannual technical progress reports on fusion materials. This report combines the full spectrum of research and development activities on both metallic and non-metallic materials with primary emphasis on the effects of the neutronic and chemical environment on the properties and performance of materials for in-vessel components. This effort forms one element of the materials program being conducted in support of the Fusion Energy Sciences Program of the U.S. Department of Energy. The other major element of the program is concerned with the interactions between reactor materials and the plasma and is reported separately.

The Fusion Materials Program is a national effort involving several national laboratories, universities, and industries. A large fraction of this work, particularly in relation to fission reactor experiments, is carried out collaboratively with our partners in Japan, Russia, and the European Union. The purpose of this series of reports is to provide a working technical record for the use of the program participants, and to provide a means of communicating the efforts of materials scientists to the rest of the fusion community, both nationally and worldwide.

This report has been compiled and edited under the guidance of A. F. Rowcliffe by Gabrielle Burn, Oak Ridge National Laboratory. Their efforts, and the efforts of the many persons who made technical contributions, are gratefully acknowledged.

F. W. Wiffen
International and Technology Division

Reports previously listed in this series are as follows:

DOE/ER-0313/1	Period ending September 30, 1986
DOE/ER-0313/2	Period ending March 31, 1987
DOE/ER-0313/3	Period ending September 30, 1987
DOE/ER-0313/4	Period ending March 31, 1988
DOE/ER-0313/5	Period ending September 30, 1988
DOE/ER-0313/6	Period ending March 31, 1989
DOE/ER-0313/7	Period ending September 30, 1989
DOE/ER-0313/8	Period ending March 31, 1990
DOE/ER-0313/9	Period ending September 30, 1990
DOE/ER-0313/10	Period ending March 31, 1991
DOE/ER-0313/11	Period ending September 30, 1991
DOE/ER-0313/12	Period ending March 31, 1992
DOE/ER-0313/13	Period ending September 30, 1992
DOE/ER-0313/14	Period ending March 31, 1993
DOE/ER-0313/15	Period ending September 30, 1993
DOE/ER-0313/16	Period ending March 31, 1994
DOE/ER-0313/17	Period ending September 30, 1994
DOE/ER-0313/18	Period ending March 31, 1995
DOE/ER-0313/19	Period ending December 31, 1995
DOE/ER-0313/20	Period ending June 30, 1996
DOE/ER-0313/21	Period ending December 31, 1996
DOE/ER-0313/22	Period ending June 30, 1997
DOE/ER-0313/23	Period ending December 31, 1997
DOE/ER-0313/24	Period ending June 30, 1998
DOE/ER-0313/100	Technical Evaluation of the Technology of Vanadium Alloys for Use as Blanket Structural Materials in Fusion Power Systems

CONTENTS

To explore the upper operating limit of vanadium-base alloys, SS-3 tensile specimens were prepared from the 832665 and 832864 heats of V-4Cr-4Ti alloys and tested at temperatures between 600 and 800°C. The results showed the behavior of the two heats to be similar (with the 832864 heat being slightly weaker) and the reduction of strengths with temperature insignificant at least up to 750°C. Ductility for both materials is good in the test temperature range. These findings are largely consistent with previously reported results on these two heats.

A study of the thermal creep properties of V-4Cr-4Ti is being performed using pressurized tube specimens. Creep tubes nominally 4.572 mm OD and 0.254 mm wall thickness were pressurized with high-purity helium gas to mid-wall effective stress levels below the uniaxial yield strength at the test temperature of interest. Specimens are being heated to 700 and 800°C in an ultra-high vacuum furnace and held at temperature for specific time intervals. Periodically the specimens are removed to measure the change in OD with a high-precision laser profilometer. Initial results show that creep rates at 800°C are substantially greater than at 700°C.

Four Charpy impact specimens were received from General Atomics (GA) after they were exposed in the tokamak environment of the JFT-2M. These specimens were prepared from the GA's 832864 heat of V-4Cr-4Ti material. The exposed specimens were impact tested at ANL using established procedures. The results showed no appreciable degradation of impact properties of the material from the JFT-2M exposure.

A systematic study is underway at Argonne National Laboratory to evaluate the performance of several V-Cr-Ti alloys after exposure to environments containing hydrogen at various partial pressures. The goal is to correlate the chemistry of the exposure environment with hydrogen uptake by the samples and the resulting influence on the microstructures and tensile properties of the alloys. At present, the principal effort has focused on the V-4Cr-4Ti alloy of a heat identified as BL-71;

however, other alloys (V-5Cr-5Ti alloy of Heats BL-63 and T87, plus a V-4Cr-4Ti alloy from General Atomics [GA]) are also being evaluated. Other variables of interest are the effect of initial grain size on hydrogen uptake and tensile properties, and the synergistic effects of oxygen and hydrogen on the tensile behavior of the alloys. During this period, specimens of Heat BL-71 were exposed for 100 h to pH_2 in the range of 3×10^{-6} and 5×10^{-2} torr (2.7×10^{-5} to 0.45 Pa) at 200 and 350°C. Tensile test results obtained on specimens exposed for 100 h at 200, 350, and 500°C to pH_2 in the range of 1×10^{-6} to 0.01 torr, showed negligible effect of H_2 on either maximum engineering stress or uniform and total elongation. However, uniform and total elongation decreased substantially when the alloy was exposed at 500°C to 1.0 torr pH_2.

Tensile and Charpy specimens made of alloy BL-42 (with a nominal composition of V-3.1Ti-0.5Si) were irradiated in the Fast Flux Test Facility (FFTF) in Cycle 11 at 520 and 600°C to up to 51 dpa. Some of these specimens were retrieved from storage and tested in this reporting period. The interest of this material stems from recent findings that show binary alloys of this class appear to exhibit lower susceptibility to radiation-induced embrittlement than other V-base alloys in low-temperature irradiation (<≈400°C). The results of our tests show the BL-42 material to have good tensile properties and fair impact properties after the 520-600°C irradiation and that alloys of this class may warrant further development for improved low-temperature performance.

Small, pre-cracked, 1/3-sized Charpy specimens of V-4Cr-4Ti were irradiated to a dose of 0.5 dpa at a temperature of 200 ± 8°C. The specimens were tested in three point bending under static conditions to measure effective toughness-temperature curves. Fracture processes were examined by using confocal microscopy and fracture reconstruction methods. It was found that this alloy undergoes normal stress-controlled cleavage transition below a characteristic temperature, and that irradiation hardening increased the transition temperature significantly. Shifts in the transition temperature imposed by irradiation hardening can be reasonably predicted by a simple equivalent yield stress model.

Significant variations exist between the microstructures of the various batches of mechanical property specimens prepared for the 500 kg heat of V-4Cr-4Ti. The development of banded grain structures is shown to be related to non-homogeneous distribution of Ti (OCN) particles (0.1-0.3 μ in diameter) that occur in some, but not all, plate products. Precipitation of Ti (OCN) will occur during the hot

extrusion of the ingot in regions where the dislocation density is high and where the temperature falls below the Ti (OCN) solvus at 1125°C. Investigation of the potential benefits of a homogenizing treatment at 1150°C is recommended before proceeding with additional fabrication of plate products from the extruded bar.

A study was conducted to determine the crystal structure of Ti-OCN particles which are commonly observed in V-Cr-Ti based alloys. The information obtained from this study will be used to gain a better understanding of the physical metallurgy of the V-Cr-Ti based alloys. The precipitates examined in this study were those that formed in a V-4Cr-4Ti alloy (S-40) plate) that was annealed at 1000°C for 2 hours. The precipitates are characterized as having a globular shaped morphology with some degree of interfacial faceting. The structural analysis indicated that these precipitates are consistent with the m3m crystal point group.

A systematic study has been in progress at Argonne National Laboratory to examine the use of YAG or CO_2 lasers to weld sheet materials of V-Cr-Ti alloys and to characterize the microstructural and mechanical properties of the laser-welded materials. During this report period, thirty-eight weldments were made with a YAG laser; the emphasis was on determining the optimal weld parameters to achieve deep penetration in the welds while eliminating porosities found previously. A preliminary assessment was then made of the weldments on the basis of visual appearance and sectioning to determine depth of penetration and extent of porosity.

A systematic vapor transport study has been initiated to develop electrically insulating CaO coatings that are compatible with use in a liquid Li environment. Several experiments were conducted to study how the deposition of Ca on V-4Cr-4Ti substrate alloys is affected by variations in process temperature and time, and specimen location, surface preparation, and pretreatment. During this reporting period, a setup has been completed to measure the electrical resistivity of the coatings in air or in an inert gas environment as a function of temperature up to 750°C. Some preliminary data are presented.

The SiC fiber types selected for the JUPITER 14J irradiation experiment are presented together with the rationale for their selection. The fiber diameter variation

from fiber-to-fiber within a tow and along single filament lengths was assessed by image analysis and SEM for four SiC-based fibers: Hi-Nicalon, Hi-Nicalon Type S, Tyron SA, and Dow Sylramic. Because of the apparently characteristic fiber diameter variations observed across tows (6-22 μm) as well as along single filaments (up to ±1.0 μm/cm), it is not appropriate to use average fiber diameters to determine individual fiber strengths or fiber strength distributions. Generally, SiC fibers with larger diameters have lower tensile strengths. Therefore, a 3-parameter modified Wiebull analysis which includes a diameter dependence parameter is preferred over the simple 2-paramater Weibull analysis to properly describe SiC fiber strength distributions. The newly introduced diameter dependence parameter may be a sensitive measure of fiber quality or performance.

FCVI SiC/SiC composites are being fabricated and will be incorporated in the upcoming 14J experiment in conjunction with the Jupiter and Crest Projects. Three different fiber compositions, three different fiber architectures, and two different interface thicknesses are being evaluated simultaneously. All of the fibrous preforms received a pyrolytic carbon surface coating between the fiber and matrix interface. Many of the non-irradiated samples have been characterized and trends examined.

Joining methods are required to allow affordable fabrication of large or complex SiC/SiC components for fusion energy systems. Previous analysis of the criteria for successful and functional joints indicate that reaction-formed and polymer-derived silicon carbide should be considered as candidate joint materials. Efforts have been initiated to investigate the issues involved with fabrication and durability of these joints. This report summarizes initial investigations of the long-term thermal stability of silicon carbide joints formed by a reaction-based approach. Results indicate that the joint may contain unreacted phases that react further during high-temperature exposure. These results, and their implications, must be confirmed by additional investigations.

Single crystal silicon carbide (SiC) has been 2 MeV silicon ion irradiated in various irradiation temperature and ion flux ranges to measure the effect of these parameters on the critical dose for amorphization. The temperature and flux range for which amorphization was observed ranged from 80 to 400 K and 0.066 to 3×10^{-4}

dpa/s, respectively. The critical dose, D_{crit}, was found by locating the depth of the boundary between partially crystalline and fully amorphous material using dark field TEM from samples prepared in cross section. This depth was compared to the damage profile as calculated using the TRIM-96 code. The temperature dependence of D_{crit} is found to agree well with previously reported values, though new evidence suggests a defect species becoming mobile in the 250-300 K range. Also of significance is that D_{crit} was dependent on flux at 340 K, ranging from 0.79 displacements per atom at the lowest ion flux to ~0.6 dpa at the highest flux level. The dose rate dependence of D_{crit} is compared with a chemical rate theory model previously described by the authors. It is seen that the dose rate dependence is substantially weaker than theorized. An extrapolation of the measured dose rate dependence is also compared with recent data on fast neutron amorphized SiC.

SiC/SiC composites were fabricated from Hi-Nicalon™ fibers with carbon, pseudo-porous SiC and multilayer SiC interphases. These materials were then irradiated in the High Flux Beam Reactor with fast neutrons to a dose level equivalent to 1.1 dpa. Results are presented for bend strength of both non-irradiated and irradiated materials. Degradation in ultimate bend stress was seen for all materials studied, while the matrix micro-cracking stress was unchanged. Within the interphases studied the multilayer SiC interphase material showed the least degradation (8-20%) in ultimate bend stress, while porous SiC underwent the greatest degradation (~35%). The fiber matrix interphases are studied with TEM for both non-irradiated and irradiated materials. While no irradiation induced microstructural evolution of the interphase was observed, debonding of the interphase from the fiber was observed for all cases. This debonding is attributed tensile stresses developed at the interface due to densification of the Hi-Nicalon™ fiber. Residual stress analysis of the fiber matrix interface clearly indicates that for densification of Hi-Nicalon™ and volumetric expansion of the CVD SiC matrix corresponding to these irradiation conditions tensile stresses occur well in excess of those which can be withstood by these, or any other viable SiC composite interphase.

The International Energy Agency (IEA) Working Group on Ferritic/Martensitic Steels for Fusion held a workshop at ECN Nuclear Research, Petten, The Netherlands, 1-2 October 1998. The Working Group, consisting of researchers from Japan, the European Union, the United States, and Switzerland, met to review research that has been completed since the previous meeting and to continue planning and coordinating an international collaborative test program on reduced-activation ferritic/martensitic steels for fusion applications. At the workshop, data were presented from the continuing research on the IEA heats of steel that are being studied in the collaboration. Data on these and other reduced-activation steels in the irradiated and unirradiated condition were presented. Other subjects that were

discussed included effects of a ferromagnetic steel in a fusion machine, the effect of helium on properties, and the development and application of oxide dispersion-strengthened steels for fusion. A Working Group status-review meeting is planned in conjunction with the International Conference on Fusion Reactor Materials (ICFRM-9) in Colorado Springs, 10-15 October 1999, at which time plans for a workshop to be held in 2000 will be finalized.

3.2 MECHANICAL PROPERTIES OF TWO 7-9Cr FERRITIC/MARTENSITIC STEELS – G .R. Odette, G. E. Lucas, and P. Spätig (University of California, Santa Barbara)   119

Tensile and fracture tests were performed on two ferritic/martensitic stainless steels. The temperature dependence of the yield stress and the thermal stress dependence of the activation volume were found to be in good agreement with a model based on the propagation of double kinks on screw dislocation segments. Effective fracture toughness-temperature curves were developed for two specimen sizes, and a constraint correction based on a critical stress (σ)-critical area (A) model was found to rationalize the differences. The status of the Master Curve Experiment is discussed.

3.3 EFFECT OF SMALL AMOUNTS OF RHENIUM AND OSMIUM ON MECHANICAL PROPERTIES OF A 9Cr-2W-0.25V-0.07Ta-0.1C Steel – R. L. Klueh, D. J. Alexander, and M. A. Sokolov (Oak Ridge National Laboratory)   125

The nuclear transmutation of tungsten to rhenium and osmium in a tungsten-containing steel irradiated in a fission or fusion reactor could change substantially the chemical composition of the steel. To determine the possible consequences of such changes on mechanical properties, tensile and Charpy impact properties were determined on five 9Cr-2W-0.25V-0.07Ta-0.1C steels that contained different amounts of rhenium, osmium, and tungsten. The mechanical properties changes due to these changes in composition were relatively minor. Observations were also made on the effect of carbon concentration. The effect of carbon on tensile behavior was relatively minor, but there was a large effect on Charpy properties. The steels showed relatively little effect of tempering temperature on the Charpy transition temperature, which was tentatively attributed to the silicon and/or manganese concentration.

3.4 SHEAR PUNCH TESTING OF IRRADIATED ISOTOPICALLY TAILORED FERRITIC/MARTENSITIC STEELS – M. L. Hamilton, D. S. Gelles (Pacific Northwest National Laboratory, S. Ohnuki (Hokkaido University), K. Shiba (JAERI), Y. Kohno (University of Tokyo), and A. Kohyama (Kyoto University)   136

Single variable experiments are being conducted to study effects of H/He/dpa on properties based on isotopically tailored alloys. ^{54}Fe has been used to prepare an isotopically tailored duplicate of the commercial steel F82H, and a small number of TEM disks have been irradiated in order to study radiation embrittlement. From single disk specimens, mechanical properties were obtained using a shear punch technique that produces a 1 mm blank from the 3 mm disk. Results indicate that shear punch testing can be used successfully to provide mechanical property data from single TEM disks. Little effect of helium on properties was found, either in ^{54}Fe isotopically tailored specimens or in a boron-doped specimen.

3.5 MICROSTRUCTURAL EXAMINATION OF IRRADIATED ISOTOPICALLY TAILORED FERRITIC/MARTENSITIC STEELS FOLLOWING SHEAR PUNCH TESTING – D. S. Gelles (Pacific Northwest National Laboratory), S. Ohnuki (Hokkaido University), K. Shiba (JAERI), Y. Kohno (University of Tokyo), A. Kohyama (Kyoto University), J. P. Robertson (Oak Ridge National Laboratory), and M. L. Hamilton (Pacific Northwest National Laboratory)   143

Single variable experiments are being conducted to study effects of H/He/dpa on properties based on isotopically tailored alloys. ^{54}Fe has been used to prepare an isotopically tailored duplicate of the commercial steel F82H, and a small number of TEM disks have been irradiated in order to study radiation embrittlement. From single disk specimens, mechanical properties were obtained using a shear punch technique that produces a 1 mm blank from the 3 mm disk. The 1 mm blanks have been thinned and examined by TEM. The novel thinning procedures are described and microstructural observation presented in detail. Little effect of helium on microstructure was found, either in ^{54}Fe isotopically tailored specimens or in a boron doped specimen.

3.6 HYDROGEN PRODUCTION EFFECT ON MICROSTRUCTURE OF HFIR-IRRADIATED LOW-ACTIVATION F82H STEEL USING ^{54}Fe ISOTOPE – E. Wakai (Japan Atomic Energy Research Institute), N. Hashimoto (Oak Ridge National Laboratory), K. Shiba and Y. Miwa (JAERI), and J. P. Robertson and R. L. Klueh (Oak Ridge National Laboratory)   151

Reduced-activation F82H-std and a similar F82H doped with ^{54}Fe (F82[(^{54}Fe]) steels were irradiated at 250°C to 2.8 dpa in HFIR and examined by TEM. The produced hydrogen concentration in the F82H(^{54}Fe) steel is estimated to be 68 appm. Pre-irradiation microstructures of F82H(^{54}Fe) steel were very similar to those of F82H-std steel. A few small cavities were formed in the irradiated F82H(^{54}Fe) steel, but the swelling is insignificant, while in the F82H-std steel no cavities were observed. Precipitates with contrast similar to α′ phase were observed on many dislocation loops in these steels. The number density and mean size for dislocation loops in the F82H-std and Fu2H(^{54}Fe) steels are 1.4×10^{22} m^{-3} and 7.9 nm, and 2.1×10^{22} m^{-3} and 6.6 nm, respectively. These types of loops are b=(a/2)<111> for the F82H-std and b=(a/2)<111> and a<100> for the F82H(^{54}Fe) steel. The concentration of a<111> type to all loops in the F82H(^{54}Fe) steel is about 73%.

3.7 SWELLING OF THE HFIR-IRRADIATED F82H, F82H+ ^{10}B AND F82H+ ^{58}Ni STEELS – E. Wakai (Japan Atomic Energy Research Institute), N. Hashimoto (Oak Ridge National Laboratory), K. Shiba, and Y. Miwa (JAERI), and J. P. Robertson and R. L. Klueh (Oak Ridge National Laboratory)   161

Swelling of reduced-activation F82H-std and F82H steels doped with natural boron (311 appm), isotope ^{10}B (325 appm), 1.35 at% ^{58}Ni, and 1.31 at% ^{60}Ni irradiated at 300 and 400°C to 52 dpa in the HFIR have been examined by TEM. The swelling of F82H-std irradiated at 400°C to 52 dpa is about 0.6% and the natural B and ^{10}B doped F82H steels is about 0.9 and 1.1%, respectively. In the ^{58}Ni and ^{60}Ni doped F82H steels, swelling is 0.02 and 0%, respectively, even though the ^{58}Ni-doped specimen has the highest helium production. Large cavities in the F82H-std are observed in the matrix but not observed near many lath boundaries, while in the ^{10}B

doped specimens, cavities are formed even near lath boundaries. While the cavities formed at 300°C to 52 dpa are observed in only F82H+ ^{10}B and F82H+ ^{58}Ni steels, the swelling value is insignificant. The number densities of dislocation loops formed in these steels at 300°C to 52 dpa are very high (i.e., on the order of 10^{22} m^3), and at 400°C to 52 dpa the number densities are very low (i.e., on the order of 10^{20} m^3). A high density of precipitates is formed in the matrix of the Ni-doped F82H steels. The low swelling of Ni-doped specimens at 400°C of 52 dpa may be caused by the formation of a high density of precipitates.

Microstructures of reduced-activation ferritic/martensitic steels, F82H (8Cr-2W-0.2V-0.04Ta), 8Cr-2WVTa doped with 58Ni, HT9 (12Cr-1MoVW) and HT9 doped with ^{58}Ni, irradiated at 400°C to 7 dpa in the High Flux Isotope Reactor (HFIR), were investigated by transmission electron microscopy. Cavities were observed in the standard F82H (f82H-std.) and 8 Cr-2WVTa-^{58}Ni, but not in the standard HT9 (HT9-std.) and HT9-^{58}Ni alloys. The irradiation induced a_0<100> and (a_0/2)<111> type dislocation loops in all alloys; the number density and the mean diameter of ($a_0$2)<111> type loops were lower and smaller than that of a_0<100> type loops. Also, there is a tendency that the number density of loops in the F82H and 8Cr-2WVTa-^{58}Ni alloys were lower than those in the HT9 alloys.

A reduced activation ferritic/martensitic steel F82H (F82H-std) and a heat with the addition of isotope ^{10}B (F82H+^{10}B) were irradiated at 673 K to 7 and 51 dpa in HFIR. The swelling behavior of these alloys was examined by transmission electron microscopy. In the F82H-std irradiated to 7 dpa, small cavities (~8 nm in dia) were observed in lath cells, but not on the interfaces of lath boundaries or precipitates. The cavity number density (N_c) was about 4×10^{21} m^{-3}. The swelling was about 0.2%. In the F82H+^{10}B irradiated to 7 dpa, smaller cavities (~5 nm in dia) were observed in lath cells, and some cavities occurred on the interfaces of lath boundaries or small precipitates. The N_c was about 1.5×10^{22} m^{-3}, and the swelling was about 0.2%. In the F82H std irradiated to 51 dpa, large and small cavities were observed in lath cells, but not on the interfaces of lath boundaries or precipitates. The N_c was about 1×10^{21} m^{-3}, and the swelling was about 0.6%.

Previous reports presented the effects of strain rate and test temperature on the tensile properties of GlidCop™ Al25 and Hycon 3HP™ tested in air. The present report summarizes the results of a similar set of tests on solution annealed (SA)

CuCrZr. The SA CuCrZr proved to have only a slight dependence on test temperature up to 350°C in comparison to the other alloys tested in this series. Tests conducted at 450°C, irrespective of the strain rate used, produced a low level of precipitate aging in the solution annealed alloy that masked any potential effect of strain rate and test temperature. For a given strain rate the yield and ultimate strength decreased slightly up to 350°C, then increased significantly at 450°C as the aging began. The uniform and total elongation both decreased steadily as the test temperature was increased to 450°C. The reduction in area was less sensitive to temperature up to 250°C, then decreased steadily up to 450°C. In general the tensile results showed little dependence on strain rate with the exception that the reduction in area was somewhat higher at the two highest strain rates (1.5×10^{-1} and 1.5 s^{-1}) when tested at 350 and 450°C, which may be a consequence to the age hardening. Failure mode in the material appeared ductile throughout the range of strain rate and test temperatures.

5.0 AUSTENITIC STAINLESS STEELS   195

5.1 MICROSTRUCTURAL EVOLUTION OF COLD-WORKED AUSTENITIC STAINLESS STEELS IRRADIATED TO 17 dpa IN SPECTRALLY TAILORED EXPERIMENTS OF THE ORR AND HFIR AT 400°C – E. Wakai (Japan Atomic Energy Research Institute), N. Hashimoto and J. P. Robertson (Oak Ridge National Laboratory), and T. Sawai and A. Hishinuma (JAERI)   197

The microstructural evolution of cold-worked JPCA, 316R, C, K steels irradiated at 400°C in spectrally tailored experiments of the ORR and HFIR was investigated. The helium generation rates were about 12-16 appm He/dpa on the average up to 17.3 dpa. The number density and average diameter of dislocation loops in the steels had ranges of 3×10^{21} to 8×10^{21} m^{-3} and 14.4 to 23.7 nm, respectively. Carbides were formed in all steels by the irradiation, and the number density and average diameter had ranges of 2×10^{21} to 1×10^{22} m^{-3} and 3.4 to 17.7 nm, respectively. The number density and root mean cube of radius for cavities were 6×10^{21} to 2×10^{22} m^{-3}, and 1.2 to 2.4 nm, respectively, in these steels, and the swelling was 0.007 to 0.1% in these steels. JPCA-CW which has the lowest swelling shows the highest number density of carbides, while K-CW which has the highest swelling shows the lowest density of carbides.

6.0 INSULATING CERAMICS AND OPTICAL MATERIALS   203

6.1 EFFECT OF LOW TEMPERATURE ION IRRADIATION ON THE MICROSTRUCTURE OF NITRIDE CERAMICS – S. J. Zinkle, L. L. Snead, W. S. Eatherly, J. W. Jones, and D. K. Hensley (Oak Ridge National Laboratory)   205

Cross-section transmission electron microscopy was used to investigate the microstructure of polycrystalline silicon nitride (Si_3N_4) and aluminum nitride (AlN) following 2 MeV Si ion irradiation at 80 and 400 K up to a fluence of 4×10^{20} ions/m^2 (maximum damage of ~10 displacements per atom, dpa). A buried amorphous band was observed at both temperatures in Si_3N_4 in the region corresponding to the peaks in the implanted ion and displacement damage. From a comparison of Si_3N_4 specimens irradiated at different fluences, it is concluded that the amorphization is primarily controlled by the implanted Si concentration rather than the displacement

damage level. Si_3N_4 amorphization did not occur in regions well-separated from the implanted ions for doses up to at least 3 dpa at 80 K, whereas amorphization occurred in the ion implanted region (calculated Si concentration >0.01 at.%) for damage levels as low as ~0.6 dpa. The volumetric swelling associated with the amorphization of Si_3N_4 is <10%. Amorphization was not observed in any of the irradiated AlN specimens. A moderate density of small (~3 nm) defect clusters were observed in the crystalline damaged regions of both the Si3N4 and AlN specimens at both irradiation temperatures. Aligned network dislocations were also observed in the AlN specimen irradiated to high dose at 80 K.

The phonon scattering rate due to dislocation loops has been calculated. The dislocation loops are modeled as plate-like inclusions in the lattice. Using the calculated value of the phonon scattering relaxation time the reduction in the lattice thermal conductivity is estimated. It is found that for characteristic values of loop size and number density in irradiated alumina dislocation loops will produce a fractional reduction in the thermal conductivity of approximately 33 percent, assuming this is the only scattering mechanism other than intrinsic scattering.

No contributions.

In this study extensive computer simulations were carried out to calculate the yield strengths arising from the presence of two defect populations. The motion of an individual dislocation through a random obstacle field containing varying ratios of obstacles with two different barrier strengths (strong and weak) was computed based on equilibrium bowing of dislocation segments between adjacent obstacles. Yield stress was determined as the minimum stress necessary for the dislocation to successfully traverse the obstacle field. The results show that the superposition law is neither linear nor root sum square, but can be approximately represented by a superposition weighting parameter that is a simple analytical function of the individual strong and weak barrier strengths. Illustrations of the implications of this law are provided.

The main thrust of the current modeling effort is to identify the mechanisms which lead to localization of plastic deformation, the accelerated cavitation at grain

boundaries, the detrimental influence of helium transmutations, and the loss of ductile crack propagation in irradiated materials. We report here our initial research findings on the problem of accumulation of nano-scale prismatic defect clusters in the vicinity of dislocations. Under irradiation conditions, small defect clusters are produced in collision cascades. These mobile clusters interact with dislocations hindering its motion. Thus, radiation hardening takes place as a result of these interactions. However, it is shown here that once these nano-phase clusters approach dislocations, they may be trapped in their elastic strain fields. Trapping is shown to occur by elastic interactions within a zone of 10 nm in bcc Fe, and 20 nm in fcc Cu at RT. If the local stress (i.e. applied plus internal) is high, clusters are absorbed in the core of grown-in dislocations as a result of unbalanced moments, providing sufficient energy for rotation of their Burgers vectors in a zone of 2-3 nm in Fe. Near the dislocation core, sessile defect clusters in Cu are shown to convert to a glissile configuration.

This work demonstrates the use of confocal microscopy and fracture reconstruction methods to measure the critical crack tip opening displacement for several candidate fusion reactor structural materials – including both tempered martensitic steels and V-4Cr-4Ti – as well as other alloys for a variety of testing conditions and specimen sizes and configurations. Extensions of the method to regimes that deviate from small scale yielding, including stable crack growth and small specimens, based on local measures of toughness combined with simulations of crack tip fields are also described.

Extended Abstract

IFFS-VI was initiated at the JUPITER Workshop on Theory and Modeling for Fusion Materials held October 30, 1997, during ICFRM-8 in Sendai, Japan. The original initiative is described, participants and collaborations are identified, and recent progress and future plans are discussed.

.

Energetic atoms which have been knocked off their lattice sites by neutron or ion irradiation leave a trail of vacancies and interstitials in their wake. Most of these defects recombine or cluster within their own collision cascade. Some fraction, however, escape to become freely migrating defects (FMD) in the bulk of the material. The interaction of FMD with the microstructure has long been linked to changes in the macroscopic properties of materials under irradiation. We calculate the fraction of FMD in pure vanadium for a wide range of temperatures and primary knock-on atom (PKA) energies. The collision cascade database is obtained from molecular dynamics (MD) simulations with an embedded atom method (EAM) potential. The actual FMD calculation is carried out by a kinetic Monte Carlo (kMC) code with a set of parameters extracted either from the experimental literature or from MD simulations. We take two different approaches to the problem and compare them. The first consists of an idealized simulation for single cascades. Annealing each cascade at different temperatures allows the mobile species to escape and account for FMD. The second analyzes bulk diffusion and damage accumulation in a specimen irradiated at a low dose rate in the presence of impurities, in order to mimic experimental conditions. At the temperature studied, beginning of stage V, we observe that only vacancies are free to move whereas most interstitials are stopped by impurities. The fraction of FMD obtained is 11% for high purity vanadium, which is in good agreement with the figures reported in literature. We also analyze the role of impurities in damage accumulation.

Extended abstract.

No contributions.

The ARIES-ST design incorporates a number of materials for which data and design criteria are required. The materials input includes the present status of the materials database, as well as progress in fabrication techniques and materials development which can be reasonably achieved over the next 25-50 years. During the past year, input was provided for the copper alloys considered for the electrically-conducting center post, the aluminum alloys proposed for the toroidal field return outer shell, the ferritic steels (low-activation and ODS) to be used as first-wall and blanket

structural material, the compatibility between the slow-flowing Pb-Li breeder and the SiC thermal barrier and the ferritic steel structural material, and the tungsten selected for both the plasma-facing divertor material and the divertor coolant pipes. Some guidance was also provided with regard to fabrication and joining techniques. The level of detail provided with regard to the database and design guidelines for the various components depended on the functional importance of the component and the status of the database.

Iron alloys enriched in Fe-54 were irradiated in the High Flux Isotopes Reactor (HFIR). Measurements and calculations have been performed to demonstrate and to predict the accelerated helium production due to higher fast and/or thermal neutron cross sections for helium-producing reactions on the iron isotopes of Fe-54 and Fe-55. A helium/dpa ratio of 2.3 was achieved for a 1.25-year irradiation.

A high-sensitivity analysis system has been developed for the measurement of hydrogen in solid materials. The system is based on a low-volume hot crucible hydrogen extraction furnace in combination with a modulated-beam quadrupole mass spectrometer detector system. Calibration of the system is conducted using a commercially available hydrogen leak source attached to the detector volume input line. Initial tests on the system using 5 to 10 mg sized specimens cut from a hydrogen-containing steel standard of 5.2 ± 0.3 wppm gave an average concentration of 5.8 ± 0.2 wppm. The ultimate system detection limit is currently ~5 x 10^{14} atoms, or ~5 appm for a 10 mg specimen. Future work will now involve analysis of a number of irradiated materials from various fission and fusion research programs.

The specific requirements of this task were to complete the conceptual designs of irradiation capsules to a neutron dose of approximately 20 dpa in BOR-60. The

specimen matrix will include sheet tensile, compact tension, bend bars, irradiation creep tubes, and TEM disks. The irradiation temperatures will be approximately 500, 550, 600, and 650°C; the temperature changes related to changes in reactor operating conditions are to be minimized; and all specimens are to be encapsulated in lithium. In addition, the possibility of a multi-temperature assembly and reconstitution of assemblies was assessed.

Irradiation of the HFIR-MFE-RB-13J irradiation experiment began during this reporting period. Four cycles of operation were completed and the fifth cycle began during the reporting period. While the operating temperatures of the experiment are slightly higher than anticipated, control of the experiment has worked as expected including temperature control during reactor startup.

The HFIR MFE-RB-11J and –12J experiments are being conducted under the auspices of the Japanese Monbusho, the Japan Atomic Energy Research Institute (JAER), and the U.S. Fusion Energy Sciences Program. The irradiation of the experiments was completed in July of 1998, and the disassembly of the experiments is scheduled to be complete in early 1999. The operating history of both experiments, including the operating temperatures of the specimens, is discussed.

The HFIR-MFE-RB-10J experiment is being conducted under the auspices of the U.S. Department of Energy (DOE)/Japan Atomic Energy Research Institute (JAERI) Collaborative Testing Program. The final specimen loading lists, operating constraints, and operating history of the experiment are discussed. The experiment has undergone approximately ten (10) days of irradiation, but has been removed from HFIR due to the development of a leak in the primary containment vessel. The associated europium liner has also been removed. Efforts are underway to apply for approval to continue the irradiation of the RB-10J experiment as soon as possible.

Significant progress continues to be made in the post-irradiation examinations (PIE) of the specimens from the DOE ORNL/JAERI collaborative capsules and in the design and fabrication of additional capsules. This report serves as a summary of the irradiation parameters for the capsules and the Fusion Materials progress reports related to the design, loading, operation, and dosimetry.

1.0 VANADIUM ALLOYS

TENSILE PROPERTIES OF 832665 AND 832864 HEATS OF V-4Cr-4Ti ALLOY AT HIGH TEMPERATURES*

- H. Tsai, L. J. Nowicki, T. S. Bray, M. C. Billone, D. L. Smith (Argonne National Laboratory) and W. R. Johnson (General Atomics)

Summary

To explore the upper operating limit of vanadium-base alloys, SS-3 tensile specimens were prepared from the 832665 and 832864 heats of V-4Cr-4Ti alloy and tested at temperatures between 600 and 800°C. The results showed the behavior of the two heats to be similar (with the 832864 heat being slightly weaker) and the reduction of strengths with temperature insignificant at least up to 750°C. Ductility for both materials is good in the test temperature range. These findings are largely consistent with previously reported results on these two heats.

Objective

The objective of this task is to determine the high-temperature tensile properties of the 832665 and 832864 heats of V-4Cr-4Ti alloys. The 832665 heat[1] is the "500-kg" heat procured by the U.S. DOE and the 832864 heat[2] is the "1200-kg" heat procured by General Atomics (GA) for the DIII-D radiative divertor upgrade[3].

Background

Susceptibility of vanadium-base alloys to low-temperature embrittlement[4,5,6] during neutron irradiation may limit the application of these alloys in low-temperature (<≈400°C) regimes. To extend the service window, it is necessary to assess the performance of the materials in the high-temperature end, i.e., in the ≈700-800°C range. While the performance at high-temperature may be limited by many factors, including helium effects and creep, adequate tensile properties remain an important consideration.

The tensile properties for the GA's 832864 heat have been measured up to 380°C[7]. Those for the 832665 heat have been measured to 700°C and recently to 800°C[8,9].

Test Specimens

The test specimens for this study were prepared from the 832665 and 832864 heats of V-4Cr-4Ti alloys. The compositions of the two heats are shown in Table 1.

Table 1. Chemical composition of the two alloys investigated

Heat Number	Ingot Size (kg)	Nom. Composition (wt.%)	Interstitial Content (wppm)			
			O	N	C	Si
832665	500	V-3.8Cr-3.9Ti	310	85	80	780
832864	1200	V-3.8Cr-3.8Ti	370	120	30	270

The specimens had nominal gauge dimensions of 0.76 (t) x 1.52 (w) x 7.6 (l) mm. The longitudinal direction was parallel to the final rolling direction of the sheets. The 832665 specimens were cut by electric-discharge machining (EDM) from a cold-rolled sheet with the appropriate thickness. For the 832864 heat, as sheets of the required thickness were not available, EDM was used to slice sheets of the correct thickness from a 4.8-mm-thick plate and then prepare the specimens from the sliced sheets. This method avoided rolling of the plate, thus

preserving the plate's as-rolled microstructure. (4.8-mm-thick plate is a major product form for the DIII-D application.)

After the machining, all specimens were held in a Ti boat and annealed at 1000°C for 1 h in a vacuum better than 10^{-7} torr.

Experimental Procedure

The tests were performed with the specimens and the test train contained in a quartz tube purged with high-purity argon. An impurity getter made of Ti foil was used to protect the specimen at temperature. Heating was achieved with a radiant furnace and the specimen temperature was indirectly measured with a thermocouple attached to the lower specimen grip. As no extensometer was used, gauge section extension was determined from the crosshead displacement after the slack in the grip and the deformation of the load frame were subtracted. The strain rate for all tests was 1.09×10^{-3}/s, except one, which was conducted at 1.09×10^{-4}/s to investigate strain-rate effects.

Results and Discussion

The results of our tests are summarized in Table 2. For both materials, in the 600-800°C-test range, the maximum strength appears to occur at 700°C. All specimens display substantial ductility, with uniform elongation ranging from 7.4 to 12.3% and total elongation from 15.2 to 20.9%. In comparison, as has been seen before in lower-temperature tests[7], the 832864 heat appears to be slightly weaker than the 832665 heat. Not unexpectedly, the 832864 heat exhibits slightly greater ductility. Serrations in the load curve, due to dynamic strain aging, were observed in both materials only at 600°C. At higher test temperatures, serrations could not be identified. Strain-rate effects at 750°C appear to be slight.

Our results exhibit fairly good agreement against previously reported tensile data, as shown in Figs. 1 and 2. The overall database indicates that degradation of the tensile properties due to high temperatures appears not to be an issue, at least at temperature up to ≈750°C.

Table 2. Summary results of the high-temperature tensile tests

Heat/ Material	Specimen No.	Test Temp.(°C)	Strain Rate (s^{-1})	0.2% OS YS (MPa)	UTS (MPa)	UE (%)	TE (%)
832665	133	600	1.09×10^{-3}	227	413	9.8	18.6
(V-4Cr-4Ti)	134	700	1.09×10^{-3}	238	428	10.6	17.3
	135	750	1.09×10^{-3}	233	395	9.6	18.4
	137	750	1.09×10^{-4}	230	401	7.4	15.8
	136	800	1.09×10^{-3}	217	357	7.8	15.2
832864	114	600	1.09×10^{-3}	199	382	10.0	18.7
(V-4Cr-4Ti)	115	700	1.09×10^{-3}	223	398	12.3	20.9
	116	750	1.09×10^{-3}	174	388	11.5	16.3
	117	800	1.09×10^{-3}	173	350	10.5	16.3

Future Activities

The fracture surface of the specimens will be examined with scanning electron microscopy to delineate the fracture mode and to determine areal reduction.
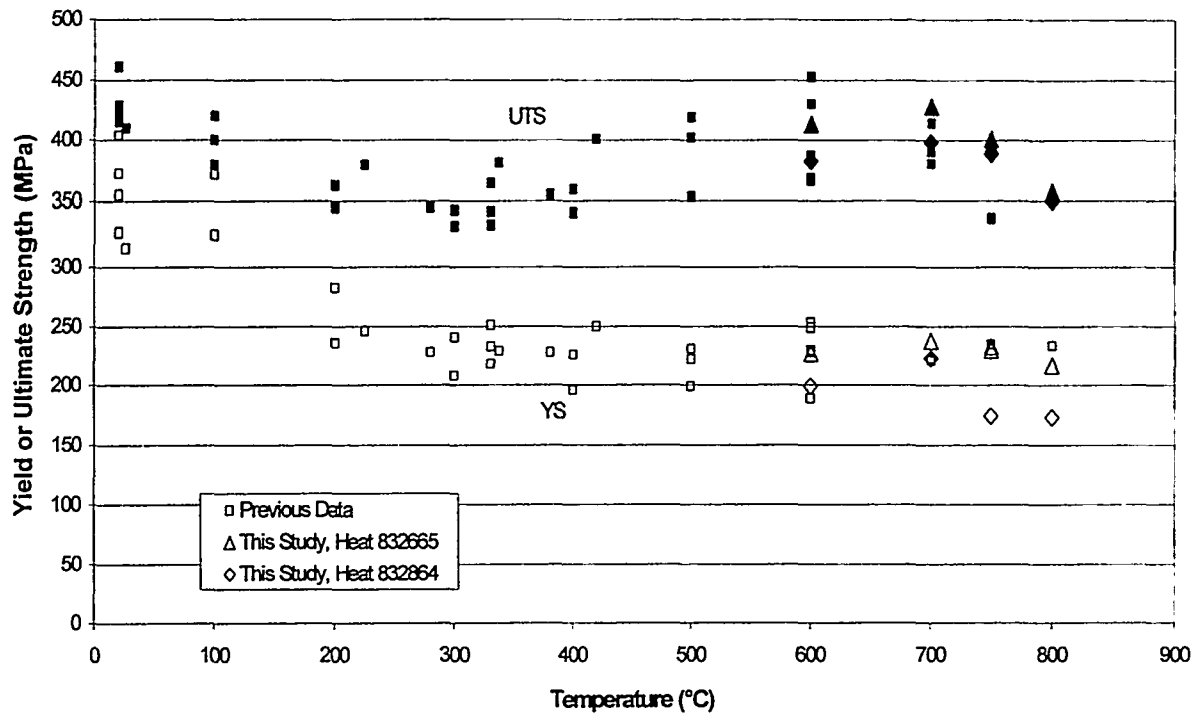
Fig. 1 Comparison of tensile strength of 832665 and 832864 heats with the existing database[7,8,9,10,11,12]. Filled symbols depict ultimate tensile strength and open symbols depict 0.2% offset yield strength.
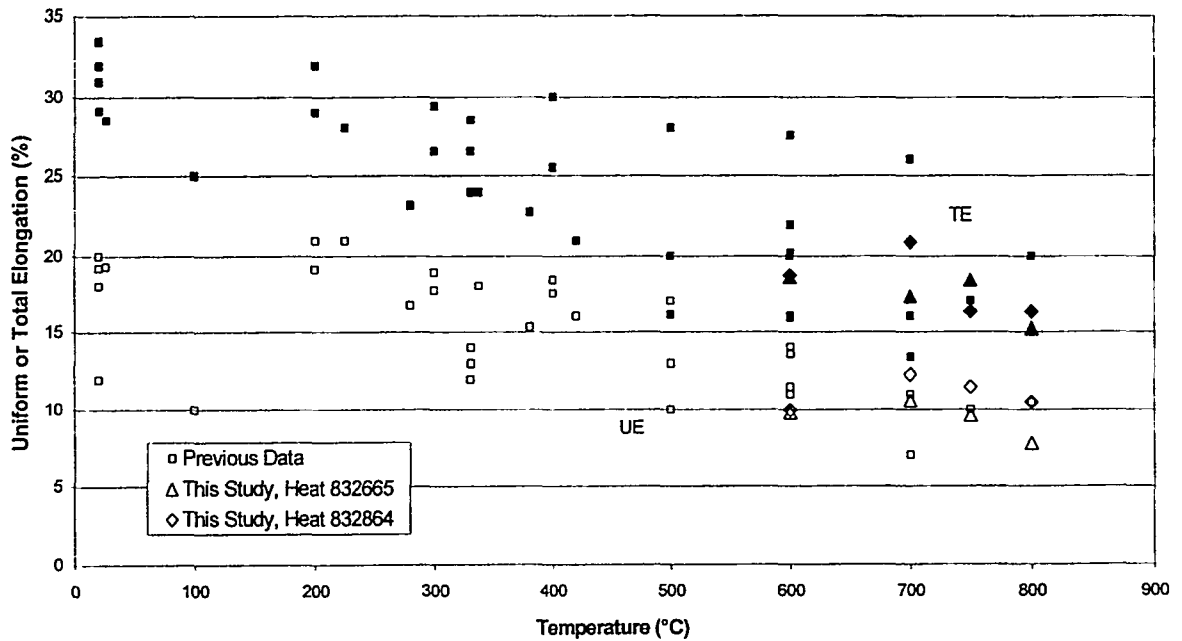
Fig. 2 Comparison of tensile elongation of 832665 and 832864 heats with the existing database[7,8,9,10,11,12]. Filled symbols depict total elongation and open symbols depict uniform elongation.

Acknowledgements

References:

1. H. M. Chung, H. Tsai, D. L. Smith, R. Peterson, C. Curtis, C. Wojcik, and R. Kinney, Fusion Materials Semiannual Progress Report, DOE/ER-0313/17, September 1994, pp. 178-182.
2. W. R. Johnson, J. P. Smith and R. D. Stambaugh, , Fusion Materials Semiannual Progress Report, DOE/ER-0313/20, June 1996, pp. 3-10.
3. J. P. Smith, W. R. Johnson, R. D. Stambaugh, P. W. Trester, D. Smith and E. Bloom, Proc. of the 7th International Conference on Fusion Reactor Materials, September 25-29, 1995.
4. H. M. Chung, H. Tsai, L. Nowicki, and D. L. Smith, Fusion Materials Semiannual Progress Report, DOE/ER-0313/22, June 1997, pp. 18-21.
5. D. J. Alexander et al., "Effects of Irradiation at Low Temperature on V-4Cr-4Ti," Fusion Materials Semiannual Progress Report for Period Ending June 30, 1996, DOE/ER-0313/20, pp.87-95.
6. H. Tsai, J. Gazda, L. J. Nowicki, M. C. Billone, and D. L. Smith, Fusion Materials Semiannual Progress Report for Period Ending June 30, 1998, DOE/ER-0313/24, pp.15-19.
7. H. Tsai, L. J. Nowicki, J. Gazda, M. C. Billone, D. L. Smith and W. R. Johnson, Fusion Materials Semiannual Progress Report, DOE/ER-0313/24, June 1998, pp. 3-10.
8. H. M. Chung, L. Nowicki, D. Busch and D. L. Smith, Fusion Materials Semiannual Progress Report, DOE/ER-0313/19, December 1995, pp. 17-21.
9. S. J. Zinkle, A. F. Rowcliffe, and C. O. Stevens, Fusion Materials Semiannual Progress Report, DOE/ER-0313/24, June 1998, pp. 11-14.
10. M. C. Billone, Fusion Materials Semiannual Progress Report, DOE/ER-0313/23, December 1997, pp. 3-61.
11. A. N. Gubbi, A. F. Rowcliffe, W. S. Eatherly and L. T. Gibson, Fusion Materials Semiannual Progress Report, DOE/ER-0313/20, June 1996, pp. 38-52.
12. E. V. van Osch and M. I. de Vries, Proc. of the 8th International Conference on Fusion Reactor Materials, October 26-31, 1998.

BIAXIAL THERMAL CREEP OF V-4Cr-4Ti AT 700°C AND 800°C – R. J. Kurtz and M. L. Hamilton (Pacific Northwest National Laboratory)*

OBJECTIVE

To determine the biaxial thermal creep characteristics of V-4Cr-4Ti over the temperature range 600 to 800°C at realistic stresses for comparison with uniaxial creep tests and irradiation creep experiments.

SUMMARY

A study of the thermal creep properties of V-4Cr-4Ti is being performed using pressurized tube specimens. Creep tubes nominally 4.572 mm OD and 0.254 mm wall thickness were pressurized with high-purity helium gas to mid-wall effective stress levels below the uniaxial yield strength at the test temperature of interest. Specimens are being heated to 700 and 800°C in an ultra-high vacuum furnace and held at temperature for specific time intervals. Periodically the specimens are removed to measure the change in OD with a high-precision laser profilometer. Initial results show that creep rates at 800°C are substantially greater than at 700°C.

PROGRESS AND STATUS

Introduction

Vanadium-base alloys are attractive candidate materials for fusion first-wall/blanket structural materials, in part, because of their potentially high service temperatures. Information on the time-dependent, high-temperature deformation properties of vanadium and vanadium alloys is limited, and within the existing data base there are uncertainties which may have influenced the results such as the interstitial impurity content of test specimens and vacuum quality. Because of this paucity of data it is a priority for the U.S. Advanced Materials Program to characterize the creep and creep rupture properties of the reference vanadium alloy V-4Cr-4Ti.

To develop a suitable test matrix, the pertinent data on thermal creep of pure vanadium and vanadium alloys was collected and summarized [1-8]. Wheeler, et al. [1] determined the secondary creep rate of pure polycrystalline vanadium over the temperature range from 477 to 1600°C. Their results showed that the activation energy for creep increased linearly from 234 to 507 kJ/mole as the stress decreased from 147 MPa to 2.5 MPa. The activation energy for creep was seen to be larger than that for self-diffusion at any given temperature.

A fifth power dependence of the minimum creep rate on applied stress was found when the ratio of strain rate to diffusivity was less than 10^9 cm^{-2}. Above this ratio a stronger stress dependence was observed. Figure 1 presents a graph of the stress dependence of the minimum creep rate for pure vanadium over the temperature range of 600 to 850°C. The 650 and 800°C data in Figure 1 were generated by Shirra [2]. Note the stress exponent is about 11.3 at stresses above 40 MPa but drops to 6.2 at stress levels below 30 MPa.
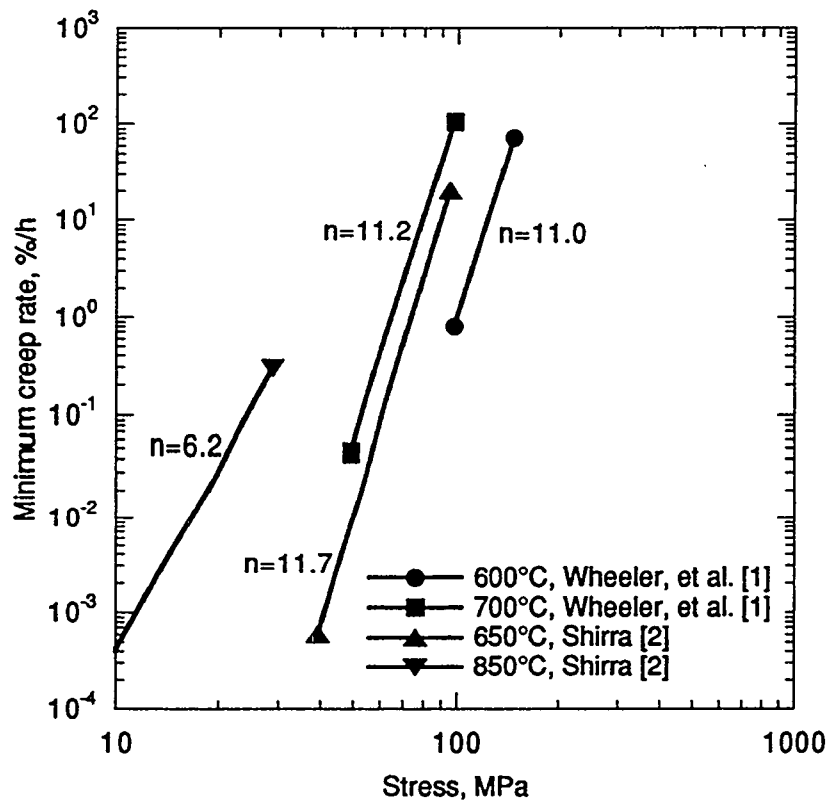
Figure 1 . Stress dependence of the minimum creep rate of pure vanadium.

The stress dependence of the secondary creep rate for V-Ti alloys is similar to that for pure vanadium [3-6]. The available data suggests that for Ti concentrations around 5 w/o, temperatures in the 650 to 700°C range, and stress levels above about 200 MPa the stress exponent is around 11. The stress exponent decreased to values between 2 and 6 for specimens with higher Ti content and tested at higher temperatures and lower stresses. Higher titanium levels have been observed to increase the secondary creep rate.

The creep behavior of V-Cr-Ti alloys tested between 600 and 800°C is plotted in Figure 2 [7,8]. The Ti concentration was about 4 to 5 w/o while the Cr concentration ranged from 4 to 15 w/o. The creep resistance of V-Cr-Ti alloys appears to increase with increasing Cr level, although this observation is not unequivocal. The stress exponent is between 10 and 11 for the bulk of these data. It should be noted that all of the creep data shown in Figure 2 was generated at stress levels greater than 200 MPa. Recently summarized tensile property data for V-4Cr-4Ti [9-11] shows that stresses of this magnitude are very close to the yield strength at temperatures between 300 and 700°C. Furthermore, a preliminary design analysis for V-4Cr-4Ti using the procedures given in the ASME Boiler and Pressure Vessel Code and the ITER Interim Structural Design Criteria indicates that the primary membrane stress limit in the temperature range of 500 to 700°C is about 110 MPa [12]. Thus, the initial test matrix was selected to explore the thermal creep properties of V-4Cr-4Ti at stress levels bounding the conditions that a vanadium first-wall structural material might experience.
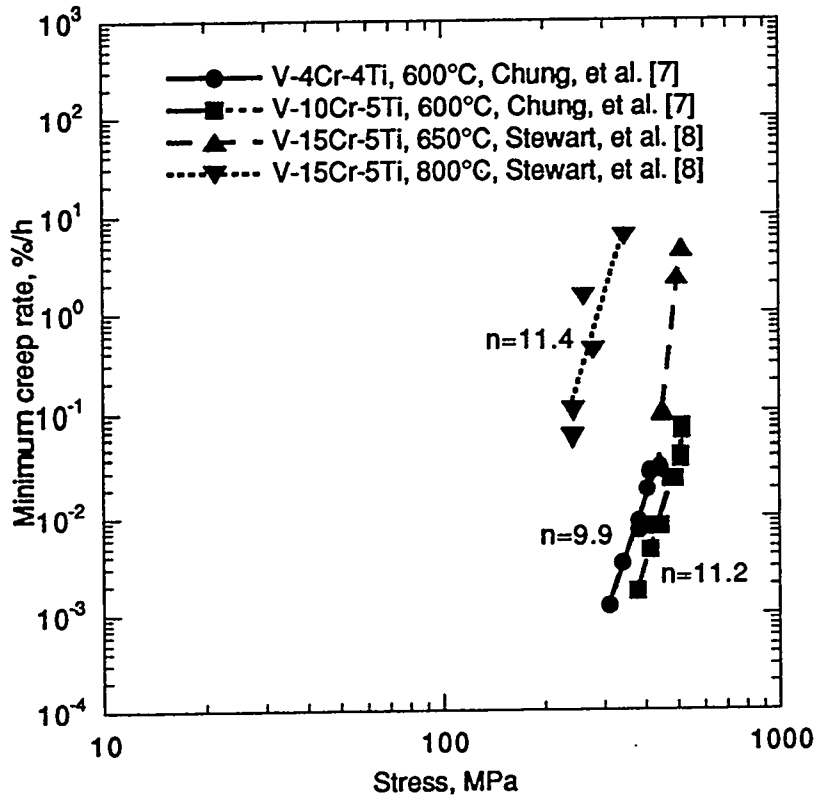
Figure 2. Stress dependence of the minimum creep rate of V-Cr-Ti alloys between 600-800°C.

Table 1 lists the temperatures and mid-wall hoop stress levels planned for the initial series of experiments. Since the ratio of inner radius to wall thickness for our creep tubes is less than 10, it is more appropriate to calculate tube stresses using the expressions for a thick-wall cylinder rather than the approximate thin-wall equations. The mid-wall hoop stresses given in Table 1 were obtained from

$$\sigma_h = \frac{pR_i^2}{R_o^2 - R_i^2}\left[1 + \frac{R_o^2}{R_m^2}\right] \tag{1}$$

where R_o is the outer radius, R_i is the inner radius, p is the internal pressure at the test temperature and R_m is the mid-wall radius. As highlighted in Table 1 by bold italicized entries the first tests will focus on the 700 and 800°C temperatures since these should be completed in the shortest time. It should be noted the stress levels and test temperatures may be revised and updated to reflect early results.

Experimental Procedure

Sections of V-4Cr-4Ti tubing with a nominal 4.572 mm OD, 0.254 mm wall thickness and ~45% cold work level were obtained from Argonne National Laboratory (ANL) for fabricating

Table 1. Planned matrix for biaxial thermal creep experiments. Italicized values represent specimens tested during the first campaign.

Test Temp., °C	Mid-Wall Hoop Stress, MPa					
600	100	150	175	200	225	250
700	*75*	*100*	*125*	*150*	*175*	200
800	25	50	*75*	*100*	*125*	*150*

creep specimens. Figure 3 shows a sketch of the specimen geometry including end-caps. Details of the tubing fabrication have been reported previously [13]. Specimen blanks 25.4 mm long were cut from the tubing and measurements of the ID and OD were performed at two axial locations (x/L = 1/3 and 2/3) and at 45° azimuthal intervals prior to cleaning. Specimen blanks and end-caps were then prepared for welding by cleaning in accordance with modified ANL Procedure IPS-181-00-00. The modifications to this procedure included a somewhat shorter exposure to the pickling solution (~3 min.) and deletion of the oven drying step. Following cleaning, specimen thickness was measured using a metallurgical microscope at eight equally spaced azimuthal locations around each tube end. Five TEM disks punched from pure titanium foil were inserted into each specimen and end-caps were electron-beam welded to the tubes. Following end-cap welding the specimens were loosely wrapped with titanium foil and annealed in a vacuum ($\leq 10^{-7}$ torr) at 1000°C for 1 h. After heat treatment specimen ODs were re-measured using a laser profilometer. The sensitivity of the laser profilometer is $\pm 5 \times 10^{-4}$ mm which translates to a strain measurement sensitivity of about ±0.01%. The diameter measurements were made at five axial locations (x/l of 0.1, 0.3, 0.5, 0.7 and 0.9). Specimens were then filled with 99.999% purity helium gas to the desired pressure and sealed by laser welding. Fill pressures were determined with a computer code that accounted for the thermal expansion of the tubing and compressibility of the helium fill gas at the test temperature of interest. The specimen OD was again measured using the laser profilometer to determine the elastic diametral displacements for each tube. Table 2 summarizes the pre-fill dimensional measurements for each specimen currently under test along with the fill pressures and mid-wall hoop stresses.
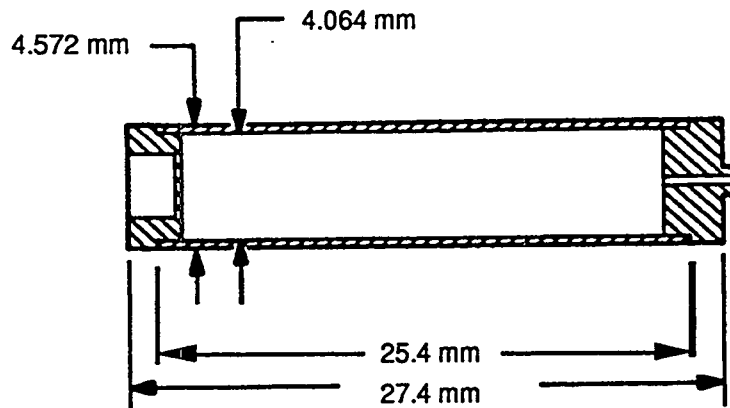
Figure 3. Sketch of creep tube specimen geometry.

Table 2. Unpressurized creep tube dimensions, fill pressures and mid-wall hoop stress levels.

Test Temp., °C	Specimen Code	Specimen OD, mm	Specimen Wall, mm	Fill Press., MPa	Mid-Wall Hoop Stress, MPa
700	AR11	4.5674	0.2601	2.896	72.5
	AR12	4.5662	0.2532	3.909	99.9
	AR13	4.5672	0.2456	4.937	129.6
	AR14	4.5657	0.2499	5.930	151.9
	AR15	4.5659	0.2553	6.964	173.4
800	AR16	4.5684	0.2477	2.654	77.3
	AR17	4.5667	0.2507	3.571	101.2
	AR18	4.5664	0.2461	4.482	128.7
	AR19	4.5667	0.2543	5.419	149.4

Prior to insertion into the vacuum furnace each specimen was loosely wrapped with titanium foil to provide additional protection against oxygen pickup during the experiment. Initially tube diameters were measured weekly until it was apparent that longer intervals could be tolerated. Testing will be conducted for several months to permit measurement of secondary creep rates and in some cases the time to failure. Two tube sections without end-caps were also included with the pressurized specimens at each test temperature to enable periodic assays for oxygen pickup.

Results

Tube diameters were measured as a function of time using the same equipment, procedures and personnel as before test. Tables 3 and 4 give the time dependence of the specimen diameter and effective mid-wall creep strains for the 700 and 800°C test temperatures, respectively. To preclude end effects only the middle three measurements along the length of the tube were used to compute the average diametral strain. For failed specimens the creep strain is based on the diameter measurement taken nearest to the failure location. Creep strains were calculated from the total measured strain minus the elastic contribution. Conversion from outer diameter strain to mid-wall strain was done using the expression derived by Gilbert and Blackburn [14]. It should be noted the conversion factor is only a constant for very small strain levels. The conversion factor decreases with increasing strain. The Gilbert and Blackburn expressions were evaluated numerically to give values of the conversion factor up to diametral strains of 0.3. The results are plotted in Figure 4. Mid-wall hoop strains were converted to effective strains by

$$\varepsilon_e = \frac{2}{\sqrt{3}} \varepsilon_h \qquad (2)$$

where ε_e is the effective mid-wall creep strain and ε_h is the mid-wall hoop strain. The results in Tables 3 and 4 are plotted in Figures 5 and 6. Effective mid-wall stresses obtained from the Von Mises distortion energy criterion are presented in Figures 5 and 6 rather than the mid-wall hoop stresses. The principal stresses inserted into the Von Mises equation were

the appropriate expressions for stress in a thick-wall, closed end cylinder. The ratio of mid-wall effective stress to mid-wall hoop stress is given by

$$\frac{\sigma_e}{\sigma_h} = \frac{\sqrt{3}R_o^2}{R_o^2 + R_m^2} \qquad (3)$$

where σ_e is the effective mid-wall stress and all other variables are the same as above.
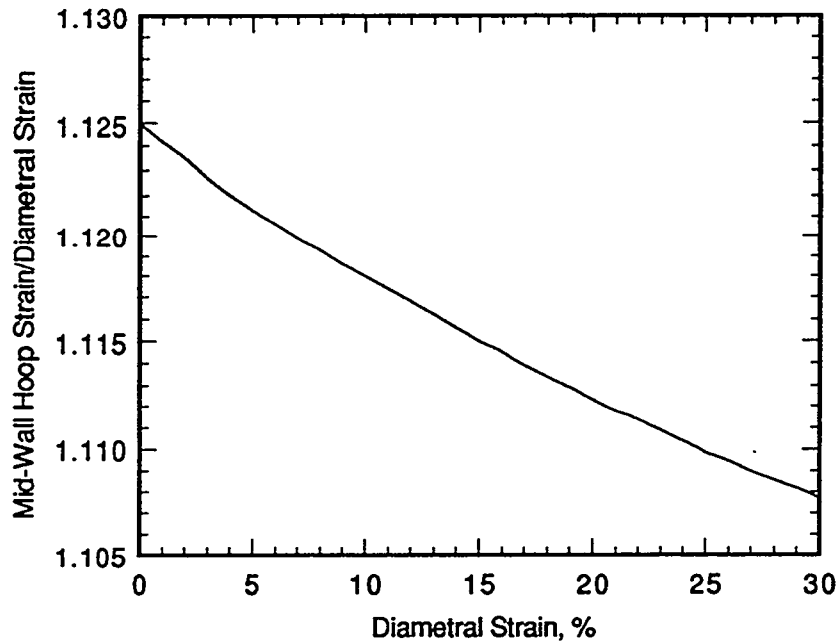
Figure 4. Ratio of mid-wall hoop strain to diametral strain as a function of diametral strain.

Table 3. Time dependence of specimen diameter and effective mid-wall creep strain for 700°C tests.

Time, h	AR11		AR12		AR13		AR14		AR15	
	OD*	ε_e**	OD	ε_e	OD	ε_e	OD	ε_e	OD	ε_e
0	4.5682	0.0000	4.5674	0.0000	4.5687	0.0000	4.5672	0.0000	4.5674	0.0000
168	4.5684	0.0072	4.5674	0.0000	4.5690	0.0072	4.5674	0.0072	4.5682	0.0217
242	4.5684	0.0072	4.5674	0.0000	4.5690	0.0072	4.5677	0.0145	4.5687	0.0361
357	4.5684	0.0072	4.5677	0.0072	4.5690	0.0072	4.5682	0.0289	4.5702	0.0795
598	4.5684	0.0072	4.5682	0.0217	4.5692	0.0145	4.5692	0.0578	4.5748	0.2096
1375	4.5684	0.0072	4.5679	0.0145	4.5695	0.0217	4.5715	0.1229	4.5999	0.9246
1523	4.5684	0.0072	4.5674	0.0000	4.5700	0.0361	4.5720	0.1373	4.6124	1.2783

*Outer diameter in mm.
**ε_e = effective mid-wall strain, %

Table 4. Time dependence of specimen diameter and effective mid-wall creep strain for 800°C tests.

Time, h	AR16		AR17		AR18		AR19	
	OD*	ε_φ**	OD	ε_φ	OD	ε_φ	OD	ε_φ
0	4.5695	0.0000	4.5674	0.0000	4.5679	0.0000	4.5677	0.0000
168	4.5705	0.0289	4.5697	0.0650	4.5730	0.1445	4.6942	3.5917
242	4.5707	0.0361	4.5715	0.1156	4.5898	0.6212	5.0874	14.709
412	4.5735	0.1156	4.5959	0.8089	4.7724	5.7999	-	-
488	4.5758	0.1806	4.6213	1.5306	4.9507	10.832	-	-
578	4.5817	0.3466	4.6708	2.9363	5.4242	24.141	-	-
727	4.5989	0.8375	4.7937	6.4173	-	-	-	-
864	4.6228	1.5156	5.0013	12.290	-	-	-	-
1031	4.6622	2.6327	-	-	-	-	-	-
1343	4.7615	5.4454	-	-	-	-	-	-
1491	4.8204	7.1108	-	-	-	-	-	-
1784	4.9525	10.835	-	-	-	-	-	-

*Outer diameter in mm.
**ε_φ = effective mid-wall strain, %
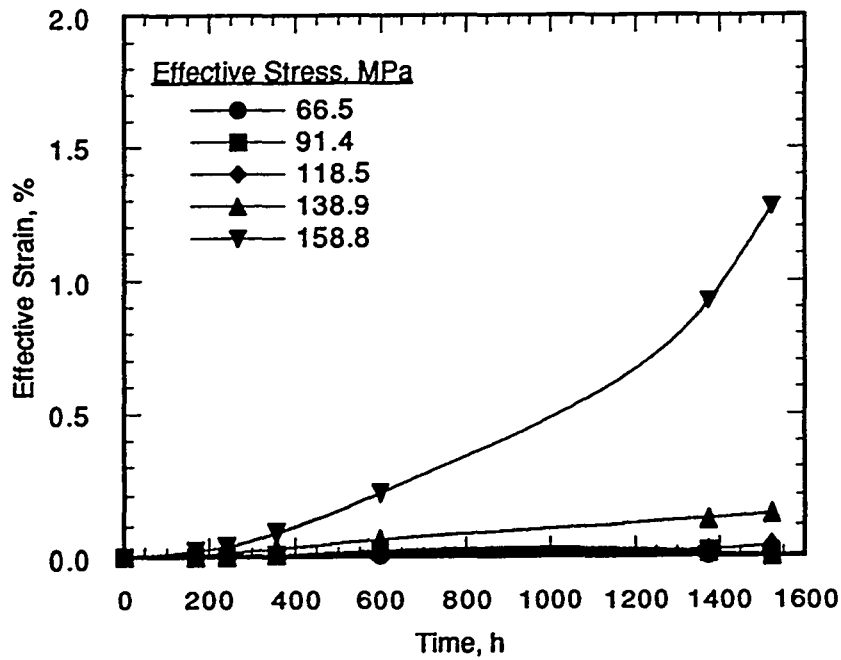
Figure 5. Time dependence of effective mid-wall creep strain at 700°C for unirradiated V-4Cr-4Ti.
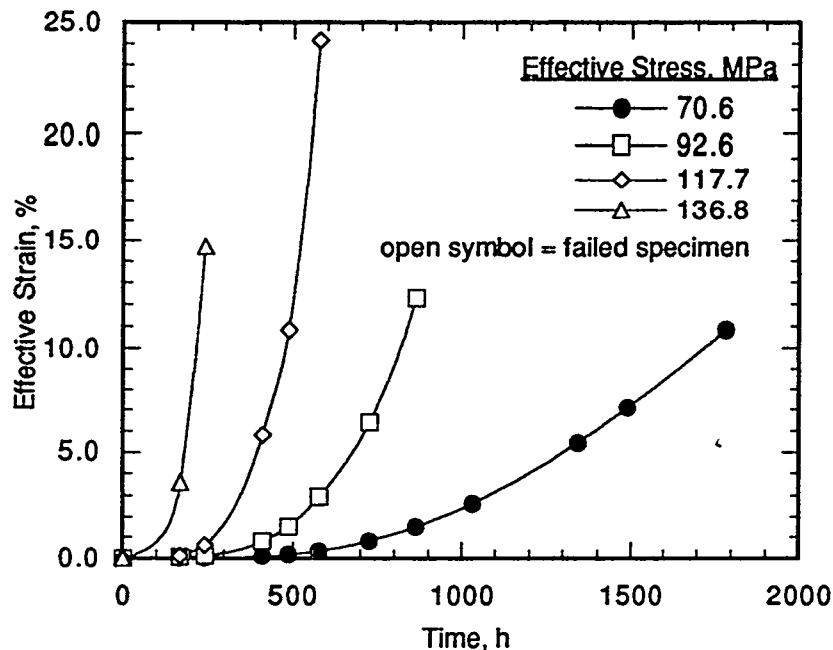
Figure 6.   Time dependence of effective mid-wall creep strain at 800°C for unirradiated V-4Cr-4Ti.

Discussion

It is apparent from the results to date that the creep rate at 800°C is considerably higher than the creep rate at 700°C. For the three highest stresses at 800°C it appears that the secondary creep regime was very short in duration. Even at the lowest stress the results suggest the specimen is exhibiting tertiary rather than secondary creep. Only the highest stress level for the 700°C tests exhibits measurable strain at this juncture. The other stress levels may be too low to cause significant creep at this temperature. These tests will be continued to give an adequate opportunity to accurately measure the secondary creep rate. Significantly more testing is required before meaningful interpretation of the data can be made and comparison of results with those obtained by other investigators.

FUTURE WORK

Considerable work remains to be done on the specimens which have failed at 800°C. We plan to perform fractographic and microstructural analyses to determine deformation and failure mechanisms. Chemical analyses are also planned to determine if oxygen pickup has influenced the deformation behavior in any way.

15

ACKNOWLEDGEMENTS

We acknowledge the substantial contributions of L. K. Fetrow and R. M. Ermi in performing the experiments described in this report.

REFERENCES

1. K. R. Wheeler, E. R. Gilbert, F. L. Yaggee and S. A. Duran, "Minimum-Creep-Rate Behavior of Polycrystalline Vanadium from 0.35 to 0.87 Tm," Acta Metallurgica 19 (1971) 21.

2. M. Shirra, "Das Zeitstandfestigkeits- und Kriechverhalten von Vanadin-Basis-Legierungen," KfK 2440, Kernforschungszentrum Karlsruhe, (1989).

3. H. Boehm and M. Schirra, "Zeitstand und Kriechverhalten von Vanad-Titan und Vanad-Titan-Niob Legierungen," KfK 774, Kernforschungszentrum Karlsruhe, (1968).

4. F. L. Yaggee, Data presented at an AEC/RDT Working Group Meeting, Washington DC (1970).

5. W. Pollack, R. W. Buckman, R. T. Begley, K. C. Thomas and E. C. Bishop, "Development of High Strength Vanadium Alloys - Final Report," WCAP-3487-16, Westinghouse Electric Corporation (1968).

6. T. Kainuma, N. Iwao, T. Suzuki and R. Watanabe, "Creep and Creep Rupture Properties of Unalloyed Vanadium and Solid-Solution-Strengthened Vanadium-Base Alloys," J. Less Common Metals 86 (1982) 263.

7. H. M. Chung, B. A. Loomis and D. L. Smith, "Thermal Creep of Vanadium-Base Alloys," in U.S. Contribution, 1994 Summary Report, Task T12: Compatibility and Irradiation Testing of Vanadium Alloys, ANL/FPP/TM-287, ITER/US/95/IV MAT 10 (1995) 87.

8. J. R. Stewart, J. C. LaVake and S. S. Christopher, Data presented at an AEC/RDT Working Group Meeting, Ames, Iowa (1968).

9. A. N. Gubbi, A. F. Rowcliffe, W. S. Eatherly and L. T. Gibson, "Effects of Strain Rate, Test Temperature and Test Environment on Tensile Properties of Vanadium Alloys," in Fusion Materials: Semiannual Progress Report for Period Ending June 30, 1996, DOE/ER-0313/20 (1996) 38.

10. S. J. Zinkle, "Thermophysical and Mechanical Properties of V-(4-5)Cr-(4-5)Ti Alloys," in Fusion Materials: Semiannual Progress Report for Period Ending December 31, 1997, DOE/ER-0313/23 (1998) 99.

11. M. C. Billone, "Revised ANL-Reported Tensile Data for Unirradiated and Irradiated (FFTF, HFIR) V-Ti and V-Cr-Ti Alloys," in Fusion Materials: Semiannual Progress Report for Period Ending December 31, 1997, DOE/ER-0313/23 (1998) 3.

12. M. C. Billone, "Design Lifetime Evaluation for V-4Cr-4Ti First-Wall Structural Material for Fusion Demo Reactors," Argonne National Laboratory, March 25, 1996.

13. H. Tsai, M. C. Billone, R. V. Strain, D. L. Smith and H. Matsui, "Irradiation Creep of Vanadium-Base Alloys," in Fusion Materials: Semiannual Progress Report for Period Ending December 31, 1997, DOE/ER-0313/23 (1998) 149.

14. E. R. Gilbert and L. D. Blackburn, "Creep Deformation of 20 Percent Cold Worked Type 316 Stainless Steel," J. Eng. Mater. & Tech., ASME Trans. (1977) 168.

IMPACT PROPERTIES OF GA'S 832864 HEAT OF V-4Cr-4Ti ALLOY AFTER EXPOSURE IN THE JFT-2M TOKAMAK - H. Tsai (Argonne National Laboratory), W. R. Johnson, P. W. Trester (General Atomics), S. Sengoku (Japan Atomic Energy Research Institute)

SUMMARY

Four Charpy impact specimens were received from General Atomics (GA) after they were exposed in the tokamak environment of the JFT-2M. These specimens were prepared from the GA's 832864 heat of V-4Cr-4Ti material. The exposed specimens were impact tested at ANL using established procedures. The results showed no appreciable degradation of impact properties of the material from the JFT-2M exposure.

OBJECTIVE

The objective of this task was to determine the impact properties of the 832864 heat specimens after the exposure in the JFT-2M tokamak.

BACKGROUND

A long-term test has been conducted in the JFT-2M tokamak fusion device to determine the effects of environmental exposure on the mechanical and chemical behavior of a V-4Cr-4Ti alloy. Test specimens of the alloy were exposed in the outward divertor chamber of JFT-2M in a region away from direct contact with the plasma, and were held in a fixture which contained a heater to preheat the specimens to 300C prior to plasma discharges. During their nine-month residence in JFT-2M, the specimens experienced exposure to air, low-pressure hydrogen and deuterium ($\approx 10^{-2}$ Pa), titanium (during vessel interior conditioning via sputtering of titanium by Ar ions with magnetron-type RF discharges), and interaction with neutral high energy particles, including metallic species, during 2,210 plasma shots and disruptions. The latter included approximately 200 lower-single-null divertor shots for which high energy particle fluxes to the test specimens were significant, and a number of non-divertor disruptions and upper-single-null divertor shots for which high energy particle fluxes to the test specimens were very low.

Similar specimens from a different heat of V-4Cr-4Ti alloy (Heat 832665) have been exposed to the DIII-D tokamak environment. Results to date from those tests[1] indicate the absorption of interstitials is limited to the very near surface, and that neither the strength nor the Charpy impact properties of the alloy are significantly changed.

EXPERIMENTAL PROCEDURE

Test Specimens

The test specimens for this study were prepared from the 832864 heat[2] of V-4Cr-4Ti alloy. The composition of the material is shown in Table 1.

Table 1. Chemical composition of the 832864 heat

Heat Number	Ingot Size (kg)	Nom. Composition (wt.%)	Interstitial Content (wppm)			
			O	N	C	Si
832864	1200	V-3.8Cr-3.8Ti	370	120	30	270

The Charpy impact specimens were 1/3-size, 3.3 mm (t) x 3.3 mm (w) x 25.4 mm (l), with a 30°,

0.61-mm-deep, 0.08-mm-root radius machined notch. The notch orientation (i.e., crack propagation direction) was perpendicular to the final rolling direction and into the thickness of the plate. This Charpy specimen design is a de facto standard and has been used extensively in previous fusion materials tests.

Test Procedure

The Charpy impact tests were conducted in air with a Dynatup drop-weight tester following established procedures. Specimen temperature during the impact test was measured with a thermocouple spot-welded to the end of the specimen. For the above-ambient-temperature tests, a hot-air blower was used to provide the heating. For the below-room-temperature tests, liquid nitrogen was used to chill the specimens.

RESULTS AND DISCUSSION

The results of the Charpy tests are summarized in Table 2 and Fig. 1. From Fig. 1, which also shows the baseline data for the 832864[3] heat and other relevant data of the sibling 832665 heat, it appears that the impact properties of the JFT-2M-exposed 832864 specimens are essentially unchanged from the nonexposed baseline. The exposed material still possesses excellent impact properties at temperatures as low as –150°C.

SEM fractographic examination of the tested specimens confirmed these positive findings. Even at a low temperature of –150°C, the fracture was ductile tear. Only at –195°C, did the specimen show brittle cleavage fracture. These results are shown in Fig. 2.

Table 2. Charpy impact properties of the 832864 specimens after the JFT-2M exposure

Spec.	Test temperature	Absorbed
G1	23	9.7
G2	-195	3.5
G3	-150	11.8
G4	200	9.9
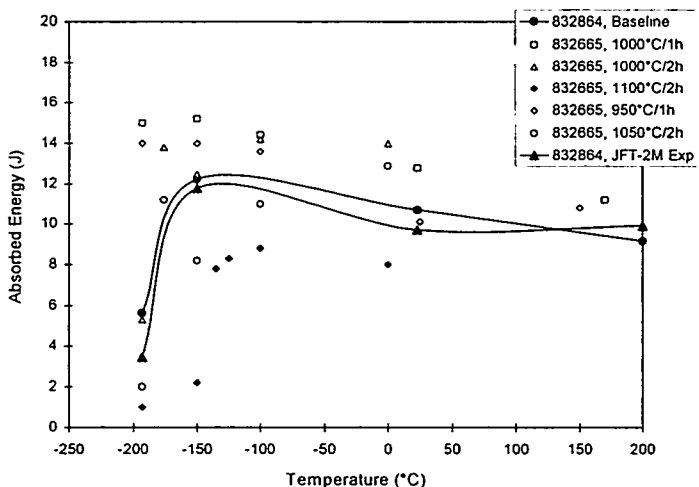
Fig. 1. Charpy impact properties of Heat 832864 specimens after the JFT-2M exposure
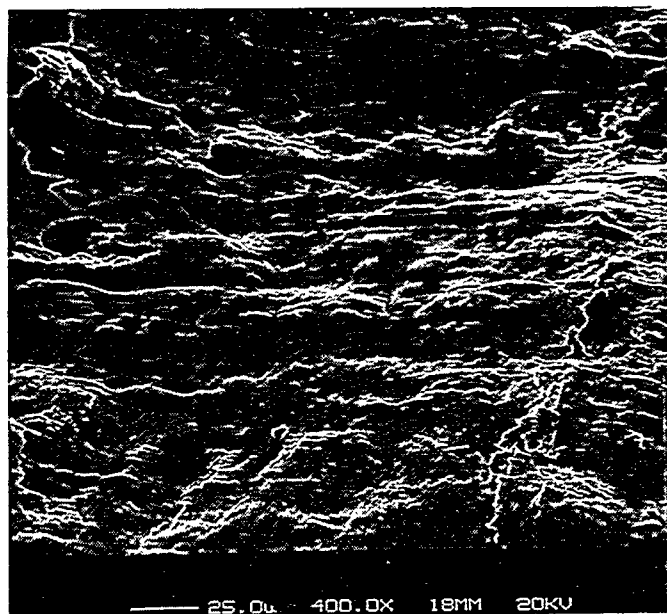
-150°C
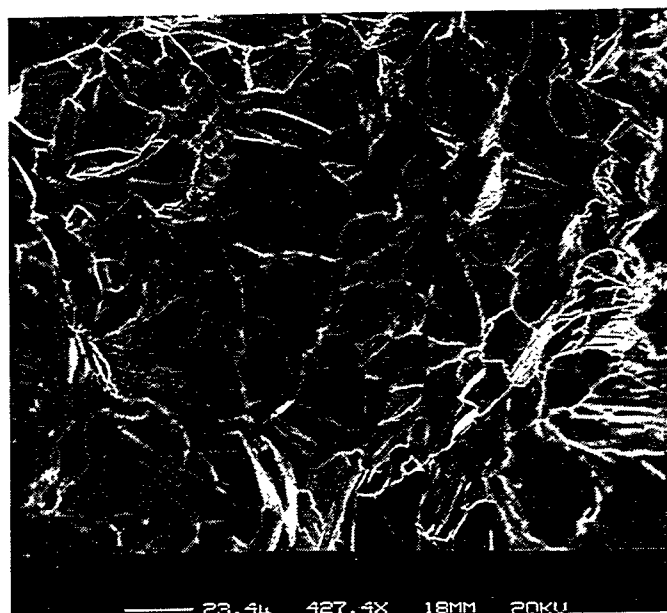
-195°C

Fig. 2.   SEM fractography of the JFT-2M-exposed Charpy specimens showing ductile tear at -150°C and brittle cleavage at –195°C.

REFERENCES

1. H. Tsai, W. R. Johnson, D. L. Smith, J. P. Smith and H. M. Chung, J. of Nuclear Mat'ls, Vol. 258-263, 1998, pp. 1466-1470.
2. W. R. Johnson, J. P. Smith and R. D. Stambaugh, Fusion Materials Semiannual Progress Report, DOE/ER-0313/20, June 1996, pp. 3-10.
3. H. Tsai, L. J. Nowicki, J. Gazda, M. C. Billone, D. L. Smith and W. R. Johnson, Fusion Materials Semiannual Progress Report, DOE/ER-0313/24, June 1998, pp. 3-10.

TENSILE PROPERTIES OF V-Cr-Ti ALLOYS AFTER EXPOSURE IN HYDROGEN-CONTAINING ENVIRONMENTS*

K. Natesan and W. K. Soppet (Argonne National Laboratory)

OBJECTIVE

The objectives of this task are to (a) determine the hydrogen uptake of V-Cr-Ti alloys as a function of temperature and partial pressure of hydrogen (pH_2) in the exposure environment, (b) examine the microstructural characteristics of surfaces and cross sections of the alloys after exposure, (c) evaluate the influence of hydrogen uptake in low-pH_2 environments on the tensile properties and cracking propensity of the alloys at room and elevated temperatures, and (d) determine the effects of oxygen/hydrogen interactions on the tensile properties of the alloys.

SUMMARY

A systematic study is underway at Argonne National Laboratory to evaluate the performance of several V-Cr-Ti alloys after exposure to environments containing hydrogen at various partial pressures. The goal is to correlate the chemistry of the exposure environment with hydrogen uptake by the samples and the resulting influence on the microstructures and tensile properties of the alloys. At present, the principal effort has focused on the V-4Cr-4Ti alloy of a heat identified as BL-71; however, other alloys (V-5Cr-5Ti alloy of Heats BL-63 and T87, plus a V-4Cr-4Ti alloy from General Atomics [GA]) are also being evaluated. Other variables of interest are the effect of initial grain size on hydrogen uptake and tensile properties, and the synergistic effects of oxygen and hydrogen on the tensile behavior of the alloys. During this period, specimens of Heat BL-71 were exposed for 100 h to pH_2 in the range of 3×10^{-6} to 5×10^{-2} torr (2.7×10^{-5} to 0.45 Pa) at 200 and 350°C. Tensile test results, obtained on specimens exposed for 100 h at 200, 350, and 500°C to pH_2 in the range of 1×10^{-6} to 0.01 torr, showed negligible effect of H_2 on either maximum engineering stress or uniform and total elongation. However, uniform and total elongation decreased substantially when the alloy was exposed at 500°C to 1.0 torr pH_2.

EXPERIMENTAL PROGRAM

The nominal compositions of the heats of vanadium alloys selected for the study were V-5 wt.% Cr-5 wt.% Ti (designated as BL-63 and T87) and V-4 wt.% Cr-4 wt.% Ti (designated as BL-71 and 44 from the GA heat). Detailed chemical analyses of these heats were presented in an earlier report.[1] The tensile specimens were fabricated according to ASTM Standard E8-69 specifications and had a gauge length of $\approx$19 mm and a gauge width of $\approx$4.5 mm. Specimens were annealed for 1 h at 1000°C before hydrogen exposure and tensile testing. During this period, tensile specimens of Heat BL-71 were exposed for 100 h at 200 and 350°C to environments with pH_2 levels of 1×10^{-6} and 1×10^{-2} torr; they were subsequently tensile-tested at a strain rate of 1.8×10^{-4} s^{-1} in room-temperature air. The specimens were loaded by means of pins that pass through holes in the grips and the enlarged end sections of the specimen, thus minimizing misalignment. Total elongation was measured with a vernier caliper and load/elongation chart records. The fracture surfaces and longitudinal and axial cross sections of the tested specimens are being examined by scanning electron microscopy. The specimens are also being analyzed for hydrogen content.

RESULTS AND DISCUSSION

The engineering stress/engineering strain plots at room temperature for V-4Cr-4Ti and V-5Cr-5Ti materials in as-annealed condition and after exposure at 500°C in pH_2 levels of 3×10^{-6} and 1 torr were reported in Refs. 1 and 2. The results showed that in the pH_2 range of the present study, BL-

71 exhibited a small decrease in uniform and total elongation after exposure to hydrogen at 500°C. During this period, additional tensile specimens of V-4Cr-4Ti were exposed for 100 h at 200 and 350°C to pH_2 levels of 1×10^{-6}, 1×10^{-4}, and 5×10^{-2} torr. Engineering stress/engineering strain curves from various tests at room temperature were analyzed to evaluate the tensile properties of the alloy after several exposures to hydrogen. Table 1 shows the values for maximum engineering stress and uniform and total elongation of the alloy after exposure at several pH_2 levels and at various temperatures.

Figure 1 shows the engineering stress-engineering strain curves for V-4Cr-4Ti alloy specimens that were exposed to various pH_2 levels at 200, 350, and 500°C and subsequently tensile tested at room temperature air. Figure 2 shows the maximum engineering stress values as a function of hydrogen concentration for the alloy at 200, 350, and 500°C. The results show that pH_2 levels in the range of the present study have little or no effect on the maximum engineering stress for the alloy. The uniform and total elongation values for the alloy are 0.14-0.20 and 0.19-0.31, respectively, at pH_2 levels of 1×10^{-6} to 5×10^{-2} torr. After exposure at a pH_2 of 1 torr at 500°C, the alloy showed a significant decrease in uniform and total elongation, indicating that this pH_2 level may be the threshold for embrittlement of the alloy. Figures 3 and 4 are plots of uniform and total elongation values as a function of H_2 concentration for the alloy exposed at 200, 350, and 500°C and tested at room temperature. The hydrogen concentration in the alloy after exposure for 100 h at 500°C in 1 torr pH_2 was 358 wppm. Examination of the fracture surfaces and specimen cross sections, and measurements of hardness profiles are in progress, and the results will be used to correlate the microstructure, hydrogen concentration, and hardness data with the tensile properties of the alloys.

Table 1. Effects of 100-h hydrogen exposure at 200, 350, and 500°C on room-temperature tensile properties of V-Cr-Ti alloys, initially annealed for 1 h at 1050°C in vacuum

Exposure temperature (°C)	pH_2 in exposure environment (torr)	Maximum engineering stress (MPa)	Uniform elongation	Total elongation
200	3×10^{-6}	421	0.199	0.302
	1×10^{-4}	420	0.178	0.313
	5×10^{-2}	419	0.138	0.207
350	3×10^{-6}	434	0.133	0.184
	1×10^{-4}	525	0.182	0.242
	5×10^{-2}	460	0.183	0.294
500	-	424	0.186	0.322
	3×10^{-6}	440	0.174	0.263
	1×10^{-4}	467	0.154	0.227
	1×10^{-4}[a]	491	0.148	0.206
	1×10^{-2}	459	0.169	0.263
	5×10^{-2}	477	0.142	0.191
	1	468	0.0016	0.0016

[a]Repeat
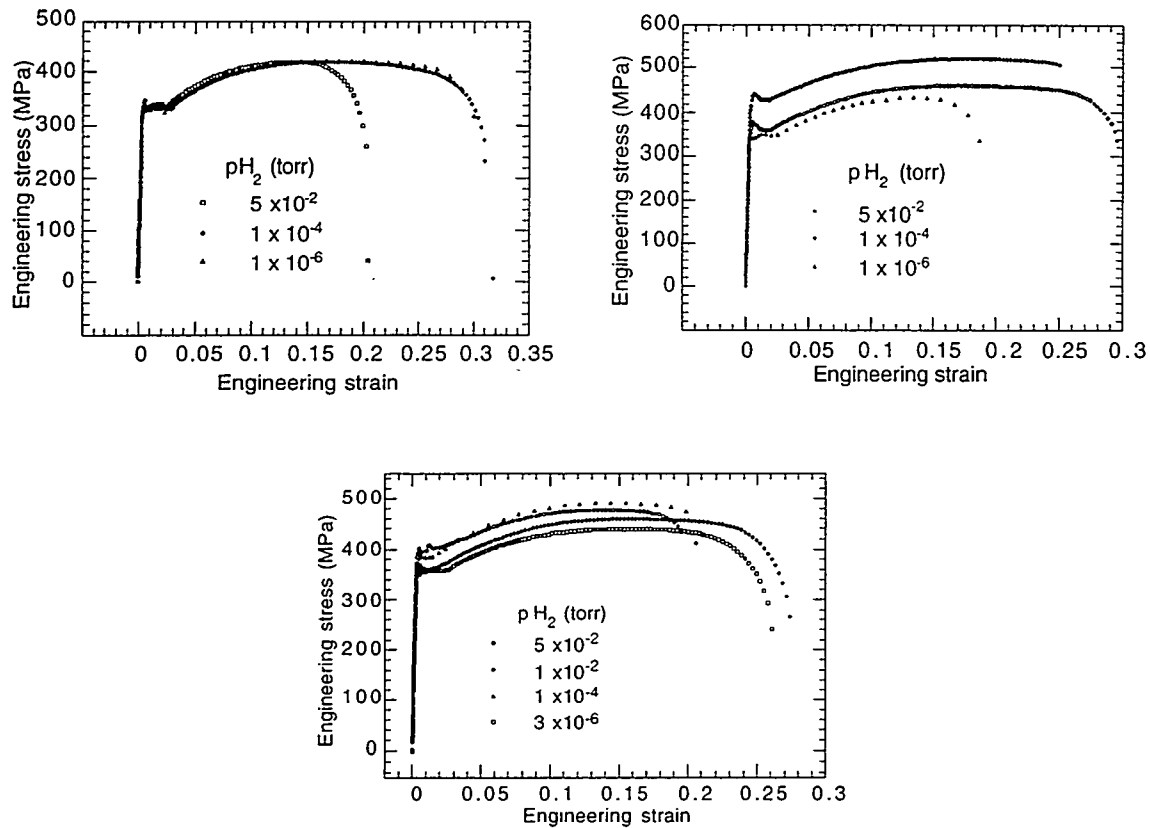
. Figure 1. Engineering stress/engineering strain curves for V-4Cr-4Ti alloy at room temperature after 100 h exposure to hydrogen at 200°C (top left), 350°C (top right), and 500°C (bottom).
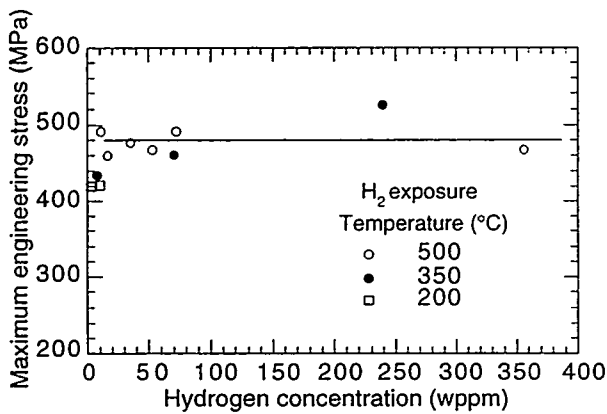
Figure 2. Maximum engineering stress as a function of hydrogen concentration for V-4Cr-4Ti alloy tested at room temperature
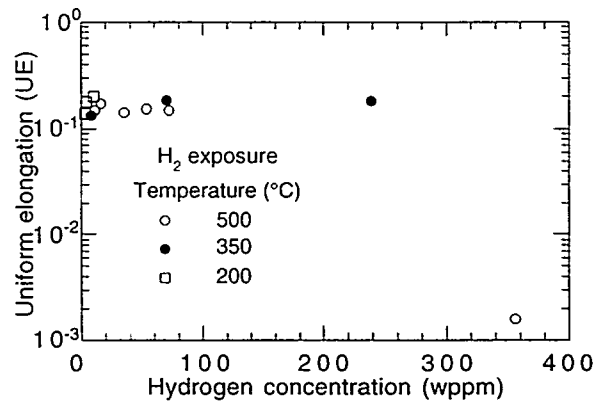
Figure 3. Uniform elongation as a function of hydrogen concentration for V-4Cr-4Ti alloy tested at room temperature
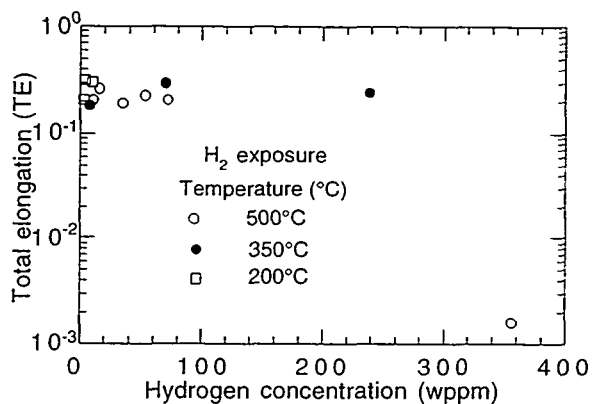
Figure 4. Total elongation as a function of
hydrogen concentration for V-4Cr-4Ti alloy
tested at room temperature

REFERENCES

1. K. Natesan and W. K. Soppet, "Tensile Properties of V-Cr-Ti Alloys after Exposure in Hydrogen-Containing Environments," Fusion Reactor Materials Progress Report for the Period Ending December 31, 1997, Argonne National Laboratory, DOE/ER-0313/23, p. 127, March 1998.

2. K. Natesan and W. K. Soppet, "Tensile Properties of V-Cr-Ti Alloys after Exposure in Hydrogen-Containing Environments," Fusion Reactor Materials Progress Report for the Period Ending June 30, 1998, Argonne National Laboratory, DOE/ER-0313/24, p. 68, September 1998.

TENSILE AND IMPACT PROPERTIES OF A V-3.1Ti-0.5Si ALLOY AFTER IRRADIATION IN THE FAST FLUX TEST FACILITY - H. Tsai, L. J. Nowicki, T. S. Bray, M. C. Billone, and D. L. Smith (Argonne National Laboratory)

SUMMARY

Tensile and Charpy specimens made of alloy BL-42 (with a nominal composition of V-3.1Ti-0.5Si) were irradiated in the Fast Flux Test Facility (FFTF) in Cycle 11 at 520 and 600°C to up to 51 dpa. Some of these specimens were retrieved from storage and tested in this reporting period. The interest of this material stems from recent findings that show binary alloys of this class appear to exhibit lower susceptibility to radiation-induced embrittlement than other V-base alloys in low-temperature irradiation (<≈400°C). The results of our tests show the BL-42 material to have good tensile properties and fair impact properties after the 520-600°C irradiation and that alloys of this class may warrant further development for improved low-temperature performance.

OBJECTIVE

The objective of this task was to determine the tensile and impact properties of the BL-42 specimens (with a nominal composition of V-3.1Ti-0.5Si) irradiated in FFTF at 520 and 600°C to 41-51 dpa.

BACKGROUND

In the last several years, significant efforts have been devoted to the development of ternary alloy V-4Cr-4Ti for fusion reactor applications. Prior to that, binary V-(3-5)Ti alloys with Si additions up to ≈1% were also considered as promising candidates. The V-4Cr-4Ti alloys were selected as the reference because of their overall superior performance in terms of strength, ductility, and most importantly, radiation resistance determined in irradiation tests in temperatures >≈400°C. Recent irradiation experiments at temperatures <≈400°C, however, show these alloys may be susceptible to significant low-temperature embrittlement[1,2,3]. In the same low-temperature irradiation experiments, the binary V-Ti alloys appear to exhibit less irradiation hardening and embrittlement than the V-4Cr-4Ti alloys[4,5]. For this reason, it was decided to retrieve the BL-42 V-3.1Ti-0.5Si specimens from storage and to complete their postirradiation evaluation.

EXPERIMENTAL PROCEDURE

Test Specimens

BL-42 was a small laboratory heat produced by Teledyne Wah Chang. The composition of the material is shown in Table 1.

Table 1. Composition of the BL-42 alloy

Concentration (wt.%)		Interstitial Concentration (ppm)			
Ti	Fe	O	N	C	Si
3.1	0.02	580	190	140	5400

The tensile specimens were of the SS-3 design, which is the de facto standard for the fusion materials program. The nominal dimensions of the gauge section were 0.76 (t) x 1.52 (w) x 7.6 (l) mm, and the longitudinal direction of the gauge was parallel to the final rolling direction of the plate.

The Charpy impact specimens were 1/3-size, 3.3 mm (t) x 3.3 mm (w) x 25.4 mm (l), with a 45°, 0.61-mm-deep, 0.08-mm-root radius machined notch. The notch orientation (i.e., crack propagation direction) was perpendicular to the final rolling direction and into the thickness of the plate. This Charpy specimen design is also a de facto standard and has been used extensively in previous fusion materials tests.

The test specimens were irradiated in Li-bonded capsules in the Materials Open Test Assembly (MOTA) of FFTF in Cycle 11. The irradiation conditions of the specimens are summarized in Table 2.

No hydrogen-outgassing (e.g., at 400°C for one hour) was performed on these specimens prior to the mechanical testing.

Table 2. Irradiation conditions of the BL-42 test specimens in FFTF Cycle 11

Specimen Type	Specimen No.	MOTA Capsule No.	Irradiation Temp. (°C)	dpa
SS-3 Tensile	143	V549	520	41
	144	V552	520	46
	146	V653	600	47
	147	V656	600	51
	148	V656	600	51
	149	V657	600	51
1/3-Size Charpy	152	V656	600	51
	153	V656	600	51
	154	V657	600	51
	155	V657	600	51

Test Procedure

Only one tensile test (with specimen 149) was conducted at room temperature; all others were conducted at the specimens' respective irradiation temperatures. The room-temperature test was conducted in air; the elevated-temperature tests were conducted in high-purity flowing argon with the specimens protected by a Ti-foil impurity getter. The tests were performed with an Instron machine without an extensometer attached to the specimen gauge. Extensions due to slack in the grip and deformation of the load frame were subtracted from the crosshead displacement to obtain the correct gauge-section extension. The strain rate for all tests was 1.09 x 10^{-3}/s, which is the reference used in many previous fusion materials tensile tests.

All Charpy impact tests were conducted in air with a Dynatup drop-weight tester. Specimen temperature during the impact test was measured with a thermocouple spot-welded to the end of the specimen. For the above-ambient-temperature tests, a hot-air blower was used to provide the heating. For the below-room-temperature tests, liquid nitrogen was used to chill the specimens.

RESULTS AND DISCUSSION

Tensile Tests

The results of the tensile tests are summarized in Table 3. A representative load/displacement

curve (for specimen 146) is shown in Fig. 1. Reduction-in-area measurements and fractographic examinations have not yet been conducted.

Table 3. Tensile properties of BL-42 specimens after the FFTF irradiation

Spec. No.	dpa	Irradiation Temp. (°C)	Test Temp. (°C)	0.2% Yield Strength (MPa)	Ultimate Tensile Strength (MPa)	Uniform Elongation (%)	Total Elongation (%)
143	41	520	520	525	624	4.2	8.1
144	46	520	520	453	559	7.7	16.4
146	47	600	600	373	541	11.0	15.9
147	51	600	600	368	566	10.4	14.4
148	51	600	600	380	539	11.7	17.2
149	51	600	22	424	615	11.7	15.0
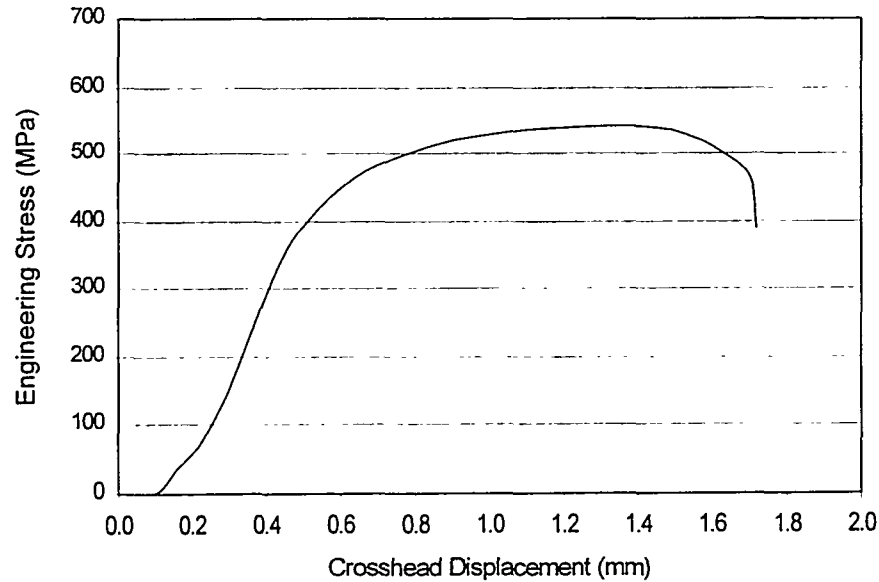
Fig. 1. Load-displacement curve for a 600°C tensile test (with specimen 146)

In all six tests, the specimens show only moderate irradiation hardening when compared with the nonirradiated yield and ultimate tensile strengths of ≈300 and 480 MPa, respectively, for this heat of material at 520°C[6]. As shown in Figs. 2 and 3, these measured strengths are fairly consistent with previously reported data for MOTA-irradiated specimens of several other vanadium-base alloys.

All BL-42 specimens tested displayed high ductility, with the uniform elongation ranging from ≈4 to 12% and total elongation from ≈8 to 17%.
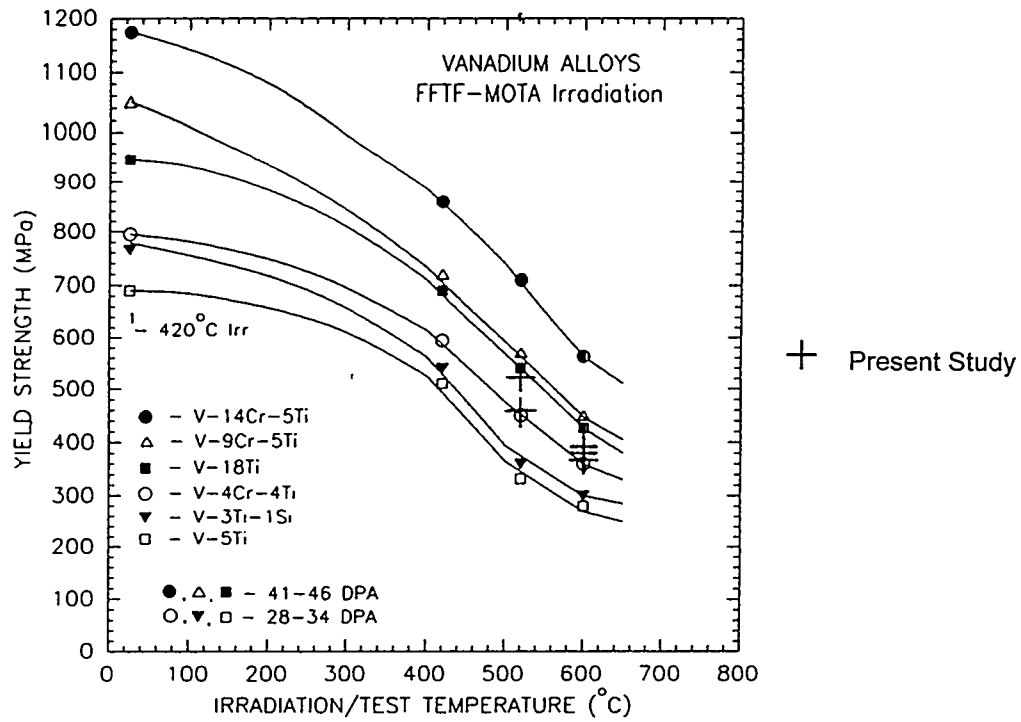
Fig. 2   Comparison of the yield strength from this work with the existing database.
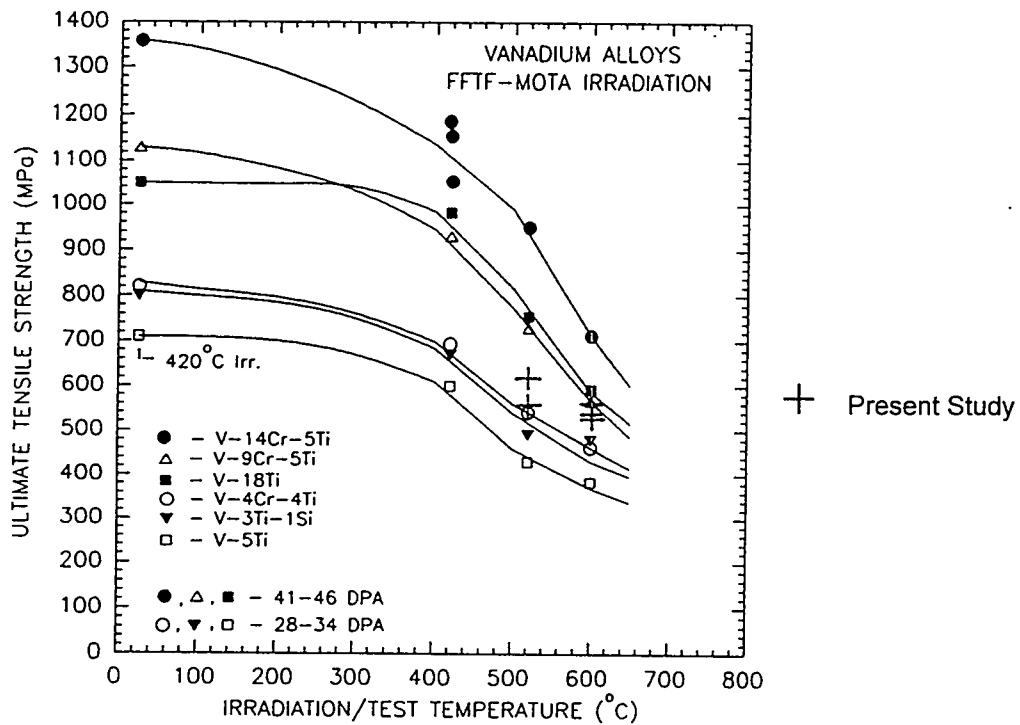
Fig. 3   Comparison of the ultimate tensile strength from this work with the existing database.

Charpy Impact Tests

The results of the Charpy tests are summarized in Table 4 and Fig. 4. There appears to be no clear ductile-to-brittle transition and the absorbed energies are relatively low (<5 J). SEM fractography showed the mode of fracture to be ductile tear at 23 and 100°C and a mixture of ductile tear and brittle cleavage at –50 and –195°C (Fig. 5). The mixed-mode fracture at low temperatures is consistent with the "non-zero" absorbed-energy measurement at –195°C and at least partially explains the lack of marked ductile-to-brittle transition in the absorbed-energy curve. Further evaluation is necessary to fully assess the fracture behavior of these specimens. (Ref. 7 reported an absorbed energy of 5.5 J at room temperature from a test of a specimen from this group. That data point, also shown in Fig. 4, is essentially consistent with the present work.)

Table 4. Charpy impact properties of BL-42 specimens after the FFTF irradiation

Spec. No.	dpa	Irradiation Temp. (°C)	Test Temp. (°C)	Absorbed Energy (J)
152	51	600	23	4.6
153	51	600	100·	3.9
154	51	600	-50	3.6
155	51	600	-195	2.2
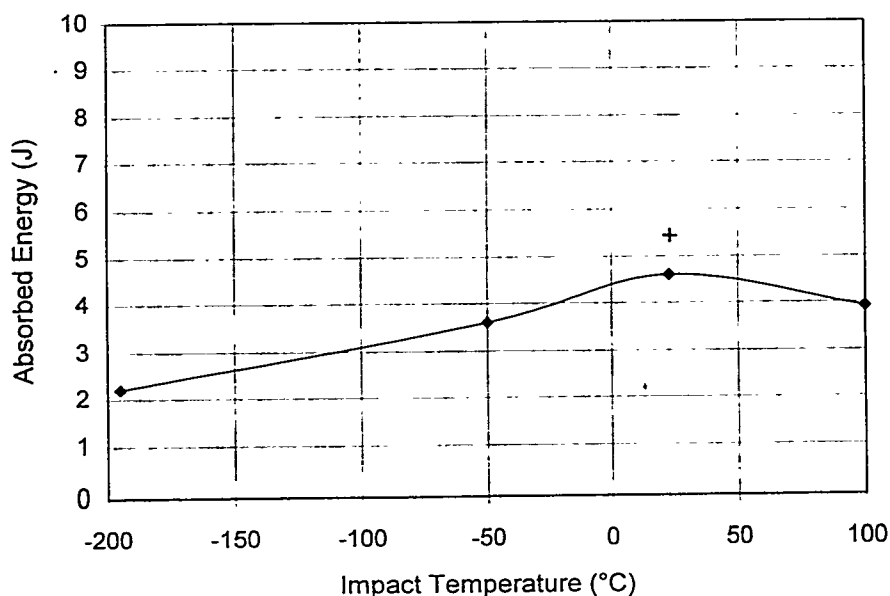
Fig. 4. Charpy impact properties of BL-42 specimens after the FFTF irradiation. "+" denotes the data point reported in Ref. 7.
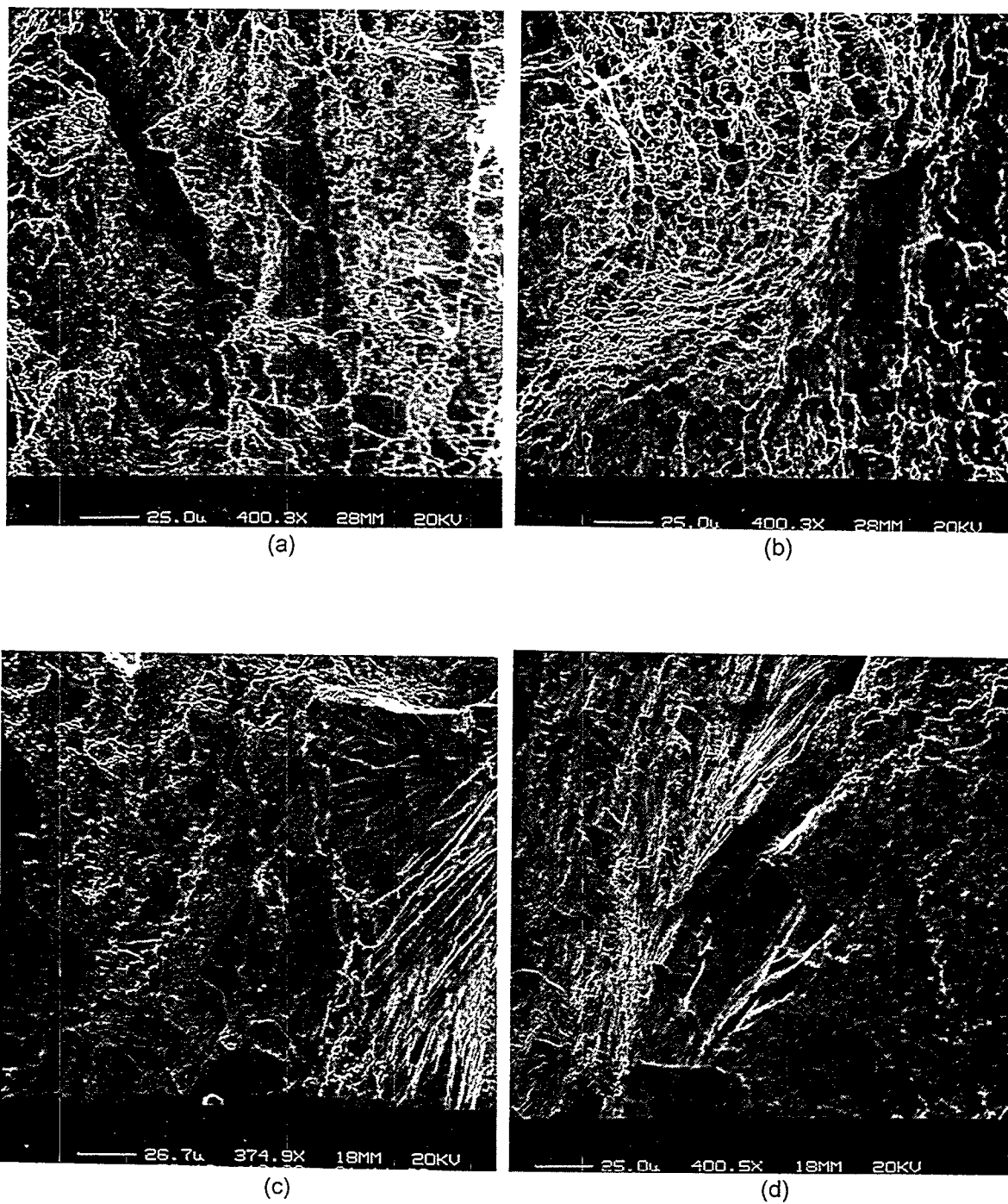
Fig. 5   SEM fractography of the BL-42 Charpy specimens showing ductile tear in the 23°C (a) and 100°C (b) specimens and mixed ductile tear and brittle cleavage in the –50°C (c) and –195°C (d) specimens.

FUTURE ACTIVITIES

Fractographic examination of the test specimens will be completed to determine the areal reduction in the tensile specimens and to further elucidate the fracture behavior of the Charpy specimens.

REFERENCES

1. H. M. Chung, H. Tsai, L. Nowicki, and D. L. Smith, Fusion Materials Semiannual Progress Report, DOE/ER-0313/22, June 1997, pp. 18-21.
2. D. J. Alexander et al., "Effects of Irradiation at Low Temperature on V-4Cr-4Ti," Fusion Materials Semiannual Progress Report for Period Ending June 30, 1996, DOE/ER-0313/20, pp.87-95.
3. H. Tsai, J. Gazda, L. J. Nowicki, M. C. Billone, and D. L. Smith, Fusion Materials Semiannual Progress Report for Period Ending June 30, 1998, DOE/ER-0313/24, pp.15-19.
4. H. M. Chung, H. Tsai, L. Nowicki, and D. L. Smith, Fusion Materials Semiannual Progress Report, DOE/ER-0313/22, June 1997, pp. 18-21.
5. H. M. Chung, H. Tsai, L. Nowicki, and D. L. Smith, Fusion Materials Semiannual Progress Report, DOE/ER-0313/22, June 1997, pp. 33-38.
6. M. C. Billone, Fusion Materials Semiannual Progress Report, DOE/ER-0313/23, December 1997, pp. 3-61.
7. B. A. Loomis, ANL memorandum to D. L. Smith, "Vanadium and Vanadium-Base Alloys – Summary of Current and Previous Irradiations, November 23, 1992.

EFFECT OF IRRADIATION ON TOUGHNESS-TEMPERATURE CURVES IN

V-4CR-4TI — E. Donahue, G. R. Odette, G. E. Lucas, and J. W. Sheckherd (University of California, Santa Barbara); A. Rowcliffe (Oak Ridge National Lab)

OBJECTIVE

The objective of this work is to explore the variation of effective fracture toughness with test temperature in V-based alloys, and to assess the effect of neutron irradiation on this toughness-temperature relationship.

SUMMARY

Small, pre-cracked, 1/3-sized Charpy specimens of V-4Cr-4Ti were irradiated to a dose of 0.5 dpa at a temperature of 200 $\pm$ 8 °C. The specimens were tested in three point bending under static conditions to measure effective toughness-temperature curves. Fracture processes were examined by using confocal microscopy and fracture reconstruction methods. It was found that this alloy undergoes normal stress-controlled cleavage transition below a characteristic temperature, and that irradiation hardening increased the transition temperature significantly. Shifts in the transition temperature imposed by irradiation hardening can be reasonably predicted by a simple equivalent yield stress model.

PROGRESS AND STATUS

Introduction

Vanadium alloys are attractive candidates for structural applications in fusion reactors because of their low neutron activation, favorable thermal properties and potential for radiation stability. However, a potential problem that these alloys share with other body centered cubic (bcc) metals is a transition in fracture mode from ductile to brittle cleavage transition below a temperature (T_t), with an attendant loss in fracture toughness. Moreover, T_t may be significantly elevated as a consequence of irradiation. Preliminary studies using nonstandard tests — including one-third-size Charpy V-notch and disc bend specimens — have suggested that alloy compositions in the range V-4Cr-4Ti are highly resistant to embrittlement, with T_t in the vicinity of or below -196°C [1-5].

However, T_t depends on the details of the test procedure[6], and it cannot be used to quantify structural stress and strain limits; hence, it is neither a fundamental material property nor a useful engineering parameter. A more useful quantitative measure of fracture resistance is the effective toughness as a function of temperature, $K_e(T)$; however, this too depends on variables such as size scales and flaw geometry, loading rate, irradiation and other sources of embrittlement (e.g., hydrogen). As discussed in detail elsewhere[7], it may be possible to develop a method to predict the stress and strain limits of flawed fusion structures using a $K_e(T)$ curve adjusted on an absolute temperature scale using measured shifts to account for variables such as irradiation, constraint, and strain rate. Hence, in support of this approach the objective of this study was to examine the effects of irradiation on the $K_e(T)$ of a V-4Cr-4Ti alloy, and to evaluate these effects within the context of understanding the mechanisms of fracture and the effects of irradiation on these mechanisms in this alloy system.

Experiment

The study was carried out on a 3.8 mm thick plate in the 40% warm-rolled (400°C) condition taken from the program heat of V-4Cr-4Ti (#832665) [8]. Small, 1/3-sized Charpy V-notch specimens (3.33 x 3.33 x 25.4 mm) were electro-discharge machined from the plate. The machined specimens were annealed for 2h at 1000°C in a vacuum of better than 10^{-4} Pa to produce a re-crystallized microstructure and remove residual hydrogen. This series of heat treatments produces an average grain size of about 25 µm and a Vickers microhardness of about 150±5 [9,10]. Fatigue pre-cracking was carried out at a final $\Delta K \leq 15$ MPa√m to a nominal crack length (a) to specimen width (W) ratio of a/W ≈ 0.5. The specimens were encapsulated and irradiated in the High Flux Beam Reactor (HFBR) to a dose of 0.5 dpa at 200±8 °C.[14]

Following irradiation, the specimens were tested in three point bending over a temperature range from -60 to 20°C at approximate loading rates of 2.5 x 10^{-6} m/s. Load and load-line displacement were monitored during testing. In most cases a cleavage pop-in occurred after some permanent displacement. In most of the pop-in cases, the specimen was post-test fatigued to mark the final location of the pop-in. In all these cases K_e was determined from

$$K_e = \sqrt{J_{Ie}E'}\qquad(1)$$

where E' is the plane strain elastic modulus and J_{Ie} is the effective energy release rate determined from the area under the stress-displacement curve up to the load drop at cleavage pop-in. In several cases, a maximum load was exhibited without pop-in, and corresponding fractography indicated subcritical crack growth; in these cases K_e was also determined from equation (1), but J_{Ie} was determined from the area under the stress-displacement curve up to maximum load. Finally, the specimen tested at 20°C exhibited no pop-in and no maximum load before the test was terminated. In this case, J_{Ie} was taken from the total area under the stress-displacement curve.

Following testing, specimen fracture surfaces were examined by both scanning electron microscopy (SEM) and confocal microscopy (CM). As described elsewhere [11,12], the CM images can be used to obtain quantitative, three-dimensional topographs of conjugate fracture surfaces. These topographs can be used with fracture reconstruction (FR) methods to determine the sequence of events in front of the crack tip ultimately leading to macroscopic fracture (e.g., a macroscopic pop-in). The post-pop-in fatigue crack provides an additional reference to improve the alignment of images in FR. The CM/FR method also provides a measure of the critical crack tip opening δ* at the point of initiation of crack extension, from which an effective toughness $K_{e\delta}$ can be estimated by

$$K_{e\delta} = \sqrt{2\delta^* \sigma_y E'}\qquad(2)$$

where σ_y is the yield stress. [11,12]

Tensile tests were also performed on unirradiated and irradiated specimens of this same alloy and the results have been reported elsewhere. [13,14]

Results

Figure 1 summarizes the $K_e(T)$ data for the irradiated materials and compares these data to the trend line for the unirradiated material tested under similar conditions [13]. As can be seen, in the irradiated material K_e transitions from a lower shelf value of about 30 MPa√m to a value of about 160 MPa√m over a fairly narrow temperature range of about -30± 10°C. This is about 170°C higher than the unirradiated data trend. As noted previously, at room temperature the irradiated specimen did not fracture, but merely deformed to maximum displacement in the test fixture with a corresponding lower bound $K_{e,min}$ value of about 145 MPa√m. As shown in Figure 1, specimens primarily failed by cleavage pop-in in the lower shelf and transition regime, but in several instances the load-displacement curves showed a maximum load without a pop-in, indicative of subcritical crack growth. Indeed, both types of behavior were exhibited at the same test temperature, reflecting the statistical variability in fracture mode in the transition regime.

Figures 2-4 show representative results for selected test temperatures that corroborate some of the observations noted above. Each figure provides: 1) a load displacement trace from the mechanical test and the corresponding point on the $K_e(T)$ plot; 2) a side view and 3) a top view of the sequence of events ahead of the crack front determined from CM/FR; and 4) an SEM micrograph from a region of interest.

Figure 2 shows results for one of the tests at -30°C. In this case, the load displacement trace showed a load drop at maximum load, with a K_e of 160 MPa√m. The SEM fractography showed the formation of a cleavage pop-in corresponding to this load drop. The CM/FR images show side views of the fracture surface overlaps (shaded regions being separated) and top views of the crack plane (again shaded regions being separated and white intact) at several values of δ.
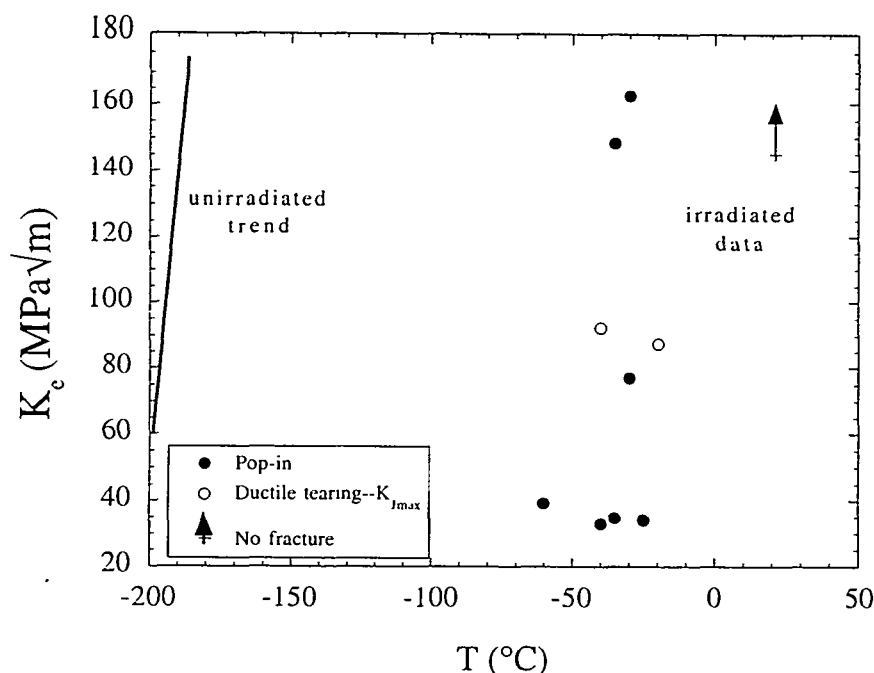
Figure 1   Variation of K_e with test temperature for irradiated and unirradiated V-4Cr-4Ti.
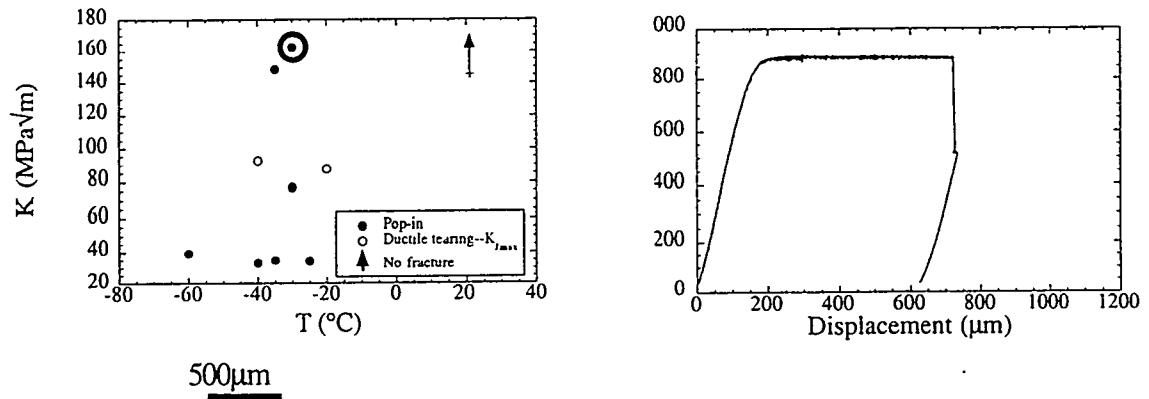
Figure 2   Load-displacement curve, CM/FR results and representive SEM micrograph for a specimen tested at -30°C.

These show that the pop-in was preceded by the formation of microcleavage cracks ahead of the crack tip; these microcracks accumulate in a single process zone and coalesce to form the pop-in at a δ^* of about 125 μm corresponding to a $K_{e\delta}$ of 168 MPa$\sqrt{m}$. SEM in the pop-in region shows well-formed cleavage facets with some out-of-plane fissures and little or no evidence of inter-granular fracture.

Figure 3 shows results for a second test at -30°C. In this case, the load displacement trace shows two load drops, the first occurring before maximum load after substantially less displacement than that shown in Figure 2; the corresponding K_e was about 75 MPa$\sqrt{m}$. Again the CM/FR showed the initial formation of microcleavage cracks ahead of the crack tip, which accumulate in approximately three process zones; microcrack coalescence to form the pop-in occurred at a δ^* of about 30 μm corresponding to a $K_{e\delta}$ of 82 MPa$\sqrt{m}$. The SEM micrograph shows the well formed interface between the cleavage facets in the pop-in region and the post-pop-in fatigue crack.Figure 4 shows results for the test at -20°C. In this case, the load displacement trace exhibited a maximum, indicative of subcritical crack growth, and the test was terminated after about 1000μm of displacement; the corresponding $K_{e,max}$ obtained at the maximum load was about 90 MPa$\sqrt{m}$. The SEM and CM/FR indeed showed two regions of subcritical crack growth at the flanks of the pre-crack front, with crack initiation occurring at a δ^* of about 35 μm corresponding to a $K_{e\delta}$ of 87 MPa$\sqrt{m}$. The SEM micrograph taken from one of these regions shows discrete steps along the crack front, perhaps indicative of localized plastic flow.

As shown in Figure 5, the values of K_e measured from the load-displacement data were in very good agreement with the values of $K_{e\delta}$ determined from CM/FR.

Discussion

Cleavage fracture is believed to occur in this alloy system (as well as other bcc systems) when the tensile stresses ahead of a crack tip exceed some critical value (σ^*) over a sufficiently large area (A^*) [11,12,15]. Hence, σ^*/A^* are local measures of toughness that are intrinsic to the material and its microstructure. Since the peak stresses σ_t ahead of a crack tip are some multiple M of the yield stress, where M reflects the degree of constraint imposed by the specimen size and crack geometry, the onset of cleavage requires sufficiently low temperatures for $\sigma_t = M\sigma_y$ to exceed σ^*. Hence, increasing σ_y (e.g., by irradiation hardening or strain rate) results in the onset of cleavage at higher temperatures; and decreasing M (for instance by decreasing specimen size or notch/crack acuity decreases T_t. Indeed, the previously reported low transition temperatures in the V-4Cr-4Ti system are consistent with a relatively low σ_y in the unirradiated material combined with specimen sizes and geometries with low M.

If — as is the case for bcc steel alloys [11,15] — σ^* and A^* are relatively insensitive to temperature, strain rate and the fine scale damage imposed by irradiation, a simple way to model shifts in a reference transition temperature (ΔT_r) due to irradiation hardening (or loading rate) is to define transition temperatures at an *equivalent* reference yield stress $\sigma_{y,ref}$. The appropriate reference condition is near the highest temperature of elastic cleavage fracture, here about $K_e = 60$ MPa$\sqrt{m}$. Hence, ΔT_r can be modeled from a knowledge of the dependence of σ_y on temperature, irradiation and strain rate. For instance, assuming that the overall constitutive relation $\sigma(\varepsilon)$ for different temperatures, strain rates and levels of irradiation hardening ($\Delta\sigma_i$) are similar if the σ_y are the same, and that $\Delta\sigma_i$ is independent of temperature and strain rate, the effects of irradiation on shift can be predicted from $\Delta\sigma_i$ by an equivalent yield stress model (EYSM) as follows.
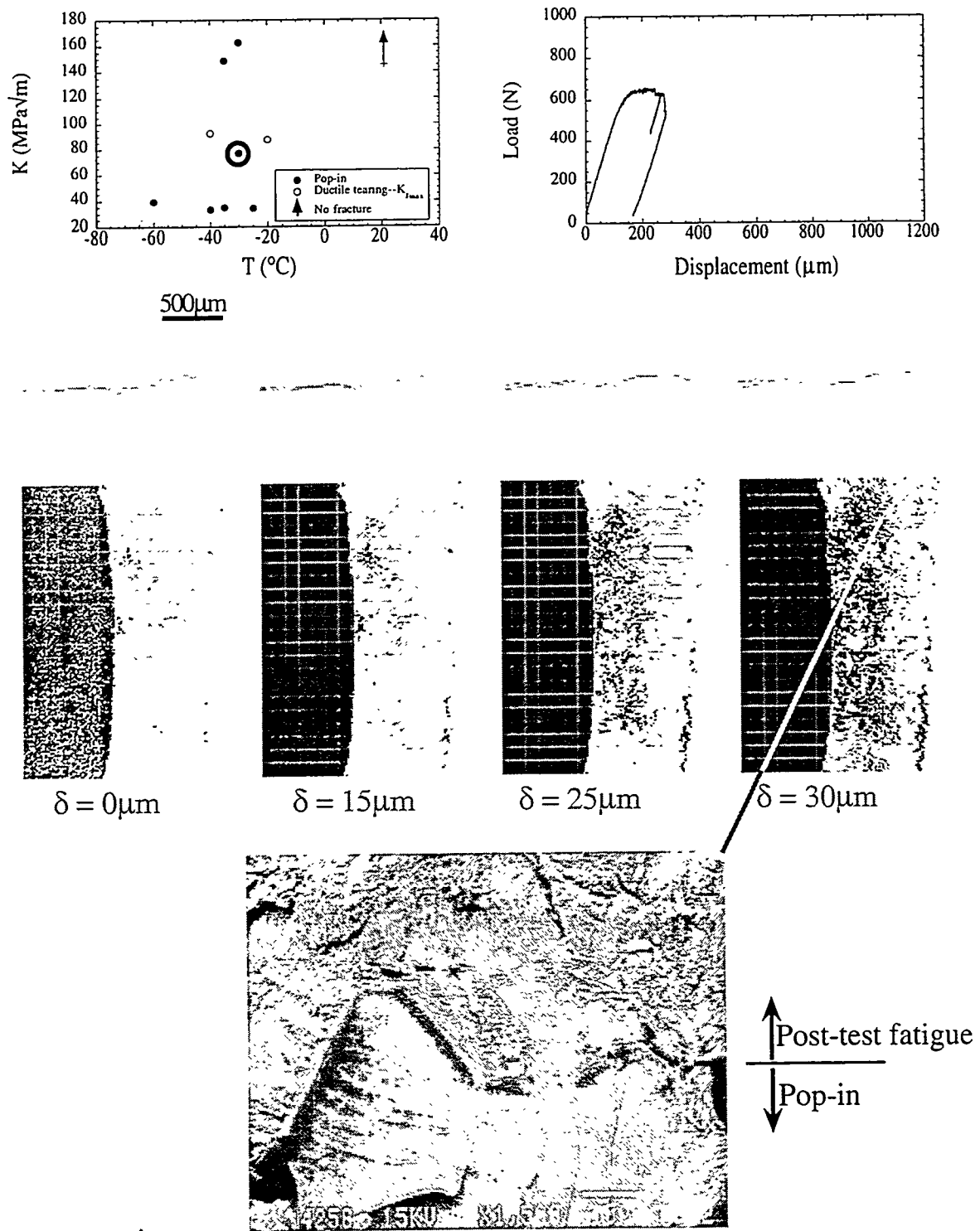
Figure 3   Load-displacement curve, CM/FR results and representive SEM micrograph for a second specimen tested at -30°C.
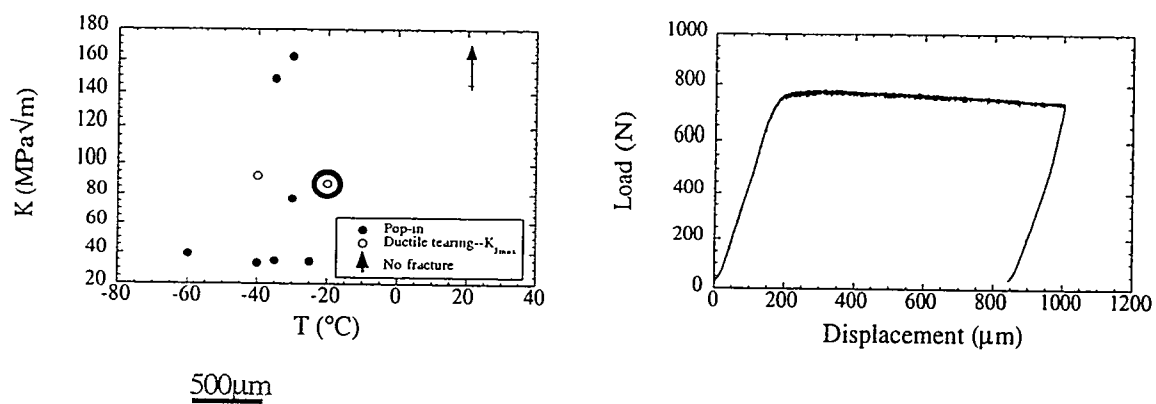
Figure 4   Load-displacement curve, CM/FR results and representive SEM micrograph for a specimen tested at -20°C.
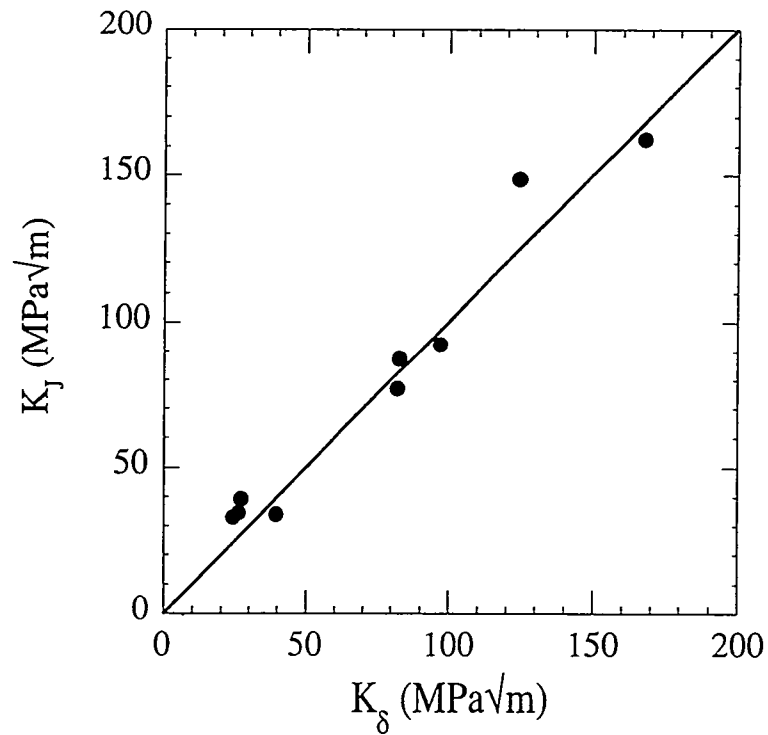
Figure 5   Comparison of K_e determined from load-displacement data with $K_{e\delta}$ determined from CM/FR.ith
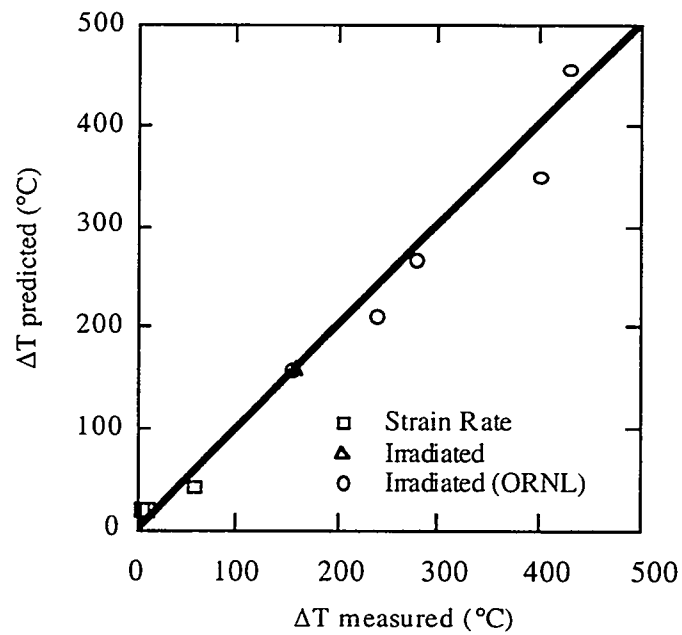
Figure 6   Comparison of measured transition temperature shifts and shifts predicted by the equivalent yield stress model.

$$\Delta T_r = T_{ri} - T_{ru}, \text{where } \sigma_{yi}(T_{ri}) = \sigma_{yu}(T_{ru}) + \Delta\sigma_i \qquad (3)$$

and the "u" and "i" subscripts refer to the unirradiated and irradiated condition, respectively.

Using the irradiation hardening results obtained for this alloy from previous work [16], estimates of ΔT_r were obtained from equation (3); and these are compared to values measured in this study in Figure 6. Also shown for comparison are the measured and predicted values of ΔT_r for other irradiation conditions of the same alloy reported by Alexander and Snead [16], and for the effects of strain rate on shift determined from static and dynamic data previously reported for this alloy [13]. In the latter case, the effects of strain rate can be predicted from the EYSM by

$$\Delta T_r = T_{rd} - T_{rs}, \text{ where } \sigma_y(\dot\varepsilon_s, T_{rs}) = \sigma_y(\dot\varepsilon_d, T_{rd}) \qquad (4)$$

and the "d" and "s" subscripts refer to dynamic and static conditions, respectively. In all cases the agreement between predicted and measured values is quite good, supporting both the assumptions and the physics underlying the EYSM.

SUMMARY AND CONCLUSIONS

In summary, the data and analysis presented here demonstrate that the program heat of V-4Cr-4Ti undergoes a "normal" stress-controlled ductile-to-cleavage transition, typical of bcc alloys. The temperature delineating this transition is shifted by irradiation hardening by an amount that is predictable by an equivalent yield stress model. This demonstrates the primary role of irradiation hardening in embrittlement of these alloys, and strongly contradicts alternate *ad hoc* explanations (e.g., impurity pickup).

ACKNOWLEDGMENTS

REFERENCES

1. Loomis, B.A., Smith, D. L., J. Nucl. Mater., Vols. 179-181, 1991, p 783.

2. Loomis, B.A., Smith, D. L., Garner, F. A., ibid., p 771.

3. Chung, H. and Smith, D. L., J. Nucl. Mater., Vols. 191-194, 1992, p 942.

4. Loomis, B. A., Nowicki, L. J., Gazda, J., Smith, D. L., , DOE/ER-0313/15, March 31, 1993, p 318.

5. Loomis, B. A., Chung, H. M., Nowicki, L. J., Smith, D. L., J. Nucl. Mater., Vols. 212-215, 1994, p 799.

6. Edsinger, K., Odette, G. R., Lucas, G. E., Sheckherd, J. W., J. Nucl. Mater. , Vols. 233-237 (1996) p. 342.

7. Odette, G. R., DOE/ER-0313/20, Department of Energy (1996) 283-298.

8. Chung, H. M., Tsai, H.-C., Smith, D. L., Peterson, R., Curtis, C., Wojcik, R., Kinney, C., DOE/ER-0313/17, March, 1994.

9. Grossbeck, M. L., Alexander, D. J., Henry, J. J., Eatherly, W. S., Gibson, L. T. DOE/ER-0313/18, March 1995.

10. Gubbi, A. N., Rowcliffe, A. F., Eatherly, W. S., ibid.

11. Edsinger, K., PhD Thesis, Department of Chemical Engineering, UCSB, 1996.

12. Edsinger, K., Odette, G. R., Lucas, G. E. Proceedings of the IEA International Symposium on Miniaturized Specimens for Testing Irradiated Materials, KFA Julich, 1995, p 150.

13. Odette, G. R., Donahue, E., Lucas, G. E., Sheckherd, J. W.,DOE/ER-0313/20, Department of Energy (1996) 11-29.

14. Alexander, D. J., Snead, L., Zinkle, S., Gubbi, A., Rowcliffe, A., Bloom, E., ibid. 87.

15. Odette, G. R., J. Nucl. Mater., Vols. 212-215, 1994, p 45.

16. Alexander, D. J., Snead. L., ASTM-STP-1325 (in press).

MICROSTRUCTURAL INHOMOGENEITIES IN V-4Cr-4Ti MECHANICAL PROPERTY SPECIMENS PREPARED FOR IRRADIATION EXPERIMENTS IN HFBR, BOR-60, AND HFIR – A. F. Rowcliffe and D. T. Hoelzer (Oak Ridge National Laboratory)

SUMMARY

Significant variations exist between the microstructures of the various batches of mechanical property specimens prepared for the 500 kg heat of V-4Cr-4Ti. The development of banded grain structures is shown to be related to non-homogeneous distribution of Ti (OCN) particles (0.1-0.3 μ in diameter) that occur in some, but not all, plate products. Precipitation of Ti (OCN) will occur during the hot extrusion of the ingot in regions where the dislocation density is high and where the temperature falls below the Ti (OCN) solvus at 1125°C. Investigation of the potential benefits of a homogenizing treatment at 1150°C is recommended before proceeding with additional fabrication of plate products from the extruded bar.

PROGRESS AND STATUS

Introduction

Beginning at the end of 1994, a series of sheet and plate materials prepared from the 500 kg heat of V-4Cr-4Ti (heat No. 832665) were supplied to ORNL from Teledyne Wah-Chang, Albany (TWCA) via ANL. These batches have been used to prepare a series of SS-3 tensile specimens and one-third-size Charpy Vee-Notch (CVN) specimens for unirradiated measurements and for irradiated testing.

Variations in the processing and manufacturing conditions have resulted in small differences in final microstructure between various batches and recently it has been observed [1] that there are significant differences in fracture behavior between different batches of CVN specimens. This report: (a) summarizes the fabrication histories of the various starting materials and specimens; (b) characterizes the microstructural differences between the various batches; and (c) seeks to understand the origins of the observed microstructural inhomogeneities.

RESULTS

Table 1 summarizes the identification codes, dimensions, and metallurgical condition of plate and sheet stock supplied by TWCA via ANL. Table 2 summarizes the specimen identification codes used by ORNL researchers in various irradiation experiments. The SS-3 specimens were prepared in four separate campaigns from three different initial batches of plate-stock, as described in Table 3. The CVN specimens were prepared in four separate campaigns from three different plates, as described in Table 4.

SS-3 Tensile Specimens

A summary of physical and mechanical properties of the four batches of SS-3 tensiles is shown in Table 5 (specimens labeled RC or RD are from the same batch of material). Although the tensile specimens came from different plates and were subjected to different final processing steps, significant differences in hardness and resistivity could not be detected. However, there were some small but significant differences in RT yield strength; the ST and RC/D series being stronger by 20 to 25 MPa than the WH and WE series tensile specimens.

Table 1: Identification of Plate and Sheet Stock of V-4Cr-4Ti (832665)

ANL I.D.	Date Received	Dimensions (cm)	Thickness (cm)	TWCA Supplied Condition	ORNL I.D.	Experimental Use
Plate B	8/94	9.5 × 10	0.38	Ann. 1050°C/2h	L150	WA series CVN
Plate A	9/94	18.5 × 23.5	0.38	Ann. 1050°C/2h	M150	WB series CVN
Plate D	9/94	24 × 26.5	0.10	~50% CW	N40	WE, WH series SS-3
Plate C	9/94	16.5 × 33	0.64	Ann. 1050°C/2h	P250	Welding
Plate A Ann.	5/95	14 × 30	0.64	Ann. 1050°C/2h	Q250	QC series CVN
–	10/95	17 × 18	0.64	Ann. 1050°C/2h	–	Welding
–	10/95	19.5 × 20	0.10	~50% CW	–	–
–	2/96	23 × 39	0.64	Ann. 1000°C/1h	R250A	Welding
–	2/96	23 × 39	0.64	~50% CW	R250	RC series CVN, SS-3
–	2/96	23 × 39	0.38	~50% CW	T150	–
–	2/96	24 × 36.5	0.10	~50% CW	S40	ST series SS-3
Plate DD	8/98	20 × 39	0.38	~50% CW	V150	–
Plate D	8/98	12.5 × 27	0.64	~50% CW	V250	–

43

Table 2. Identification Codes for V-4Cr-4Ti (832665) Irradiation Specimens

Irradiation Experiment	I.D. Codes SS-3	I.D. Codes CVN	I.D. Codes DCT
HFBR-V1	WH 01-03	WB 83-151	–
HFBR-V2	WH 08-14	WB 78-159	–
HFBR-V3	WH 23-25 ST 12-44	QC 95-199	–
HFBR-V4	ST 53-75	QC 113-202	–
ATR-A1	–	QC 01-10	QA 05-06
BOR-60 (Fusion 1)	WE 01-12 WE 21-25	WB 32-77	WC 01-18
HFIR-RB-10J	RC 06-47	RC 11-97	RC 01-03

44

Table 3. Processing Histories for SS-3 Tensile Specimens

ST Series	WH Series	WE Series	RC/D Series
Plate S40 1.02 mm thick ~50% CR ↓ Machined specimens ↓ Vac. ann. 1000°C, 2h	Plate N40 1.02 mm thick ~50% CR ↓ Machined specimens ↓ Vac. ann. 1000°C, 2h	Plate N40 1.02 mm thick ~50% CR ↓ Vac. ann. 950°C, 2h ↓ 50% CR to 0.76 mm thick ↓ Machined specimens ↓ Vac. ann. 1000 or 1050°C, 2h	Plate R250 ↓ Vac. ann. 1000°C, 2h ↓ 40% cross-rolled to 3.8 mm thick in 10 passes ↓ ORNL I.D.: R150 ↓ Machined specimens ↓ Vac. ann. 1000°C, 2h

Table 4. Processing Histories for CVN Specimens

WB Series	QC (01-40)	QC (41-210)	RC Series
Plate M150 3.8 mm thick 1050°C, 2h (TWCA) ↓ Machined specimens (LT orientation) ↓ Vac. ann. 1000°C, 2h	Plate Q250 6.4 mm thick 1050°C, 2h (TWCA) ↓ Machined specimens (LT orientation) ↓ Vac. ann. 1000°C, 2h	Plate Q250 6.4 mm thick 1050°C, 2h (TWCA) ↓ 40% cross-rolled to 3.8 mm thick in 10 passes ↓ Machined specimens (LT orientation) ↓ Vac. ann. 1000°C, 2h	Plate R250 6.4 mm thick 50% CR (TWCA) ↓ Vac. ann. 1000°C, 2h ↓ 40% cross-rolled to 3.8 mm thick in 10 passes ↓ Machined specimens (LT orientation ↓ Vac. ann. 1000°C, 2h

*LT orientation in each case is with respect to the cold-rolling direction of the TWCA plate.

Table 5. Average Physical and Mechanical Properties of SS-3 Specimens Following Final Anneal (1000°C, 2h)

SS-3 Series	Grain Size ±2 μm	Hardness ±5 VHN	RT Yield ±10 MPa	Resistivity ±0.6 n Ω-m
ST	15	140	356	283.7
WH	26	134	330	280.3
WE	12/40 banded	141	334	281.4
RC/D	23	137	356	281.9

There are significant differences in grain size and in microstructural homogeneity between the batches. The ST and WH series of tensiles were machined directly from the cold-worked plates S40 and N40, followed by final annealing at 1000°C/2h. The microstructure of both batches are fairly homogeneous, with grains slightly elongated in the rolling direction (Fig. 1a and b). The average grain size of the WH series (~26 μ) is significantly larger than that of the ST series (~15 μ), probably as a result of differing final levels of CW in the two plates. On the other hand, the microstructure of the WE series is relatively inhomogeneous (Fig. 2a, b, and c), with bands of coarse grains (~40 μ dia) interspersed with regions of finer grains (15-20 μ dia). The finer grains are associated with bands of Ti (OCN) particles aligned along the rolling direction of the plate. In contrast, the microstructure of the RC/D series (Fig. 1c) is uniform, with a more uniaxed grain structure than the other three series, presumably as a result of the 40% cross-rolling treatment prior to the final anneal (Table 3).

CVN Specimens

The CVN specimens used in the HFBR, BOR-60, ATR, and HFIR irradiation experiments were fabricated in four campaigns, as shown in Table 4. In each campaign, the specimens were machined in an L-T orientation with respect to the rolling direction marked on the plate material received from TWCA. The WB series and the WC (01-40) specimens were machined directly from the TWCA annealed plate. On the other hand, the CVN specimens with ID numbers QC (41-20) and the RC series were machined from plates which had been 40% cold-rolled at ORNL in a direction perpendicular to the TWCA rolling direction.

QC Series

Both sets of specimens (01-40) and (41-210) originated from plate Q250 and both sets are characterized by dispersions of Ti (OCN) particles unevenly distributed in bands throughout the microstructure. The bands of particles are typically 200-300 μ wide in the transverse plate direction (T), around 20-100 μ thick in the short plate direction (S), and almost continuous in the longitudinal or rolling direction (L) [Figs. 3 and 4]. Within the precipitate rich regions, grain growth is restricted and a microstructure of alternating bands of coarse (30-50 μ dia) and fine (10-20 μ dia) grains develops during the final recrystallization treatment at 1000°C. The Ti (OCN) particles are believed to develop during the hot extrusion of the cast billet and to persist during subsequent cold rolling and annealing operations, as discussed below. The banded nature of the grain structure is less pronounced in the QC (41-210) series of specimens (Fig. 4) than in the QC (01-40) series (Fig. 3); as a result of differences in processing history (Table 4). Before machining the QC (41-210) series, the 6.4 mm plate was cold-rolled 40% in a direction perpendicular to the TWCA rolling direction. The cross-rolled material subsequently develops a more equiaxed and less banded grain structure during the final recrystallization treatment at 1000°C. The QC (01-40) series, on the other hand, were machined directly from the annealed plates supplied by TWCA, and the post-machining anneal at 1000°C only served to remove any hydrogen picked-up during machining and did not affect the microstructure.

WB Series

This set of specimens originated from the TWCA annealed plate M150 and the microstructure is very similar to that of the QC (01-40) specimens, with the characteristic banded grain distribution associated with a non-uniform dispersion of Ti (OCN) [Fig. 5]. The distribution of particles within a band is shown in Fib. 5b in an LS section and in Fig. 5c in an LT section.

1(a)

1(b)

1(c)
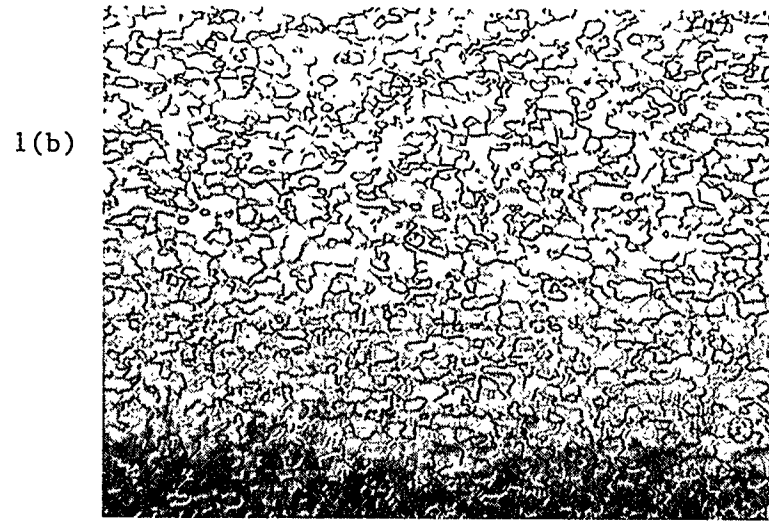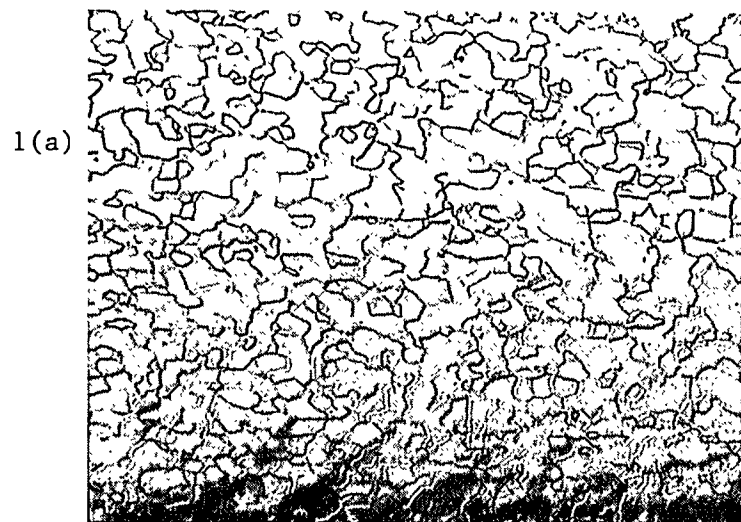
100X 50μm
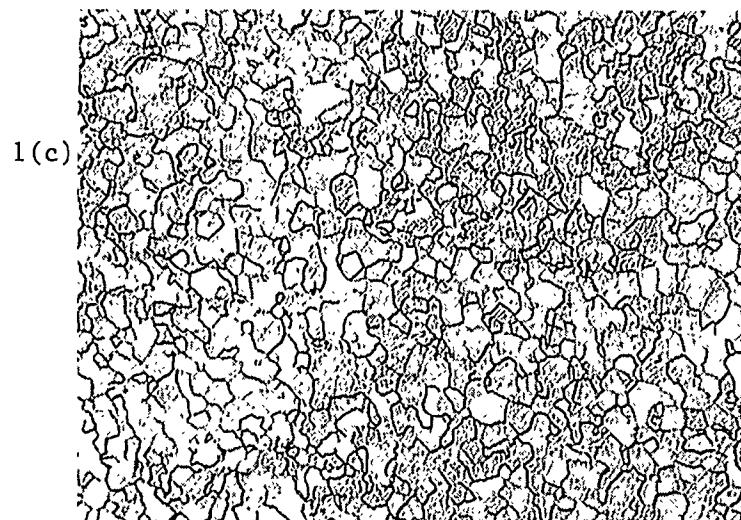
Fig. 1. Optical microstructures of 3 batches of SS-3 tensile specimens: (a) WH series, (b) ST series, and (c) RC/D series. The WH and ST series have a grain structure slightly elongated in the plate rolling direction; the RC/D series has an equi-axed grain structure.
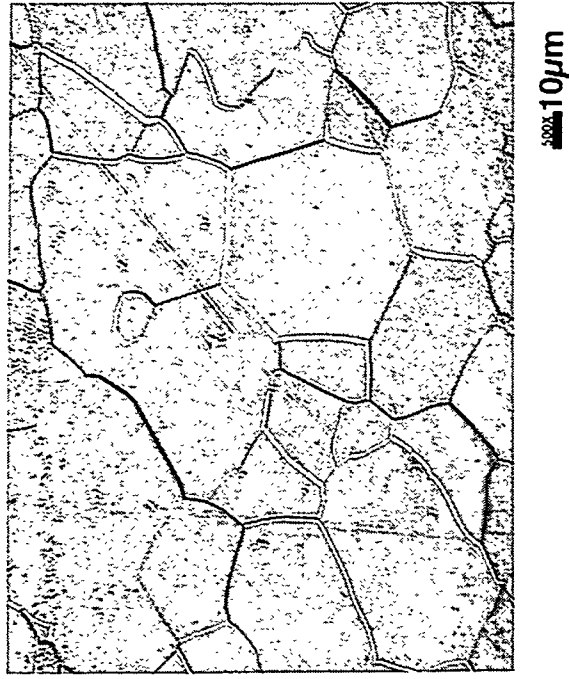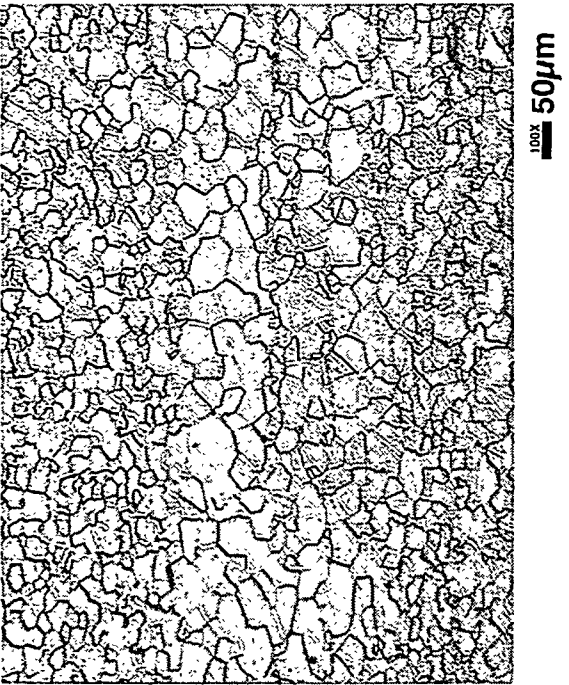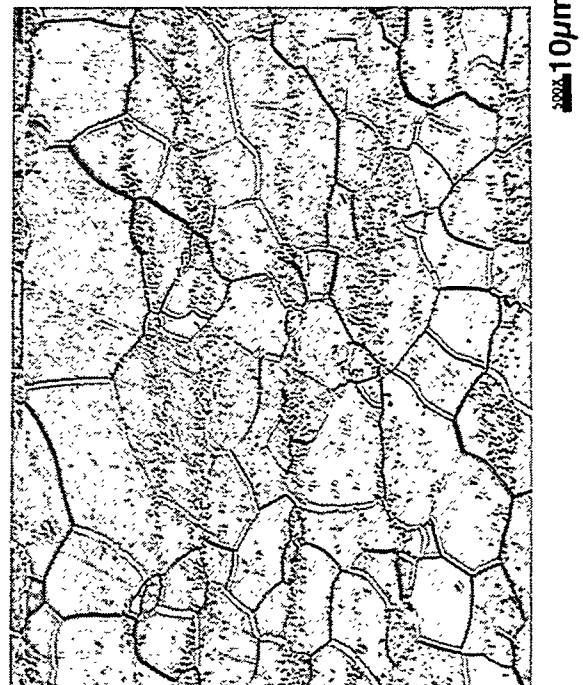
Fig. 2. Optical microstructure of the WE series SS-3 tensile specimens with an inhomogeneous banded distribution of grains (a). Areas with large grains are relatively precipitate-free (b); regions of finer grains are associated with bands of Ti (OCN) particles (c).

2(a)

2(b)

2(c)

50μm

10μm

10μm

51

3(b)

3(a)

3(c)
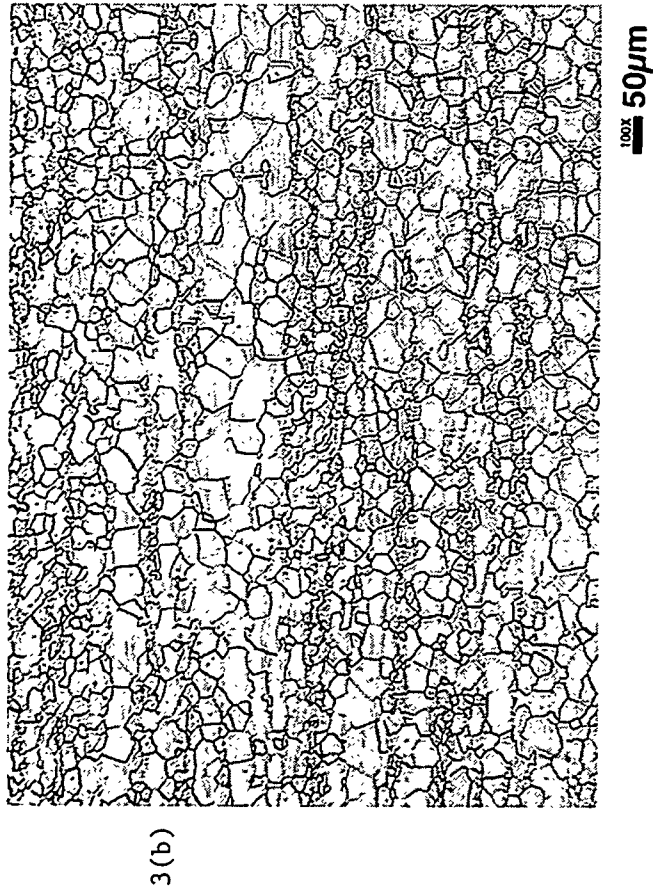
Fig. 3. Optical microstructure of CVN specimen from the QC (01-40) series showing banded grain structure associated with inhomogeneous distribution of Ti (OCN) particles: (a) LT orientation; (b) and (c) LS orientation.
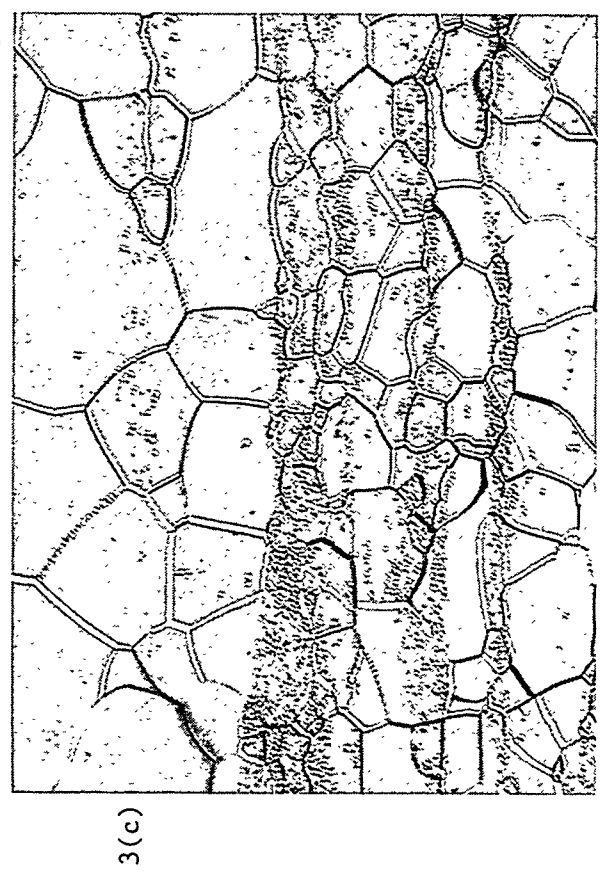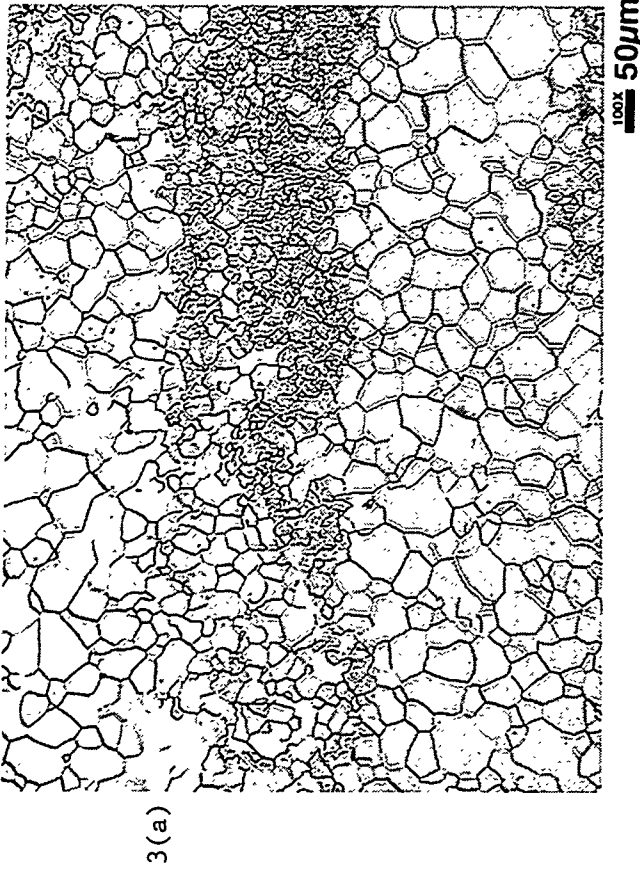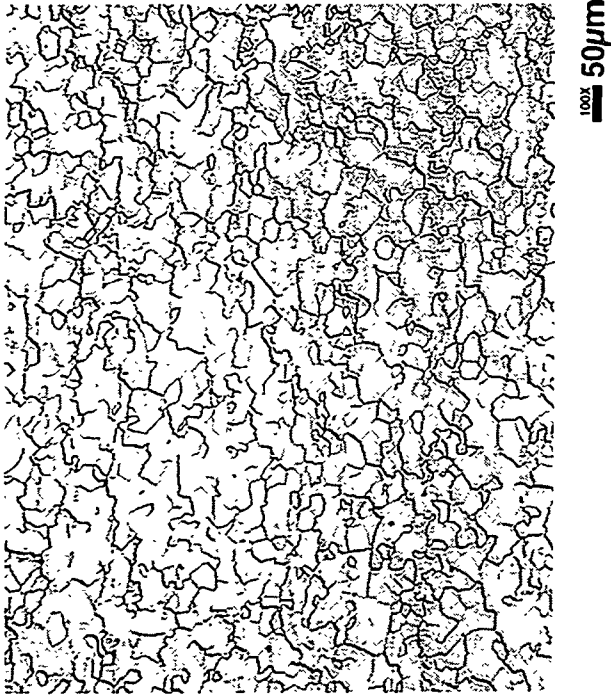
4(b)
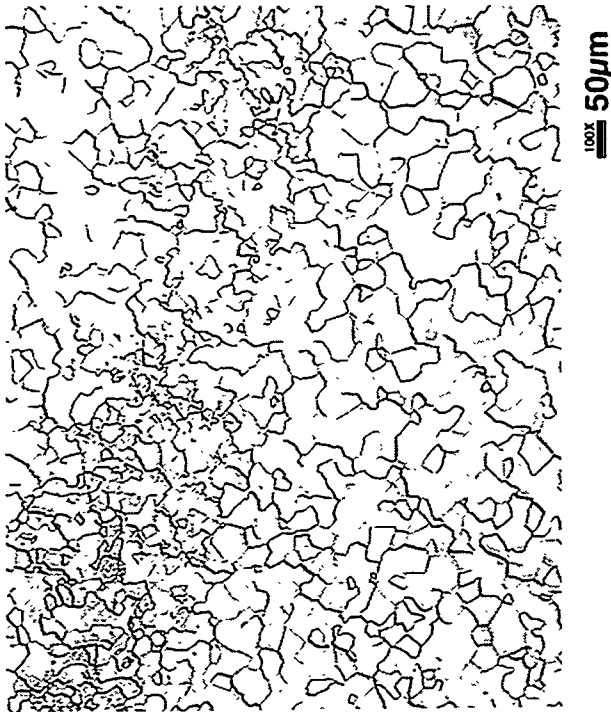
4(a)
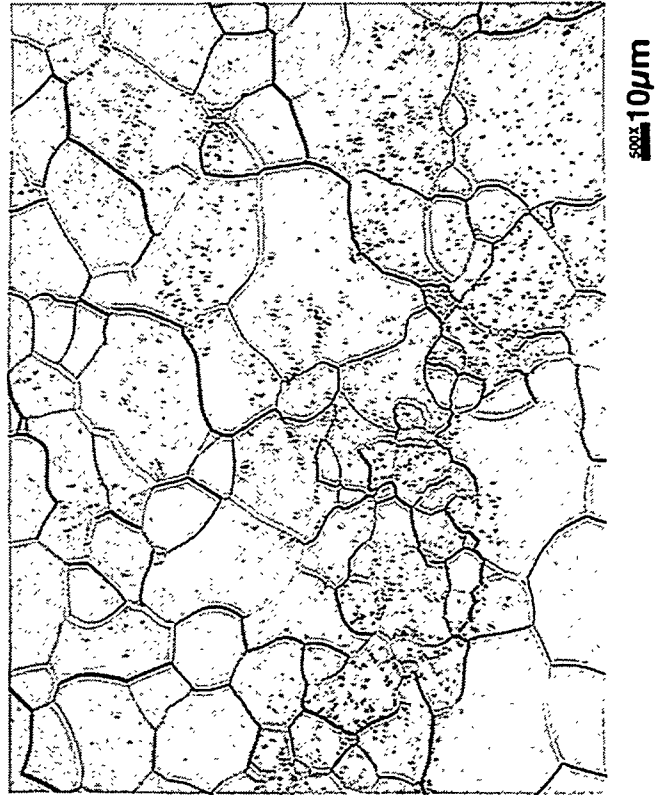
4(c)

Fig. 4. Optical microstructure of CVN specimen from the QC (41-210) series showing banded grain microstructure associated with inhomogeneous distribution of Ti (OCN) particles: (a) LT orientation; (b) and (c) LS orientation.

5 (b)

5 (a)

5 (c)

Fig. 5. Optical microstructure of CVN specimen from the WB series showing banded microstructure associated with inhomogeneous distribution of Ti (OCN) particles; (a) and (b) LS orientation; (c) LT orientation.
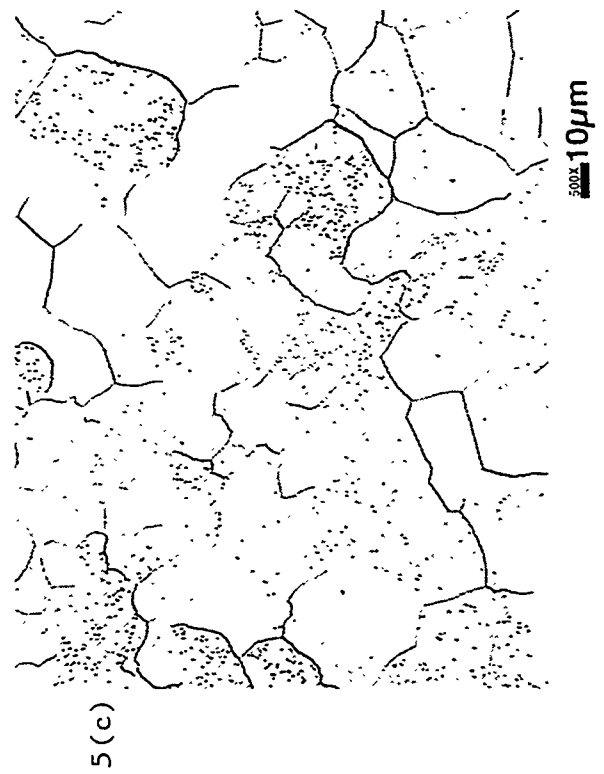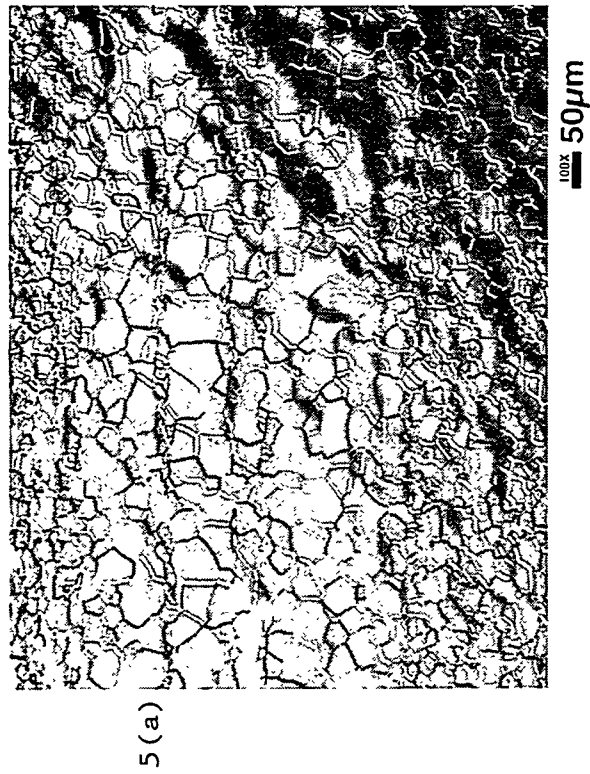
RC Series

The microstructure of these specimens, which originated from plate R250, is quite different from those of the other three sets that were derived from plates Q250 and M150. As shown in the low magnification micrographs in Fig. 6a and b, the grain structure is uniform (average grain size ~23 μ), with no evidence of the bands of fine grains that characterize the other sets. The TI (OCN) particles, while showing some tendency toward alignment in the rolling direction (Fig. 6c), are much more uniformly dispersed than in the other sets of specimens.

Precipitation of Ti (OCN)

In an accompanying article [2], it is shown that the globular phase referred to as Ti (OCN) is based upon the fcc TiC phase, which accommodates the other interstitials O and N. In an earlier progress report, Kurtz et al. [3] showed with optical microscopy that the volume fraction of globular particles in heat 832665 can be significantly reduced by heat treating at 1125°C for one hour. The coarse particles re-precipitated during a subsequent treatment at 890°C for two hours. This observation indicates that a solvus for the Ti (OCN) phase exists in the vicinity of 1125°C. As further confirmation of this solvus, a CVN specimen with an inhomogeneous banded microstructure (QC30) was heat treated at 1125°C for two hours in a vacuum of 5×10^{-7} torr. Dissolution of the Ti (OCN) occurred, accompanied by rapid grain growth in the regions between the original bands of particles. Within the banded regions, however, particle dissolution was not complete and the finer grain sizes still persisted. This is illustrated in Fig. 7. These micrographs of the specimen heat treated at 1125°C provide a graphic illustration of the inhomogeneous nature of the microstructures derived from plate Q250. To investigate the origins of this inhomogeneity, metallographic samples were prepared from sections taken from an as-extruded bar (6.3 x 6.3 x 50 cm). The extrusion of the 500 kg heat was carried out by sealing a semi-ingot in a stainless steel jacket and heating at 1150°C for three hours before extrusion [4].

The microstructure of the as-extruded material shown in Fig. 8 consists of an inhomogeneous mixture of small grains (20-60 μ), coarse grains (100-150 μ), and elongated deformed regions arranged in bands parallel to the extrusion direction. Examination of six different metallographic specimens failed to produce any evidence of Ti (OCN) precipitation, although the optical technique being used would not detect particles below about 0.1 μ.

During extrusion, non-homogeneous plastic flow patterns develop that depend upon the alloy flow properties, temperature distribution, die friction, and extrusion speed. The thermal situation is complex and temperatures are influenced by heat generation due to plastic deformation, internal shear, friction with the tooling, and the heat transfer within the billet and through the tooling. Typically, the emergent temperature increases with ram displacement, ram speed, and with reduction ratio. The temperature at the product surface is higher than at the product center.

During extrusion of the V-4Cr-4Ti, dynamic recovery and recrystallization occur to an extent that reflects the inhomogeneity of the deformation rate and temperature distribution. At the same time, precipitation of Ti (OCN) will occur whenever the temperature falls below the solvus at ~1125°C. Because of the incoherent nature of the TI (OCN) precipitate-matrix interface, precipitation will occur most rapidly in areas of high dislocation density. Precipitation of Ti (OCN) can occur (a) during hot deformation in regions where the temperature falls below ~1125°C, and, to a lesser extent, (b) in regions of high dislocation density during cool-down of the extrusion.

Because of the inhomogeneous nature of both the deformation and temperature distribution, it is very likely that precipitation of Ti (OCN) will also be distributed non-homogeneously. However, in

6(a)

^{100X} 50μm

6(b)

^{100X} 50μm

6(c)

^{500X} 10μm
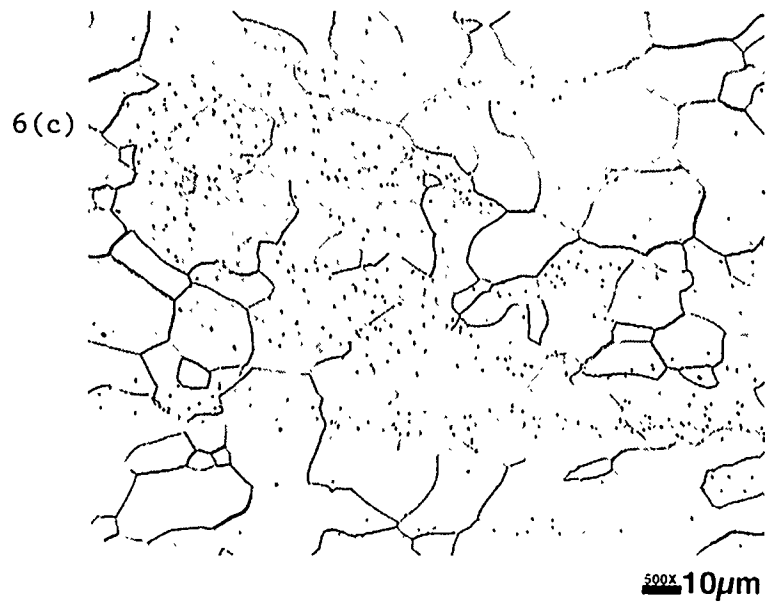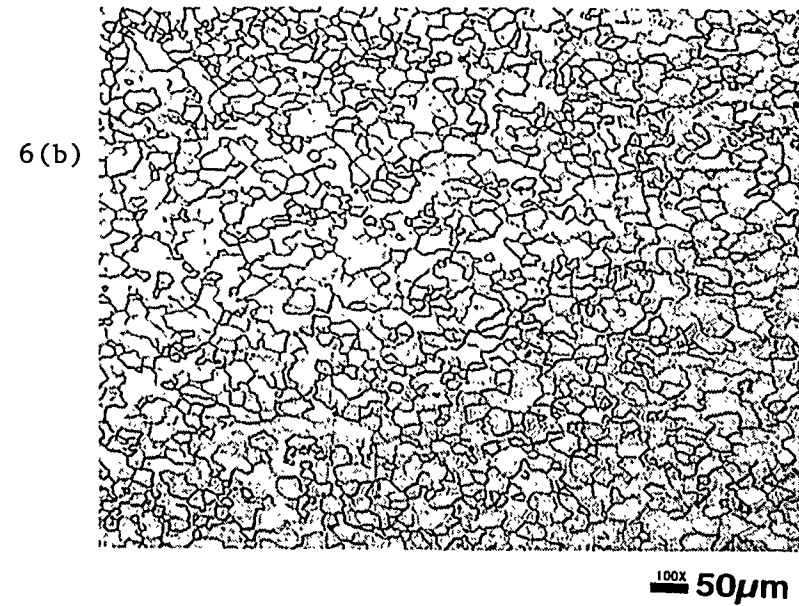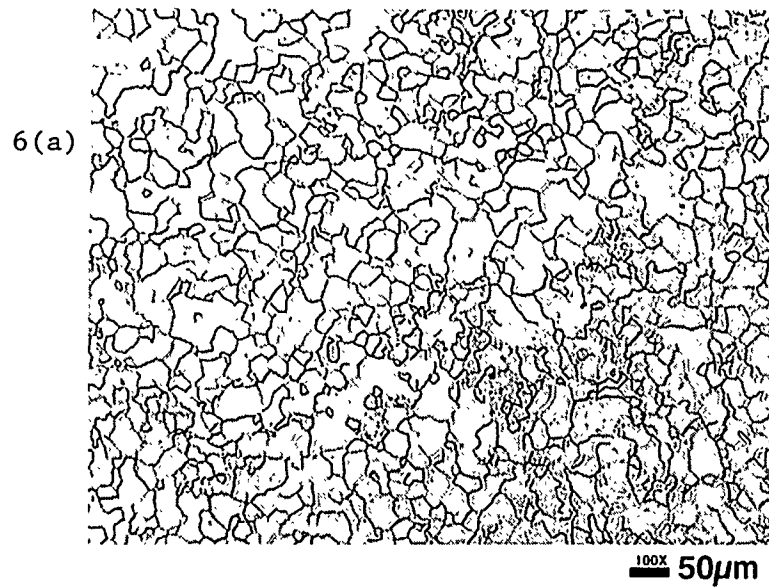
Fig. 6. Optical microstructure of CVN specimen from the RC series showing a more uniform distribution of Ti (OCN) particles and absence of banded grain structure: (a) LT orientation; (b) and (c) LS orientation.

56

7 (b)

7 (a)

7 (c)
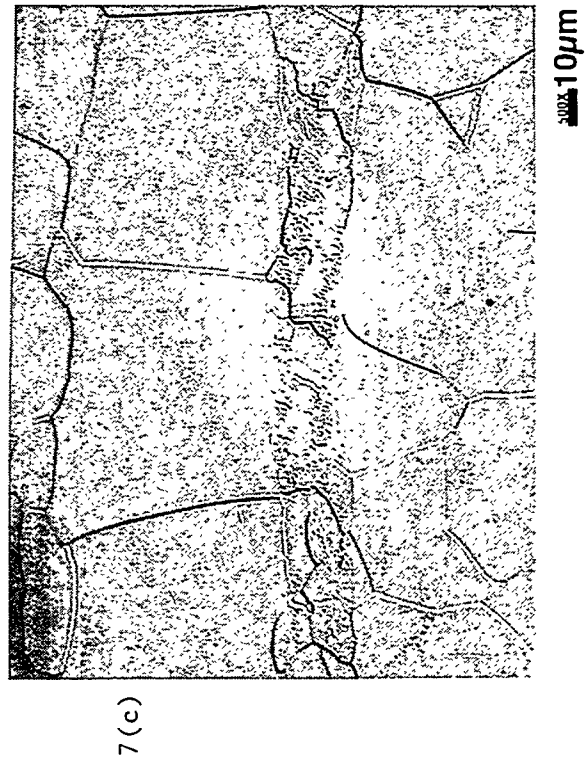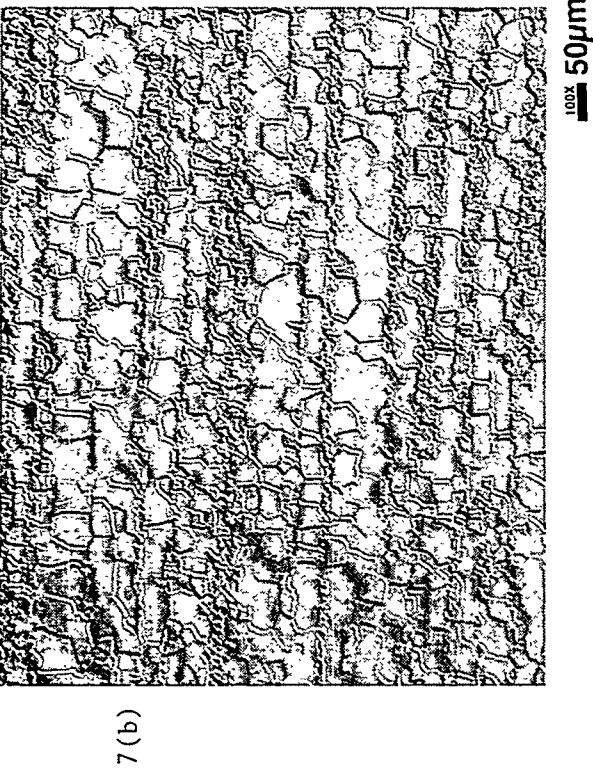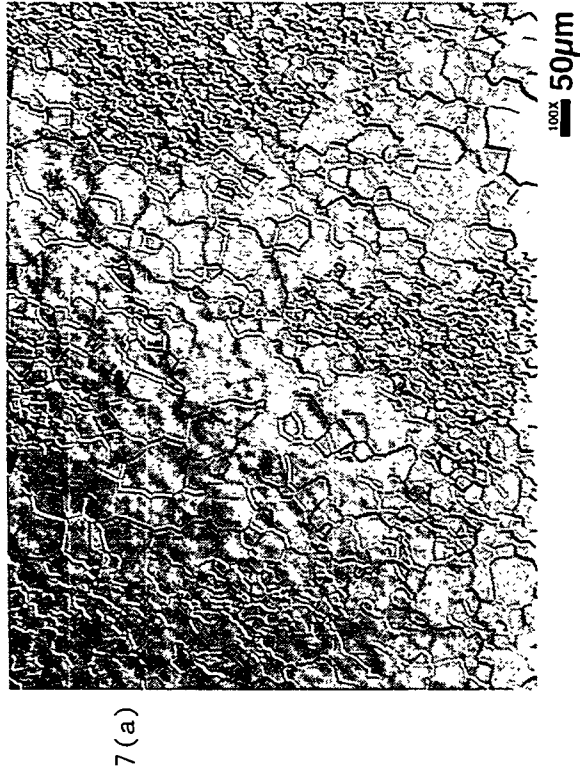
Fig. 7. Optical microstructure of CVN specimen from the QC (01-40) series after heat-treating at 1125°C for 2h, illustrating partial dissolution of Ti (OCN) and grain growth: (a) LT orientation; (b) and (c) LS orientation.

8(a)

8(b)
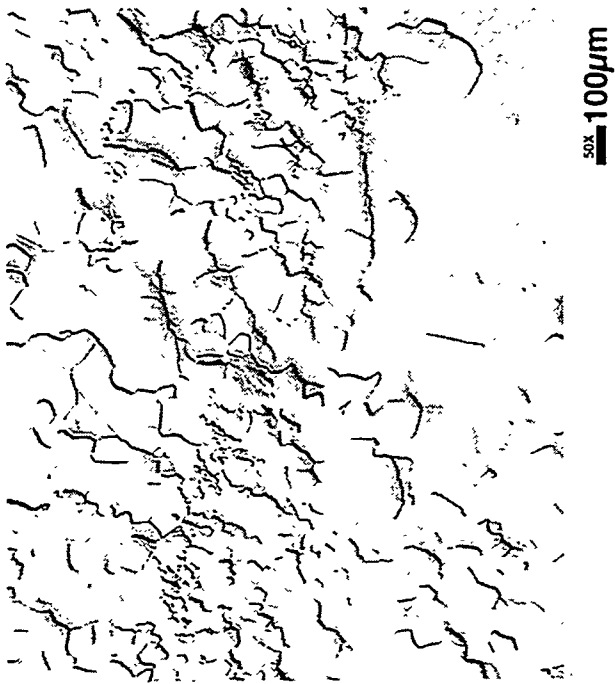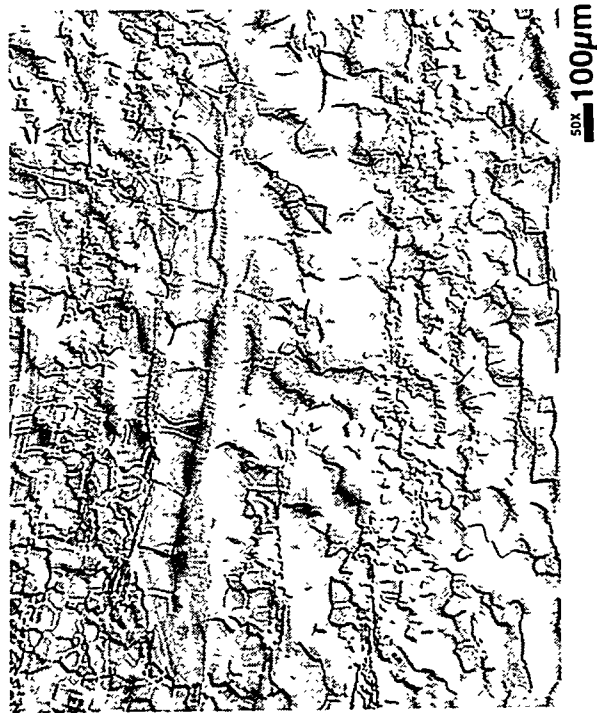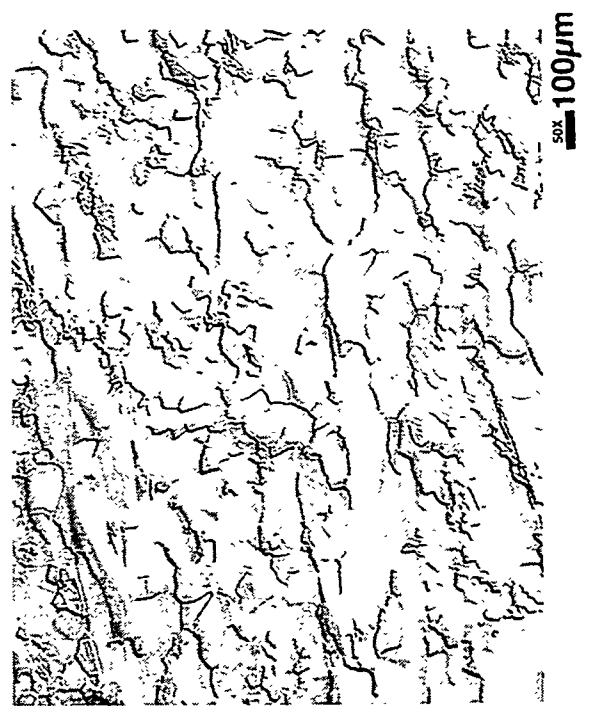
8(c)

Fig. 8. Optical microstructure of as-extruded V-4Cr-4Ti showing fine equi-axed grains, large elongated grains, and un-recrystallized regions. Sections (a) and (b) are parallel to the extrusion direction, (c) is perpendicular to the extrusion direction.

regions of the billet where the temperature remains above ~1125°C during extrusion, precipitation during deformation will not occur and subsequent precipitation of Ti (OCN) during secondary processing is likely to be much more uniformly dispersed.

Secondary processing consists of rolling to a maximum of 50% reduction at temperatures in the range RT to 400°C with intermediate annealing at 1050 to 1075°C. Since this is below the Ti (OCN) solvus, inhomogeneous distributions of Ti (OCN) developed during extrusion cannot be eliminated. Grain growth is inhibited in regions of high particle density and a banded recrystallized grain structure develops that persists in the final microstructure of the mechanical property specimen. This seems to be the situation with the QC and WB series of CVN specimens and indicates that plates M150 and Q250 came from parts of an extrusion that cooled below 1125°C during the extrusion process. In contrast, the RC series of specimens have relatively uniform microstructures, suggesting that plate R250 came from a section of the extrusion that did not cool below 1125°C during the extrusion process. With regard to the tensile specimens, the uniformity of the microstructure of the ST and RC/D series similarly indicates that plates S40 and R250 came from sections of the extrusion that were maintained >1125°C. However, the fact that one series of tensiles (WE) made from plate N40 was banded and the other (WH) was not indicates that homogeneous and non-homogeneous material can exist in a single plate.

CONCLUSIONS

A comprehensive study of the fabrication metallurgy of the V-4Cr-4Ti alloy has never been undertaken, and consequently, the program is dealing with considerable variations in the microstructures of specimens prepared by different processing paths. Understanding of the kinetics of recovery, recrystallization, and precipitation is incomplete, and we can only speculate on the dynamic interactions occurring during the hot extrusion, particularly since the extrusion temperature is so close to the Ti (OCN) solvus.

The microstructural variations discussed in this report are unlikely to have any major impact on tensile behavior, but the presence or absence of banded microstructures could introduce an anisotropy in crack propagation behavior.

Before any further processing of extruded barstock into plate is undertaken, it would be advisable to undertake a pilot study to investigate the potential benefits of introducing a homogenization treatment at 1150°C to dissolve any Ti (OCN) formed during the extrusion process. Knowledge of the kinetics of recovery, recrystallization, and precipitation needs to be expanded to provide a rational basis for selecting rolling and intermediate annealing schedules that will generate predictable and consistent microstructures.

REFERENCES

1. E. Donahue (UCSB), private communication.

2. D. T. Hoelzer, Fusion Materials Semiannual Progress Report, this volume, pp. 59-63.

3. J. Kurtz, M. L. Hamilton, and H. Li, Fusion Materials Semiannual Progress Report for Period Ending December 31, 1997 (DOE/ER-0313/23), pp. 111-118.

4. R. Petersen, Teledyne Wah Chang, Albany, private communication.

STRUCTURAL ANALYSIS OF Ti-OXYCARBONITRIDES IN V-Cr-Ti BASED ALLOYS — D.T. Hoelzer (Oak Ridge National Laboratory)

OBJECTIVE

The purpose of this work is to determine the crystal structure of globular shaped Ti-OCN (oxycarbonitrides) to assist in understanding their role in the physical metallurgy of V-Cr-Ti based alloys.

SUMMARY

A study was conducted to determine the crystal structure of Ti-OCN particles which are commonly observed in V-Cr-Ti based alloys. The information obtained from this study will be used to gain a better understanding of the physical metallurgy of the V-Cr-Ti based alloys. The precipitates examined in this study were those that formed in a V-4Cr-4Ti alloy (S-40 plate) that was annealed at 1000°C for 2 hours. The precipitates are characterized as having a globular shaped morphology with some degree of interfacial faceting. The structural analysis indicated that these precipitates are consistent with the m3m crystal point group.

INTRODUCTION

It is commonly known that an inhomogeneous distribution of Ti-oxycarbonitrides (Ti-OCN) often form in the solid solution matrix of V-Cr-Ti alloys during thermo-mechanical processing. The formation of these precipitates is significant since they have been shown to influence the ductile-to-brittle transition temperature (DBTT) of V-Cr-Ti alloy by removing interstitial elements from the matrix [1]. Furthermore, their formation may also assist in controlling grain growth during thermo-mechanical processing which can influence the mechanical properties of the V-Cr-Ti alloy. However, with the exception of chemical analysis being done on the Ti-OCN precipitates there has been very little reported regarding their crystal structure. This type of information is beneficial to understanding the precipitation process of the Ti-OCN precipitates. Thus, the purpose of this study was to apply electron diffraction techniques for determining the crystal structure of the Ti-OCN precipitates. These results will be used in a more comprehensive study of the precipitation process of the Ti-OCN.

RESULTS AND DISCUSSION

The microstructure observed in the thin foil of the V-4Cr-4Ti alloy (S-40 plate) after annealing at 1000°C for 2 hours consisted of equiaxed recrystallized grains. The matrix contained an inhomogeneous distribution of globular shaped precipitates as represented in Figure 1. The size range observed for these precipitates was typically ~0.1 to 0.3μm. There was no apparent correlation with the formation of the precipitates on grain boundaries. The EDS analysis indicated that the globular shaped precipitates contained titanium, carbon, and oxygen [2]. The presence of nitrogen could not be ascertained due to the peak overlap of N-K_α with Ti-L_α.
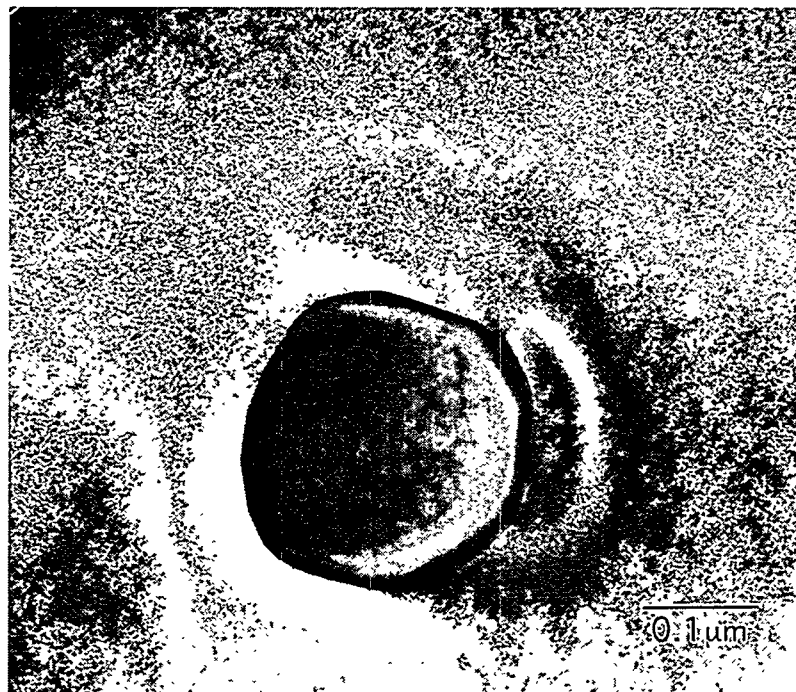
Figure 1. Globular-shaped Ti-OCN particle observed in the solid solution matrix of V-4Cr-4Ti alloys that form during thermo-mechanical processing.

The structural analysis consisted of determining the crystal point group of the precipitates. Figure 2 shows the SAED and CBED patterns that were obtained from a precipitate that was oriented along a 3-fold zone axis that could either be the [111] zone axis of a cubic structure or the [0001] zone axis of a trigonal/rhombohedral (hexagonal indexing) structure. The CBED whole pattern observed in Figure 2b shows HOLZ lines and Kikuchi bands that are consistent with 3m symmetry. The observed 3m symmetry rules out all possible structures except those based on either the $3m1_R$, 3m, or 6_Rmm_R diffraction groups [3]. There is only one crystal point group associated with the $3m1_R$ diffraction group and that is P6m2 which is a HCP structure. However, according to the powder diffraction files (PDF) in the international centre for diffraction data (ICDD) there are no phases present in the binary Ti-x (where x = O,C,N) systems that possess this point group [4]. There are two point groups associated with the 3m diffraction group and they are 3m and $\bar{4}3m$. However, there are no reported phases that exist in the binary Ti-x systems that have these point groups. The 6_Rmm_R diffraction group is also associated with two point groups which are $\bar{3}m$ and m3m. From the reported phases in the binary Ti-x systems, both the α-Ti_2O_3 and β-Ti_2O_3 phases have the $R\bar{3}c$ space group which contains the $\bar{3}m$ point group. However, these two phases are eliminated as possibilities due to inconsistencies encountered when structure factor considerations are applied to the indexing of the SAED pattern shown in Figure 2a. Finally, the TiC, TiN, and γ-TiO phases are all reported to have the Fm3m space group, which contains
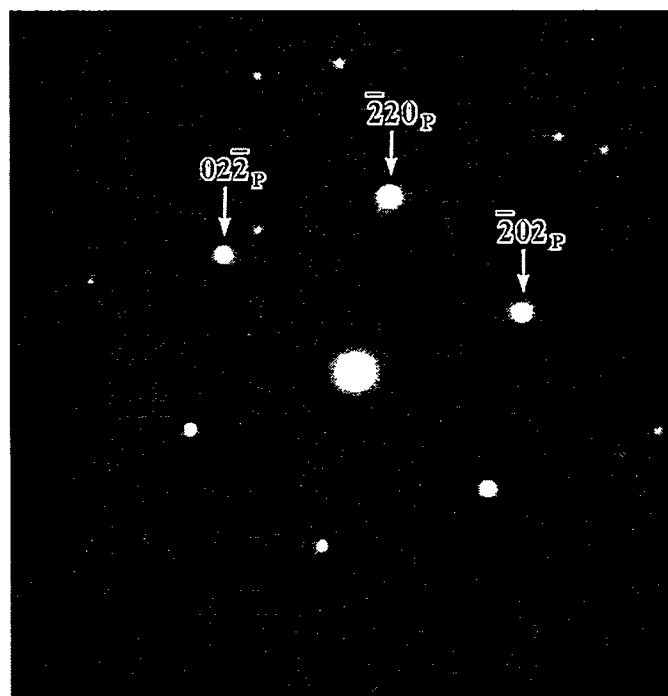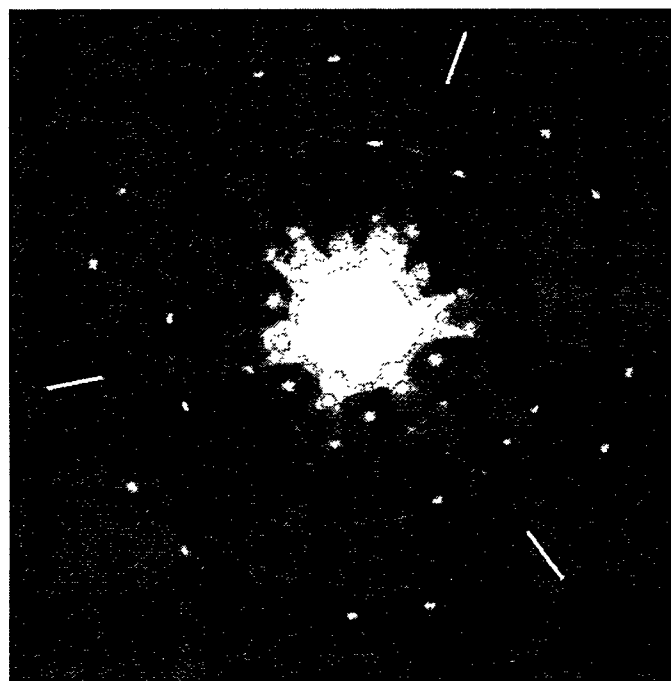
Figure 2. Structural analysis of the Ti-(OCN) phase showing (a) the [111] zone axis and (b) 3m CBED whole pattern symmetry that were consistent with the m3m point group of a fcc structure.

the m3m point group [5]. Therefore, the fcc crystal structure based on the m3m point and Fm3m space groups is the only one that is consistent with the results of the diffraction analysis.

A second zone axis of high symmetry was obtained from a representative precipitate and is shown in the SAED pattern of Figure 3. The analysis of this pattern indicated that both the structure factor and the measured interplanar d-spacings and angles were consistent with the [110] zone axis of the fcc crystal structure based on the Fm3m space group.
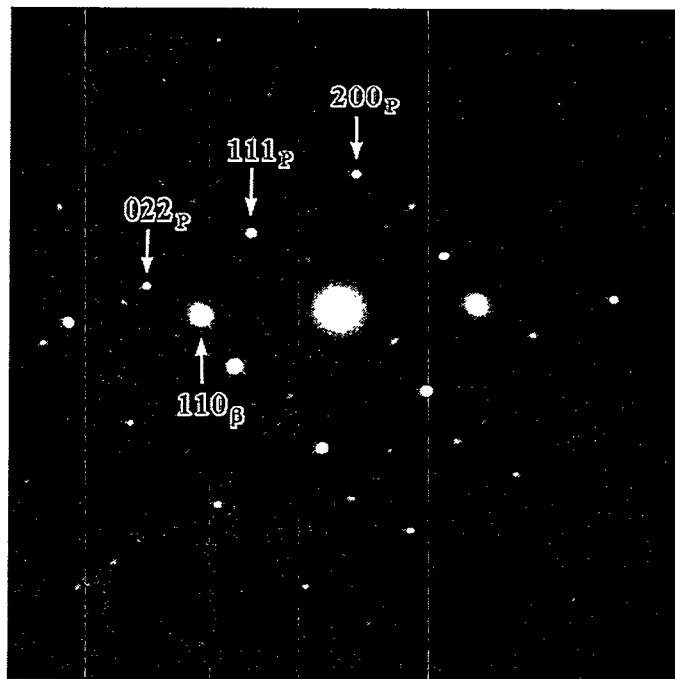
Figure 3. SAED pattern from a Ti-(OCN) particle consistent with the [110] zone axis of the fcc crystal structure. The subscripts P and β denote the diffraction spots from the Ti-OCN particle and bcc solid solution matrix, respectively.

Although it is impossible to differentiate between the TiC, TiN, and γ-TiO phases based on symmetry information they may be differentiated based on lattice parameter. This is possible to an extent since the lattice parameter of each of these phases is slightly different as shown in Table 1. The lattice parameter of several precipitates was calculated from reflections present at appropriate zone axes and was found to be 4.36Å (± 0.09Å). From Table 1 it is seen that this value agrees the best with the lattice parameter of the TiC phase. Thus, the results of this study suggests that the Ti-OCN precipitates are based on the fcc TiC phase but that this structure can accommodate other interstitials such as O and N in solid solution. This is possible because the three binary Ti-x phases have the same Fm3m space group and are therefore isomorphous with each other.

Table 1. Compositional ranges and lattice parameters of the Ti-x (x = O, N, and C) phases.

Phase	Composition (at.%)	Space Group	Lattice Parameter	PDF Number	References
γ-TiO	34.9 to 55.5	Fm3m	4.177Å	8-0177	4,6
TiN	28 to >50	Fm3m	4.256Å	6-642	4,6
TiC	32 to 48.8	Fm3m	4.3285Å	6-614	4,6

REFERENCES

1. S.J. Zinkle, H. Matsui, D.L. Smith, A.F. Rowcliffe, E. van Osch, K. Abe, and V.A. Kazakov, Journal of Nuclear Materials, Vol. 258-263, 1998, p. 205.
2. P.M. Rice, Unpublished results.
3. B.F. Buxton, J.A. Eades, J.W. Steeds, and G.M. Rackham, Philisophical Transactions of the Royal Society, Vol. 281, 1976, p. 181.
4. JCPDS International Centre for Diffraction Data, 1998.
5. T. Hahn, ed., International Tables for Crystallography, Dordrecht, Holland ; Boston, U.S.A. : Published for the International Union of Crystallography by D., 1983.
6. T.B. Massalski, J.L. Murray, L.H. Bennet, and H. Baker, eds., Binary Alloy Phase Diagrams, 1986.

LASER-WELDED V-Cr-Ti ALLOYS: MICROSTRUCTURAL AND MECHANICAL PROPERTIES*
K. Natesan, C. B. Reed, Z. Xu, and D. L. Smith (Argonne National Laboratory)

OBJECTIVE

The objectives of this task are to (a) determine the optimal parameters for laser beam welding of sheets of V-Cr-Ti alloys; (b) examine the microstructural characteristics of welded sections, including base metal, heat-affected-region, and core of weld; (c) evaluate the influence of different postwelding heat treatments on microstructural characteristics; and (d) evaluate the mechanical properties, such as tensile and impact, of laser-welded materials.

SUMMARY

A systematic study has been in progress at Argonne National Laboratory to examine the use of YAG or CO_2 lasers to weld sheet materials of V-Cr-Ti alloys and to characterize the microstructural and mechanical properties of the laser-welded materials. During this report period, thirty eight weldments were made with a YAG laser; the emphasis was on determining the optimal weld parameters to achieve deep penetration in the welds while eliminating porosities found previously[1]. A preliminary assessment was then made of the weldments on the basis of visual appearance and sectioning to determine depth of penetration and extent of porosity.

EXPERIMENTAL PROGRAM

The heat of vanadium alloy selected for the study had a nominal composition of V-4 wt.%Cr-4 wt.%Ti (designated as BL-71). A 4-mm-thick sheet of the alloy was used for the welding study. Earlier microstructural and hardness results were presented in a previous report [1] from welding of a 4-mm-thick plate with a YAG laser in a pulsed mode. The purpose of that study was to increase the weld penetration from ≈1.2 mm in earlier welded samples to as deep as 3 mm or more. Welding parameters such as power, traverse speed, pulse time, overlap, etc., were examined to obtain optimal quality in the final weld. Those welds lacked the full 4 mm penetration desired, and also contained some porosity. During this period, a series of welding tests was conducted, the main purpose of which was to obtain ideal welds which have enough penetration for Charpy impact specimens (weld depth > 2.74 mm) but no root porosity, surface splatter or plate-out. Two different focal length lenses (5" and 3") were tested under different laser parameters and beam travel speeds. To avoid the cracking and oxidation of the welds, high-purity argon (99.999%) was used as the shielding gas with a flow rate of 25 L/s, provided by a 9.5-mm diameter tube at 30° from horizontal. Some tests were also conducted using an environmental control box to improve the quality of the welding atmosphere.

RESULTS AND DISCUSSION

In the last report [1], we presented microstructural and hardness data on laser-welded V-4Cr-4Ti alloy. The welds in that study were made with a YAG laser in the pulsed mode, the energy of the laser beam was 4.5-5.5 J/ms; pulse width was maintained at 3 ms, and workpiece traverse speed was varied between 10 and 40 mm/s. Weld depth in those specimens reached 2.23 mm; still inadequate for Charpy specimens. Root porosity was also found.

During this period, the series of welds listed in Table 1 was completed.

Table 1 Laser Welding of Vanadium

Weld No.	Penetration (mm)	Laser Schedule E-L-R*	Feed (cm/s)	Lens	Focal Position	Porosity? **	Irregular or splatter surface ?	Ideal Welds
1	2.74	4/3/66	1	5"	@ Surface			Y
2	3.15	4/3/66	0.5	5"	@ Surface			Y
3	2.53	4/3/66	1	5"	@ Surface		Y	
4	3.42	4/3/66	0.5	5"	@ Surface			Y
5	2.81	4/3/66	1	5"	@ Surface			Y
6	2.91	4/3/66	1	5"	@ Surface			Y
7	2.38	4/3/66	1.5	5"	@ Surface	Y		
8	2	6/2/66	1.5	5"	@ Surface		Y	
9	1.17	6/2/66	2	5"	@ Surface		Y	
10	1.86	4/3/66	2	5"	@ Surface			
11	2.43	4/3/66	1.5	5"	@ Surface	Y		
12	1.48	4/3/66	2	5"	1/2 mm into			
13	2.53	4/3/66	1.5	5"	@ Surface			
14	2.54	5/2.5/64	1.5	5"	@ Surface	Y		
15	1.94	5/2.5/64	2	5"	@ Surface		Y	
16	1.89	5/2.5/64	2	5"	@ Surface		Y	
17	2.26	4/3/66	1.5	5"	@ Surface			
18	2.02	4/2/100	1.5	5"	1 mm into		Y	
19	2.2	4/3/66	1.5	5"	1 mm into			
20	2.17	4/3/66	1.8	5"	1 mm into	Y		
21	2.16	4/3/66	2	5"	1 mm into	Y		
22	2.82	4/3/66	1.5	3"	1 mm into			Y
23	2.81	4/3/66	2	3"	1 mm into	Y		
24	1.66	4/3/66	4	3"	1 mm into			
25	1.75	4/3/66	3	3"	1 mm into			
37	2.43	5/3/53	2	3"	1 mm into			
38	1.79	5/3/53	3	3"	1 mm into		Y	
39	2.5	5/3/53	2.5	3"	1 mm into	Y		
40	1.92	5.5/3/48	3	3"	1 mm into		Y	
41	2.5	5.5/3/48	2.5	3"	1 mm into	Y	Y	
42	2.37	5.2/3/51	2.5	3"	1 mm into	Y		
43	2.8	5.2/3/51	2	3"	1 mm into	Y		Y
44	2.18	5.2/3/51	3	3"	1 mm into			

* The meanings of the E-L-R in the laser schedule, a control program used to control the firing of the laser are as follows:
E: energy per unit time in joules/millisecond,
L : the pulse width in milliseconds and
R: the repetition rate in Hz or Pulses per second.

The laser schedule can be run under normal mode or alternative mode. In normal mode, the two rods fire the laser at same time, and in alternative mode, they fire alternatively. Alternative mode was used for all the V welds. In alternative mode, the real repetition rate is two times of the R number. For example, Laser Schedule E4L0.5R100 (ALT), gives energy per unit time of 4 J/millisecond, pulse width of 0.5 milliseconds, and repetition rate of 2 X 100 = 200 Hz.

* *Porosity was examined at a single, randomly selected cross section via 400X optical microscopy.

The welds were metallurgically analyzed to characterize the weld depths and the microstructures. Root porosity was found in welds produced under relatively high beam travel speeds. Porosity was examined at a single, randomly selected cross section via 400X optical microscopy. Splatters were generated when the peak power of the laser beam was too high. Ideal welds (no porosity or irregular surface, and weld depth>2.74 mm) were achieved for each of the following three conditions:

1) 5" lens, laser schedule E4R3L66, and beam travel speed, F<= 1 cm/s,
2) 3" lens, laser schedule E4L3R66 and beam travel speed, F<= 1.5 cm/s, and
3) 3"lens, laser schedule E5.2L3R51 and beam travel speed, F<= 2 cm/s.

Weld depths of larger than 3 mm without porosity were obtained at beam speeds of 0.5 cm/s for 5" lens, and > 2.8 mm at 1,5 cm/s for 3" lens. The weld depth required by the Charpy impact test specimen is larger than 2.74 mm. The ideal welds produced using 5" lens and 3" lens are shown in Figures 1 and 2.
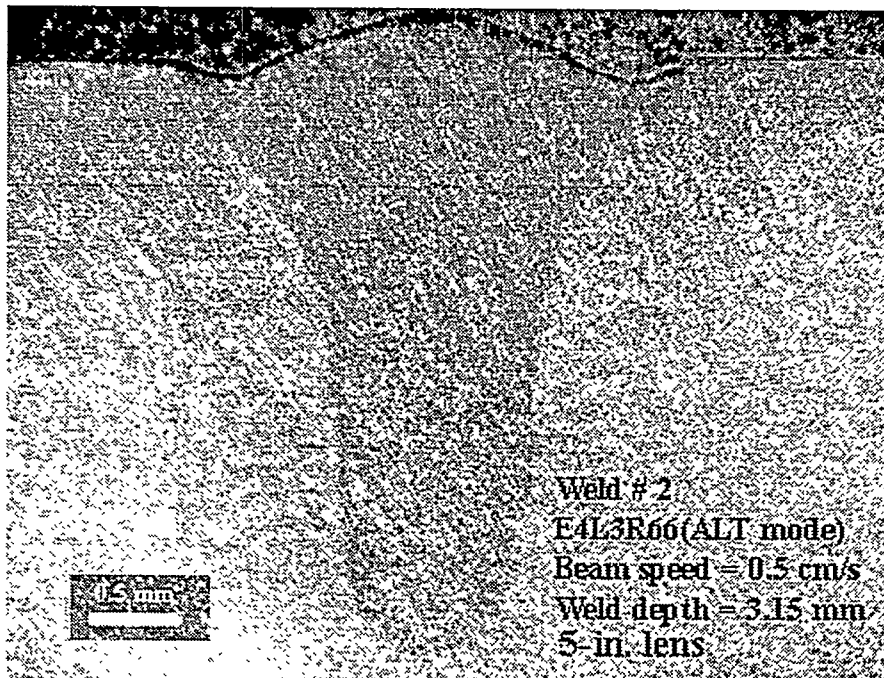
Figure 1 Weld produced under laser schedule of E4L3R66 and beam travel speed of 0.5 cm/s for 5" lens.
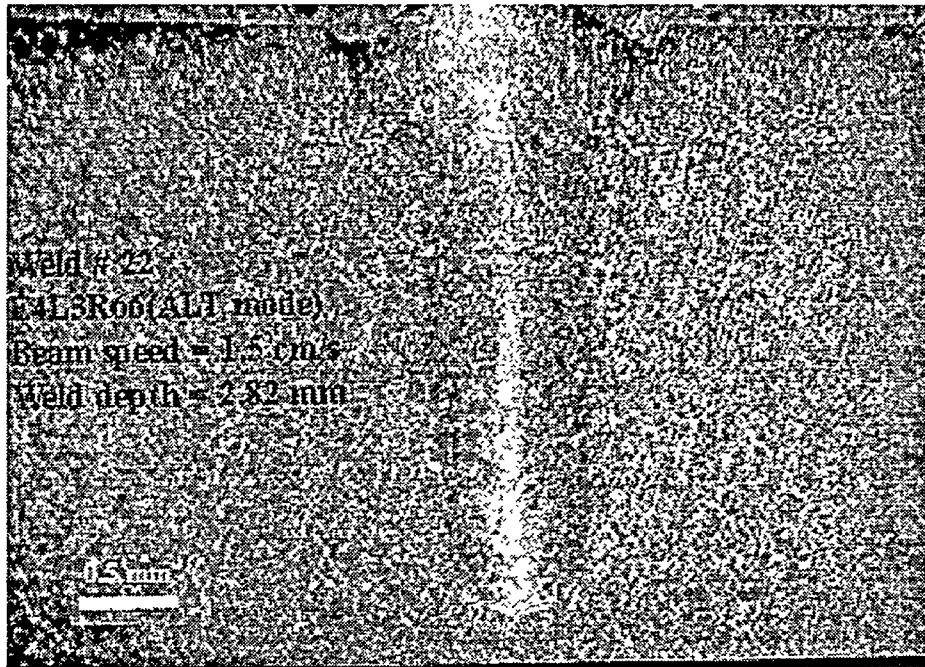
Figure 2 Weld produced under laser schedule of E4L3R66 and beam travel speed of 1.5 cm/s for 3" lens.

In the next report period, the deepest welds achieved so far will be sectioned longitudinally to comprehensively examine for porosity. Sections of weld metal will also be analyzed for oxygen content and correlated with weld hardness.

A welding environment control (containment) box was assembled within the laser system. The gas lines and vacuum ports were tested. The use of the containment box is expected to provide a controlled atmosphere for laser welding of vanadium and protect it from oxidation, splatter and plate-out.

Five preliminary welds were produced with the environmental control box. The laser schedule used was E4L3R66 (ALT). A 3-inch focal length lens was used, which was focussed at 1 mm into the 4-mm thick plate. The environmental gas was 99.996% purified argon. The environmental control box was first evacuated to 20 in. Hg by a vacuum pump, then the argon was allowed to flow into the box at a flow rate of 30 L/s for 10 to 15 seconds before the laser started firing. The beam travel speed was 1 cm/s for all welds except weld No. 4, which was 0.5 cm/s. Both antireflective coated and non-coated windows were tested. The welds are shown in Figure 3. Though a shiny weld (weld No.1 in Fig. 3) was achieved, a vapor was deposited on the window after a single run. This deposit significantly reduced the transmission coefficient of laser beam through the window and a significant amount of energy was absorbed by the window leading to glazing and cracking of the glass. As a result, the weld depth decreased from the beginning to the end of the welds (see Fig. 3). Further work is necessary to effectively utilize the containment box.
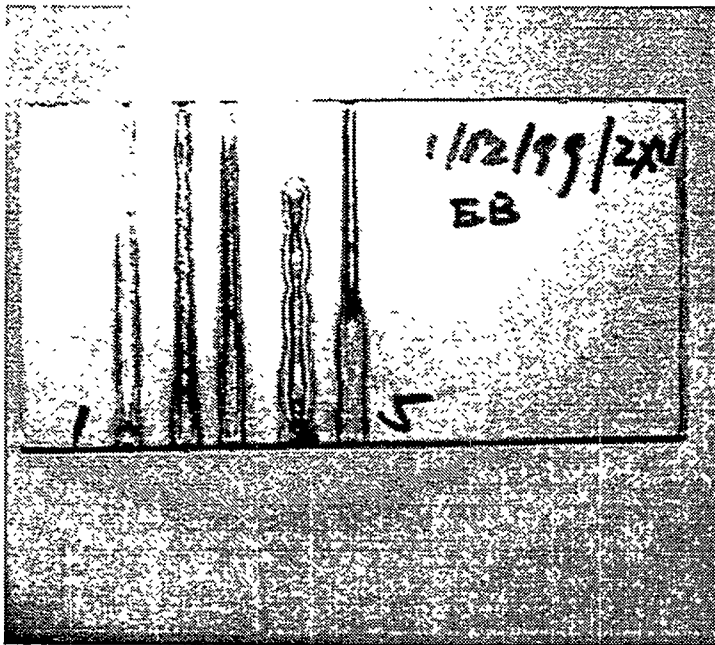
Figure 3 Top view of the welds produced within the environmental control box.

REFERENCES
1. K. Natesan, D. L. Smith, Z. Xu, and K. H. Leong, "Laser-Welded V-Cr-Ti Alloys: Microstructural and Mechanical Properties," Fusion Reactor Materials Progress Report for the Period Ending June 30, 1998, Argonne National Laboratory, DOE/ER-0313/24, p. 87, June 1998.

DEVELOPMENT OF ELECTRICALLY INSULATING CaO COATINGS*
K. Natesan, M. Uz, and S. Wieder (Argonne National Laboratory)

OBJECTIVE

The objectives of this task are to (a) develop electrically insulating coatings, with emphasis on the basic understanding of the thermodynamic conditions and kinetics of coating development needed to achieve stable coatings of CaO that are compatible in a Li/Li-Ca environment; (b) perform detailed postexposure analysis of the surface layers by several electron/optical techniques to characterize the elemental and phase compositions, quantify stratification in the layers, and establish the role of compositional changes in the coating defects and microstructure; (c) measure the electrical resistance of the coatings, before and after exposure external to Li; and (d) establish optimal procedures from the standpoint of sample preparation procedures, exposure time and temperature, and sequence of operations in order to obtain reliable and reproducible coatings with adequate electrical resistance for use in an Li environment.

SUMMARY

A systematic vapor transport study has been initiated to develop electrically insulating CaO coatings that are compatible with use in a liquid Li environment. Several experiments were conducted to study how the deposition of Ca on V-4Cr-4Ti substrate alloys is affected by variations in process temperature and time, and specimen location, surface preparation, and pretreatment. During this reporting period, a setup has been completed to measure the electrical resistivity of the coatings in air or in an inert gas environment as a function of temperature up to 750°C. Some preliminary data are presented.

EXPERIMENTAL PROGRAM

In an attempt to gain further fundamental understanding, experiments were conducted to develop Ca-rich coatings by using the pack diffusion process. The experiments involved exposure of V alloy specimens to a pack of fine Ca pellets at 700-800°C. The specimens were either completely enclosed within the pack or were hung above the pack material in a static Ar environment. The vapor pressure of Ca at 700-800°C is sufficient to deposit a layer of Ca on the specimens. Several geometrical arrangements were examined to obtain a uniform coating of Ca on the specimens, which were typically coupons that measured 5-10 x 5 x 1 mm. The alloys included V-4Cr-4Ti and V-5Cr-5Ti with and without prealuminization. In addition, specimens with various surface roughnesses (polished, grit-blasted, etc.) were included in the evaluation. The effort during this period concentrated on setting up an apparatus for measuring the electrical resistivity of the coated specimens as a function of temperature up to 750°C. The apparatus has been used to measure the resistance of thin coating layers developed by the pack diffusion process.

RESULTS AND DISCUSSION

Coating by Vapor Phase Transport

Twelve runs have been conducted to study the deposition of Ca or Ca/Mg on V alloys.[1] After deposition, the specimens were oxidized in air at 600°C to convert the deposited metals into their respective oxides. The specimens exhibited insulating characteristics after this oxidation step. Detailed X-ray diffraction studies on these specimens showed good correlation between high resistance values at room temperature and a high concentration of Ca/Mg in oxide form. Calcium concentrations in the range of 60-80 wt.% were obtained in several specimens. However, coating thicknesses in a given specimen or between various specimens were not uniform; in some

specimens, coating spallation was noted.

The results also showed that Ca and/or Mg deposition via vapor phase transport is possible but that the coating thickness and the adhesive bonding of the coating with the substrate that was obtained by a single deposition/oxidation procedure was not adequate to produce the desired insulating characteristics. Additional experiments, with several procedural modifications, were conducted and, finally, double deposition/oxidation seemed to produce a thicker coating that was more adherent and exhibited adequate insulating characteristics at room temperature. To examine the stability of the coating and its electrical resistivity at elevated temperature, experiments were conducted with some of the coated samples at temperatures up to ≈700°C in which a two-probe method was used to measure resistance.

Figure 1 shows typical scanning electron microscopy (SEM) photomicrographs of cross sections and surfaces of V-4Cr-4Ti alloy in various stages of coating development, i.e., after Ca deposition, after oxidation of the Ca deposit, and after repeated oxidation of the Ca deposit. The top left photomicrograph shows a cross section of a specimen after Ca deposition by pack diffusion. Even though Ca is the deposited element, some CaO is present in the layer because the low flow rate of 99.999 vol.% Ar used in the experiment contained sufficient oxygen to partially oxidize Ca to CaO. The top right photomicrograph shows the cross section of the specimen after Ca deposition and subsequent oxidation in 99.999% Ar. The average thickness of the coating layer was ≈4 μm but the thickness was not uniform. The bottom left photomicrograph shows a cross section of a specimen in which the sequence was Ca deposition, oxidation, and deposition. It is evident that the coating after this sequence is much thicker and denser than the coating observed after single-stage deposition.

The bottom right photomicrograph shows the surface of a specimen after dual deposition/oxidation treatments. The sample was mechanically weak and broke into several pieces, especially after resistance measurements at elevated temperatures in air. The results showed that reaction after long-term exposure at high temperature (especially at anticipated service temperatures) should be one of the criteria for an acceptable coating.

The variation in the product of resistance times area as a function of temperature obtained on specimens of V-4Cr-4Ti alloy with Ca deposition/oxidation and with Ca deposition/oxidation and redeposition of Ca is shown in Figure 2. The specimen with single-step deposition of Ca and oxidation exhibited (see left graph in Figure 2) a low value of ≈10 $\Omega \cdot cm^2$ at room temperature. Upon heating the specimen during the resistance measurement, the value decreased further to as low as 0.5 $\Omega \cdot cm^2$ at 546°C. The specimen was maintained at 546°C overnight and the resistance gradually increased to a value of 10 $\Omega \cdot cm^2$; it was then given a second cycle of heating and cooling, as shown in the figure. The resistance during the second heating remained the same as it was during the cooling part of the first cycle. However, a further increase in resistance was observed during the cooling part of the second cycle. The product of the resistance times area still remained in the range of 15-20 $\Omega \cdot cm^2$ in a temperature range of 200-500°C.

The right-hand graph in Figure 2 shows the variation in values for resistance times area for a specimen that was treated with Ca deposition/oxidation/redeposition of Ca. During the heating cycle, the value ranged between 10^7 to 10^2 $\Omega \cdot cm^2$ as the temperature increased from room temperature to ≈500°C, with a sharp drop in the temperature range of 200-500°C. The specimen was maintained overnight at 546°C in air, during which time the value for resistance times area increased from ≈400 to 2 x 10^5 $\Omega \cdot cm^2$. Upon cooling, the value showed further increase to ≈10^7 $\Omega \cdot cm^2$ at room temperature. It is evident that the dual treatment of Ca deposition improved the coating from the standpoint of thickness as well as resistance.

The behavior of the coatings of the above two specimens at 546°C as a function of exposure time is shown in Figure 3. At temperature, with a single Ca deposition treatment, the specimen exhibited a gradual increase in resistance to 5 $\Omega \cdot cm^2$, while the specimen with a double Ca treatment exhibited

values in the range of 10^4 to 10^5 $\Omega \cdot cm^2$. Additional experiments are in progress to evaluate the characteristics of coatings developed on several other specimens. Furthermore, the microstructures of several of these coated specimens will be characterized and compositional gradients will be determined. Also, some of the specimens will be exposed to an Li environment; their resistances will be measured before and after exposure.
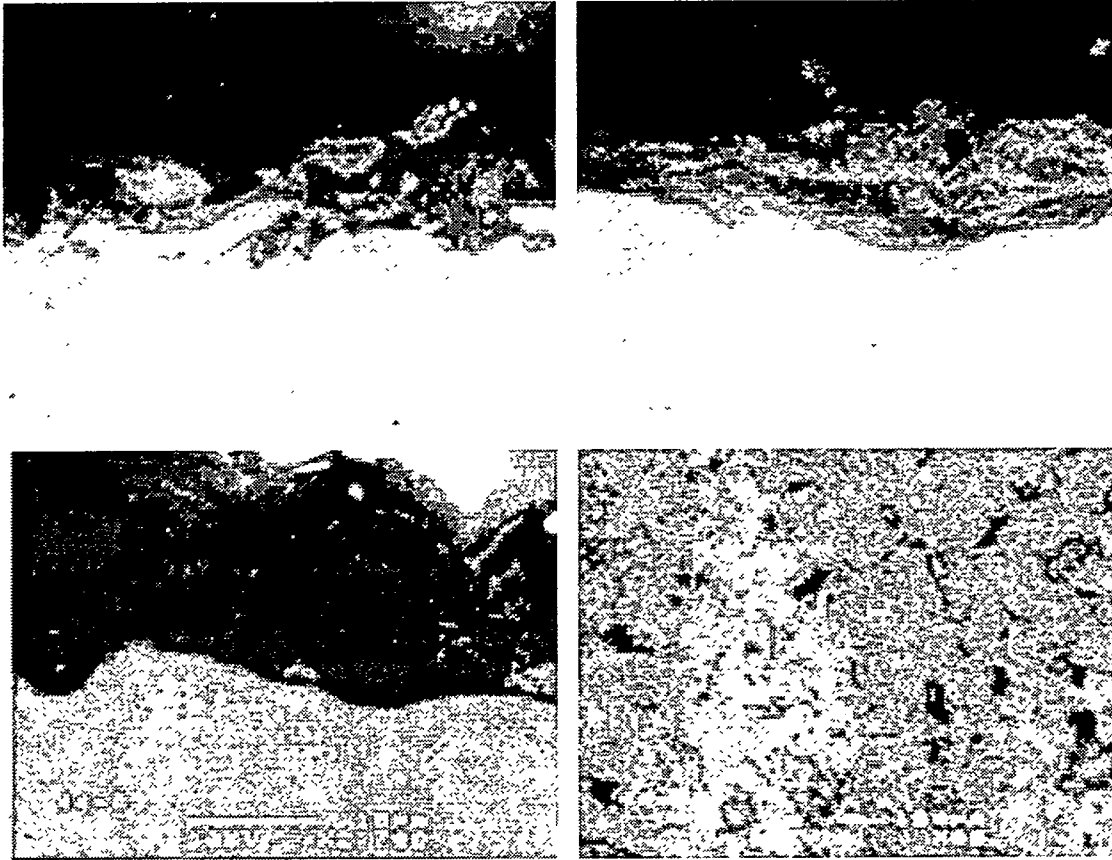
Fig.1. SEM photomicrographs of V-4Cr-4Ti alloy after Ca deposition (top left), after oxidation of Ca deposit (top right), after repeat of Ca deposition (bottom left) and after repeat of oxidation of Ca deposit (bottom right). Bottom right photomicrograph is a surface view, and the others are cross sections.
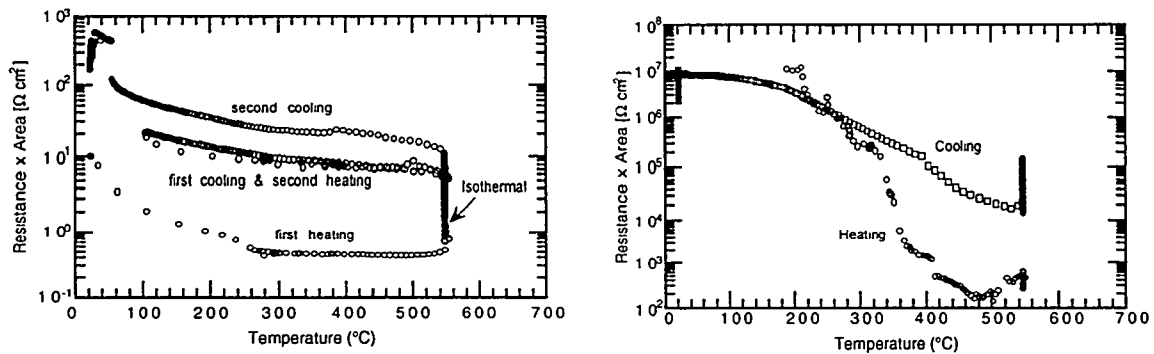
Fig. 2. Product of resistance times area as a function of temperature for V-4Cr-4Ti alloy with (left) Ca deposition/oxidation and (right) Ca deposition/oxidation/Ca deposition.
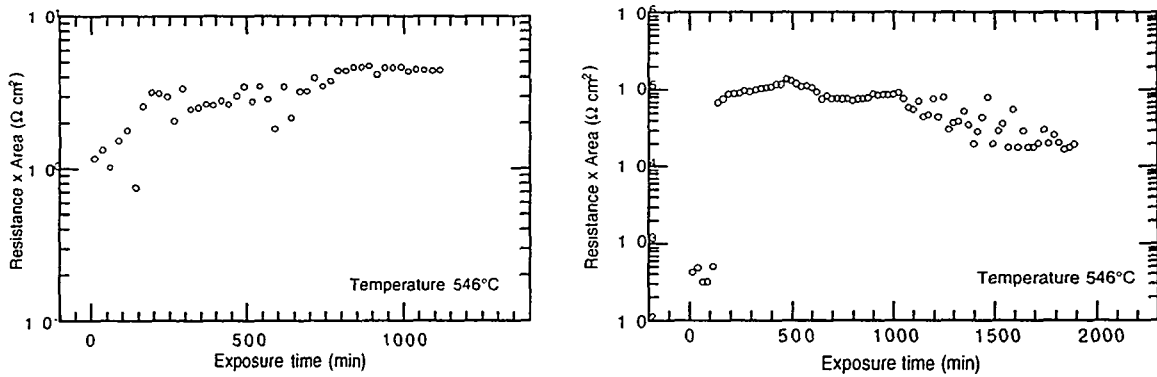
Fig. 3. Product of resistance times area as a function of time at 546°C for V-4Cr-4Ti alloy with (left) Ca deposition/oxidation and (right) Ca deposition/oxidation/Ca deposition.

REFERENCES

1. K. Natesan, C. B. Reed, M. Uz, and D. L. Rink, "Development of Electrically Insulating CaO Coatings," Fusion Reactor Materials Progress Report for the Period Ending June 30, 1998, Argonne National Laboratory, DOE/ER-0313/24, p. 82, September 1998.

2.0 SILICON CARBIDE COMPOSITE MATERIALS

SiC FIBER EVALUATIONS - G. E. Youngblood and R. H. Jones (Pacific Northwest National Laboratory)*

OBJECTIVE

The objective of this report is to evaluate the unirradiated properties of near stoichiometric β-SiC fibers which will be irradiated in the JUPITER/HFIR 14J experiment.

SUMMARY

The SiC fiber types selected for the JUPITER 14J irradiation experiment are presented together with the rationale for their selection. The fiber diameter variation from fiber-to-fiber within a tow and along single filament lengths was assessed by image analysis and SEM for four SiC-based fibers: Hi-Nicalon, Hi-Nicalon Type S, Tyranno SA and Dow Sylramic. Because of the apparently characteristic fiber diameter variations observed across tows (6-22 μm) as well as along single filaments (up to $\pm 1.0 \mu$m/cm), it is not appropriate to use average fiber diameters to determine individual fiber strengths or fiber strength distributions. Generally, SiC fibers with larger diameters have lower tensile strengths. Therefore, a 3-parameter modified Weibull analysis which includes a diameter dependence parameter is preferred over the simple 2-parameter Weibull analysis to properly describe SiC fiber strength distributions. The newly introduced diameter dependence parameter may be a sensitive measure of fiber quality or performance.

PROGRESS AND STATUS

Introduction

The JUPITER HFIR/14J neutron irradiation experiment, scheduled to commence in March, 1999 and to be completed in March, 2000, is part of the U.S./Monbusho collaboration. The irradiations will be carried out at 300, 500 and 800°C to a dose of $\approx$ 10 dpa-SiC.

Better irradiation stability of SiC/SiC composites is expected if fiber properties are closely matched to that of the SiC matrix so that differential swelling or shrinkage between the fiber and matrix can be minimized [1]. Therefore, several advanced fibers with near stoichiometric β-SiC compositions and crystalline structures were selected for the HFIR/14J irradiation. This report will discuss ongoing evaluations of these fibers.

HFIR/14J Fiber Matrix

The selected fiber types for the HFIR/14J experiment are listed in Table 1. All of the listed fibers are polymer-derived with room temperature tensile strengths in excess of 2.5 GPa and have fine diameters which make them suitable for weaving into fabric for SiC/SiC composite fabrication. Except for the Hi-Nicalon fiber, these fibers have been given a final sintering treatment at 1600°C or greater to stabilize their crystalline structures. Therefore, their bulk density and elastic modulus values ($\approx$3.1 g/cc and $\approx$400 GPa, respectively) approach monolithic β-SiC values. The Hi-Nicalon fiber has lower density and modulus values (2.7 g/cc and 270 GPa, respectively), and has exhibited long-term radiation degradation [3].

Table 1. Measured Properties* of Near Stoichiometric β-SiC Fibers to be Irradiated in 14J.

Measured Property	Hi-Nicalon (1)	Annealed Hi-Nic (2)	Hi-Nic Type S (1)	Tyranno SA (3)	Tyranno SA(2) (3)	Dow Sylramic(4)	Dow Syl. (2) (4)
Avg. Diameter (μm)	13.8/14	(14)	12.3/13	9.4/10	(10)	(10)	9.2/10
Density (g/cc)	2.69/2.74	2.82	3.08/3.1	(3.02)	(3.1)	(3.1)	(>3.1)
RT Tensile Strength (GPa)	3.4/2.8	nm	2.1/2.5	(2.8)	(2.8)	(3.2)	(3.2)
RT Modulus (GPa)	(270)	nm	(420)	(420)	(375)	(400)	(>400)
RT Elongation (%)	(1.0)	nm	(~0.6)	(0.7)	(~0.7)	(~0.8)	(<~0.8)
RT Therm. Cond. (W/mK)	4.8/5.3	nm	(18)	(65)	nm	(46)	(>46)
RT Elect. Cond. (Ω-cm)	3.0/1.4	1.1	30/0.1	nm	nm	nm	nm
Second Phases (wt. %)	Turbo C 18 v /%	nm	0.2 O	<2 Al 0.3 O	<2 Al 0.3 O	2.2 TiB$_2$ 0.8 O	< B <0.8 O
XRD Crystallite-Size (nm)	4.0/4	nm	11/22	40/38	(150**)	85/90	(~100)
Continuous Use Temp (°C)#	1078	1215	1256	~1300 est.	nm	1261	nm

Manufacturer's values are listed second or in parenthesis
(1) Nippon Carbon Co., Ltd., Yokohama, Japan
(2) Annealed at 1500°C, Argon (1 hr.)
(3) Ube Industries, Ltd., Ube City, Japan
(4) Dow Corning Corp., Midland, Michigan, USA
** Determined from TEM microstructures
# Determined from the fiber BSR thermal creep when m = 0.5 for a 100 hr. test in argon [2].

However, SiC/SiC composite with Hi-Nicalon reinforcement is commercially available. Since considerable irradiation performance data has been accumulated for this fiber, it is retained in the experimental matrix as a reference. To examine if the irradiation performance of the Hi-Nicalon fiber could be improved without degrading its other properties, a high temperature anneal (1500°C, 1 hour in argon) was given to a fiber bundle prior to insertion into 14J. The remaining stoichiometric SiC fibers listed in Table 1 currently are being evaluated for advanced aerospace applications because of their improved creep and rupture strength properties as well as improved oxidation resistance [4]. The Hi-Nicalon Type S and Dow Sylramic fibers just recently have become commercially available, although in limited amounts. Both of these fiber types have been given additional treatments to improve their creep and rupture strength properties even more.

These treated fibers, listed as Tyranno SA(2) and Dow Sylramic(2) in Table 1, are developmental and are available only on special request at this time.

Recently, the thermal diffusivity of the Hi-Nicalon fiber was determined as a function of temperature from RT to 200°C [5]. Similar measurements are planned for the other selected fibers and the upper temperature limit for the difusivity measurements will be extended to 1000°C. Other characterization measurements include crystallite size determinations by XRD and field emission SEM and RT electrical conductivity determinations. Irradiation effects on these fiber properties will be assessed after the 14J irradiations. The fiber continuous use temperature was estimated from a 100 hr. thermal creep bend stress relaxation (BSR) test as discussed previously [2]. A similar fiber BSR test to examine the potential for irradiation-enhanced creep will be carried out in HFIR/14J. To more closely simulate the time-temperature conditions expected in the HFIR/14J irradiation, a 1000 hr. fiber thermal creep BSR test will be carried out. Of particular interest is the effect of the added aluminum in the Tyranno SA fiber and the reduced boron in the Sylramic fiber. The aluninum (as Al_2O_3) stabilizes grain growth in the Tyranno fiber while reduced boron in the Sylramic should alleviate the expected helium generation problem in a neutron irradiation environment.

Effects of Diameter Variation on Fiber Tensile Strength

Initial characterization of the Hi-Nicalon, Hi-Nicalon Type S, Tyranno SA and Dow Sylramic fibers has indicated that they typically exhibit a large variation in their effective diameters (6-22 μm) as well as strength dependence on their diameters. A simple 2-parameter Weibull analysis, as recommended by ASTM D3379 [6], may not be adequate to describe fiber strength distributions before and after irradiation treatments [7]. Therefore, a study to assess the influence of diameter variation on fiber tensile strengths and strength distributions was carried out. A 3-parameter "modified" Weibull analysis method, recently developed by Zhu et al. [8], was examined as a better way to describe fiber strength distributions.

Typical fiber diameter (cross-sectional shape) variations across a tow were examined by image analysis of approximately 200 fiber cross sections per fiber. The fiber diameter sizes exhibited near normal distributions with the Hi-Nicalon and Tyranno SA fibers having 1σ standard deviations near 13%, and the Hi-Nicalon S and Dow Sylramic having standard deviations <10%. Surprisingly, the measured average aspect ratios (fiber maximum diameter/breadth) were about 1.1 for each of the four examined fibers. To investigate typical fiber diameter variation along a filament length, three neighboring 30 cm long filaments were pulled from a tow and cut sequentially into 1 cm segments. The equivalent fiber diameter was determined from multiple measurements made directly from SEM micrographs of the individual segments. Diameter variations of up to $\pm 1 \mu$m/cm length were observed for each of the four fiber types.

Because of the apparently characteristic fiber diameter variations observed across tows as well as along single filaments for SiC fibers, it is not appropriate to use average fiber diameters to determine individual fiber strengths. Particularly, fiber strength distributions are affected, as a 10% error in diameter results in about a 20% error in the calculated breaking stress. Such errors show up as additional scatter in the Weibull strength distribution. Therefore, it is necessary to measure/determine the fiber cross-sectional area (equivalent diameter) at the point of the original fracture to properly assess the fiber strength distribution.

The observed dependencies of the fiber tensile strengths on diameter for the Hi-Nicalon, Hi-Nicalon Type S and Dow Sylramic fibers are illustrated in Figure 1(a-d). In Figure 1(a-d), the fiber tensile strengths exhibit significant scatter. Nevertheless, the general trend that fibers with larger diameters have lower strengths is consistent. The tensile strength (σ) versus
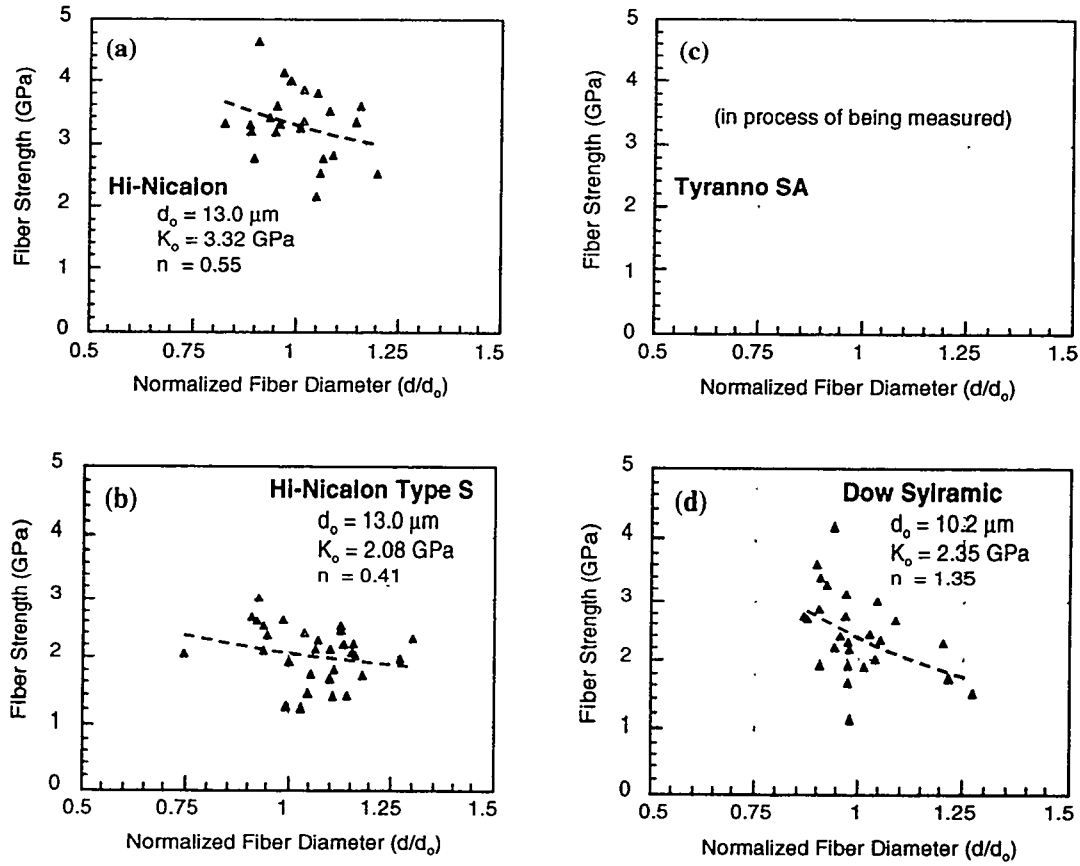
Figure 1(a-d). Tensile strength dependence on the normalized diameter for (a) Hi-Nicalon, (b) Hi-Nicalon Type S, (c) Tyranno SA and (d) Dow Sylramic fiber types.

normalized diameter (d/d_o) data were fit with a power law dependence of the form

$$\sigma = K_o(d/d_o)^{-n} \tag{1}$$

where d_o is the average diameter of the data set, n is the power law exponent and K_o is the average strength expected for a fiber with diameter d_o. The values of d_o, K_o and n are included in the plots for each fiber type. The strongest strength dependence on diameter (n=1.35) was exhibited by the Dow Sylramic fiber, while the weakest (n=0.41) was exhibited by the Hi-Nicalon Type S fiber.

The modified 3-parameter Weibull analysis, as presented by Zhu [8], was used to analyze the fiber tensile strength data. In this method, the strength data are fit by linear regression to the modified Weibull expression

$$Ln\{Ln[(N+1)/(N+1-i)]\} - hLn(d/d_o) = \beta Ln(\sigma_i) - \beta Ln(\sigma_o) \tag{2}$$

where i is the rank of the fiber tensile strengths arranged in descending order; N is the total number of tensile tests; σ_i and d_i are the corresponding measured tensile strength and diameter

values, respectively; and β and σ_o are the Weibull shape and strength parameters, respectively. In the left-hand side of Eqn (2), the second term appears as a correction factor to the first term, which is the standard Weibull failure probability ranking term. The new parameter (h) represents the fiber strength dependence on the fiber diameter. Since the Weibull mean strength (σ_{WM}) is given by

$$\sigma_{WM} = \sigma_o \Gamma(1 + 1/\beta)(d/d_o)^{-h/\beta} \tag{3}$$

where Γ is the gamma function with argument $(1 + 1/\beta)$, the identities

$$n = h/\beta \qquad \text{and} \qquad K_o = \sigma_o \Gamma(1 + 1/\beta) \tag{4}$$

are required to make Eqns (1) and (3) equivalent [8].

Iteration is necessary to derive the three parameters β, σ_o and h. To do this, conventional 2-parameter Weibull analysis yields an initial β value (β_o). A fixed n value is obtained by linear regression fitting the fiber tensile strength-diameter data to Eqn (1). An initial h value ($h_1 = n\beta_o$) is inserted into Eqn (2), and new values for β and σ_o are obtained. This cycle is repeated until the β, σ_o and h values converge which usually only requires five or six iterations. The modified Weibull analysis results for the three fiber types for which the tensile tests have been completed are given in Table 2.

Table 2. Summary of 3-Parameter Modified Weibull Analysis for SiC-Fibers

Fiber Type	β	σ_o (GPa)	h	σ_{WM} (GPa)	$\Delta \sigma_{WM}$ (GPa)
Hi-Nicalon	6.99	3.58	3.87	3.35	±0.56
Hi-Nicalon S	5.18	2.29	2.11	2.11	±0.47
Dow Sylramic	4.77	2.63	6.43	2.40	±0.57

The σ_o and β values derived from the simple 2-parameter Weibull analysis of the Hi-Nicalon, Hi-Nicalon Type S and Dow Sylramic fiber tensile strength data were 3.61, 2.31 and 2.72 GPa and 6.37, 4.93 and 3.80, respectively. The 2-parameter σ_o values were only slightly higher than the corresponding 3-parameter values listed in Table 2. However, the 3-parameter β values were significantly larger than the corresponding 2-parameter β values. The degree of difference in either value becomes larger as the fiber strength dependence on diameter becomes stronger (larger n or h values). The σ_{WM} values (Table 2) agree closely with the K_o values (Fig. 1) derived from fitting the tensile strength and normalized diameter data for each fiber type.

The scatter in the strength versus diameter data shown in Fig. 1 primarily is due to the statistical variation of flaw sizes and is the dominant mechanism responsible for the Weibull strength distribution. If h = 2.0 in Eqn (2), the modified Weibull analysis reduces to the single modal Weibull distribution that includes the fiber strength dependence on test volume (proportional to d^2 for fibers with the same length). If the fiber strength is primarily determined by surface flaws, a strength dependence on fiber surface area (proportional to d^1) is expected and h = 1.0. The tensile strength distribution for the Hi-Nicalon Type S fiber with h = 2.11 nearly falls into the former category. However, when h > 2, as appears to be the case for the Hi-Nicalon and Dow Sylramic fibers with h = 3.87 and 6.43, respectively, flaw location and type also influence the fracture mechanics [9]. In this respect, the parameter h should be sensitive to processing variables, and

also may be valuable as an indicator of the effects of fiber treatments as well as the effects of irradiation.

FUTURE WORK

The characterization of the properties for the unirradiated SiC fiber specimens will be continued through 1999.

ACKNOWLEDGMENTS

REFERENCES

1. G.E. Youngblood, C.R. Eiholzer, C.A. Lewinsohn, R.H. Jones, A. Hasegawa and A. Kohyama, "Fiber diameter variation-sample preparation and analysis," presented at the 23rd International Conference on Engineering Ceramics and Structures, Cocoa Beach FL (1999).

2. G.E. Youngblood, R.H. Jones, G.N. Morscher and Akira Kohyama, "Creep behavior for advanced polycrystalline SiC fibers," p. 75 in Fusion Materials Semiannual Progress Report for Period Ending JUne 30, 1997, DOE/ER-0313/22.

3. G.E. Youngblood, R.H. Jones, Akira Kohyama and L.L. Snead, "Radiation response of SiC-based fibers," p. 163, ibid., for Period Ending December 31, 1997, DOE/ER-0313/23.

4. H.M. Yun and J.A. DiCarlo, "Comparison of the tensile, creep and rupture strength properties of stoichiometric SiC fibers," presented at the 23rd International Conference on Engineering Ceramics and Structures, Cocoa Beach, FL (1999).

5. D.J. Senor, G.E. Youngblood, D.V. Archer and C.E. Chamberlain, "Recent progress in thermal conductivity testing of SiC-based materials for fusion," presented at the 3rd IEA/JUPITER Joint International Workshop on SiC/siC Ceramic Composites for Fusion Applications, Cocoa Beach, FL (1999).

6. "Tensile strength and Young's modulus for high-modulus single-filament materials," Standard D3379-75, American Society for Testing and Materials, West Conshocken, PA (1986).

7. Edgar Lara-Curzio and Christiana M. Russ, "Why it is necessary to determine each fiber diameter when estimating the parameters of the distribution of fiber strengths," presented at the 23rd International Conference on Engineering Ceramics and Structures, Cocoa Beach, FL (1999).

8. Yuntian T. Zhu, W.R. Blumenthal, S.T. Taylor and T.C. Lowe, "Analysis of ceramic fiber size dependence and whisker strength," J. Am. Ceram. Soc., 80[6], 1447-52 (1997).

9. S.T. Taylor, Y.T. Zhu, W.R. Blumenthal, M.G. Stout, D.P. Butt and T.C. Lowe, "Characterization of Nicalon fibers with varying diameters, Part I-Strength and fracture studies and Part II-Modified Weibull distribution," J. of Mater. Sci. 33, 0000-0006 (1998).

FABRICATION OF SIC/SIC CERAMIC COMPOSITES USING ADVANCED FIBERS – N.L. Vaughn, L.L Snead, R.A. Lowden (Oak Ridge National Laboratory); A. Kohyama and Y. Katoh (Kyoto University, Japan); J.L. Bailey, J.J. Henry, and A.M. Williams (Oak Ridge National Laboratory)

OBJECTIVE

This paper presents a summary of the development of fiber-reinforced ceramic composites using a SiC matrix derived by forced-flow chemical vapor infiltration SiC and near stoichiometric SiC-based fibers.

SUMMARY

FCVI SiC/SiC composites are being fabricated and will be incorporated in the upcoming 14J experiment in conjunction with the Jupiter and Crest Projects. Three different fiber compositions, three different fiber architectures, and two different interface thicknesses are being evaluated simultaneously. All of the fibrous preforms received a pyrolytic carbon surface coating between the fiber and matrix interface. Many of the non-irradiated samples have been characterized and trends examined.

PROGRESS AND STATUS

Experimental Details

Evaluation of three different fiber types and architectures has been investigated (see Table 1), and an initial comparison of their properties has been completed. Initial comparisons of the Hi-Nicalon™, Hi-Nicalon™ Type-S, and Tyranno™ SA fiber composites will be used to determine the next phase of study. Composites fabricated from satin weave fabric were layed up in a 0-90° orientation. Composites made from plain weave fabric were layed up in a 0±30° orientation. The bottom third of each composite was buffered using ceramic grade Nicalon to minimize waste during the initial densification attempts. Due to the satin weave architecture a volumetric fiber loading of approximately 35% was the maximum. Once the preforms were made, each received a pyrolytic carbon coating derived from decomposition of propylene at 1100°C at a pressure of 40 torr. The resulting average calculated interphase coating thickness was between 150 to 200nm. Each fibrous preform was then infiltrated/densified with a SiC matrix using forced flow chemical vapor infiltration (FCVI) from decomposition of methyltrichlorosilane. The infiltration run times varied from 11 to 17 hours at 1200°C with ambient pressure.

Table 1: Fiber Types and Respective Architectures Examined to Date

Fiber Type	Chopped	Plain Weave	Satin Weave
CG-Nicalon	●	●	·
Hi-Nicalon		●	●
Hi-Nicalon Type S		●	●
Tyranno SA		●	●

Once densified the composites were removed from their graphite holders and cut into flexure bars (30 x 6 x 2.2mm) according to the 14J irradiation capsule bend bar geometry. The samples were then weighed and measured and broken using four-point bending with an upper span of 10mm and a lower span of 20mm. Using the failure loads and dimensions the ultimate stress and matrix microcrack stress of each sample was calculated and an average determined for each composite.

Some difficulty was experienced in fully densifying the Tyranno SA fabric, especially in the satin weave. Aforementioned, the buffer layer was removed to improve infiltration, but showed minimal improvement in the Tyranno SA fabric. Thus the run conditions were altered from the standard conditions.

All of the samples described in this report have yet to be irradiated. Composite samples fabricated from all three fiber types will be incorporated into the upcoming 14J experiment in the HIFR at the Oak Ridge National Lab and planned lower dose rabbit irradiations. Further information will be available after such time. This report covers only non-irradiated samples.

Results

Twelve flexure bars were cut from each sample and six were characterized to determine as-fabricated properties. The remaining six bars from each sample will be incorporated into radiation testing or other characterization procedures. The results from flexure testing can be seen in Figure 2 and Table 2. The dimensions of the flexure bars were 30 x 6 x 2.2mm. The samples were broken using four point bending with an upper span of 10mm and a lower span of 20mm. All testing was done at room temperature.

Figure 1: Representative Load Displacement curves for the three composites of differing fiber type a) Tyranno SA fiber reinforced; b) Hi-Nicalon Type-S fiber reinforced; c) Regular Hi-Nicalon fiber reinforced

(c)
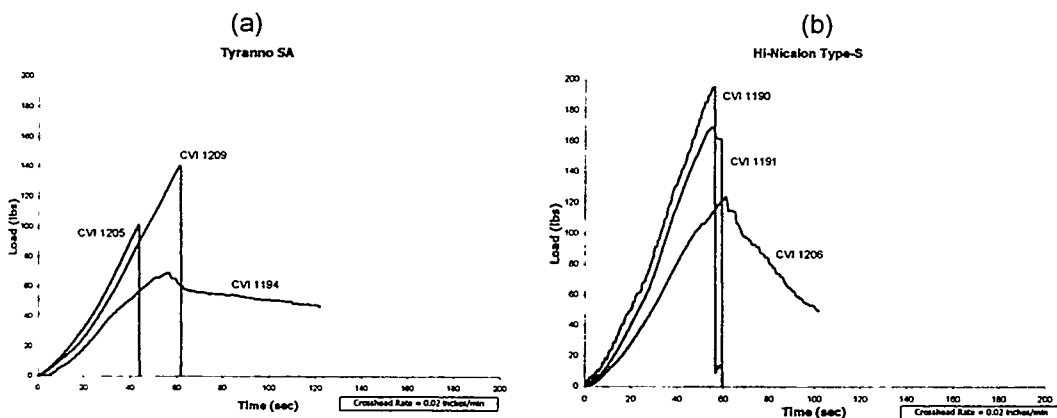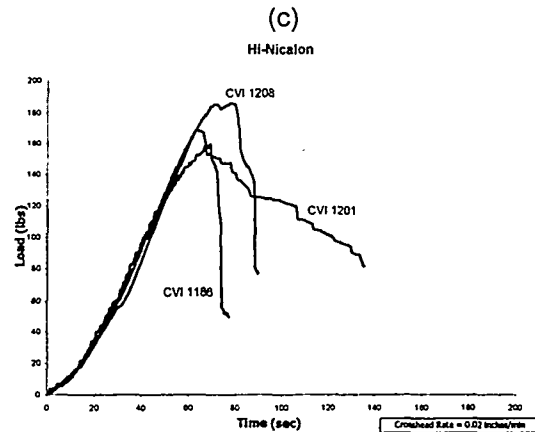
Hi-Nicalon

Table 2: Comparison of Average Strengths and Theoretical Densities (8 tests each); error represents one standard deviation

Fiber Type	UTS (MPa)	MM σ (MPa)	Theor. Density (%)
Tyranno SA	202±62	211±51	78±2%
Hi-Nicalon	367±56	342±67	85±4%
Hi-Nic Type S	352±50	327±44	84±4%

Discussion of Results

Comparing ultimate bend strength and matrix microcracking strength of each composite, it was determined that the composites made using both plain and satin weave Hi-Nicalon were the best performers of the initial composites compared. Though the Type-S and Tyranno composites did not return as high strengths as the regular Hi-Nicalon, their strengths were encouraging and they demonstrated great potential for the applications being considered. The lesser performance of the Type-S composite may be ascribed to the thinner than planned interphase coating observed through SEM of the fracture surface (see Figure 2). This most likely contributed to the brittle behavior exhibited by the Type-S composites as seen in Figure 1.

Figure 2: SEM of fracture surface from CVI 1206 a Type-S fiber composite a) fiber-matrix interface; b) brittle fracture surface; c) different fiber-matrix interface

(a)   (b)   (c)
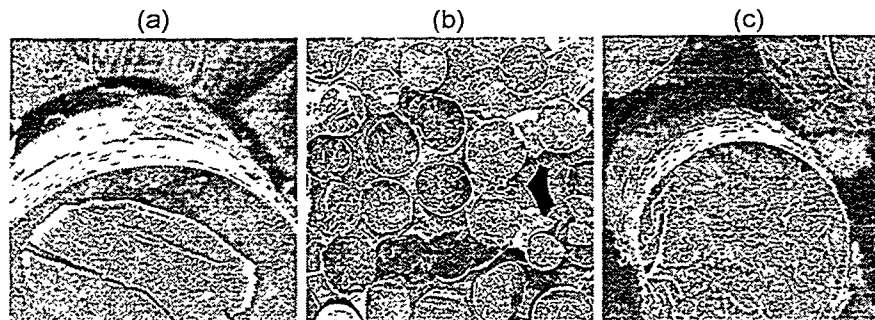
Initially the Tyranno SA fiber composites seemed inferior to the Hi-Nicalon family of composites. But after closer examination the poor performance of the Tyranno composites could be connected to the inability to properly densify the composites. Multiple factors led to the overall low density of the Tyranno composites. The fiber architecture was the first suspect. The bundles of fibers in all three composites densified well, however none of the composites had good inter-layer densification. This was most evident in the Tyranno fiber composites. Large voids between layers were created due to very rapid densification. Such voids between the layers of fabric could have the effect of reduced interlaminar shear and strength properties. Secondly, the choice to buffer the Tyranno composites (to save material) intensified the poorly infiltrated areas within the fabric. This was due to the higher growth rate within the Nicalon fabric ultimately causing sealing off of the gas flow to the Tyranno region. By removing the buffer layer and using the desired fiber types through the entire part, overall properties of the composites were enhanced. Further investigation is recommended on the effects of fiber architecture and layup on the final strength for Tyranno composites.

Figure 3: Cross-section of CVI1201 (Hi-Nicalon Composite), line indicates buffer zone
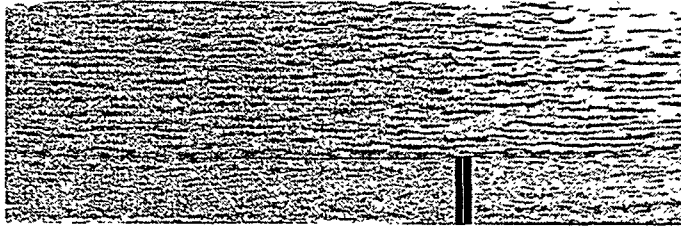
Figure 4: Schematic of Forced Flow Chemical Vapor Infiltration Process
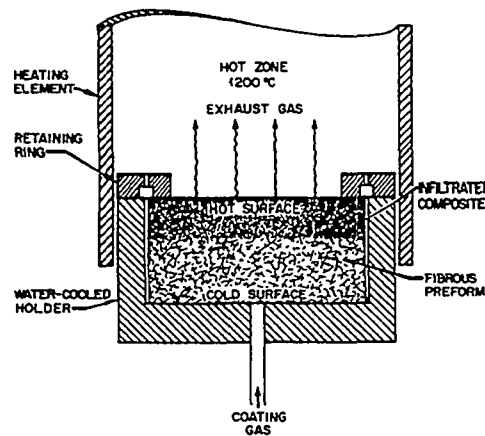
Figure 5: a) 100X picture of Type-S composite fiber bundle; b) 5X picture of Type-S composite showing porosity between fabric layers (arrows indicate pores)

(a)   (b)
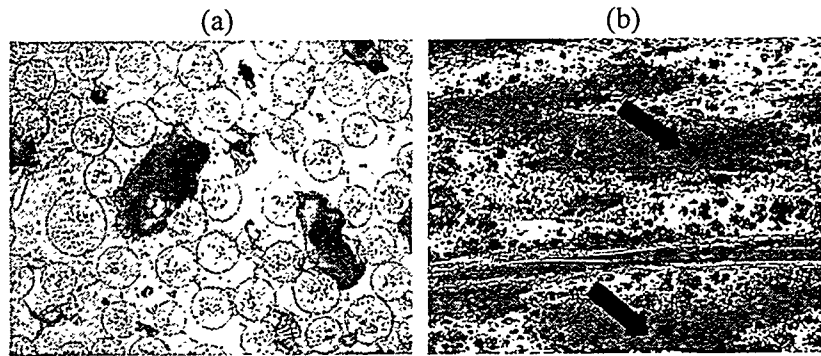
Once the buffer layer was removed, infiltration improved greatly. However, simple layup adjustment did not remedy the inter-layer pores. Therefore, the process conditions were altered. By adjusting the infiltration parameters, slightly better infiltration was achieved both in the fiber bundles and between layers. The parameters were adjusted as seen in Table 2 and improvements were noted immediately (Figure 6). Further development of the FCVI approach to infiltrating these advanced fibers is recommended.

Table 3: Changes in Run conditions for Tyranno plain weave composite.

Infiltration Parameter	Old Conditions	New Conditions
Surface Temperature ($^{\circ}$C)	1200°C	1150°C
MTS Flow Rate (g/min)	0.300	0.250
Hydrogen Flow Rate (sccm)	500	500

Figure 6: Cross-section of CVI1205 and CVI1209 respectively – Tyranno Composite with No Buffer fabricated using a) old run conditions and b) new run conditions

(a)

(b)
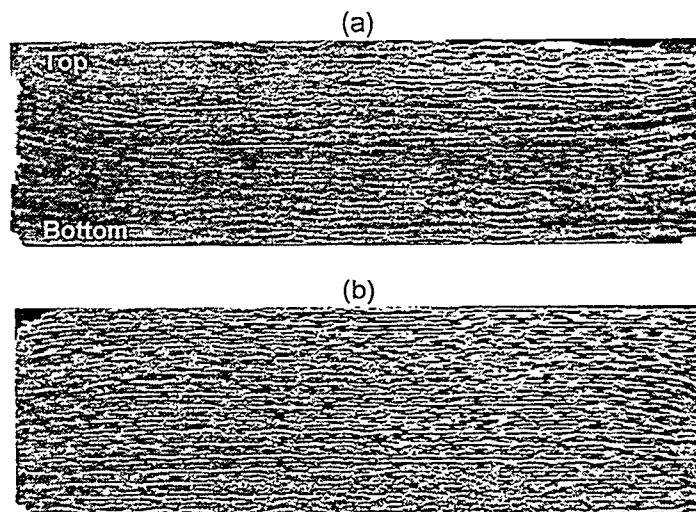
CONCLUSIONS

The advanced fibers performed well when used to replace current lower-grade ceramic fibers in regards to matrix microcracking and ultimate bend strength. Initially, no processing conditions were altered to accommodate the advanced fibers though parameters such as thermal conductivity, fiber diameter and fabric weave need to be considered for a more thorough evaluation of these materials. Ordinarily these factors and others are considered to predict the optimum deposit kinetics during infiltration. By incorporating factors such as fabric architecture and fiber surface roughness, further property improvements will be achieved. Ultimate bend strengths near the 400 MPa range indicate great promise for the use of these new fibers. Though low theoretical density of the composites contributed to inferior properties, further development of the infiltration process should further improve properties. It is recommended that alternate forms of infiltration be investigated alongside FCVI, such as liquid-phase infiltration. Additionally, development of new and current interface coatings is an essential part of the development of these fibers for ceramic composites. Each fiber type reacted differently to the pyrolytic carbon coating, therefore coatings may need to be derived specifically for a given fiber type and architecture. Though the Tyranno fibers did not perform exceptionally during initial studies, past research indicates good results from both Nicalon and Tyranno fibers as preforms for FCVI. Further development of SiC/SiC composites using Type-S, Tyranno, and other advanced fibers is therefore recommended.

METHODS FOR JOINING SILICON CARBIDE COMPOSITES FOR HIGH TEMPERATURE STRUCTURAL APPLICATIONS

METHODS FOR JOINING SILICON CARBIDE COMPOSITES FOR HIGH TEMPERATURE STRUCTURAL APPLICATIONS — C. A. Lewinsohn[1], R. H. Jones[1], M. Singh[2], T. Shibayama[3], T. Hinoki[4], M. Ando[4], Y. Katoh[4], and A. Kohyama[4]. (1) Pacific Northwest National Laboratory*, Richland, WA 99352 USA; (2) NASA Lewis Research Center, Cleveland, Ohio, USA; (3) Center for Advanced Research of Energy Technology, Hokkaido University, Sapporo, Japan; (4) Institute of Advanced Energy, Kyoto University, Gokasho, Uji, Kyoto 611, Japan.

OBJECTIVE

Reliable and practical joining techniques are required to enable the use of silicon carbide composites in fusion energy systems. The variety of demanding criteria for the properties of joints will be described, including those pertaining to fusion energy systems. Issues concerning practical fabrication of joints will also be discussed. Preliminary results on the thermal stability of joints formed by a reaction based joining approach will be presented.

SUMMARY

Joining methods are required to allow affordable fabrication of large or complex SiC/SiC components for fusion energy systems. Previous analysis of the criteria for successful and functional joints indicate that reaction-formed and polymer-derived silicon carbide should be considered as candidate joint materials. Efforts have been initiated to investigate the issues involved with fabrication and durability of these joints. This report summarizes initial investigations of the long-term thermal stability of silicon carbide joints formed by a reaction-based approach. Results indicate that the joint may contain unreacted phases that react further during high-temperature exposure. These results, and their implications, must be confirmed by additional investigations.

PROGRESS AND STATUS

INTRODUCTION

The development of fusion energy systems creates many demanding criteria for the materials to be used in this application. One criterion, is the need for a hermetic material that can chemically and mechanically withstand high-temperatures and neutron fluxes as the "first-wall" material. In addition, the radioactivation of the material to be used as the first wall should be below the limits for a safe and environmentally benign lifecycle. A candidate material for this application is silicon carbide fiber-reinforced, silicon carbide (SiC/SiC). These composites possess desirable thermal, mechanical, and radiation stability. A limitation of these materials, however, is that they can only be produced in limited sizes and shapes. Therefore, to fabricate a complete fusion energy system a method of joining SiC/SiC components, without compromising the properties that are needed, is required.

Since silicon carbide has many desirable properties for use as a "first-wall" in a fusion energy system [1-4], it is undesirable to use a joining technique that introduces dissimilar materials at the inner face of the first wall. In addition, to avoid poisoning the plasma the first wall must be hermetic. Thus, it is highly likely that a means of joining SiC/SiC components to each other is required. Two attractive methods of joining silicon carbide with other forms of silicon carbide have been developed: reaction bonding [5-8], and preceramic polymer adhesives [9-15]. In this paper, preliminary results obtained from joints formed by reaction based forming will be presented. Although other investigators have demonstrated that joints with required values of strengths can be formed [5-8], the long term stability of the joint, and consequent affects on the mechanical properties of the joint, require further attention. In this study joints were annealed under long term static and cyclic, high temperature conditions and the resulting microstructures were examined.

Issues Concerning Joining for Fusion Energy Systems

The criteria typically required for successful ceramic-to-ceramic joints for high temperature applications are usually: (1) adequate mechanical properties, and (2) chemical stability with respect to the components being joined and with the service atmosphere. In addition to these basic requirements, materials for joining silicon carbide composites required for use in fusion energy systems must meet other criteria that assure that fusion energy systems produce economically viable power, and operate in a safe and environmentally benign manner over their lifetimes. Hence, any joining method used for fusion energy systems must also satisfy the conditions of radiation resistance, mechanical integrity, desirable thermal properties, safety during operation and maintenance, prevention of injuries in the case of accidental release, and environmentally benign waste disposal.

The requirements of safety, injury, and waste disposal have been considered from the perspective of identifying elements that form transmutation products, after exposure to fusion energy system operating conditions, that exceed the accepted limits [16,17]. From this point of view, several elements that may potentially be attractive for use in joining must be excluded. Nickel, molybdenum, niobium, and cobalt are unacceptable. In addition, since joining will occur at the construction site of a fusion energy system it is preferable that the joining technique be performed in the ambient environment without applied pressure. Furthermore, the temperature used for joining must be below that which causes degradation of the fibers: believed to be 1200-1400 C. The joining technique must be compatible with the other materials and processes used during assembly of the fusion energy system. Consideration of these factors has led to the selection of silicon carbide formed by two different methods as potential joining compounds: (1) reaction-forming, and (2) pyrolysis of preceramic polymers. In this report, however, only joints fabricated by reaction-forming will be discussed.

EXPERIMENTAL TECHNIQUE

To evaluate the suitability of joints formed by the reaction-based forming approach, plates of monolithic silicon carbide (Hexoloy SA, Carborundum Co., Niagara, NY) were joined using the ARCjoinT technique [6-8]. Two plates of monolithic silicon carbide were cut into 25 mm-long by 4 mm-thick pieces. A carbonaceous mixture was applied to the ends of the plates that were to be joined and this was cured at 110-120°C for 10 to 20 minutes. Subsequently, a slurry of pure silicon powder was applied to the surface of the joint region and heated up to 1425°C for 5-10 minutes. Capillary forces drew the molten silicon into the joint region where it reacted with the carbon to form silicon carbide. The resulting joint material consisted of silicon carbide with controllable amounts of silicon and other phases as determined by the composition of the raw materials and infiltrant. A limited number of joints between pieces of silicon carbide composite material were also fabricated. This composite was reinforced with Hi-Nicalon fibers (Nippon Carbon Co., Yokohama, Japan) that had

been coated with a 1 μm-thick layer of carbon prior to matrix infiltration via chemical vapor infiltration. In addition, an approximately 2 μm-thick layer of silicon carbide was deposited on the outside of the composite to inhibit oxidation at high-temperatures.

The plates that were joined using the method described above were cut into bars that were 44 x 4 x 4 mm. The bars were cut so that the joint was at the middle of the bar and the plane of joining was aligned so that it was parallel to the applied load. Several of the bars were annealed in a resistively-heated, quartz-image, furnace under vacuum. A series of specimens was annealed at 1100°C for ten consecutive 10 h long cycles. The microstructure of untreated and annealed specimens was investigated via scanning electron microscopy (SEM), energy dispersive X-ray analysis (EDX), transmission electron microscopy (TEM), and high-resolution transmission electron microscopy (HRTEM).

RESULTS
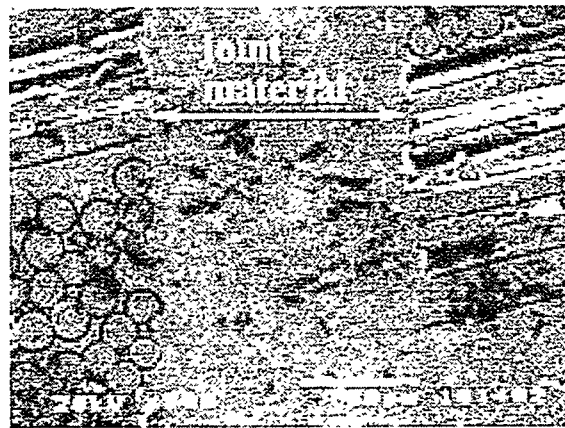
Figure 1. Micrograph of a cross section of two pieces of silicon carbide joined with reaction-bonded silicon carbide.
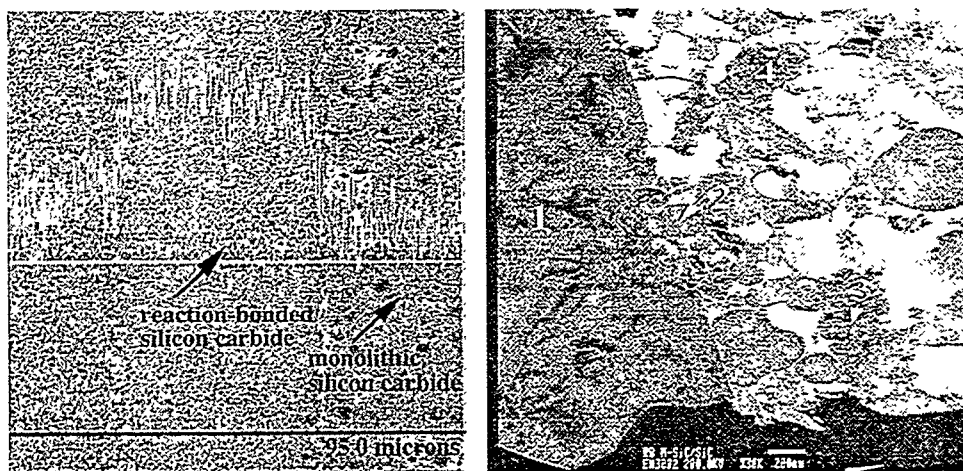
Figure 2. Micrographs of a cross section of two pieces of monolithic silicon carbide joined by reaction-bonded silicon carbide: (a) SEM image, with EDX signal from silicon superimposed, and (b) low magnification TEM micrograph. In (b), 1 indicates monolithic silicon carbide, (2) epitaxial carbon, (3) indicates reaction bonded silicon carbide, and (4) indicates a pore.

To demonstrate the suitability of the joining technique, some joints were made between pieces of a silicon carbide composite material (Figure 1). Joining pieces directly or between the outer coating of silicon carbide was equally successful and no evidence of a deleterious reaction between the joint material and the composite was observed, despite the high-temperature used to melt the pure silicon infiltrant. Apparently, these composite materials are not affected by exposure to the liquid silicon during the short infiltration time.

The microstructure of a joint between two pieces of monolithic silicon carbide is shown in Figure 2. The image shown in Figure 2a shows that the joint region contains an excess of silicon relative to
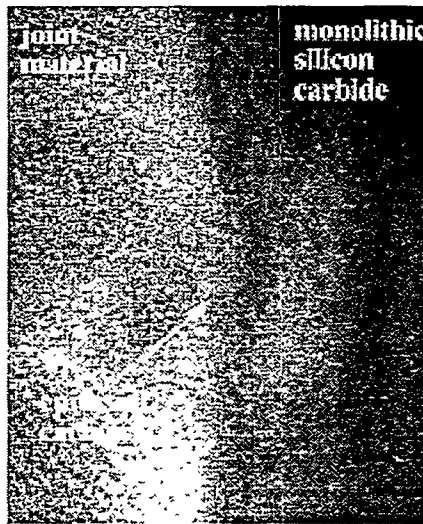
Figure 3. High resolution transmission electron micrograph indicating the presence of carbon with an epitaxial relationship to the monolithic silicon carbide in untreated joints.
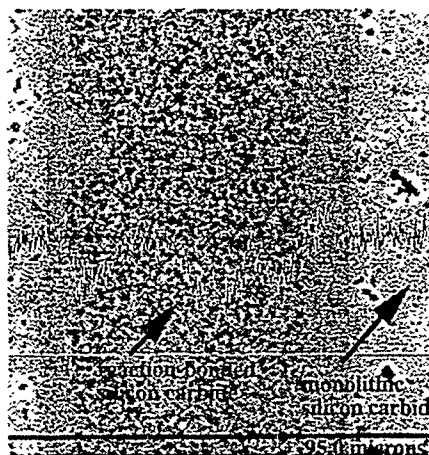
Figure 4. Scanning electron micrograph, with EDX spectra from silicon superimposed, of a cross section of two pieces of monolithic silicon carbide joined by reaction-bonded silicon carbide after annealing for ten cycles to 1100 C.

the monolithic material. This silicon may be silicon that did not react completely during the joint fabrication process. A low resolution transmission electron microscope (TEM) image, Fig. 2b, indicates that the joint material is actually a mixture of three phases: carbon, silicon carbide, and porosity. The porosity may be an artifact of ion thinning. These phases were identified from selected area diffraction patterns. It should be noted that the particle size of the carbon and the reaction-formed silicon carbide are extremely small; i.e., a few hundred nanometers.

It appears that in addition to unreacted silicon in the joint there is also unreacted carbon. Although TEM observations were only limited to the interface between the reaction-bonded silicon carbide and the monolithic silicon carbide, close examination of the EDX spectra of an untreated joint indicates a slight decrease in the silicon signal in the joint near the interface. This suggests that carbon may segregate to the interface region. As shown in Figure 3, carbon particles in an epitaxial relationship with the monolithic silicon carbide were found via HRTEM.

Experiments were conducted to investigate the long term stability of the reaction-formed joint material at elevated temperatures. Several specimens were annealed in a treatment that involved heating the specimens from 25 C to 1100 C in 55 min, holding the temperature at 1100 C for ten hours, rapidly cooling the specimens to 25 C (about 30 min), and repeating this cycle until the specimen had been subject to ten hold periods. Initial SEM microscopy and EDX results, Figure 4, indicates that after this treatment the silicon signal across a typical cross section of a joint is relatively constant. In addition, the appearance of the joint material near the interface with the monolithic silicon carbide is different from that in the middle of the joint. It is possible that further reactions between unreacted silicon and the extremely fine-grained carbon in the untreated joints occurred during annealing. Further microscopy will be conducted to investigate this hypothesis.

CONCLUSIONS

Preliminary studies have shown that joints between silicon carbide and silicon carbide composites can be fabricated by a reliable, low-cost reaction-forming technique. Annealing appears to promote further reaction-forming between unreacted silicon and carbon. Additional work is required to characterize the microstructure and mechanical properties of untreated and annealed joints.

REFERENCES

(1)   R.H. Jones, C.H. Henager, and G.W. Hollenberg, J. Nuc. Mat., **191-194**, 75-83 (1992).
(2)   P. Fenici and H.W. Scholz, J. Nuc. Mat., **212-215** (1994).
(3)   P. Rocco, H.W. Scholz, M. Zucchetti, "Silicon Carbide and the New Low Activation Requirements for a Fusion Reactor First Wall," J. Nuc. Mat., **191-194**, 1474-1479 (1992).
(4)   P. Rocco, M. Zucchetti, "The Impact of Low-activation Criteria on the Development of Novel Materials for Fusion," J. Nuc. Mat., **212-215**, 649-654 (1994).
(5)   B.H. Rabin, and G.A. Moore, "Joining of SiC-Based Ceramics by Reaction Bonding Methods," J. Mat. Synth. & Proc., **1** [3], 195-201 (1993).
(6)   M. Singh, "A Reaction Forming Method for Joining of Silicon Carbide-Based Ceramics," Scripta Mater., **37** [8], 1151-1154 (1997).
(7)   M. Singh, S.C. Farmer, and J.D. Kiser, "Joining of Silicon Carbide-Based Ceramics by Reaction Forming Approach," Cer. Eng. Sci. Proc. 18 [3], 161-166 (1997).
(8)   M. Singh, "Joining of Sintered Silicon Carbide Ceramics For High Temperature Applications," J. Mat. Sci. Lett, in press.

(9)   S. Yajima, K. Okamura, T. Shishido, Y. Hasegawa, and T. Matsuzawa, "Joining of SiC to SiC Using Polyborosiloxane," Am. Ceram. Soc. Bull., **60**, 253, (1981).

(10) A. Donato, P. Colombo, and M.O. Abadirashid, "Joining of SiC to SiC using a preceramic Polymer," pp. 431-436 in <u>High-Temperature Ceramic -Matrix Composites I</u>, A.G. Evans and R. Naslain (eds.), Ceram. Trans., **57**, The American Ceramic Society, Westerville, Ohio, USA, 1995.

(11) W.J. Sherwood, C.K. Whitmarsh, J.M Jacobs, and L.V. Interrante, "Joining Ceramic Composites Using Active Metal/HCPS Preceramic Polymer Slurries," Cer. Eng. Sci. Proc., **18**, 177-184 (1997).

(12) O. Unal, I.E. Anderson, M. Nostrati, S. Ijadi-Maghsoodi, T.J. Barton, and F.C. Laabs, "Mechanical Properties and Microstructure of a Novel SiC/SiC Joint," pp. 185-194 in <u>Ceramic Joining</u>, I.E. Reimanis, C.H. Henager, Jr., and A.P. Tomsia (Eds.), Ceramic Transactions, vol. 77, The American Ceramic Society, Westerville, Ohio, USA, 1997.

(13) P. Colombo, "Joining Ceramics Using Preceramic Polymers," in <u>Interfacial Science in Ceramic Joining</u>, NATO Advanced Research Workshop, Bled, Slovenia, November 12-15, 1997.

(14) P. Colombo, V. Sglavo, E. Pippel, and J. Woltersdorf, "Joining of Reaction-Bonded Silicon Carbide Using a Preceramic Polymer," J. Mat. Sci., **33**, 2409-2416 (1998).

(15) E. Pippel, J. Woltersdorf, P. Colombo, and A. Donato, "Structure and Composition of Interlayers in Joints Between SiC Bodies," J. Eur. Ceram. Soc., **17**, 1259-1265 (1997).

(16) L.R. Greenwood, and F.A. Garner, "Transmutation of Mo, Re, W, Hf, and V in Various Irradiation Test Facilities and STARFIRE," J. Nuc. Mat., **212-215**, 635-639 (1994).

(17) E.T. Cheng, G. Saji, "Activation and Waste Management Considerations of Fusion Materials," J. Nuc. Mat., **212-215**, 621-627 (1994).

DOSE RATE DEPENDENCE OF THE AMORPHIZATION OF SILICON CARBIDE –

L. L. Snead, S. J.Zinkle, W. S.Eatherly, D. K.Hensley, N. L.Vaughn, J. W. Jones (Oak Ridge National Laboratory)

OBJECTIVE

The obejective of this work is to provide information on the dose rate dependence for amorphization of SiC in order to determine under which environments this phenomenon will be an issue for fusion applications.

SUMMARY

Single crystal silicon carbide (SiC) has been 2 MeV silicon ion irradiated in various irradiation temperature and ion flux ranges to measure the effect of these parameters on the critical dose for amorphization. The temperature and flux range for which amorphization was observed ranged from 80 to 400 K and 0.066 to 3×10^{-4} dpa/s, respectively. The critical dose, D_{crit}, was found by locating the depth of the boundary between partially crystalline and fully amorphous material using dark field TEM from samples prepared in cross section. This depth was compared to the damage profile as calculated using the TRIM-96 code. The temperature dependence of D_{crit} is found to agree well with previously reported values, though new evidence suggests a defect species becoming mobile in the 250-300 K range. Also of significance is that D_{crit} was dependent on flux at 340 K, ranging from 0.79 displacements per atom at the lowest ion flux to ~0.6 dpa at the highest flux level. The dose rate dependence of D_{crit} is compared with a chemical rate theory model previously described by the authors. It is seen that the dose rate dependence is substantially weaker than theorized. An extrapolation of the measured dose rate dependence is also compared with recent data on fast neutron amorphized SiC.

PROGRESS AND STATUS

1. Introduction

The amorphization of SiC has been widely studied in support of SiC electronic applications. The bulk of the work utilized high-energy ions and electrons to cause atomic displacement-driven amorphization. Numerous studies [1-10] have shown that SiC becomes amorphous during ion-beam irradiation at temperatures between 77 K and room temperature for damage levels of ~0.1 to 0.5 displacements per atom (dpa.) Over the past several years there has been substantial effort to understand the role of irradiation temperature on D_{crit} [9,11-17]. From this work the onset of dynamic recovery stages have been identified for which D_{crit} increase with increasing temperature. The absolute value of D_{crit} and the onset of these dynamic recovery stages appear to be dependent not only on the irradiation temperature but also on the irradiating species. For example, D_{crit} for electrons has been shown [15] to be ~0.7 dpa at ~50 K, increases to a plateau region of ~ 1 dpa in the 80 to 200 K range and then to increase rapidly with the crystal becoming non-amorphizable above ~300 K. This is compared with a heavy Xe ion irradiation [18] where D_{crit} was approximately ~0.19 dpa at 40 K, increases to ~ 0.24 dpa at 100K and then increases rapidly with temperature at ~500 K. It is noted that the reported doses for these two examples have been recalculated assuming sublattice-averaged displacement energy of 40 eV.

Other variables such as crystal structure (α vs β) [10,14,15] and the effect of implanted species [17] on the amorphization of SiC have been studied. However, the effect of dose rate on the amorphizability of SiC has not been investigated to this point, though it is known that displacement dose rate has a strong influence on the amorphizability of the silicon crystal [19]. This paper presents evidence for dose rate effects in the amorphization of SiC under silicon ion

irradiation. The data are then compared to a chemical rate theory model previously used to describe the dose rate and temperature effects on the amorphization of SiC. Finally, the dose rate data is compared with some limited recent work demonstrating that SiC becomes amorphous by very low dose rate fission-neutron irradiation [20].

2. Experimental Procedure

Single crystal 6H alpha silicon carbide was procured as on-axis n-type wafers from Cree Systems, Inc. The doping level was approximately 4×10^{17} nitrogen atoms/cm^3. Discs, 3 mm in diameter were cut from the 0.36 mm thick wafers and mounted with either Aquadag™ or silver paint to a copper target block. Wafers were received with both sides polished and no further surface preparation was performed prior to irradiation. Two MeV Si ion implantation was carried out with the Tandem Van de Graaff accelerator in the Surface Modification and Characterization (SMAC) user facility of the Solid State Division of ORNL. Temperature was measured by a thermocouple embedded in the target block and controlled by a combination of resistive heating, forced air and liquid nitrogen cooling within ±3°C during irradiation.

Transmission electron microscopy (TEM) samples were prepared by bonding the irradiated wafer face to an identical, non-irradiated sample, followed by diamond slicing of the sandwich. Specimens were mechanically thinned and ion milled with argon ions at 6 keV and 15° using a liquid nitrogen cooled stage during milling. A final mill was performed at 3 keV, 11° for 10 minutes at liquid nitrogen temperature to reduce near-surface amorphization associated with argon implantation. A Phillips CM-30 microscope was used for the TEM. Data on amorphization was found by measuring the depth of the transition from partially crystalline to completely amorphous using weak beam dark field (WBDF) TEM imaging in a (g,3g), g=0006 diffracting condition. This is a departure from our earlier work [9,17] which used the transition range found by TEM bright field imaging. Data on the amorphization threshold, D_{crit}, are found by comparing the measured transition depth with a TRIM-96 [21] calculation. Figure 1 shows the calculated dpa and ion concentration levels for a representative irradiation. Amorphization depth data were only obtained at < 1 nm depths in order to avoid the implanted region.
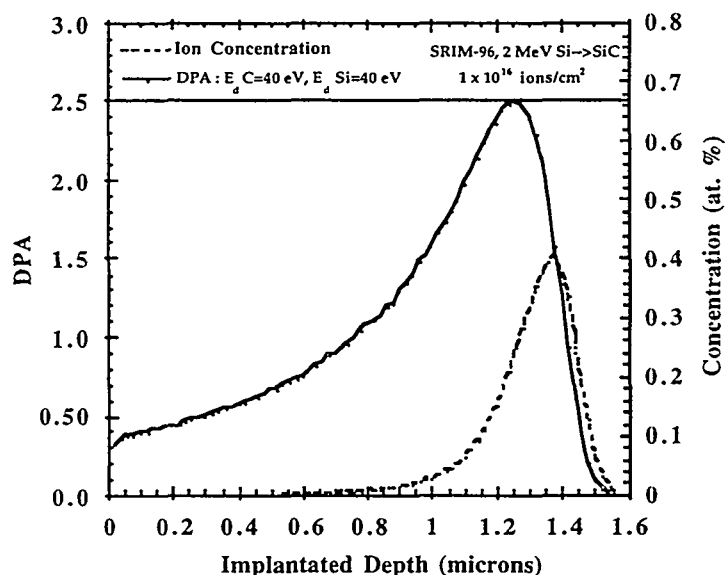
Figure 1

TRIM-96 Simulation of SiC implanted with 2 MeV Si to an ion fluence of 1×10^{16} ions/cm^2 assuming average displacement energy of 40 eV on both the silicon and carbon sublattices.

A cross sectional WBDF image for a sample which has been amorphized by a 2 MeV Si ion irradiation is shown in Figure 2A. Inset in the figure are the diffuse rings of the mid-range

diffraction patterns and diffraction pattern depicting the 6H diffracting conditions used for the WBDF image. Figure 2B is a higher magnification WBDF image showing the transition from partially crystalline to fully amorphous structure at ~340 nm.
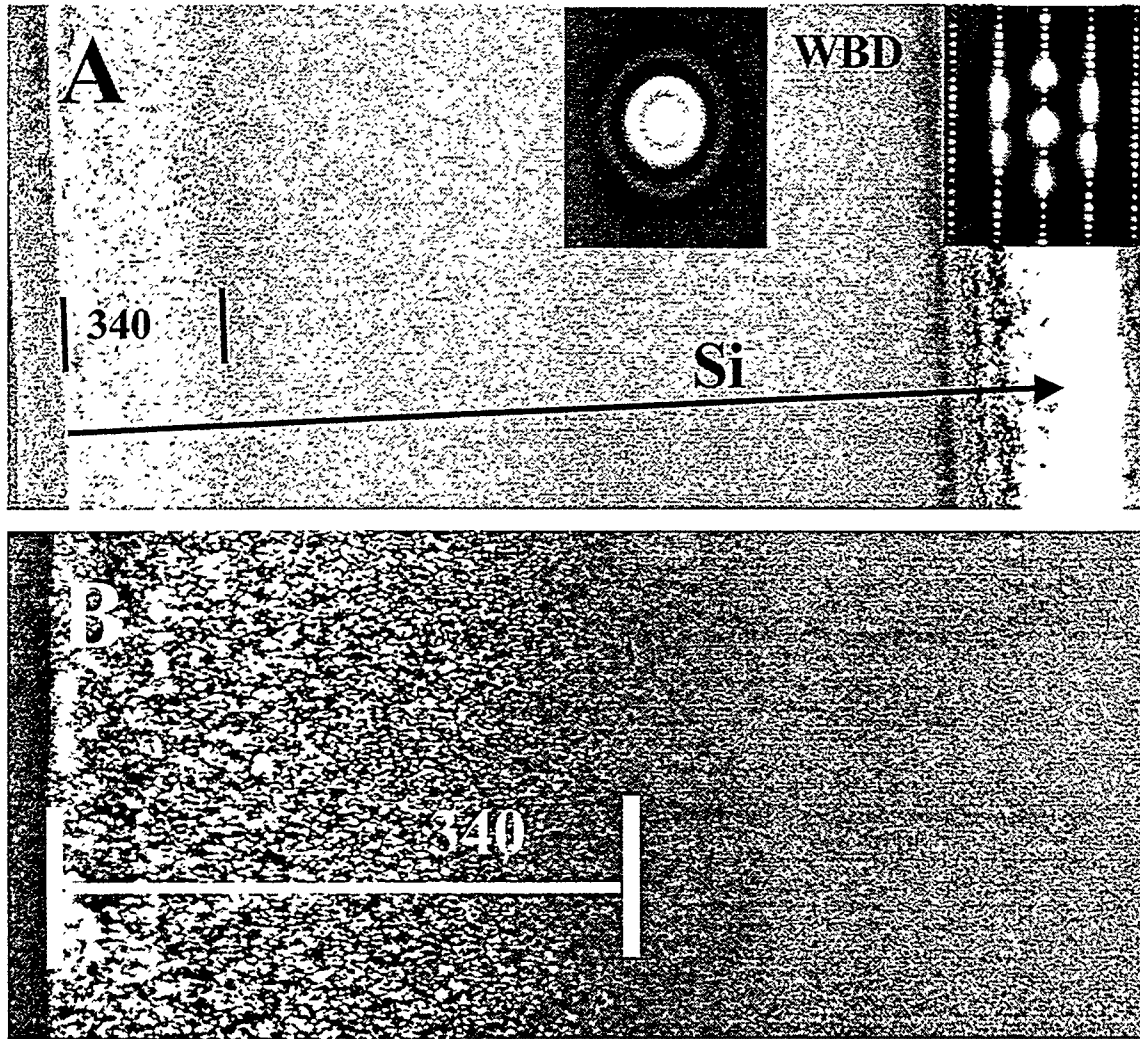
Figure 2: TEM WBDF images of 2 MeV Si ion irradiated SiC at 340 K to 1.2×10^{16} ion/cm^2.

Figure 3 shows the effect of D_{crit} as a function of irradiation temperature at a dose rate of 6.6×10^{-6} dpa/s. The 2 MeV Si ion displacement dose rate for this series varied in the range of $1-5 \times 10^{-4}$ dpa/s. In Figure 3, D_{crit} has increased from about 0.2 to ~0.25 dpa as the irradiation temperature increased from 80 to 100 K. Above this temperature an apparent plateau region exists until approximately 250 K at which point the D_{crit} begins to increase. Though the data is rather limited, it appears that the increase in D_{crit} begins to level off above 300 K and then rapidly increases above ~340 K.

Figure 4 gives the effect of dose rate on D_{crit} at an irradiation temperature of ~340 K. The figure shows the critical dose decreasing with increasing dose rate, dropping from 0.79 dpa to 0.6 dpa as the dose rate increased from $\sim 6.6 \times 10^{-6}$ dpa/s to 1.8×10^{-4} dpa/s. At the highest flux studied (2.9×10^{-4} dpa/s) the critical dose for amorphization increases slightly. The reason for this is unclear, though the trend is consistent with the increased beam heating at the elevated flux rate.
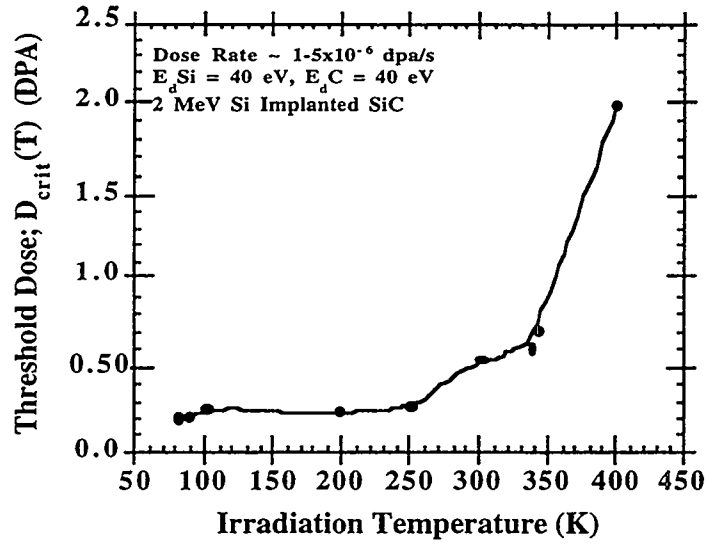
Figure 3: Threshold dose for amorphization as a function of irradiation temperature for Si ion irradiated single crystal alpha SiC.
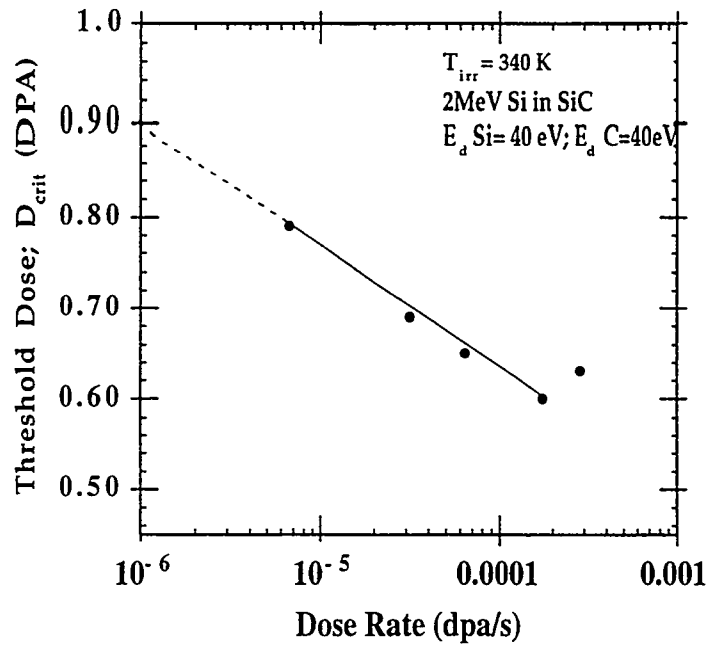
Figure 4: Threshold dose for amorphization as a function of dose rate for Si ion irradiated single crystal alpha SiC.

3. DISCUSSION

As was originally observed by Inui[14] for 2 MeV electron irradiation and by Weber and Wang[18] for 1.5 MeV xenon ion irradiation, the Si ion irradiations of this study show a measurable jump in the critical dose for amorphization above an irradiation temperature of ~90 K. It is noted that such a jump was not seen by Weber [22] for Ne and Ar results, which have closer atomic masses to Si, and therefore more similar cascade events, as compared with Xe. The increase in dose for amorphization (fig 3) demonstrates an increase in dynamic recovery for the crystal possibly due to the onset of carbon interstitial migration. The absolute value of D_{crit} for the Si ion irradiations of this paper increases from ~0.2 to 0.25 dpa which is in good agreement with earlier xenon and argon ion irradiation results [8] but substantially lower than the electron irradiation (~0.4->0.6 dpa) [14] results. This difference is likely due to the difference between the crystal lattice damage produced by high energy electrons, which is limited to the production simple point defects, as compared with the complex defects which can form within and contiguous to heavy-ion induced cascades. The amount of chemical disordering on a dpa-normalized basis is substantially higher for heavy ions as compared with high-energy electron irradiation. If chemical disordering assists the amorphization of SiC (by increasing the lattice free energy), this may explain the lower D_{crit} for ion irradiation as compared with electron irradiations and may also explain the increased temperature for which amorphization is possible with heavy ions. This assumes that in-cascade amorphization is not occurring in SiC, which has not been adequately demonstrated. Results from molecular dynamics simulations[23] and high-resolution TEM observations[10,15] argue against such in-cascade amorphization of SiC.

Above the 90 K dynamic recovery stage a rather broad plateau region (figure 3) exists for which no significant new recovery processes occur. At approximately 250 K the critical dose for amorphization begins to increase indicating the beginning of a second dynamic recovery stage. The trend for increasing amorphization dose for temperatures greater than 300 K was seen for the previous ion irradiations [22]. From figure 3 it appears that the temperature increase begins at a lower temperature than previously seen and may reached a second plateau region before rapidly increasing above 340 K. While additional data points are needed for confirmation, this data suggests a new, intermediate, dynamic recovery stage may be operating.

From the data of figure 4 it is apparent that the rate at which atoms are displaced in SiC does affect the critical dose required to drive the crystal amorphous. Specifically, the dose rate was increased by a factor of almost 50 leading to a reduction in the critical dose for amorphization of about 25%. The temperature at which this dose rate study was performed was 340 K, chosen based on the assumption that this temperature was well within the upper dynamic recovery stage. For this reason a reduction in D_{crit} with increasing dose rate is intuitive if one considers the amorphization occurring as a competition between irradiation-induced atomic displacements and thermally driven replacement of point defects.

In a previous paper [17] the authors modified the chemical rate theory model of Motta and Olander [24] to explain the temperature and dose rate dependent amorphization in SiC. In this model the dose rate (ϕ) dependence scales as the inverse square root of the damage dose rate. By manipulating the data of figure 3, a range in interstitial migration energies for the upper dynamic recovery was determined. [17] With this information the model was applied for the dose rate variation in this study. Analysis revealed that the dose rate dependence measured here is substantially weaker than predicted yielding a dose rate dependence proportional to $\phi^{-1/8}$ as compared with $\phi^{-1/2}$ for the model. One possible explanation for this discrepency may be that at the chosen irradiation temperature, ~340 K, was not sufficiently high for both carbon and silicon interstitials to be mobile. If in fact the evidence for a second plateau region in the range of ~300-350 K is accurate, both Si and C atoms are not fully mobile and the model should not be applied.

Furthermore, the dose rate dependence would be expected to increase from zero at the plateau to the predicted $\phi^{-1/2}$ dependence well above the plateau where full mobility is achieved. Clearly, this model needs to be reexamined regarding its dose rate dependence. Further evidence for the discrepancy between the model and empirical data is the existence of data [20,25] on neutron irradiated Cree β-SiC which fully amorphized at a dose rate of ~8 x 10^{-7} dpa/s. In this case the (above critical) dose was 2.6 dpa at an irradiation temperature of ~332 K, which may also reside on the second plateau. Applying the chemical rate theory model ($\phi^{-1/2}$) would have estimated a threshold dose of more than 10 dpa for amorphization. Furthermore, analysis of a cylindrical sample which was partially amorphized in the same neutron irradiation described above indicates amorphization occurred at approximately 0.9 dpa, which is in good agreement with the empirical $\phi^{-1/8}$ dependence depicted as the solid and dotted line in figure 4.

CONCLUSIONS

(1) A dynamic recovery stage was observed near 90 K for 2 MeV Si ion amorphized alpha SiC in good agreement with previous high-energy electron and xenon irradiations. Evidence indicated that the upper dynamic recovery stage previously identified at ~350 to 400 K may be a combination of at least two independent stages.

(2) A weak dose rate dependence on the amorphization of single crystal alpha-SiC exists at 340 K. As the dose rate is increased, the damage level required to drive the crystal amorphous is decreased. The dose rate dependence is empirically shown to follow a $\phi^{-1/8}$ dependence at 340 K compared with the $\phi^{-1/2}$ of the model previously discussed by the authors. It is speculated that this weaker than predicted dependence relates to a second, previously unidentified annealing stage. The calculated critical dose for amorphization of a fast neutron irradiation induced amorphous SiC sample is consistent with the extrapolated dose rate data from this study.

ACKNOWLEDGEMENT

REFERENCES

1. C.W. White, C.J. McHargue, P.S. Sklad, L.A. Boatner, and G.C. Farlow, Mater. Sci. Reports **4** (2-3), 41 (1989).
2. R.R. Hart, H.L. Dunlap, and O.J. Marsh, Radiat. Eff. **9**, 261 (1971).
3. J.M. Williams, C.J. McHargue, and B.R. Appleton, Nucl. Instrum and Meth. **209/210**, 317 (1983).
4. J.A. Spitznagel, S. Wood, W.J. Choyke et al., Nucl. Instrum. Meth. in Phys. Res. **B16**, 237 (1986).
5. J.A. Edmond, R.F. Davis, S.P. Withrow, and K.L. More, J. Mater. Res. **3** (2), 321 (1988).
6. N.G. Chechenin, K.K. Bourdelle, A.V. Suvorov, A.V. Suvorov, and A.X. Kastilio-Vitloch, Nucl. Instrum. and Meth. in Phys. Res. **B65**, 341 (1992).
7. P. Musumeci, e. al, e. al et al., Nucl. Instrum in Phys. Res. **B 116**, 327 (1996).
8. W.J. Weber, N. Yu, L.M. Wang, and N.J. Hess, J. Nucl. Mat. **244**, 258 (1997).
9. L.L. Snead and S.J. Zinkle, in *MRS Symposium on Microstructure of Irradiated Materials*, edited by I.M. Robertson, L.E. Rehn, S.J. Zinkle, and W.J. Phythian (MRS, Inc., Boston MA., 1995), Vol. 373, p. 377.

10. W.J. Weber, L.M. Wang, and N. Yu, Nucl. Instrum. Meth. Phys. Res. B **116**, 322 (1996).

11. A. Heft, E. Wendler, J. Heindl et al., Nucl. Instr. Meth. **B 113**, 239 (1996).

12. C. Kinoshita and S.J. Zinkle, J. Nucl. Mater. **233-237**, 100 (1996).

13. A. Matsunaga, C. Kinoshita, K. Nakai, and Y. Tomokiyo, J. Nucl. Mater. **179-181**, 457 (1991).

14. H. Inui, H. Mori, and H. Fujita, Phil. Mag. **B 61**, 107 (1990).

15. H. Inui, H. Mori, and T. Sakata, Phil. Mag. **B 66** (6), 737 (1992).

16. H. Inui, Phil. mag. **B 65**, 1 (1992).

17. L.L. Snead and S.J. Zinkle, in *Microstructure Evolution During Irradiation*, MRS Symposium Proceedings, edited by I.M. Robertson, G.S. Was, L.W. Hobbs, and T. Diaz de la Rubia (MRS, Pittsburgh, 1997), Vol. 439, p. 595.

18. W.J. Weber and L.M. Wang, Nucl. Instrum. Meth. Phys. Res. B **106**, 298 (1995).

19. J. Linros, R.G. Elliman, and W.L. Brown, J. Mater. Res. **3** (6), 1208 (1988).

20. L.L. Snead, S.J. Zinkle, J.C. Hay, and M.C. Osborne, Nucl. Instrum. Meth. in Phys. Res. **B141**, 123 (1997).

21. J.F. Ziegler, J.P. Biersak, and U. Littmark, *The Stopping and Range of Ions in Solids* (Pergamon Press, New York, 1985).

22. W.J. Weber, L.M. Wang, N. Yu, and H.J. Hess, Mat. Sci. Eng. **A253**, 62 (1998).

23. T. Diaz de la Rubia, M.-J. Caturla, and M. Tobin, in *Microstructure of Irradiated Materials*, MRS Symposium Proceedings, edited by I.M. Robertson, L.E. Rehn, S.J. Zinkle, and W.J. Phythian (Materials Research Society, Pittsburgh, 1995), Vol. 373, p. 555.

24. A.T. Motta and D.R. Olander, Acta Metall. Mater. **38**, 2175 (1990).

25. L.L. Snead and J.C. Hay, accepted J. Nucl. Mater. (1998).

INTERPHASE INTEGRITY OF NEUTRON IRRADIATED SILICON CARBIDE COMPOSITES – L. L. Snead and E. Lara-Curzio (Oak Ridge National Laboratory)

OBJECTIVE

The objective of this study is to apply a residual stress analysis to the interface between Nicalon™ fiber and the interphase coating to explain the experimental result of debonding during neutron irradiation.

SUMMARY

SiC/SiC composites were fabricated from Hi-Nicalon™ fibers with carbon, pseudo-porous SiC and multilayer SiC interphases. These materials were then irradiated in the High Flux Beam Reactor with fast neutrons to a dose level equivalent to 1.1 dpa. Results are presented for bend strength of both non-irradiated and irradiated materials. Degradation in ultimate bend stress was seen for all materials studied, while the matrix micro-cracking stress was unchanged. Within the interphases studied the multilayer SiC interphase material showed the least degradation (8-20%) in ultimate bend stress, while porous SiC underwent the greatest degradation (~35%). The fiber matrix interphases are studied with TEM for both non-irradiated and irradiated materials. While no irradiation induced microstructural evolution of the interphase was observed, debonding of the interphase from the fiber was observed for all cases. This debonding is attributed tensile stresses developed at the interface due to densification of the Hi-Nicalon™ fiber. Residual stress analysis of the fiber matrix interface clearly indicates that for densification of Hi-Nicalon™ and volumetric expansion of the CVD SiC matrix corresponding to these irradiation conditions tensile stresses occur well in excess of those which can be withstood by these, or any other viable SiC composite interphase.

PROGRESS AND STATUS

1. Introduction

Both the physical and dimensional properties of ceramic grade Nicalon™ fiber are unstable at relatively low neutron fluence [1-3]. The general behavior of these fibers is the inverse of what occurs in fully dense SiC. For example, fully dense SiC undergoes minor isotropic expansion under irradiation while Nicalon™ fiber shows a substantial densification. The elastic modulus and strength of stoichiometric SiC decrease slightly under neutron irradiation while Nicalon™ shows a significant increase. The significant densification of the ceramic grade Nicalon™ (about 5% at 1 displacement per atom, dpa) has been blamed for the substantial (~40%) reduction in bend strength which occurs in CVI SiC matrix composites [4]. The densification of ceramic grade Nicalon™, Hi-Nicalon™ and Morton CVD SiC is given in Figure 1 [5]. Recently, the Nicalon™ fiber thermomechanical properties have been improved by altering the method of cross-linking the spun polymer thereby reducing the oxygen content from 15%. (ceramic grade Nicalon™ fiber) to less than 0.5 % (Hi-Nicalon™) [6]. The average SiC crystallite size for this product increases by more than a factor of two over the ceramic grade fiber, and the fiber elastic modulus undergoes a large increase while the strength decreases slightly. The density of the Hi-Nicalon™ fiber is also increased from 2.55 g/cc (ceramic grade Nicalon™ fiber) to 2.74 g/cc, which is approximately 85 % theoretical SiC density. Also of interest for nuclear applications, the Hi-Nicalon™ fiber density did not to undergo the dramatic densification seen in ceramic grade Nicalon™ fiber [5]. Composites produced similarly to those in this study fibers show similar degradation to those fabricated with the ceramic grade Nicalon™, albeit to a lesser extent [5].
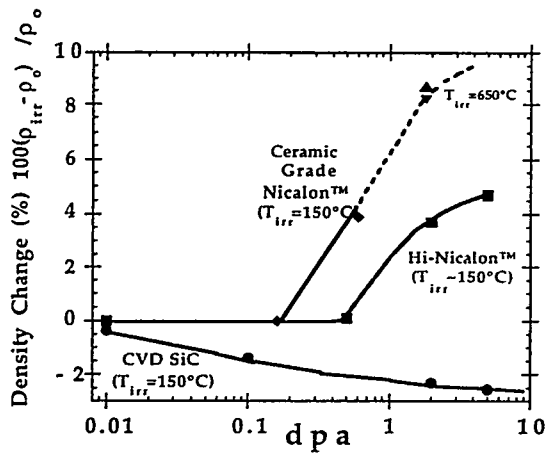
Figure 1: Volumetric changes under irradiation.
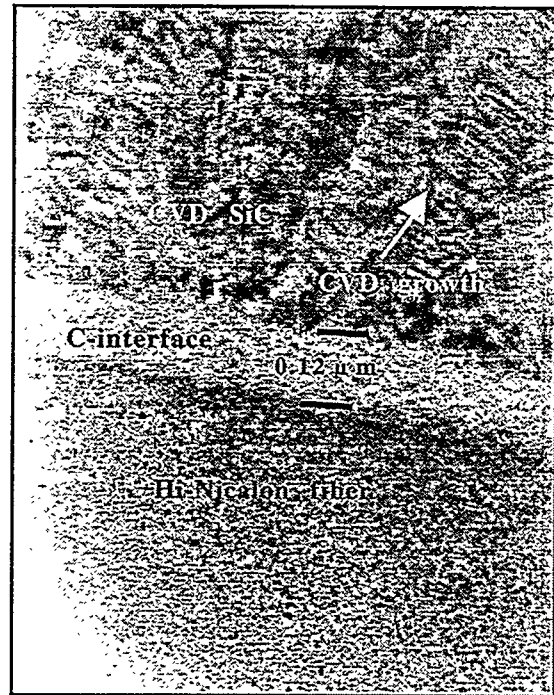
Figure 2: TEM of pyrolitic C interphase.

2. EXPERIMENTAL

Materials

A series of composites were fabricated to deposit a porous SiC interphase first on ceramic grade Nicalon fiber to optimize the process and then on low oxygen content Hi-Nicalon fiber for the irradiation study. The carbon interface was applied to the composite prior to SiC infiltration by decomposition of propylene gas at 1100 °C. Figure 2 shows a TEM micrograph for the 0.12 μm carbon interphase. Previous work has shown that the structure of this interphase deposited onto Nicalon™ in a similar manner is only partially graphitic with basal planes preferentially lying normal to the axis of the fiber [7]. The interface between the Hi-Nicalon™ fiber and the carbon interphase does not show evidence of the silica layer present in ceramic grade Nicalon™ materials processed in a similar fashion. Deposition variables for the porous SiC interphase were infiltration temperature and the relative mixture of methyltrichlorosilane, argon, methane and hydrogen flow gasses. A substantial degradation of the standard Nicalon fiber was seen due to interaction with the (porous SiC) reactant gasses leading to very low composite strengths, especially on the higher temperature surface of the preform, presumably due to accelerated kinetics. For this reason, a thin (0.1 μm) coating of carbon from a propylene precursor was deposited on fibers prior to the porous SiC deposition as a reaction barrier. The results of the process development led to a composite infiltrated at 900°C. Figure 3 shows a high resolution TEM image of the "porous" SiC interphase. This micrograph shows interconnected β-SiC surrounding islands of poorly graphitized carbon. This interphase is best described as a two component mixture of carbon and β-SiC, where the SiC is the predominant phase. The porous and pyrolitic carbon SiC interfacial composites were processed at the High Temperature Materials Laboratory at the Oak Ridge National Laboratory using the forced chemical vapor infiltration (FCVI) method [8]. The infiltrated silicon carbide matrix was deposited from methyltrichlorosilane with a typical infiltration time of 18 hrs. The dimensions of the as fabricated discs were 4.45 cm diameter and 1.25 cm thickness.
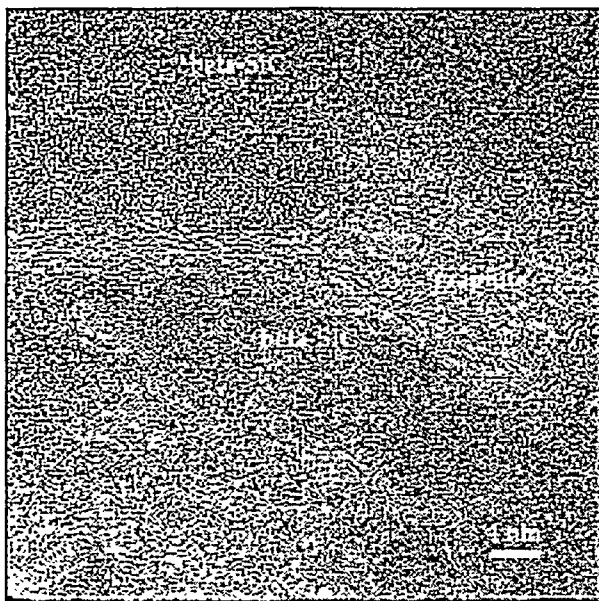
Figure 3: HRTEM of porous SiC interphase.

Figure 4: TEM image of interface between fiber and first multilayer SiC interphase.

Composites containing a multilayer SiC fiber coating were fabricated using isothermal CVI of Hi-Nicalon™ fiber preforms by Hyper-Therm High-Temperature Composites, Inc. The fabric was cut into individual plies 15 x 30 cm and laid-up in a $(0,90)_s$ fiber architecture containing 8 plies per preform. The preform was compacted to ~35% fiber volume within a graphite holding tool during deposition of the fiber coating and subsequent SiC matrix densification. An initial layer of pyrolytic carbon 20 nm thick was deposited on the fiber preform to prevent the previously discussed interaction with the SiC processing phases. The first SiC layer of the multilayer fiber coating is then deposited followed by a 20 nm interrupted layer of pyrolytic carbon. A TEM image of the interface between the fiber and the first interlayer is given in Figure 4. The composite architecture for all composites was 1800 denier (500 filament yarn) plain weave fabric and was laid-up inside a graphite holder with a fiber volume fraction of approximately 40 %. The fabricated composite void fraction was 10-12%.

Irradiation

Composite samples were machined to dimensions of 2.5 x 3 x 25 mm for the irradiation study. The porous SiC material surfaces were machined such that the top and bottom surfaces had exposed fabric where the surface layer had been ground flat. The multilayer SiC material had a thin CVD SiC overcoat (~100 μm) so that the top and bottom fabric layer were not exposed. The fabric orientation was such that the fabric was in the plane of the width and length axes of the bend bar. All edges of the bend bars were ground flat, thus some of the fibers were machined away for the porous SiC interfacial materials. All materials were cleaned in acetone and isopropyl alcohol prior to the irradiation capsule assembly.

A single irradiation capsule, SiC-1, was assembled consisting of subcapsules which contained the samples. The bend bar samples had at least one side in flush contact with the inside of sub-capsule to allow for heat transfer. Sub-capsules were either 6061 aluminum alloy or V-4Cr-4Ti alloy. The sample temperature was achieved by machining gas gaps into the sub-capsule so that the nuclear heating was conducted through the helium cover gas. A single type-K thermocouple was embedded in each sub-capsule and the temperature was continuously recorded. Following

welding of the aluminum capsule exterior the capsule was evacuated using a turbomolecular pump and back-filled with ultra-high purity helium. This procedure was repeated three times with a final backfill to helium over pressure of 15 psi. The positive pressure of helium was monitored during the irradiation period.

The SiC-1 capsule was inserted into the V-16 in-core thimble of the High Flux Beam Reactor at the Brookhaven National Laboratory. The duration of the irradiation was one reactor cycle which corresponds to an approximate fast neutron fluence of 1.1×10^{25} n/m^2 (E>0.1 MeV). This corresponds to ~1.1 displacements per atom (dpa) in SiC, assuming a sublattice-averaged displacement energy of 40 eV. The irradiation temperature for the multilayer-SiC interfacial composite was 385°C and was constant within 5°C throughout the irradiation. Two subcapsules were used for the porous-SiC interfacial composite. The lower temperature subcapsule which was made of type 6061 aluminum alloy had a constant irradiation temperature of 260°C, constant within 5°C throughout the irradiation. The higher temperature subcapsule, which was fabricated from vanadium, initially achieved a temperature of 1060°C and then decreased in temperature linearly with time to a final temperature of 910°C. It is believed that this decrease in temperature is due to swelling of the vanadium subcapsule (associated with interstitial pickup from the capsule gas) which narrowed the gas gap thus reducing the temperature. Other factors such as increased emissivity of the vanadium subcapsule surface would also cause a reduction of the subcapsule temperature. Post-irradiation examination of the SiC samples did not show any evidence of reaction with the subcapsules.

Testing

All transmission electron microscopy was carried out on mechanically thinning and polished samples. For the case of the neutron irradiated specimens, the thickness of the foil was left at greater than 200 μm to minimize grinding damage to the supposed weakened interface. Argon ion milling of was carried out at 15° and 6 keV. All bend testing was conducted at room temperature using a four-point bend fixture with load and support spans of 0.5 and 2.0 cm, respectively. The cross-head displacement speed was 8.5×10^{-4} cm/s. Where possible, a furnace anneal at temperature and atmosphere comparable to the in-reactor tests were performed to ensure oxidation or other factors were not responsible for any composite degradation.

RESULTS AND DISCUSSION

Results from the room temperature bend testing for both non-irradiated and 1.1 dpa irradiated composites are given in Table 1. It is noted that data of irradiated bend bars are from two samples at each condition, thus are statistically limited. However, several samples of each type were tested in the non-irradiated condition yielding more statistically meaningful data. The matrix micro cracking stress was taken from the load-displacement curve as the departure from linearity and is therefore a macroscopic matrix stress. Undoubtedly, limited matrix micro cracking occurs at stresses below this value. From the table it is seen that the results from the furnace anneal of control samples was within statistical scatter of the non-annealed control samples. Though it is noted that the ultimate fracture stress for the multilayer SiC interphase appears low.

From Table 1, within statistical limitations, the macroscopic matrix microcracking stress is unchanged. The ultimate fracture stress appears to be reduced in each case, with the multilayer SiC interphase showing the least reduction (~8-20%) and the porous SiC interphase showing the most (~35%).

Interphase Type	Matrix Microcracking Stress (MPa)	Ultimate Fracture Stress (MPa)
Multilayer SiC		
Non-irradiated	250±32 (6 tests)	507±75
Non-irradiated,385°C anneal	264±17 (5 tests)	438±21
Irradiated, 385°C	290,244	462,371
Pyrolytic Carbon		
Non-irradiated	214±38 (4 tests)	375±51
Irradiated, 385°C	172, 285	235,347
Porous SiC		
Non-irradiated	298±22 (8 tests)	515±19
Non-irradiated,260°C anneal	335, 332	507,510
Irradiated, 260°C	268, 251	347,344
Non-irradiated,1000°C anneal	287, 415	457,507
Irradiated, 1042→910°C	210,201	332,304

Table 1 :Bend Test Results for Hi-Nicalon™/CVI SiC Composites
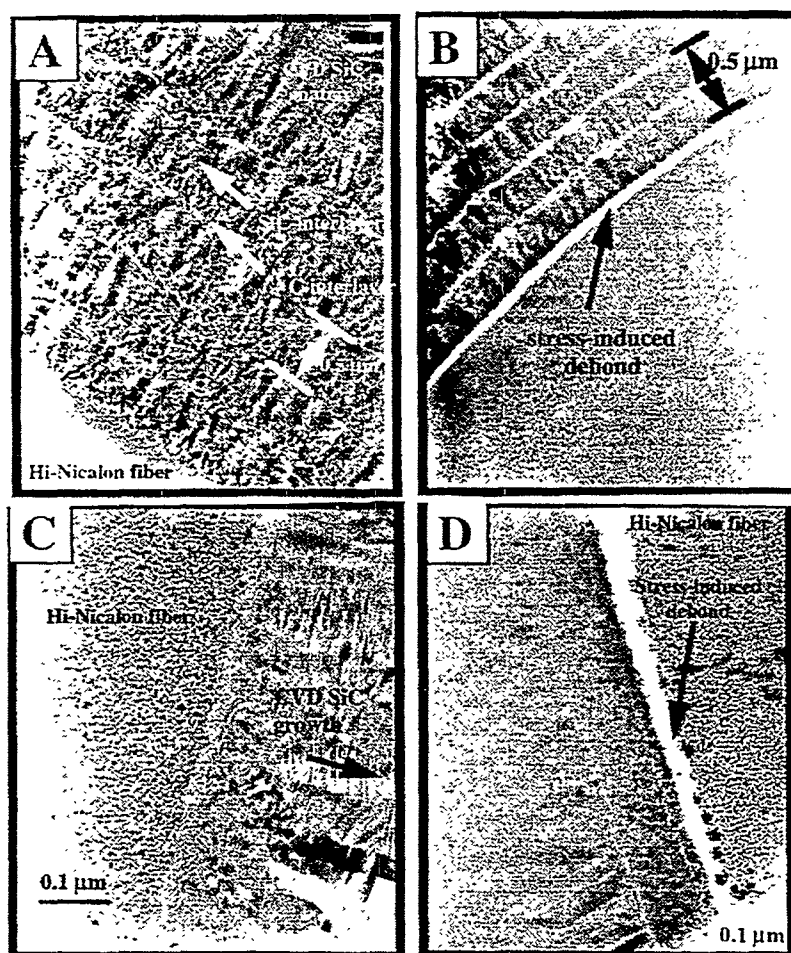
Figure 5: TEM of non-irradiated and irradiated multilayer and porous SiC interphase interfaces.

Transmission electron microscopy reveals debonding at the fiber-interphase boundary for all three interphase materials. For the case of the porous SiC interphase, debonding within the fiber also occurred, though debonding at the boundary was still more common. Non-irradiated (fig 5A,C) and irradiated (fig 5B,D) interphases are shown in Figure 5. A debond width of ~50 nm is clearly visable at the boundary between the fiber and first multilayer (fig 5B). Debonding was observed for regions opaque to the 300 keV electrons indicating that debonding is not due to preferential milling by the argon ions. The micrograph depicting debonding for the porous SiC interphase (fig 5D) is one which exhibited debonding within the fiber. Debond width in this case is on the order of 80 nm. Debonding for the pyrolitic carbon interphase (not shown) occurs at the interface between the fiber and the carbon interphase.

Assuming unirradiated physical properties for fiber and matrix and the irradiation-induced volumetric changes for Hi-Nicalon™ and CVD SiC given in figure 1, a residual stress analysis for the fiber/matrix interface can be performed. The micromechanical analysis of the infiltrated bundle can be simplified by considering a system of three concentric cylinders of increasing radii, a and b, where the inner cylinder represents a fiber that is coated by a thin layer of thickness (b-a). This bundle is embedded in a matrix represented by a cylinder of radius c of thickness (c-b). The magnitude of c is selected so that $v_F = a^2/c^2$, where v_F is the fiber volume fraction in the composite. The values of a and b are selected from actual values of the fiber radius and the thickness of the fiber coating. To further simplify the analysis, the following assumptions are made: (1) all the phases in the composite are linear elastic and isotropic, (2) no relaxation of stresses during irradiation or during cooling from the fabrication temperature, and (3) fibers and matrix exhibit volumetric changes as a result of neutron irradiation.

Equilibrium of forces in a long cylindrical differential element result in $\sigma_r = \frac{d}{dr}(r\sigma_\theta)$ and

$\sigma_\theta = \frac{d}{dr}(r\sigma_r)$ where σ_p and σ_θ are the radial and tangential stresses, respectively and r is the

radial position. When combined, these equations yield solutions of the form: $\sigma_r = A - \frac{B}{r^2}$ and

$\sigma_\theta = A + \frac{B}{r^2}$ where A and B are integration constants that have different values for each of the

three phases in the model composite. Boundary conditions require continuity of traction at the fiber-fiber interphase, and at the fiber-interphase-matrix interfaces and zero-normal forces acting on the free surface, i. e.: $\sigma_r^f(r=a) = \sigma_r^c(r=a)$, $\sigma_r^c(r=b) = \sigma_r^m(r=b)$,

and $\sigma_r^m(r=c) = 0$. Upon enforcement of the boundary conditions, the unknown integration constants A and B can be eliminated in favor of the still unknown interfacial normal stresses, P_1 and P_2 as follows

$$\sigma_r^f = \sigma_\theta^f = -P_1 \qquad r \leq a \tag{1}$$

$$\sigma_r^c = \frac{P_1 a^2 - P_2 b^2}{b^2 - a^2} + \frac{a^2 b^2 (P_2 - P_1)}{r^2 (b^2 - a^2)} \qquad a \leq r \leq b \tag{2}$$

$$\sigma_\theta^c = \frac{P_1 a^2 - P_2 b^2}{b^2 - a^2} - \frac{a^2 b^2 (P_2 - P_1)}{r^2 (b^2 - a^2)} \qquad a \leq r \leq b \tag{3}$$

$$\sigma_r^m = \frac{P_2\, c^2}{c^2 - b^2}\left(1 - \frac{c^2}{r^2}\right) \qquad b \leq r \leq c \tag{4}$$

$$\sigma_\theta^m = \frac{P_2\, c^2}{c^2 - b^2}\left(1 + \frac{c^2}{r^2}\right) \qquad b \leq r \leq c \tag{5}$$

Deformation compatibility requires that the radial displacement (e.g., the tangential strains) be the same at the interface for the phases meeting there. Mathematically this is expressed as: $\varepsilon_\theta^f = \varepsilon_\theta^c$, $r = a$ and $\varepsilon_\theta^c = \varepsilon_\theta^m$, $r = b$. By assuming a long cylindrical assembly, end-effects are neglected and mathematically the plane-strain assumption is expressed as: $\varepsilon_z^f = \varepsilon_z^c = \varepsilon_z^m$, which means that plane cross-sections will remain plane after deformation.

Equilibrium of axial forces requires that the sum of forces in the z direction be equal to zero, i.e.,

$$\frac{a^2}{c^2}\,\sigma_z^f + \frac{(b^2 - a^2)}{c^2}\,\sigma_z^c + \frac{(c^2 - b^2)}{c^2}\,\sigma_z^m = 0 \tag{6}$$

Because the phases are assumed to be both isotropic and perfectly elastic, the relationship between the stresses and the strains will be given by:

$$\varepsilon_r = \frac{\sigma_r}{E} - \frac{v}{E}\left(\sigma_r + \sigma_\theta + \sigma_z\right) + \alpha\,\Delta T + \varepsilon_r^o \tag{7}$$

$$\varepsilon_\theta = \frac{\sigma_\theta}{E} - \frac{v}{E}\left(\sigma_r + \sigma_\theta + \sigma_z\right) + \alpha\,\Delta T + \varepsilon_\theta^o \tag{8}$$

$$\varepsilon_z = \frac{\sigma_z}{E} - \frac{v}{E}\left(\sigma_r + \sigma_\theta + \sigma_z\right) + \alpha\,\Delta T + \varepsilon_z^o \tag{9}$$

where α is the linear coefficient of thermal expansion, ΔT is the change in temperature from the fabrication temperature to room temperature and ε^o is the transformation strain resulting from neutron irradiation. Substituting the expression for the stresses (Equations 1-5) into the constitutive equations (Equations 7-9) and enforcing the boundary conditions in Equations (6-8) yields a 4 x 4 system of linear simultaneous equations for the unknown interfacial pressures P_1, P_2 and the axial stresses in the fiber and the fiber coating. The axial stress in the matrix can then be readily determined from Equation 6.

Figure 6 shows the predicted radial stress at the fiber-fiber coating interface as a function of neutron irradiation. Note that those stresses would exist if there continuity of radial displacement existed at the interface. At the 1.1 dpa dose level of this study figure 6 yields a residual stress above one GPa, which is clearly higher than could be withstood by the interphases leading to debonding.
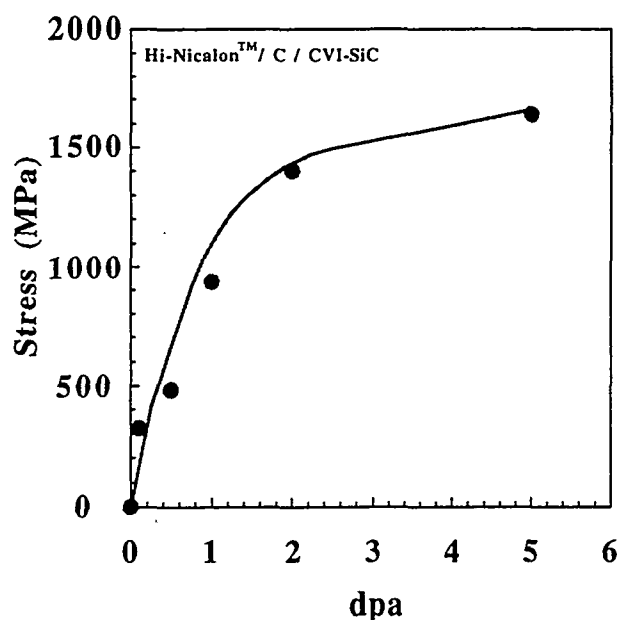
Figure 6: Residual stress at interphase.

CONCLUSIONS

(1) Bend strength results indicate that at 1.1 dpa ultimate fracture strength is decreased for Hi-Nicalon™ composites. The relative degree of decrease appears to depend on the interphase type with multilayer SiC interphase suffering the least reduction (~8-20%), followed by the pyrolitc carbon interface (~22%) and the porous SiC interphase (~35%).

(2) Transmission electron microscopy reveals debonding at or near the interface between the fiber and interphase.

(3) Residual stress analysis indicates that radial tensile stresses develop at the interphase during irradiation due to induced densification of the Hi-Nicalon™ fiber. These stresses are considerably higher than can be withstood by these or any viable SiC/SiC interphase, indicating that high Nicalon™ is of limited application in neutron irradiation environments.

REFERENCES

[1] K. Okamura, A. Matasuzawa, and M. Sato, J. Nucl. Mater. 155-157 (1985) 329.
[2] A. Kohyama, H. Tezuka, and S. Saito, J. Nucl. Mater. 155-157 (1988) 334.
[3] L.L. Snead, M. Osborne, and K.L. More, J. Mater. Res. 10 (1995) 736.
[4] L.L. Snead, D. Steiner, and S.J. Zinkle, J. Nucl. Mat. 191-194 (1992) 566.
[5] L.L. Snead et al., J. Nucl. Materl 253 (1998) 20.
[6] T. Seguchi, N. Kasai, and K. Okamura, Proceedings of International Conference on Evolution in Beam Applications , 1991) p. .
[7] R.A. Lowden and K.L. More, in Interfaces in Composites, Vol. 170, eds. C.G. Pantano and E.J.H. Chen (MRS, Pittsburgh, 1990) p. 273.
[8] T.M. Besmann et al., J. de Physique 50 (1988) 273.

3.0 FERRITIC/MARTENSITIC STEELS

SUMMARY OF IEA WORKSHOP/WORKING GROUP MEETING ON FERRITIC/MARTENSITIC STEELS FOR FUSION—R. L. Klueh (Oak Ridge National Laboratory)

OBJECTIVE

The objective of this report is to describe the working group meeting and workshop held to review planned and completed work that is being undertaken to prove the feasibility of using ferritic/martensitic steels for fusion applications.

SUMMARY

The International Energy Agency (IEA) Working Group on Ferritic/Martensitic Steels for Fusion held a workshop at ECN Nuclear Research, Petten, The Netherlands, 1-2 October 1998. The Working Group, consisting of researchers from Japan, the European Union, the United States, and Switzerland, met to review research that has been completed since the previous meeting and to continue planning and coordinating an international collaborative test program on reduced-activation ferritic/martensitic steels for fusion applications. At the workshop, data were presented from the continuing research on the IEA heats of steel that are being studied in the collaboration. Data on these and other reduced-activation steels in the irradiated and unirradiated condition were presented. Other subjects that were discussed included effects of a ferromagnetic steel in a fusion machine, the effect of helium on properties, and the development and application of oxide dispersion-strengthened steels for fusion. A Working Group status-review meeting is planned in conjunction with the International Conference on Fusion Reactor Materials (ICFRM-9) in Colorado Springs, Colorado, USA, 10-15 October 1999, at which time plans for a workshop to be held in 2000 will be finalized.

PROGRESS AND STATUS

Introduction

The IEA Working Group on Ferritic/Martensitic Steels for Fusion under the auspices of the IEA Executive Committee for the Implementing Agreement on Fusion Materials conducted a workshop at ECN Nuclear Research, Petten, The Netherlands, 1-2 October 1998. Researchers from Japan (4), the European Union (5), the United States (3), and Switzerland (1) participated. Russian Federation participation was invited, but no one from there attended the meeting. The objective of the Working Group is the establishment and coordination of an international collaborative test program to determine the feasibility of using ferritic/martensitic steels for fusion.

This workshop was the ninth meeting of the Working Group, which was formed as a result of a workshop on ferritic/martensitic steels in Tokyo in October 1992. At the first meeting following the Tokyo workshop, the Working Group developed specifications for large heats of reduced-activation steels and outlined a collaborative research program. Two 5-ton heats of the IEA-modified F82H steel and two 1-ton heats of JLF-1 steel were produced, fabricated into plates, and distributed to the participants of the collaboration. Subsequent meetings have been used to plan a test program and to coordinate the acquisition of the data needed to prove feasibility for the steels for fusion.

The Petten meeting was a follow up to the meeting at Tokyo, Japan, 3-4 November, 1997, in which information was presented that indicated helium has an embrittling effect on ferritic/ martensitic steels irradiated at 250-400°C. At the Tokyo meeting and at ICFRM-8 at Sendai, Japan, 27-31 October 1997, several investigators presented data on oxide dispersion-strengthened (ODS) steels as possible structural materials that will allow higher operating temperatures. At Petten, information was presented on both of these subjects, along with recently developed information on the properties of the IEA heats of reduced-activation steels and other reduced-activation steels. Information was also presented on work designed to determine the effects produced by ferritic/martensitic steels in the high magnetic fields of a magnetically confined fusion reactor.

Research and Development Activities

The following is a brief description of the information presented at the Petten workshop. Copies of viewgraphs and other information presented at the workshop are appended to this summary.

Ferromagnetic Effects

At one time it was believed that the expected strong interaction of a ferromagnetic material with the magnetic fields of a magnetically confined fusion system would make it impossible to use the ferritic/martensitic steels as structural materials. Calculations in the early 1980s indicated that the effect could be taken into account in the design of the reactor. Because these early studies were but cursory analyses of the problem, questions as to the magnitude of the effect persist, and detailed design studies as well as experimental investigations are required to eliminate this uncertainty.

P. Ruatto has been involved in a program at FZK Karlsruhe to study the transient eddy current problems and magnetic fields and forces that can develop with the use of ferritic/martensitic steels. Ruatto's presentation (given by E. Materna-Morris) discussed some of the information derived with the three-dimensional finite element method program AENEAS that was developed at FZK. Results were presented for calculations that examined the effect of plasma disruptions on the outboard blanket segment of the DEMO helium-cooled pebble bed outboard blanket segment and the European Helium cooled pebble bed test blanket module in ITER. A centered plasma disruption was considered for the DEMO, and the forces on the components were calculated and described for the MANET steel. The force calculations for a plasma disruption in ITER were also summarized. The conclusion was that for a correct mechanical design of a fusion power plant it is necessary to include an electromagnetic analysis, and the AENEAS is an appropriate tool for this task.

K. Shiba discussed the Japan Atomic Energy Research Institute (JAERI) research effort on the effect of a ferromagnetic material (ferritic/martensitic steel) on the operation of a fusion machine. (Note that this presentation was part of Shiba's presentation in the section on Steel Properties— Irradiated, and the viewgraphs on the ferromagnetic effects are included in his presentation in that section.) Three subject areas are being pursued by JAERI: (1) an experimental study of the use of a ferritic steel for plasma ripple reduction in ITER by the installation of a "ferritic board" on the JFT-2M tokamak, (2) an experimental study of the possibility of producing rippleless plasma operation with a reduced-activation martensitic steel as the vacuum vessel by the installation of a reduced-activation (F82H) ferritic steel liner in a small tokamak, and (3) using this lined tokamak to conduct research on possible undesirable effects due to ferritic/martensitic steels on plasma production and control. Work began on (1) this past year and involved a computer simulation and preliminary experiment using JFT-2M. The results indicated a reduction in ripple magnitude and a modification of the magnetic field over the whole plasma region due to the insertion of the ferritic board.

R. Klueh has attempted to determine what work has been conducted and what work is ongoing throughout the world on ferromagnetic effects, and the results of that have been summarized. A copy of that summary is included in the appended material following Ruatto's presentation.

Steel Properties—Unirradiated

The work of the Monbusho fatigue test program in Japan to develop mini-sized test techniques, study size effects, develop a strain-control test technique without contacting the specimen, and determine the fatigue behavior of JLF-1 steel was described by A. Kohyama. A hydraulic servo-controlled testing machine using laser measurements has been developed that should be applicable to hot-lab testing. Testing of full-sized hour-glass specimens (100 mm long, 9 mm at the center of the specimen) and miniature specimens (25.4 mm long, 1.25 mm at the center) measured comparable properties except under the condition of very low cycle fatigue. The machine was used to test JLF-1 base metal and TIG weldments, and the results indicated that fatigue strength (S-N curve) of the base

metal was less than that of the weld metal. A correlation was developed between the fatigue limit and Vicker hardness that was related to the tensile strength, which was shown to provide good predictions for the fatigue limit.

A. Alamo presented data on the effect of thermal aging on the tensile and Charpy behavior of six European Union (EU) reduced-activation ferritic/martensitic steels and F82H and JLF-1. Aging was for up to 13400 hours at 250, 350, 400, 450, and 550°C. The EU steels included steels with high carbon and nitrogen (LA12Ta), low C with (LA12TaLC) and without (LA12LC) tantalum and low nitrogen (LA12TaLN). There was also high (11%) chromium (LA4Ta) and high (3%) tungsten (LA13Ta).

There was little effect of aging on the yield stress of the F82H after aging 13400 h, but the reduction of area was significantly reduced above 400°C. The Charpy results for the EU steels indicated that there were chemical composition effects. For example, aging the high-tungsten steel to 10000 h at 350, 400, 450, and 550°C, resulted in a reduction of upper-shelf energy (USE) and an increase of transition temperature for the higher temperatures, which was associated with Laves phase. There were also indications of chromium effects, especially at 400°C aging, which may be due to chromium-rich α' formation. The F82H and JLF-1 showed a reduction in USE and an increase in transition temperature after thermal aging 13400 h at 550°C, but little effect after aging at 250, 350, 400, and 450°C. Laves phase formation may play a role in this behavior. Tensile, creep, and Charpy tests were also made on thermally aged F82H weldments produced by the TIG and electron beam (EB) processes. TIG welds, which were post-weld heat treated (PWHT), displayed a similar strength but a slightly lower ductility and USE compared to the base metal. In particular, some degradation of impact properties was found after aging at 550°C. However, the results for EB welds without a post-weld heat treatment still need to be compared with steels that have a PWHT to fully evaluate the properties of the EB weldments.

K. Shiba reported on the continued progress on the JAERI round robin tests that are generating a range of mechanical and physical properties data for the IEA heat of F82H. Mechanical property tests that have been made or that are in progress include hardness, tensile, Charpy impact, fatigue, fracture toughness, and creep. The range of physical properties include density, specific heat, thermal expansion, thermal and electrical conductivity, melting point, Young's modulus, Poisson's ratio, modulus of rigidity, and magnetic hysteresis. Other measurements include the determination of a continuous-cooling-transformation diagram, water corrosion, hydrogen permeability, and hydrogen cracking. Some of the mechanical property tests have also been conducted on aged steel and on weldments. Shiba presented recent tensile, Charpy, fatigue, and fracture toughness results on thermally aged and unaged F82H steel. Analysis of the extracted precipitates from the aged steel indicated a tendency toward the production of Laves phase for steel aged at 550, 600, and 650°C. Mechanical properties of the weldments were generally comparable to the base metal.

Fabrication of the blanket structure of a fusion power plant presents many difficulties, especially welding and joining, and A. Hishinuma presented information on a potential joining technique. Hot Isostatic Pressing (HIP) bonding is a potential technique for certain geometries. However, the optimum conditions for HIP bonding are 150 MPa at 1040°C for 2 h followed by tempering. Such a high temperature and long hold time can have negative effects on the properties due to austenite grain growth. Spark plasma sintering (SPS) bonding, which involves the formation of a plasma between the parts being joined, is being studied by JAERI as an alternative to HIP bonding. SPS conditions are 20-50 MPa at 800-900°C with hold times of 0.08-1 h. Excellent joints have been obtained with this technique; the joints are improvements over HIP-bonded material in metallographic appearance and strength.

Steel Properties—Irradiated

The status of the JAERI irradiation program on F82H was reviewed by K. Shiba. Irradiations are being carried out in the High Flux Isotope Reactor (HFIR) in the U.S./JAERI collaboration and in the Japan Materials Test Reactor (JMTR) and the Japan Research Reactor (JRR-2/JRR-3/JRR-4). Accelerator (dual/triple beam) irradiations are also being conducted. The program involves tensile, Charpy, and fracture toughness measurements and microstructural studies of the irradiated steel.

E. V. van Osch reported on results of work at ECN at Petten on post-irradiation properties of the IEA F82H plate and welds. Irradiation was in the High Flux Reactor (HFR) to 2-3 dpa and the testing (tensile, impact, and static fracture toughness) is in progress. A 65 kg heat of steel (ECN-BS) was obtained and irradiated with F82H. ECN-BS contained somewhat more Cr, C, and Ta and less B than the F82H. The ECN-BS steel showed improved Charpy properties over the F82H after irradiation to 2.5 dpa at 300°C. Comparison was made between EB and TIG weldments of the IEA F82H. Before irradiation, the EB welds had a higher strength and ductility; testing of the irradiated welds is in progress. Irradiations to 10 dpa at 300°C are in progress, with the testing to be performed under the next EU Framework Program (1999-2002). The F82H is included in this experiment, but emphasis of this framework program will be on the new EUROFER steels. This experiment will also include work on B-doped steels to investigate the effect of helium on properties, to investigate the distribution of the boron in the steel, and to measure the helium content.

The Japanese universities (Monbusho) program on the properties of irradiated reduced-activation ferritic steels for fusion reactors was reviewed by A. Kohyama. Most of this work was on the JLF-1. The first irradiations were carried out in FFTF. The results included: tensile studies conducted on steels irradiated to 60 dpa at 365-600°C, swelling data obtained after irradiation to 70 dpa at 420°C, ΔDBTT (change in ductile-brittle transition temperature) data obtained from irradiations to 50°C at ≈400°C, and pressurized-tube irradiation creep tests for specimens irradiated to 35 dpa at 520°C. Current work involves experiments in HFIR, JOYO, and JMTR. At present a dual-beam ion-irradiation facility (DuET) is being constructed at Kyoto University that will be used for future in-beam studies. The facility is expected to begin operation in FY 1999.

Another Monbusho effort is the Ferritic Isotopic Tailoring (FIST) experiment in which isotopic-tailored F82H disks were irradiated in HFIR to simulate the fusion environment effects of producing hydrogen and helium in the steel. Preliminary results from TEM and shear-punch tests have been obtained and are being evaluated.

The effect of tantalum in the ORNL 9Cr-2WVTa steel on Charpy and tensile properties after irradiation was discussed by R. L. Klueh. The steel has excellent strength and impact toughness before and after irradiation in the Fast Flux Test Facility (FFTF) and the High Flux Reactor (HFR). The ductile-brittle transition temperature (DBTT) increased only 32°C after 28 dpa at 365°C in FFTF, compared to a shift of ≈60°C for a 9Cr-2WV steel—the same as the 9Cr-2WVTa steel but without tantalum. This difference occurred despite the two steels having similar tensile properties before and after irradiation. The 9Cr-2WVTa steel has a smaller prior-austenite grain size, but otherwise microstructures are similar before irradiation and show similar changes during irradiation. The irradiation behavior of the 9Cr-2WVTa steel differs from the 9Cr-2WV steel and other similar steels in two ways: (1) the shift in DBTT of the 9Cr-2WVTa steel irradiated in FFTF does not saturate with fluence by ≈28 dpa, whereas for the 9Cr-2WV steel and most similar steels, saturation occurs by <10 dpa, and (2) the shift in DBTT for 9Cr-2WVTa steel irradiated in FFTF and HFR increased with irradiation temperature, whereas it decreased for the 9Cr-2WV steel, as it does for most similar steels. The improved properties of the 9Cr-2WVTa steel and the differences with other steels were attributed to tantalum in solution and the loss of that tantalum during irradiation by precipitation. The precipitation still needs to be confirmed.

ODS Steels and Alloy Development

B. van der Schaaf reviewed the possibility of oxide dispersion-strengthened (ODS) steels for fusion applications. These steels contain a high number density of (TiO_2 or Y_2O_3) oxide particles that provide enhanced creep strength. One problem with the conventional and reduced-activation ferritic/martensitic steels being investigated for fusion is that the upper operating temperature will be limited to ≈550°C, and this limits the systems in which they can be used (e.g. water-cooled system). ODS steels with their improved creep properties offer the possibility of extending that temperature to 600°C and higher. Because they are strengthened by a high number density of small oxide particles, the oxide particles could provide sites for defect recombination and helium trapping and thus reduce swelling and suppress helium bubble effects. Most of the prior work on these materials for nuclear applications were for fuel canning for fast breeder reactors. The results for that application indicated significant improvement in creep strength over conventional steels with the helium effects suppressed. The major problems

involved the anisotropy due to the powder metallurgy fabrication techniques used to make the tubes. There is limited experience on thick-wall parts, and although reduced-activation ODS steels are being developed, there is as yet no literature information available on them.

Van der Schaaf concluded that the ODS reduced-activation steels being developed show considerable promise that indicates they could, if developed, extend operating temperatures above 600°C (assuming creep controls and not corrosion) and reduce helium effects. However, the fabrication route needs to be developed for the larger sections needed in a fusion reactor blanket. Joining may present some difficulty and should be addressed early in the development stage.

Work on the development of ODS steels was described by A. Alamo. The high-chromium ferritic steels (MA 956 and MA 957) had elongated grains (recrystallized grain size d>1 mm, recrystallization temperature >1300°C) with a high texture, anisotropic properties, and low ductility. The creep and aging behavior of these steels was studied. The MA 957 with an optimized grain size showed excellent creep resistance at 650°C relative to a 15-15 austenitic stainless steel, especially for longer rupture times (>10^4). Precipitation of intermetallic phases (χ, Laves, and α' phases) was detected in the thermal aging studies and irradiation experiments.

The development of a 9Cr ODS steel which can transform to martensite is being pursued. The objective is to avoid intermetallic phase precipitation and reduce the anisotropy of the properties compared to the fully ferritic materials. 9Cr-Mo and 9Cr-W steels containing Y_2O_3 are being examined. These steels developed an eqiaxed grain structure when normalized and tempered, and there was no grain growth in the range 1000-1250°C. The yield stress for each of these steels was higher than that for MA 957 with a somewhat reduced, but still high, reduction of area. This development study is continuing.

A. Hishinuma reported on the JAERI efforts to produce an ODS reduced-activation ferritic/ martensitic steel. The compositions that have been investigated were variations on the F82H with 8% Cr, 0-1.75% W, 0.1-0.28% Ti, 0.15% O, 0.1-0.23% Y, 0.12% C. The manufacturing process involved mechanical alloying the powders followed by hot extrusion at 1050°C to fabricate the steel, after which it was normalized and tempered. Microstructures have been produced that have a fine-grain structure that appears relatively equiaxed. Excellent Charpy and tensile properties were obtained from several of the experimental steels. The compositional variations indicated that the tensile properties depended on the Y_2O_3 and tungsten content, but much less on the titanium content.

G. R. Odette discussed the recent review of the fusion materials program in the U.S. by The Fusion Energy Systems Advisory Committee of which Odette was a member. They recommended that the fusion materials program seek to integrate modeling, experiment, and data-base development to develop advanced materials for fusion. This means bringing more modeling into the materials program, as the committee viewed the program as being deficient in this area. Odette feels that one area where such an approach can be applied is the study of fracture of fusion reactor components. Since fracture behavior of irradiated materials is of critical importance for fusion, micromechanical-based local fracture models need to be applied with small specimen measurement of fracture resistance on unirradiated and irradiated material to provide the resultant properties necessary to predict limits for fusion structures. These results need to be further combined with microstructure-property models that reflect the effect of alloy composition, processing variables, and irradiation. The implementation of such an integrated approach was discussed in terms of work being conducted at the University of California at Santa Barbara. As one example, work on reactor pressure vessel embrittlement was cited and discussed.

Helium Effects Studies

Electron microscopy studies of the reduced-activation ferritic/martensitic steels IEA F82H and OPTIMAX A were discussed by R. Schaüblin. The F82H was irradiated to 0.5 and 1.7 dpa with 590 MeV protons at PSI in Switzerland, and F82H and OPTIMAX A were irradiated to 2.5 dpa at 250°C in HFR in Petten. The dislocation structure, carbide composition and size distribution, and grain/lath boundary chemistry of the F82H irradiated with protons were determined for the unirradiated (before and after tensile deformation) and irradiated steels. The

results for the proton irradiation of the IEA F82H generally indicated that there was essentially no difference in the microstructural defects in the as-received (unirradiated), deformed (material taken outside the necked region), and irradiated conditions. The $M_{23}C_6$ particles, which constituted the majority of the precipitate, were found to be coherent with the matrix. Chromium enrichment at prior austenite grain boundaries was detected for the normalized-and-tempered steel, but after irradiation, chromium depletion was observed.

Neutron irradiation of OPTIMAX A at 250°C produced no defects, but faceted cavities were observed. For the F82H, on the other hand, no cavities were present, but black dot (loops) damage was observed.

Helium effects studies using boron-doped F82H steel irradiated in HFIR and JMTR were reported by K. Shiba. Standard F82H, which contains a small amount of natural boron, F82H to which natural boron was added, and F82H to which ^{10}B was added were compared. The ^{10}B is transmuted to helium; natural boron contains $\approx$20% ^{10}B. Irradiation in HFIR at 300-500°C up to $\approx$30 dpa produced very little effect on the tensile properties (yield stress and total elongation). Tensile specimens irradiated in JMTR to 0.7 dpa and 120 appm He for the ^{10}B-doped steel had little effect on the yield stress, but there was an indication of a slight reduction in total elongation and reduction of area. Although the standard F82H and the F82H containing the ^{10}B addition had similar Charpy impact properties in the unirradiated condition, irradiation to 0.2-0.6 dpa at 250-350°C in JMTR produced a much larger shift in the Charpy transition temperature for the ^{10}B-doped ($\approx$100 appm He) steel. At temperatures above $\approx$400°C, there was only a small difference in the Charpy behavior of the steels with and without ^{10}B. Microstructural examination of steels irradiated to 57 dpa in HFIR indicated 2×10^{21} m^{-3} (3 nm) cavities present in the ^{10}B-doped steel but none in the non-doped steel.

E. Matera-Morris reported on the effect of helium on steels after dual-beam irradiation and neutron irradiation in the HFR. MANET I hardened more than the F82H did during dual-beam irradiation to 0.3 dpa and 500 appm He. For irradiations in HFR at 300°C, a larger shift in Charpy transition temperature was observed for MANET I and OPTIFER II than for the ORNL 9Cr-2WVTa and F82H. Dual-beam irradiation of the F82H to 0.8 dpa and 300 appm He at 250°C produced a larger shift in the transition temperature than for a similar irradiation in HFR. The excess shift was attributed to helium. Likewise, to explain the relative Charpy transition temperature behavior of MANET I, OPTIFER II, F82H, and 9Cr-2WVTa (listed in order of decreasing transition temperature shift) after irradiation in HFR, the results were correlated with ^{10}B content, which transmuted to helium, although it was stated that the helium contribution to the shift in transition temperature cannot be determined quantitatively because it is not possible to separate helium and alloying effects. Scanning electron microscopy observations of relative amounts of cleavage and intergranular fracture on the fracture surfaces were correlated with the Charpy results (change in transition temperature).

A. Kimura discussed a small punch test procedure used to evaluate the effect of helium on the DBTT of 9Cr-2W steels. Disk specimens 3-mm in diameter and 0.22-mm thick were irradiated in a 36 MeV α-particle beam from a cyclotron. An energy degrader was used to uniformly implant 120 and 580 appm He (0.048 and 0.23 dpa) in the disk. Irradiation was at <150°C. Hardness data were used to estimate a yield stress and yield stress increase ($\Delta\sigma_y$) during irradiation. Data from JMTR irradiations where no helium was present indicated that the shift in yield stress fit a dpa$^{1/4}$ law, which agreed with the results for the cyclotron-irradiated specimens, indicating no helium effect on hardening (just the effect of displacement damage). The data for the cyclotron-irradiated material fit the linear correlation between $\Delta\sigma_y$ and ΔDBTT obtained from the JMTR data, indicating that helium did not affect the shift in DBTT. From hardening changes during annealing, it was found that helium reduced the rate of recovery of the irradiation hardening, suggesting that helium stabilizes the defect clusters. TEM indicated that helium decreased the size of the clusters but increased the number density. In this experiment, irradiation to 0.23 dpa and 580 appm He at <150°C did not affect irradiation hardening and embrittlement .

E. V. van Osch reported on work being started to study the post-irradiation welding of helium-containing steel at ECN in Petten. Neutron irradiated F82H plates of 1, 3, and 5 mm thickness that were irradiated in HFR to 2 dpa ($\approx$5 appm He) and some 1 mm plates that were irradiated to 2.5 dpa were available for the study. The irradiated 1, 3, and 5 mm plates were successfully TIG welded to unirradiated plates with no external defects

detected by SEM. The 1 and 3 mm plates were welded in a single pass with no filler metal, and the 5 mm plate contained a Y-groove and was welded with 4-6 passes. Further inspection of the welds is planned. Heats of steel have been ordered with ^{10}B, ^{11}B, and natural boron, so that it will be possible to generate various amounts of helium up to 250 appm He and higher.

Strategy for the Development of Ferritic/Martensitic Steels for Fusion

Presentations were made on the strategy for the development of ferritic/martensitic steels in Japan, EU, and the U.S. by A. Hishinuma, B. van der Schaaf, and F. W. Wiffen, respectively. The stated goal of this session was the development of a united strategy that could be presented by representatives from the Working Group (van der Schaaf and Hishinuma) to an IEA panel that was meeting in Copenhagen the following week, 5-9 October 1998, to consider a coordinated strategy for fusion materials development.

The strategies for Japan and the EU are pointed toward a DEMO using a martensitic steel, and this gives rise to dates for selecting a given material for the construction of the plant. Japan has a potential date of 2015 for selecting a material for DEMO, and the EU has a date for a DEMO-relevant design by 2009 based on conventional-type ferritic/martensitic steels. Should ODS steels be successfully developed, the date for a DEMO-relevant design for this material would be 2015.

In contrast to Japan and the EU, the U.S. has no plans for a DEMO and instead is involved in a science-based approach in which the technical program will emphasize, "enabling technologies for plasma experiments, domestic and internationally." The materials work will be targeted at developing materials that will support economically attractive, environmentally attractive, and safe fusion energy source designs.

A. Kohyama presented some further views on the Japanese strategy. He expressed concern about what should be done beyond the work presently being carried on the large heats of the IEA F82H and JLF-1 that are being studied in the IEA collaboration. He emphasized the need for a clear strategy for ferritic/martensitic steel development to be presented to the fusion community.

The discussion on the strategies of the various programs indicated that at present it appears there are common features in the strategies of the three programs, starting with the need to coordinate the materials development with the design and engineering community. The question of whether ferromagnetic structural materials are acceptable for magnetically confined fusion still needs to be answered, as do questions on the effect of the simultaneous helium and displacement damage on properties (embrittlement). An expansion of the design window for ferritic/martensitic steels is desirable, and it is agreed that the ODS steels offer the best approach to achieve that goal by raising the operating temperature. This development needs to be pursued.

Other questions vital to the application of ferritic/martensitic steels to fusion include nuclear transmutations that will burn out elements of the steel (e.g., W, Ta, etc.), the effect of tungsten on the breeding ratio, compatibility issues and the need for barriers or other coatings for the steel. The urgent need for a 14 MeV neutron source was again emphasized.

Despite different objectives of the European Union, Japan, and the United States and given the time and financial constraints on the programs, the complexity of the common problems standing in the way of the three programs meeting their respective goals makes a coordinated effort of international collaboration by the three programs essential if their goals are to be achieved.

Action Items

No formal action items were set forth at this meeting. However, the following action item from the Tokyo meeting has not yet been completed:

Considerable work has now been completed on the IEA heats of ferritic/ martensitic steels. Compilations of the work on the IEA heat of F82H by the Japanese and European Union are being prepared by K. Shiba and R. Lindau, respectively, who will consult on an exchange of reports and a distribution of the reports to other members involved in the IEA collaboration. In the future, a report summarizing the work being carried out in the European Union, Japan, and the United States will be prepared.

K. Shiba has agreed to continue this cooperative effort with R. Lindau. In addition, E. van Osch has expressed his interest to Shiba in participating in the effort.

On an informal basis, the EU approached Shiba requesting the JAERI irradiation matrix for F82H, so they can avoid duplication in their program. Shiba has this information in his data base, but he also agreed to prepare a hard copy and distribute it.

Other Information

Although it was not discussed formally in the meeting, the EU has ordered a 4000 kg heat of EUROFER 97, the EU reduced-activation reference steel for DEMO. Delivery is expected in the spring of 1999. Most of the ingot will be processed into plate to be used for the EU testing program for wrought and weld products. Tens of meters of tubes will be produced that will be used for welding trials and component mock-ups. Welds for testing will be made by fusion and HIP processes. There will be a limited number of forged bars, some of which will be atomized for powder products that will be made by the HIP process for qualification of the process. There are plans to offer material to participants in the IEA program for evaluation.

Next Meeting

The next meeting of the Working Group will occur on one evening of the ICFRM-9 Conference in Colorado Springs, Colorado, USA, during the week of 10-15 October 1999. This meeting will serve as the planning meeting for the next workshop, which will be held in the fall of 2000.

MECHANICAL PROPERTIES OF TWO 7-9CR FERRITIC/MARTENSITIC STEELS

G. R. Odette, G. E. Lucas and P. Spätig (University California, Santa Barbara)

OBJECTIVE

The objective of this work is to generate a data base in support of developing fracture assessment methods of fusion structures comprised of ferritic/martensitic steels.

SUMMARY

Tensile and fracture tests were performed on two ferritic/martensitic stainless steels. The temperature dependence of the yield stress and the thermal stress dependence of the activation volume were found to be in good agreement with a model based on the propagation of double kinks on screw dislocation segments. Effective fracture toughness-temperature curves were developed for two specimen sizes, and a constraint correction based on a critical stress ($\tilde{\sigma}$)-critical area ($\tilde{A}$) model was found to rationlaize the diffrences. The status of the Master Curve Experiment is discussed.

PROGRESS AND STATUS

Introduction

Design and operation of fusion reactor structures will require appropriate data compilations and advanced integrity assessment methods in order to safely and effectively manage irradiation embrittlement without undue conservatism. The data will largely come from a limited number of tests on small specimens, compatible with both available irradiation volumes and the practical constraints of time and resources. A method has been proposed based on the concept of a set of master toughness-temperature curves, $K_e(T)$, which are indexed by temperature shifts (ΔT) that efficiently account for the effects of strain rate, irradiation, specimen/component size and geometry [1]. The MC-ΔT method not only directly links to specifying engineering design and operation limits, but is also compatible with the more fundamental micromechanics-, and ultimately microstructure-, based understanding and predictive models. Indeed, such connections are required for the effective use of small specimens and tractable irradiation programs. This work is part of an ongoing study to develop constitutive relations and effective toughness-temperature data in support of developing an MC-ΔT approach for ferritic/martensitic steels.

Materials

Two normalized and tempered martensitic steels were investigated. The first one is a reduced activation, tungsten-stabilized steel (Fe-7.65Cr-2.0W-0.1C-0.18V-0.04Ta) being studied as part of an International Energy Agency (IEA) program. The second alloy is a modified vanadium and niobium-stabilized steel, close to the T91 designation (Fe-8.26Cr-0.1C-0.95Mo-0.2V-0.075N). The heat treatment of these two steels was:

      i) 0.5h at 1313K for normalization and 2h at 1013K for tempering (IEA)
      ii) 2.5h at 1343K for normalization and for 4.75h at 1038K for tempering (T91)

Tensile tests

Tensile properties have been studied over the temperature range 77K - 293K. For the IEA steel, the tensile tests were performed on round specimens (3mm diameter, 18 mm gauge length) and on small flat tensile specimens for the T91 steel (0.5 mm thick and 9 mm gauge length). This study focuses on the temperature and strain rate dependence of the yield stress, as part of an overall effort to develop rigorous constitutive models for ferritic-martensitic steels.

Like other bcc metals and alloys, these steels exhibit a strong temperature and strain rate dependence of the yield stress associated with thermally activated dislocation slip. Baseline tests were carried out over a wide range of temperatures at a strain rate of 2×10^{-4} s^{-1}. The constant strain rate tests were supplemented by strain rate jump tests described elsewhere [2]. Figure 1 shows the temperature dependence of the yield stress for both steels where previous data for IEA steel of Spätig et al. (1998) [3] at high temperature have been included. Figure 2 gives an example of a strain rate jump test. The analysis involves decomposition of the yield stress into thermal, σ^*, and athermal components. The thermal component is described by a Arrhenius–type equation with a temperature independent pre-exponential term and an exponential argument that contains a temperature dependent activation energy term minus a stress times activation volume term, V. The activation volumes were measured from the strain rate jump tests and the activation energy of the rate controlling dislocation slip process was deduced from the activation volumes. The temperature dependence of the yield stress and the thermal stress dependence of the activation volume were compared with the model of Dorn and Rajnak [4]. This model is based upon the nucleation and propagation of double kinks on screw dislocation segments. Figures 3 and 4 show the temperature dependence of σ^* and the thermal stress dependence of V in dimensionless units, respectively. Here, σ_p is the Peierls stress and $2U_k$ is the thermal activation energy for nucleating a pair of kinks at T_c. A good agreement between the experimental data and the model has been found up to about 200K for both steels. At temperatures above 200K, it is found that the plastic flow cannot be described in terms of a single rate controlling process, since other mechanisms become operative.

Fracture tests

The effective fracture toughness K_e was measured for the T91 steel as a function of temperature T with fatigue pre-cracked compact tension specimens. Figure 5a shows the experimental $K_e(T)$ curve for this alloy. Six 0.2T specimens at each temperature of 148K, 168K and 188K and six 0.5T specimens at 198K were tested to characterize the intrinsic scatter of toughness data in the transition region. An additional nine 0.2T tests were carried out over a range of temperatures from the lower shelf to lower knee region. All specimens failed by quasi-cleavage, in some cases after a large amount of plastic deformation. Indeed, the effective toughness measured with 0.2T specimens at 198K is higher than that obtained with the 0.5T specimens, illustrating the effect of constraint loss assoicated with large scale yielding, i.e. when the plastic zone at the crack tip is no longer small with respect to the specimen dimensions [5]. However, the K_e values obtained with small specimens can be adjusted to those which would be measured in small scale yielding by application of correction factors, $K_{ssy} = CFK_e$, where $CF = (J/J_{ssy})^{1/2}$ derived from finite element method simulations [6] of crack tips fields and by using a critical stress, $\tilde{\sigma}$, critically stressed area, $\tilde{A}$, local fracture criterion. The ratio is the J required to produce the same $\tilde{\sigma}/\tilde{A}$ as the corresponding small scale yielding J, J_{ssy}. The corrected data are presented on Figure 5b.
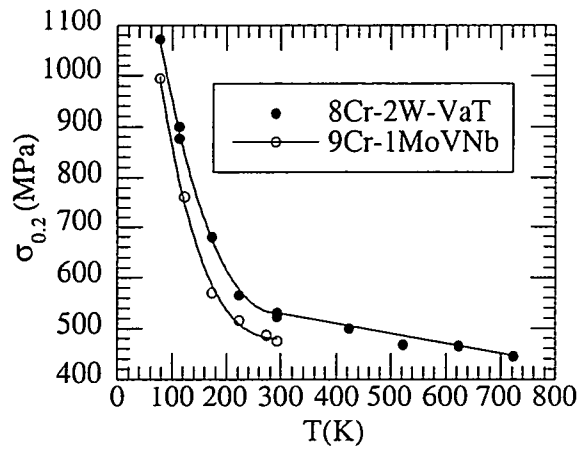
Fig. 1: Temperature dependence of the yield stress
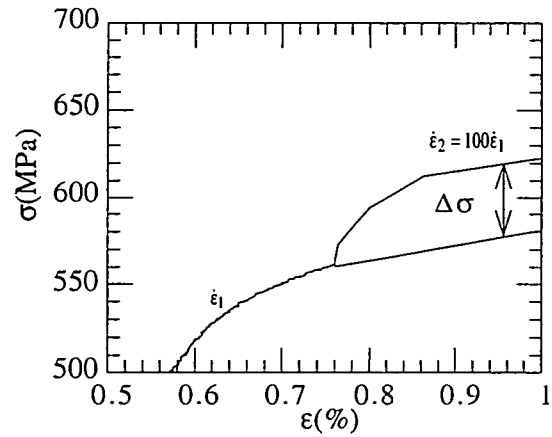
Fig.2: Example of strain rate jump at 223K at the yield stress, IEA steel
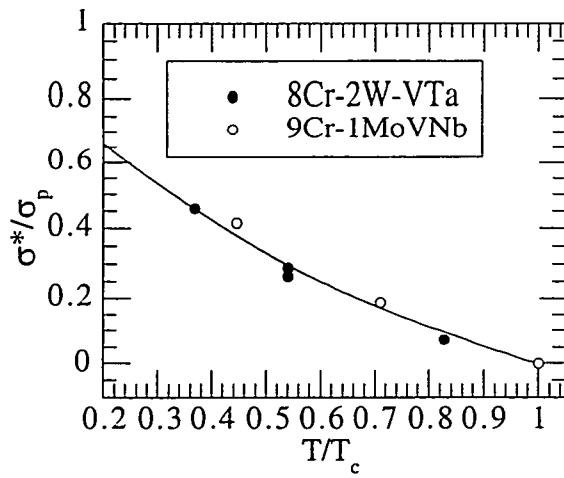
Fig. 3: Temperature dependence of the thermal stress
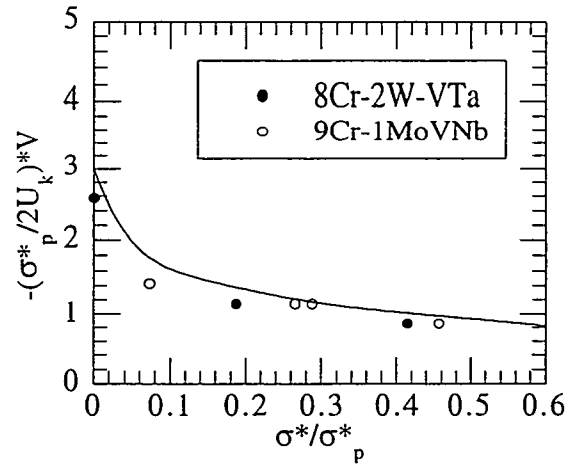
Fig. 4: Thermal stress dependence of the activation volume
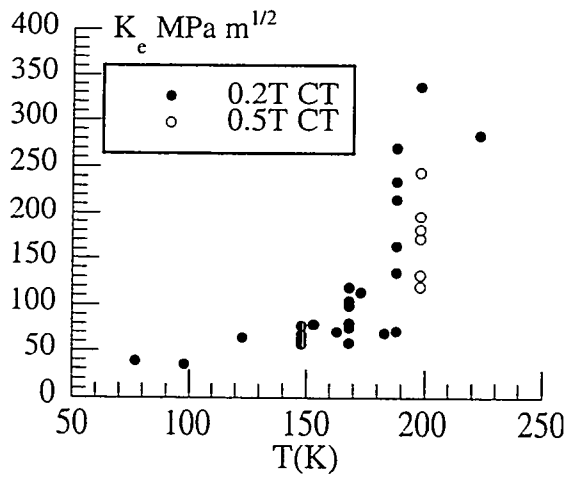
Fig. 5a: Temperature-dependent fracture toughness for T91 steel
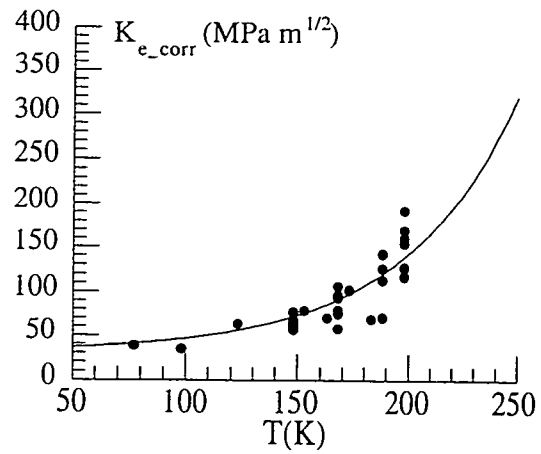
Fig. 5b: Constraint corrected fracture toughness data for T91 steel
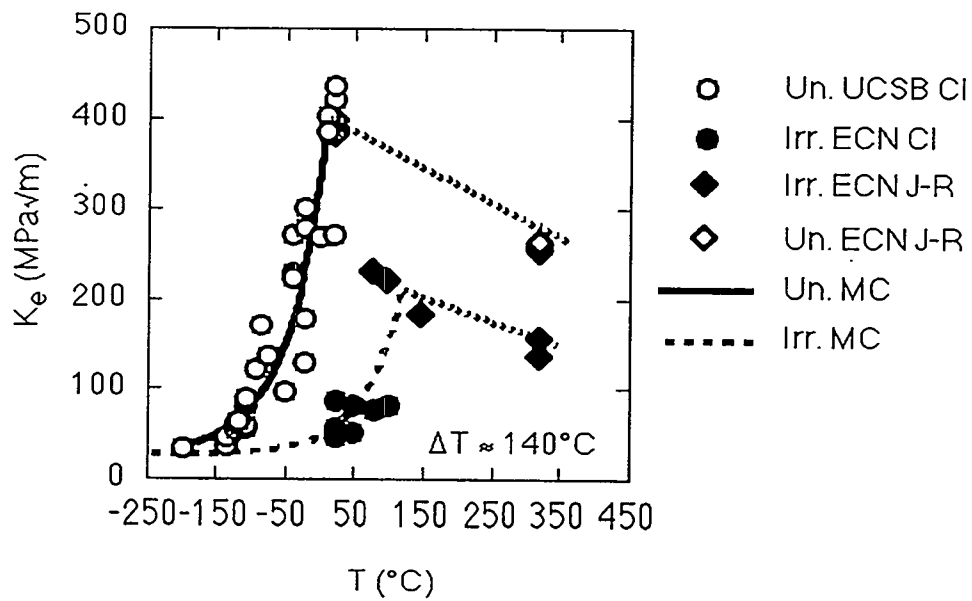
Fig. 6: Irradiation shift for F82H steel, 2.5 dpa and T_{irr} =573K

Clearly, constraint loss corrections are a promising approach to analyzing small specimen data [5]. Note, to complement previous work, a similar study will be carried out on the IEA alloy in the near future.

Recently, measurements of $K_e(T)$ of the IEA steel following neutron irradiation to 2.5 dpa at 573K were reported by van Osch et al. [7]. In combination with previous measurements of $K_e(T)$ for the IEA steel in the unirradiated condition, these results can be used to evaluate both cleavage initiation temperature shift, ΔT, and J_R-da ductile toughness decrease, ΔK_{Jr}, for these irradiation conditions. The results, shown in Figure 6, indicate a $\Delta T \approx 140K$ and a $\Delta K_{Jr} \approx -120$ MPa$\sqrt{m}$. The $\Delta T = T_{oi} - T_{ou}$ is primarily due to irradiation hardening, $\Delta\sigma_I \approx 175$ MPa. The ΔT can be estimated using the equivalent yield stress model (EYSM): $\sigma_y(T_{oi}) = \sigma_y(T_{ou}) + \Delta\sigma_i$ [8,9], where $T_{ou} \approx 160K$ and T_{oi} are the temperatures of the unirradiated and irradiated steels, respectively, at a reference toughness of 60 MPa$\sqrt{m}$. The predicted ΔT based on the EYSM is 133K compared to a measured value of 140K.

MACE current status:

We have planned a related set of irradiation experiments called the Master Curve Experiments (MACE), in which tensile, fracture, and microstructural specimens of ferritic/martensitic steels will be irradiated over a range of temperatures and doses in a facility being installed at the Budapest Research Reactor KFKI AEKI. At the end of August 98, the authorization was given by the Hungarian safety authorities to run the new irradiation rig BAGIRA (Budapest Advanced Gas-cooled Irradiation Rig) at KFKI AEKI. Thermal tests with dummy material and dosimetry measurements started last September. The preliminary tests include a sequence of three loadings of 16%, 40% and 100% of the ultimate target. The fast neutron flux exceeded initial calculated estimates resulting in higher than expected heating rates. This problem was solved by increasing the cooling gas flow. Currently, the test with 40% of the target loading is running with a stable operating temperature of about 245±15°C, with a gradient of about 15°C between the middle and the end of the sample assembly. A final test is planned with a loading near the target level. Dosimetry measurements will be performed at this time. Initiation of actual specimen irradiations in MACE at 250°C with a target dose of 0.5 dpa are expected to begin within 6 weeks of the completion of this final test.

REFERENCES

[1] Odette, G. R., Edsinger, K., Lucas, G. E., E. Donahue, ASTM-STP-1328, American Society for Testing and Material, Philadelphia, PA (1998) 298-327.

[2] P. Spätig, G. R. Odette, G. E. Lucas, submitted to J. Nucl. Mater (1999).

[3] P. Spätig, R. Schäublin, S. Gyger, M. Victoria, J. Nucl. Mater. 258-263 (1998) 1345.

[4] J. E. Dorn and S. Rajnak, Trans. AIME 230 (1964) 1052.

[5] G. R. Odette, K. Edsinger, G. E. Lucas, E. Donahue, Small Specimen Test Techniques, ASTM STP 1329, American Society for Testing and Materials (1998) p. 298

[6] M. Nevalainen and R. H. Dodds, Inter. J. Fracture 74 (1995) 131.

[7] E. V. van Osch, M. G. Horsten, G. R. Odette, G. E. Lucas ASTM-STP 1325, American Society for Testing and Materials (in press).

[8] G. R. Odette, E. Donahue, G. E. Lucas, J. W. Sheckherd, DOE/ER-0313/20, Department of Energy (1996) p. 11.

[9] G. R. Odette, P. M. Lombrozo, R. A. Wullaert, Effects of Irradiation on Materials, ASTM-STP-970, American Society for Testing and Materials (1985) p.841.

EFFECT OF SMALL AMOUNTS OF RHENIUM AND OSMIUM ON MECHANICAL PROPERTIES OF A 9Cr-2W-0.25V-0.07Ta-0.1C STEEL—R. L. Klueh, D. J. Alexander, and M. A. Sokolov (Oak Ridge National Laboratory)

OBJECTIVE

The experiments in this work were meant to determine the effect of small amounts of rhenium and osmium on the mechanical properties of a 9Cr-2W-0.25V-0.07%a-0.1C steel. These effects could become important because tungsten is transmuted to rhenium and osmium when irradiated with neutrons in a fission or fusion reactor.

SUMMARY

The nuclear transmutation of tungsten to rhenium and osmium in a tungsten-containing steel irradiated in a fission or fusion reactor could change substantially the chemical composition of the steel. To determine the possible consequences of such changes on mechanical properties, tensile and Charpy impact properties were determined on five 9Cr-2W-0.25V-0.07Ta-0.1C steels that contained different amounts of rhenium, osmium, and tungsten. The mechanical properties changes due to these changes in composition were relatively minor. Observations were also made on the effect of carbon concentration. The effect of carbon on tensile behavior was relatively minor, but there was a large effect on Charpy properties. The steels showed relatively little effect of tempering temperature on the Charpy transition temperature, which was tentatively attributed to the silicon and/or manganese concentration.

PROGRESS AND STATUS

Introduction

Irradiation of the first wall and blanket structure of a fusion power plant by neutrons from the fusion reaction will induce the transmutation of constituent elements of the structural material, which will result in the replacement of the transmuted atom with one solid and one gas (helium or hydrogen) atom in the matrix of the material. The production of the solid radioactive transmutants are the impetus for the development of reduced-activation materials designed to ameliorate the radioactive waste disposal of components of a fusion power plant after the service lifetime [1]. Efforts have been made to determine the effect of the gaseous helium and hydrogen formed this way on the mechanical properties of the material. However, it has been assumed that the solid transmutants will have little effect on the mechanical properties, since only small amounts of such elements are expected to form and only small amounts of the elements of the structural material will be transmuted.

Recently, Greenwood and Garner [2] pointed out that significant amounts of transmutants can be produced when certain materials are irradiated in the fission reactors being used in the United States Department of Energy Fusion Reactor Materials Program. They concluded that the effect is most acute for certain elements irradiated in the High Flux Isotope Reactor (HFIR) [2], because of the thermal neutrons present in the mixed-spectrum of this reactor. The HFIR is the principle fission reactor used in the United States Fusion Materials Program. Elements of concern to Greenwood and Garner included molybdenum, tungsten, vanadium, and rhenium.

Tungsten is important because it has been used in the new reduced-activation steels as a replacement for molybdenum [1]. Steels with 9 % Cr-2% W are the leading reduced-activation steels under consideration (compositions are in wt. % unless otherwise stated). Figure 1, taken from Greenwood and Garner [2], shows that a considerable portion of the tungsten could be burned out of the steel during irradiation in the Fast Flux Test Facility (FFTF) and HFIR (two fission reactors), and the conceptual fusion power plant, STARFIRE. Tungsten transmutes to rhenium [2], and then much of the rhenium transmutes to osmium. This change in composition for a steel with 2% W could significantly affect the tungsten composition of the steel, and thus, it could conceivably affect the mechanical properties. The
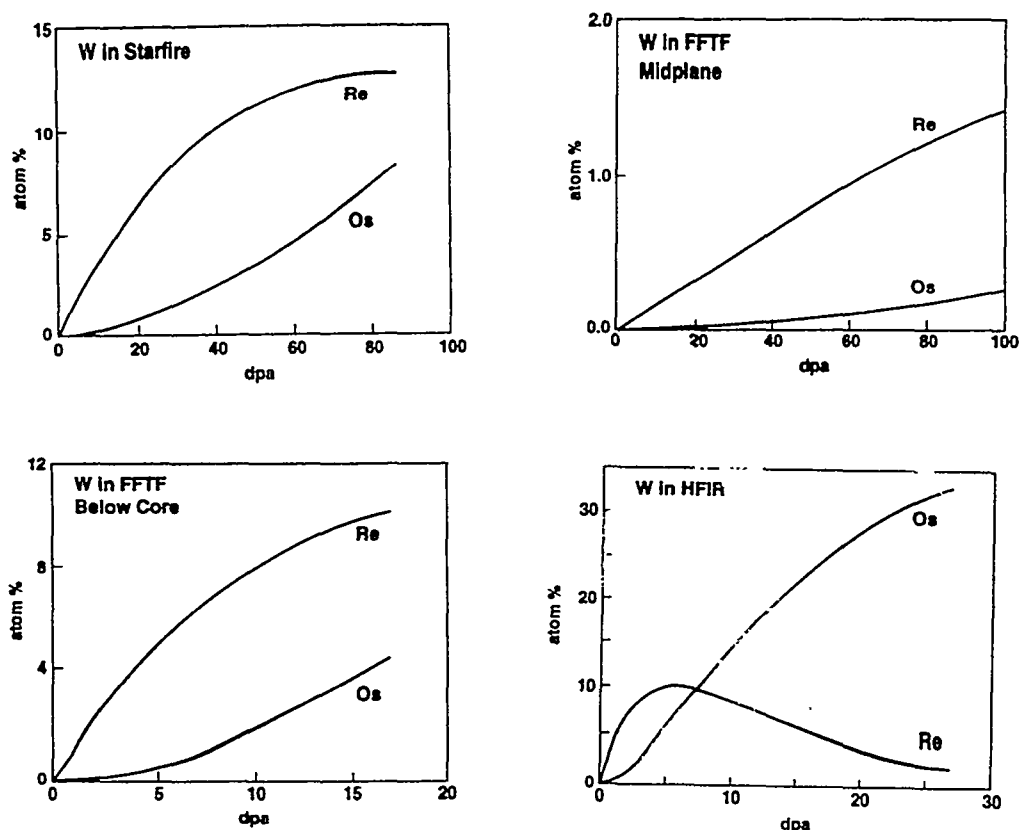
Figure 1. The transmutation of tungsten to rhenium and osmium in the conceptual fusion reactor Starfire, in two positions of the Fast Flux Test Facility (FFTF), and in the High Flux Isotope Reactor (HFIR). Taken from Greenwood and Garner [2].

largest effect occurs for HFIR (Fig. 1). Therefore, if the mechanical properties are affected by the change in composition, the properties could differ after irradiation in HFIR and irradiation in a fast reactor, such as FFTF [2], or irradiation in a fusion power plant.

Tensile and Charpy impact properties were measured on steels of nominal composition 9% Cr-2% W-0.25% V-0.07 % Ta-0.1% C (9Cr-2WVTa) with and without the addition of rhenium and osmium to determine if these elements have a significant effect on the mechanical properties. The 9Cr-2WVTa steel was used as the base because this is a reduced-activation steel with excellent properties in the normalized-and-tempered condition [3-5] and after irradiation [6].

Experimental Procedure

Small 450-g vacuum arc-melted heats of 9Cr-2WVTa steel and this composition with various levels of rhenium and osmium were made. Compositions of the experimental steels are given in Table 1.

Rhenium and osmium were added to the basic 9Cr-2WVTa composition with the objective of producing steels with 0.2 Re and 0.2 Os (ReOs-1), 0.1 Re and 0.6 Os (ReOs-2), and a third steel with the latter combination of rhenium and osmium, but with less tungsten to account for the tungsten that is transmuted during irradiation (ReOs-3). The first attempt to produce ReOs-3 resulted in an alloy with twice the desired carbon (ReOs-4), and although this high carbon was beyond that for the 9Cr-2WVTa,

Table 1. Chemical composition of steels (wt. %)

Element	9Cr-2WVTa	ReOs-1	ReOs-2	ReOs-3	ReOs-4
C	0.081	0.077	0.078	0.060	0.20
Mn	0.01	0.01	0.01	0.02	0.01
P	0.007	0.004	0.006	0.012	0.003
S	0.006	0.005	0.006	0.005	0.007
Si	0.09	0.20	0.10	0.06	0.01
Cr	8.96	8.76	8.76	8.72	8.76
V	0.20	0.21	0.20	0.23	0.21
Ta	0.06	0.06	0.08	0.06	0.07
W	2.17	2.29	2.26	1.47	1.58
Os		0.25	0.79	0.76	0.84
Re		0.20	0.07	0.11	0.14
Fe	Balance	Balance	Balance	Balance	Balance

the steel was still included in the tests as it provided an opportunity to examine the effect of carbon on the mechanical properties on this type of steel.

Chemical analyses of the heats of steel indicated that the rhenium and osmium values achieved were close to those desired; the Os of the high-Os steels was measured as ≈0.8% instead of the 0.6% desired (Table 1). Further, the objective for ReOs-3 was to reduce the 2% W in proportion to the amount of rhenium and osmium added, resulting in a 1.25% W steel. However, because the tungsten was high in the other steels (closer to 2.25% instead of 2%), ReOs-3 and ReOs-4 contained ≈1.5% W. The five steels will be referred to as 9Cr-2WVTa, 9Cr-2WVTa-0.2Re-0.2Os (ReOs-1), 9Cr-2WVTa-0.1Re-0.8Os (ReOs-2), 9Cr-1.5WVTa-0.1Re-0.8Os-0.1 (ReOs-3), and 9Cr-1.5WVTa-0.1Re-0.8Os-0.2C (ReOs-4).

The 9Cr-2WVTa was meant to be a reproduction of a larger heat (18 kg) of this composition produced for the original work to develop the reduced-activation steels and for which a range of data have been obtained (Table 2) [3-5]. The small 450-g heat of 9Cr-2WVTa was used as the control for this experiment in order to compare steels made by the same process. The nominal composition of the large heat for Cr, W, V, and Ta, the primary alloying elements, was achieved in the small heat. However, the silicon and manganese contents of the 18-kg heat were adjusted to ≈0.2% Si and ≈0.45% Mn [3], which are typical compositions for these elements when such steels are produced by a commercial vendor. The small heats for the present study were made from the individual elements and contained less manganese and, in most cases, less silicon: the manganese level was 0.01-0.02%, and silicon varied from 0.01 to 0.2% (Table 1). Carbon concentration was also different: in the small experimental steels, analyses indicated that it varied from 0.06% for ReOs-3 to ≈0.08% for the other three heats, compared to 0.11% in the large heat. The ReOs-4 was analyzed as containing 0.2% C. For the general discussion of the steels, they will be referred to as containing ≈0.1 and ≈0.2% C.

Half of each 12.7 x 25.4 x 127 mm ingot was hot rolled to a thickness of 6.4 mm and half to a thickness of 0.76 mm. Mechanical properties tests were made on normalized-and-tempered steel. The steels

Table 2. Chemical composition of different heats of 9Cr-2WVTa steels

Element	450-g Heat	18-kg Heat
C	0.081	0.11
Mn	0.01	0.44
P	0.007	0.015
S	0.006	0.008
Si	0.09	0.21
Cr	8.96	8.90
V	0.20	0.23
Ta	0.06	0.06
W	2.17	2.01
Fe	Balance	Balance

were austenitized for 0.5 h at 1050°C in a helium atmosphere, after which they were quickly cooled in flowing helium. Specimens were tested in two tempered conditions: 1 h at 700°C and 1 h at 750°C.

Tensile specimens 44.5-mm long with a reduced gage section of 20.3 x 1.52 x 0.76 mm were machined from the 0.76-mm sheet with gage lengths parallel to the rolling direction. The specimens were heat treated after machining. Tensile tests were conducted over the range room temperature to 600°C in vacuum on a 44-kN Instron universal testing machine at a nominal strain rate of $\approx 4 \times 10^{-4}$ s^{-1}.

One-third-size Charpy specimens 3.3 x 3.3 x 25.4 mm with a 0.51-mm-deep 30° V-notch and a 0.05- to 0.08-mm-root radius were machined from the normalized 6.4-mm plate along the rolling direction with the notch transverse to the rolling direction. Specimens were tempered after machining. Charpy tests were carried out in a pendulum-type impact machine specially modified to accommodate subsize specimens [7]. The absorbed energy values were fitted with a hyperbolic tangent function to permit the upper-shelf energy (USE) and ductile-brittle transition temperature (DBTT) to be evaluated. The DBTT was determined at the energy midway between the upper- and lower-shelf energies. Note that for these miniature specimens different DBTT and USE values are obtained than for full-size specimens. However, it has been shown that a low transition temperature for miniature specimens translates to a low value for full-size specimens [8,9]. A correlation likewise exists for the USE [8,9].

Results

Metallography and Microhardness

The steels were examined by optical microscopy. All of the microstructures were 100% tempered martensite. There was some variation in the estimated prior-austenite grain size, determined by comparing the microstructure with ASTM Grain Size charts. The three steels with 2% W and different amounts of Re and Os had similar grain sizes (Table 3), while the two steels with 1.5% W had different values: the 1.5% W steel containing ≈0.1% C (ReOs-3) had the largest grain size of all five steels, and the 1.5% W steel with 0.2% C (ReOs-4) had the smallest grain size of the steels.

Table 3. Microhardness and prior austenitized grain size of steels

Steel	Vickers Hardness (average of 5 readings)	Prior Austenite Grain Size mm (ASTM No.)
ReOs-0	253.8	0.016 (9)
ReOs-1	235.0	0.015 (9.25)
ReOs-2	254.6	0.016 (9)
ReOs-3	246.8	0.0205 (8.25)
ReOs-4	262.7	0.0095 (10.25)

Hardnesses showed a relatively small variation (Table 3), with the 2% W steel with 0.2% Re and 0.2% Os (ReOs-1) having the lowest hardness. There was less variation among the other steels. The 1.5% W steel containing 0.2% C had highest hardness.

Tensile Behavior

There was considerable variation in the strength (Figs. 2 and 4) and ductility (Figs. 3 and 5). The amount of variation for the yield stress (YS) [Figs. 2(a) and 4(a)] was greatest for the room temperature tests and least at 600°C. Variability was less for the ultimate tensile strength (UTS) of the different steels [Figs. 2(b) and 4(b)] than for the YS, but again, the variation for the UTS was greatest at the lowest temperatures. At most test temperatures below 600°C, the YS and UTS of the 9Cr-2WVTa-0.2Re-0.2Os steel (ReOs-1) was the smallest. The steels with 1.5% W, 0.8% Os and 0.1% Re with 0.1% C (ReOs-3) and 0.2% C (ReOs-4) were near the strongest of all the steels below 600°C. There was not much difference between the YS of those two steels below 600°C, but the UTS of the steel with 0.2% C (ReOs-4) was generally the highest of these two steels as well as of the other steels below 600°C.

The variation in ductility—uniform elongation [Figs. 3(a) and 5(a)] and total elongation [Figs. 3(b) and 5(b)]—was also quite wide for the steels tempered at both 700 (Fig. 3) and 750°C (Fig. 5). The relative ductilities of the steels were not always inverse to the strength, as might be expected. For example, the
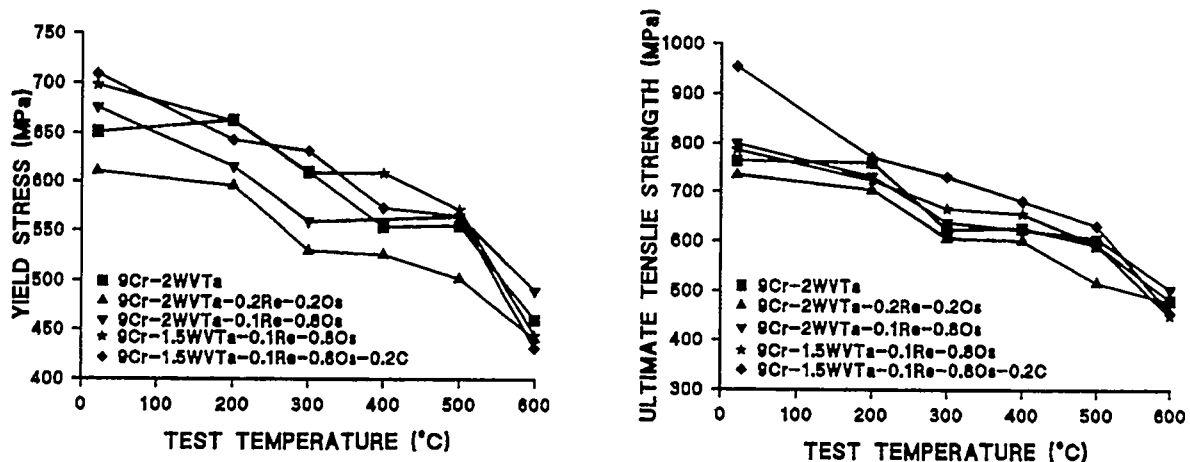
Figure 2. The yield stress and ultimate tensile strength of the 9Cr-2WVTa steels containing varying amounts of rhenium and osmium after normalizing and tempering 1 h at 700°C.
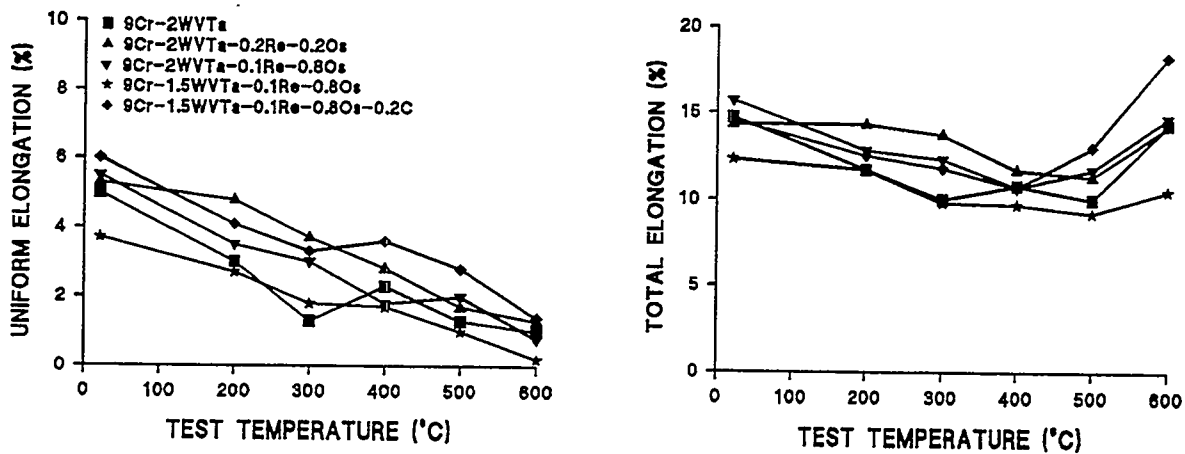
Figure 3. The uniform and total elongation of the 9Cr-2WVTa steels containing varying amounts of rhenium and osmium after normalizing and tempering 1 h at 700°C.
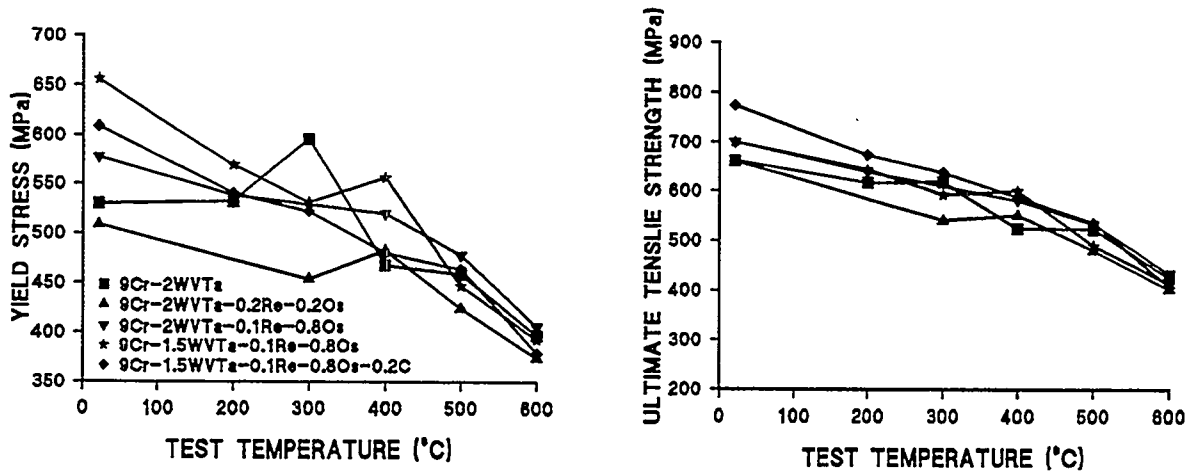
Figure 4. The yield stress and ultimate tensile strength of the 9Cr-2WVTa steels containing varying amounts of rhenium and osmium after normalizing and tempering 1 h at 750°C.
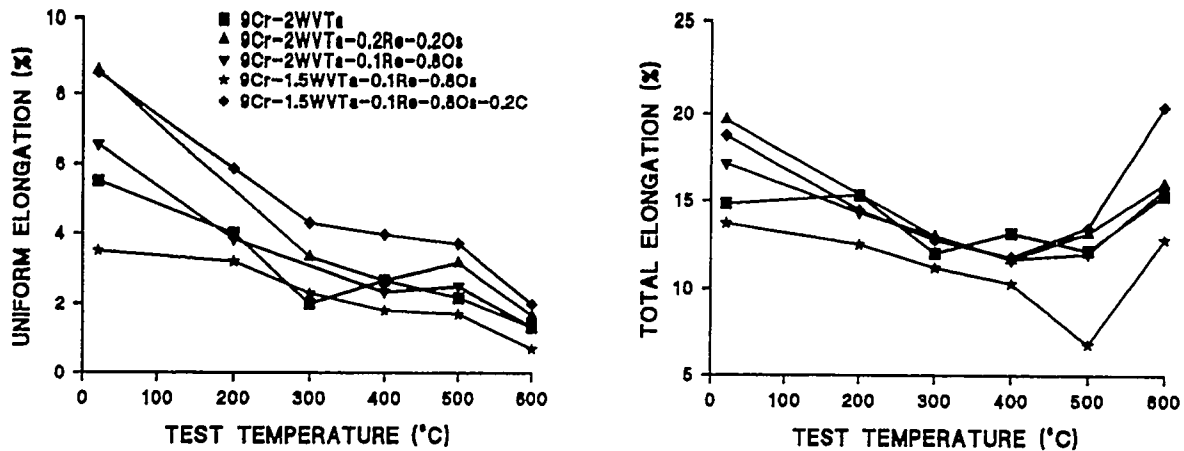
Figure 5. The uniform and total elongation of the 9Cr-2WVTa steels containing varying amounts of rhenium and osmium after normalizing and tempering 1 h at 750°C.

1.5% W steel with 0.1% C (ReOs-3) generally had the lowest uniform and total elongation, while the steel with 0.2% C (ReOs-4) often had the highest ductility, even though these were two of the strongest steels. The total elongation of all the steels increased with temperature above ≈400°C, with the largest change occurring for the steel with 0.2% C.

Yield stress results for the small 450-g heat and the large 18-kg heat of 9Cr-2WVTa steel at room temperature and 600°C are compared in Table 4. The large heat was substantially stronger than the small heat.

Table 4. A comparison of properties of the 450-g and 18-kg heats of 9Cr-2WVTa steel

Heat Size	Tempering Temperature (°C)	YS (MPa)		UTS, MPa		Charpy	
		RT	600°C	RT	600°C	TT(°C)	USE (J)
450-g	1 h at 700°C	651	460	764	481	-103	13.7
	1 h at 750°C	530	397	661	425	-120	15.4
18-kg	1 h at 700°C	823	651	942	696	-43	7.5
	1 h at 750°C	645	489	774	526	-88	11.2

Charpy Impact Properties

The transition temperature (DBTT) and upper-shelf energy (USE) for the steels tempered at 700 and 750°C are given in Table 5 and Fig. 6.

As expected, the USE of all five steels is higher after the 750°C temper than after the 700°C temper [Fig. 6(b)]. For the four steels with ≈0.1% C, there was relatively little difference in DBTT, all of which were lower than for the steel with 0.2% C (Figs. 7 and 8), which was also expected. The lower DBTT after the 750°C temper than after the 700°C temper observed for the 9Cr-2WVTa and the 9Cr-2WVTa-0.1Re-0.8Os-0.1C steels was the expected behavior, since the strength decreases with tempering temperature. What was not expected was the relatively small difference in DBTT for the other three steels after the different tempering treatments. These steels showed essentially no effect of tempering temperature on the DBTT (Table 2 and Fig. 6). For some of the steels (ReOs-3 and ReOs-4), the measured values after tempering at 700°C were lower than after tempering at 750°C.

Table 5. Charpy impact properties of steels

Steel	Tempering Temperature (°C)	Transition Temperature (°C)	Upper-Shelf Energy (J)
9Cr-2WVTa	1 h at 700°C	-103	13.7
	1 h at 750°C	-120	15.4
9Cr-2WVTa-0.2Re-0.2Os-0.1C	1 h at 700°C	-103	12.7
	1 h at 750°C	-105	14.2
9Cr-2WVTa-0.1Re-0.8Os-0.1C	1 h at 700°C	-102	13.3
	1 h at 750°C	-133	14.3
9Cr-1.5WVTa-0.1Re-0.8Os-0.1C	1 h at 700°C	-114	12.6
	1 h at 750°C	-113	13.8
9Cr-1.5WVTa-0.1Re-0.8Os-0.2C	1 h at 700°C	-84	8.6
	1 h at 750°C	-78	9.4
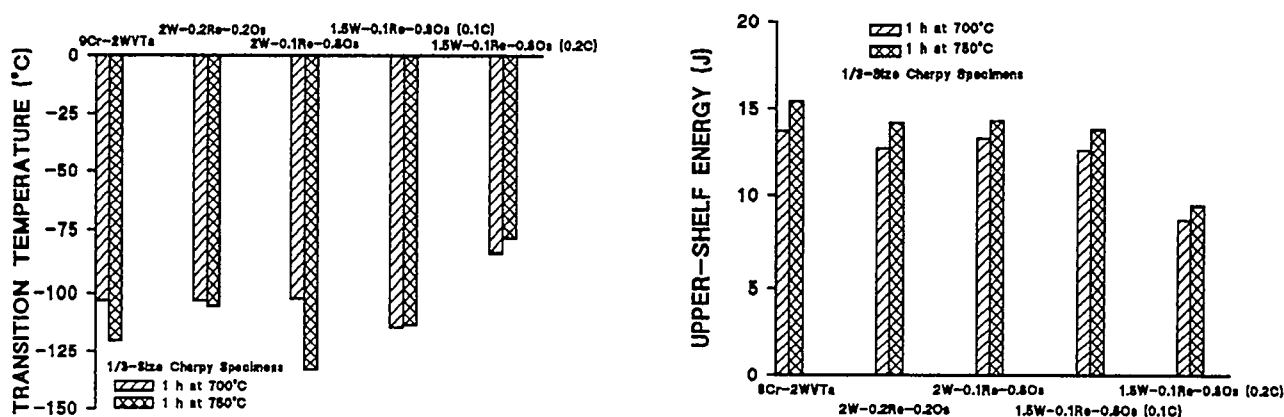
Figure 6. The Charpy transition temperature and upper-shelf energy of the 9Cr-2WVTa steels containing varying amounts of rhenium and osmium after normalizing and tempering 1 h at 700°C and 1 h at 750°C.

The 450-g heat of 9Cr-2WVTa steel used in this experiment had a lower DBTT and a relatively smaller difference after tempering at 700 and 750°C than the 18-kg heat tested previously (Table 4). The DBTTs of the large heat after tempering at 700 and 750°C were -43 and -88°C, respectively, compared to -103 and -120°C, respectively, for the small heat. The small heat also had a significantly higher USE in each case (Table 4).

Discussion

During irradiation in HFIR, tungsten transmutes to rhenium, which subsequently transmutes to osmium (Fig. 1). The objective of these experiments was to determine the possible effect rhenium and osmium and the substitution of rhenium and osmium for tungsten could have on the mechanical properties of the 9Cr-2WVTa steel. Such compositional changes occur when tungsten is transmuted to rhenium and

osmium when the steel is irradiated in a reactor, such as HFIR (and in a future fusion reactor). After tungsten is irradiated to ≈25 dpa in HFIR, ≈32% will be transmuted to ≈29% Os and ≈3 % Re. For the 2% W in the 9Cr-2WVTa steel, this means ≈0.58% Os and ≈0.06% Re form, thus reducing the tungsten composition by about this amount. Steels containing 0.6% Os and 0.1% Re were proposed. The actual alloys produced contained somewhat more osmium. In addition, the tungsten was somewhat higher than desired (Table 1). Of course, the mechanical properties after irradiation will also be affected by radiation damage. Nevertheless, the results provide information on the effect of osmium and rhenium on the properties of the 9Cr-2WVTa steel.

The objective of testing the two Re-Os alloys with 2% W (9Cr-2WVTa-0.2Re-0.2Os and 9Cr-2WVTa-0.1Re-0.8Os) was to determine the effect of the rhenium and osmium on the steel (Figs. 2-5). The steel containing 0.2% Re and 0.2% Os was generally the weakest of the five steels. The 9Cr-2WVTa and 9Cr-2WVTa-0.1Re-0.8Os steels had similar strengths and ductility that were more in line with those of the two 1.5% W steels.

The Charpy properties of the three 2% W steels were quite similar (Fig. 6), with the only unusual observation being that there was essentially no difference in the DBTT of the 0.2Re-0.2Os steel after the 700 and 750°C tempers. For all three steels, the USE after the 750°C temper was greater than after the 700°C temper.

When the tungsten concentration was reduced from ≈2.2% to ≈1.5% with no change in carbon, the 1.5% W steel was generally the strongest of these steels—at least below 600°C. The stronger 1.5% W steel with ≈0.1% C generally had the lowest uniform and total elongation of the five steels. However, the Charpy impact properties of the steel with 1.5% W were similar to those for the 2% W steels. Although the 1.5% W steel with ≈0.1% C had a similar strength to the 1.5% W steel with ≈0.2% C, the steel with 0.2% C was close to having the highest ductility of the five steels. A possible explanation is that the higher carbon content means that not all carbides are dissolved during austenitization, which could cause the smaller prior austenite grain size that can probably affect ductility. Whether undissolved carbides remained during austenitization needs to be verified by transmission electron microcopy (TEM).

Charpy properties of the 1.5% W steels reflected the carbon content. The steel with the highest carbon had the highest DBTT and the lowest USE of all five steels (Fig. 6); this occurred despite the high-carbon steel having the smallest prior austenite grain size and not necessarily always being the strongest of the steels. This was probably due to larger carbides in this steel, although that needs to be established by TEM.

Tempering temperature apparently had no effect on the DBTT of either of the 1.5% W steels, just as there was no effect on the 0.2Re-0.2Os steel, although for the 1.5% W steels, the DBTT was slightly higher after the 750°C temper than the 700°C temper, which is contrary to expectations. The reason for this lack of effect of tempering temperature is not known. In all cases, these steels did have the expected effect of tempering temperature on USE (i.e., the USE was always higher for the higher tempering temperature).

Basically, the results of these tests give little indication that the tensile and Charpy properties will be affected significantly by the amounts of rhenium and osmium estimated to form in a 9Cr-2WVTa steel irradiated to ≈25 dpa in HFIR. Likewise, the reduction of tungsten that would accompany the increase in rhenium and osmium also appears to have little effect—at least in the presence of the additional Re and Os. Under the influence of irradiation at temperatures below ≈400°C where irradiation hardening is expected, the effect of the compositional changes would probably be of even less significance.

The largest effect of composition on mechanical properties involved the apparent effect of carbon concentration on the Charpy properties (Figs. 6-8). Although there was relatively little difference in the strength of the 1.5% W steels with ≈0.1 and 0.2% C, there was a substantial difference in the Charpy behavior. Carbon can play a role on the properties through its effect on the strength and the carbide

morphology. Since there was relatively little difference in strength for the two steels, the difference in the carbides in the two steels must be the cause, especially since the steel with 0.2%C had a much smaller prior austenite grain size than the steel with ≈0.1% C. TEM is required to verify these suggestions.

The difference in properties noted between the small (450-g) heat of steel (0.08% C) produced for this experiment and the larger (18-kg) heat (0.11% C) previously studied [3-6] (Table 4) may also be at least partially due to the difference in carbon concentration. As Table 4 indicates, the large heat is stronger and has a lower DBTT and higher USE. Without further experiments, it is not possible to determine if the difference in properties for these two steels is attributable to the carbon, but based on the small difference in the strength of the 1.5% W steels with ≈0.1% C (measured as 0.06%) and ≈0.2% C, there would appear to be other reasons for the differences. That is, the DBTTs of the 1.5% W steels with ≈0.1 and ≈0.2% C after tempering at 700°C were -114 and -84°C, respectively, and after tempering at 750°C they were -113 and 78°C, respectively. This compares with the 450-g heat of 9Cr-2WVTa steel that had DBTTs of -103 and -120°C after tempering at 700 and 750°C, respectively, compared to the DBTTs of the 18-kg heat that were -43 and -88°C, respectively. The relative difference for the latter steels seems to be somewhat larger than for that attributed to carbon for the 1.5% W steels, especially when it is considered that there is much less difference in carbon for the 450-g and 18-kg heats of 9Cr-2WVTa steels.

As pointed out in the previous section, the 9Cr-2WVTa steels also contain different amounts of manganese and silicon; both manganese and silicon are thought to strengthen by solid solution hardening [10]. If this is the case here, then the increased strength and reduced Charpy properties of the large heat might also be partially attributed to the higher silicon and manganese in the 18-kg heat, which contains about 40 times more manganese (0.44 vs. 0.01) and twice as much silicon (0.21 vs. 0.09). Again, further work is required to make a clear determination on the cause for the differences that have been observed. Should manganese be the cause, that could be important because fairly large amounts of manganese are expected to form in such a steel by transmutation in a magnetically confined fusion reactor [11].

When reasons for the observations of little or no change in DBTT with tempering temperature for the steels of this experiment (Table 5) compared to the previous experiment are considered, manganese and silicon concentration differences for the heats of this experiment and heats used previously appear to be the only possible reasons that can be cited. Further work is required to elucidate a relationship to the composition. If there is such a relationship, it might be possible to exploit it in the development of such steels.

Summary and Conclusions

Tensile and Charpy impact properties were determined for the following five steels: 9Cr-2WVTa, 9Cr-2WVTa with additions of ≈0.2% Re and ≈0.2% Os, 9Cr-2WVTa with additions of≈0.1%Re and ≈0.8% Os, one 9Cr-1.5WVTa with additions of ≈0.1Re and ≈0.8Os, and a 9Cr-1.5WVTa with additions of ≈0.1Re, ≈0.8Os, and ≈0.2% C. All but the last steel contained ≈0.1% C. There were only minor variations in the tensile properties due to the addition of the rhenium and osmium to the 9Cr-2WVTa or the simultaneously reduction of the tungsten content to 1.5% and the addition of rhenium and osmium. The change in carbon concentration had the major effect on the Charpy impact properties by causing an increase in the transition temperature and a reduction in the USE. For most of the steels, there was little difference in the transition temperature after tempering at 700 and 750°C, much less than for a heat of 9Cr-2WVTa tested previously. A smaller amount of silicon and manganese in the steels used in the present experiments may be the cause for these differences, although that still needs to be verified.

References

[1] R. L. Klueh and E. E. Bloom, Nucl. Eng. & Design/Fusion 2 (1985) 383.

[2] L. R. Greenwood and F. A. Garner, J. Nucl. Mater. 212-215 (1994) 635.

[3] R.L. Klueh and P.J. Maziasz, Met. Trans. 20A (1989) 373.

[4] R.L. Klueh, Met. Trans. 20A (1989) 463.

[5] R.L. Klueh and W.R. Corwin, J. Eng. Mater. 11 (1989) 169.

[6] R. L. Klueh and D. J. Alexander, in: Effects of Radiation on Materials: 18th International Symposium, ASTM STP 1325, R. K. Nanstad, M. L. Hamilton, F.A. Garner, and A.S. Kumar, Eds. (American Society for Testing and Materials, 1999) p. 911.

[7] D.J. Alexander, R.K. Nanstad, W.R. Corwin, and J.T. Hutton, in: Application of Automation Technology to Fatigue and Fracture Testing, ASTM STP 1092, A.A. Braun, N.E. Ashbaugh, and F.M. Smith, Eds. (American Society for Testing and Materials, Philadelphia, 1990) 83.

[8] W.R. Corwin and A.M. Hougland, in: The Use of Small-Scale Specimens for Testing Irradiated Material, ASTM STP 888, W.R. Corwin and G.E. Lucas, Eds. (American Society for Testing and Materials, Philadelphia, 1986) 325.

[9] D.J. Alexander and R.L. Klueh, in: Charpy Impact Test: Factors and Variables, ASTM STP 1072, J. M. Holt, Eds. (American Society for Testing and Materials, Philadelphia, 1990) 179.

[10] G. Krauss, Steels: Heat Treatment and Processing Principles (ASM International, Materials Park, OH, 1989) 139.

[11] R. Sanz, R. de la Fuente, and J. M. Perlado, J. Nucl. Mater., 155-157 (1988) 592.

SHEAR PUNCH TESTING OF IRRADIATED ISOTOPICALLY TAILORED FERRITIC/MARTENSITIC STEELS

SHEAR PUNCH TESTING OF IRRADIATED ISOTOPICALLY TAILORED FERRITIC/MARTENSITIC STEELS - M. L. Hamilton, D. S. Gelles (Pacific Northwest National Laboratory)*, S. Ohnuki (Hokkaido University), K. Shiba (JAERI), Y. Kohno (University of Tokyo), and A. Kohyama (Kyoto University)

OBJECTIVE

The objective of this effort is to provide an understanding of the effect of hydrogen and helium production during irradiation on post-irradiation mechanical properties in ferritic/martensitic steels for first wall applications in a fusion reactor.

SUMMARY

Single variable experiments are being conducted to study effects of H/He/dpa on properties based on isotopically tailored alloys. ^{54}Fe has been used to prepare an isotopically tailored duplicate of the commercial steel F82H, and a small number of TEM disks have been irradiated in order to study radiation embrittlement. From single disk specimens, mechanical properties were obtained using a shear punch technique that produces a 1 mm blank from the 3 mm disk. Results indicate that shear punch testing can be used successfully to provide mechanical property data from single TEM disks. Little effect of helium on properties was found, either in ^{54}Fe isotopically tailored specimens or in a boron-doped specimen.

PROGRESS AND STATUS

Introduction

A concern in developing structural materials for fusion power systems is the consequences of transmutation-induced helium and hydrogen on material properties. For the advanced ferritic steel fusion materials option, helium (in appm) will be generated at about ten times the dpa rate, and hydrogen will be generated approximately ten times more rapidly. Experiments to define the effect of helium remain controversial[1,2] but severe effects of helium accumulation on fracture toughness have been claimed.[3,4] It is therefore very important to evaluate these transmutation effects in order to establish whether steels can be successfully adapted for fusion applications.

Single variable experiments have been conducted to study effects of H/He/dpa on properties by preparing isotopically tailored alloys. Initially, alloys containing small additions of different nickel isotopes were studied,[5] but the present approach considers alloys made from iron isotopes in order to vary H/He/dpa rates.[6] The controlling reactions are:

^{54}Fe (n,p) ^{54}Mn

^{54}Fe (n,) ^{55}Fe

^{55}Fe (n,) ^{52}Cr or ^{55}Fe (n,p) ^{55}Mn (n,) ^{56}Fe

[54]Fe was used to prepare an isotopically tailored duplicate of the commercial steel F82H,[7] and, because of cost and irradiation space limitations, only a small number of TEM disks were irradiated in order to study radiation embrittlement.

Very recently, individual TEM disks were made available for post-irradiation examination. It was possible to obtain mechanical properties from three alloy conditions for which only a single disk was available, and from a fourth condition where several disks were available in order to compare with results on unirradiated controls. Mechanical properties were obtained using a shear punch technique that produces a 1 mm blank from the 3 mm disk.

Experimental Procedure

A 4 g. batch of isotopically tailored F82H martensitic steel was prepared as described previously,[7] and specimens 3 mm in diameter, intended for transmission electron microscopy (TEM), were obtained along with a specimen of standard F82H and a specimen of boron-doped F82H, following irradiation in either the JP17 irradiation experiment to 2.3 dpa at 250°C or the JP22 irradiation experiment to 34 dpa at 300°C in the High Flux Isotope Reactor (HFIR) in Oak Ridge, TN.[8] Also available were unirradiated control specimens of the isotopically tailored alloy, the standard alloy and another heat of the steel, designated the IEA heat.[9] F82H has the approximate composition (in weight %) Fe-7Cr-2W-0.2V-0.1C-.04Ta-0.01N. Composition details are provided in Table 1.

Table 1. Composition of alloys of interest

Alloy	Cr	C	W	V	Ta	B	Mn	N	Si
F82H [54]Fe	7.1	0.097	1.8	0.17	0.04	-	0.4	0.007	0.55
F82H STD	7.46	0.097	2.1	0.18	0.03	0.0004	0.07	0.004	0.09
F82H [10]B	7.25	0.098	2.1	0.22	0.04	0.0058	0.5	0.002	0.17

Room temperature mechanical properties information was obtained using a shear punch technique that produces 1 mm blanks from 3 mm disks.[10-12] Shear punch testing is essentially a blanking operation which is common to sheet metal forming. A 1 mm diameter punch is driven at a constant rate of 0.127 mm/min. (0.005 in./min.) through a TEM-sized disk (nominally 0.25 mm thick and 2.8 mm in diameter). The load on the punch is measured as a function of punch travel, which is taken to be equivalent to the crosshead displacement. This assumes that the test machine and punch are completely stiff relative to the response of the test specimen.

Figure 1. Schematic of shear punch test apparatus.

A plot of punch load versus punch displacement was obtained for each specimen. A diagram of the apparatus that is required is provided in Figure 1.

The curve obtained from a shear punch test is of a similar form to that obtained from a tensile test. Initially a linear relationship exists between load and punch displacement during which no plastic deformation occurs. This is followed by a deviation from linearity or yield point when permanent penetration of the punch into the specimen occurs. Beyond the yield point, further deformation forms a shear process zone between the die and punch. Work hardening compensates for thinning until a maximum load is achieved. The points of interest on the curve were the yield load and maximum load. Effective shear yield strength (τ_{sy}) and an effective maximum shear strength (τ_{sm}) can be evaluated from these values, respectively, by the following equation:[10]

$$\tau_{sy,sm} = P/(2\pi rt)$$

Where P is the appropriate load, r is the average of bore and punch radii and t is the specimen thickness. Previous work has shown that an empirical relationship can be developed between data from shear punch testing and that from tensile testing.[10-12] In this instance, however, no tensile data were available and the shear punch test was used only as a tool to identify trends in the mechanical properties that might occur as a result of differing helium and hydrogen levels as has successfully been done before.[5]

Results

Fourteen shear punch tests were performed in this study, comprising nine control tests and five tests on irradiated samples. The results of shear punch testing are provided in Table 1 and examples of test curves are provided in Figures 2a and b. Table 2 includes irradiation conditions and calculated values of effective shear yield strength, τ_{sy}, and effective shear maximum strength, τ_{ms} for each of the specimens tested. Figure 2a shows test curves for all ^{54}Fe isotopically tailored samples tested and Figure 2b compares response for the three specimens that were tested following irradiation to highest dose. It is apparent from the test traces shown in Figure 2, that shear punch tests are well behaved and that materials differences are evidenced as differences in yield and maximum strength, whereas differences in ductility are modest, being inversely proportional to strength changes.

The results of Table 2 are plotted as a function of dose in Figure 3 to demonstrate the fluence dependence of hardening. Figure 3a provides comparison of all conditions as a function of effective shear yield strength and Figure 3b gives similar results for effective shear maximum strength. Strength values for unirradiated controls are restricted to a narrow range whereas irradiation of the isotopically tailored alloy to 2.3 dpa at 250°C increased strength and irradiation to 34 dpa at 300°C increased strength further. In comparison, other conditions of F82H have lower strengths, particularly following irradiation to 34 dpa. The response is complex, as comparison of relative strengths for yield differ from those for maximum strength. This complex response may be an indication of inadequate statistics.

Discussion

This work demonstrates that it is possible to obtain mechanical property information on very limited quantities of material: TEM samples weigh about 0.1 gm and the 1 mm blank about 0.01 gm. The techniques described above not only allow for experiments where material is very limited, very expensive or very difficult to obtain in the desired treatment or irradiation condition, but it also allows sampling of complex conditions. For example, in irradiation creep experiments

Figure 2. Shear punch test traces for (a) isotopically tailored specimens and (b) high dose specimens. Note that He levels are measured values while H levels are calculated estimates.
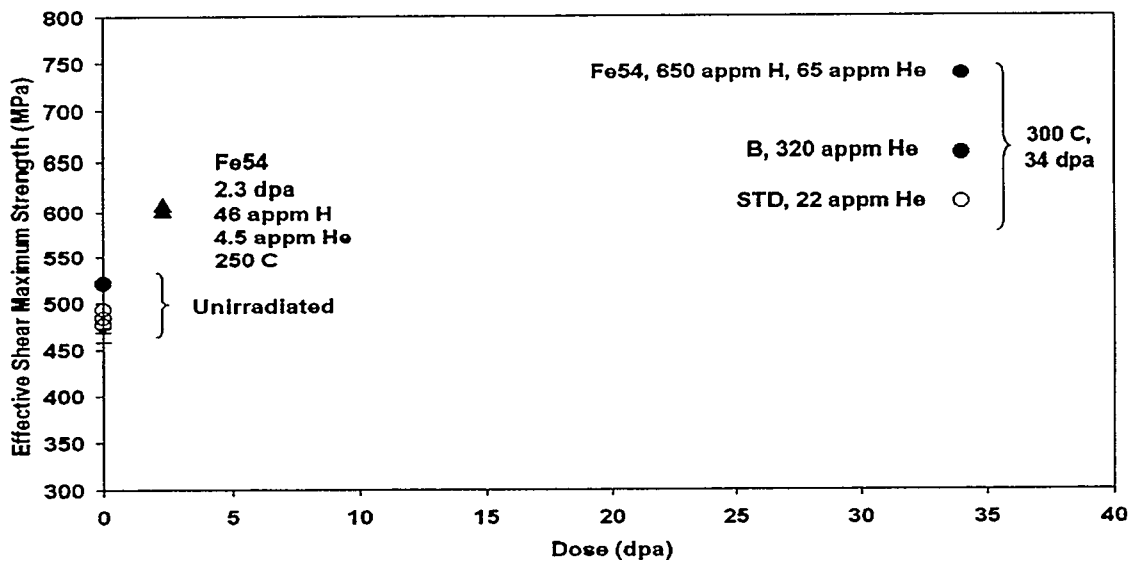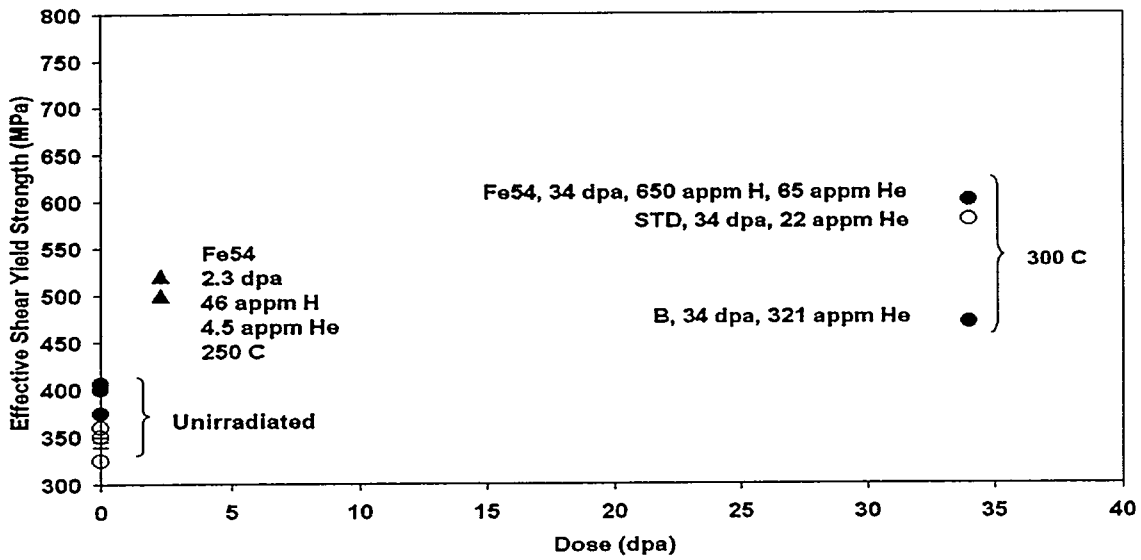
Figure 3. Shear punch test results as a function of dose for (a) effective shear yield strength and (b) effective shear maximum strength. Note that He levels are measured values while H levels are calculated estimates.

where strong gradients exist in temperature or flux, it may now be possible to provide understanding of property and microstructural variation over distances of one or two mm. The added advantages of effectively smaller TEM sample volumes that reduce radioactivity or magnetic interactions are also of benefit.

Table 2. Results of shear punch testing at room temperature.

ID	MATERIAL	CONDITION*	τ_{sy}	τ_{ms}
A943-5	F82H IEA	Unirradiated	340, 345, 350	458, 469, 473
F191-3	F82H STD	Unirradiated	325, 350, 360	476, 482, 492
C103	F82H STD	300°C, 34 dpa, 21.8 appm He	580	609
FN91-3	F82H ^{54}Fe	Unirradiated	390, 400, 406	519, 520, 522
FN51-2	F82H ^{54}Fe	250°C, 2.3 dpa,6 appm H,4.5 appm He	500, 520	602, 608
C603	F82H ^{54}Fe	300°C, 34 dpa,650 appm H,65.3 appm He	600	738
C203	F82H ^{10}B	300 C, 34 dpa, 321 appm He	470	656

* H values are predicted, but He values are measured.[14]

The intent of isotopic tailoring experiments is to assess the effect of hydrogen and helium production during irradiation on properties and microstructure. Because mechanical properties for the different alloys following irradiation at 300°C are very similar, the present results do not demonstrate a significant effect of helium on mechanical properties, and any effect of hydrogen is probably small, although hydrogen production levels are not completely understood. However, it should be noted that concerns about a large effect of helium on ductile brittle transition behavior are centered on irradiation temperatures in the 400°C range. Therefore, the present results are probably not pertinent to that issue.

CONCLUSIONS

Isotopic tailoring is being used to study effects of transmutation on mechanical properties. Shear punch tests can provide mechanical properties information with limited numbers of TEM samples.

ACKNOWLEDGMENTS

FUTURE WORK

This work will be continued within the confines of funding and specimen availability.

REFERENCES

1. R. L. Klueh, J. Nucl. Mater. 218 (1995) 151.

2. D. S. Gelles, R. L. Klueh and D. J. Alexander, J. Nucl. Mater. 230 (1996) 187.

3. A. Hishinuma, A. Kohyama, R. L. Klueh, D. S. Gelles, W. Dietz, and K. Ehrlich, J. Nucl. Mater. 258-263 (1998) 193.

4. A. Kohyama, A. Hishinuma, D. S. Gelles, R. L. Klueh, W. Dietz, and K. Ehrlich, J. Nucl. Mater. 233-237 (1996) 138.

5. D. S. Gelles, G. L. Hankin and M. L. Hamilton, J. Nucl. Mater. 251 (1997) 188.

6. L. R. Greenwood and F. A. Garner, J. Nucl. Mater. 212-215 (1994) 635.

7. M. Suzuki, A. Hishinuma, N. Yamanouch, M. Tamura and A. F. Rowcliffe, J. Nucl. Mater. 191-194 (1992) 1056.

8. J. E. Pawel and K. E. Lenox, in Fusion Materials Semiannual Progress Report for the Period Ending December 31, 1995, DOE/ER-0313/19 (1996) 312.

9. K. Shiba in Proceedings of the IEA Working Group Meeting on Ferritic/Martensitic Steels, ed. R. L. Klueh, October 1996, ORNL/M-5674.

10. M. L. Hamilton, M. B. Toloczko, and G. E. Lucas, Miniaturized Specimens for Testing of Irradiated Materials, eds. Hans Ullmaier and Peter Jung (Forschungszentrum Julich GmbH, January, 1995) 46.

11. G. L. Hankin, M. A. Khaleel, M. B. Toloczko, M. L. Hamilton, and R. G. Faulkner, presented at the 19th ASTM International Symposium on Effects of Radiation on Materials, held June 1998 in Seattle, WA, to be published in the symposium proceedings.

12. M. L. Hamilton, G. L. Hankin, F. A. Garner, and R. G. Faulkner, IBID.

13. L..R. Greenwood, B. M. Oliver, S. Ohnuki, K. Shiba, Y. Kohno, A. Kohyama, J. P. Robertson, and D. S. Gelles, this report.

MICROSTRUCTURAL EXAMINATION OF IRRADIATED ISOTOPICALLY TAILORED FERRITIC/MARTENSITIC STEELS FOLLOWING SHEAR PUNCH TESTING

- D. S. Gelles (Pacific Northwest National Laboratory), S. Ohnuki (Hokkaido University), K. Shiba (JAERI), Y. Kohno (University of Tokyo), A. Kohyama (Kyoto University), J. P. Robertson (Oak Ridge National Laboratory) and M. L. Hamilton (Pacific Northwest National Laboratory)[*]

OBJECTIVE

The objective of this effort is to provide understanding of the effect of hydrogen and helium production during irradiation on post-irradiation mechanical properties in Ferritic/Martensitic steels to be used for first wall applications in a fusion reactor based on microstructural examination.

SUMMARY

Single variable experiments are being conducted to study effects of H/He/dpa on properties based on isotopically tailored alloys. ^{54}Fe has been used to prepare an isotopically tailored duplicate of the commercial steel F82H, and a small number of TEM disks have been irradiated in order to study radiation embrittlement. From single disk specimens, mechanical properties were obtained using a shear punch technique that produces a 1 mm blank from the 3 mm disk. The 1 mm blanks have been thinned and examined by TEM. The novel thinning procedures are described and microstructural observation presented in detail. Little effect of helium on microstructure was found, either in ^{54}Fe isotopically tailored specimens or in a boron doped specimen.

PROGRESS AND STATUS

Introduction

A concern in developing structural materials for fusion power systems is the consequences of transmutation-induced helium and hydrogen on material properties. For the advanced ferritic steel fusion materials option, helium (in appm) will be generated at about ten times the dpa rate, and hydrogen approximately ten times more rapidly than helium. Experiments to define the effect of helium remain controversial[1,2] but severe effects of helium accumulation on fracture toughness have been claimed.[3,4] It is therefore very important to evaluate these transmutation effects in order to establish whether steels can be successfully adapted for fusion applications.

Single variable experiments have been conducted to study effects of H/He/dpa on properties by preparing isotopically tailored alloys. Initially, alloys containing small additions of different nickel isotopes were studied,[5] but the present approach considers alloys made from iron isotopes in order to vary H/He/dpa rates.[6] The controlling reactions are:

$$^{54}\text{Fe (n,p) }^{54}\text{Mn}$$

$$^{54}\text{Fe (n,}\gamma\text{) }^{55}\text{Fe; }^{55}\text{Fe (n,}\alpha\text{) }^{52}\text{Cr or }^{55}\text{Fe (n,p) }^{55}\text{Mn (n,}\gamma\text{) }^{56}\text{Fe.}$$

^{54}Fe was used to prepare an isotopically tailored duplicate of the commercial steel F82H,[7] and, because of cost and irradiation space limitations, a small number of TEM disks were irradiated in order to study radiation embrittlement.

Very recently, individual TEM disks were made available for post-irradiation examination. It was possible to obtain mechanical properties from three alloy conditions for which only a single disk was available, and from a fourth condition where several disks were available in order to compare with results on unirradiated controls. Mechanical properties were obtained using a shear punch technique that produces a 1 mm blank from the 3 mm disk, and microstructural information was obtained from the 1 mm blanks thinned to electron transparency. The purpose of this paper is to document the experimental technique used in preparing TEM specimens and to describe microstructural observation.

Experimental Procedure

A 4 g batch of isotopically tailored F82H ferritic/martensitic steel was prepared as described previously,[7] and specimens 3 mm in diameter, intended for transmission electron microscopy (TEM), were obtained along with a specimen of standard F82H and a specimen of boron-doped F82H, following irradiation in either the JP17 irradiation experiment to 2.3 dpa at 250°C or the JP22 irradiation experiment to 34 dpa at 300°C in the High Flux Isotope Reactor (HFIR) in Oak Ridge, TN.[8-9] Also available were unirradiated control specimens of the isotopically tailored alloy, the standard alloy and another heat of the steel, designated the IEA heat.[10] F82H has the approximate composition (in weight %) Fe-7Cr-2W-0.2V-0.1C-.04Ta-0.01N. Composition details are provided in Table 1 and irradiation details are given in Table 2.

Table 1. Composition of alloys of interest.

Alloy	Cr	C	W	V	Ta	B	Mn	N	Si
F82H ^{54}Fe	7.1	0.097	1.8	0.17	0.04	-	0.4	0.007	0.55
F82H STD	7.46	0.097	2.1	0.18	0.03	0.0004	0.07	0.004	0.09
F82H ^{10}B	7.25	0.098	2.1	0.22	0.04	0.0058	0.5	0.002	0.17

Room temperature mechanical properties information was obtained using a shear punch technique that produces 1 mm blanks from 3 mm disks.[12] Fourteen shear punch tests were performed comprising nine control tests and five tests on irradiated samples. The results of shear punch testing are reported elsewhere.[12]

Preparation of miniature TEM specimens has been a goal for many years because of the inherent benefits arising from reduced magnetic moment and reduced radioactivity. However, previous attempts were not completely successful, either because the smaller specimens were punched from thinned TEM samples, causing excessive deformation, or specimens were prepared from disks smaller than 3 mm, requiring nickel or chrome plating before thinning in order to increase the sample size for simplified handling. Also, it was found that the composite samples tended to come apart during examination because bonding was not ideal. The present effort provided an alternative approach, based on the observation that 1 mm shear punch blanks were free of surface buckling and with well defined cylindrical shear surfaces. Finite element analysis supported the view that 1 mm blanks would provide acceptable material

Table 2. Irradiation conditions for TEM samples.

ID	MATERIAL	CONDITION*
A943-5	F82H IEA	Unirradiated
F191-3	F82H STD	Unirradiated
C103	F82H STD	300°C, 34 dpa, 21.8 appm He
FN91-3	F82H ^{54}Fe	Unirradiated
FN51-2	F82H ^{54}Fe	250°C, 2.3 dpa, 6 appm H, 4.5 appm He
C603	F82H ^{54}Fe	300°C, 34 dpa, 650 appm H, 65.3 appm He
C203	F82H ^{10}B	300°C, 34 dpa, 321 appm He

* H values are predicted, but He values are measured.[11]

for microstructural examination, because the stress state induced by punching at the center of the 1 mm blank remained well below yield.[13] Also, the punching process could be used to provide a 3 mm support disk and then thinning could be accomplished by standard procedures. The need for a glue joint was apparent, but superglue did not allow sufficient positioning control to work properly.

Therefore, specimens for TEM were prepared from the punched 1 mm blanks by pressing them into 3 mm punched 316 stainless steel disks and using thermal setting epoxy to ensure good bonding. Surfaces were then ground to remove excess epoxy and samples were electropolished to perforation in a standard Tenupol twin jet polishing apparatus. The epoxy bond was found to be resistant to chemical attack and provided a good bond as well as a supporting rim for the thin foil adjacent to the perforation. Examples of an unpunched disk, a punched disk with 1 mm blank and a thinned 1 mm specimen in a 3 mm stainless steel disk are shown in Figure 1.

Results

TEM specimen preparation was successful for all seven conditions available. However, the control condition for the IEA heat of F82H was not examined in this study. All thin foils prepared from the 1 mm blanks could be considered very good to excellent, with negligible bending and sufficient thin area at the center of the disk. No problems were encountered due to magnetic interactions or excessive radioactivity. Examples of the microstructures at low magnification are shown in Figure 2. Micrographs have been selected to show prior-
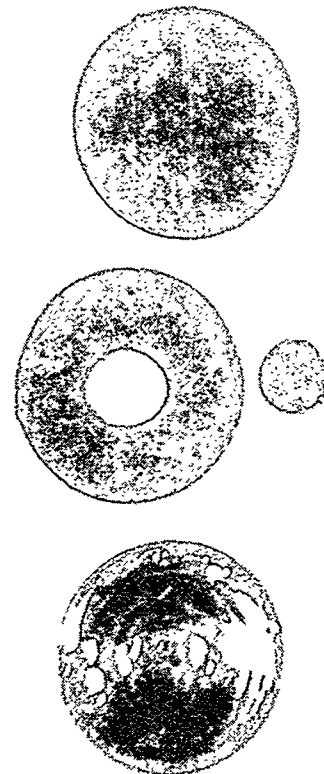
Figure 1. Sample Configurations for TEM Specimen Preparation.
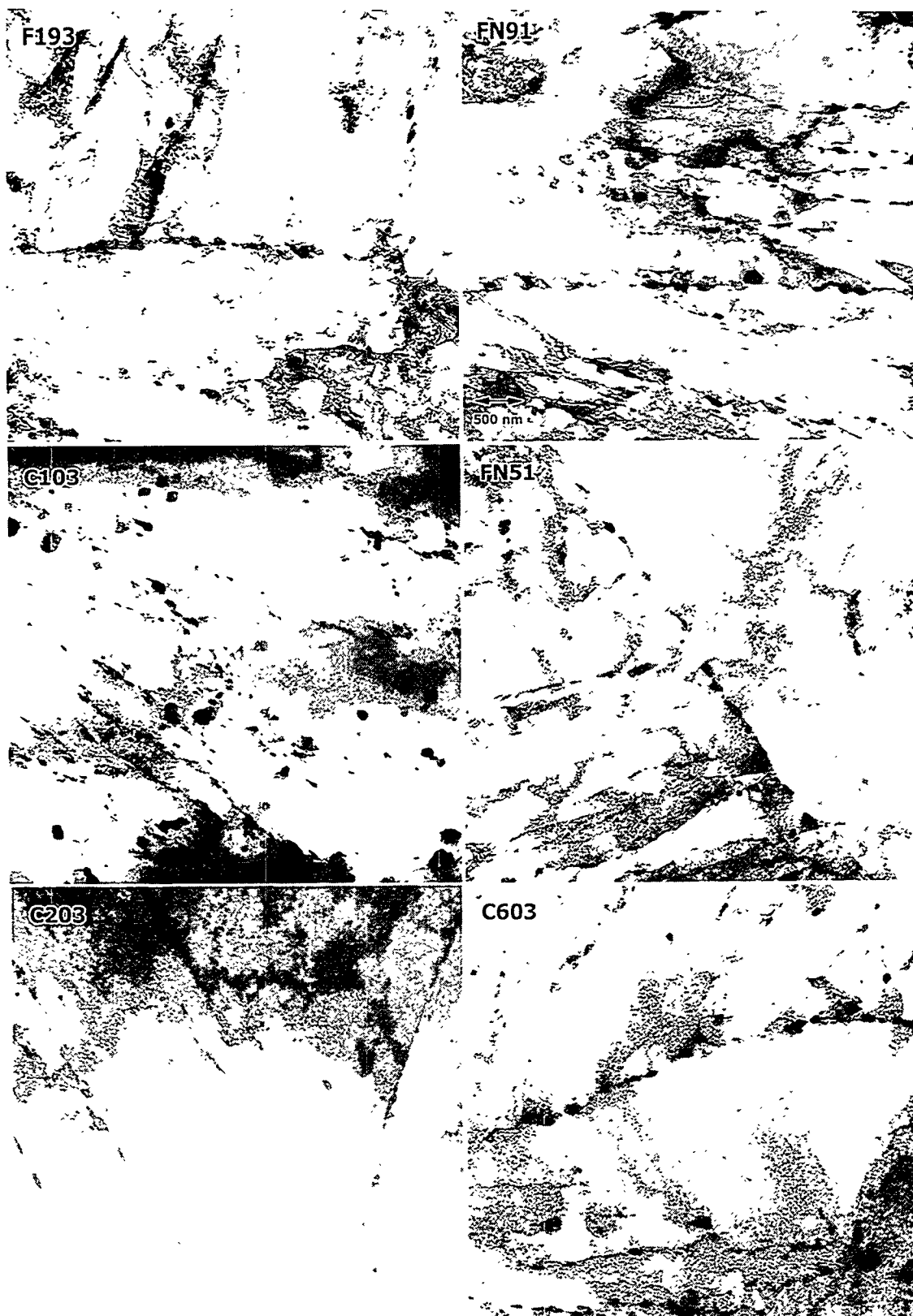
Figure 2. Microstructures at low magnification.

austenite boundary structure when they could be found, and are arranged with standard F82H on the upper left, [54]Fe F82H on the right with increasing dose from top to bottom, and [10]B F82H at the bottom left. Figure 2 demonstrates that foils provided abundant thin area. However, foils of specimens C103 and C203 had limited thin area compared to the other conditions. From Figure 2, it can be shown that all conditions appear typical of F82H. Lath boundaries are decorated with carbides and dislocation structures tend to be subgrain boundaries in the unirradiated conditions: F193 and FN91. Figure 2c of specimen C103 shows coarser carbide structure than the control condition of F193 in Figure 2a, but differences should probably be ascribed to area-to-area differences in the carbide distribution. The effect of irradiation is seen as damage on a fine scale that tends to obscure subgrain structure.

In order to examine the fine scale damage due to irradiation, the microstructures were imaged under conditions approaching weak beam using $\vec{g}$ = [200] and [011] for foils oriented near (011). Dislocation microstructures for the six conditions are given in Figure 3. Figure 3 is arranged to show [011] dark field contrast images with $\vec{g}$ vertical for all conditions, and in the three cases where two images dark field images for a given condition are provided, a 200 dark filed image is provided on the left (3c, 3e and 3g) with $\vec{g}$ horizontal. Therefore, Figure 3 provides examples of the unirradiated microstructures for F82H STD in a and F82H [54]Fe in b, F82H [54]Fe is then shown with increasing dose in c, d e and f, and then F82H STD in g and h can be compared with F82H [10]B in i and j for the high dose condition. Figure 3i presents a bright field image in order to assess cavitation development in F82H [10]B. From Figure 3, it can be noted that dislocation structure prior to irradiation consists of subgrain boundaries and a low density of straight dislocations within laths. Following irradiation, fine dislocation structure develops consisting of both $\frac{a}{2}$<110> and a<100>. [Under [200] contrast, strong vertical images show one set of a<001> and all other images are of $\frac{a}{2}$<111> type with all sets visible.] In F82H [54]Fe, irradiation to 2.3 dpa at 250°C produces $\frac{a}{2}$<111> dislocations with loops as large as 20 nm, as well as a few a<100> loops as large as 13 nm. Irradiation to 34 dpa increases both the total dislocation density and the fraction of a<100> dislocations. In comparison, the F82H STD and F82H [10]B at 34 dpa produce microstructures similar to F82H [54]Fe. The bright field image of F82H [10]B irradiated to 34 dpa reveals no significant cavitation despite the He level at 321 appm He. Therefore, irradiation of this isotopically tailored series of alloys at 250 to 300°C develops both $\frac{a}{2}$<110> and a<100> dislocation structure and this structure should be responsible for changes in mechanical properties due to irradiation.

Examination included limited efforts at FEG-STEM compositional analysis. Compositional analysis of carbide precipitates was possible and sufficiently detailed to demonstrate transmutation of approximately a third of the W to Os, with no evidence for the intermediate product, Re, following irradiation of standard F82H to 34 dpa. This can be shown from Figure 4, which provides x-ray spectra for a carbide precipitate in F82H STD irradiated at 300°C to 34 dpa after subtraction of a hole count. The spectrum has been labelled to show peak positions for W, Re and Os. The Os peak is approximately one third of that for W with Re absent. Therefore, it can be concluded that ⅓ of the W has transmuted to Os with little of the intermediate product Re retained, and the Os is retained in the chrome carbides. This transmutation response has been predicted by Garner and Greenwood.[14]

Discussion

This effort demonstrates that it is possible to obtain mechanical property and microstructural information on very limited quantities of material: TEM samples weigh about 0.01 g and the 1 mm blank about 0.001 g. The techniques described above not only allow for experiments
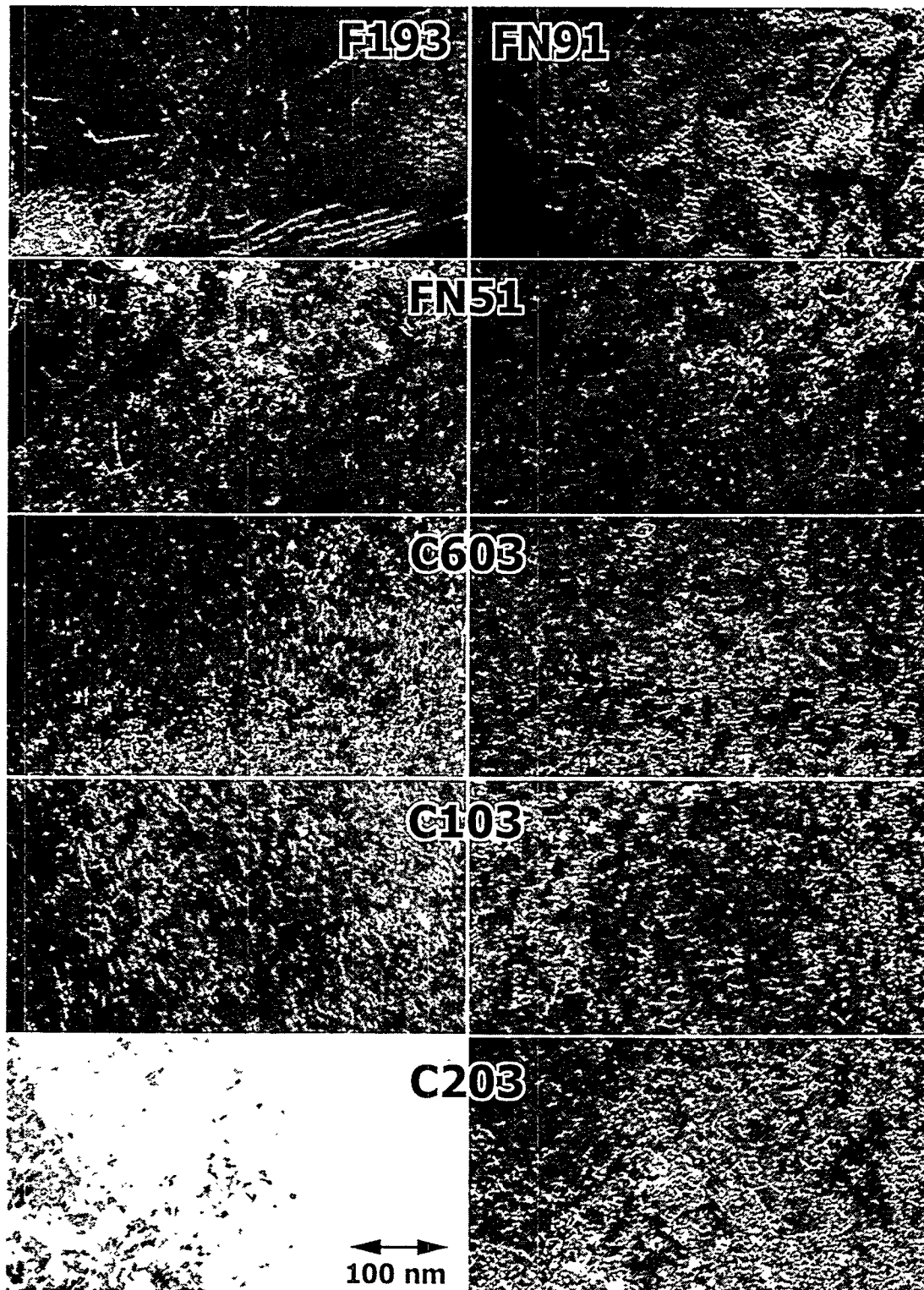
Figure 3. Microstructures at higher magnification showing dislocation structures in dark field a-h and j and in bright field i. See text for details.

where material is very limited, very expensive or very difficult to obtain in the desired treatment or irradiation condition, but they also allow sampling of complex conditions.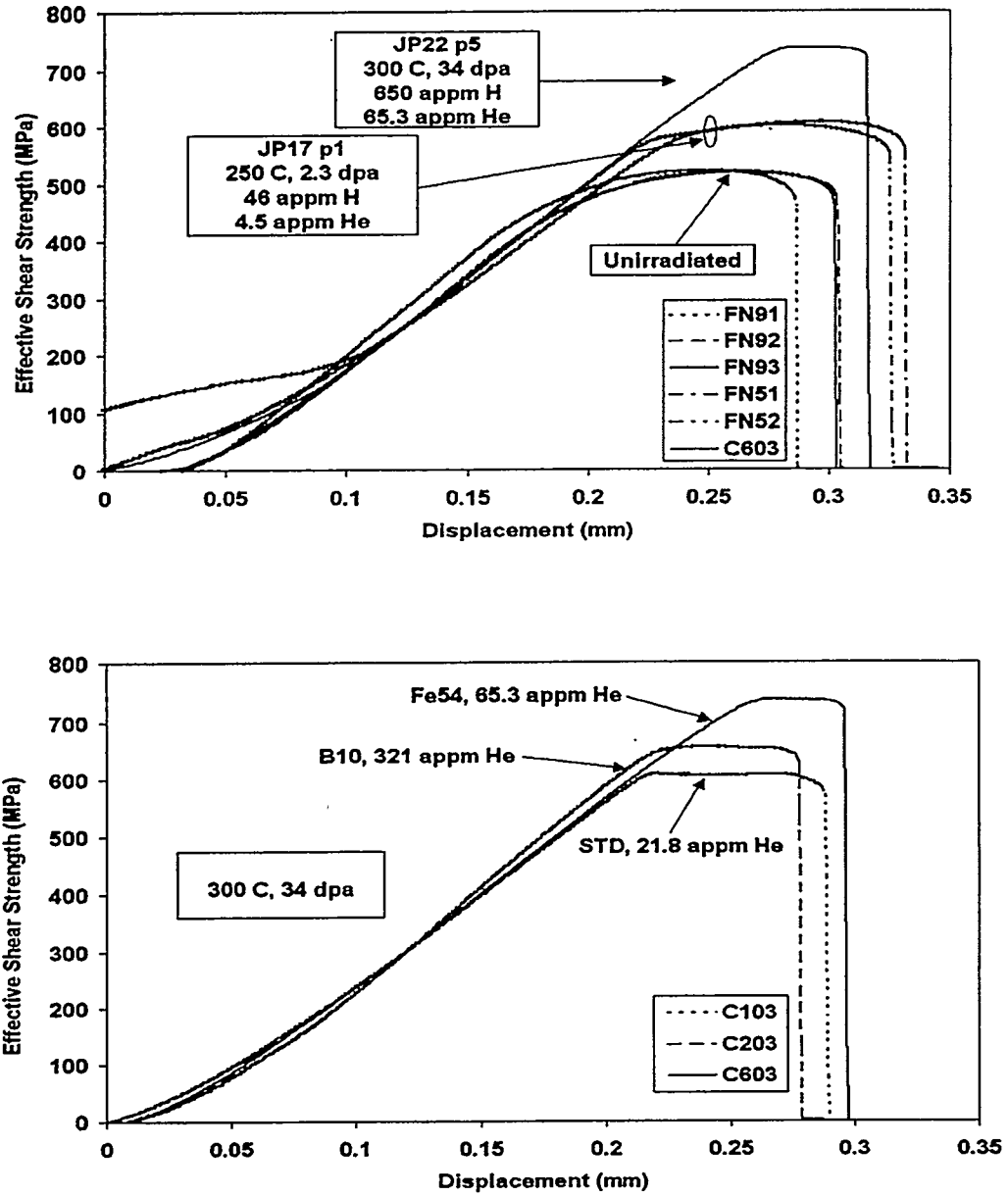 For example, in irradiation creep experiments where strong gradients exist in temperature or flux, it may now be possible to provide understanding of property and microstructural variation over distances of one or two mm. The added advantages of effectively smaller TEM sample volumes that reduce radioactivity or magnetic interactions are also of benefit.
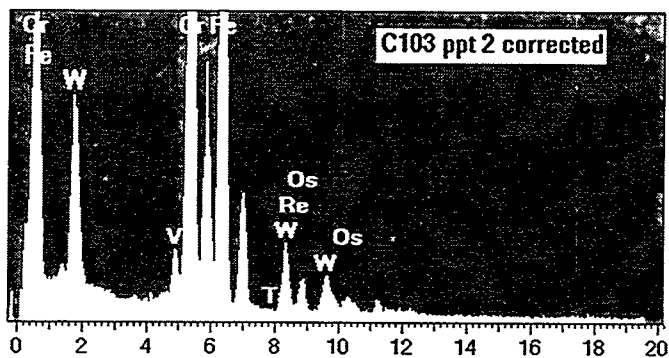
Figure 4. X-ray spectrum for carbide particle in specimen C103 (with background removed).

The intent of isotopic tailoring experiments is to assess the effect of hydrogen and helium production during irradiation on properties and microstructure. Because mechanical properties for the different alloys following irradiation at 300°C are very similar, the present results do not demonstrate a significant effect of helium on mechanical properties, and any effect of hydrogen is probably small, although hydrogen production levels are not completely understood. However, it should be noted that concerns about a large effect of helium on ductile brittle transition behavior are centered on irradiation temperatures in the 400°C range. Therefore, the present results are probably not directly pertinent to that issue. However, the absence of precipitate formed during irradiation as found in the these ^{54}Fe isotopically tailored alloys differs from the case where Ni isotopic tailoring was used.[ref]

CONCLUSIONS

Isotopic tailoring is being used to study effects of transmutation on mechanical properties.

Shear punch tests can provide mechanical properties information with limited numbers of TEM samples creating 1 mm blanks that can be successfully prepared for microstructural examination.

Microstructural comparisons show that hardening is due to development of $\frac{a}{2}<110>$ and a$<100>$ dislocation structure with little difference between the different alloys following irradiation to 34 dpa at 300°C.

FUTURE WORK

This work will be continued within the confines of funding and specimen availability.

REFERENCES

1. R. L. Klueh, J. Nucl. Mater. 218 (1995) 151.

2. D. S. Gelles, R. L. Klueh and D. J. Alexander, J. Nucl. Mater. 230 (1996) 187.

3. A. Hishinuma, A. Kohyama, R. L. Klueh, D. S. Gelles, W. Dietz, and K. Ehrlich, J. Nucl. Mater. 258-263 (1998) 193.

4. A. Kohyama, A. Hishinuma, D. S. Gelles, R. L. Klueh, W. Dietz, and K. Ehrlich, J. Nucl. Mater. 233-237 (1996) 138.

5. D. S. Gelles, G. L. Hankin and M. L. Hamilton, J. Nucl. Mater. 251 (1997) 188.

6. L. R. Greenwood and F. A. Garner, J. Nucl. Mater. 212-215 (1994) 635.

7. M. Suzuki, A. Hishinuma, N. Yamanouch, M. Tamura and A. F. Rowcliffe, J. Nucl. Mater. 191-194 (1992) 1056.

8. A. W. Longest, D. W. Heatherly, K. R. Thoms and J. E. Corum, in Fusion Materials Semiannual Progress Report for the Period Ending March 31, 1992, DOE/ER-0313/12 (1992) 24.

9. J. E. Pawel, A. W. Longest, R. L. Senn, D. W. Heatherly, R. G. Sitterson, in Fusion Materials Semiannual Progress Report for the Period Ending September 30, 1993, DOE/ER-0313/15 (1994) 3.

10. K. Shiba in Proceedings of the IEA Working Group Meeting on Ferritic/Martensitic Steels, ed. R. L. Klueh, October 1996, ORNL/M-5674.

11. L. R. Greenwood, B. M. Oliver, S. Ohnuki, K. Shiba, Y. Kohno, A. Kohyama, J. P. Robertson and D. S. Gelles, this report.

12. M. L. Hamilton, S. Ohnuki, K. Shiba, Y. Kohno, A. Kohyama, J. E. Roberston, and D. S. Gelles, this report.

13. G. L. Hankin, M. A. Khaleel, M. B. Toloczko, M. L. Hamilton, and R. G. Faulkner, presented at the 19th ASTM International Symposium on Effects of Radiation on Materials, held June 1998 in Seattle, WA, to be published in the symposium proceedings.

14. F. A. Garner and L. R. Greenwood, Rad. Eff. & Def in Solids 144 (1998) 251.

HYDROGEN PRODUCTION EFFECT ON MICROSTRUCTURE OF HFIR-IRRADIATED LOW ACTIVATION F82H STEEL USING ^{54}Fe ISOTOPE

E. Wakai (Japan Atomic Energy Research Institute), N. Hashimoto (Oak Ridge National Laboratory), K. Shiba, Y. Miwa(JAERI), J. P. Robertson, and R. L. Klueh(ORNL)

OBJECTIVE

The purpose of the present study is to investigate the effect of hydrogen production on the microstructure and mechanical properties of ^{54}Fe-doped F82H steel irradiated in HFIR.

SUMMARY

Reduced-activation F82H-std and a similar F82H doped with ^{54}Fe (F82H(^{54}Fe)) steels were irradiated at 250°C to 2.8 dpa in HFIR and examined by TEM. The produced hydrogen concentration in the F82H(^{54}Fe) steel is estimated to be 68 appm. Pre-irradiation microstructures of F82H(^{54}Fe) steel were very similar to those of F82H-std steel. A few small cavities were formed in the irradiated F82H(^{54}Fe) steel, but the swelling is insignificant, while in the F82H-std steel no cavities were observed. Precipitates with contrast similar to α' phase were observed on many dislocation loops in these steels. The number density and mean size for dislocation loops in the F82H-std and F82H(^{54}Fe) steels are 1.4 $\times 10^{22}$ m^{-3} and 7.9 nm, and 2.1x10^{22} m^{-3} and 6.6 nm, respectively. The types of loops are b=(a/2)<111> for the F82H-std and b=(a/2)<111> and a<100> for the F82H(^{54}Fe) steel. The concentration of a<111> type to all loops in the F82H(^{54}Fe) steel is about 73%.

PROGRESS AND STATUS

1. Introduction

Ferritic/martensitic steels are candidate materials for the first wall and blanket structure of fusion reactors. In the D-T fusion reaction, the high-energy neutrons produced induce displacement damage and generate hydrogen and helium gas atoms in the materials from (n, p) and (n, α) reactions. The presence of these gases could lead to degradation of mechanical properties. In order to investigate the effect of hydrogen gas atoms on ferritic steels using a fission reactor, hydrogen gas atoms can be generated in F82H by doping with the ^{54}Fe isotope. Irradiation of such an alloy in a mixed-spectrum fission reactor with thermal neutrons like the High Flux Isotope Reactor (HFIR) results in the following transmutation reactions:

^{54}Fe(n, p)^{54}Mn,

^{54}Fe(n, α)^{52}Cr.
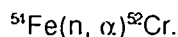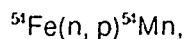
The effects of neutron irradiation on the tensile deformation of F82H steel have been reported. Shiba et al. [1-2] have described the tensile data, obtained under the U.S. DOE/JAERI program, following irradiation in HFIR at 200 to 600°C for doses in the range 3-34 dpa; The effect of helium production on mechanical properties were investigated using an isotope of boron (^{10}B). A summary of the tensile data for 9-12Cr ferritic/martensitic steels irradiated under a variety of

conditions has been presented by Rowcliffe et al. [3] and Zinkle et al.[4]. Klueh et al. [5] have reported that DBTT shifts of F82H-std, OPTIFER-1a, and 9Cr-2WVTa steels increase for irradiation temperatures below 300°C even for low damage levels of 1-3 dpa.

The purpose of the present study is to analyze the radiation-induced microstructural changes under hydrogen production in the ^{51}Fe-doped F82H steels.

2. Experimental procedure

The chemical compositions of the F82H-std and F82H(^{54}Fe) specimens used in this study are given in Table 1. The mass ratio of iron for these specimens was analyzed to be as shown in Table 2, correcting for the presence of ^{54}Cr. This means that about 96 % of iron atoms in the doped alloy were composed of ^{54}Fe in the F82H(^{54}Fe) specimen [6]. Normalizing and tempering were performed in a vacuum followed by air-cooling as given in Table 3. The details of the preparation process for the F82H(^{54}Fe) is described in ref. [6].

Table 1   Chemical compositions of the specimens used in this study (wt%)

Alloys	Cr	B	C	N	P	S	Al	Si	V	Mn	Ta	W
F82H-std	7.46	0.0004	0.094	0.002	0.003	0.003	0.019	0.09	0.18	0.07	0.03	2.1
F82H(^{54}Fe)	7.1	-	0.097	0.007	<0.002	0.0015	0.03	0.55	0.15	0.40	0.04	1.8

Table 2   Mass ratio analysis of the isotopically tailored F82H steel using ^{54}Fe

Alloy	Relative mass ratio		
	54/56	57/56	58/56
F82H-std	0.083	0.023	0.0003
F82H(^{54}Fe)	40	0.0083	0.00087

Table 3   Heat treatment

Alloy	Normalizing	Tempering
F82H-std	1040°C, 0.67h	740°C, 2h
F82H(^{54}Fe)	1040°C, 0.33h	745°C, 0.67h

Table 4   Neutron fluence (n/cm^2) and damage value for the F82H steel

Total	Thermal (<0.5 eV)	0.5 eV - 0.1 MeV	>0.1 MeV	>1 MeV	Damage (dpa)
1.26×10^{21}	4.78×10^{21}	4.09×10^{20}	3.73×10^{20}	1.96×10^{20}	~2.8

Standard 3 mm-diameter disks punched from 0.25 mm-thickness sheet stock were irradiated in the HFIR target in the HFIR-MFE-JP17 capsule as part of the JAERI/US collaborative program. The irradiation began on December 31, 1991, at the start of HFIR fuel cycle 304 and ended February 27, 1992, at the end of HFIR cycle 305. The exposure for the irradiation was 3702 MWd, or approximately 43.6 days at 85 MW reactor power. The complete description and details of the design, construction, and installation of the capsule have been previously reported [7-9]. The irradiation temperatures and displacement damage were 250 °C and about 2.8 dpa for the F82H steel in the JP17 capsule. The neutron fluence data [10] are given in Table 4. Hydrogen and helium production in the F82H(^{54}Fe) steel irradiated to 2.8 dpa were estimated to be 68 appm H and about 1 or 2 appm He, respectively, using only a reference data for spectral averaged cross section (^{54}Fe(n, p) ^{54}Mn--1.19×10^{-2} barn, ^{54}Fe(n, α) -- (1.9 or 3.6) $\times 10^{-4}$ barn) [11]. In the F82H-std steel, the values of hydrogen and helium production were also estimated to be 5 appm H and 5 appm He (4 appm He produced from impurity boron), respectively, using impurity boron concentration and the reference data (^{54}Fe(n, p) ^{54}Mn--1.19×10^{-2} barn, ^{55}Fe(n, p) ^{56}Mn--2.4×10^{-4} barn) [11].

Microstructures of these specimens were examined using a JEM-2000FX transmission electron microscope with a LaB$_6$ gun operated at 200 kV. Microstructures of unirradiated control specimens were also examined.

3. Results

3.1 Pre-irradiation microstructures of the F82H-std and F82H(^{54}Fe) steels

The microstructure after normalizing and tempering was a lath martensitic structure in both the F82H-std and F82H(^{54}Fe) steel, and these steels are very similar to each other as shown in Figs. 1(a) and 1(b). Large precipitates of M$_{23}$C$_6$ carbides were observed in the matrix and on grain boundaries in these steels. MC carbides also formed in the matrix for these steels. The dislocation density for the two steels was nearly equal. The mean width of the lath boundaries for the F82H(^{54}Fe) was close to that for F82H-std. The microstructural features are summarized in Table 5.
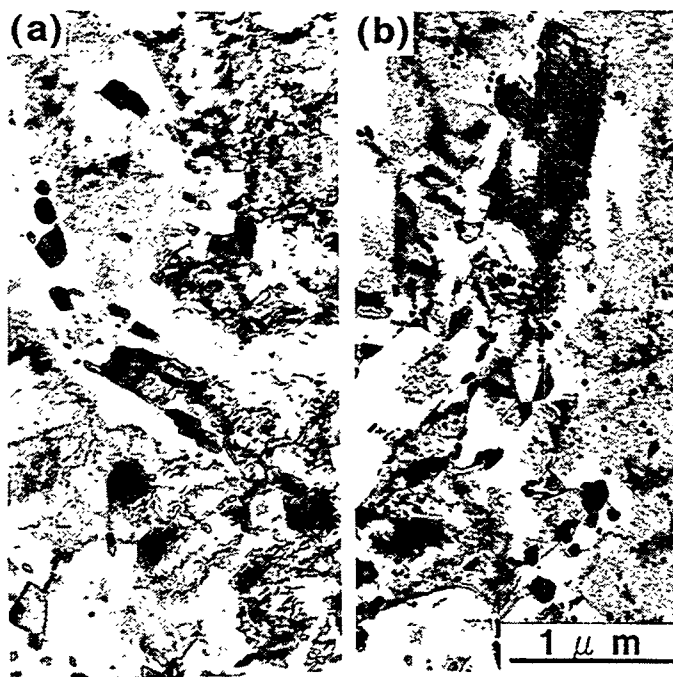
Fig. 1 Pre-irradiation microstructures of (a) F82H-std and F82H(^{54}Fe) steels

Table 5 Summary of defect clusters formed in the F82H and F82H(^{54}Fe) steels.
RMC denotes root mean cube.

	F82H-std unirradiated	F82H(^{54}Fe) unirradiated	F82H-std 250°C, 2.8 dpa	F82H(^{54}Fe) 250°C, 2.8 dpa
Dislocation loops Number density Mean size	-	-	1.4×10^{22} m^{-3} 7.9 nm	2.1×10^{22} m^{-3} 6.6 nm
Dislocations Areal number density	9×10^{13} m^{-2}	1×10^{14} m^{-2}	1×10^{14} m^{-2}	9×10^{13} m^{-2}
Cavities Number density RMC radius Swelling	-	-	0 m^{-3} 0 nm 0 %	5×10^{19} m^{-3} 1.9 nm 0.0001%
M$_{23}$C$_6$ Number density Mean size	3×10^{20} m^{-3} 62 nm	5×10^{20} m^{-3} 76 nm	3×10^{20} m^{-3} 73 nm	3×10^{20} m^{-3} 65 nm
MC Number density Mean size	$<1 \times 10^{20}$ m^{-3} 14 nm	2×10^{20} m^{-3} 12 nm	1×10^{20} m^{-3} 13 nm	2×10^{20} m^{-3} 13 nm
Lath Mean width of lath	440 nm	480 nm	410 nm	450 nm

3.2 Standard F82H steel irradiated at 250°C to 2.8 dpa

Figures 2(a)-(c) show microstructures of the F82H-std steel irradiated at 250°C to 2.8 dpa; these micrographs were taken in the [001] direction using g=110 at a low and high magnification of bright-field image condition, and a high magnification of weak beam dark-field image condition, respectively. Dislocation loops were observed on {111} planes with (a/2)<111> Burgers vectors. Some loops were arranged along dislocation lines. The number density and mean size of the loops were 1.4×10^{22} m^{-3} and 7.9 nm, respectively. Precipitates with contrast like α'-phase were observed on many dislocation loops. A few MC carbides were observed in the matrix. No cavities were observed. The microstructural features are also summarized in Table 5.
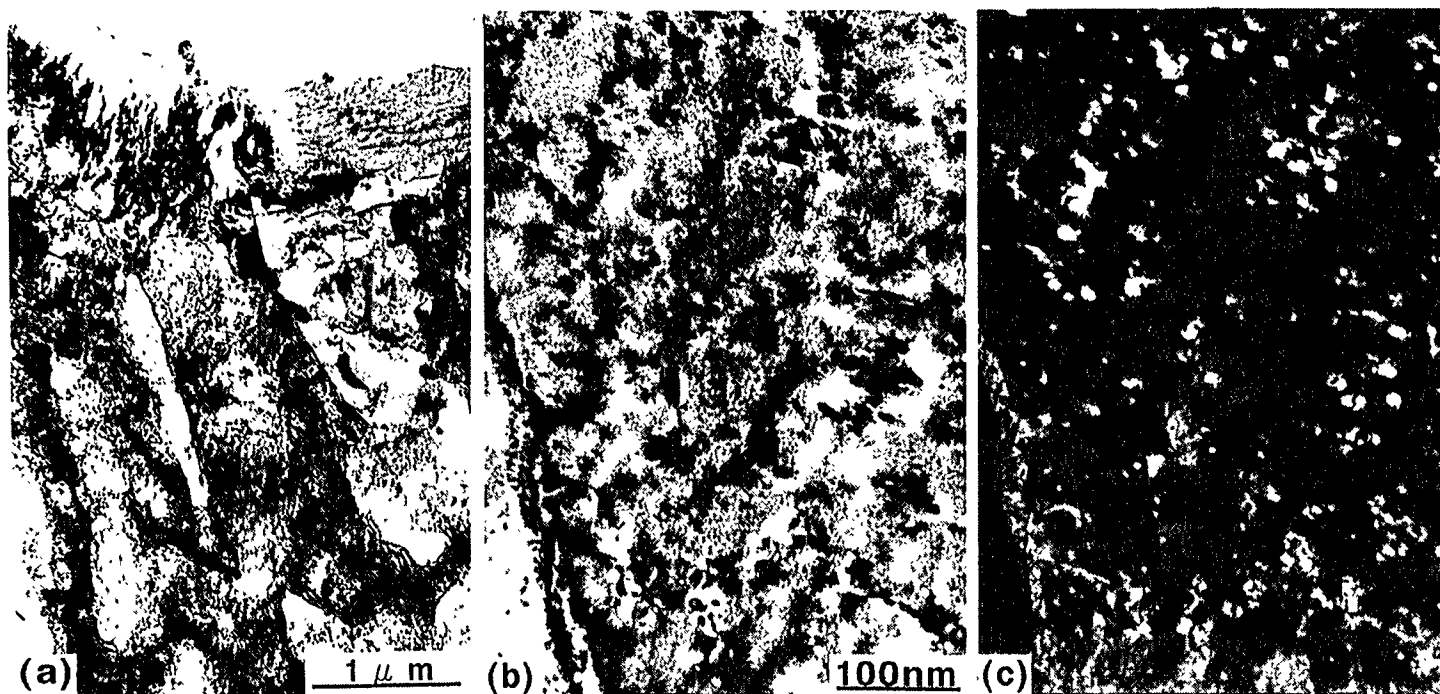
Fig. 2 Microstructures of (a) a bright-field image in low magnification, (b) a bright-field image in high-magnification, and (c) a weak beam dark-field image in high-magnification in the **F82H-std** steel irradiated at 250°C to 2.8 dpa. Precipitates with contrast like α'-phase are seen on many dislocation loops.

3.3 F82H(^{54}Fe) steel irradiated at 250°C to 2.8 dpa

Figures 3(a)-(c) show microstructures of the F82H(^{54}Fe) steel irradiated at 250°C to 2.8 dpa; these micrographs were also taken from the [001] direction using g =110 at a low and high magnification of bright-field image condition, and a high magnification of weak beam dark-field image condition, respectively. Two types of dislocation loops were observed: those on {111} planes with (a/2)<111> Burgers vectors and those on {100} planes with a<100> ones. The concentration of <111> type to all loops was about 73%. The total number density and mean size of loops was 2.1×10^{22} m^{-3} and 6.6 nm, respectively. Precipitates contrast like α'-phase were also observed on many dislocation loops. A few MC carbides were observed in the matrix. As shown in Fig. 4, several small cavities were observed, and the number density, root mean cube of radius, and swelling of cavities were 5×10^{19} m^{-3}, 1.9 nm, and 0.0001%, respectively .
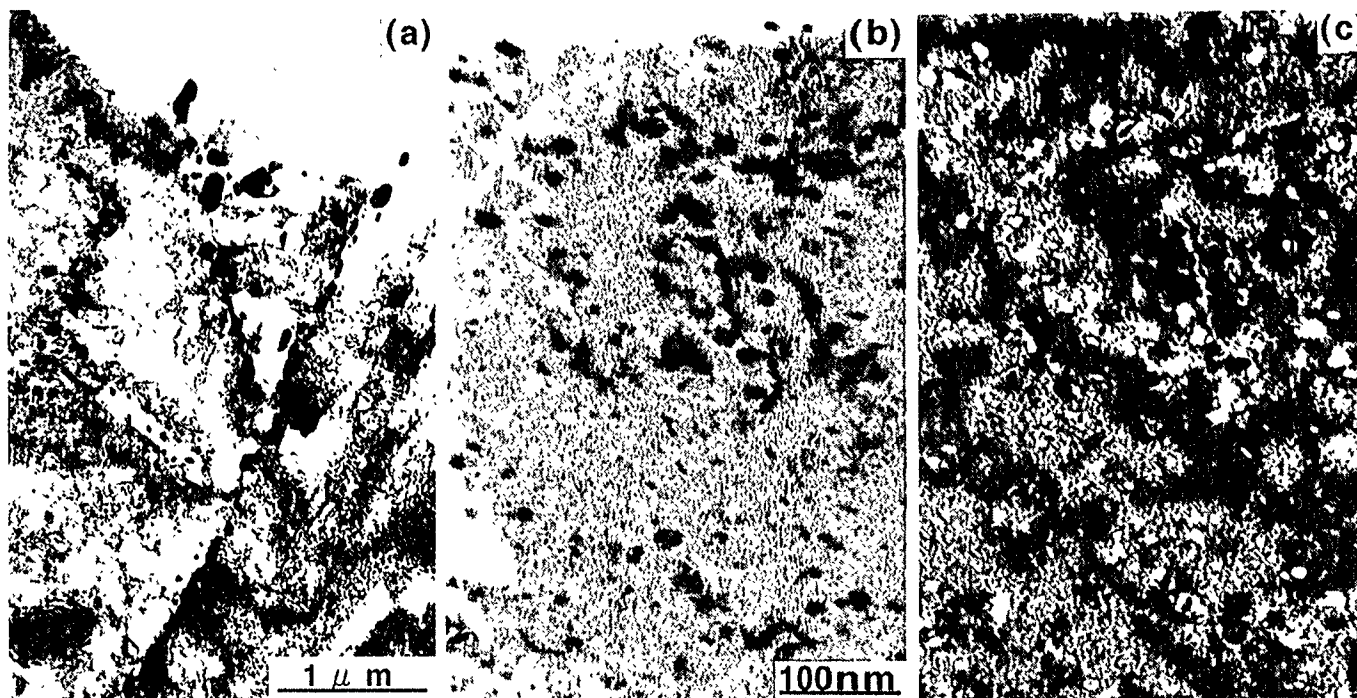
Fig. 3 Microstructures of (a) a bright-field image in low magnification, (b) a bright-field image in high-magnification, and (c) a weak beam dark-field image in high-magnification in the F82H(^{54}Fe) steel irradiated at 250°C to 2.8 dpa. Precipitates with contrast like α'-phase are also seen on many dislocation loops.
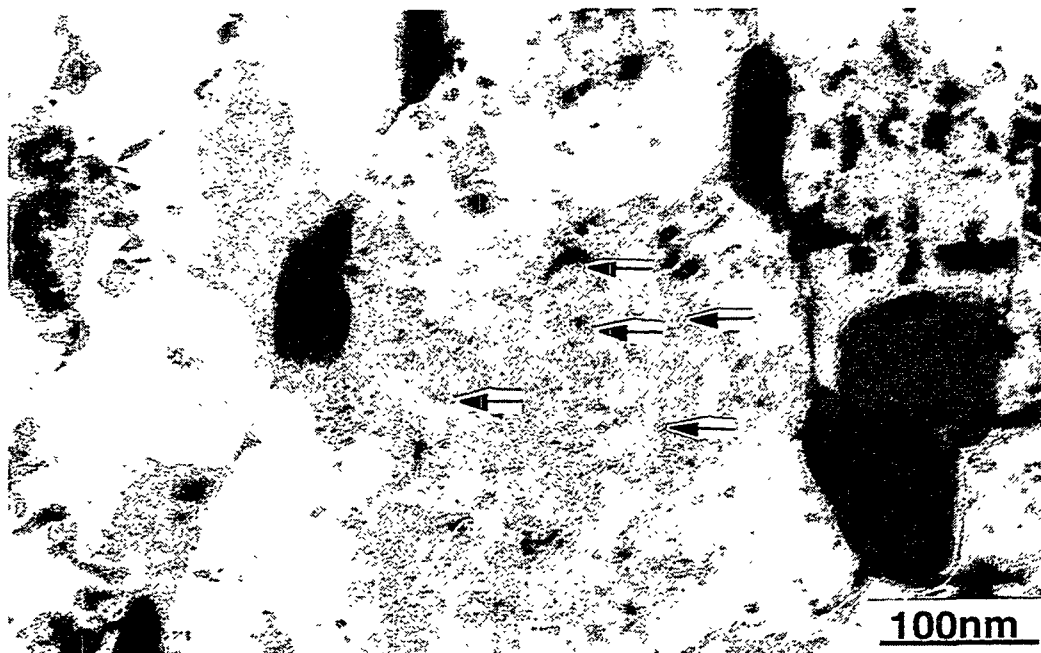
Fig. 4 Cavities formed in the the $F82H(^{54}Fe)$ steel irradiated at 250°C to 2.8 dpa.

4. Discussion

4.1 Precipitates with contrast like α'-phase observed on dislocation

According to ref. [12-16] for radiation effects of binary Fe-(9-50)Cr alloys, dislocation loop formation was affected by the purity level of the alloys, and in many case Cr-rich-precipitates (α'-phase) on the loops were formed. Under 1 MeV electron irradiation, α' precipitate formation on dislocation loops was observed at temperatures below 600°C in an Fe-9Cr alloy. As the irradiation temperature decreased the dislocation loop density increased and α' precipitate density also increased. In case of neutron irradiation, the α' precipitate density on the dislocation loops was less than that in case of electron irradiation, and the cause of it may be considered to be due to cascades and low damage rates in the neutron environment. This formation of α' precipitate on dislocation loops in Fe-Cr alloys could cause large shifts of DBTT and large increases of yield strength (Y.S.), such as $\Delta DBTT = 145°C$ and $\Delta Y.S. = 260$ MPa seen for high-purity Fe-9Cr alloys irradiated at 330°C to 0.3 dpa in JRR-3M (Modified Japan Research Reactor-3) [13, 14]. Therefore, the cause of the large shift of DBTT, +130°C, in the F82H-std irradiated at 250°C to 2.8 dpa [5] may be explained by the idea that the precipitates seen on dislocation loops in this experiment are α'-phase .

4.2 Type of dislocation loops

It is well known that the formation energy of (a/2)<111> loops is smaller than that of a<100> loops. Recently, purity effects of Fe-(9-50)Cr alloys, corresponding to 99.7% (including about 100 wt.ppm carbon) and 99.99% purity (including about 3 - 60 wt.ppm carbon), on dislocation loops under irradiation were investigated [12,16]. The number density of loops increased with increasing impurity level, such as carbon and nitrogen atoms, and the mean size of loops decreased with impurity level. The loops on {100} planes with a<100> Burgers vector were observed in all specimens. In addition to this, another type of loops on {111} planes with (a/2)<111> formed in high-purity Fe-Cr alloys. Carbon concentration was very sensitive to the type of loop formation, and no formation of (a/2)<111> type was in the Fe-Cr alloys with more than 60 wt.ppm carbon. The number ratio percentage of (a/2)<111> type to all types was about 60-70% at 300°C and 80-90% at 500 °C in the high-purity Fe-Cr alloys (including 3-5 wt.ppm carbon). These reference data suggest that the formation of a<100> type is very difficult in the higher purity Fe-Cr alloys with less than 3 wt.ppm carbon. F82H(^{54}Fe) steels irradiated at 250°C to 2.8 dpa have two types of loops of (a/2)<111> and a<100>, while F82H-std has only one type of (a/2)<111>. This results may be related to the free carbon concentration in the matrix. The tempering time for the former steel is shorter than that of F82H-std, and the carbide formation may not be saturated. Therefore, it can be considered that the free carbon concentration in the matrix in F82H-std steel may be very low.

ACKNOWLEDGMENTS

REFERENCES

[1] K. Shiba, I. Ioka, J. P. Robertson, M. Suzuki, and A. Hishinuma, Euromat-9 6(1996), p.265.

[2] K. Shiba et. al, unpublished data.

[3] A. F. Rowcliffe, J. P. Robertson, R. L. Klueh, K. Shiba, D. J. Alexander, M. L. Grossbeck, and S. Jitsukawa, J. Nucl. Mater., 258-263(1998), pp. 1275-1279.

[4] S. J. Zinkle, J. P. Robertson, and R. L. Klueh, Fusion Reactor Materials Semiannual Progress Report for Period Ending June 30, 1988, Office of Fusion Energy, DOE/ER-0313/24, pp. 135-143.

[5] R. L. Klueh, D. J. Alexander, and M. Rieth, Fusion Reactor Materials Semiannual Progress Report for Period Ending June 30, 1988, Office of Fusion Energy, DOE/ER-0313/24, pp. 150-162.

[6] M. Suzuki, A. Hishinuma, N. Yamonouchi, M. Tamura, and A. F. Rowcliffe, J. Nucl. Mater., 191-194(1992), pp. 1056-1059.

[7] A. W. Longest, D. W. Heatherly, K. R. Thoms, and J. E. Corum, Fusion Reactor Materials Semiannual Progress Report for Period Ending March 31, 1991, Office of Fusion Energy, DOE/ER-0313/10, p.3.

[8] A. W. Longest, D. W. Heatherly, J. E. Wolfe, K. R. Thoms, and J. E. Corum, Fusion Reactor Materials Semiannual Progress Report for Period Ending September 30, 1991, Office of Fusion Energy, DOE/ER-0313/11, p.30.

[9] A. W. Longest, D. W. Heatherly, K. R. Thoms, and J. E. Corum, Fusion Reactor Materials Semiannual Progress Report for Period Ending March 31, 1992, Office of Fusion Energy, DOE/ER-0313/12, p.24.

[10] L. R. Greenwood and C. A. Balwin, Fusion Reactor Materials Semiannual Progress Report for Period Ending March 31, 1996, Office of Fusion Energy, DOE/ER-0313/19, pp. 286-290. G. [11] R. Odette, J. N. Mater., 141-143(1986), pp. 1011-1017.

[12] E. Wakai, A. Hishinuma, K. Yano, S. Takaki, and K. Abiko, J. Physique (IV) ,5 (1995), C7-pp. 277-286.

[13] A. Hishinuma, E. Wakai, S. Takaki, and K. Abiko, Proc. Ultra High Purity Base Metals, 1998, pp. 27-34.

[14] E. Wakai, A. Hishinuma, S. Takaki, and K. Abiko, to be applied, in Proc. Ultra High Purity Base Metals, 1999.

[15] E. Wakai, A. Hishinuma, T. Sawai, S. Kato, S. Isozaki, S. Takaki, and K. Abiko, Phys. Stat. Sol. (a), 160(1997), p.441.

[16] E. Wakai, A. Hishinuma, Y. Kato, S. Takaki, and K. Abiko, Proc. Ultra High Purity Base Metals, Eds. K. Abiko, K. Hirokawa, and S. Takaki, The Japan Institute of Metals Sendai (Japan), (1994), p.522.

SWELLING OF HFIR-IRRADIATED F82H, F82H+^{10}B AND F82H+^{58}Ni STEELS - E. Wakai (Japan Atomic Energy Research Institute), N. Hashimoto (Oak Ridge National Laboratory), K. Shiba, Y. Miwa (JAERI), J. P. Robertson, and R. L. Klueh(ORNL)

OBJECTIVE

The purpose of the present study is to investigate the swelling of ferritic/martensitic F82H steels following neutron irradiation in the range 200 - 500°C and the effect of dopant elements on the swelling of isotopically tailored F82H steels.

SUMMARY

Swelling of reduced-activation F82H-std and F82H steels doped with natural boron (311 appm), isotope ^{10}B (325 appm), 1.35 at% ^{58}Ni, and 1.31 at% ^{60}Ni irradiated at 300 and 400 °C to 52 dpa in the HFIR have been examined by TEM. The swelling of F82H-std irradiated at 400 °C to 52 dpa is about 0.6 % and the natural B and ^{10}B doped F82H steels is about 0.9 and 1.1 %, respectively. In the ^{58}Ni and ^{60}Ni doped F82H steels, swelling is 0.02 and 0%, respectively, even though the ^{58}Ni-doped specimen has the highest helium production. Large cavities in the F82H-std are observed in the matrix but not observed near many lath boundaries, while in the ^{10}B doped specimens, cavities are formed even near lath boundaries. While the cavities formed at 300°C to 52 dpa are observed in only the F82H+^{10}B and F82H+^{58}Ni steels, the swelling value is insignificant. The number densities of dislocation loops formed in these steels at 300°C to 52 dpa are very high(i.e., on the order of 10^{22} m^{-3}), and at 400°C to 52 dpa the number densities are very low (i.e., on the order of 10^{20} m^{-3}). A high density of precipitates is formed in the matrix of the Ni-doped F82H steels. The low swelling of Ni-doped specimens at 400 °C of 52 dpa may be caused by the formation of a high density of precipitates.

PROGRESS AND STATUS

1. Introduction

Ferritic/martensitic steels are candidate materials for the first wall and blanket structure of fusion reactors. In the D-T fusion reaction, the high-energy neutrons produced induce displacement damage and generate gas atoms (helium) in the materials from (n, p) and (n, α) reactions. The presence of these gases could lead to degradation of mechanical properties. The effect of gas atoms generated from the (n, α) reaction can be simulated by using a steel doped with ^{10}B or ^{58}Ni and irradiating with thermal neutrons in a mixed-spectrum fission reactor, such as the High Flux Isotope Reactor (HFIR). Helium is produced according to the following reactions:

^{10}B(n, α)^{7}Li,
^{58}Ni(n, γ)^{59}Ni(n,α)^{56}Fe,
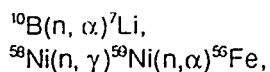
The effect of neutron irradiation on the tensile deformation of F82H steel has been reported. Shiba et al. [1,2] have described the tensile data, obtained under the U.S. DOE/JAERI program, following irradiation in HFIR at 200 to 600°C for doses in the range 3-34 dpa, and the helium

production effect on mechanical properties was investigated using isotope [10]B doping. A summary and discussion of the tensile data for 9-12Cr ferritic-martensitic steels irradiated under a variety of conditions has been presented by Rowcliffe et al. [3]. Recently, the swelling of F82H and the other 7-9Cr low-activation ferritic steels irradiated at 430°C to 67 dpa in FFTF was reported by Morimura et al. [4]; the swelling of F82H was 0.1%, and those of the other steels were 0.1-0.7%. Maziasz and Klueh[5] had investigated the swelling versus helium production rate in 9Cr-1MoVNb (-0, -2Ni) and 12Cr-1MoVW(-0, -2Ni) steels irradiated at 400°C to 47 dpa, using the efficiency of helium production rate for HFIR and FFTF, and they indicated that the swelling of 0.1 to 0.4% depended on helium production. The purpose of the present study is to investigate the swelling of F82H, for different helium production rates after irradiation in HFIR and the effect of the additional element (B and Ni) on microstructures.

2. Experimental procedure

The standard F82H steel and the F82H steel doped with [10]B were prepared to examine the effect of helium on the microstructures. The F82H+natural B and F82H+[10]B steels were prepared from F82H doped with 0.0060% natural boron and 0.0058% [10]B with 94.37 at% purity level, respectively. The F82H+[58]Ni and F82H+[60]Ni steels were prepared from F82H doped with isotope [58]Ni and [60]Ni, respectively. The F82H-std and these F82H+ B specimens were first normalized at 1040°C for 30 minutes in a vacuum followed by air-cooling. In the F82H+Ni specimens, the normalizing was performed at 1200°C for 2 hours. After that the F82H-std and these F82H+B specimens were tempered at 740°C for 2 hours and 1.5 hours, respectively, in a vacuum followed by air-cooling. The chemical compositions of the specimens used in this study are given in Table 1. Boron concentration in the F82H+Ni steels are now analyzing.

Table 1. Chemical compositions of the specimens used in this study(wt%)

	Cr	C	Si	V	Mn	Ta	W
F82H-std	7.44	0.1	0.14	0.20	0.49	0.04	2
F82H+natural B	7.49	0.099	0.15	0.20	0.50	0.04	2.1
F82H+[10]B	7.23	0.098	0.17	0.22	0.50	0.04	2.1
F82H+[58]Ni	7.8	0.04	0.2	0.2	0.4	0.04	2.1
F82H+[60]Ni	7.8	0.04	0.2	0.2	0.4	0.04	2.1

	B (wt%)	Ni (wt%)	[10]B (at%)	[11]B (at%)	[58]Ni (at%)	[60]Ni (at%)
F82H-std	0.0004	-	0.0004	0.0017	-	-
F82H+natural B	0.0060	-	0.0064	0.0248	-	-
F82H+[10]B	0.0058	-	0.0325	-	-	-
F82H+[58]Ni		1.4			1.35	-
F82H+[60]Ni		1.4			-	1.31

Table 2. Midplane fluence for HFIR JP-12

Neutron Fluence (n/cm^2)				
Total	Thermal (<0.5 eV)	0.5 eV- 0.1 MeV	> 0.1 MeV	>1 MeV
26.3x10^{22}	10.9 x10^{22}	8.39 x10^{22}	7.06 x10^{22}	3.67 x10^{22}

Table 3. Helium production of these steels for HFIR-JP12. α is due to impurity level of boron in the F82H+Ni steels, and β is α/52.

	F82H-Std	F82H+natural B	F82H+^{10}B	F82H+^{58}Ni	F82H+^{60}Ni
He (appm)	~26	~90	~350	~500+α	~28+α
(appm)He/dpa					
(0-54 dpa)	0.5	1.7	6	10	0.5
(0-1.4 dpa)	0.5	45	230	3.4+β	1.4+β
(1.4-54 dpa)	0.5	0.5	0.5	10	0.5

Standard 3 mm-diameter TEM disks punched from 0.25 mm-thick sheet stock were irradiated in the HFIR target in the HFIR-MFE-JP12 capsule as part of the JAERI/US collaborative program. The capsule irradiation began on July 20, 1990, at the start of HFIR fuel cycle 289 and was completed 35 cycles on April 1, 1994. The exposure was 64904 MWd at 85 MW reactor power and achieved a peak fluence of 52 dpa for the F82H-std steel in the midplane of the capsule. The dpa level is based on 0.00873 dpa/MWd in the target position. The complete description and details of the design, construction, installation of the capsule, and neutron dosimetry, and damage calculation for JP12 have been previously reported [6-10]. The midplane fluences for HFIR JP-12 are given in Table 2. The irradiation temperatures and displacement damage were 300 and 400°C and 52 dpa for the JP12 capsule. He generation in these steels at 52 dpa is given in Table 3.

Microstructures of these specimens were examined using a JEM-2000FX transmission electron microscope with a LaB$_6$ gun operated at 200 kV. Microstructures of unirradiated control specimens were also examined.

3. Results and discussion

3.1 Initial microstructures of the F82H-std, F82H+B, F82H+Ni steels

The microstructure after normalizing and tempering was a lath martensitic structure for the F82H-std, natural B, isotope ^{10}B, ^{58}Ni and ^{60}Ni doped steels as shown in Figs. 1(a)-1(e). In the F82H-std, the dislocation line density was about 1x10^{14} m^{-2}. M$_{23}$C$_6$ carbides were observed in the matrix and on grain boundaries, and the number density and mean size were 6x10^{19} m^{-3} and 73 nm, respectively. Only a few MC carbides were observed in the matrix, and the number density and mean size were <1x10^{20} m^{-3} and 14 nm, respectively. The mean width of the lath structure was about 440 nm.

Microstructures of B-doped specimens are similar to the F82H-std. On the other hand, Ni-doped specimens have a higher MC carbide number density and no M$_{23}$C$_6$ carbides: a few M$_6$C carbides formed at lath boundaries and unidentified precipitates were sometimes observed in the matrix of some grains. The detail of the microstructures will be reported in next progress report.
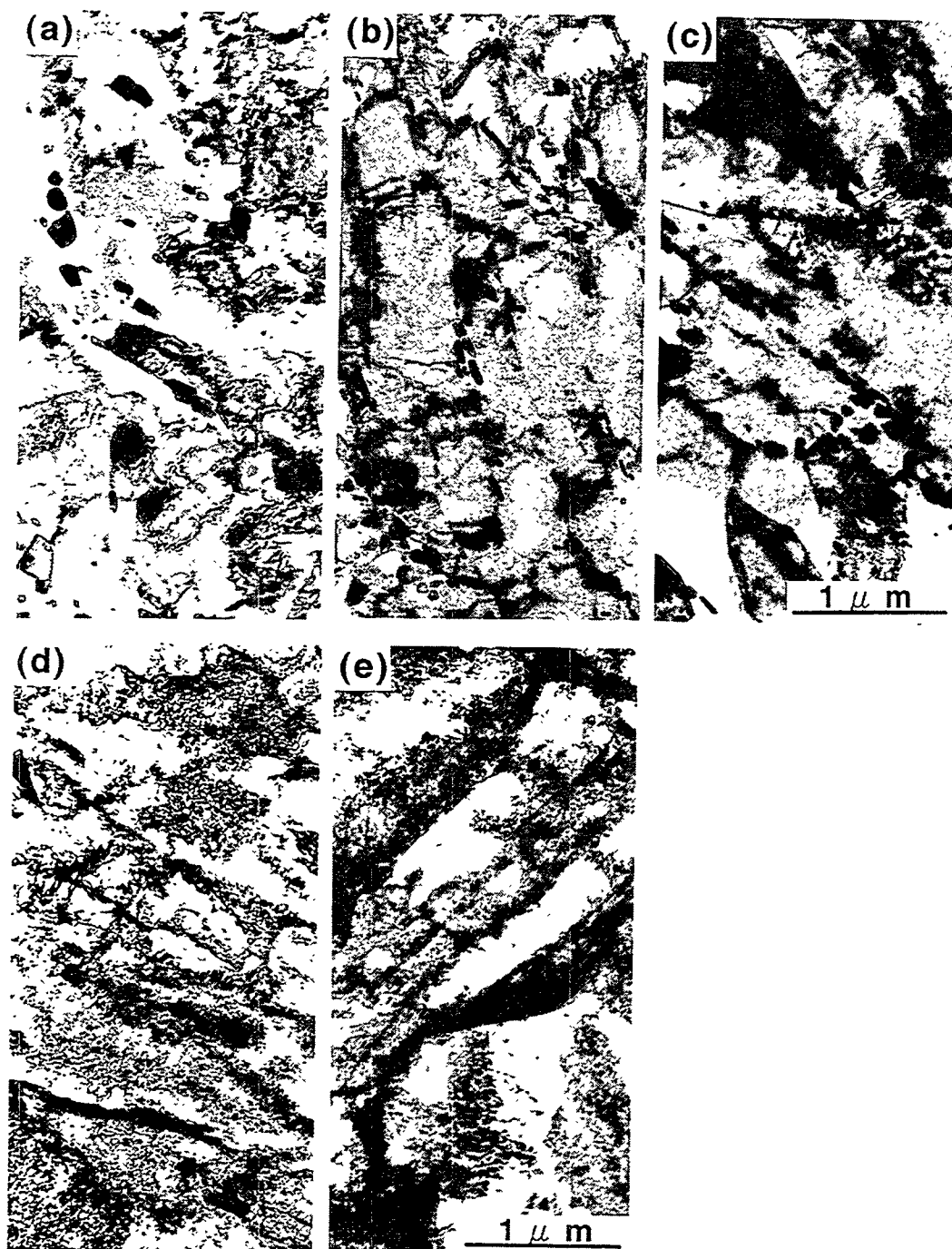
Figure 1. Pre-irradiation microstructure of (a) F82H-std, (b) F82H+natural B, (c) F82H+^{10}B, (d) F82H+^{58}Ni, and (e) F82H+^{60}Ni steels

3.2 Swelling of F82H steels irradiated at 400°C to 52 dpa
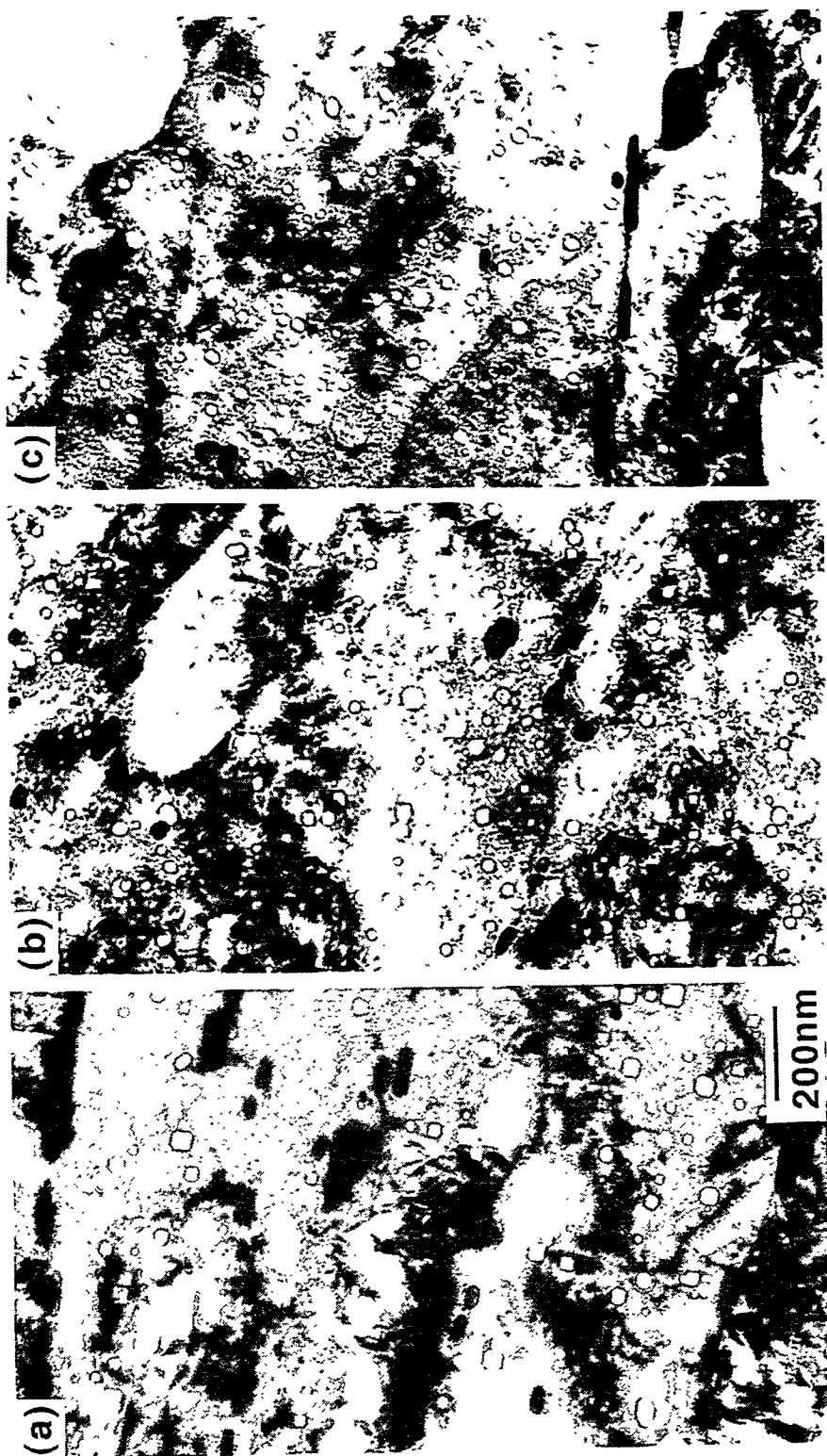
Figure 2. Cavities formed in the (a) F82H-std, (b) F82H+natural B, and (c) F82H+^{10}B steels irradiated at 400°C to 52 dpa. In the F82H-std, cavities can not be seen near the lath boundaries, while in the F82H+natural B and F82H+^{10}B steels cavities can be observed near these lath boundaries.

Figures 2(a)-2(c) show cavities observed in the F82H-std, F82H+natural B, and F82H+^{10}B steels, respectively, irradiated at 400°C to 52 dpa. Lath boundaries and many $M_{23}C_6$ precipitates can be seen in these micrographs. In Fig. 2(a), cavities can not be seen near the lath boundaries, while in Figs. 2(b) and 2(c) cavities can be observed near these lath boundaries. The swelling of the F82H-std steel was about 0.5% in average of all regions, and it was about 0.7-0.8 % in the matrix region in which cavities exist. The average swelling in all regions of F82H+natural B and F82H+^{10}B steels is about 0.9 and 1.1%, respectively. Figs. 3(a) and 3(b) show microstructures of F82H+^{60}Ni and F82H+^{58}Ni irradiated at 400°C to 52 dpa. Small cavities were observed for the F82H+^{58}Ni steel and the swelling was 0.02%, but no cavities were observed for the F82H+^{60}Ni. The number density, root mean cube radius, and swelling of cavities of these steels are summarized in Table 4. The low swelling in the Ni-doped specimens may be caused by the high density of precipitate formation as descried in the next paragraph.

The growth of $M_{23}C_6$ carbides was observed on lath boundaries at bending curves in F82H-std, F82H+natural B, and F82H+^{10}B steels. Many small M_6C precipitates were formed on the $M_{23}C_6$ carbides, and a few M_6C precipitates were formed in matrix by the irradiation. In the Ni-doped F82H+^{60}Ni and F82H+^{58}Ni steels, a high density of precipitates were formed by the irradiation as seen in Fig. 4. A low density of loops was also observed in all steels. The details of precipitates and loops will be presented in the next report.
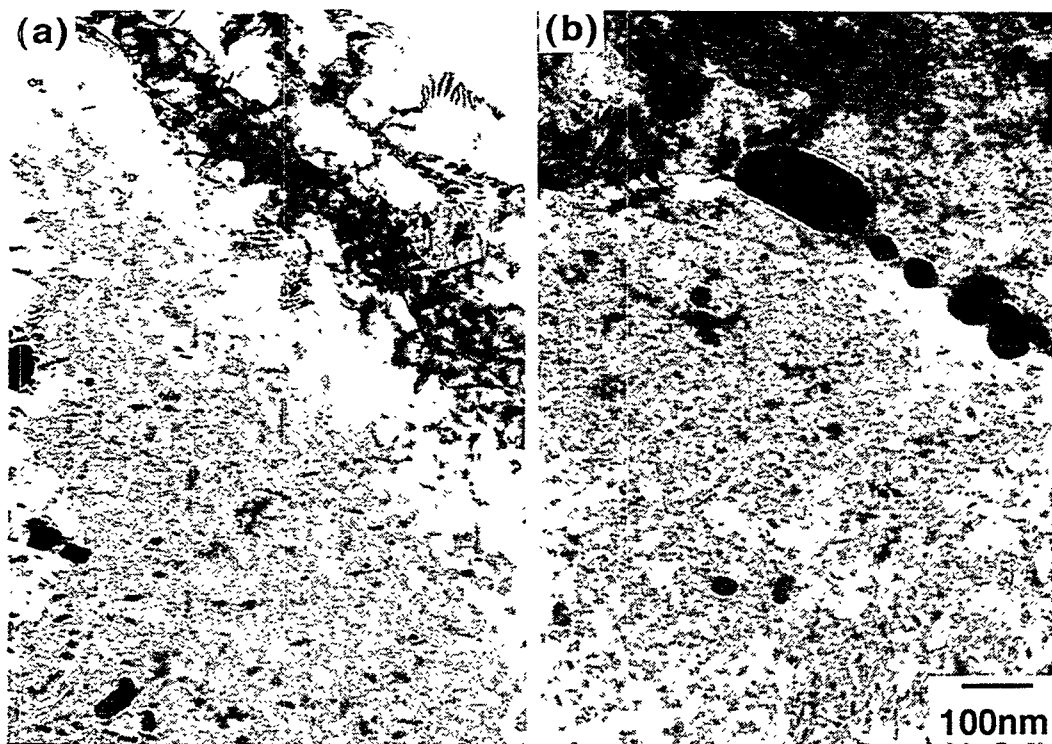
Figure 3. Microstructure of (a) F82H+^{60}Ni and (b) F82H+^{58}Ni steels irradiated at 400°C to 52 dpa. Cavities were formed in the F82H+^{58}Ni steel, but no cavities were formed in the F82H+^{60}Ni steel.
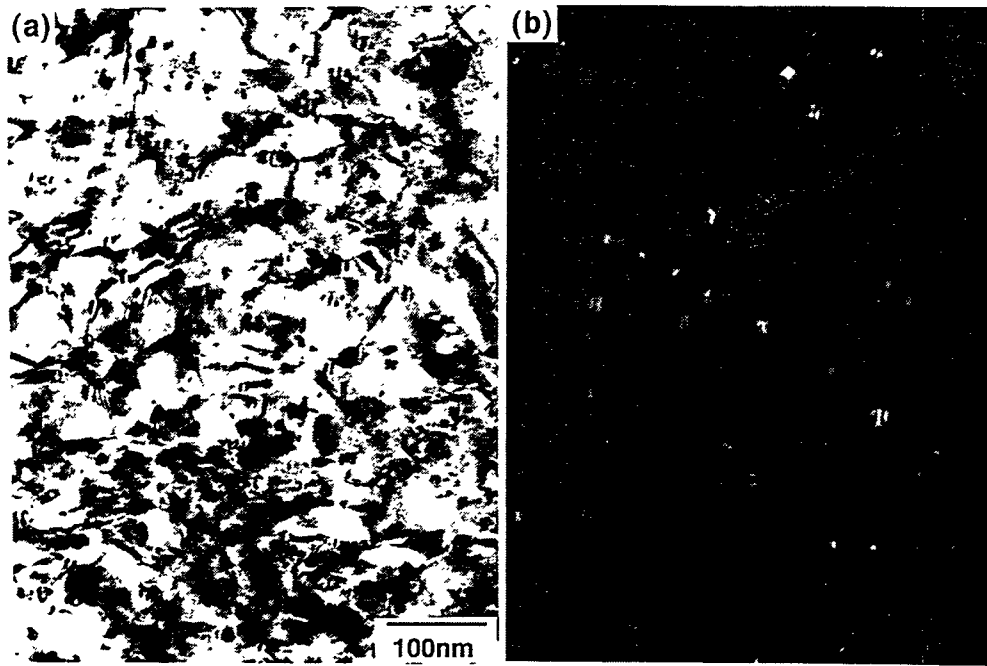
Figure 4.   A high number density of precipitates formed in F82H+^{58}Ni steel irradiated at 400°C to 52 dpa

Table 4.   Cavities formed at 300 and 400°C to 52 dpa in the F82H steels.   RMC radius denotes root mean cube of cavity radius.

Alloy	Cavity (300°C to 52 dpa)			Cavity (400°C to 52 dpa)		
	Number Density	RMC radius	Swelling	Number Density	RMC radius	Swelling
F82H		-		6×10^{20} m^{-3}	~13 nm	~0.6%
F82H+natural B		-		2×10^{21} m^{-3}	~11 nm	~0.9%
F82H+^{10}B	2×10^{21} m^{-3}	3 nm	0.002%	4×10^{21} m^{-3}	~8 nm	~1.1%
F82H+^{58}Ni	4×10^{21} m^{-3}	4 nm	0.02%	2×10^{21} m^{-3}	~3 nm	~0.02%
F82H+^{60}Ni		-			-	

3.3 Swelling of these F82H steels irradiated at 300°C to 52 dpa

Figures 5(a) - 5(e) show microstructures of F82H-std, F82H+natural B, and F82H+^{10}B steels, F82H+^{60}Ni and F82H+^{58}Ni, respectively, irradiated at 300°C to 52 dpa.   Cavities were observed in only the F82H+^{10}B and F82H+^{58}Ni steels, and the values of swelling were 0.02 and 0.002%, respectively.

Many small M$_6$C precipitates were also formed on the M$_{23}$C$_6$ carbides.   The size of M$_{23}$C$_6$ carbides in the F82H-std was smaller than that in the F82H+B steels.   Many dislocation loops were formed in all steels.   A summary of the results for the microstructures of these irradiated steels is given in Table 5.   Further details of precipitates and loops will be described in the next progress report.
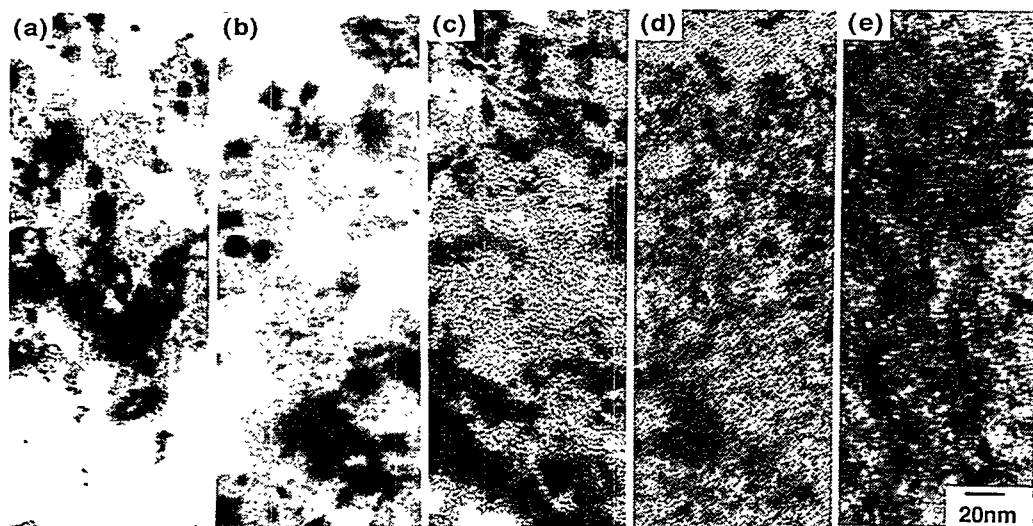
Figure 5. Microstructure of (a) F82H-std, (b) F82H+natural B, and (c) F82H+^{10}B , (d) F82H+^{60}Ni, and (e) F82H+^{58}Ni steels irradiated at 300°C to 52 dpa. Small cavities were observed in only the F82H+^{10}B and F82H+^{60}Ni steels.

Table 5. Summary of radiation-induced defect clusters formed at 300 and 400°C to 52 dpa in the F82H steels

Alloy	300°C to 52 dpa			400°C to 52 dpa		
	Loop	Cavity (swelling)	Precipitate	Loop	Cavity (swelling)	Precipitate
F82H	high	No	M_6C on $M_{23}C_6$	low matrix	large (~0.6%)	M_6C on $M_{23}C_6$ few M_6C in ($M_{23}C_6$ growth)
F82H+natural B	high	No	M_6C on $M_{23}C_6$	low	large (~0.9%)	M_6C on $M_{23}C_6$ few M_6C in matrix ($M_{23}C_6$ growth)
F82H+^{10}B	high	small (0.002%)	M_6C on $M_{23}C_6$	low	large (~1.1%)	M_6C on $M_{23}C_6$ few M_6C in matrix ($M_{23}C_6$ growth)
F82H+^{58}Ni	high	small (0.02%)	MC in matrix	low	small (0.02%)	M_6C in matrix others
F82H+^{60}Ni	high	No	MC in matrix	low	No	M_6C in matrix others

ACKNOWLEDGMENTS

REFERENCES

[1] K. Shiba, I. Ioka, J. P. Robertson, M. Suzuki, and A. Hishinuma, Euromat-9 6(1996), p.265.

[2] K. Shiba, unpublished data.

[3] A. F. Rowcliffe, J. P. Robertson, R. L. Klueh, K. Shiba, D. J. Alexander, M. L. Grossbeck, and S. Jitsukawa, J. Nucl. Mater., 258-263(1998), pp. 1275-1279.

[4] T. Morimura, A. Kimura, and H. Matsui, J. Nucl. Mater., 239(1996)118-125.

[5] P. J. Maziasz and R. L. Klueh, American Society for Testing and Materials-1046, Philadelphia, 1990, p. 35.

[6] R. L. Senn, Fusion Reactor Materials Semiannual Progress Report for Period Ending September 30, 1988, Office of Fusion Energy, DOE/ER-0313/3, p.8.

[7] R. L. Senn, Fusion Reactor Materials Semiannual Progress Report for Period Ending March 31, 1988, Office of Fusion Energy, DOE/ER-0313/4, p.7.

[8] R. L. Senn, Fusion Reactor Materials Semiannual Progress Report for Period Ending September 30, 1989, Office of Fusion Energy, DOE/ER-0313/5, p.6.

[9] J. E. Pawel, K. E. Lenox, A. W. Longest, R. L. Senn, and K. Shiba, Fusion Reactor Materials Semiannual Progress Report for Period Ending September 30, 1994, Office of Fusion Energy, DOE/ER-0313/17, p.3.

[10] L. R. Greenwood and C. A. Baldwin, Fusion Reactor Materials Semiannual Progress Report for Period Ending September 30, 1998, Office of Fusion Energy, DOE/ER-0313/23, p. 301.

MICROSTRUCTURE OF ISOTOPICALLY-TAILORED F82H AND HT9 IRRADIATED AT 400°C IN HFIR

- N. Hashimoto, J.P. Robertson, A.F. Rowcliffe (Oak Ridge National Laboratory), Y. Miwa , and K. Shiba (Japan Atomic Energy Research Institute)

OBJECTIVE

The objective of this report is to present recently generated TEM data for isotopically-tailored ferritic/martensitic steels, F82H and HT9, irradiated in the temperature range for swelling.

SUMMARY

Microstructures of reduced-activation ferritic/martensitic steels, F82H (8Cr-2W-0.2V-0.04Ta), 8Cr-2WVTa doped with ^{58}Ni, HT9 (12Cr-1MoVW) and HT9 doped with ^{58}Ni, irradiated at 400°C to 7 dpa in the High Flux Isotope Reactor (HFIR), were investigated by transmission electron microscopy. Cavities were observed in the standard F82H (F82H-std.) and 8Cr-2WVTa-^{58}Ni, but not in the standard HT9 (HT9-std.) and HT9-^{58}Ni alloys. The irradiation induced $a_0<100>$ and $(a_0/2)<111>$ type dislocation loops in all alloys; the number density and the mean diameter of $(a_0/2)<111>$ type loops were lower and smaller than that of $a_0<100>$ type loops. Also, there is a tendency that the number density of loops in the F82H and 8Cr-2WVTa-^{58}Ni alloys were lower than those in the HT9 alloys.

PROGRESS AND STATUS

1. Introduction

Ferritic/martensitic steels are attractive candidate structural first wall materials for fusion reactors [1]. The high-energy neutrons produced by the D-T fusion reaction induce displacement damage and generate gas atoms in the materials from (n,p) and (n,α) reactions. Simultaneous production of helium atoms from (n,α) reactions is considered to strongly influence the nucleation processes of cavities. To clarify the effect of helium atoms on the microstructural development and mechanical property changes in ferritic/martensitic steels under fast neutron irradiation, F82H (8Cr-2W-0.2V-0.04Ta), 8Cr-2WVTa doped with ^{58}Ni, HT9 (12Cr-1MoVW) and HT9 doped with ^{58}Ni were irradiated with neutrons in the High Flux Isotope Reactor (HFIR). Irradiation of ^{58}Ni-doped alloys in a mixed spectrum reactor like the HFIR results in the following transmutation reaction with the thermal neutrons:

$$^{58}Ni\,(n,\gamma)\,^{59}Ni(n,\alpha)\,^{56}Fe$$

Thus this nickel doping allows for the simultaneous production of helium and displacement damage.

2. Experimental Procedure

F82H, 8Cr-2WVTa doped with ^{58}Ni, HT9, and HT9 doped with ^{58}Ni were included in this experiment; the compositions and heat treatment are given in Table 1. The heat treatment for 8Cr-2WVTa-^{58}Ni was not enough so that there is a possibility that it has much carbon in matrix. Standard 3-mm diameter transmission electron microscopy (TEM) disks were punched from 0.25-mm thick sheet stock. Irradiation was carried out at 400°C in the HFIR-MFE-JP-20 capsule in the High Flux Isotope Reactor (HFIR) to neutron fluences of ~ 5.16 x 10^{25} n/cm^2 (E> 0.1 MeV), resulting in displacement values of about 7.4 dpa. The details of the design, construction, and installation of JP-20 have been reported [2-5]. The damage level and helium concentration in the steels are given in Table 2.

Table 1. Chemical compositions of the specimens (wt.%) (Balance Fe) and heat treatment.

Steel	Cr	^nNi	^{58}Ni	Si	C	N	P	S	Mn	W	V	Ta	Ti	Nb	Mo	B
HT9-std.	12.0	0.5	-	0.18	.20	.02	-	-	0.5	0.5	0.3	-	-	.01	1.0	-
HT9-^{58}Ni	12.0	-	1.4	0.18	.20	.02	-	-	0.5	0.5	0.3	-	-	.01	1.0	-
F82H-std.	7.46	0.03	-	0.14	.100	.002	.001	.001	0.49	2.00	0.20	.04	.008	-	-	.0004
8Cr-2WVTa-^{58}Ni	8.00	-	1.40	0.21	.043	.004	.001	.003	0.40	2.11	0.20	.04	.001	-	-	-

Heat treatment:
HT9-std. and HT9-^{58}Ni; 1050°C/1 h/ AC + 780°C/2.5 h/ AC
F82H-std.; 1040°C/0.5 h/ AC + 740°C/2 h/ AC

Table 2. Damage level and helium concentration.

	dpa	appm He	He/dpa
HT9-std.	7.4	10	1.3
HT9-^{58}Ni	7.4	40	5.2
F82H-std.	7.4	8	1.0
8Cr-2WVTa-^{58}Ni	7.4	50	6.6

TEM specimens were thinned using an automatic Tenupole electropolishing unit located in a glove box. TEM disks were examined using a JEM-2000FX (LaB$_6$) transmission electron microscope equipped special objective lens polepiece that lowers magnetic field at the ferro-magnetic specimen. The foil thicknesses were measured by thickness fringes in order to evaluate quantitative defect density values.

3. Results and discussion

3.1 Dislocations and dislocation loops

Figure 1 shows the dislocation segments and loops which were obtained in HT9-std. and HT9-^{58}Ni after irradiation at 400 °C to 7.4 dpa using the diffraction conditions: B=[001], g=200, (g, 4g). The irradiation induced a<100> and (a$_0$/2)<111> type dislocation loops in both alloys, the number density and the mean diameter of (a$_0$/2)<111> type loops are lower and smaller than those of a<100> type loops. On the other hand, there is no significant difference in number density and mean diameter of loops between HT9-std. and HT9-^{58}Ni. Figure 2 shows the dislocation segments and loops which were obtained in F82H-std. and 8Cr-2WVTa-^{58}Ni after irradiation at 400°C to 7.4 dpa using the diffraction conditions: B=[011], g=200, (g, 4g). The irradiation induced a<100> and (a$_0$/2)<111> type dislocation loops in both alloys, and the number density and the mean diameter of (a$_0$/2)<111> type loops are lower and smaller than those of a<100> type loops. And, the number density and the mean diameter of loops in 8Cr-2WVTa-^{58}Ni are higher and smaller than that in F82H-std. From comparison between the HT9 and the F82H, it appears that the number density of loops in the F82H are lower than those in the HT9. Table 3 summarizes the quantitative results of dislocation loops and total dislocation density.

Table 3. The summary of dislocation loops in alloys after irradiation at 400°C to 7.4 dpa in HFIR.

Steel	a$_0$<100> type loops		(a$_0$/2)<111> type loops		Total
	Number density (m^{-3})	Mean diameter (nm)	Number density (m^{-3})	Mean diameter (nm)	density (m^{-2})
HT9-std.	1x10^{22}	14	3x10^{21}	10	6x10^{14}
HT9-^{58}Ni	1x10^{22}	16	5x10^{21}	8	6x10^{14}
F82H-std.	6x10^{21}	16	2x10^{21}	8	4x10^{14}
8Cr-2WVTa-^{58}Ni	7x10^{21}	11	3x10^{21}	9	4x10^{14}
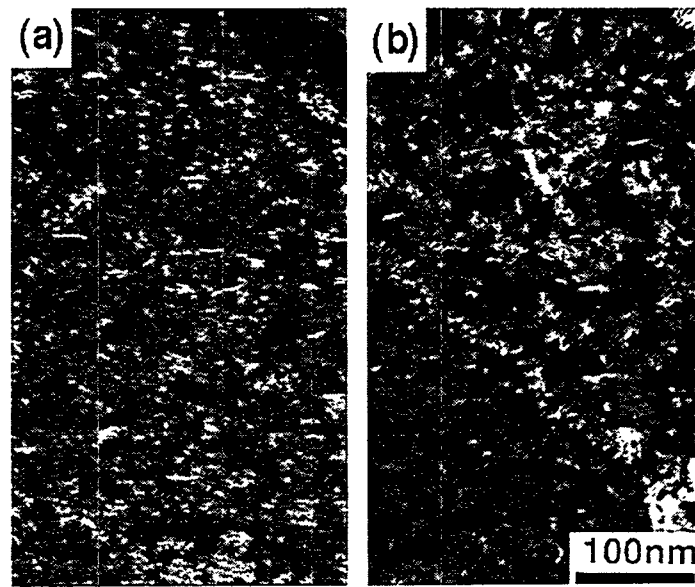
Figure 1 Microstructures of the dislocation segments and loops in HT9-std. (a) and HT9-^{58}Ni (b) after irradiation at 400°C to 7.4 dpa in HFIR, the diffraction conditions: B=[001], g=200, (g, 4g).
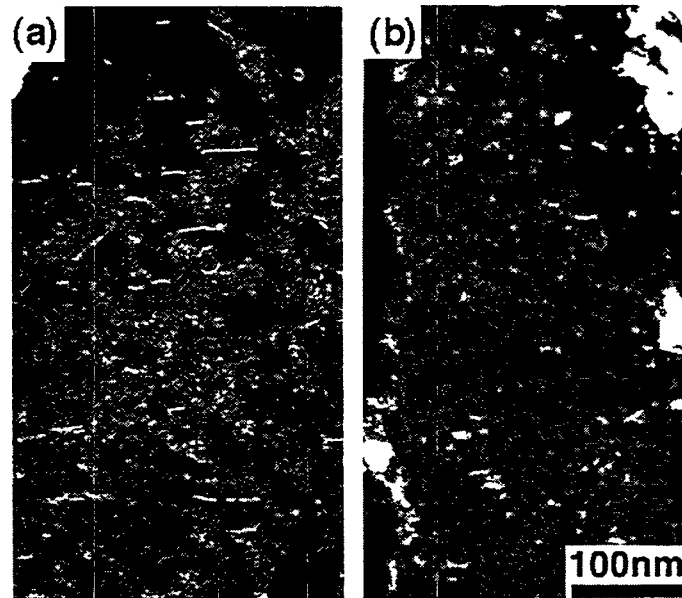
Figure 2 Microstructures of the dislocation segments and loops in F82H-std. (a) and 8Cr-2WVTa-^{58}Ni (b) after irradiation at 400°C to 7.4 dpa in HFIR, the diffraction conditions: B=[011], g=200, (g, 4g).

During irradiation of Fe-Cr binary alloys, dislocation evolution in an initially almost dislocation-free condition proceed by the formation of interstitial-type dislocation loops with an a_0<100> and/or $(a_0/2)$<111> Burgers vector [6,7]. According to an investigation of dislocation loop evolution in ferritic alloys irradiated to high fluence [8,9], the a_0<100> type dislocation loops were sensitive to chromium content, and a number of a_0<100> type dislocation loops were present in an Fe-12Cr alloy irradiated at 420°C to 140 dpa, while in Fe-6Cr and Fe-9Cr alloys, their number density was

extremely low. This difference in the nucleation of interstitial loops could be explained by chromium stabilization of interstitial clusters, and/or the α' precipitation promotes the loop nucleation in the Fe-12Cr alloy. Further analysis concerning the nucleation of precipitates under irradiation should be carried out. On the other hand, according to a previous paper which investigated the relationship between type of dislocation loop and content of interstitial impurities, there is a tendency for the $a_0<100>$ type loops to form in alloys which have much carbon [10]. The HT9 alloys and 8Cr-2WVTa-^{58}Ni used in this study have more carbon and nitrogen than the F82H, which means there is a possibility that the difference in impurity content affects the loop formation.

3.2 Cavities

Figure 3 (a) - (d) show the microstructures in HT9-std., HT9-^{58}Ni, F82H-std. and 8Cr-2WVTa-^{58}Ni after irradiation at 400°C to 7.4 dpa. No cavities were observed in HT9-std. and HT9-^{58}Ni, while in F82H-std. and 8Cr-2WVTa-^{58}Ni, cavities were observed with number densities of 4×10^{21} and 5×10^{21} m^{-3}, and mean diameters of 4 and 2 nm, respectively. From this result, swelling of F82H-std. and 8Cr-2WVTa-^{58}Ni was estimated to be 0.2 and 0.018 %, respectively. Table 4 contains the cavity number densities, mean diameters and swelling of the alloys

Table 4. The summary of cavities in alloys after irradiation at 400°C to 7.4 dpa in HFIR.

Steel	Cavity		
	Number density (m^{-3})	Root mean cube (nm)	Swelling (%)
HT9-std.	-	-	-
HT9-^{58}Ni	-	-	-
F82H-std.	4×10^{21}	4	0.2
8Cr-2WVTa-^{58}Ni	5×10^{21}	2	0.018
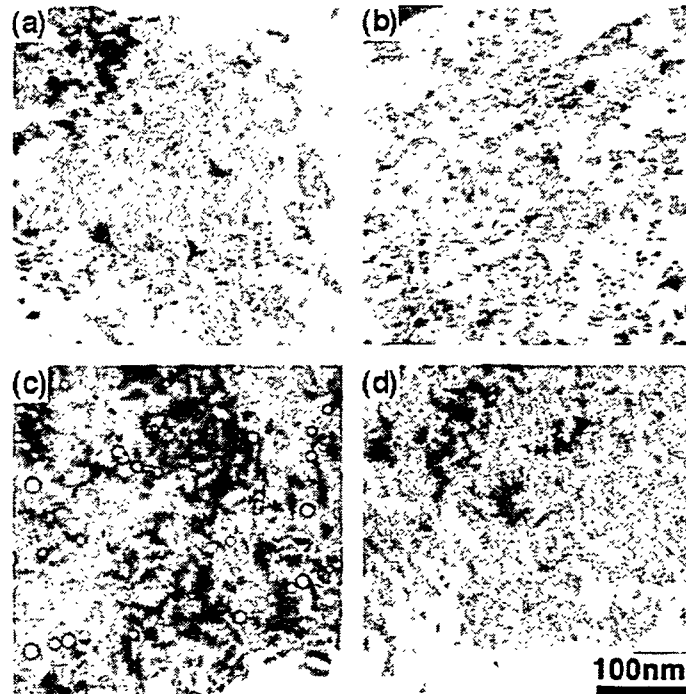
Figure 3 Microstructures of the cavities in HT9-std. (a), HT9-^{58}Ni (b), F82H-std. (c) and 8Cr-2WVTa-^{58}Ni (d) after irradiation at 400°C to 7.4 dpa.

FUTURE WORK

Further analysis of precipitates in the alloys will be carried out.

ACKNOWLEDGMENTS

REFERENCES

1) R.L. Klueh, K. Ehrlich, and F Abe, J. Nucl. Mater. **191-194** (1992) 116.
2) J.E. Pawel and R.L. Senn, "Status of U.S./Japan Collaborative Program Phase 2 HFIR Target Capsules", Fusion Reactor Materials Semiannual Report for Period Ending March 31, 1995, DOE/ER-0313/12, 1992, p. 15.
3) J.E. Pawel, A.W. Longest, R.L. Senn, K. Shiba, D.W. Heatherly, and R.G. Sitterson, "Status of U.S./Japan Collaborative Program Phase 2 HFIR Target and RB* Capsules", Fusion Reactor Materials Semiannual Report for Period Ending September 30, 1993, DOE/ER-0313/15, 1992, p. 3.
4) J.E. Pawel, K.E. Lenox and I. Ioka, "Status of U.S./Japan Collaborative Program Phase 2 HFIR Target and RB Capsules", Fusion Reactor Materials Semiannual Report for Period Ending March 31, 1995, DOE/ER-0313/18, 1995, p. 3.
5) L.R. Greenwood and C.A. Baidwin, "Neutron Dosimetry and Damage Calculations for The HFIR-JP-20 Irradiation", Fusion Reactor Materials Semiannual Report for Period Ending December 31, 1997, DOE/ER-0313/23, 1997, p. 305.
6) N. Yoshida, et al., J. Nucl. Mater., **155-157** (1988), 1232.
7) D.S. Gelles, Annual Progress Report for Fusion Year, (1991), 348.
8) Y. Katoh, A. Kohyama and D.S. Gelles, J. Nucl. Mater., **225** (1996) 154.
9) D.S. Gelles, J. Nucl. Mater., **225** (1995) 163.
10) E. Wakai et al., Proceeding of Ultra High Purity Base metals, UHPM-94, 488.

Swelling of F82H irradiated at 673 K to 7 dpa in HFIR - Y. Miwa, E. Wakai, K. Shiba (Japan Atomic Energy Research Institute), N. Hashimoto, J. P. Robertson and A. F. Rowcliffe (Oak Ridge National Laboratory)

OBJECTIVE

The objective of this work is to study the effect of neutron irradiation on swelling behavior of reduced activation ferritic/martensitic steels for first wall applications in fusion energy system.

SUMMARY

A reduced activation ferritic/martensitic steel F82H (F82H-std) and a heat with the addition of isotope ^{10}B (F82H+^{10}B) were irradiated at 673 K to 7 and 51 dpa in HFIR. The swelling behavior of these alloys was examined by transmission electron microscopy. In the F82H-std irradiated to 7 dpa, small cavities (~ 8 nm in diameter) were observed in lath cells, but not on the interfaces of lath boundaries or precipitates. The cavity number density (N_c) was about 4×10^{21} m^{-3}. The swelling was about 0.2%. In the F82H+^{10}B irradiated to 7 dpa, smaller cavities (~ 6 nm in diameter.) were observed in lath cells, and some cavities occurred on the interfaces of lath boundaries or small precipitates. The N_c was about 1.5×10^{22} m^{-3}, and the swelling was about 0.2%. In the F82H-std irradiated to 51 dpa, large and small cavities were observed in lath cells, but not on the interfaces of lath boundaries or precipitates. The N_c was about 1×10^{21} m^{-3}, and the swelling was about 0.6%.

PROGRESS AND STATUS

Introduction

The reduced activation ferritic/martensitic steel F82H is one of the candidate materials for the first wall structure of fusion reactors. The effect of neutron irradiation on mechanical properties and microstructures in F82H is being examined in the Japan/US collaborative program on fusion reactor materials. The swelling behavior of F82H irradiated at 673 K up to 51 dpa is presented in this report.

Experimental Procedure

Two types of F82H, one containing a low concentration of normal boron (F82H-std) and the other containing an addition of isotopic ^{10}B (F82H+^{10}B), were prepared to examine the effect of helium on the microstructures. The chemical compositions and notations of these alloys are given in Table 1. C106 and FM19 are F82H-std specimens, and C205 is the F82H+^{10}B specimen. Heat treatment conditions of each specimen are listed in Table 2.

Standard transmission electron microscopy specimens of 3 mm in diameter were punched out from 0.25-mm-thickness plates. These specimens were irradiated at about 673 K in HFIR target position in the capsule of HFIR-MFE-JP12/position 8 [1] and HFIR-MFE-JP20/position 9 [2]. The resulting thermal and fast neutron fluences, taking into account the specimen position in reactor are 1.08×10^{27} n/m^2 (E<0.5 eV) and 3.65×10^{26} n/m^2 (E>1MeV) for HFIR-MFE-JP12 [3] and 1.83×10^{26} n/m^2 (E<0.5 eV) and 5.16×10^{25} n/m^2 (E>1MeV) for HFIR-MFE-JP20 [4], respectively. These fluences correspond to 51.3 and 7.4 dpa for HFIR-MFE-JP12 and HFIR-MFE-JP20, respectively. The dose dependence of He generation in each specimen is shown in Figure 1.

Microstructural observation was carried out using a JEM-2000FX transmission electron microscope with a LaB$_6$ gun operated at 200 kV. The root mean cube of cavity radius, r_{RMC}, was obtained by

$$r_{RMC} = \{(\Sigma r_i^3)/N\}^{1/3}$$

The distribution of cavities was not uniform, so that the cavity number density (N_c) and the swelling were measured in cavity rich region in order to estimate the maximum swelling.

Results and Discussion

Swelling in F82H-std (C106) irradiated to 7 dpa

Figures 2(a)~(c) show the cavity distribution in F82H-std irradiated to 7 dpa. The calculated He concentration is about 8 appm. As seen in Figures 2(a) and (b), small cavities were observed in lath cells, and aligned along dislocation lines. Small cavities were also observed on dislocation loops that were formed during irradiation. A few cavities were observed on the interfaces of small precipitates, but no cavities were observed on larger

precipitates. Cavities were not observed on the lath boundaries (Figure 2(c)). The width of cavity free zone from lath boundaries was about 50 nm. Relatively larger cavities were facetted which suggested some conversion to bias-driven voids was occurring.

Figure 3 shows the size distribution of cavities. The diametral size distribution had a peak at 5 nm with a maximum diameter of about 20 nm. The r_{RMC} and N_c were about 4.3 nm and about 4.0×10^{21} m^{-3}, respectively. The swelling was about 0.2%.

Swelling in F82H+^{10}B (C205) irradiated to 7 dpa

Figures 4(a)~(c) show the cavity distribution in F82H+^{10}B irradiated to 7 dpa. The calculated He concentration is about 330 appm. Cavities were observed associated with dislocations within the lath cells. The average diameter was smaller and the number density higher than in the F82H-std (Figures 4(a) and (b)). Some cavities were observed on the interfaces on lath boundaries or small precipitates (Figures 4(b) and (c)). All cavities were spherical with no evidence of facetting.

Figure 5 shows the size distribution of cavities. The diametral size distribution had a peak at about 4 nm with a maximum diameter of about 15 nm. These are smaller than those in C106. The fraction of larger cavities (~ 10 nm in diameter) was smaller than that in C106. The r_{RMC} and N_c were about 3.1 nm and about 1.5×10^{22} m^{-3}, respectively. The swelling was about 0.2%. The N_c was higher and r_{RMC} was smaller than that in C106, swelling was about the same as that in C106. The addition of ^{10}B results in He generation of about 320 appm from ^{10}B(n,α)^{7}Li reaction in steel at an early stage (about 1 dpa) of the neutron irradiation up to 7 dpa. The rapid generation of helium in ^{10}B-doped material (Figure 1) is thought to be directly responsible for the four times increase in the measured cavity density.

Swelling in F82H-std (FM19) irradiated to 51 dpa

Figures 6(a)~(c) show the cavity distribution in F82H-std irradiated to 51 dpa. The calculated He concentration is about 26 appm. As seen in Figures 6(a)~(c), cavities were observed in lath cells, and not on lath boundaries or precipitates/matrix interfaces. The width of the void free zone at lath boundaries was about 50 nm, which is similar to that in F82H-std irradiated to 7 dpa (C106). Small and large cavities are shown in Figure 6(b); the

larger cavities were frequently observed at dislocation kinks or bowed-out dislocations. Many of the small cavities occurred in close proximity to a large cavity, frequently less than a small cavity diameter away.

Figure 7 shows the size distribution of cavities. The diametral size distribution has a peak at about 8 nm, and the maximum diameter is about 55 nm. These are much larger than those in C106. The r_{RMC} and N_c were about 11 nm and about 1×10^{21} m^{-3}, respectively. The N_c is lower and r_{RMC} is larger than that in C106. The swelling was about 0.6 %, significantly larger than that in the 7 dpa specimen.

The details of microstructures of a series of F82H alloys irradiated at 673 K to 54 dpa are reported by Wakai et. al. elsewhere [5] in this report.

ACKNOWLEDGMENTS

REFERENCES

[1] R. L. Senn, Fusion Reactor Materials Semiannual Progress Report, DOE/ER-0313/5, p.6 (1988)

[2] J. E. Pawel, Fusion Reactor Materials Semiannual Progress Report, DOE/ER-0313/15, p.3 (1993)

[3] L. R. Greenwood, Fusion Reactor Materials Semiannual Progress Report, DOE/ER-0313/23, p.301 (1997)

[4] L. R. Greenwood, Fusion Reactor Materials Semiannual Progress Report, DOE/ER-0313/23, p.305 (1997)

[5] E. Wakai, in this semi-annual report.

Table 1   Chemical compositions (mass %)

	C	Si	Mn	P	S	Cr	W	V	Ta	T. Al	T. N	Ni	Ti	B
FM19	0.100	0.14	0.49	0.001	0.001	7.44	2.0	0.20	0.04	0.019	0.002			tr.[*1]
C106	0.097	0.09	0.07	0.002	0.003	7.46	2.1	0.18	0.03	0.014	0.004	0.03	0.008	0.0004
C205	0.098	0.17	0.5	0.001	0.001	7.23	2.1	0.22	0.04	0.021	0.002			0.0058[*2]

*1: tr. means trace quantity.

*2: all boron is ^{10}B.

Table 2   Heat treatment conditions

	Normalizing	Tempering
FM19	1313 K / 0.5 h /AC	1013 K / 2 h / AC
C106	1313 K / 0.667 h / AC	1013 K / 1.5 h / AC
C205	1313 K / 0.5 h / AC	1013 K / 1.5 h / AC

AC: air-cooling.   Normalizing and tempering was carried out in vacuum.
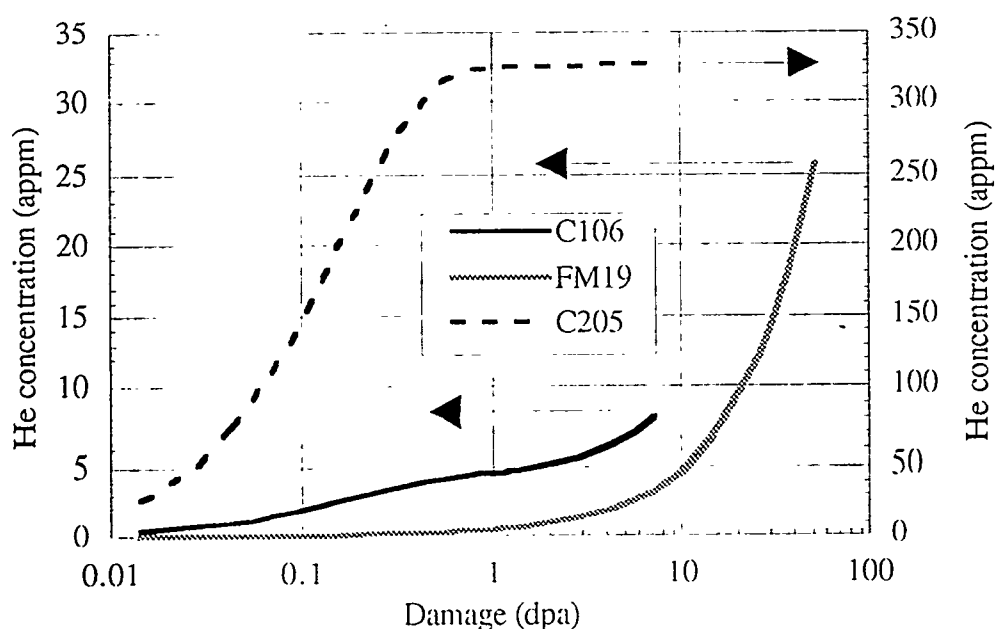
Figure 1 Dose dependence of He concentration in F82H-std (C106, FM19) and F82H+^{10}B (C205). He concentrations are 8, 26 and 330 appm in C106, FM19, and C205, respectively.

180
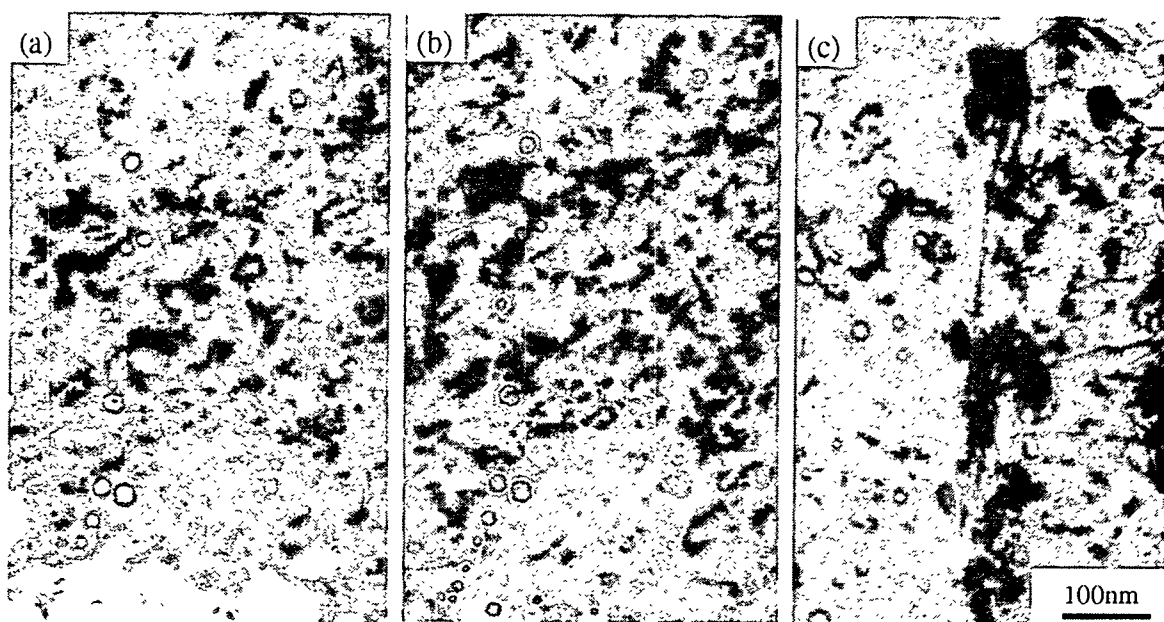
Figure 2   Cavities in F82H-std irradiated at 673 K to 7 dpa.

The calculated He concentration is about 8 appm. (a) and (b): Underfocus and overfocus image in the same position of matrix. (c): Cavities near lath boundary.
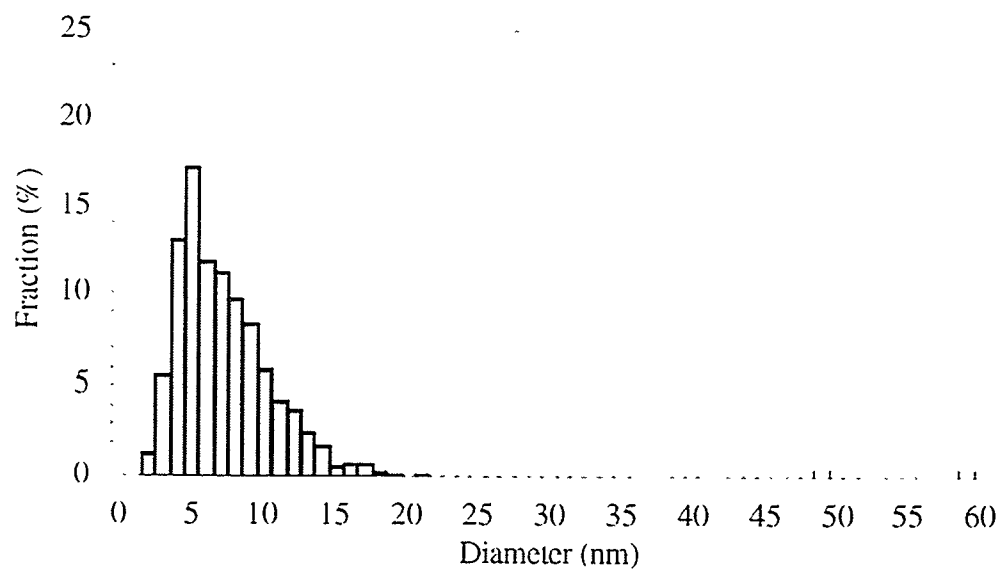
Figure 3   Cavity size distribution in F82H-std irradated at 673 K to 7 dpa.
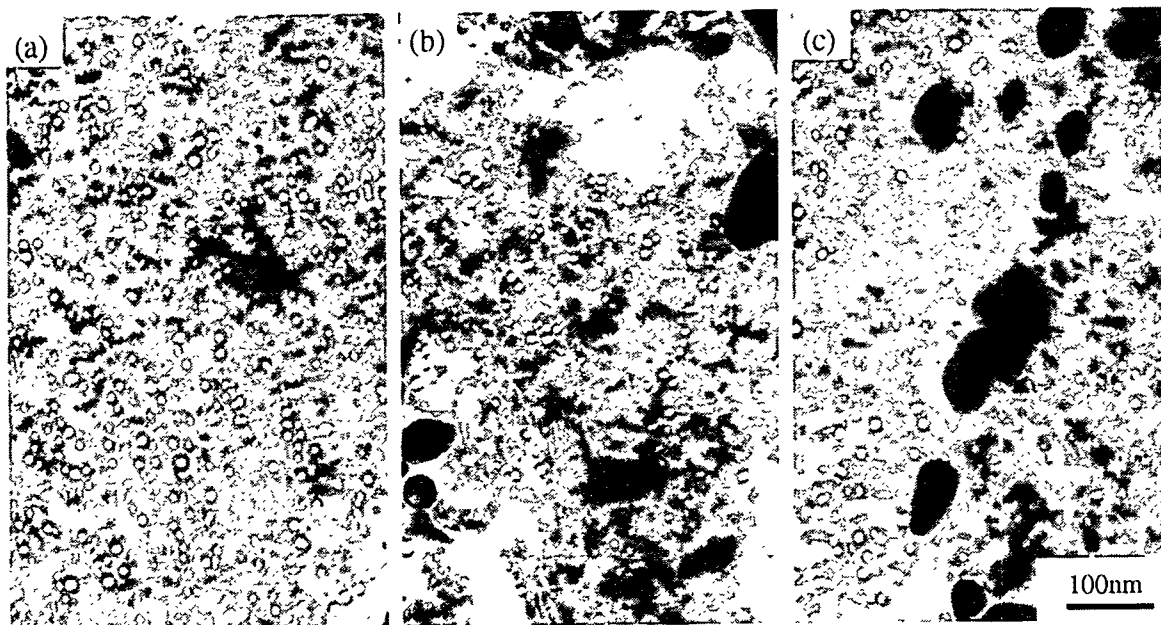
Figure 4   Cavities in F82H+^{10}B irradaited at 673 K to 7 dpa.

The calculated He concentration is about 330 appm. (a) and (b): Many cavities were observed along dislocations. (c): Some cavities on small precipitates and lath boundaries.
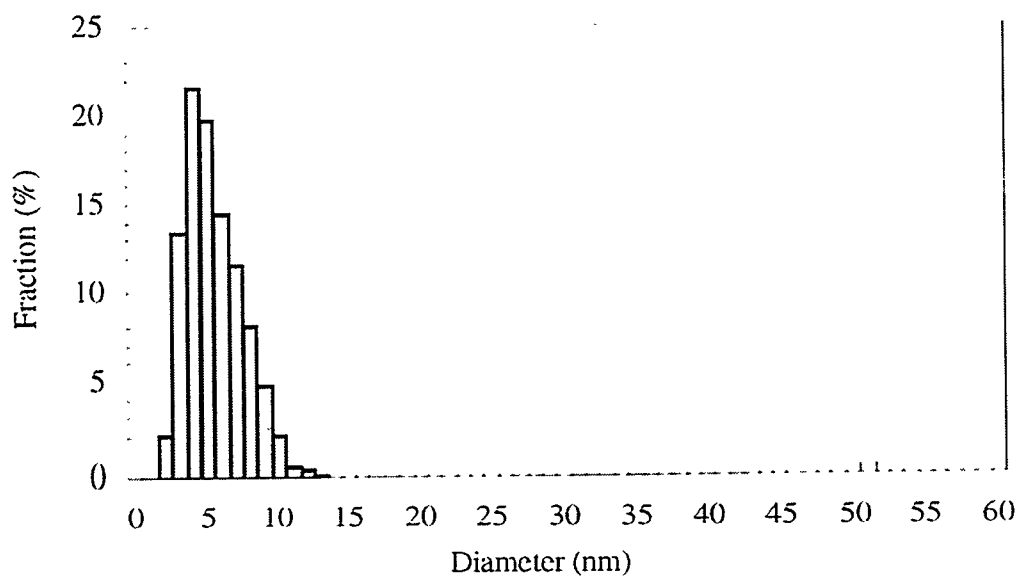
Figure 5   Cavity size distribution in F82H+^{10}B irradaited at 673 K to 7 dpa.
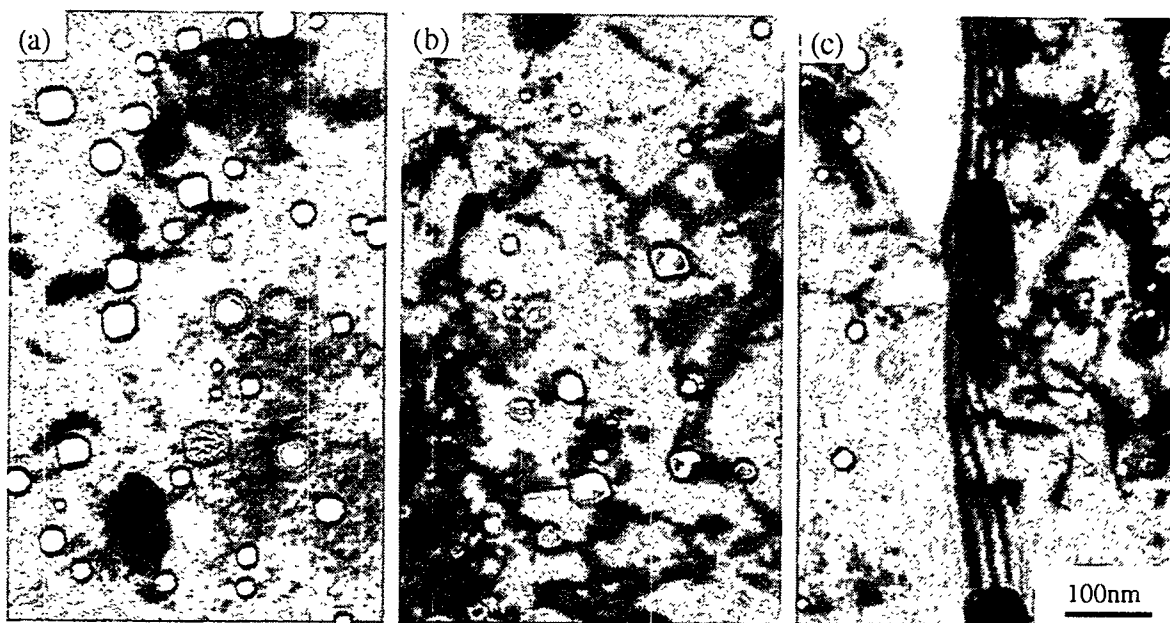
Figure 6   Cavities in F82H-std irradaited at 673 K to 51 dpa.

The calculated He concentration is about 26 appm. (a): Cavities in the matrix (s>>0). (b): Cavities in matrix (s~0), and large cavities were observed at dislocation. (c): No cavities near lath boundaries.
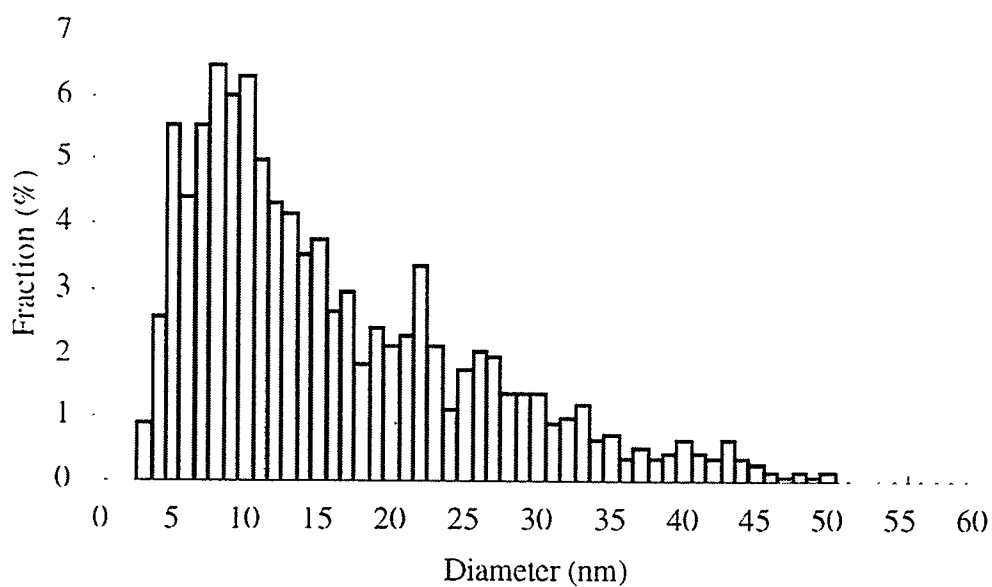
Figure 7   Cavity size distribution in F82H-std irradaited at 673 K to 51 dpa.

4.0 COPPER ALLOYS AND HIGH HEAT FLUX MATERIALS

TEMPERATURE AND STRAIN RATE EFFECTS IN SOLUTION ANNEALED CuCrZr –

D.J. Edwards (Pacific Northwest National Laboratory)*

OBJECTIVE

The objective of this work is to investigate the strain rate and temperature dependence of the tensile properties of solution annealed CuCrZr.

SUMMARY

Previous reports presented the effects of strain rate and test temperature on the tensile properties of GlidCop™ Al25 and Hycon 3HP™ tested in air. The present report summarizes the results of a similar set of tests on solution annealed (SA) CuCrZr. The SA CuCrZr proved to have only a slight dependence on test temperature up to 350°C in comparison to the other alloys tested in this series. Tests conducted at 450°C, irrespective of the strain rate used, produced a low level of precipitate ageing in the solution annealed alloy that masked any potential effect of strain rate and test temperature. For a given strain rate the yield and ultimate strength decreased slightly up to 350°C, then increased significantly at 450°C as the ageing began. The uniform and total elongation both decreased steadily as the test temperature was increased to 450°C. The reduction in area was less sensitive to temperature up to 250°C, then decreased steadily up to 450°C. In general the tensile results showed little dependence on strain rate with the exception that the reduction in area was somewhat higher at the two highest strain rates (1.5×10^{-1} and 1.5 s^{-1}) when tested at 350 and 450°C, which may a consequence to the age hardening. Failure mode in the material appeared ductile throughout the range of strain rate and test temperatures.

PROGRESS AND STATUS

Introduction

As shown in previous reports (1-9), there is a growing recognition that the copper alloys currently considered as candidate materials for the first wall, divertor and limiter structures do not possess the required combination of properties to adequately meet the design criteria for future generation fusion reactors. One of the problems that has arisen is the sensitivity to strain rate, test temperature, and test atmosphere that is found to vary with each alloy and the different heat treatments that can be given to the respective alloys. The degradation in strength and ductility can be quite severe depending on the alloy and test conditions. Unfortunately the actual mechanism remains unclear and may be different for each alloy, particularly the oxide dispersion strengthened GlidCop™ and the precipitation strengthened CuNiBe alloy Hycon 3HP™. CuCrZr, another precipitation strengthened alloy, can be distinguished from the other two alloys for two reasons – namely the mechanical properties appear to be relatively unaffected by test temperature and strain rate in the unirradiated state [6], and the toughness remains higher after irradiation than the other two alloys despite suffering from a severe loss of ductility and work hardening capability when irradiated at temperatures less than 180°C.

An experiment to study the effects of strain rate and test temperature, as well as test environment has been initiated on these three alloys to compare their behavior. The range of strain rates and temperatures was also extended over work reported in the literature to

encompass a broader range of behavior. This report concerns the results on tensile properties of the CuCrZr alloy in the solution annealed condition (no cold work or ageing treatment). Results on the GlidCop™ and Hycon alloy have been presented previously [7].

Experimental Procedure

The CuCrZr used in this experiment was manufactured by Zollern GmbH Laucherthal (Heat Z822). This material was used in a previous study on the effect of heat treatment on the tensile and electrical conductivity [5]. The composition of the material is reported as 0.85 wt% Cr, 0.09% Zr, and <0.001 wt% P. The bar was solution annealed at 970°C for 20 minutes and then water quenched.

The tensile tests were conducted in open air over a strain rate range of 3.9×10^{-4} to 1.5 s^{-1} and covering the temperature range of 25 to 450°C. The testing was conducted on an MTS servo hydraulic frame. The specimens were taken to temperature and then held for 5 minutes to allow the temperature to equilibrate through the entire specimen. Since the tests were conducted in open air, thermal convection was sufficient to equilibrate the temperature in the short period of time. Oxidation of the specimens did occur during the testing, but from comparison with previously published data [5] the oxide scale does not appear to have affected the tests. The specimen geometry and orientation with respect to the original rolling or extrusion direction is the same as that reported earlier [7]. To aid in gripping and aligning the specimens 3.2 mm diameter pin holes were drilled in the center of the specimens grips at each end. The 0.2% offset yield, ultimate, uniform and total elongation, and the reduction in area (RA) were measured on 2 specimens each from computerized data for the two highest strain rates, and from chart recordings for the two lower strain rates. The reduction in area was measured in an optical comparator.

Results and Discussion

The tensile results for the solution annealed CuCrZr are presented in Table 1. The values represent an average of two tensile tests per condition, with the variation usually less than ±5% for the strength, elongation and reduction in area. Figures 1 through 3 show how the tensile properties vary as a function of test temperature. Only a small decrease occurs in the yield and ultimate strength up to 350°C, irrespective of the strain rate, and the elongation, though more variable, decreases steadily as the test temperature increases. The reduction in area appears to be slightly higher for the two highest strain rates as the test temperature is increased, with a difference of approximately 10-15% at 350 and 450°C. Unfortunately the tests conducted at 450°C result in limited age hardening that causes the yield and ultimate strengths to increase well above the values measured at 350°C. The decrease in elongation and reduction in area may therefore be due to the influence of the age hardening as well as the higher test temperature.

Unlike the GlidCop™ Al25 [3, 7], the tensile properties of the solution annealed CuCrZr are essentially independent of the strain rate, and no evidence of the embrittlement found in the case of the Hycon alloy is observed. The yield strength and elongation for the solution annealed CuCrZr are plotted as a function of strain rate in Figures 4 and 5. The strain rate sensitivity parameters for the yield are lower than those reported for the GlidCop™ and Hycon alloys by Zinkle and Eatherly [3] and separately by Edwards [7]. The elongation remains independent of strain rate at test temperatures up to 450°C despite the limited age hardening that occurred in the specimens tested at 450°C.

Table 1. Temperature and strain rate dependence for solution annealed CuCrZr (JET)

Alloy	Test Temp. (°C)	YS (MPa)	UTS (MPa)	e_u (%)	e_{tot} (%)	RA (%)
3.9 x 10⁻⁴ s⁻¹	25	112	240	44.2	56.1	62.7
	150	101	202	40.6	50.0	57.0
	250	91.5	193	37.3	46.5	63.0
	350	95	206	30.2	36.4	51.2
	450	169	222	19.1	35.6	43.3
1.5 x 10⁻³ s⁻¹	25	118	242	43.3	57.4	64.6
	150	102	212	40.4	55.2	59.9
	250	95	191	34.1	42	64.4
	350	91.4	196	30.1	36.3	55.5
	450	166	226	21.2	35.7	46.5
1.5 x 10⁻¹ s⁻¹	25	104	255	46.0	60.7	64.0
	150	102	219	41.7	55.9	57.5
	250	98	196	37.2	48.1	66.1
	350	95	185	30.7	40.6	62.2
	450	165	240	20.0	32.6	53.2
1.5 s⁻¹	25	121	263	41.8	53.7	63.9
	150	108	227	40.0	52.1	64.8
	250	96	200	37.1	49.6	68.3
	350	94	182	33.7	43.2	65.0
	450	177	253	21.3	31.6	54.2

The tensile data for the solution annealed CuCrZr thus confirm previous experiments that found that the CuCrZr is apparently less susceptible to the effects of test temperature and strain rate compared to the other two high strength alloys. However, further testing is warranted since the solution annealed CuCrZr will not remain in the same condition under irradiation at low temperatures (25-200°C). Irradiation-induced precipitation and radiation hardening will both lead to dramatic increases in strength and loss of ductility, whereas irradiation at higher temperatures could easily promote hardening at low doses and softening at higher doses as precipitate overaging occurs. The CuCrZr must also be tested in the condition more representative of its actual in-service condition, most likely a solution annealed and aged condition. This condition has been investigated to a limited extent by Zinkle and Eatherly [5] for the same material tested in vacuum.

FUTURE WORK

Specimens from solution annealed and aged CuCrZr are also planned for testing to compare the results with those obtained in this study and the previously reported tests on the GlidCop™ and Hycon 3HP™. The fracture surfaces of the solution annealed CuCrZr specimens will be selectively examined and reported at a later date.

ACKNOWLEDGEMENTS

REFERENCES

1. R.R. Solomon, J.D. Troxell, and A. V. Nadkarni, J. of Nucl. Matls., **233-237**, (1996), p. 542.

2. D.J. Alexander, Fusion Materials Semiannual Progress Report for the Period ending June 30, 1996, DOE/ER-0313/20, (Oak Ridge National Laboratory, 1996), p. 217.

3. S.J. Zinkle and W.S. Eatherly, Fusion Materials Semiannual Progress Report for the Period ending December 31, 1996, DOE/ER-0313/21, (Oak Ridge National Laboratory), p. 165.

4. D.J. Alexander, S.J. Zinkle and A.F. Rowcliffe, Fusion Materials Semiannual Progress Report for the Period ending December 31, 1996, DOE/ER-0313/21, (Oak Ridge National Laboratory, 1996), p. 217.

5. S.J. Zinkle and W.S. Eatherly, Fusion Materials Semiannual Progress Report for the Period ending June 30, 1997, DOE/ER-0313/22, (Oak Ridge National Laboratory), p. 143.

6. K. Leedy, J.F. Stubbins, D.J. Edwards, R.R. Solomon and D. Krus, Fusion Materials Semiannual Progress Report for the Period ending June 30, 1997, DOE/ER-0313/22, (Oak Ridge National Laboratory), p. 149.

7. D.J. Edwards, Fusion Materials Semiannual Progress Report for the Period ending December 31, 1997, DOE/ER-0313/23, (Oak Ridge National Laboratory), p. 213.

8. M. Li, J.F. Stubbins and D.J. Edwards, Fusion Materials Semiannual Progress Report for the Period ending June 30, 1998, DOE/ER-0313/24, (Oak Ridge National Laboratory), p. 173.

9. S.J. Zinkle and W.S. Eatherly, Fusion Materials Semiannual Progress Report for the Period ending June 30, 1998, DOE/ER-0313/24, (Oak Ridge National Laboratory), p. 189.
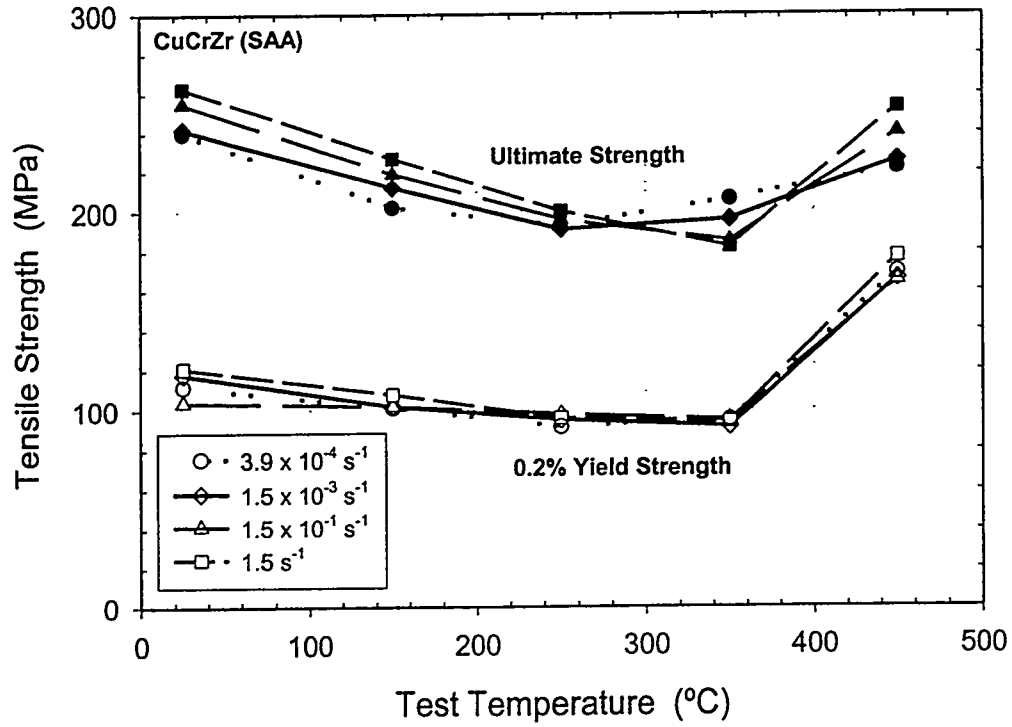
Figure 1. The temperature dependence of the yield and ultimate strength of the solution annealed CuCrZr shows that the strength decreases somewhat up to 450°C, where a limited degree of age hardening is thought to be responsible for the sudden increase in strength.
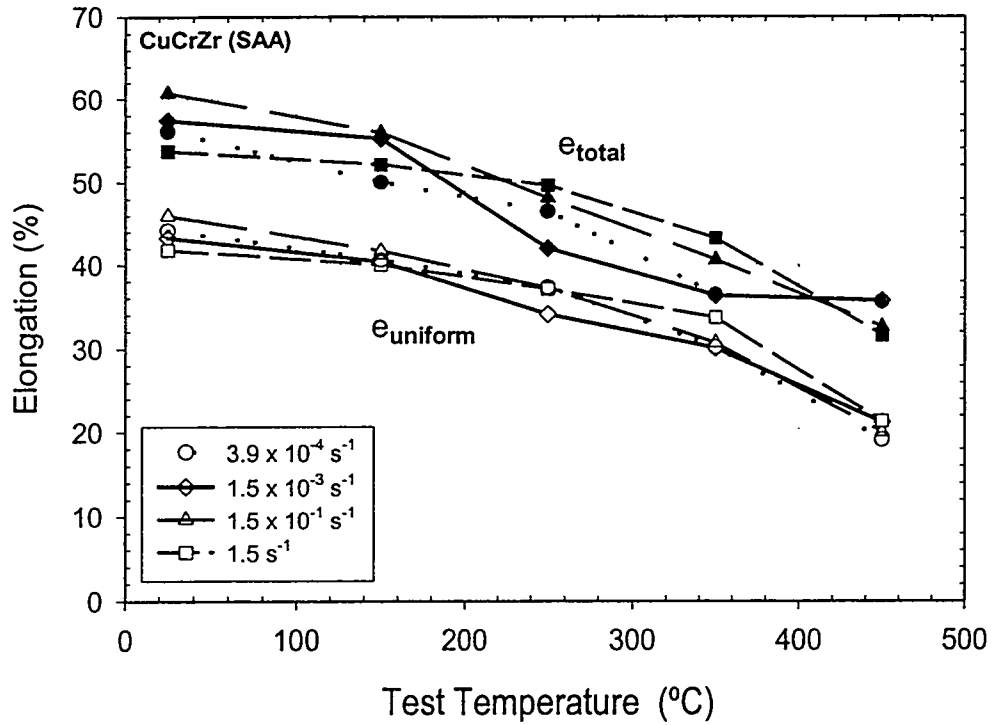
Figure 2. Shown is the temperature dependence of the uniform and total elongation of the solution annealed CuCrZr. Elongation decreases steadily as the test temperature is increased, though the 450°C tests are influenced both by the age hardening and the high test temperature.
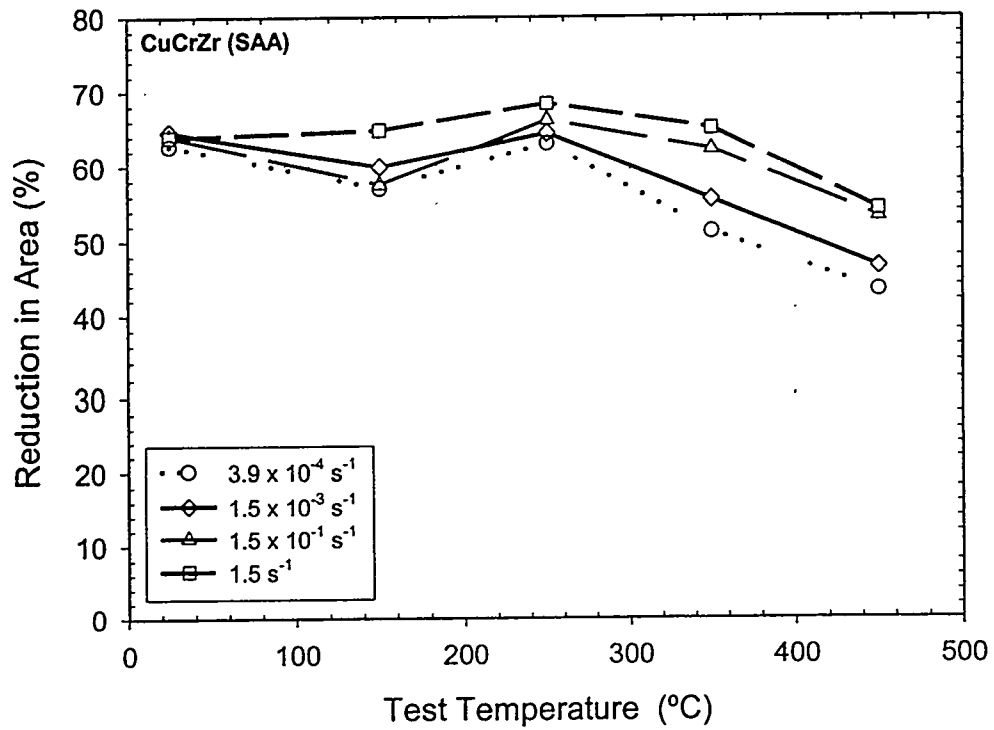
Figure 3. Changes in the reduction in area as a function of test temperature were found to be variable, however, even at 450°C the reduction in area remained above 40%. The two lower strain rates produced a noticeably smaller reduced area at 350°C and above, which might be a consequence of the age hardening.
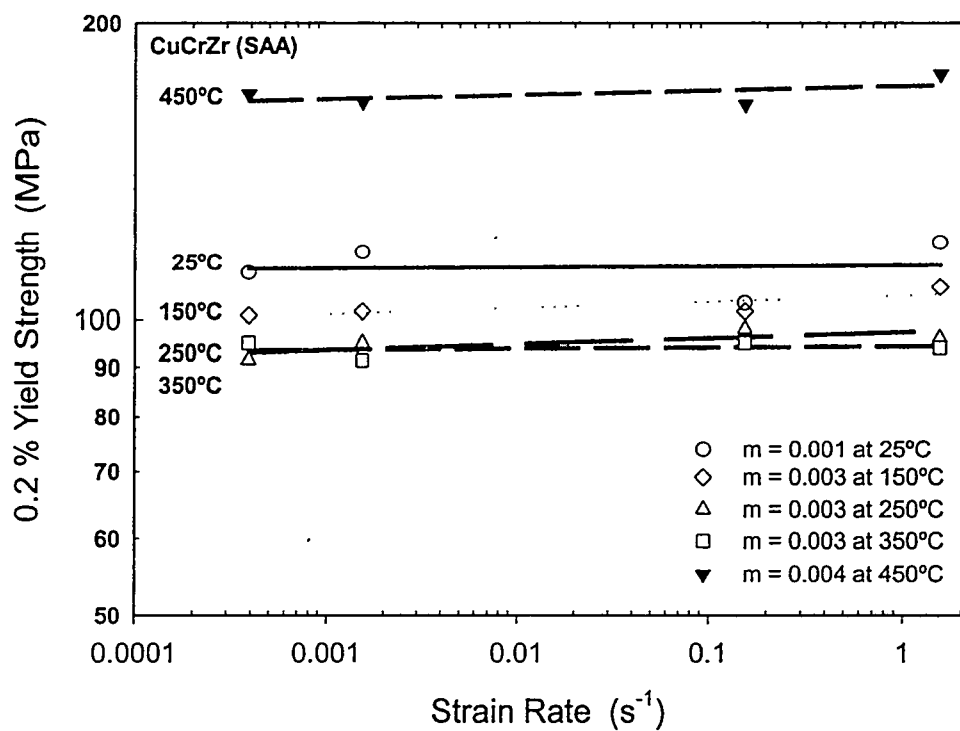
Figure 4. The yield strength of the solution annealed CuCrZr proved to be rather insensitive to the strain rates used in this experiment. The strain rate sensitivity was lower in general than those measured for the GlidCop™ Al25 and Hycon 3HP™.
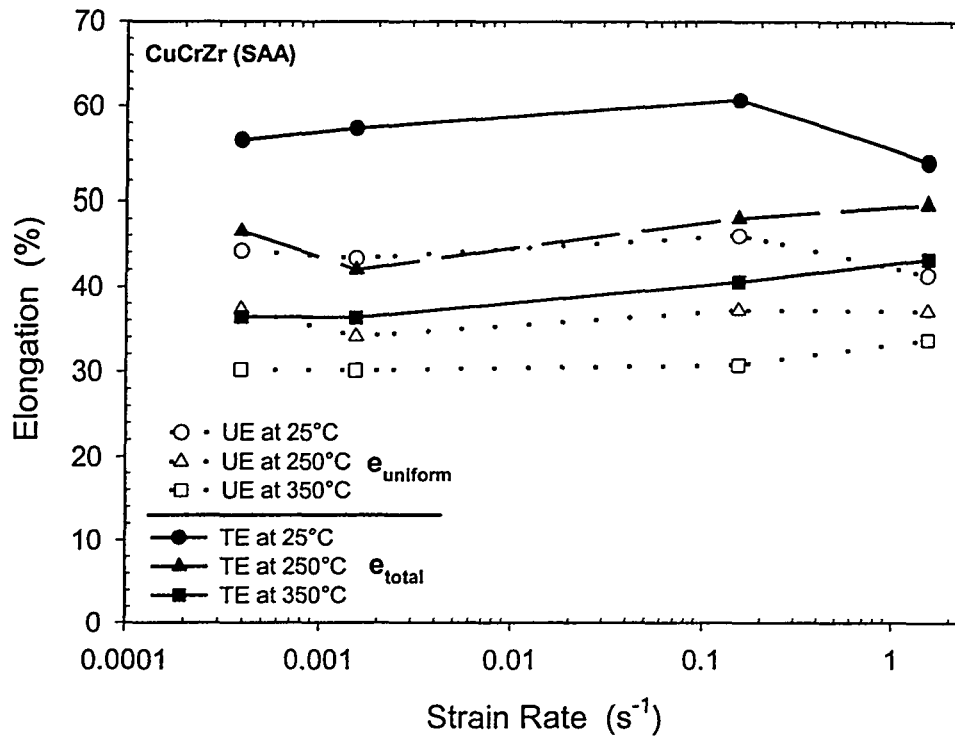
Figure 5. As in the case of the yield strength, the uniform and total elongation were not sensitive to the variation in strain rates used in this experiment. The curves for the tests conducted at 450°C are not shown for simplicity, but they show the same trend.

5.0   AUSTENITIC STAINLESS STEELS

MICROSTRUCTURAL EVOLUTION OF COLD-WORKED AUSTENITIC STAINLESS STEELS IRRADIATED TO 17 DPA IN SPECTRALLY TAILORED EXPERIMENTS OF THE ORR AND HFIR AT 400°C — E. Wakai (Japan Atomic Energy Research Institute), N. Hashimoto, J. P. Robertson (Oak Ridge National Laboratory), T. Sawai, and A. Hishinuma (JAERI)

OBJECTIVE

The purpose of this work is to summarize the microstructural evolution of cold worked austenitic steels irradiated at 400 °C to 17.3 dpa in the spectrally tailored experiments of the ORR and HFIR.

SUMMARY

The microstructural evolution of cold-worked JPCA, 316R, C, K steels irradiated at 400 °C in spectrally tailored experiments of the ORR and HFIR was investigated. The helium generation rates were about 12-16 appm He/dpa on the average up to 17.3 dpa. The number density and average diameter of dislocation loops in the steels had ranges of 3×10^{21} - 8×10^{21} m^{-3} and 14.4- 23.7 nm, respectively. Carbides were formed in all steels by the irradiation, and the number density and average diameter had ranges of 2×10^{21}- 1×10^{22} m^{-3} and 3.4- 17.7 nm, respectively. The number density and root mean cube of radius for cavities were 6×10^{21} to 2×10^{22} m^{-3} and 1.2 to 2.4 nm, respectively, in these steels, and the swelling was 0.007 - 0.1% in these steels. JPCA-CW which has the lowest swelling shows the highest number density of carbides, while K-CW which has the highest swelling shows the lowest density of carbides.

PROGRESS AND STATUS

1. Introduction

One of the favored first wall and blanket concepts for near term fusion systems such as the International Thermonuclear Experimental Reactor (ITER) is a low pressure water-cooled austenitic stainless steel structure [1]. The neutron sources with a maximum energy of 14 MeV in the D-T fusion reactor create displacement damage in the first wall materials, and also produce hydrogen and helium atoms from (n, p) and (n, α) reactions. In the absence of operating fusion reactors, the necessary irradiation experience has to be gained from a partial simulation of the fusion environment using fission reactors. For austenitic stainless steels, it is possible to reproduce the damage rate, neutron fluence, and helium generation rate typical of the fusion environment using spectral tailoring [2-6]. Spectral tailoring involves progressively changing the ratio of thermal to fast neutron flux through the use of removable shields surrounding the experimental assembly [2]. In this way the two-step thermal neutron reaction with ^{58}Ni [7] can be mainly manipulated so that the ratio of helium generation rate to displacement rate (He/dpa ratio) approximates that for fusion throughout the irradiation. In this study the microstructural evolution of several types of austenitic stainless steels has been examined under the controlled He/dpa ratio. This experiment is being conducted under the DOE/JAERI Collaborative Agreement.

2. Experimental Procedure

The spectrally tailored experiments were performed in two stages. The first stage of the irradiation was carried out in the Oak Ridge Research Reactor (ORR) in capsule ORR-MFE-7J (330 and 400°C) [8-11]. After accumulating approximately 7.4 dpa in the ORR, the 400 °C specimens were transferred to the High Flux Isotope Reactor (HFIR) in capsule HFIR-RB-400J-1 for the second stage [12-14]. In each reactor, the specimens were irradiated at 400 °C. Temperatures were continuously measured and controlled in these experiments during irradiation. The thermal and fast (E >0.1 MeV) neutron fluences in the ORR were 8.1×10^{25} and 9.5×10^{25} n/m^2 [12], and those of the HFIR were 4.0×10^{25} and 1.6×10^{26} n/m^2[8], respectively. The experiments achieved a total peak damage level of 17.3 dpa. The helium concentrations generated in type 316 and JPCA stainless steel were 200 and 280 He appm, respectively, and the controlled average ratios of He/dpa were 12 and 16 appm for the 316 and JPCA, respectively, in this irradiation. The summary is given in Table 1.

Transmission electron microscopy (TEM) disks of several different austenitic stainless steels were irradiated in these capsules. The steels are the JPCA, 316R, C, and K. Chemical compositions of these alloys are given in Table 1. The JPCA steel contains boron, phosphorus, and titanium. The 316R is a standard of type 316 stainless steel. The C and K stainless steels have low carbon concentration, and they are modified exploratory alloys with titanium and/or niobium. The JPCA, 316R, C, and K alloys were solution-annealed or 20 % cold-worked before irradiation.

Microstructures of these specimens were examined using a JEM-2000FX transmission electron microscope with a LaB$_6$ gun operated at 200 kV. In order to evaluate defect density the foil thickness of each TEM specimen was measured by thickness fringes or by the improved CSS method [15, 16].

Table 1. Damage levels, helium concentrations, and the ratios of He/dpa of type 316 and JPCA stainless steels irradiated in the spectrally tailored experiments of the ORR and HFIR

	316 (13 wt%Ni)			JPCA (16 wt%Ni)		
	Damage (dpa)	He (atppm)	He/dpa	Damage (dpa)	He (atppm)	He/dpa
ORR (MFE-7J)	7.4	100	14	7.4	155	21
HFIR (RB-400J-1)	9.9	100	10	9.9	125	13
ORR + HFIR	17.3	200	12	17.3	280	16

Table 2. Chemical compositions of austenitic stainless steels used in this study (wt%)

Alloy	Fe	Cr	Ni	B	C	N	P	S	Si	Ti	Mn	Nb	Mo
JPCA	Bal	14.2	15.6	0.003	0.06	0.0039	0.027	0.005	0.50	0.24	1.77	-	2.3
316R	Bal.	16.8	13.5	-	0.06	-	0.028	0.003	0.61	0.005	1.80	-	2.5
C	Bal.	15.4	15.6	-	0.02	0.0018	0.017	0.007	0.51	0.25	1.56	0.08	2.4
K	Bal	18.0	17.6	-	0.02	0.004	0.015	0.005	0.48	0.29	1.46	-	2.6

3. Results and Discussion

Microstructures of austenitic stainless steels under spectrally tailored experiments

The microstructural data obtained is summarized in Table 3-5. Dislocation loops, carbides, and cavities were formed by the irradiation at 400°C to 17.3 dpa The number density and average diameter of dislocation loops in the steels had ranges of 3×10^{21}- 8×10^{21} m^{-3} and 14.4-23.7 nm, respectively. In 316-CW steels, the loops were not observed in some area of high density dislocation prior to the irradiation. In the JPCA- CW steels, the number density was somewhat higher than those of the other steels. Carbides were formed in all the steels by the irradiation, and the number density and mean size of carbides in these steels had ranges of 2×10^{21}- 1×10^{22} m^{-3} and 3.4- 17.7 nm, respectively. The steels with the lowest and highest number density of carbides were K-CW and JPCA-CW alloys, respectively. The number density of cavities were 6×10^{21} to 2×10^{22} m^{-3} in these steels. The swelling was 0.007 - 0.1% in these steels. JPCA-CW which has the lowest swelling shows the highest number density of carbides, while K-CW which has the highest swelling shows the lowest density of carbides.

In many steels, the number density of dislocation loops, carbides, and cavities in these cold-worked steels are very close to those in the solution-annealed steels[17], but the swelling in most part of CW steels is lower than that of these SA steels.

Table 4. Mean size and number density formed in these steels irradiated at 400 °C to 17.3 dpa with a helium generation rate of about 12 -16 appm He/dpa on the average throughout this experiment. *data are previous data[17].

Alloy	Mean Size (nm)	Number Density (m^{-3})
JPCA-CW	19.3	8×10^{21}
JPCA-SA*	18.7	7×10^{21}
316R-CW	14.4	5×10^{21}
316R-SA*	20.2	1×10^{22}
C-CW	23.7	3×10^{21}
C-SA*	26.3	3×10^{21}
K-CW	20.2	4×10^{21}
K-SA*	22.1	5×10^{21}

Table 5. Mean size and density of precipitates formed in these steels irradiated at 400 °C to 17.3 dpa. *data are previous data[17].

Alloy	Mean Size (nm)	Number Density (m^{-3})
JPCA-CW	3.4	1×10^{22}
JPCA-SA*	3.4	8×10^{21}
316R-CW	17.7	5×10^{21}
316R-SA*	15.1	5×10^{21}
C-CW	4.3	5×10^{21}
C-SA*	5.3	6×10^{21}
K-CW	15.1	2×10^{21}
K-SA*	19.3	1×10^{21}

Table 6. Swelling data of the cavities formed in these steels irradiated at 400 °C to 17.3 dpa with a helium generation rate of about 12 -16 appm He/dpa on the average throughout this experiment. *data are previous data[17].

Alloy	Root Mean Cube of Cavity Radius (nm)	Number Density (m^{-3})	Swelling (%)
JPCA-CW	1.3	8×10^{21}	0.007
JPCA-SA*	1.5	1×10^{22}	0.01
316R-CW	2.4	6×10^{21}	0.04
316R-SA*	1.8	6×10^{21}	0.02
C-CW	1.2	3×10^{22}	0.02
C-SA*	2.5	1×10^{22}	0.07
K-CW	2.4	2×10^{22}	0.01
K-SA*	4.0	1×10^{22}	0.3

ACKNOWLEDGMENTS

REFERENCES

1. G. L Kulcinski, J. Nucl. Mater., 1 2 2 & 1 2 3(1984)457.

2. M. L. Grossbeck et al., in: Proc. Conf. on Fast, Thermal, and Fusion Reactor Experiments, Salt Lake. City, Utah, April 1985, Vol. 1, pp. 199-210.

3. A. F. Rowcliffe, A. Hishinuma, M. L. Grossbeck, and S. Jitsukawa, J. Nucl. Mater., 179-181 (1991)125.

4. R. E. Stoller, P. J. Maziasz, A. F. Rowcliffe, and M. P. Tanaka, J. Nucl. Mater., 155-157 (1988)1328.

5. T. Sawai, P. J. Maziasz, H. Kanazawa and A. Hishinuma, Fusion Reactor Materials Semiannual Progress Report for Period Ending September 30, 1990, Office of Fusion Energy, DOE/ER-0313/9, 1990, p. 152.

6. T. Sawai. P. J. Maziasz, H. Kanazawa, and A. Hishinuma, J. Nucl. Mater., 191-194 (1992) 712.

7. A. A. Bauer and M. Kangilaski, J. Nucl. Mater., 4 2(1972)91.

8. J P. Robertson, I. loka, A. F. Rowcliffe, M. L. Grossbeck, and S. Jitsukawa, Effects of Radiation on Materials: 1 8th International Symposium, ASTM STP 1325, R. K. Nastad, et. al . Eds., American Society for Testing and Materials, Philadelphia, 1997.

9. I. I Siman-Tov, Fusion Reactor Materials Semiannual Progress Report for Period Ending September 30, 1987, Office of Fusion Energy, DOE/ER-0313/2, 1988, p. 18.

10. L. R. Greenwood, Fusion Reactor Materials Semiannual Progress Report for Period Ending March 31, 1989, Office of Fusion Energy, DOE/ER-0313/6, 1989, p. 23.

11. L. R. Greenwood, Alloy Development for Irradiation Performance Semiannual Progress Report for Period Ending March 31, 1989, Office of Fusion Energy, DOE/ER-0045/16,1986, p. 17.

12. L. R. Greenwood, C. A. Baldwin and B. M. Oliver, Fusion Reactor Materials Semiannual Progress Report for Period Ending September 30, 1994, Office of Fusion Energy, DOE/ER-0313/17, 1995, p. 28.

13. A. W. Longest, J. E. Pawel, D. W. Heatherly, R. G. Sitterson, and R. L. Wallace, Fusion Reactor Materials Semiannual Progress Report for Period Ending March 31, 1993, Office of Fusion Energy, DOE/ER-0313/14, 1993, p. 14.

14. A. W. Longest, D. W. Heatherly, E. D. Clemmer, and J. E. Corum, Fusion Reactor Materials Semiannual Progress Report for Period Ending March 31, 1993, Office of Fusion Energy, DOE/ER-0313/14, 1993, p. 14.

15. T. Sawai, M. Suzuki, P. J. Maziasz, and A. Hishinuma, J. Nucl. Mater., 187(1992)146.

16. T. Sawai, and M. Suzuki, Scripta Metall., 24(1990)2047.

17. E. Wakai, N. Hashimoto, T. Sawai, J. P. Robertson, L. T. Gibson, I. Ioka, and A. Hishinuma, Fusion Reactor Materials Semiannual Progress Report for Period Ending June 30, 1997, Office of Fusion Energy, DOE/ER-0313/22, 1997, pp. 159-168.

6.0   INSULATING CERAMICS AND OPTICAL MATERIALS

EFFECT OF LOW TEMPERATURE ION IRRADIATION ON THE MICROSTRUCTURE OF NITRIDE CERAMICS

– S.J. Zinkle, L.L. Snead, W. S. Eatherly, J.W. Jones and D.K. Hensley (Oak Ridge National Laboratory)

OBJECTIVE

The objective of this study is to gain some insight into point defect mobilities in silicon nitride and aluminum nitride by examining the low-temperature irradiated microstructure.

SUMMARY

Cross-section transmission electron microscopy was used to investigate the microstructure of polycrystalline silicon nitride (Si_3N_4) and aluminum nitride (AlN) following 2 MeV Si ion irradiation at 80 and 400 K up to a fluence of 4×10^{20} ions/m^2 (maximum damage of ~10 displacements per atom, dpa). A buried amorphous band was observed at both temperatures in Si_3N_4 in the region corresponding to the peaks in the implanted ion and displacement damage. From a comparison of Si_3N_4 specimens irradiated at different fluences, it is concluded that the amorphization is primarily controlled by the implanted Si concentration rather than the displacement damage level. Si_3N_4 amorphization did not occur in regions well-separated from the implanted ions for doses up to at least 3 dpa at 80 K, whereas amorphization occurred in the ion implanted region (calculated Si concentration >0.01 at.%) for damage levels as low as ~0.6 dpa. The volumetric swelling associated with the amorphization of Si_3N_4 is <10%. Amorphization was not observed in any of the irradiated AlN specimens. A moderate density of small (~3 nm) defect clusters were observed in the crystalline damaged regions of both the Si_3N_4 and AlN specimens at both irradiation temperatures. Aligned network dislocations were also observed in the AlN specimen irradiated to high dose at 80 K.

PROGRESS AND STATUS

Introduction

AlN and Si_3N_4 are being considered for ceramic insulator applications in magnetic fusion reactors. Both of these materials have high strength and high electrical resistivity at moderate temperatures. Despite the widespread interest in these materials for electronic and structural ceramic applications, relatively little is known about their point defect behavior. We are unaware of any studies on self-interstitial atom (SIA) mobility in Si_3N_4. Atobe and coworkers found that the nitrogen vacancies (F centers) in AlN accumulated linearly with fast neutron fluence during irradiation at 20 K, whereas the accumulation was sublinear (proportional to the square root of fluence) at 360 K [1]. This indicates [2] that nitrogen SIAs are immobile in AlN at 20 K and mobile at 360 K.

Examination of the irradiated microstructure of ceramics, and in particular the temperature-dependent amorphization behavior, can provide insight into the mobility of point defects [3-5]. Several previous microstructural investigations of irradiated AlN and Si_3N_4 have been performed. Elevated temperature neutron irradiations of AlN [6,7] and Si_3N_4 [8] have observed faulted dislocation loops on basal and prism habit planes, respectively. Amorphization did not occur during 1 MeV electron irradiation at 140 K up to a fluence of 3×10^{26}/m^2 (~0.5 dpa) in AlN [9] or during 1-2 MeV electron irradiation at 100-170 K up to fluences of $3-18 \times 10^{26}$/m^2 (~0.5-4 dpa) in Si_3N_4 [9-11]. AlN and Si_3N_4 were found to remain crystalline following room temperature bombardment with 3 MeV Kr ions up to a fluence of 2×10^{21}/m^2 (~150 dpa peak damage) [12]. Conversely, numerous ion irradiation studies at temperatures from 80 to 450 K have found that Si_3N_4 can be amorphized after ~1 to 2 dpa in the region corresponding to the peak in the

implanted ion (Ni, Ti, Si, Fe, Cr) and displacement damage profiles [3,13-17]. The discrepancy in the Si_3N_4 amorphization behavior observed by Cartz et al. [12] and the implanted Ni, Ti, Si, Fe, Cr studies [3,13-17] highlights the importance of obtaining amorphization data under conditions where implanted ion effects are negligible [3]. Silicon nitride was recently shown to be resistant to amorphization up to 7 dpa during room temperature 3.6 MeV Fe ion irradiation in regions well separated from the implanted ions, whereas amorphization occurred readily in ion-implanted regions for doses of ~2 dpa [3]. Unfortunately, many ion beam amorphization studies have not attempted to separate implanted ion and displacement damage effects, with the notable exceptions of in-situ thin foil [18] and cross-section [3] MeV ion irradiation studies.

Table 1. Summary of properties of the investigated AlN and Si_3N_4 ceramics [7,19].

Material	Crystal structure	Lattice parameters	Density (g/cm^3)	Thermal conductivity (W/m-K)	Ionicity	Sublimation temperature
AlN (Cercom)	Hexagonal (wurtzite)	a=0.311 nm c=0.498 nm c/a=1.60	3.25	115	0.40	2790 K
β-Si_3N_4 (Kyocera)	Hexagonal (P6$_3$ space group)	a=0.760 nm c=0.290 nm c/a=0.290	3.21	29	0.28	2151 K

EXPERIMENTAL PROCEDURE

Small blocks of hot isostatically pressed Si_3N_4 (Kyocera SN733) and sintered AlN (Cercom) were obtained from commercial vendors. Table 1 summarizes some of the physical properties of AlN and Si_3N_4 [7,19]. Transmission electron microscope (TEM) specimens (3 mm diameter by 0.5 mm thick) were machined by a combination of diamond sawing and ultrasonic cutting. The top surfaces of the specimens were mechanically polished using 0.05 μm diamond paste.

The specimens were thermally anchored to a copper block using either silver paint or Aquadag™ adhesive. Duplicate specimens of each material were simultaneously irradiated for each irradiation condition using a 1.2 cm diameter beam spot. The irradiations were performed using 2 MeV Si beam currents of 0.3-1 μA/cm^2 at the Surface Modification And Characterization (SMAC) facility in the Solid State Division at ORNL. The irradiation temperature was continuously monitored by a thermocouple embedded in the support block. The maximum calculated beam heating was <1°C. Specimens were irradiated to fluences of either $4x10^{19}$ or $4x10^{20}/m^2$ at 78-82 K and 400 K. The displacement damage and implanted ion profiles were calculated using the TRIM96 program [20]. Figure 1 shows the calculated results for Si_3N_4; similar profiles were calculated for AlN. All calculations assumed a sublattice-averaged displacement energy of 40 eV.

Following the irradiation, cross-section TEM specimens were prepared by gluing the irradiated disks to polished unirradiated disks, sectioning, grinding to 0.1 mm, dimpling to 20 μm, and then dual-gun ion beam thinning at ~80 K with 6 keV Ar ions until perforation occurred near the interface. The specimen surfaces were cleaned using 3 keV Ar ions at an angle of 11° and then coated with a thin (~5 nm) layer of carbon prior to examination. The specimens were examined using conventional bright-field and dark-field imaging techniques in a Philips CM-30 microscope operating at 300 kV.
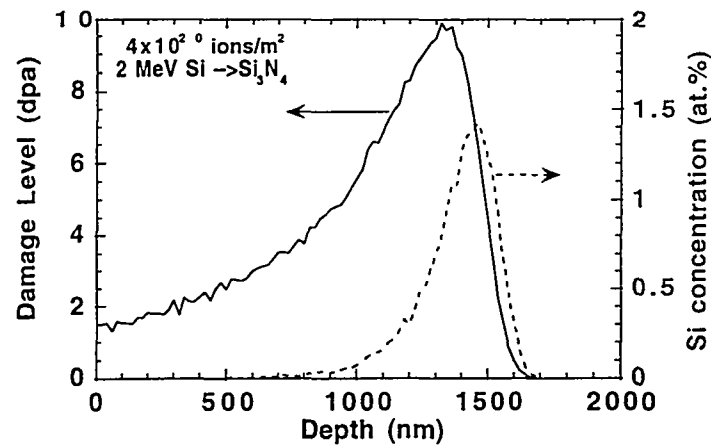
Fig. 1. Calculated damage and implanted ion distributions for 2 MeV Si ions in Si_3N_4.

Results

Figure 2 shows the general cross-section microstructure of silicon nitride irradiated at 80 K to fluences of 4×10^{19} and 4×10^{20} ions/m². A buried amorphous band was observed at both fluences, with a width of 0.7 µm at the lower fluence and 1.0 µm at the higher fluence. The residual dark contrast in the amorphous regions is due to Y_2O_3-enriched grain boundaries (0.5 µm mean grain diameter). The amorphization dose was comparable at grain boundaries and in the grain interior. The measured maximum damage range at both fluences was 1.70 ±0.02 µm. The similarity in damage range for the two doses implies that the volumetric swelling associated with amorphization of Si_3N_4 is <10%, which is much less than the value of 22-25% suggested in some previous ion irradiation studies [15,16]. A recent modeling study found that the crystalline and amorphous Si_3N_4 densities were comparable [21], in agreement with the present results. From a comparison with the calculated TRIM profiles (Fig. 1), amorphization occurred at 80 K when the damage level was >0.6 dpa and the implanted Si concentration was c_{Si}>0.01 at.% in the lower fluence specimen and when the damage level was >3.3 dpa and c_{Si}>0.01 at.% in the higher fluence specimen. This implies that the implanted ion concentration is the controlling factor in the low temperature amorphization of Si_3N_4 (for damage levels >0.6 dpa).

Small defect clusters (~3 nm diameter) were visible in the crystalline damaged regions of Si_3N_4 irradiated at 80 K to a fluence of 4×10^{20} ions/m², whereas these defect clusters were not visible in the lower fluence specimen. This implies that these defect clusters were formed as the result of nucleation and growth (or perhaps multiple overlapping cascades), as opposed to direct formation within a single cascade.

Irradiation of Si_3N_4 at 400 K also produced a buried amorphous layer, although the band width at a given fluence was smaller than at 80 K. For example, the amorphous layer was ~0.17 µm wide for irradiation at 400 K to a fluence of 4×10^{19} ions/m². Analysis of the amorphization behavior at 400 K showed a good correlation with implanted Si concentration and a poor correlation with damage level. Amorphization of Si_3N_4 at 400 K occurred when the calculated Si concentration exceeded 0.1 at.% (for damage levels >0.9 dpa). Small defect clusters (~3 nm diameter) were observed in the damaged crystalline regions of Si_3N_4 at both of the 400 K irradiation fluences.

Fig. 2. Cross-section microstructures of Si_3N_4 irradiated with 2 MeV Si ions at 80 K.
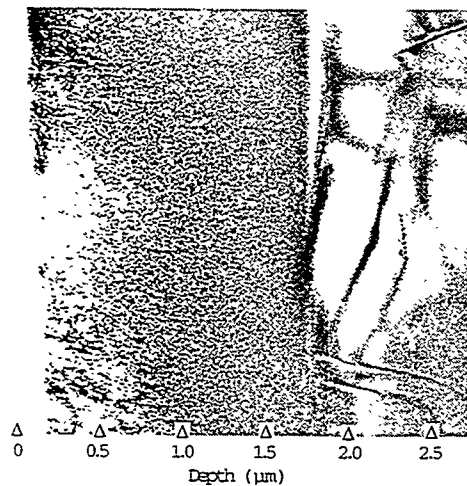
Fig. 3. Cross-section microstructure of aluminum nitride irradiated with 2 MeV Si ions at 78 K to a fluence of 4×10^{20} ions/m^2.
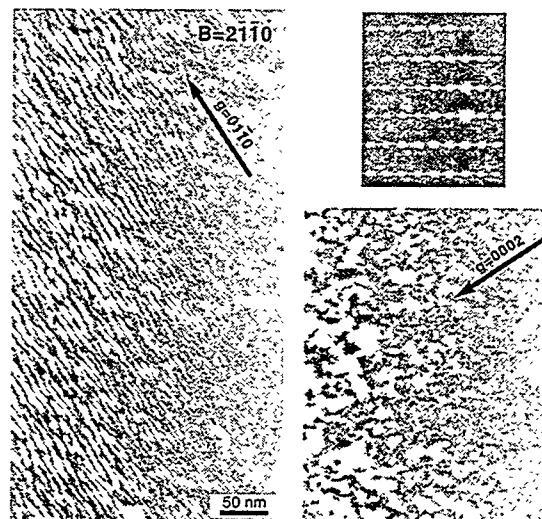
Fig. 4. Aligned network dislocations and defect clusters in AlN irradiated at 78 K to a fluence of 4×10^{20} ions/m^2.

Figure 3 shows the general cross-section microstructure of aluminum nitride irradiated at 78 K to a fluence of 4×10^{20} ions/m^2. A high density of small defect clusters (mean diameter of ~3 nm) was formed up to a maximum depth of 1.74 µm, with no evidence for amorphous regions in the grain interior (~8 µm grain diameter). A similar damage range and defect microstructure was observed in the specimen irradiated at 400 K to the same fluence. The initially crystalline grain boundary phase in AlN (easily visible at grain boundary triple points) was amorphized during irradiation at 78 K.

The irradiated microstructure of AlN is shown in finer detail in the centered dark field images of Fig. 4. A network of aligned dislocations were visible with a diffraction vector of $g = 01\bar{1}0$ but were not present for g=0002. Streaking was observed along the 0002 systematic row in the diffraction pattern.

Discussion

According to ionicity model for amorphization susceptibility [22], Si$_3$N$_4$ and AlN would both be expected to have moderate resistance to radiation-induced amorphization due to their largely covalent bonding. However, both of these materials have an amorphization resistance at 80 K that is comparable or superior to the predominantly ionic bonded Al$_2$O$_3$ which is amorphized after ~5 dpa [23,24]. Similarly, according to structural freedom considerations [25], Si$_3$N$_4$ should become amorphous at lower doses than Al$_2$O$_3$. As discussed elsewhere, point defect mobility is another important factor for amorphization [4]. In particular, amorphization generally does not occur in irradiated ceramics if the anion and cation SIAs are mobile.

The observation of a well-developed network dislocation structure in AlN at 80 K (Fig. 4) is evidence for significant SIA mobility. This conclusion is based on the assumption that the network dislocation structure was formed by the growth and unfaulting of interstitial dislocation loops produced at lower doses. As discussed in the introduction, the earlier optical absorption study by Atobe et al. [1] suggested that nitrogen SIAs in AlN are immobile at 20 K and mobile at 360 K. The present microstructural observations suggest that both the anion and cation interstitials in ion irradiated AlN are mobile at a temperature as low as 80 K. Further work is needed to determine if there is any possible influence of ionization induced diffusion [26] which could produce enhanced point defect mobility during ion irradiation.

There is a lack of microstructural data to which the present low-temperature irradiation results can be compared. It is interesting to note that the predominant habit plane for dislocation loops observed in previous high-temperature neutron irradiation studies were [0001] and $\{10\bar{1}0\}$ for AlN and Si$_3$N$_4$, respectively [7,8]. This difference may be due to the large difference in c/a lattice parameter ratios for these two materials (Table 1). The microstructural evolution in AlN irradiated to ~10 dpa at 80 K in the present study appeared to be more advanced than in a previous neutron irradiation study to a similar dose at ~770 K [7]. The neutron irradiation study reported the presence of interstitial dislocation loops on the basal plane with a Burgers vector of c/2[0001], but a network dislocation structure was not observed. The formation of network dislocations in irradiated materials generally requires high doses at elevated temperatures. Work is in progress to investigate the dose and temperature dependence of the microstructure of ion-irradiated AlN.

As summarized in the introduction, there are no known observations of amorphization in AlN, although relatively few studies have been performed [9,12]. In contrast, numerous studies have reported ion beam amorphization of Si$_3$N$_4$. The results of the present study and ref. [3] demonstrate that certain implanted ions have a pronounced effect on promoting amorphization of Si$_3$N$_4$. One possible mechanism for the implanted ion effect is that the impurity atoms may

effectively trap migrating SIAs in Si_3N_4. The physical reason why AlN is able to accommodate >1% Si without amorphization whereas Si_3N_4 becomes amorphous for implanted metal ion concentrations above 0.01-0.1 at.% is worthy of further study. From the present study and previous work, strong implanted ion effects on the amorphization of Si_3N_4 appear to exist for Ni, Ti, Si, Fe, and Cr ions [3,13-17]. Amorphization has not been observed in Si_3N_4 irradiated at room temperature to moderate (3.5 dpa) or high (150 dpa) damage levels with He [3] or Kr [12] ions, respectively.

Conclusions

Aluminum nitride exhibits a high resistance to ion beam amorphization at temperatures as low as 80 K. The pronounced microstructural evolution of the defect clusters in the irradiated AlN specimens suggests that there is high mobility of the self interstitial atoms on both sublattices at 80 K. Therefore, amorphization is not expected to occur at temperatures $\geq$80 K even at higher doses (>10 dpa) unless implanted ions begin to trap point defects or the composition becomes significantly different from AlN due to the implanted ions.

The amorphization of beta-silicon nitride is extremely sensitive to small concentrations of implanted ions (Cr, Ti, Fe, Si). Amorphization at 80 K occurred when the implanted Si concentration exceeded ~100 appm for damage levels greater than ~0.5 dpa. Amorphization did not occur at 80 K outside of the implanted ion region (c_{Si}<100 appm) for damage levels as high as 3 dpa. Amorphization at 400 K was also sensitive to the implanted ion concentration, with a critical concentration of Si needed to induce amorphization of ~0.1 at.% for damage levels >0.9 dpa.

The development of resolvable defect clusters (and a network dislocation structure in the case of AlN) during irradiation at ~80 K is an indication that both anion and cation self-interstitial atoms are mobile in these two nitride ceramics. Further work at temperatures <80 K is needed to determine the migration kinetics of self-interstitial atoms in these materials.

REFERENCES

1. K. Atobe, M. Honda, N. Fukuoka, M. Okada, and M. Nakagawa, Jap. J. Appl. Phys. **29** (1), 150 (1990).
2. S.J. Zinkle and C. Kinoshita, J. Nucl. Mater. **251**, 200 (1997).
3. S.J. Zinkle and L.L. Snead, Nucl. Instr. Meth. B **116**, 92 (1996).
4. S.J. Zinkle and G.P. Pells, J. Nucl. Mater. **253**, 120 (1998).
5. A. Meldrum, S.J. Zinkle, L.A. Boatner, and R.C. Ewing, Phys. Rev. B, in press (1999).
6. T. Yano, M. Tezuka, H. Miyazaki, and T. Iseki, J. Nucl. Mater. **191-194**, 635 (1992).
7. T. Yano and T. Iseki, J. Nucl. Mater. **203**, 249 (1993).
8. R.A. Youngman and T.E. Mitchell, Radiat. Eff. **74**, 267 (1983).
9. A. Matsunaga, C. Kinoshita, K. Nakai, and Y. Tomokiyo, J. Nucl. Mater. **179-181**, 457 (1991).
10. H. Inui, H. Mori, and H. Fujita, Acta Metall. **37** (5), 1337 (1989).
11. H. Mori, T. Sakata, H. Yasuda, and M. Maeda, J. Vac. Sci. Technol. B **12** (4), 2376 (1994).
12. L. Cartz, F.G. Karioris, and R.A. Fournelle, Radiat. Eff. **54**, 57 (1981).
13. R.S. Bhattacharya, A.K. Rai, and P.P. Pronko, J. Appl. Phys. **61** (10), 4791 (1987).
14. R.G. Vardiman, in *Processing and Charaterization of Materials using Ion Beams*, MRS Symposium Proceedings, edited by L.E. Rehn, J. Greene, and F.A. Smidt (Materials Research Society, Pittsburgh, 1989), Vol. 128, p. 369.
15. W. Bolse, S.D. Peteves, and F.W. Saris, Appl. Phys. A **58**, 493 (1994).
16. F. Brensheidt, E. Wieser, W. Matz, A. Mücklich, and W. Möller, Appl. Phys. A **65**, 281 (1997).

17. F. Brensheidt, S. Oswald, A. Mücklich, E. Wieser, and W. Möller, Nucl. Instr. Meth. B **129**, 483 (1997).
18. L.M. Wang, S.X. Wang, W.L. Gong, R.C. Ewing, and W.J. Weber, Mater. Sci. Eng. A **253**, 106 (1998).
19. C.-M. Wang, X. Pan, M. Rühle, F.L. Riley, and M. Mitomo, J. Mater. Sci. **31**, 5281 (1996).
20. J.F. Ziegler, J.P. Biersak, and U. Littmark, *The Stopping and Range of Ions in Solids* (Pergamon Press, New York, 1985).
21. F. de Brito Mota, J.F. Justo, and A. Fazzio, Phys. Rev. B **58** (13), 8323 (1998).
22. H.M. Naguib and R. Kelly, Radiat. Eff. **25**, 1 (1975).
23. H. Abe, S. Yamamoto, and H. Naramoto, Nucl. Instr. Meth. B **127/128**, 170 (1997).
24. R. Devanathan, K.E. Sickafus, W.J. Weber, and M. Nastasi, Nucl. Instr. Meth. B **141**, 366 (1998).
25. L.W. Hobbs, A.N. Sreeram, C.E. Jesurum, and B.A. Berger, Nucl. Instr. Meth. B **116**, 18 (1996).
26. S.J. Zinkle, in *Microstructure Evolution During Irradiation*, MRS Symposium Proceedings, edited by I.M. Robertson, G.S. Was, L.W. Hobbs, and T. Diaz de la Rubia (Materials Research Society, Pittsburgh, 1997), Vol. 439, p. 667.

PHONON SCATTERING RATE AND THERMAL CONDUCTIVITY REDUCTION DUE TO DISLOCATION LOOPS IN ALUMINA - D.P. White (Oak Ridge National Laboratory and Merrimack College)

OBJECTIVE

The objective of this work is to calculate the phonon scattering rate (inverse relaxation time) due to dislocation loops in alumina. From this calculation an estimate of the effect of this scattering mechanism on the thermal conductivity is made.

SUMMARY

The phonon scattering rate due to dislocation loops has been calculated. The dislocation loops are modeled as plate-like inclusions in the lattice. Using the calculated value of the phonon scattering relaxation time the reduction in the lattice thermal conductivity is estimated. It is found that for characteristic values of loop size and number density in irradiated alumina dislocation loops will produce a fractional reduction in the thermal conductivity of approximately 33 percent, assuming this is the only scattering mechanism other than intrinsic scattering.

PROGRESS AND STATUS

Introduction

The thermal properties of ceramic materials used in fusion reactors change as a result of being in a radiation environment. Point defects are known to reduce the thermal conductivity and their effect on the thermal conductivity of irradiated ceramics has been calculated [1-3]. Ceramic materials are also known to develop dislocation loops as a result of irradiation. The effect of dislocation loops on the thermal conductivity of ceramics has not been as well developed in the literature as that due to point defects. Estimates of the effect in irradiated ceramics have been presented [4] but a detailed calculation of the phonon relaxation time has not been presented. A calculation of the phonon relaxation time due to dislocation loops is presented below. Using this relaxation time an estimate of the reduction in the thermal conductivity due to dislocation loops is calculated.

Theory

In order to calculate the phonon relaxation time of a dislocation loop the loop will be considered to be a plate-like assembly of atoms within the material. This plate of material will perturb the local phonon velocity and this will give rise to phonon scattering. If this scattering is strong enough then it will lead to a reduction of the thermal conductivity of the material.

First consider a single atom placed into an existing lattice. Assume that this atom occupies a volume, V_0, equal to the average atomic volume of the lattice. (This would not be true for an individual interstitial atom, however we will shortly be considering an assembly of these defects forming the plate-like inclusion and the majority of the atoms in the plate will occupy the average atomic volume). The model to be considered for this inclusion is that of a spherical inclusion in an elastic continuum.

A spherical inclusion at the origin causes a displacement, $\vec{d}(\vec{r}) = a\vec{r} + b\vec{r}/r^3$ [5-6]. This displacement causes a dilation of the lattice. It is this dilation, a part of which will cause a local variation in the phonon velocity, which gives rise to phonon scattering.

By analogy between the strain field and the electromagnetic field the dilation caused by this inclusion can be calculated [5,7,8]. The dilation is given by;

$$\vec{\nabla} \cdot \vec{d}(\vec{r}) = a\vec{\nabla} \cdot \vec{r} + b\vec{\nabla} \cdot \frac{\vec{r}}{r^3}. \tag{1}$$

The second term in the dilation is 0 for r >0 however it can be evaluated at r = 0 using the divergence theorem and Eq. 1 becomes:

$$\vec{\nabla} \cdot \vec{d}(\vec{r}) = 3a + 4\pi b\delta(\vec{r} - \vec{r}_\alpha), \tag{2}$$

which covers the case when the inclusion is at a position $\vec{r}_\alpha$ other than the origin. The first term in Eq. 3 is a uniform dilation of the lattice, this uniform dilation will not lead to a local variation of the phonon velocity and therefore does not give rise to phonon scattering. The second term will lead to phonon scattering.

The uniform dilation of the lattice is given by 3a, so:

$$3a = \frac{V_0}{GV_0} = \frac{1}{G} \tag{3}$$

where G is the number of atoms in the lattice, so a is a very small number. The magnitude of the displacement at the edge of the inclusion is:

$$r_0 = ar_0 + \frac{b}{r_0^2} \tag{4}$$

but since a is so small $r_0 \approx b/r_0^2$ and so $b \approx r_0^3$. The second term in the dilation now becomes;

$$4\pi r_0^3 \delta(\vec{r} - \vec{r}_\alpha) = 3V_0\delta(\vec{r} - \vec{r}_\alpha) = \theta_2(\vec{r}). \tag{5}$$

The inclusion site, $\vec{r}_\alpha$, is a lattice site, $\vec{x}_i$, and the lattice expression for Eq. 6 is;

$$\theta_2(\vec{x}_i) = 3\delta(\vec{x}, \vec{x}_i), \tag{6}$$

where $\delta(\vec{x}, \vec{x}_i)$ is the Kronecker delta. The change in the local phonon velocity due to this dilation is given by [9,10];

$$\delta v(\vec{x}_i) = \gamma v_0 \theta_2(\vec{x}_i) = 3\gamma v_0 \delta(\vec{x}, \vec{x}_i), \tag{7}$$

where γ is the Gruneisen constant (which typically has a value close to 1), and v_0 is the unperturbed phonon velocity. The scattering of phonons can be described in terms of a perturbation Hamiltonian of the form,

$$H' = \sum_{\vec{q},\vec{q}'} c_2(\vec{q},\vec{q}') a^*(\vec{q}') a(\vec{q}) \quad , \qquad \vec{q} \neq \vec{q}', \tag{8}$$

where $\vec{q}$ and $\vec{q}'$ are the wave vectors of the incident and scattered phonons respectively and a^* and a are phonon creation and annihilation operators respectively. If this perturbation is due to a change in the local phonon velocity the coefficient $c_2(\vec{q},\vec{q}')$ has the following form [10];

$$c_2(\vec{q},\vec{q}') = \frac{2Mv}{G} qq' \sum_{\vec{x}_i} \delta v(\vec{x}_i) e^{i(\vec{q}-\vec{q}')\cdot\vec{x}_i} (\vec{\varepsilon}\cdot\vec{\varepsilon}'), \tag{9}$$

where M is the mass of the average atom in the lattice, and $\vec{\varepsilon}$ and $\vec{\varepsilon}'$ are the phonon polarization unit vectors. The lattice sum in Eq. 10 is a sum over impurity sites. In this model of a dislocation loop the inclusions are considered to be oriented so that they form a plate of radius R and thickness h. It has been shown [11] that the phonon relaxation time for such an orientation of defects is;

$$\frac{1}{\tau(q)} = \frac{4h}{v_0} \frac{R^2 h}{v_{plat}} \left(\frac{\delta v}{v_0}\right)^2 \omega^2 A(q), \tag{10}$$

where,

$$A(q) = 4\pi \int_0^z [J_1(t)]^2 / t(1 - t^2/z^2)^{1/2} dt, \tag{11}$$

where $z = qR$ and $J_1(t)$ is the Bessel function.

Calculation, Results, and Conclusions

The scattering rate given by Eqs. 11 and 12 can now be evaluated. Assuming that the thickness of the platelet is one atomic layer, h = 2.04 X 10^{-10} m for alumina. The term, $1/v_{plat}$, in Eq. 11 is identified as the number of platelets per unit volume, n_{plat}. Irradiated alumina has been observed to have dislocation loops with an average radius of, R = 1 X 10^{-9} m, at a density of, n_{plat} = 10^{22} m^{-3} [12]. The phonon velocity in alumina is, v_0 = 1 X 10^4 m/s [3]. Figure 1 is a plot of the phonon scattering rate (Eq. 11) for these conditions up to the Debye frequency of 1.31 X 10^{14} s^{-1}.

At low frequency the scattering rate is very low, the platelets are transparent to long wavelength phonons. At high frequencies, above approximately 20% of the Debye frequency, the term $A(q)$ approaches a constant value of 2π and the scattering rate is proportional to ω^2. This result is what would be expected for an infinite sheet defect, that is the platelets appear infinite to short wavelength phonons.

This last result may be used in order to estimate the effect of these defects on the thermal conductivity of alumina at high temperatures. At high temperatures Eq. 11 becomes;

$$\frac{1}{\tau(q)} = 2\pi n_{plat} \frac{4h}{v_0} R^2 h \left(\frac{\partial v}{v_0}\right)^2 \omega^2. \tag{12}$$

This expression may be substituted into the thermal conductivity integral in order to calculate the change in thermal conductivity it produces. As mentioned, the expression in Eq. 13 only applies to phonons with frequencies above 20% of the Debye frequency but since equal frequency intervals contribute equally to the thermal conductivity integral this will not produce an error of more than 20% in the calculated thermal conductivity. This approximation will overestimate the effect of platelet (dislocation loop) scattering.

The intrinsic phonon scattering rate has the form, $1/\tau_i = B\omega^2$, where $B = (2\gamma^2 K_B T)/(Mv^2\omega_D)$ and where K_B is Boltzmann's constant, M is the average atomic mass, T is the temperature, and ω_D is the Debye frequency. The platelet scattering rate in this approximation has the same form as the intrinsic scattering rate and is $1/\tau_{plat} = A\omega^2$ with A given by Eq. 13. The thermal conductivity without any defects present can be estimated by substituting the intrinsic relaxation time into the thermal conductivity integral,

$$K = \frac{1}{3} \int_0^{\omega_D} S(\omega) v^2 \tau(\omega) d\omega \tag{13}$$

where $S(\omega)$ is the lattice specific heat, it is found that $K_{unint} = K_B \omega_D / (2\pi^2 v B)$. Similarly the combined intrinsic-loop scattering relaxation time, $1/\tau_c = (A+B)\omega^2$, may be substituted into Eq. 14 to estimate the thermal conductivity with platelet scattering. It is found that the fractional reduction in the thermal conductivity is given by:

Fig. 1. A plot of the phonon scattering rate due to dislocation loops in alumina. This plot was produced by evaluating Eq. 11 for the case when $h = 2.04 \times 10^{-10}$ m, $R = 1 \times 10^{-9}$ m, and $n_{plat} = 10^{22}$ m^{-3}.

scattaring rate (10^{-10} s^{-1})

angular frequency (10^{13} s^{-1})

$$\frac{K_{unirr} - K_{plat}}{K_{unirr}} = \frac{\delta K_{plat}}{K_{unirr}} = 1 - \left(\frac{A}{B} + 1\right)^{-1}. \tag{14}$$

For the platelet size and number density we have been considering in this paper, $A = 9.4 \times 10^{-18}s$ and at 300K $B = 1.86 \times 10^{-17}s$. Substituting these values into Eq. 15 it is found that the expected fractional reduction in the thermal conductivity due to dislocation loops of the size and number density given above is about 33%. The actual fractional reduction in thermal conductivity attributable to dislocation loops will be less that the 33% reduction calculated above because this reduction was calculated assuming the only scattering mechanisms were intrinsic and dislocation loop scattering. For example, in the presence of strong point defect scattering, which preferentially scatters high frequency phonons, the frequency range over which dislocation loop scattering is important will be diminished and the actual fractional reduction due to dislocation loops will be similarly diminished.

This calculation shows that dislocation loop scattering can lead to a significant reduction in the thermal conductivity in alumina and must be taken into account in a discussion of the reduction of the thermal conductivity due to irradiation.

FUTURE WORK

This calculation of the effect of dislocation loops on the thermal conductivity of alumina has not considered the effect of the scattering due to the strain field of the dislocation line surrounding the loop. Although is has been suggested that this scattering is less important that that due to the stacking fault [13] it should be estimated and compared to the results of this paper.

ACKNOWLEDGMENTS

REFERENCES

1.   D.P. White, J. Nucl. Mater. 219 (1995) 165.
2.   P.G. Klemens, Nucl. Instr. and Meth. 229 (1984) 204.
3.   D.P. White, J. Appl. Phys. 73 (1993). 2254.
4.   P.G. Klemens, G.F. Hurley, and F.W. Clinard, Jr., 2nd Topical Meeting on Technology of Controlled Nuclear Fusion, USERDA Rept. CONF-760935, (1976) 957.
5.   M.W. Ackerman and P.G. Klemens, J. Appl. Phys. 42 (1971) 968.
6.   Arnold Sommerfeld, Mechanics of Deformable Bodies (Academic Press, NY, 1950).
7.   P. Carruthers, Rev. Mod. Phys. 33 (1961) 92.
8.   C.A. Ratsifaritana and P.G. Klemens, Int. J. Thermophys. 8 (1987) 737.
9.   P.G. Klemens, J. Appl. Phys. 39 (1968) 5304.
10.   P.G. Klemens, in Thermal Conductivity, edited by R.P. Tye (Academic Press, NY, 1969).
11.   Lawrence A. Turk and P.G. Klemens, Phys. Rev. B 9 (1974) 4422.
12.   L.L. Snead and S.J. Zinkle, personal correspondence.
13.   P.G. Klemens, Can. J. Phys. 35 (1957) 441.

7.0   SOLID BREEDING MATERIALS

No contributions.

8.0 RADIATION EFFECTS, MECHANISTIC STUDIES, AND EXPERIMENTAL METHODS

DEVELOPMENT OF SUPERPOSITION RULES FOR HARDENING IN ALLOYS CONTAINING MULTIPLE DEFECT POPULATIONS — G. R. Odette, G. E. Lucas and G. Tedeski, and B. D. Wirth (University of California, Santa Barbara)

OBJECTIVE

The objective of this work is to develop a superpositiuon law to assess the net contribution of two defect population to hardening.

SUMMARY

In this study extensive computer simulations were carried out to calculate the yield strengths arising from the presence of two defect populations. The motion of an individual dislocation through a random obstacle field containing varying ratios of obstacles with two different barrier strengths (strong and weak) was computed based on equilibrium bowing of dislocation segments between adjacent obstacles. Yield stress was determined as the minimum stress necessary for the dislocation to successfully traverse the obstacle field. The results show that the superposition law is neither linear nor root sum square, but can be approximately represented by a superposition weighting parameter that is a simple analytical function of the individual strong and weak barrier strengths. Illustrations of the implications of this law are provided.

PROGRESS AND STATUS

Introduction

Radiation hardening in structural materials in general, and in fusion reactor materials in particular, can arise from the evolution of more than one defect type. Numerous studies have shown that the contributions to hardening from a single defect type can be reasonably predicted by simple barrier hardening models, [1-8] where the yield stress contribution produced by dispersed obstacles, σ_o, is given by

$$\sigma_o = M\alpha' Gb\sqrt{N_o} \qquad (1)$$

where N_o = areal density of obstacles, b is the Burgers vector of the dislocation moving in the obstacle field, M is the Taylor factor (~3), G is the shear modulus, and α' is an effective barrier strength for the obstacle type and field. Note that the morphology of a dislocation in the obstacle field results in an effective strength α' which is smaller than the individual obstacle strength α, where $0 < \alpha < 1$; i.e., $\alpha' < \alpha$.

The total yield stress σ_t from two types of obstacles (σ_1, α_1 and σ_2, α_2) falls between a linear sum (LS) and a root-sum square (RSS) limit, and it can be expressed in terms of a superposition parameter S given by

$$\sigma_t = S(\sigma_1^2 + \sigma_2^2) + (1-S)\sqrt{\sigma_1^2 + \sigma_2^2} \qquad (2)$$

Hence, S=1 corresponds to LS superposition and S=0 corresponds to RSS. In general, the value of S lies in between; i.e., $0 < S < 1$. The magnitude of S has a significant impact on not only hardening but post-irradiation annealing (PIA). For instance, consider the addition of an irradia-

tion defect strength contribution of σ_2 = 200 MPa to a material with a pre-existing population of defects which impart a strength of σ_1 = 200 MPa. The irradiation hardening $\Delta\sigma_t$ would be the full 200 (i.e., 200 + 200 - 200) MPa for LS superposition (S=1) compared to $\Delta\sigma_t$ = 82 MPa ($\sqrt{200^2 + 200^2} - 200$) for RSS (S=0); and for an intermediate value of S, say S=0.5, an intermediate value of $\Delta\sigma_t$ = 141MPa would obtain. If after PIA, the value of σ_2 were reduced to 100 MPa by recovery, LS superposition would lead to a 50% recovery, and RSS a 71%. If PIA also altered S, an additional component of recovery would obtain; for example, if S were to decrease from 0.5 to 0 in this same example, the recovery would increase to 83%.

This study was undertaken to investigate this superposition law and develop a simple model for S by using computer simulations to calculate the yields strength for various defect populations.

Computer Simulations

The motion of an individual dislocation through a random obstacle field containing varying ratios of obstacles with two different barrier strengths (strong, α_s, and weak, α_w) was computed based on equilibrium bowing of dislocation segments between adjacent obstacles, using the methods pioneered by Foreman and Makin. [9]

Figure 1 illustrates various characteristics of the calculational results. For a dislocation passing through a field of weak obstacles, the dislocation remains fairly linear. When it passes through a field of strong obstacles, it bows significantly between adjacent particles before surmounting the obstacle, and the effective linear obstacle density along the dislocation line increases accordingly. In a mixed filed the dislocation is bowed between strong obstacles, but the front is only slightly perturbed by the weaker obstacles in between. The yield stress in all cases is taken as the value of applied stress when the dislocation successfully passes through the obstacle field.
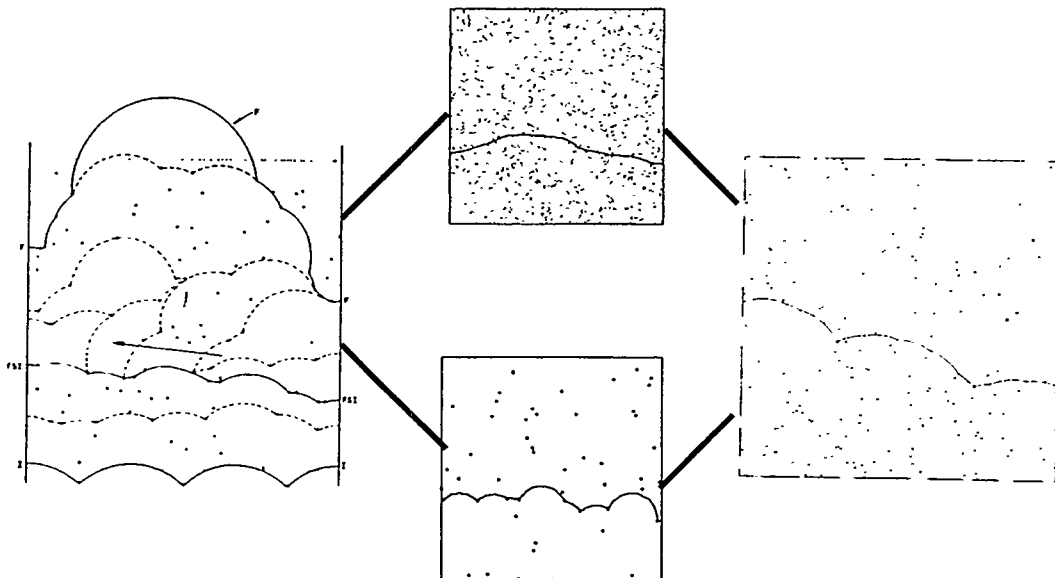
Figure 1.   Illustration of dislocation moving through obstacle fields in computer simulations.

Results

It was found that obstacles with similar barrier strengths obey a RSS type of superposition law, with S=0. However, a mix of weak obstacles (α_w) and strong obstacles (α_s) was found to result in an intermediate behavior, with $0 < S < 1$, and S increasing as α_w decreases and α_s increases as

$$S \sim \alpha_s - \alpha_w \, (4.3\text{-}2.4 \, \alpha_s) \tag{3}$$

This is illustrated in Figure 2 which compares the values of S obtained from the computer simulations with that calculated from eqn (3). There was a relatively weak dependence observed on the relative concentrations of strong and weak obstacles.

The consequence of this is that the contribution of a defect to hardening can depend strongly on the relative strength of obstacles to the pre-existing defects. Addition of dissimilar strength barriers results in more significant net hardening per increment of individual barrier strength (approaching LS) than addition of similar barriers (approaching RSS).

APPLICATION

This effect can be illustrated for irradiation hardening in reactor pressure vessel (RPV) steels. The initial strength in these steels is strongly affected by the presence of an array of strong barriers (Mo_2C) with an estimated α_s of 0.9 giving rise to a strengthening contribution of about σ_c ~ 200 MPa. [10] In RPV steels containing significant copper impurity content (Cu > 0.1), irradiation hardening tends to be dominated by the formation of copper rich precipitates (CRPs) which may be alloyed with Ni and Mn, along with the formation of a matrix defect (MDs) population. [11]
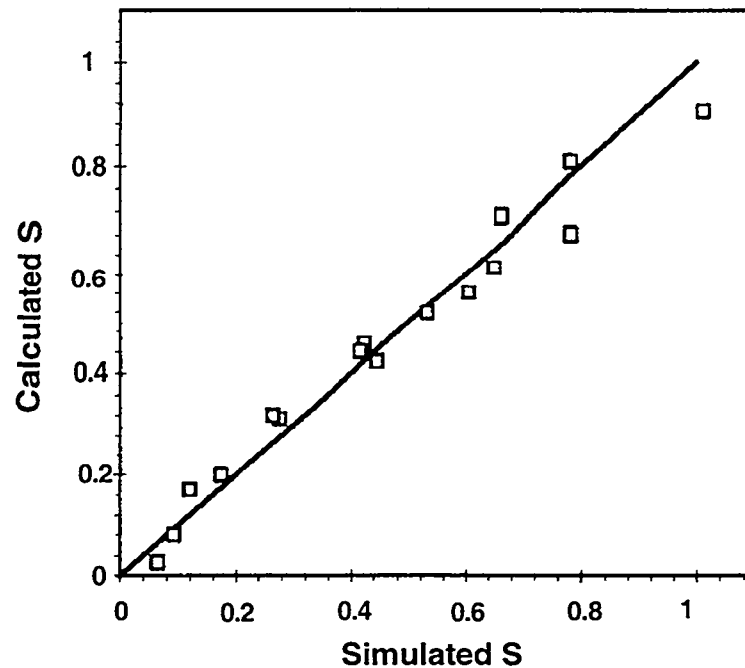
Figure 2.   Comparison of calculated values of superposition parameter S with values determined from computer simulations

Similarly, the post-irradiation annealing response is related to changes in these defect populations with time at temperature. The hardening contribution of the CRPs, σ_p, and hence their barrier strength α_p, can be estimated from a Russell-Brown modulus interaction model, [12] along with the knowledge of the size, number density and composition of the precipitates, which can be obtained from small angle neutron scattering (SANS) measurements. [11] The contribution from MDs of the order σ_m (where $\alpha_m \ll 1$), can be added in empirically. The total irradiation hardening can be estimated from

$$\Delta\sigma_i = S(\sigma_c + \sigma_p) + (1 - S)\sqrt{\sigma_c^2 + \sigma_p^2} - \sigma_c + \sigma_m \qquad (4)$$

Figure 3 shows that predictions of hardening based on microstructural measurements combined with equation (4) are in very good agreement with measured values of yield strength change.

Figure 4 shows the influence of superposition on the post-irradiation annealing (PIA) response. Data points were obtained from microhardness measurements, and the solid lines are predictions of the hardening from application of the Russel-Brown model and the corresponding SANS data combined with the superposition law. [13] Figure 4a corresponds to PIA in a A533B-type model steel containing no Mo (and hence no Mo_2C); hence the hardening and PIA recovery is almost entirely due to the formation and recovery of CRPs and matrix damage (i.e., $\Delta\sigma = \sigma_p + \sigma_m$), and the sluggish coarsening of the CRPs during PIA results in substantial residual hardening even after 1000h at temperature. On the other hand, Figure 4b corresponds to PIA in an A533B-type model steel containing 0.5Mo (and hence Mo_2C). In the as-irradiated condition, the CRPs have a small α_w relative to the strong carbide α_s, and the superposition is between LS and RSS; hence, the total hardening is less than the CRP contribution alone. Upon annealing, MDs anneal out reducing σ_m and CRP dissolution and coarsening reduces both σ_p and S, resulting in significantly higher recovery.
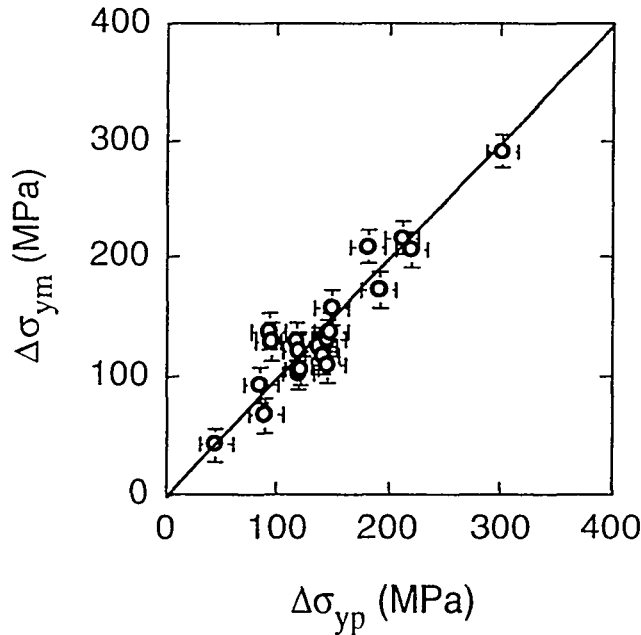
Figure 3. Comparison of measured values of yield stress change with values calculated from microstructural data using the superposition law.
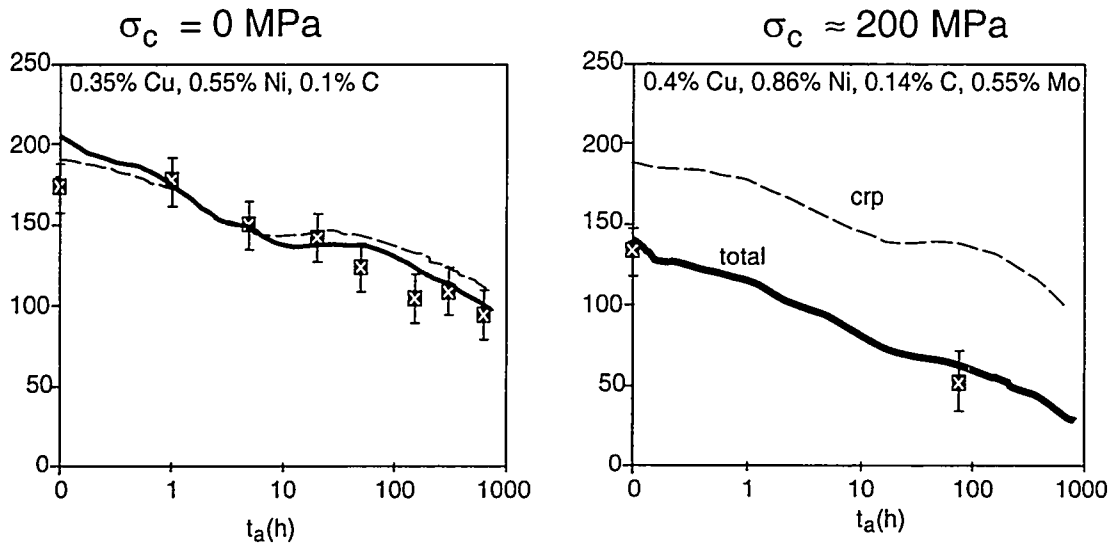
Figure 4. Calculated and measured changes of residual hardening during post-irradiation annealing for A533B-type alloys a) without and b) with Mo additions. In a) the recovery corresponds to the linear superposition of contributions from CRPs and matrix defects (MD). In b) recovery is enhanced by a reduction in σ_m, σ_p and S.

CONCLUSIONS

Computer simulations of dislocations moving in obstacle fields have been used to derive a simple analytical model of the superposition of strengthening from two obstacle types. The superposition model is particularly useful in evaluating changes in strength attributed to the addition (and removal) of a weak(er) obstacle field to (from) a pre-existing strong obstacle field, a situation which is typical for irradiation hardening (and post-irradiation annealing) in structural materials.

ACKNOWLEDGMENTS

REFERENCES

1. G. R. Odette, D. Frey, J. Nucl. Mater., 85/86 (1979) 817-822.

2. M. Grossbeck, P. Maziasz, A. Rowcliffe, J. Nucl. Mater., 191/194 (1992)

3. F. Garner, M. Hamilton, N. Panayotou, G. Johnson, J. Nucl. Mater., 103/104 (1981) 803-808.

4. U. F. Kocks, Physics of Strength and Plasticity, MIT Press, Cambridge (1969) 143.

5. J.J. Holmes, R. E. Robbins, J.L. Brimhall, B. Mastel, Acta Met, 16 (1968) 955.

6. G. L. Kulcinski, J. L. Brimhall, G. E. Kissinger, Acta Met (1972).

7. A. L. Bement, Rev. Roum. Phys., 17, 3 (1972) 361-380.

8. H. R. Brager, F. A. Garner, N. Panayotou, J. Nucl. Mater., 103/104 (1981) 955-960.

9. A. J. E. Foreman and M. J. Makin, Can. J. Phys., 45 (1967) 511

10. E. Mader, G. R. Odette, G. E. Lucas, Proceedings of the 6th International Symposium on Environmental Degradation of Materials in Nuclear Power Systems — Water Reactors, San Diego, CA, August 1993, TMS/ANS/NACE (1994) 739-746.

11. G. R. Odette, MRS Soc. Symp. Proc., 373 (1995) 137.

12. K. C. Russell and L M. Brown, Acta Met., 20 (1972) 969.

13. E. Mader, "Kinetics of Irradiation Embrittlement and the Post-Irradiation Annealing of Nuclear Reactor Pressure Vessel Steels," PhD Thesis, Department of Materials (1995).

MECHANISMS OF PLASTIC AND FRACTURE INSTABILITIES OF FUSION STRUCTURAL MATERIALS – N. M. Ghoniem (University of California, Los Angeles)

ABSTRACT

Research progress at UCLA on the DOE grant *#DE FG03-98ER54500 is* outlined in this report, for the period July 15, 1998 through January 14, 1999. The main objectives of the work is to develop new methodologies for modeling a number of mechanisms which control plastic instabilities and fracture of V, Fe and Cu alloys under fusion irradiation conditions. These phenomena appear to be generic, and are believed to present substantial challenges to the structural integrity of first-wall fusion material systems. The main thrust of the modeling effort is to identify the mechanisms which lead to localization of plastic deformation, the accelerated cavitation at grain boundaries, the detrimental influence of helium transmutations, and the loss of ductile crack propagation in irradiated materials. We report here our initial research findings on the problem of accumulation of nano-scale prismatic defect clusters in the vicinity of dislocations. Under irradiation conditions, small defect clusters are produced in collision cascades. These mobile clusters interact with dislocations, hindering its motion. Thus, radiation hardening takes place as a result of these interactions. However, it is shown here that once these nano-phase clusters approach dislocations, they may be trapped in their elastic strain fields. Trapping is shown to occur by elastic interactions within a zone of 10 *nm* in bcc Fe, and 20 *nm* in fcc Cu at RT. If the local stress (i.e. applied plus internal) is high, clusters are absorbed in the core of grown-in dislocations as a result of unbalanced moments, providing sufficient energy for rotation of their Burgers vectors in a zone of 2-3 *nm* in Fe. Near the dislocation core, sessile defect clusters in Cu are shown to convert to a glissile configuration. The current work is performed in collaboration with LLNL (Dr. T. de la Rubia), and is partially supported by the Institute of Materials Research at LLNL. The UCLA group has an active collaboration program on this problem with the Danish RISO National Labs (Dr. B. Singh), and the German Forschungszentrum Julich (Dr. H. Trinkaus). Additionally, collaborative efforts have started with UCSB (Professors Lucas and Odette) on the problem of Ductile-to-Brittle Transition in V and Fe, where our dislocation dynamics method is to be coupled with their fracture mechanics approach at different length scales.

SUMMARY

The main thrust of the current modeling effort is to identify the mechanisms which lead to localization of plastic deformation, the accelerated cavitation at grain boundaries, the detrimental influence of helium transmutations, and the loss of ductile crack propagation in irradiated materials. We report here our initial research findings on the problem of accumulation of nano-scale prismatic defect clusters in the vicinity of dislocations. Under irradiation conditions, small defect clusters are produced in collision cascades. These mobile clusters interact with dislocations, hindering its motion. Thus, radiation hardening takes place as a result of these interactions. However, it is shown here that once these nano-phase clusters approach dislocations, they may be trapped in their elastic strain fields. Trapping is shown to occur by elastic interactions within a zone of 10 *nm* in bcc Fe, and 20 *nm* in fcc Cu at RT. If the local stress (i.e. applied plus internal) is high, clusters are absorbed in the core of grown-in dislocations as a result of unbalanced moments, providing sufficient energy for rotation of their Burgers vectors in a zone of 2-3 *nm* in Fe. Near the dislocation core, sessile defect clusters in Cu are shown to convert to a glissile configuration.

OBJECTIVES

The general objectives of the modeling activities at UCLA are:

(1) To integrate three material length scales for determination of basic mechanisms of plastic and fracture instabilities under irradiation conditions. These length scales are: i- atomistic, using Molecular Dynamics , ii- mesoscopic, using Dislocation Dynamics (DD) and Fokker-Planck (FP) theory approaches, and macroscopic utilizing fracture mechanics.

(2) To apply developed computational tools to the study of four basic types of plastic and fracture instabilities which occur in Fe, V and Cu alloy systems. Those are: (1) transition from a state of uniform deformation (elongation) to localized plastic flow, (2) transition from a ductile mode of crack propagation, associated with extensive plasticity and micro-void formation to a brittle mode associated with cleavage fracture, (3) transition from transgranular crack growth to intergranular crack separation, (4) irradiation effects on thermo-mechanical instabilities.

(3) To focus on important and challenging problems of material deformation under irradiation. Important questions in this regard are: (a) why does plastic flow under irradiation tend to localize in shear bands? (b) what are the effects of material alloying, temperature, neutron irradiation and strain rate on flow localization? (c) What is the connection between radiation hardening and mechanical instabilities? (d) are there any fundamental differences between instabilities occurring in BCC materials (Fe and V) and FCC materials (Cu and steels) ? (e) Is there a relationship between global thermodynamic variables (e.g. stress, temperature, etc) and microstructure transitions from uniform to cellular to banded? (f) what is the relevance of these phenomena to the development of fusion materials? (g) What types of degradation mechanisms does helium

introduce in irradiated alloys?, and what is its role on transition from transgranular to intergranular cracking? (h) What are the exact conditions for the sudden transition in crack propagation from a ductile to a brittle mode? And finally, (i) how do non-metallic interstitial elements influence the ductility of Fe, V, and Cu fusion materials alloys?

(4) To analyze the deformation characteristics of three main fusion material systems; namely reduced-activation ferritic/ martensitic, low-activation vanadium , and copper alloys.

The specific objective of this task is to determine the conditions for the accumulation of nano-scale defect clusters at slip dislocations. Nano-scale defect clusters are produced from collision cascades under irradiation. Their accumulation hinders slip od dislocations, and thus leads to radiation hardening.

BACKGROUND

The deformation behavior of both BCC (e.g. Fe and V) and FCC (e.g. Cu and austenitic steels) metals is sensitive to neutron irradiation, temperature, strain rate and alloying, exhibiting a variety of complex mechanisms which render them brittle. Under low temperature (< 0.4 T_m) neutron irradiation, the flow stress increases because of resistance to dislocation glide on slip planes. At critical neutron fluence, cracks propagate in a brittle fashion, dissipating small amounts of energy in plastic deformation. Resistance to dislocation motion increases as a result of accumulation of dispersed barriers through radiation-induced lattice defects, as well as general mobility reductions at high strain rates through phonon and electron damping mechanisms. Additionally, heavily irradiated fusion materials generally exhibit extreme hardening associated with localized deformation in "dislocation channels", which lead to pre-mature loss of ductility and failure. At higher temperatures, on the other had, helium migration to grain boundaries results in the accelerated formation of gas-filled cavities leading to transition form matrix to grain boundary cracking. Non-metallic interstitial elements (e.g. nitrogen, carbon, hydrogen and oxygen) are transported in the strong stress fields around notches and crack tips, and their segregation results in dramatic weakening and cracking of stressed components. Modeling of the detrimental effects of irradiation on the mechanical properties is required to guide experimental efforts of alloy optimization. Through mechanistic models, one can identify material controlling parameters (e.g. alloying elements, operating conditions (flux, fluence, temperature, stress, etc.), material processing variables, etc.), where the impact could be minimized.

. Under the current DOE grant at UCLA, research on four tasks has been started. The first one: *Atomistic Computer Simulations*, is concerned with the utilization of MD computer simulations to determine defect production and properties, collision cascade effects on dislocation motion and dislocation recovery mechanisms, cascade interactions with radiation-induced barriers to dislocation motion, and the short-range interactions between dislocation segments and dispersed barriers. In the second task: *Atomic Clustering*, we plan to develop efficient computational methods for atomic clustering problems which

lead to the formation of dispersed barriers under irradiation. This will include determination of size and composition of precipitate clusters, helium clusters, point defect clusters, as well as their spatial distribution statistics. Task 3: *3-D Dislocation Dynamics,* is concerned with further development of a breakthrough computational method for studying localized plastic instabilities. In this method, the elastic field of dislocations (i.e. displacement, strain, stress, forces, self and interaction energies) is determined on the basis of segmenting arbitrarily curved and oriented dislocation loops into 3D parametric curves. The equations of motion for each loop segment is developed with inertial and viscous drag mobility effects, thus allowing for studies of irradiation effects on plastic deformation. Finally, *Plastic And Fracture Instabilities Under Irradiation* are analyzed in task 4. The onset of flow localization in irradiated materials will be determined by combining the interaction between the hardening effects of radiation-induced barriers and the destruction of these obstacles by leading dislocations in heterogeneous spatial locations. Several other fracture mechanisms will be simulated for Fe, V and Cu alloys, including dislocation-crack interactions, the dynamic structure and size of the plastic zone, and the segregation of interstitial elements under irradiation to crack tips. Coupling of the computational methods developed here with the US experimental program is expected to provide an additional tool for alloy development of fusion structural materials.

SUMMARY OF RESEARCH PROGRESS

Radiation Hardening of FCC and BCC Metals

It has been experimentally established that exposure of all metals to fast-neutron irradiation results in an increase in their flow stress. It has also been established that when BCC metals are irradiated at high temperature, or when they are annealed after irradiation, the stress-strain curve of the unirradiated material is substantially recovered. This is a direct indication of the role of radiation-induced defect clusters on hardening. Several studies discuss the relative roles of both alloying elements in ferritic steels (e.g. Ni, Si, C, Mn, Mo and Co), and intrinsic defect clusters (point defects, dislocation loops, and bubbles) produced by irradiation on the shift in the Ductile-to-Brittle-Transition-Temperature (DBTT) of ferritic alloys [1-4]. Radiation hardening and the shift in DBTT have been qualitatively and phenomenologicaly related to the interaction of mobile dislocations with dispersed barriers as well as with relatively immobile forest dislocations.

Under irradiation conditions of almost all-metallic alloys, localized deformation patterns have been observed. Bloom et al. Observed localized slip traces of {111} planes with type 304 stainless steel specimens, after being irradiated at 120 °C, and deformed to 10%[5]. In FCC alloys, the stress required to unpin small clusters of defects is increased because of the decrease in inter-barrier separation as a result of irradiation. If dislocation pile-ups form behind dispersed barriers, leading dislocations experience a sufficient force on them to break them loose, and with additional dynamic inertia they destroy other irradiation-induced obstacles. The phenomenon is thus intimately related to the dynamics of dislocation motion, and cannot be captured by static considerations alone. Dislocation

channels form in a manner similar to avalanche propagation, and the final result is the well-documented plastic instability [5-7]. Plastic deformation in this case is concentrated on slip planes, leading to pre-mature fracture.

Intensive experimental investigations of hardening mechanisms in both FCC and BCC alloys indicated that two types of phenomena govern the increase in flow stress: (1) source hardening; (2) friction hardening. Source hardening operates when the critical resolved shear stress level is low, and is increased slowly until dislocations are unpinned from the influence of small barriers to their motion. The phenomenon is common in BCC alloys, and is related to the fast diffusion rates of impurities, point defects or other elements (e.g. carbon) to dislocation cores. In FCC alloys, impurity atom diffusion is not sufficiently fast to catch up with moving dislocations and result in the associated phenomenon of source hardening. Source hardening is manifest in a yield drop (from upper to lower yield points), and can be observed in unirradiated BCC alloys. The required critical stress to release the dislocation line from a row of carbon atoms has been roughly estimated [6]. When the dislocation is free from the locking action of solute atoms, point defects or impurities, the dislocation can move at a lower stress, causing the drop in the yield point. In FCC alloys, however, source hardening can only be observed under irradiation conditions, where small point defect clusters form the pinning obstacles to dislocation motion.

Friction hardening, on the other hand, is thought to be responsible for the characteristics of plastic stress-strain behavior, as expressed in the work hardening exponent, and several other measures (yield surface, Bauschinger plastic anisotropy, etc.). It can also be decomposed into two parts: (1) flow stress increase by long-range dislocation reactions; (2) flow stress increase by short-range dislocation reactions. Without the influence of irradiation, both types of reactions occur, but irradiation introduces additional features of the microstructure, which can modify or totally change the nature of these types of interactions. Long-range reactions are qualitatively understood by applying simplified elasticity solutions for long, straight dislocations. However, the quantitative predictions of long-range interaction effects on increasing the flow stress are uncertain by factors of 2-4 [8-10]. Several reasons are behind such uncertainties, such as the curved and tangled nature of interacting dislocations, the influence of forest dislocations on the strength of reactions, the formation of dipoles and higher order clusters, and the possible annihilation of close by dislocation segments. On the other hand, the nature and magnitude of short range interactions are not well-understood, because of uncertainties in the applicability of elasticity theory, and uncertainties in estimating the overall energetics of close-range interactions with radiation-induced obstacles (e.g. voids, bubbles, vacancy loops, interstitial loops, and point defect-impurity clusters).

Starting in 1997, a small effort on the development of a new computational method for simulation of dislocation microstructure evolution was initiated at UCLA. Funding for this fundamental work is provided by the ASCI (Accelerated Scientific Computing Initiative) through a collaborative program with LLNL. This research effort is continuing, and has the objective of developing general efficient computational methods for material deformation under general loading conditions. The work is in collaboration with IBM, WSU, and LLNL, and is backed up by a systematic experimental program. Under the current DOE

grant, the work is to be extended to the specific conditions of fusion structural materials. This leveraging of knowledge is now leading to wide recognition of the fusion materials problems within the materials science and mechanics communities. There are generic aspects of plastic and fracture instabilities that touch upon many material systems outside the specific conditions of the fusion environment. However, the current effort supported by DOE/OFE is dedicated to the specialized irradiation conditions of the fusion environment. We report here on some of the general methodologies developed at UCLA so far, and point to specific results obtained in collaboration with a number of national and international colleagues.

Development of the Parametric Dislocation Method

In this method, the geometry of dislocation segments is represented in parametric vector form as: $\hat{r}^{(j)}(u) = q_i^{(j)} N_i(u)$, where the vector $\hat{r}^{(j)}(u)$ represents the spatial position of segment (j). A set of parametric functions $N_i(u)$, and generalized coordinates $q_i^{(j)}$ completely determine the shape of the segment. The displacement vector, $\mathbf{u}$, the stress tensor σ_{ij}, and the interaction energy between two loops, E_I, can now be obtained as fast numerical sums, over the number of quadrature points Q_{max}, the loop segments N_s, and the number of loops N_{loop}. These are given by (see our references [11-14] for details):

$$u_i = \frac{1}{4\pi} \sum_{\gamma=1}^{N_{loop}} \{ -b_i \Omega + \frac{1}{2} \sum_{\beta=1}^{N_s} \sum_{\alpha=1}^{Q_{max}} w_\alpha (\varepsilon_{ikl} b_l R_{,pp} + \frac{\varepsilon_{kmn} b_n R_{,mij}}{1-\nu}) \hat{x}_{k,u} \}$$

$$\sigma_{ij} = \frac{\mu}{4\pi} \sum_{\gamma=1}^{N_{loop}} \sum_{\beta=1}^{N_s} \sum_{\alpha=1}^{Q_{max}} b_n w_\alpha [\frac{1}{2} R_{,mpp} (\varepsilon_{jmn} \hat{x}_{i,u} + \varepsilon_{imn} \hat{x}_{j,u}) + \frac{1}{1-\nu} \varepsilon_{kmn} (R_{,ijm} - \delta_{ij} R_{,ppm}) \hat{x}_{k,u}]$$

$$E_I = -\frac{\mu b_i^{(1)} b_j^{(2)}}{8\pi} \sum_{\beta^{(1)}=1}^{N^{(1)}} \sum_{\beta^{(2)}=1}^{N^{(2)}} \sum_{\alpha^{(1)}=1}^{Q_{max}^{(1)}} \sum_{\alpha^{(2)}=1}^{Q_{max}^{(2)}} w_{\alpha^{(1)}} w_{\alpha^{(2)}} [R_{,kk} (\hat{x}_{j,u}^{(2)} \hat{x}_{i,u}^{(1)} + \frac{2\nu}{1-\nu} \hat{x}_{i,u}^{(2)} \hat{x}_{j,u}^{(1)}) + \frac{2}{1-\nu} (R_{,ij} - \delta_{ij} R_{,ll}) \hat{x}_{k,u}^{(2)} \hat{x}_{k,u}^{(1)}]$$

Comparisons of our method with analytical solutions show that the accuracy of calculating the Peach-Kohler force can be less than 0.5% at distances as close as 1.5 b from the dislocation core. The calculations of the interaction and self-energies (as well as self-forces) are absolutely convergent with increasing the number of segments and/or quadrature. Computational speed tests show that the method is as fast as a purely analytical one for straight segments, hence we describe it as a **fast sum method.**
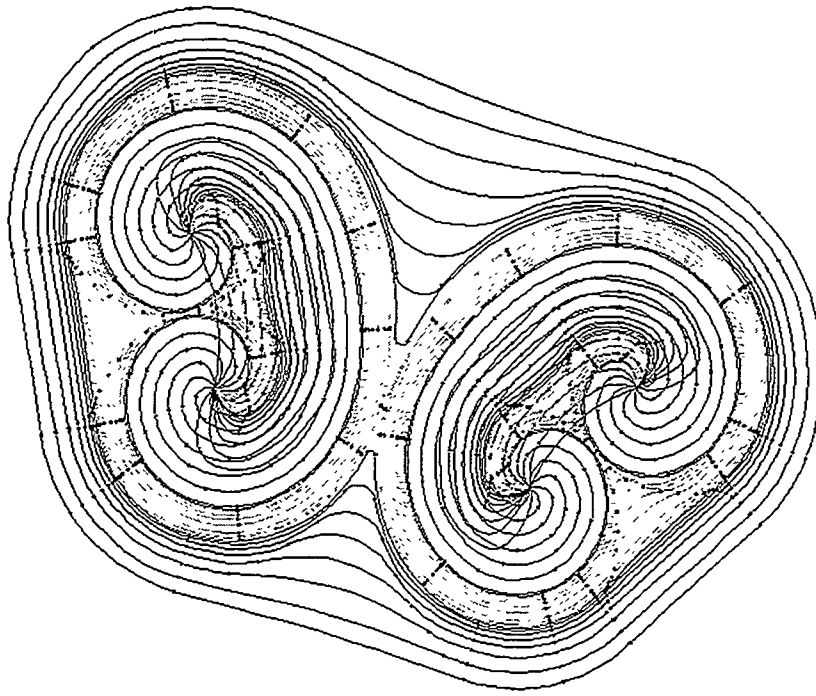
Figure (1); Interaction between Frank-Read sources in Cu
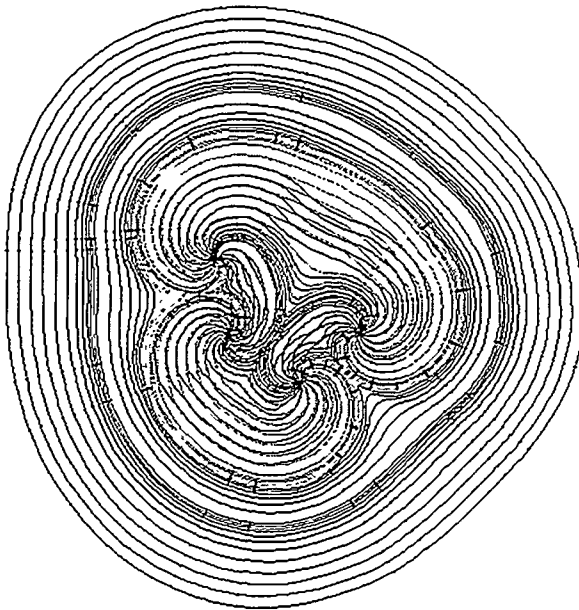
Fig.(2): Formation of Complex Dislocation Loops in FCC Cu.

The equations of motion for dislocation segments have been derived from a Galerkin minimum energy principle, in the same way as customary in FEM techniques in continuum mechanics. The position, tangent and normal vectors of specific nodes on continuous dislocation lines are updated for every time step. Our approach provides a great degree of flexibility in changing the shape and length of each dislocation segment without particular limitations. When additional crystallographic constraints are included, the influence of the crystal structure on dislocation shapes can be clearly seen. Figures (1-3) show the interaction between Frank-Read dislocation sources in FCC Cu. In Figures (1-2), complex loops form as a result of dislocation source interactions, while Lomer-Cottrel junction forms in Figure (3). The time step is adjusted to capture annihilation interaction within one FR source, or junction formation along the common line on two conjugate slip planes.
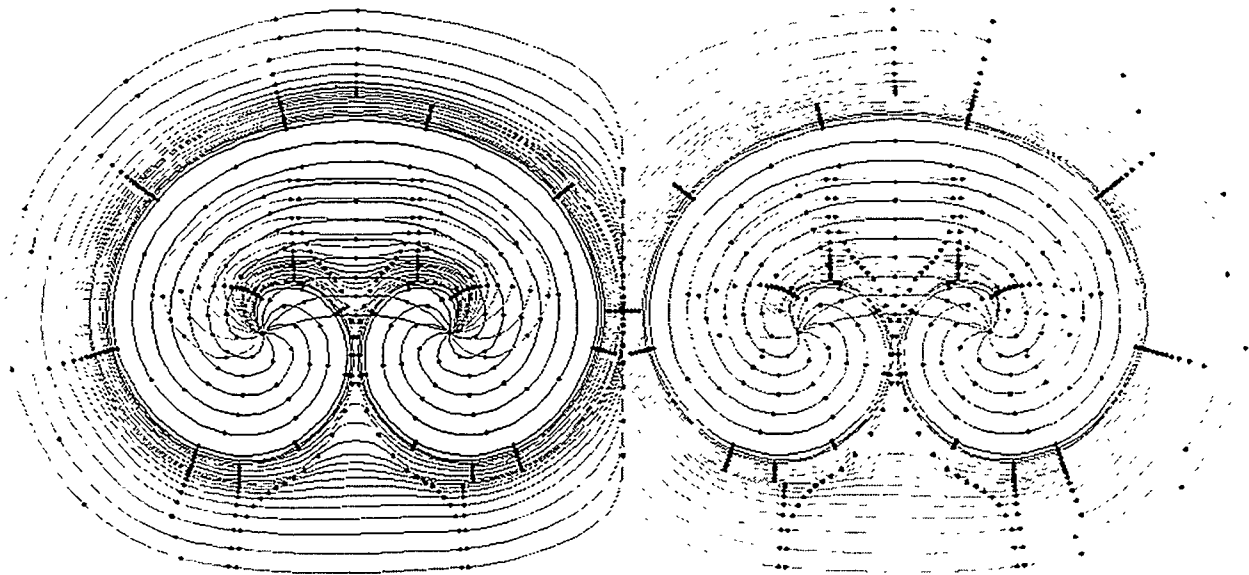
Figure (3): Formation of a Lomer-Cottrel Lock as a result of interaction between two dislocation loops.

Dislocation Decoration with Nano-scale Defect Clusters in Irradiated Metals

Collaborators: N.M. Ghoniem (UCLA), L. Sun (UCLA), B.N. Singh (RISO), and T. Diaz de la Rubia (LLNL)

Under neutron or charged particle irradiation, nano-scale point defect clusters nucleate directly from atomic collision cascades in irradiated materials. Once these clusters nucleate, they assume the shape of small prismatic dislocation loops of radial dimensions in the range of 1-3 *nm*. Molecular Dynamics (MD) computer simulations [15-17], as well as experimental evidence suggest that, at least in bcc metals, these clusters can be rather mobile, and that they migrate predominantly along close-packed crystallographic directions. The most stable clusters in bcc Fe are glissile sets of co-linear <111> crowdions,

with a dislocation loop character of $\frac{a}{2}$<111>{111} [15]. In fcc Cu, hexagonal faulted Frank

loops of type $\frac{a}{3}$<111>{111} are found to be stable and sessile. Vacancy clusters in Cu are

found to be {111}-platelets of Stacking Fault Tetrahedra (SFT's). Experimental evidence [18,19] suggest that under electron irradiation, where defect clusters are not directly produced in collision cascades, grown-in dislocations are not heavily *decorated* with small defect clusters. The work of Sigle et al [18] indicates that only SFT's are found within *20 nm* of dislocation cores, and their position is on the compression side of edge dislocations.

Fig. 4 shows a TEM micrographs of pure single crystal Mo irradiated with fission neutrons at 320 K [19]. Grown-in (slip) dislocations are clearly decorated with small defect clusters, without any preference to either side of pre-existing dislocations. The zone of *attraction* is on the order of 10 *nm* in bcc metals [20], and about 20 *nm* in fcc metals [19]. While defect clusters nucleate homogeneously under electron irradiation, they can be directly produced heterogeneously by collision cascades under ion or neutron irradiation. Experimental evidence of their interaction with dislocations is consistent with a high degree of cluster mobility. The decoration of existing dislocations with nano-scale defect clusters appears to be a consequence of in-cascade nucleation, followed by coherent transport along closely packed crystallographic directions.

It is well established that neutron irradiation leads to a substantial increase in the yield strength and hardening of metals. This phenomenon is particularly severe at low temperatures (i.e., below recovery stage V). The decoration of slip dislocation with defect clusters appears to be the controlling mechanism for blocking dislocation

Fig. 4: Dislocation decoration and "raft" formation in single crystal molybdenum irradiated at 320 K to a neutron fluence of 1.5×10^{21} n/m^2 (E> 1 MeV). After ref. [20].

motion on its glide plane. Moreover, once plastic deformation commences, it is observed to be rather heterogeneous and concentrated in ``soft" deformation channels, while the vast majority of the matrix is in a state of elastic deformation. The onset of this type of plastic instability is thus associated with the initiation and propagation of dislocation channels that are nearly free of defect clusters. Decoration of dislocations with irradiation-produced defect clusters is possibly the root cause of localized plastic deformation, leading to premature fracture. At low applied stress levels, defect clusters (of both vacancy and interstitial type) inhibit dislocation mobility by acting as barriers to their motion. As the stress is increased in a local region, clusters are absorbed in the dislocation core, and are hence cleared from the glide plane of a moving dislocation loop. This qualitative picture can explain the initial radiation hardening, and the subsequent onset of flow localization. However, quantitative determination of the detailed mechanisms by which the phenomenon occurs remain largely unexplored [21].

We consider here the conditions for the interaction and accumulation of small, prismatic-type point defect clusters with grown-in (deformation) dislocation loops. In particular, we provide theoretical estimates for the attractive elastic interaction region around dislocations, and compare the results to experimental observations. In addition, we give theoretical results for the spatial structure of the accumulation, or elastic trapping, region around dislocation loops. The interaction of point defects with slip loops is also analyzed and compared to the case of nano-scale defect clusters. In fcc metals of low stacking fault energy, small defect clusters are faulted, and are hence sessile. We wish to show that, as a result of their elastic interaction with the internal stress field of dislocations, these clusters can acquire enough energy to convert to a more glissile configuration. We first present the main features of a new the computational model for accurate evaluation of the elastic field of dislocation aggregates. We describe the geometry of interacting dislocations of arbitrary 3-D shapes. The stress, interaction energy, interaction forces, and moments on the small defect clusters are then outlined. Results of the model are given next, and compared to existing experimental observations.
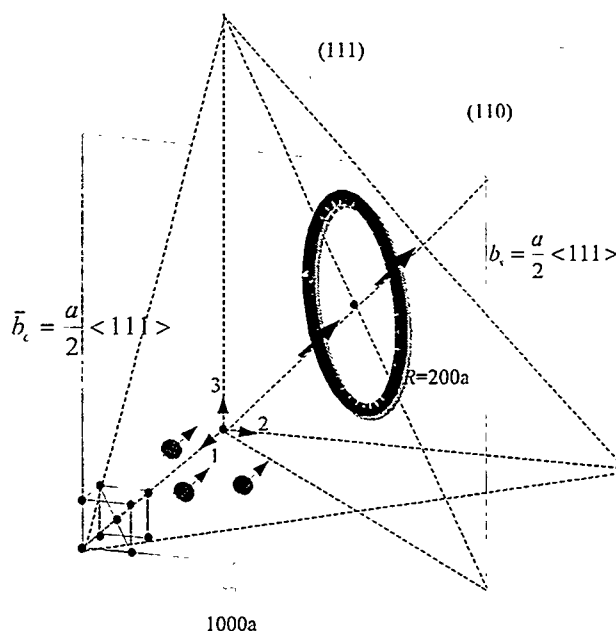
Fig. 5: Geometric arrangement of a proto-typical slip loop and interacting defect clusters in bcc crystals.

Fig. 5 shows a typical geometric representation for interaction between prismatic defect clusters and deformation slip loops on the primary glide plane of bcc crystals. The medium is assumed to be infinite and elastically isotropic, but the cube size of Fig. 5 is taken as (1000 a), where (a) is the lattice parameter. The slip loop is at the center of the cube, and has a diameter of (400 a), while the clusters have a diameter of 3 nm. For fcc crystals, the slip loop is assumed to be on the <111>-plane, with Burgers vector $\frac{a}{2}$<110>. The habit plane of defect clusters in fcc is (110), while their Burgers vector is of the $\frac{a}{2}$<110>$-type. Several combinations of loop and cluster Burgers vectors have been studied. Our analysis indicates that are only four independent interaction energy surfaces between slip loops and defect clusters existing in bcc crystals.

A dislocation loop of arbitrary 3-D shape is discretized into parametric segments. For each segment (j), we choose a set of generalized coordinates, and the corresponding shape functions to represent the configuration of the segment. In this case, the generalized coordinates are just the position and tangent vectors, associated with the beginning and end nodes on segment (j). Following Kroner [22] and DeWit \cite [23], the stress field of a dislocation loop is given by a line integral over the dislocation loop. We extend their treatment to the specific case of parametric geometric representation. An efficient numerical integration scheme has been developed to solve for the stress field at any point of the material as a fast summation over quadrature points, as indicated in section 2.2. above. The interaction energy of two dislocation loops over is calculated by equation (3). However, if one of the loops is infinitesimal, the interaction energy can be simplified, as shown by Kroupa [24]. We assume here (the elastic dipole approximation) that the stress tensor of a grown-in dislocation loop is constant over the cross-section of a small point-defect cluster. In case we treat one single vacancy or interstitial atom as a center of dilatation, the interaction energy simplifies to the method of Bullough and Willis [25].
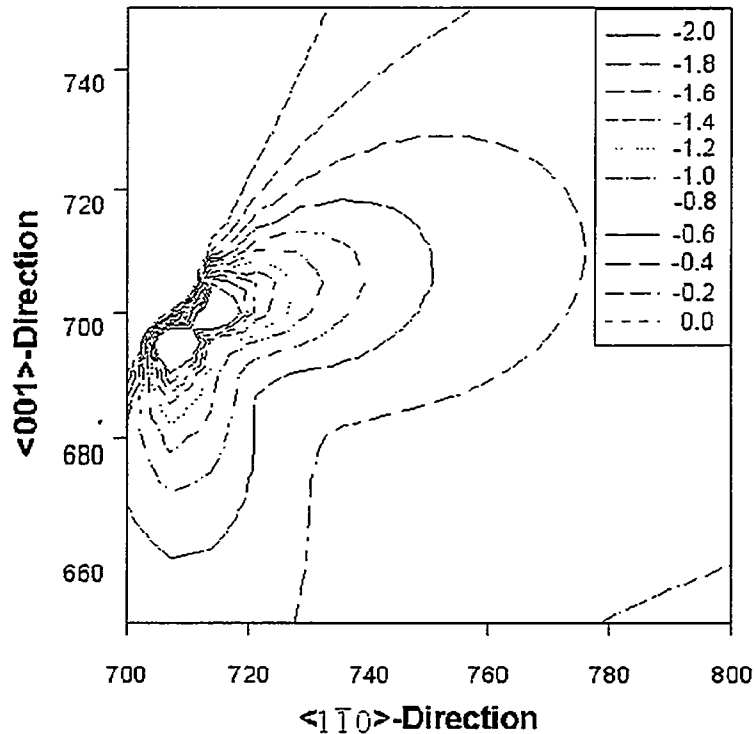
Fig. 6: Interaction Energy Contours (in units of kT) for Cu

Fig. 6 shows a cut in the interaction energy surfaces between interstitial defect clusters of Burgers vector $\frac{a}{2}$<111> and a proto-typical slip loop on the <110>-plane in bcc-Fe at RT. The vectors<001> and <110> define the plane of the contours, and the energy units are in (kT). In this particular orientation of the cluster's Burgers vector, the iso-energy surfaces are anti-symmetric with respect to the $<001>$-direction. The symmetry properties of the iso-energy surfaces depend on the relative orientations of the slip loop and cluster Burgers vectors. Generally, the surface bounding a value of {- kT} is considered a trapping surface, and clusters which enter into this zone will oscillate within the surface. A 3-D picture of one of
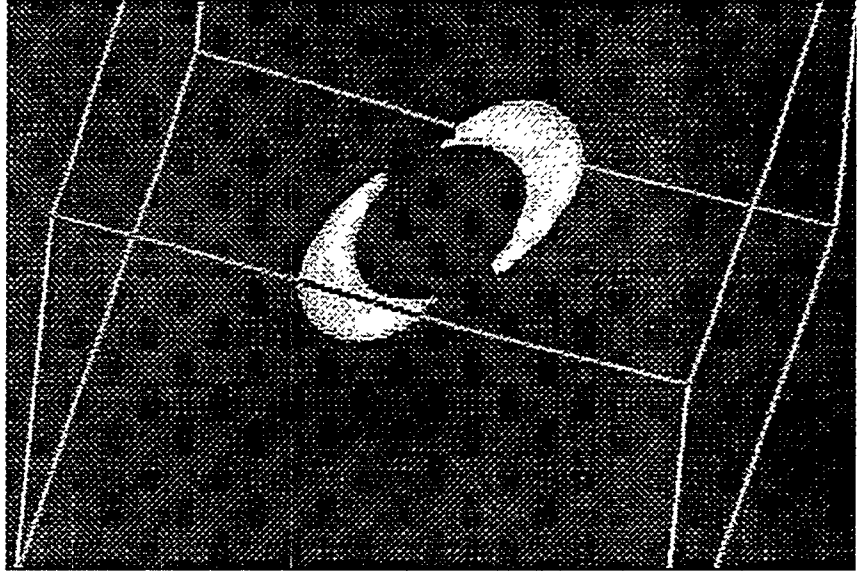
Fig. 7: 3-D picture of one of the four trapping zones in bcc at RT

the four trapping zones in bcc at RT is shown in Fig. 7. It is clear that the zone assumes a {\it crescent}-shape, of maximum width around the edge component of the slip loop. The trapping zone size diminishes for mixed character segments on the slip loop, and vanishes at the purely screw component. These results are consistent with experimental observation [20].

The total force and its moment on the cluster due to the slip loop can also be computed (see reference 14 for details). They are derived on the basis of the infinitesimal loop approximation of Kroupa [22], where we extended his formulation by introducing geometric parameterization of the loops. As the defect cluster moves closer to the core of the slip loop, the turning moment on its habit plane increases. If the amount of mechanical work of rotation exceeds a critical value (taken as 0.1 eV/crowdion, as a result of MD calculations [26], it will change its Burgers vector and habit plane and move to be incorporated into the dislocation core. The mechanical work for cluster rotation is equated to this critical value. The critical surface for cluster rotation and hence subsequent absorption into the dislocation core has been determined. It is found that this stand-off zone is about one cluster diameter 3 nm. Fig. 7 indicates that the maximum capture zone size (at the edge component) decreases with temperature, and is greater for fcc-Cu as compared to bcc-Fe. Both observations result from an increase in the cluster thermal energy, and a decrease in its modulus with temperature.

In fcc metals of low stacking fault energy, small clusters may exist in the form of faulted Frank loops. However, if the cluster size is large enough, it is energetically more

favorable to unfault and become glissile. Another unfaulting mechanism is by assistance of large local stress fields. An *induced surface tension* can change the critical unfaulting radius, depending on whether it adds or subtracts from the stacking fault energy. For a circular Frank loop to unfault, the loop containing the fault and its perfect counterpart is attained by an additional Schokley partial $\frac{a}{6}[1\bar{1}2]$. If clusters are produced very near dislocation cores, it is found that the critical unfauling radius can be as small as *6 nm* in fcc-Cu (see Ref. 14 for details). This point is illustrated in Fig. 8, where the critical unfaulting radius is
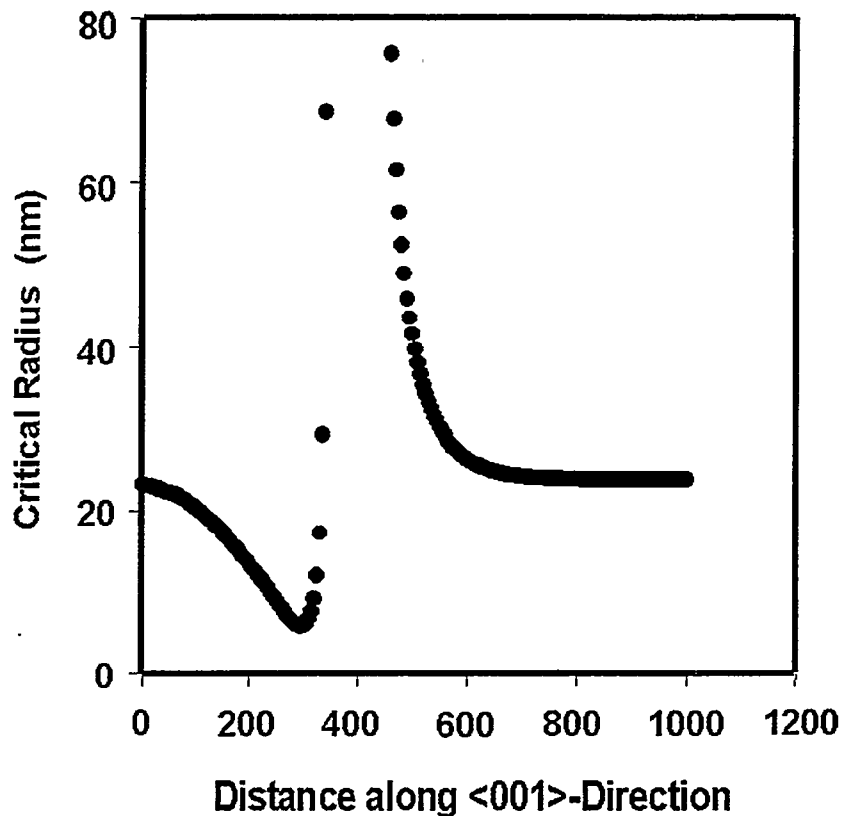
Fig. 8: Dependence of the critical unfaulting cluster radius on its distance from the core of the slip loop

plotted against distance along the <001>-direction in Cu. The stress-free unfaulting radius of 22 *nm* is dramatically altered near the core of the slip loop. On the compressive side, the stress field shrinks the critical radius to 6 *nm*, while it expands it significantly on the tensile side.

It is concluded that the interaction between nano-scale clusters and slip loops is highly orientation dependent, unlike the situation with defect dilatation centers used in calculations of dislocation [25]. The size of the elastic capture zone is primarily determined by the interaction between the edge components of slip loops, and is not very sensitive to cluster-cluster interaction. Calculated trapping zone sizes are in reasonable agreement with experimental results. On the other hand, clusters that are very near dislocation cores (within 3 *nm*) can be absorbed into the core by rotation of their Burgers vector as a result of unbalanced moments. Clusters that glide on prismatic cylinders are trapped above and below the slip plane in a *crescent* shape, obstructing the motion of edge components. The expansion of loops is thus anisotropic upon further deformation, where screw components will first propagate. It appears that the initiation of a dislocation channel on the slip plane is associated with the stress required for the dislocation to overcome the collective elastic potential of trapped clusters, rather than by cutting through dispersed obstacles on the glide plane in the normal Orowan hardening mechanism.

RECENT RELEVANT PUBLICATIONS & PRESENTATIONS:

Publications:

(1) N.M. Ghoniem and M. Bacaloni, "Finite Segment Method for 3-D Dislocation Dynamics," Eng. Report No. {**UCLA/MATMOD-97-01**}, (1997).
(2) H. Huang, N.M. Ghoniem, T. Diaz de la Rubia, M. Rhee, H. Zbib and J. Hirth, "Stability of dislocation short-range reactions in bcc crystals," *J. Eng. Mat. & Tech.*, in the press, April 1999.
(3) N.M. Ghoniem, "Curved parametric segments for the stress field of 3-D dislocation loops," *J. Eng. Mat. & Tech.,* in the press, April 1999.
(4) N. M. Ghoniem, L. Sun, "A Fast Sum Method for the Elastic Field of 3-D Dislocation Ensembles," *Phys. Rev.,* Submitted.
(5) N.M. Ghoniem, B. N. Singh, L. Z. Sun, and T. Diaz de la Rubia, "Dislocation Decoration with Nano-scale Defect Clusters in Irradiated Metals," Submitted, *J. Nucl. Mater.*

Conference Presentations:

(1) M. Ghoniem, "Three-dimensional Dislocation Dynamics with Parametric Dislocation Segments," Second Euro-Conference on Fracture and Plastic Instabilities in Materials, Thessaloniki, Greece, September 1997.
(2) N.M. Ghoniem, "Principles of 3-D Dislocation Dynamics," 13th US Congress on Applied Mechanics, Gainesville, Florida, June 1998.
(3) N.M. Ghoniem, " Stability of short-range Reactions in 3-D Dislocation Dynamics, " Society of Engineering Science Conference, Pullman, Washington, September 1998.
(4) N.M. Ghoniem, "Simulations of Dislocation Loop Interactions in Single and Multiple Slip," Seventh International Symposium on Plasticity and Its Current Applications, Cancun, Mexico, January 1999.

RESEARCH COLLABORATIONS

The present research is a result of collaborations with the following national and international groups:

(1) Dr. Tomas Diaz de la Rubia, Lawrence Livermore National laboratory.
(2) Dr. Klaus Schwarz, IBM Watson Research Center.
(3) Professors H. Zbib and John Hirth, Washington State University.
(5) Dr. Bachu N. Singh, RISO Danish National Laboratory.
(5) Dr. Helmut Trainkaus, German Forschungszentrum Julich.

A new collaborative research initiative has been started with Professors Lucas and Odette at UCSB, to link Dislocation Dynamics to macroscopic fracture mechanics.

REFERENCES

(1) G.E. Lucas, G.R. Odette, R. Maiti, and J.W. Sheckherd, "Tensile Properties of Irradiated Pressure Vessel Steels," , in *Influence of Radiation on Material Properties: Thirteenth International Symposium*, STP 956, F. Garner, C. Henager, and N. Igata, Ed., American Society for Testing of Materials, Philadelphia, 1987, pp. 379 - 394.

(2) D. Pachur, "Apparent Embrittlement Saturation and Radiation Mechanisms of Reactor Pressure Vessels," in *Radiation Effects on Materials: Tenth International Symposium*, STP 725, D. Kramer, H.R. Brager, and J.S. Perrin, Ed., American Society for Testing of Materials, Philadelphia, 1981, pp. 5-19.

(3) C. Guionnet, Y. Robin, C. Flavier, A. Lefort, D. Gros, and R. Perdreau, " Radiation Embrittlement of a PWR Vessel Steel: Effects of Impurities and Nickel Content," in Ref. 5 above, pp. 20-37.

(4) J.R. Hawthorne, H.E. Watson, and F.J. Loss, " Experimental Investigation of Multicycle Irradiation and Annealing Effects on Notch Ductility of A533-B Weld Deposits," in Ref. 5 above, pp. 63-75.

(5) E.E. Bloom, et al., J. Nucl. Mater., 22 (1967) 68.

(6) D. Hull, *Introduction to Dislocations*," Sec. 10.4, Pergamon Press, Inc., New York, 1965.

(7) F.R. Smidt, Jr. "Dislocation Channeling in Irradiated Metals," *NRL Report*, NRL-7078, Naval Research Laboratory, 1970.

(8) M.J. Makin, *Phil. Mag.*, Vol. 10, 1964, pp. 695.

(9) F. Kroupa, *Phil. Mag.* Vol. 7, 1962, pp. 783.

(10) A.J.E. Forman, *Phil. Mag.* Vol. 17, 1968, pp. 353.

(11) N.M. Ghoniem and M. Bacaloni, "Finite Segment Method for 3-D Dislocation Dynamics," Eng. Report No. {**UCLA/MATMOD-97-01**}.(1997).

(12) N.M. Ghoniem, "Curved parametric segments for the stress field of 3-D dislocation loops," *J. Eng. Mat. & Tech.,* in the press, April 1999.

(13) N. M. Ghoniem, L. Sun, "A Fast Sum Method for the Elastic Field of 3-D Dislocation Ensembles," *Phys. Rev.*, Submitted.

(14) N.M. Ghoniem, B. N. Singh, L. Z. Sun, and T. Diaz de la Rubia, "Dislocation Decoration with Nano-scale Defect Clusters in Irradiated Metals," Submitted, *J. Nucl. Mater*.

(15) Yu. N. Osetsky, M. Victoria, A. Serra, S.I. Golubov, and V. Priego, J. Nucl. Mater. **251**, 34 (1997).

(16) T. Diaz de la Rubia and M. Guinan, Phys. Rev. Lett. **66**, 2766 (1991).

(17) D.J. Bacon and T. Diaz de la Rubia, J. Nucl. Mater. **216**, 275 (1994).

(18) B.N. Singh, A.J.E. Foreman and H. Trinkaus, J. Nucl. Mater. **249**, 103 (1997).

(19) W. Sigle, M.L. Jenkins and J.L. Hutchinson, Phil. Mag. Lett. **57**, 2766 (1988).

(20) B.N. Singh and J. Evans, J. Nucl. Mat., to be published.

(21) H. Trinkaus, B.N. Singh and A.J.E. Forman, J. Nucl. Mater. **251**, 172 (1997).

(22) F. Kr"oner, Ergeb. Angew. Math. **5**, 1 (1958).

(23) R. DeWit, Sol. State Phys. **10**, 249 (1960).

(24) F. Krupa, in *Theory of Crystal Defects*, edited by B. Gruber (Academia Publishing House, Prague), 275 (1966).

(25) R. Bullough and J.R. Willis, Phil. Mag. **31**, 855 (1975).

(26) A.J.E. Forman,C.A. English and W.J. Phythian, Phil. Mag. **A66**, 655 (1992).

EVALUATION OF FRACTURE TOUGHNESS, CONSTRAINT AND SIZE EFFECTS FROM CRITICAL CRACK TIP OPENING MEASUREMENTS USING CONFOCAL MICROSCOPY AND FRACTURE RECONSTRUCTION METHODS —G. R. Odette, G. E. Lucas , K. Edsinger, E. Donahue and H. Rathbun (University of California, Santa Barbara)

SUMMARY

This work demonstrates the use of confocal microscopy and fracture reconstruction methods to measure the critical crack tip opening displacement for several candidate fusion reactor structural materials — including both tempered martensitic steels and V-4Cr-4Ti — as well as other alloys for a variety of testing conditions and specimen sizes and configurations. Extensions of the method to regimes that deviate from small scale yielding, including stable crack growth and small specimens, based on local measures of toughness combined with simulations of crack tip fields, are also described.

PROGRESS AND STATUS

Introduction

Design and operation of fusion reactors will require accurate and conservative predictions of loading conditions which might result in rapid and catastrophic fracture by the unstable propagation of cracks presumed to exist in any large, complex structure. The critical crack tip opening displacement (δ^*) represents a material's fracture toughness in a way that is fully equivalent to more frequently cited measures like J_{Ic}. Based on standard assumptions of elastic-plastic fracture mechanics (EPFM) and in combination with an appropriate constitutive law, δ^* can be used to evaluate the remote loads (stresses) and displacements (strains) leading to fracture initiation in cracked specimens or structures. Further, since δ^* represents a permanent record on the fracture surface, it is highly robust and can be used for conditions where conventional methods are difficult or impossible to apply, viz., dynamic loading rates; thin specimens with limited length of crack front under plane strain; wedge loading; complex (e.g. three dimensional) crack configurations; and subcritical crack growth. However, δ^* is not frequently used because it is difficult and tedious to measure. These limitations are avoided using a new method based on confocal microscopy fracture reconstruction (CM/FR). This paper demonstrates the use of confocal microscopy and fracture reconstruction methods to measure the critical crack tip opening displacement for several candidate fusion reactor structural materials as well as other alloys for a variety of testing conditions and specimen sizes and configurations.

Confocal Microscopy and Fracture Reconstruction

Kobayashi and co-workers have pioneered the development of fracture reconstruction using topographic maps of conjugate fracture surfaces to reconstruct the sequence of events involved in the fracture process [1-4]. We have further developed the fracture reconstruction method using confocal microscopy (CM) to obtain the topographic maps of fracture surfaces and a set of algorithms to construct, align and analyze conjugate fracture surfaces. These methods are described in more detail elsewhere [5,6], but are reviewed here.

The confocal microscope effectively, optically sections a surface by using a depth of focus which is small relative to the height variation of the surface features; hence, the surface is illuminated

only at the points where the focal plane intersects the fracture surface. By systematically chang-
ing the specimen position in z for a fixed focal length, a series of illumination patterns is obtained
as a function of z, and these images can be recorded digitally and used to computationally recon-
struct a quantitative, three-dimensional, digital image of the surface.

With conjugate topographs, it is possible to approximately reconstruct the sequence of events
leading up to fracture. Conjugate fracture surfaces are matched and computationally overlapped
until the position of the pre-crack is accurately represented; the surfaces are then computationally
separated by an amount δ corresponding to the crack tip opening displacement. Since the recon-
struction is computational, the process can be viewed from any direction, and regions of material
separation represent damage evolution.

Fracture reconstruction data can be represented in a variety of ways, and several examples are
illustrated in Figure 1 for ductile crack growth in an edge-cracked specimen of HT-9, a tempered
martensitic stainless steel, loaded in three point bending at 20°C. Figure 1a shows both a side
and top view of material separation of a crack advancing by stable, ductile fracture taken at a
specific δ (= 225 µm). Intact material is represented in white, and separation in black. The top
view shows damage nucleation ahead of the crack, and the side view shows the relationship
between the two fracture surfaces along a specific plane perpendicular to the fracture surface and
the crack front (approximately at the center of the figure above). Figure 1b shows the degree of
overlap between the upper and lower fracture surfaces for a given δ (= 0 µm) as a function of
position ahead of the crack tip. The upper figure illustrates this from a top view, where overlap is
represented by gray scales (increasing white corresponds to increasing overlap). The lower figure
represents the degree of overlap (vertical) ahead of the pre-crack tip (horizontal) averaged over
the length of the crack front. As such, the lower figure can also be interpreted as the degree of
crack tip opening δ_{remote} (vertical) as a function of crack advance Δa (horizontal), and thus directly
corresponds to J vs Δa. Finally, a sequence of top views onto a crack plane for a series of in-
creasing δ's is shown in Figure 1c. These images are useful for observing the sequence of events
in crack initiation and growth, as well as for detecting the critical value, δ^*, at which initiation
occurs. This can be used to estimate fracture toughness from [5]

$$K_{J\delta} \sim \sqrt{J_{I\delta}E'} \sim \sqrt{m\delta^* \sigma_y E'} \tag{1}$$

where σ_y is the yield stress, and m is a factor that depends on the alloy stress-strain or constitu-
tive properties and the specimen/structure-crack configuration. For deep cracks in bending and
typical strain hardening rates, m is approximately equal to 2.

Finally, the observations of damage evolution and crack initiation can be combined with finite ele-
ment analysis (FEA) of crack tip stress and strain fields to develop micromechanical models of
fracture and quantify local fracture parameters.

Examples

Quasi-cleavage

Figure 2 illustrates a CM/FR sequence for fracture in an F-82H specimen (W=10mm, a/W=0.5)
tested in three point bend at -73°C. Damage in the form of microcleavage cracks begins to form
at a δ of about 62µm. These microcleavage cracks ultimately coalesce into a process zone crack
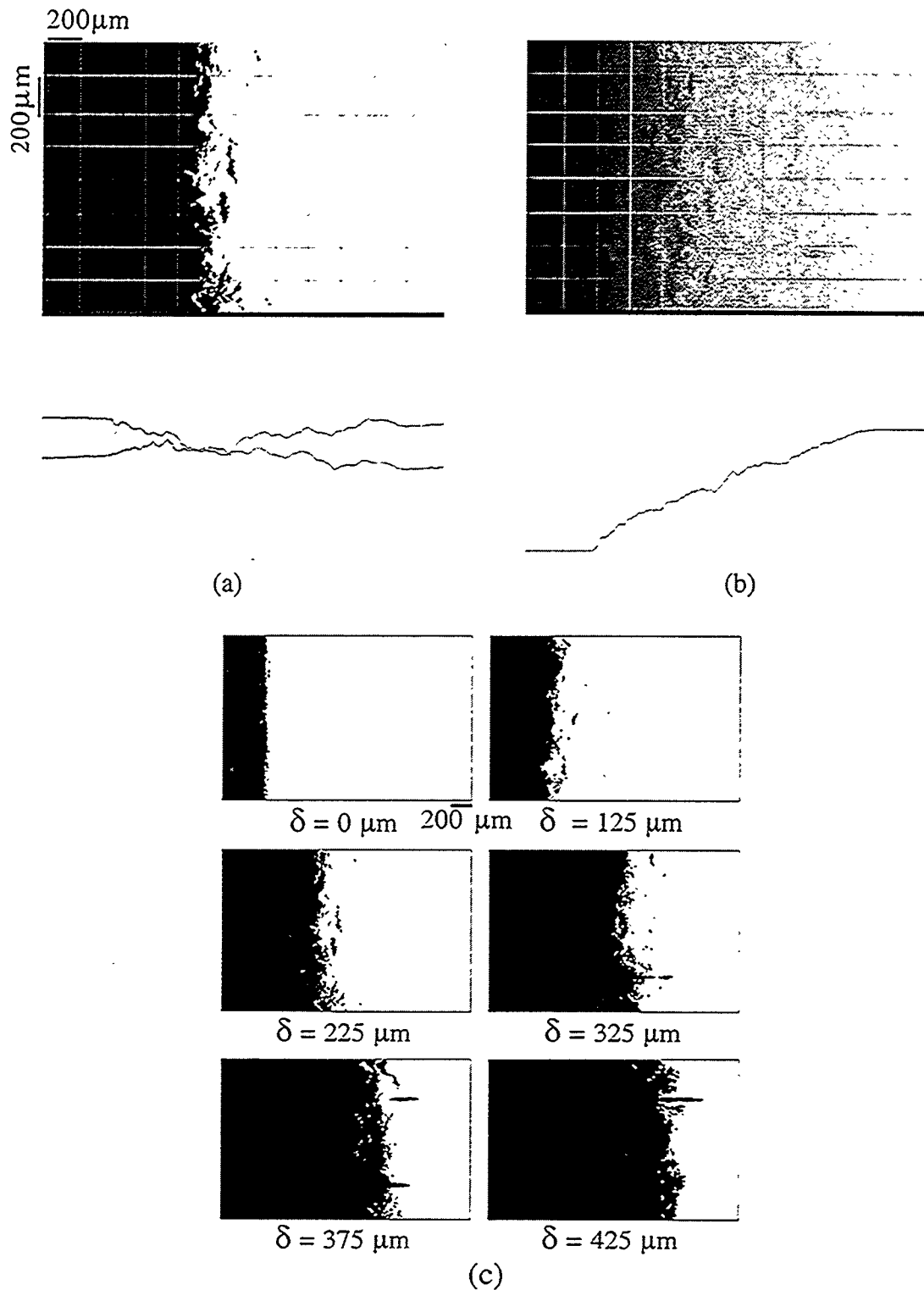
Figure 1.   Illustration of the several representations of CM/FR data for HT-9: a) fracture surface separations at a fixed δ; b) conjugate fracture surface overlap at a fixed δ; c) fracture surface separations at a sequence of δ's.

$\delta = 62\ \mu m$ 200 μm $\delta = 64\ \mu m$

$\delta = 66\ \mu m$ $\delta = 68\ \mu m$

$\delta = 70\ \mu m$
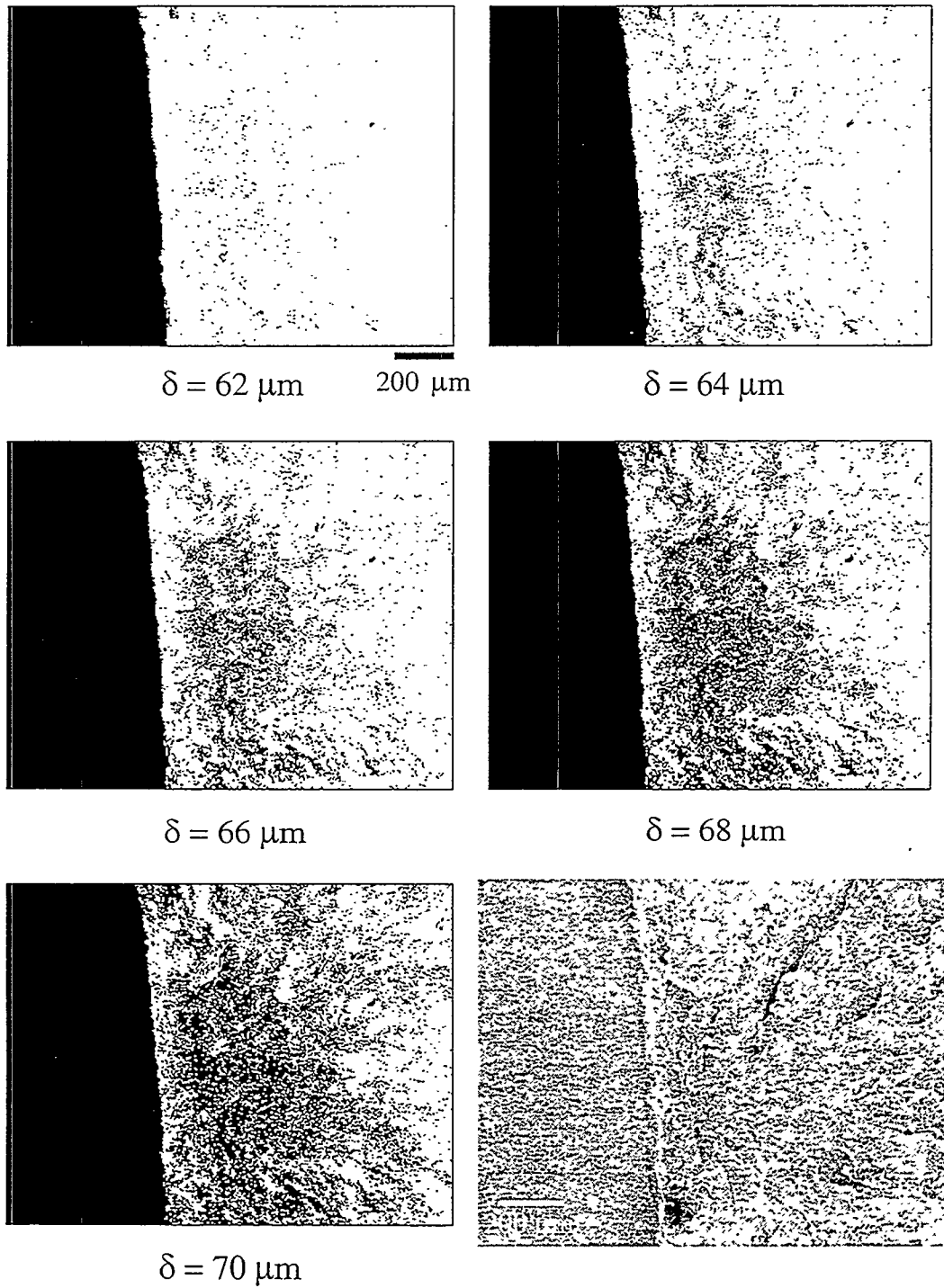
Figure 2.   CM/FR sequence for fracture in an F-82H specimen (W=10mm, a/W=0.5) tested in three point bend at -73°C

that propagates unstably beyond a δ^* of 70μm. Corresponding FEA shows the initial peak damage region corresponds with peak stresses ahead of the crack tip. Similar observations and related analyses have been used to develop a micromechanical model for quasi-cleavage (and cleavage) fracture based on crack tip stresses exceeding a critical value σ^* over a critical area A^* ahead of the crack tip. [7]

Ductile Fracture

Figure 3a illustrates a CM/FR sequence for fracture in a low-alloy steel tested in three point bend at 20°C. Here, damage in the form of microvoid nucleation and growth initiates ahead of the crack tip and coalesces with the crack tip in a stable, subcritical crack growth process. The variation of δ_{remote} with Δa shown in Figure 3b closely corresponds to the mechanical J-Δa curve determined for this test and shown in Figure 3c. The minima/arrests, respectively, in these curves correspond to damage coalescence with the crack tip. The location of damage initiation observed by CM/FR can be used with high resolution scanning electron microscopy (SEM) to examine the surface for microstructural features that may play a role in crack initiation; in the case of the specimen shown in Figure 3, SEM identified a number of large particles in the damage initiation region. [5]

Fracture Toughness

Figure 4 illustrates that measures of $K_{J\delta}$ determined from CM/FR are in good agreement with values of fracture toughness, K_{Jc}, determined from analysis of mechanical load-displacement data for a wide range of alloys, specimen sizes and test conditions. Hence, CM/FR provides an opportunity to measure fracture toughness under conditions where standard techniques may not be easily applied (dynamic loading, small specimens, part through cracks, etc.)

Size Effects

All measures of toughness respond to size and geometry effects. Small or shallow cracked specimens have a higher toughness and hence higher δ^*. This is illustrated in Figure 5, where δ_{remote} vs x (distance ahead of the crack) data are plotted for pre-cracked Charpy specimens (PCC) from a low alloy steel tested at -40°C; as seen the specimen containing the shallow crack (i.e., crack length to specimen width ratio a/W=0.1) blunts to a larger δ before the onset of unstable fracture than the deeply cracked specimen (a/W=0.5). These size effects (as well as effects of irradiation and strain rate) can be modeled using the critical stress/area criteria described above in conjunction with stress fields calculated by FEA for geometries of interest. This is illustrated in Figure 6, where both pre-cracked Charpy and pre-cracked 1/3-sized-Charpy (MPCC) data on F-82H are fit by the same σ^*/A^* criteria on the lower shelf and knee, where quasi-cleavage initiation predominates .

$\delta = 125\ \mu m$ 200 μm $\delta = 175\ \mu m$

$\delta = 250\ \mu m$ $\delta = 350\ \mu m$
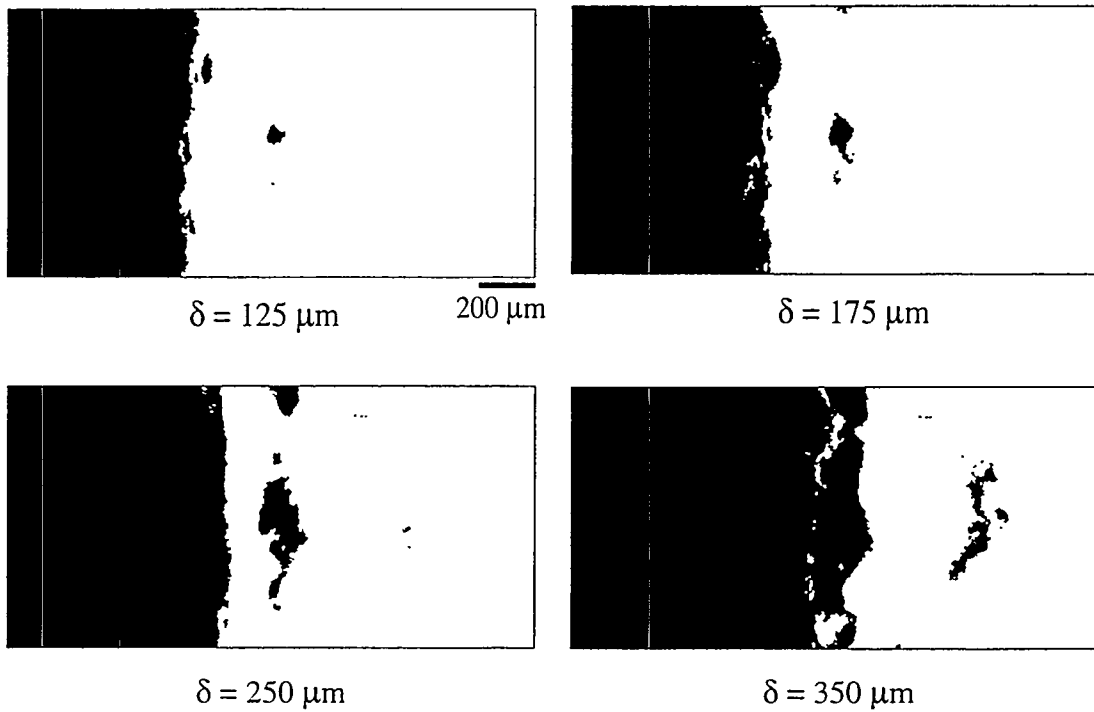
(a)
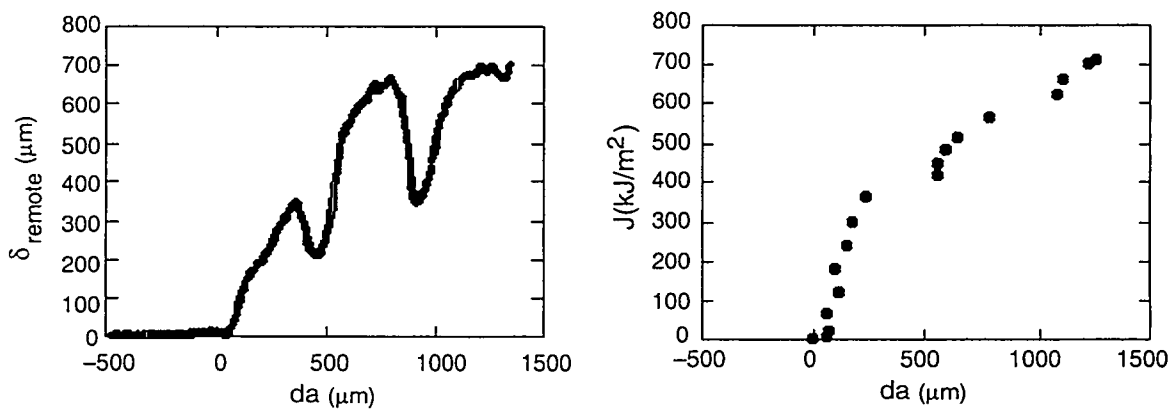
(b)

Figure 3. a) a CM/FR sequence; b) the variation of δ_{remote} with Δa; and c) mechanical J-Δa
curve determined for a low-alloy steel tested in three point bend at 20°C
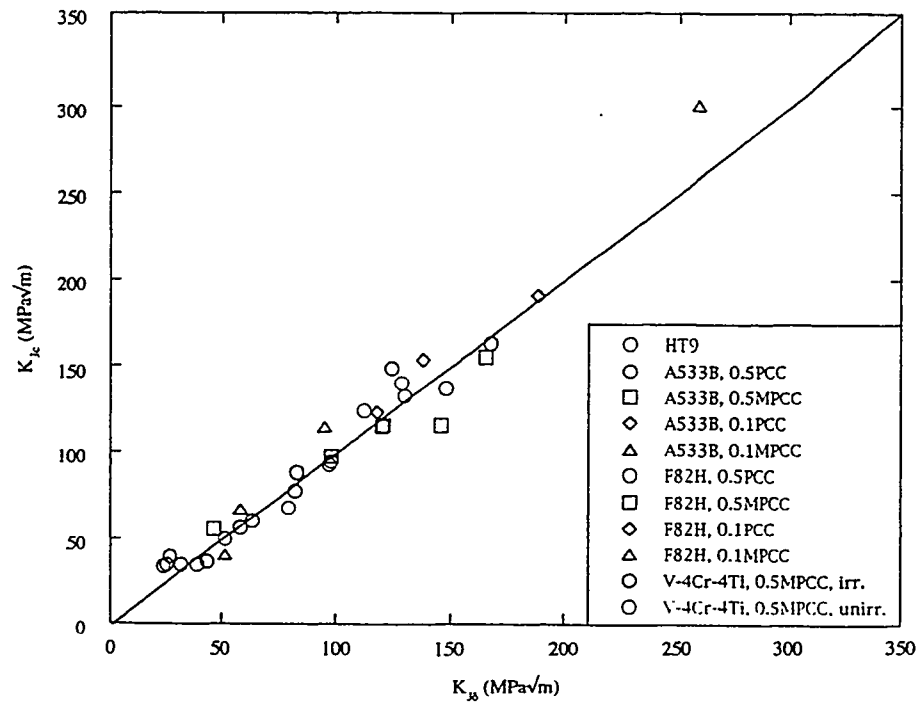
Figure 4. Comparison of $K_{\delta c}$ determined from CM/FR with K_{Jc} determined from analysis of mechanical load-displacement data for a range of alloys, test conditions and specimen sizes, including pre-cracked Charpy (PCC) and 1/3-sized Charpy (MPCC) specimens with crack length to specimen width ratios of 0.1 and 0.5.
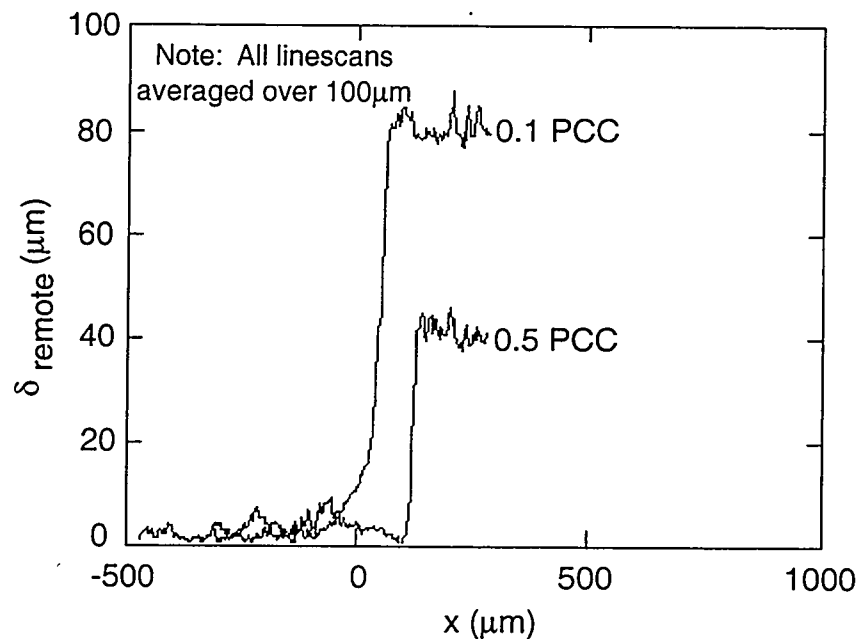
Figure 5. δ_{remote} vs x for pre-cracked Charpy specimens from a low alloy steel tested at -40°C
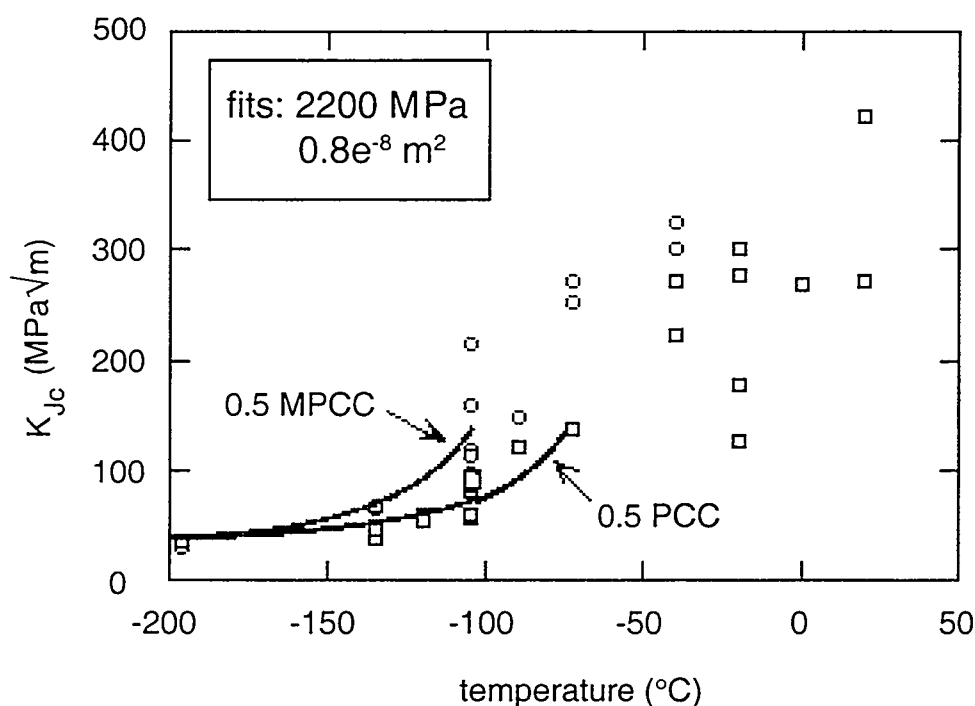
Figure 6. Effective toughness versus temperature for both pre-cracked Charpy and 1/3-sized-Charpy data in F-82H. Lines represent predictions of σ*/A* model.

SUMMARY AND CONCLUSIONS

The use of confocal microscopy and fracture reconstruction to observe the sequence of events in the fracture process and to measure the evolution of the crack tip opening displacement δ has been demonstrated for a variety of alloys. Values of δ* at the point of crack initiation can be used to obtain measures of fracture toughness for a large variety of specimens and test conditions. The evolution of δ provides insight into the mechanisms of fracture; and measures of δ* can be combined with finite element analyses of crack tip stress and strain fields to provide direct measures of local fracture parameters.

Knowledge of fracture micromechanics, quantification of local fracture parameters, and FEA can be combined to predict fracture under a variety of specimen/structure sizes/geometries and test/service conditions.

ACKNOWLEDGMENTS

REFERENCES

1. Ogawa, K., Zhang, X. J., Kobayashi, T., Armstrong, R. W., Irwin, G. R., ASTM-STP-833 American Society for Testing and Materials (1984) p. 393.

2. Kobayashi, T. and Shockey, D. A., Metallurgical Transactions., Vol. 18A (1987) p. 1941.

3. Kobayashi, T. and Shockey, D. A, Advanced Materials and Processes, Vol. 140-5 (1991) p. 28.

4. Kobayashi, T. and Shockey, D. A, Advanced Materials and Processes, Vol. 140-6 (1991) p. 24.

5. Edsinger, K., PhD Thesis - Department of Chemical and Nuclear Engineering, University of California, Santa Barbara (1995).

6. Edsinger, K., Odette, G. R., Lucas, G. E., Proceedings of the IEA International Symposium on Miniaturized Specimens for Testing Irradiated Materials, KFA Julich, September 22-23, 1994 (1995) p. 150.

7. Odette, G. R., Journal of Nuclear Materials, Vols. 212-215 (1994) p. 45.

COMPARISON OF SWELLING AND IRRADIATION CREEP BEHAVIOR OF FCC-AUSTENITIC AND BCC-FERRITIC/MARTENSITIC ALLOYS AT HIGH NEUTRON EXPOSURE

COMPARISON OF SWELLING AND IRRADIATION CREEP BEHAVIOR OF FCC-AUSTENITIC AND BCC-FERRITIC/MARTENSITIC ALLOYS AT HIGH NEUTRON EXPOSURE - F. A. Garner (Pacific Northwest National Laboratory)*, M. B. Toloczko (Washington State University), and B. H. Sencer (New Mexico Tech)

(Summary of a presentation at the Basic Differences in Irradiation Effects Between fcc, bcc and hcp Metals and Alloys, Congas de Onis, Spain, October 1998)

EXTENDED ABSTRACT

It is well-known that ferritic and ferritic/martensitic steels develop much less swelling than austenitic steels during neutron or charged particle irradiation. The prevailing assumption is usually that the steady-state swelling rate of bcc steels is inherently much lower than that of fcc steels, at least a factor of ten or more. It is shown in this paper that this perception is incorrect, with bcc steels having steady-state swelling rates perhaps only a factor of two lower. The creep compliance of the two types of alloys also differs only by a factor of about two.

This misperception arose from a dose assignment error made ~15 years ago, where both Fe-Cr-Ni ternary austenitic alloys and Fe-Cr binary ferritic alloys in one important EBR-II experiment were assigned dpa exposure levels that were too large for the lowest temperature capsules. When the error was recently corrected, it was found that an apparent low-temperature tendency toward saturation of swelling in Fe-Cr-Ni alloys disappeared, and that the very low steady-state swelling rate of Fe-Cr binaries was strongly underestimated and still may not have been attained at the termination of the experiment. Figure 1 presents the corrected EBR-II data. Recent Russian data on the swelling of cold-worked iron and Fe-Cr alloys tends to confirm a possible steady-state swelling rate approaching ~0.5%/dpa.

The lower swelling observed in both model and commercial bcc steels is shown in this paper to be a consequence of much longer transient regimes prior to the onset of steady-state swelling. Several other commonly held perceptions concerning the swelling of both bcc and fcc steels are examined in this paper and also shown to require revision. These involve the effect of cold-work on swelling and the extent of the temperature regime of swelling.

It also appears that the use of well-controlled in-reactor materials tests that employ active temperature control in FFTF-MOTA tend to yield significantly lower values of void swelling compared to that obtained under more representative conditions typical of actual reactor operation in EBR-II. Not only was this observed in fcc Fe-Cr-Ni alloys but also in Fe-Cr binary alloys, as shown in Figure 2.
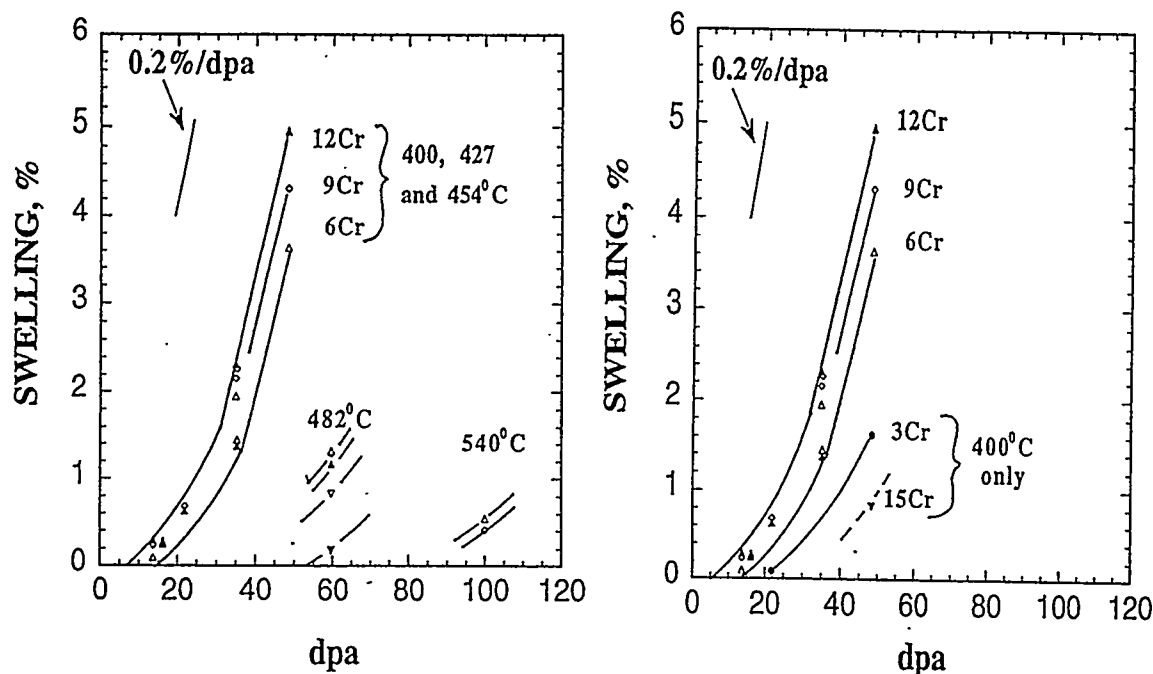
Figure 1. Corrected compilation of Fe-Cr swelling data from an early EBR-II experiment, showing that the primary influence of both chromium content and temperature lies in the duration of the transient regime. This behavior was also seen in the fcc Fe-Cr-Ni ternary alloys irradiated in the same capsules.
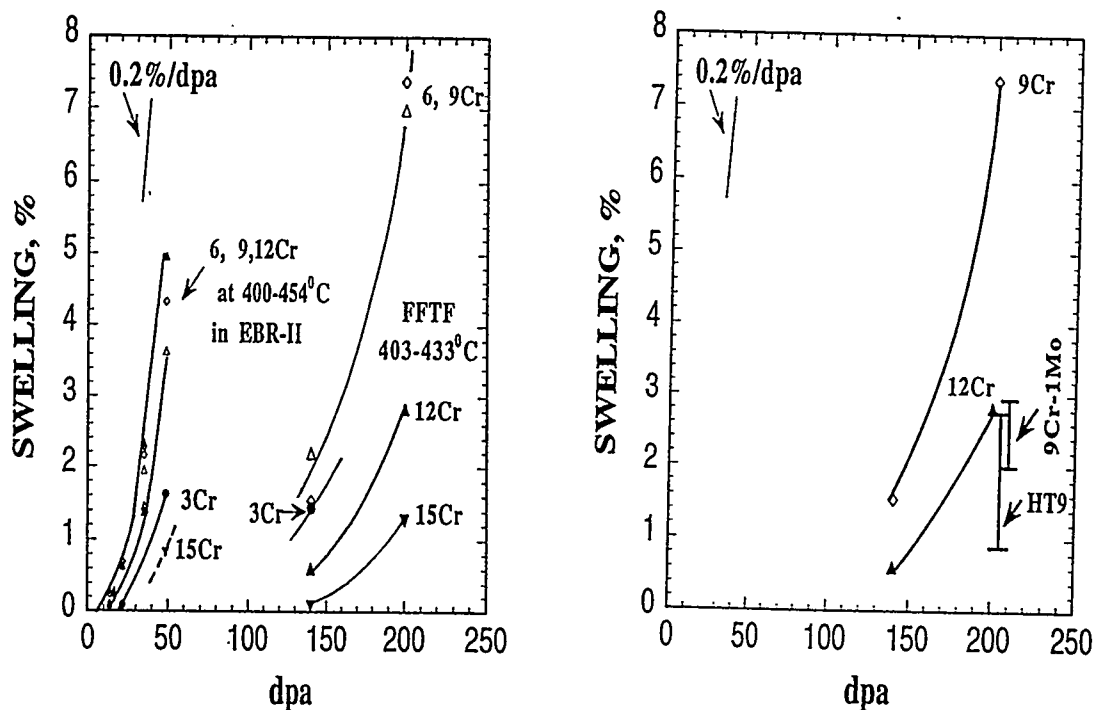
Figure 2. Comparison of EBR-II and FFTF-MOTA data for identical Fe-Cr alloys. Note that HT9 and 9Cr-1Mo irradiated in FFTF-MOTA appear to have only slightly longer transient regimes of swelling.

PROGESS ON THE INTEGRATED FOCUS ON FUNDAMENTAL STUDIES – VANADIUM INITIATIVE – H.L. Heinisch (Pacific Northwest National Laboratory*) and N. Sekimura (University of Tokyo)

OBJECTIVE

The objective of the Integrated Focus on Fundamental Studies – Vanadium Initiative (IFFS-VI) is to foster direct collaborations, integration of efforts, and joint utilization of resources by the US and Japan under the JUPITER Fusion Materials Collaboration agreement. The basic concept of IFFS-VI is to integrate theory, modeling and experiments, as well as the efforts of Japanese and US participants, toward a common focus on a specific technological problem in Fusion Materials research.

SUMMARY

IFFS-VI was initiated at the JUPITER Workshop on Theory and Modeling for Fusion Materials held October 30, 1997, during ICFRM-8 in Sendai, Japan. The original initiative is described, participants and collaborations are identified, and recent progress and future plans are discussed.

PROGRESS AND STATUS

Introduction

IFFS-VI is a program of theory, modeling, simulation and experiments focused on the specific problem of understanding and predicting the effects of temperature variation during fission reactor irradiation on the microstructure development and property changes of V-4Cr-4Ti. This program was devised and embraced by both sides of the JUPITER collaboration as a means of focusing our individual and joint efforts. The problem chosen aims our theory and modeling programs at the prime candidate material that has received the least attention in that regard so far, but it does not preclude advancements in the general fundamental understanding of irradiation effects. The primary temperature variation experiments, already planned before IFFS-VI was started, are currently underway as a major JUPITER irradiation in HFIR. They will provide experimental information on defect accumulation and property changes under well-controlled and monitored conditions. The temperature variation experiments will provide a good comparative data base against which to evaluate the theories and models in V alloys, as well as in general. V-4Cr-4Ti, other V alloys of interest and some pure metals are among the materials included in the experiments. Separate low-dose irradiations will be performed in the JMTR reactor and with heavy ions in Japan.

IFFS-VI is expected to continue throughout the remainder of the JUPITER collaboration and become a strong basis upon which to build future Japan/US collaborations on theory, modeling and experiments.

IFFS-VI Tasks

The experimental tasks associated with the neutron irradiations in HFIR and JMTR are underway or in the development stage, and their performance will not be directly affected by IFFS-VI. At present, the theory and modeling tasks fall into the broad categories of

Interatomic Potentials, Defect Properties, Cascade Generation, Annealing Simulation and Comparison with Experiments. A more detailed breakdown of the tasks is indicated below. It is not anticipated that sufficient resources will exist for the completion of all the tasks within the remainder of the JUPITER collaboration. However, the task lists serves as an important instrument for focussing and integrating the activities of both sides.

1. Interatomic Potentials

    a) Design and evaluate interatomic potentials for V, Ti, Cr and their interactions among themselves and with He (and O?).

    b) Evaluate applicability and feasibility of Tight Binding molecular dynamics (MD) for defect simulations.

2. Defect Properties

    a.) Calculate properties of defects in vanadium

        i.) Formation energies, binding energies
            Vacancy clusters, loops ,SFT, voids
            SIA clusters, loops
        ii.) Migration energies, diffusivities
            Vacancies, vacancy clusters
            SIAs, SIA clusters, SIA loops

    b.) Determine alloy and impurity properties

        i.) Binding energies of Ti atoms to point defects and clusters
        ii.) Binding energies of Cr atoms to point defects and clusters

    c.) Simulate defect interactions

        i.) V point defect – dislocation interactions
        ii.) Loop – dislocation interactions
        iii.) Role of Ti, Cr near dislocations
        iv.) Oxide precipitate formation

    d.) Evaluate helium interactions

        i.) He diffusivity in V
        ii.) He binding energies to defects, impurities
        iii.) He at grain boundaries

3.. <u>Cascade Generation</u>

    a.)   Create data base of cascades in vanadium for relevant recoil energy spectra

    b.)   Examine effects of Ti and Cr alloying elements on defect production

    c.)   Examine effects of cascade overlap

4. <u>Monte Carlo and Analytical Simulations of Microstructural Evolution</u>

a.) Determine the fractions of surviving defects for individual cascades as a function of temperature and energy

b.) Simulate damage accumulation in bulk as a function of temperature and recoil spectrum

c.) Determine the effects of temperature variation on damage accumulation

d.) Examine the role of grain boundaries on damage accumulation and He accumulation

5. Comparison with Experiments

The Varying Temperature Irradiation Experiment in HFIR will subject test specimens to cyclic changes in temperature during irradiation. Each cycle will consist of 0.05 dpa at a lower temperature, followed by 0.45 dpa at a higher temperature. Ten temperature cycles are planned for each of two low-high temperature pairs (200-350 C and 300-500 C). TEM specimens and mini-tensile, -Charpy and -bend bar specimens will be irradiated. Materials include ferritic and austenitic steels, refractory alloys, copper alloys and vanadium alloys. The vanadium alloys include pure vanadium, binary and ternary alloys, as well as the V-4Cr-4Ti alloy that is the subject of IFFS-VI. Pure Fe, Cu, Mo and W are also included in the experiment matrix.

Prior to obtaining the results from repeated cycles in HFIR, several irradiations will be carried out in JMTR for conditions identical to one cycle of the HFIR Varying Temperature Irradiation Experiment.

Some irradiation effects data for vanadium, V-4Cr-4Ti and other vanadium alloys already exists, although effects of temperature variation are not included.

IFFS-VI Proposed Schedule

IFFS-VI was initiated as a two-year program, with a goal of predicting the outcome of the HFIR experiments, from which experimental data should be available starting in late 1999 or early 2000. Good progress toward this goal is expected to be made by building on existing models and using the experimental data that already exist for vanadium. Although there is a logical sequence of activities toward meeting the goal, many of the IFFS-VI tasks can be worked on simultaneously and at various levels of physical realism until all the pieces fit together with the requisite level of physical reality.

It is expected that many of the ongoing developments in theory and modeling of irradiation effects are directly relevant to IFFS-VI without being developed specifically for V-4Cr-4Ti or pure V or even bcc metals and alloys, especially developments of models dealing with defect accumulation and microstructure evolution. These models can be developed in a general way and made specific to V-4Cr-4Ti when cascade and defect property information for that material is available from MD simulations and first principles calculations.

Basic information that must be established early on includes interatomic potentials for pure V (some cascade simulations have been done using an embedded atom potential, see below) and for the V-impurity and V-4Cr-4Ti alloy element interactions. These potentials should be developed and tested before further atomistic calculations are performed.

)

Progress is to be shared informally through email, conference presentations, and postings on a potential Internet web site. Progress will be formally reviewed at a JUPITER collaboration workshop on theory and modeling, now scheduled to be held in conjunction with the ICFRM-9, October 10-15, in Colorado Springs.

IFFS-VI Progress in Theory, Modeling and Experiments

The following is a list of papers, presentations and work in progress on fundamental studies of radiation damage relevant to IFFS-VI objectives involving US and Japanese JUPITER participants:

The following papers, specifically on vanadium, are in the Proceedings of ICFRM-8, October 26-31, 1997, Sendai, Japan, Part C, J. Nucl. Mater., in press.

"Defect Cluster Formation in Vanadium Irradiated with Heavy Ions," N. Sekimura, Y. Shirao, H. Yamaguchi, S. Yonamine and Y. Arai.

"A Molecular Dynamics Simulation Study of Displacement Cascades in Vanadium," K: Morishita and T. Diaz de la Rubia.

The following papers, on vanadium and fundamental aspects of radiation damage in BCC metals, were presented at the International Workshop on Basic Aspects of Differences in Irradiation Effects between FCC, BCC and HCP Metals and Alloys, October 15-20, 1998, Cangas de Onis, Spain. The proceedings will be published in J. Nucl. Mater.

"Damage Evolution and Accumulation in Pure Vanadium," E. Alonso, T. Diaz de la Rubia and J.M. Perlado.

"Cascade Damage in FCC and BCC Metals, N. Sekimura.

"Modeling of Irradiation Damage Evolution in FCC and BCC Metals," T. Diaz de la Rubia and N. Soneda.

"Primary Defect Formation in BCC Iron: The Role of Cascade Energy and Temperature and Pre-existing Defects," R. Stoller.

"Atomistic Simulation of Self-interstitial Dislocation Loop Structure and Mobility in BCC Iron," B.D. Wirth, G.R. Odette and G.E. Lucas.

"Kinetic Monte Carlo Studies of the Effects of One-dimensional Glide on the Reaction Kinetics of Interstitial Clusters," H.L. Heinisch, B.N. Singh and S.I. Golubov.

"New Aspects of Void Formation in Neutron-irradiated Copper and Nickel at High Temperature," Y. Shimomura and I. Mukouda.

"Deformation and Fracture Mechanisms in Irradiated FCC and BCC Metals," S.J. Zinkle and G.E. Lucas.

"Computer Simulation of Fundamental Behaviors of Interstitial Clusters in Fe and Ni," E. Kuramoto.

"Three-dimensional Dislocation Dynamics for Computer Simulation of Localized Plastic Deformation," N.M. Ghoniem.

The following papers on vanadium were presented at Symposium N on Microstructural Processes in Irradiated Materials, at the Materials Research Society 1998 Fall Meeting, November 30-December 3, 1998, Boston, MA, USA. Papers will be published in the MRS Proceedings for this symposium.

"Dislocation Loops Interaction With Dislocations in Vanadium: An Atomistic Study with Flexible Boundary Conditions," E. Alonso, T Diaz de la Rubia and J.M. Perlado.

"Effects of Neutron Irradiation on Tensile Properties of V-Ti-Cr-Si Type Alloys with Helium Pre-existence," M. Satou and K. Abe.

A direct collaboration under JUPITER was established between Q. Xu and H.L. Heinisch during Dr. Xu's assignment at PNNL. Progress on their study of "The Effects of Temperature Variation on Defect Accumulation During Irradiation" using KMC simulations will be reported at ICFMR-9, October 10-15, 1999, Colorado Springs, CO, USA.

FUTURE WORK

Progress by the participants in IFFS-VI will be reviewed at the US/Japan JUPITER Workshop on Theory and Modeling to be held in conjunction with ICFRM-9.

SIMULATION OF DAMAGE EVOLUTION AND ACCUMULATION IN VANADIUM

E. Alonso, M.-J. Caturla, T. Díaz de la Rubia and J.M. Perlado[*]

Lawrence Livermore National Laboratory, P.O. Box 808,
Livermore, CA 94550, USA

[*]Instituto de Fusión Nuclear, José Gutiérrez Abascal, 2
E.T.S.I.I
28006 Madrid, Spain

Summary

Energetic atoms which have been knocked off their lattice sites by neutron or ion irradiation leave a trail of vacancies and interstitials in their wake. Most of these defects recombine or cluster within their own collision cascade. Some fraction, however, escape to become freely migrating defects (FMD) in the bulk of the material. The interaction of FMD with the microstructure has long been linked to changes in the macroscopic properties of materials under irradiation. We calculate the fraction of FMD in pure vanadium for a wide range of temperatures and primary knock-on atom (PKA) energies. The collision cascade database is obtained from molecular dynamics (MD) simulations with an embedded atom method (EAM) potential. The actual FMD calculation is carried out by a kinetic Monte Carlo (kMC) code with a set of parameters extracted either from the experimental literature or from MD simulations. We take two different approaches to the problem and compare them. The first consists of an idealized simulation for single cascades. Annealing each cascade at different temperatures allows the mobile species to escape and account for FMD. The second analyzes bulk diffusion and damage accumulation in a specimen irradiated at a low dose rate in the presence of impurities, in order to mimic experimental conditions. At the temperature studied, beginning of stage V, we observe that only vacancies are free to move whereas most interstitials are stopped by impurities. The fraction of FMD obtained is 11% for high purity vanadium, which is in good agreement with the figures reported in literature. We also analyze the role of impurities in damage accumulation.

Introduction

Vanadium-based alloys are of great technological importance for future fusion reactors [1]. Their low activation in a 14 MeV neutron environment make them the ideal candidates for the structural material of the reactor first wall. Thus it is imperative that we fully understand the production and accumulation of radiation damage in these alloys. We present a study of damage production and accumulation in pure vanadium in a first step towards addressing this issue. .

Radiation damage production and accumulation in solids can be divided into two stages. In the production stage, the impinging particle gradually gives off its kinetic energy to the atoms of the lattice in the form of energetic recoils. These recoils deposit their energy in the lattice by generating secondary and higher order recoils that result in a displacement collision cascade. The outcome of this stage, of the time scale of ps, is a population of point or clustered defects known as the primary state of damage. In the second stage, which can extend over seconds, defects that survive recombination within their nascent cascade migrate over long distances, interacting with the microstructure. These freely migrating defects (FMD) are responsible for the changes in the macroscopic properties of metals under irradiation, such as void swelling, embrittlement, radiation enhanced diffusion, etc.

Computer simulation efforts have been conducted in an attempt to model the two stages of radiation damage. Molecular dynamics (MD) simulations studies using many-

body potentials of the embedded atom method (EAM) type have proven to be very successful in the description of the first stage of damage production [2,3]. The modeling of the second stage has historically been undertaken by rate theory [4-6]. However, the application of kinetic Monte Carlo (kMC) simulations to diffusion processes [7,8] is starting to gain acceptance among the radiation damage community. The main strength of kMC stems from the fact that the highly inhomogeneous nature of the spatial and temporal damage distribution can be easily incorporated and treated. Moreover, features such as one-dimensional migration of small interstitial clusters can also be treated within the same model.

One quantity of fundamental interest for understanding radiation effects in solids is the fraction of FMD. This fraction has been obtained by different experimental methods in the literature. The main approach has been to analyze changes in macroscopic properties believed to depend on the FMD population and to interpret these changes in terms of rate equations. Measurements of radiation-enhanced diffusion [9-13], radiation-induced segregation [14-16], dislocation pinning [17], swelling rates [18], ordering rates [19] and electrical resistivity [20] have been used during the past twenty years to estimate this fraction.

We present a calculation of the fraction of FMD in vanadium obtained by coupling MD with kMC simulations. We compare our results with the experimental data reported in the literature. We carry out two kinds of calculation. In the first, a single cascade is annealed at various temperatures. This represents the dilute upper limit of the FMD fraction corresponding to very low dose irradiation conditions. The second is a simulation of damage accumulation at a fixed dose rate and temperature with varying impurity concentration. For the sake of argument the impurities will be considered to be traps of infinite strength for interstitials and transparent to vacancies. The role of impurities will be analyzed in terms of FMD population and damage accumulation behavior.

Cascade simulations and defect production

We simulate the primary state of damage by MD simulations. In order to obtain reliable statistics a significant number of cascades has to be produced for each energy. The details of these simulations are shown in table 1. All MD simulations were performed using the MDCASK code either in its parallel or serial version. All the collision cascades were simulated at room temperature (300 K). Since little influence of the irradiation temperature on defect production has been observed [2,21,22], the defect configurations so generated were used along the entire temperature range investigated by kMC. The temperature was controlled by connecting the MD box to a thermal bath applying Langevin dynamics [23] to the two outer layers of atoms. The atomic interactions were described by the Johnson and Oh
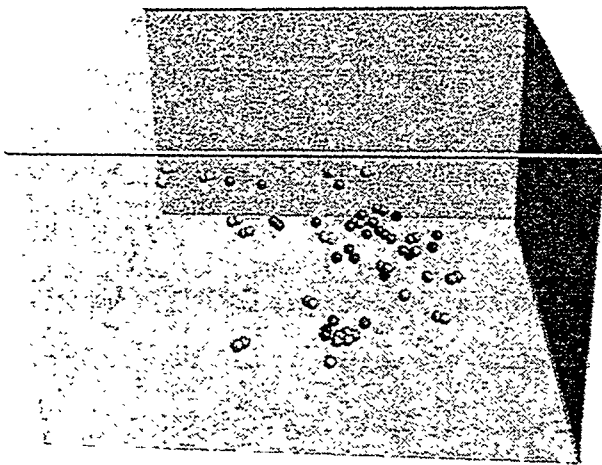
Figure 1. State of damage generated by a 10 keV PKA at 300K. The light points represent self-interstitial atoms and the dark ones vacancies. The defect population is stable 15 ps after the PKA entrance. No clusters larger than size 4 are formed.

EAM potential [24]. The short range interaction part was smoothly splined to the universal potential of Biersack and Ziegler [25]. Previous studies with this potential have accurately reproduced the melting point and the displacement threshold energies [26].
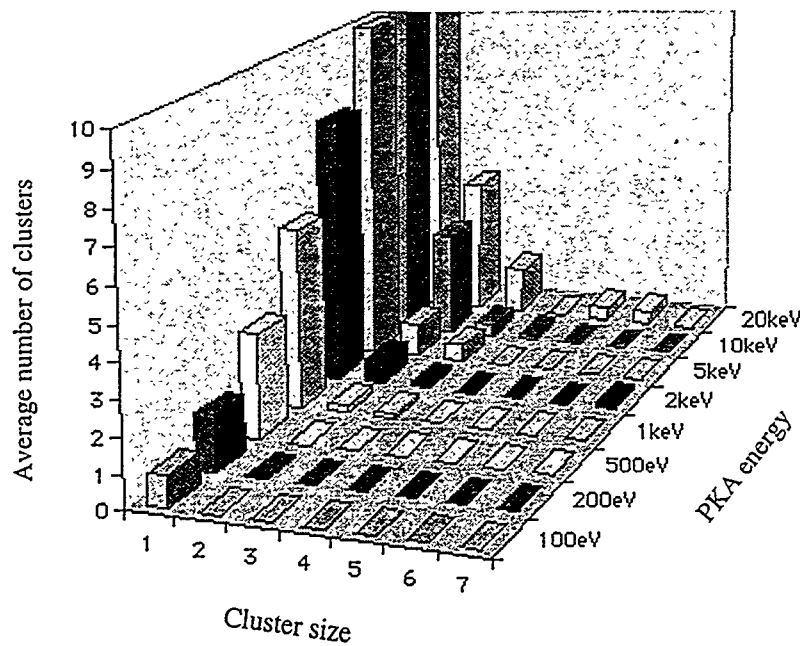
Figure 2. Average number of intersititial clusters as a function of size and PKA energy. The low clustering tendency is the same for vacancy clusters (Not shown in figure).

Due to the open character of the bcc structure, channeling occurred in most of the high energy cascades. Simulations in which channeling caused a cascade to cross the boundaries of the simulation box were eliminated. Only three of the 20 keV cascades were completed out of more than ten started. The simulations were continued until the number of defects reached a stable population. The high melting point of vanadium confines the thermal spike associated with the cascade to a small region that cools down quickly. Figure 1 shows the configuration of the damage produced by a 10 keV recoil after 15 ps. The light points correspond to self-interstitial atoms and the dark ones to vacancies. Although vacancies occupy the central part and SIAs the periphery, the trend is not so obvious as in fcc metals. The defects are spread over the simulation box mostly as point defects. Only small interstitial and vacancy clusters are formed during this stage.

Table 1: Computational box size and number of simulations for each recoil energy.

Energy (eV)	Box size (lat units)	no. of atoms	no. of cascades
20000	80x80x80	1024000	3
10000	50x50x50	250000	6
5000	45x45x45	182250	4
2000	45x45x45	182250	7
1000	30x30x30	54000	9
500	25x25x25	31250	15
200	25x25x25	31250	15
100	25x25x25	31250	15

An important result of these simulations is the low interstitial and vacancy clustering observed. We consider a defect cluster to be any group of defects in which each of its members has at least one of the other elements of the cluster in a first nearest neighbor position. Figure 2 shows the interstitial cluster distribution as a function of recoil energy and cluster size. The largest cluster obtained was of 7 units in a 2 keV cascade. Except for this cluster, no clusters greater than 3 were observed in cascades below 10 keV. This low clustering is in good agreement with previous MD simulations in bcc metals [21,22,26-28].

Another result of these simulations is the effectiveness of the thermal spike in repairing damage, in contrast to the predictions of a purely ballistic model [29]. Figure 3 depicts the efficiency of the ballistic NRT model to describe damage production. The collisional models break down at high energies because of the local melting of the material [30,31] and the damage production saturates at high energies due to subcascade formation.

The efficiency value obtained at high energy recoils is 26%, in good agreement with previous work in bcc [21,22,27,28].

Kinetic Monte Carlo simulations

In order to extend the time scale of the simulation we couple the MD output to a kMC code. The kMC simulations were performed with the BigMac code written by Mark

PKA energy(eV)

Johnson at LLNL. The details of its operation are described elsewhere [32]. The input needed for the code is the primary state of damage obtained from MD, the diffusivities of the single and clustered defects, and the binding energies of the defect clusters. The input parameters of the model are shown in table 2. All vacancy clusters are assumed to be immobile. The binding energy of vacancy clusters was computed by MD. The formation energy of different cluster configurations was calculated up to size 6

Figure 3. Efficiency of the NRT model as a function of PKA energy. The small drop from 5 keV (34%) to 20 keV (26%) indicates that the NRT efficiency is close to saturation.

minimizing the energy by a quasi-newton method [33]. A fit of this curve was made to determine the binding energy as a

function of cluster size for larger clusters. The main assumption was that the most stable configuration of large vacancy clusters is purely spherical. Although in pure metals a void will collapse to form a faulted dislocation loop, the presence of helium stabilizes spherical voids. Therefore the assumption should hold for vanadium, a material with high impurity content and in a helium producing environment. Thus another point of the curve could be computed for a better fit at large sizes. One perfectly spherical void containing more than

Table 2: Input diffusivities for kMC and reference.

	D(cm²/s)	E_m(eV)	Reference
I	1.0e-03	0.03	[28]
I2	7.5e-05	0.067	[28]
I3-I19	1.4e-04	0.17	[28].
V	1.0e-03	0.7	[37]

100 atoms was relaxed and its formation energy calculated. As expected under this assumption, the best fit of the formation energy as a function of cluster size is close to a power of (2/3).

The interstitial cluster diffusivities and binding energies are those calculated by Naoki Soneda for iron with the Johnson&Oh potential [26]. Iron and vanadium have a number of important similarities: the same type of lattice and proximity in the periodic table. Moreover, within the context of these calculations both metals are described by the same type of interatomic potential. This factor in particular led us to presume that a detailed study of cluster binding energies and cluster diffusivities in

vanadium would yield similar numbers to those of iron. Single-interstitials and interstitial clusters of sizes up to 3 were allowed to migrate three-dimensionally. Interstitial clusters of sizes between 4 and 19 were constrained to one-dimensional migration (glissile) and larger clusters were considered to be sessile.

Freely migrating defects from single cascades

FMD are those defects that escape recombination within their collision cascade. In such a case, the outgoing flux of defects through a spherical surface centered at the cascade and of sufficient radius will account for those defects that are highly unlikely to undergo recombination.

Obviously this definition is sensitive to the radius of the sphere, the simulation time and the temperature. In a real irradiation experiment cascade overlapping occurs, so it is reasonable to set a simulation time slightly lower than the time for cascade overlapping for a given dose rate. Since the simulation time is fixed by the dose rate and the

Figure 4. Escape ratio of interstitials as a function of recoil energy and annealing temperature. Mobile interstitial clusters are also inclusded in the escape ratio. Observe that the escape ratio decreases with increasing recoil energies.

temperature is another physical magnitude, the only parameter of our model that can affect the FMD so calculated is the sphere radius. Due to the details of the kMC code, the simulation box is cubic. We compute the fraction of FMD as a function of temperature and recoil energy and analyze the sensitivity of the model to the kMC box size.

The simulation details are as follows. We anneal the primary state of damage obtained in each of the cascades of our database in a kMC box of 100 nm edge. Each of the defects that leave the box are flagged as FMD and removed from the simulation. The simulation time is set to 1000 s which is equivalent to a dose rate of 10^{-9} $s^{-1}cm^{-2}$ in a 100 nm box. In order to improve the statistical validity of the simulation, the calculation was repeated for 100 different random number sequences for each cascade. The same procedure was followed over the temperature range from 150 K to 750 K. The fraction of freely migrating interstitials is displayed in figure 4 as a function of annealing temperature and PKA energy and the fraction of freely migrating vacancies in figure 5. The values shown are averaged over all the cascades available for each recoil energy.

As was shown in the previous section, the largest interstitial cluster found is of size 7, which is still mobile under our assumption. The high mobility of these clusters causes them all to leave the box over the entire range of temperatures investigated, as seen in figure 4. Another interesting feature of this simulation is the correlation between recoil energy and escape ratio. The higher the PKA energy, the more defects produced, therefore the higher the probability for those defects to recombine and the lower the escape ratio. This observation is in contrast to similar work on other metals in which the opposite or no dependence were seen [34]. The type of lattice may play an important role in this difference. In the referenced study, the material analyzed was gold, an fcc metal. In fcc metals big dislocation loops are formed after the collision cascade and the vacancy rich core is clearly separated from the interstitials in the periphery.

The picture is considerably different for vacancies as shown in figure 5. The low diffusivity of the single vacancy means its motion is not noticeable until temperatures of about 270 K, which is 100 degrees above the experimental temperature of stage III in this metal [35]. Stage III temperature is determined by the migration energy of the single vacancy. Unfortunately, the high impurity content

Figure 5. Escape ratio of vacancies as a function of recoil energy and annealing temperature. The second step corresponding to stage V starts to be visible at PKA energies of more than 1 keV.

of vanadium reflects in wide disagreements over the experimental temperatures of the annealing stages. Moreover, the annealing stages are more tied to impurity migration phenomena than to vacancy migration [36]. These factors led us to use the migration energy calculated by Bacon et al. [37] in the input parameters. Its value of 0.7 eV seems like a good compromise given that experiments report values from 0.5 eV to 1.2 eV [35]. Therefore, the 100 degree shift of stage III is a direct consequence of our vacancy migration energy choice. For low energy recoils that is the only feature of the curve due to the absence of immobile vacancy clusters. At high PKA energies only the single vacancies have escaped after stage III has been reached, but small vacancy clusters still remain in the box. Only when the temperature is high enough for those clusters to break up and emit single vacancies can all the defects escape the box. This happens in stage V, which occurs at the second step located at 550K in the curves corresponding to the 5keV, 10keV and 20 keV recoils. Once again, this temperature is 100 degrees above the experimental one [36].

The main conclusion of this study is that no production bias of vacancies occurs at any of the temperatures simulated. The fraction of FMD obtained for 20 keV recoils is 17%

after normalizing by the NRT model. This number is in the same line of previous computer simulations of metals [28,34,38].

The sensitivity of the FMD to the kMC box size was studied. The same simulation was performed for one of the 20keV cascades, varying the edge of the simulation box from 50 nm to 200 nm. No appreciable difference in the number of FMD was found. The only difference observed was at the stage III transition temperature. In that temperature regime, the motion of single-vacancies is extremely low and the box size may slightly shift the transition temperature. Some slowly moving vacancies escaped from the small boxes while they did not have enough time in the big ones. This effect is completely negligible.

Damage accumulation

The simulation of the previous section is purely ideal and no experiment would ever measure that FMD concentration. The interaction of newly produced point defects with the damage from previous cascades will dramatically lower that figure. In an attempt to calculate the fraction of FMD in a more realistic fashion we perform the following damage accumulation simulation:

- Dose rate of 10^{-4} dpa/s in a kMC box of 200 nm edge.
- Periodic boundary conditions along the three coordinate axes.

- Flat recoil spectrum of 20 keV. The fraction of FMD represented by η is calculated as follows:

$$\eta = \frac{N_{FMD}}{NRT} \tag{1}$$

The fraction of FMD so calculated is independent of recoil energy once the NRT model efficiency is constant. Figure 3 shows that the efficiency is already constant at 20 keV. Therefore, the results are directly comparable to experiments of neutron or heavy ions irradiation.

- Temperature of 650K, well above the transition temperature for stage V where vacancies clusters become unstable.
- Two spherical sinks with a capture radius of 1.5 nm, both for interstitial and vacancies. These long range sinks play a role similar to that of dislocations. Assuming an effective length for the dislocation of the order of the kMC box the dislocation density is $5 \cdot 10^9$ dis/cm^2.
- Presence of interstitial traps.

The traps can be likened to generic impurities. They are immobile, which reproduces a stable population of impurities once steady-state is reached. They are transparent to vacancies but form a tightly bound complex with single-interstitials. In other words, they are sinks of infinite strength for single-interstitials. Once the impurity-interstitial complex is formed, the arrival of new interstitials can make it grow but it will always remain infinitely bound. The only way such complexes can shrink is by the arrival of diffusing vacancies.

In a simulation of this sort, the number of FMD equals the number of mobile species immediately before the introduction of a new collision cascade and subsequent defect overlap. The population of mobile species will drop noticeably after several cascades. More defects will be available for recombination and a steady count of FMD will be reached. The fraction of FMD will be this steady-state value over the number of defects produced by the recoil energy analyzed according to the NRT model.

The absence of detrapping will have a negligible effect on the fraction of FMD. On the other hand, its influence on the damage accumulation will not allow us to establish quantitative comparisons with experiments. The no-detrapping feature speeds up the simulation driving the system towards the saturation of the damage at low doses. Despite this mismatch between damage and dose, qualitative conclusions can be drawn since the overall trend is preserved.

We repeat the calculation for two different impurity concentrations: 5 ppm and 100 ppm. In this way we can single out the role of impurities both on the fraction of FMD and on the damage accumulation. The simulation with 5 ppm is clearly more representative of a high purity sample used by experimentalists.

Figures 6 and 7 show how the damage accumulation occurs in both simulations. Damage saturation is quickly reached at about 10^{-3} dpa in the high purity case. The cluster density in the 100 ppm case keeps increasing linearly at the same dose. These curves are not quantitatively comparable to experiments, not only for the lack of detrapping previously mentioned, but also due to the small size of the clusters in the simulation. As will be explained later, none of the clusters in the simulation should be visible in the microscope.

Dose (dpa)
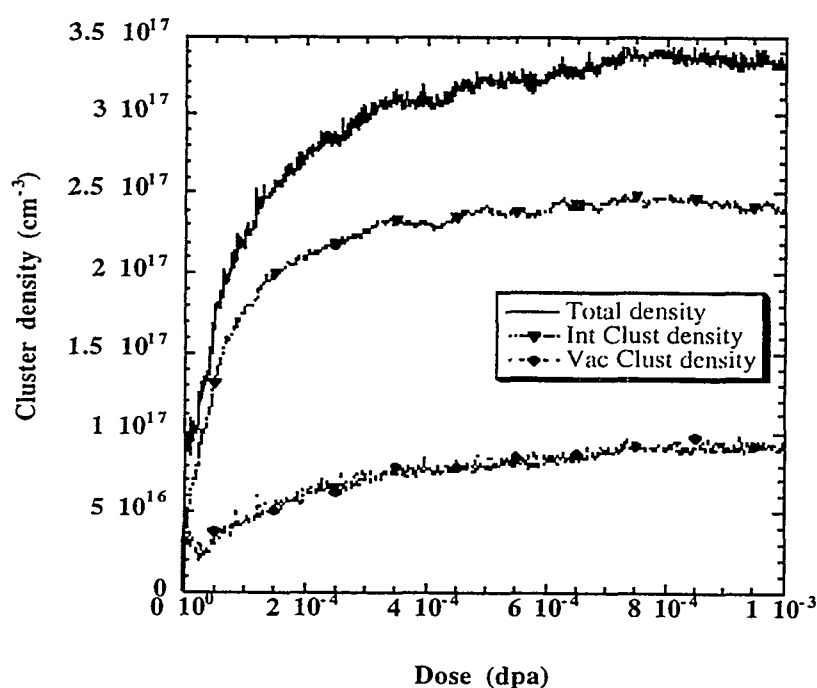
Figure 6. Interstitial and vacancy cluster density as a function of dose for vanadium with 5 ppm impurity content. All the interstial clusters represented are trapped at the impurities. The number of free interstitial clusters is negligible.

The different behavior of the two simulations is easy to explain in terms of occupied trapping sites and free defects available. Only when the vast majority of the interstitial traps have captured at least one interstitial, can cluster growth be expected. Once this trap saturation is reached the cluster density growth drops departing from linear behavior and the growth of the already existing clusters takes place.

Evidently, in the high purity case, the lower concentration of trap sites and consequent faster saturation of them leads to a saturation of the damage faster than in the low purity case. The number of trap sites not only affects the damage accumulation behavior, but also the number of freely migrating defects. Most of the cascade produced interstitials are promptly captured by impurities leaving a population of freely migrating interstitials close to zero. In any case, the dependence of this rather small number of freely migrating interstitials on the number of traps is beyond all doubt. The trap concentration plays its role on the number of freely migrating vacancies also. Although trapping sites are transparent to vacancies, saturated traps are an effective sink for them. This dependence is shown in figures 8 and 9. As seen in figure 8, the average of the population of single vacancies in the

instant before the next recoil entrance is 20 in the case of 5 ppm of impurities. This average is obtained only over the points of the curve with a steady population of free vacancies. Normalizing by the NRT collisional model we obtain a fraction of freely migrating vacancies of 11%. In the low purity case of figure 9, the number of freely migrating vacancies is 4, 2.2% of the defects predicted by the NRT model. These numbers are in line with previous experimental and computer simulation results and display the strong dependence of the fraction of FMD and the concentration of impurities[13,28,34,38]. Due to the greater effectiveness of the traps at capturing interstitials, the fraction of freely migrating interstitials is much lower than the fraction of freely migrating vacancies for the two impurity concentrations. In the case of 5 ppm, the fraction of freely migrating interstitials is 1% and for 100 ppm an almost negligible 0.07%. Very likely, the presence of vacancy traps would sway these figures towards more balanced numbers both for freely migrating vacancies and interstitials. Nonetheless, the imbalance of the two populations of FMD shows the influence of the type of impurity on the fraction of FMD.

Dose (dpa)

Figures 10 and 11 show the cluster size distribution function at two different doses for the 5 ppm case. At 10^{-3} dpa, a clear change in the shape of the curve is observed. A shift toward higher cluster sizes is shown in figure 11. Since TEM resolution is of the order of nanometers, only clusters over size 40 are visible. Since the largest clusters are of size 27, none of the clusters in our simulation would be visible in the microscope, as pointed out in the

Figure 7. Interstitial and vacancy cluster density as a function of dose in vanadium with 100 ppm impurity content. The damage has not saturated at 10^{-3} dpa because not all the trapping sites have been taken.

beginning of this section. In the case of the simulation with 100 ppm, since at 10^{-3} dpa the damage accumulation is still in the linear regime, no cluster growth has occurred. The distribution function is not displayed in this case, because no significant changes in the form of the curve can be seen in the dose range analyzed.

Conclusions

We have presented an extensive study of damage accumulation in Vanadium that couples MD to simulate damage production and kMC to reproduce damage evolution. The collision cascades showed the expected low clustering behavior of bcc metals. However, the defect production obtained is lower than in the 5 keV cascades at 10K reported by Morishita et al. [26]. The production of self-interstitial atoms (SIA) drops from 18 at 10K to 12 at 300K, which implies a 33% decrease.

Figure 8. Number of freely migrating vacancies as a function of dose in vanadium with 5 ppm impurity content. The average number is 20.

We calculated the fraction of FMD by two different approaches and compared both results. The first one is comparable to an infinitely small dose rate in a perfectly pure material. The second one consists of the simulation of low dose rate irradiation conditions in two different materials: one of high and another of low purity. The main difference detected is the imbalance in the number of freely migrating interstitials and freely migrating vacancies in the two cases with impurities. This disproportion is the result of the biased nature of the trapping sites. Therefore, different types of imbalances can be expected for different kinds of impurities. The absence of impurities evens out this imbalance as seen in the single-cascade simulation. There is a strong correlation between the impurity content and the fraction of FMD. For vacancies, this fraction is 17% in the pure case, drops down to 11% for only 5 ppm of interstitial-trapping impurities and decreases to 2.2% for 100 ppm. We

Figure 9. Number of freely migrating vacancies as a funcion of dose in vanadium with 100 ppm impurity content. The average number is 4 vacancies.
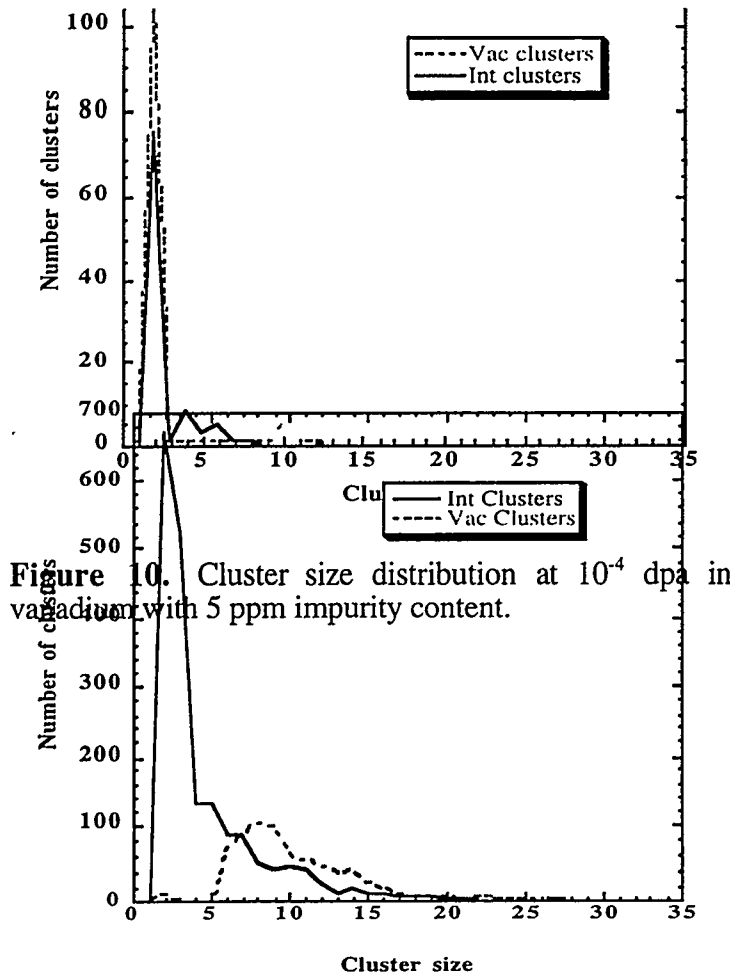
Figure 10. Cluster size distribution at 10^{-4} dpa in vanadium with 5 ppm impurity content.

Figure 11. Cluster size distribution at 10^{-3} dpa in vanadium with 5 ppm impurity content. Cluster growth has taken place after the trap sites have been saturated.

believe the damage accumulation simulation is the most valid method to compute the fraction of FMD.

We also analyze the role of impurities in the damage accumulation process. In spite of the impossibility of establishing direct comparison with experiments, qualitative conclusions can be drawn. The existence of impurities clearly increases the dose required to achieve the saturation of the damage. This saturation is reached in a state in which defect production and recombination are perfectly balanced. Until most of the trapping sites are taken, the trapping contribution is too high to allow equilibrium. Thus, the higher the content of impurities, the later the material will reach the steady state of damage.

In order to get a deeper insight into these phenomena and to reproduce experimental conditions in a more realistic manner, work is underway to include the effect of detrapping, real impurities and alloying elements. Additional work is underway to model the behavior of V-Ti-Cr alloys and to investigate radiation induced hardening and void swelling in these materials.

References

[1] H.M. Chung, B.A. Loomis, D.L. Smith, J. Nucl. Mater. **239** (1996) 139.
[2] D.J. Bacon, T. Díaz de la Rubia, J. Nucl. Mater. **216** (1994) 275.
[3] R.S. Averback, J. Nucl. Mater. **216** (1994) 49.
[4] R. Bullough, Proc. Conf. on Dislocations and Properties of Real Materials, Royal Society, London (The Institute of Metals, London, 1985) p. 382.
[5] H. Trinkaus, B.N. Singh, A.J.E. Foreman, J. Nucl. Mater. **249** (1997) 91.
[6] C.H. Woo, B.N. Singh, A.A. Semenov, J. Nucl. Mater. **239** (1996) 7.
[7] D.G. Doran, Rad. Effects 2 (1970) 249.

[8] H. L. Heinisch, J. Nucl. Mater. **117** (1983) 46.

[9] A. Müller, V. Naundorf, M.-P. Macht, J. Appl. Phys. **64** (1988) 3445

[10] V. Naundorf, M.-P. Macht, H. Wollenberger, J. Nucl. Mater. **186** (1992) 227.

[11] A. Iwase, L.E. Rehn, P.M. Baldo, L. Funk, Appl. Phys. Lett. **67** (1995) 229.

[12] P. Fielitz, M.-P. Macht, V. Naundorf, H. Wollenberger, Appl. Phys. Lett. **69** (1996) 331.

[13] P. Fielitz, M.-P. Macht, V. Naundorf, H. Wollenberger, Z. Metallkd. **87** (1996) 439.

[14] L.E. Rehn. P.R. Okamoto, R.S. Averback, Phys. Rev. B **30** (1984) 3073.

[15] T. Hashimoto, L.E. Rehn, P.R. Okamoto, Phys. Rev. B **38** (1988) 12865.

[16] R.A. Erck, L.E. Rehn, J. Nucl. Mater. **168** (1989) 208.

[17] J.A. Goldstone, D.M. Parkin, H.M. Simpson, J. Appl. Phys. **53** (1982) 4189.

[18] S.J. Zinkle, B.N. Singh, J. Nucl. Mater. **199** (1993) 173.

[19] M.A. Kirk, T.H. Blewitt. Metall. Trans. **9** (1978) 1729.

[20] S.J. Zinkle, J. Nucl. Mater. **155-157** (1988) 1201-1204.

[21] D.J. Bacon, A.F. Calder, F. Gao, V.G. Kapinos, S.J. Wooding, Nucl. Inst. and Meth. in Phys. Res. B, **102** (1995) 37.

[22] R.E. Stoller, J. Nucl. Mater. **233-237** (1996) 999.

[23] R. Biswas, D.R. Hamann, Phys. Rev. B **34** (1986) 895

[24] R.A. Johnson, D.J. Oh. J. Mater. Res. **4** (1989) 1195.

[25] W.D. Wilson, L.G. Haggmark, J.P. Biersack, Phys. Rev. B **15** (1977) 2458

[26] K. Morishita, T. Díaz de la Rubia, Mat. Res. Soc. Symp. Proc. **396** (1996) 39.

[27] W.J. Phythian, R.E. Stoller, A.J.E. Foreman, A.F. Calder, D.J. Bacon, J. Nucl. Mater. **223** (1995) 245.

[28] N. Soneda, T Díaz de la Rubia, Phil Mag A **78** N-5 (1998) 995.

[29] M.J. Norgett, M.T. Robinson, I.M. Torrens, Nucl. Eng. Design **33** (1975) 50.

[30] F. Seitz, J.S. Koehler, in: Solid State Phys, eds. F. Seitz and D. Turnbull (Academic, New York, 1956), Vol 2.

[31] T. Diaz de la Rubia, R.S. Averback, R. Benedek, W.E. King, Phys. Rev. Lett. **59** (1987) 1930.

[32] M.D. Johnson, M.-J Caturla, T. Díaz de la Rubia, J. Appl. Phys. **84** (1998) 1963.

[33] J.B. Gibson, A.N. Goland, M. Milgram, G.H. Vineyard, Phys. Rev. **120** (1960) 1229.

[34] T.Díaz de la Rubia, N. Soneda, M.J. Caturla, E. Alonso, J. Nucl. Mater. **251** (1997) 13.

[35] H. Schultz, Landolt-Börnstein New Series III/25 (1991) 115.

[36] T. Leguey, R. Pareja, E.R. Hodgson, J. Nucl. Mater. **231** (1996) 191.

[37] D.J. Bacon, J.M. Harder, J. Nucl. Mater. **155-157** (1988) 1254.

[38] H.L. Heinisch, Rad. Eff. Def. Sol. **113** (1990) 53.

KINETIC MONTE CARLO STUDIES OF THE EFFECTS OF ONE-DIMENSIONAL GLIDE
ON THE REACTION KINETICS OF INTERSTITIAL CLUSTERS - H.L. Heinisch (Pacific
Northwest National Laboratory*), B.N. Singh (Risø National Laboratory, Denmark) and S.I.
Golubov (Institute of Physics and Power Engineering, Russia)

(Summary of a paper presented at the International Workshop on Basic Aspects of
Differences in Irradiation Effects between FCC, BCC and HCP Metals and Alloys, Cangas
de Onis, Spain, October 15-20, 1998. The paper will appear in the workshop proceedings in
J. Nucl. Mater.)

EXTENDED ABSTRACT

A comparison of the available experimental results on cluster density and void swelling
clearly demonstrates that there are very significant differences in the defect accumulation
behavior between fcc and bcc metals irradiated under cascade damage conditions over a
wide temperature range [1]. In an attempt to understand the mechanisms responsible for
causing these large differences in the swelling behavior between fcc and bcc metals,
Golubov, Singh and Trinkaus [2] have analyzed the experimental results on void swelling
within the framework of the production bias model (PBM) with the assumption of one-
dimensional (1-D) diffusional transport of self-interstitial atom (SIA) clusters. Molecular
dynamics (MD) studies have demonstrated that the structure, stability, and the fraction of
glissile SIA clusters (migrating one-dimensionally) that are produced in cascades in bcc iron
are different from that in fcc copper [3,4].

The concept of "pure" 1-D diffusional transport implies that the gliding SIA clusters
(essentially small glissile dislocation loops) are assumed to maintain the same Burgers
vector throughout their lifetime (until they interact with a sink). It was found that
incorporating the assumption of pure 1-D diffusional transport of SIA clusters into the PBM
does not provide an adequate explanation for the observed large differences in the swelling
behavior between fcc and bcc metals [2]. Rather, Golubov et al. [2] have proposed that the
treatment of the damage accumulation in the PBM should include the effects of changes in
the Burgers vector of SIA clusters during their 1-D diffusional transport. MD simulation
studies have shown that such changes can occur either by thermal activation [5,6] or by
interaction with another SIA cluster [7]. The net effect of this kind of migration is a defect
migration path that is 3-D but consists of segments of 1-D random walks. The reaction
kinetics of this mixed 1-D/3-D type of migration will depend on the average length of 1-D
segments relative to the size and concentration of other defects and microstructural features
the SIAs can interact with.

Unfortunately, at present, there exists no mathematical description of the reaction kinetics for
1-D glide with random Burgers vector changes. Some guidance can be found from earlier
work by Gösele and Seeger [8], who analytically described the reaction kinetics of single
crowdions involved in defect recovery during annealing experiments. Their work
demonstrated that even a very small deviation from the pure 1-D diffusion (which in their
case involved infrequent jumps of crowdions from one row of atoms to another, continuing in
the same direction in "preferentially " 1-D migration) leads to a decisive change in the
reaction kinetics. While this conclusion has been taken to be the central argument in the
treatment of defect accumulation and void lattice formation in fcc and bcc metals by Golubov

et al. [2], there still remains the difficulty of analytically describing the effects of random Burgers vector changes and mixed 1-D/3-D migration.

In order to gain insight on these processes, we began investigating the changes in reaction kinetics as a function of changes in the Burgers vector of one-dimensionally diffusing SIA clusters, and the size and density of randomly or periodically distributed sinks using kinetic Monte Carlo simulations.

When the frequency of changes in the Burgers vector is so high that the mean transport distance between Burgers vector changes becomes of the order of the lattice parameter of the crystal, the reaction kinetics under these conditions can be assumed to be the same as in the case of "pure" 3-D diffusional transport. Thus, the Monte Carlo simulations are used to study the reaction kinetics of the two limiting cases of "pure" 1-D (i.e. when there is no change in Burgers vector) and "pure" 3-D diffusional transport, as well as when the diffusional transport occurs as a mixture of 1-D and 3-D.

Empirical computational studies of the effects of scale and Burgers vector change were performed using a simple kinetic Monte Carlo computer code, following the basic concepts of the ALSOME kinetic Monte Carlo code used for annealing studies of cascades [9] and simulations of defect accumulation under irradiation.[10]   Studies were performed to determine the effects on absorption of defects into a static array of unsaturable absorbers as a function of the number of jumps N between direction changes, varying from N=0 for "pure" 3-D migration with equally probable jumps along any of the twelve <110> directions to N=∞ for pure 1-D migration. These were done for different absorber sizes and concentrations, and were plotted in terms of the average distance between direction changes, $L = a \, (N/2)^{1/2}$, where a is the FCC lattice parameter.
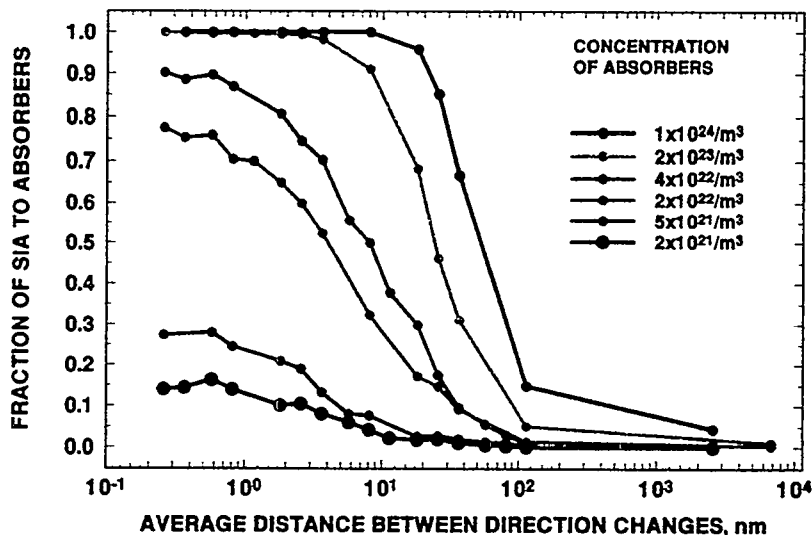
Figure 1. The fractions of mobile SIAs absorbed by a periodic array of absorbers of radius 0.9 nm as a function of the average distance traveled between direction changes for various concentrations.

As an example, Figure 1 shows the fraction of defects absorbed as a function of L for six different levels of concentration of a periodic array of absorbers of radius R=0.9 nm. Every data point represents the average value for the individual trajectories of 1000 mobile defects, initiated one at a time at random positions and with randomly chosen initial migration directions within the computational cell. When the probability of meeting an absorber increases at higher concentration, the transition from 1-D to 3-D behavior as a function of L becomes much sharper. This illustrates how defect reaction kinetics in a global sense will change differently during defect accumulation, depending on the value of L.
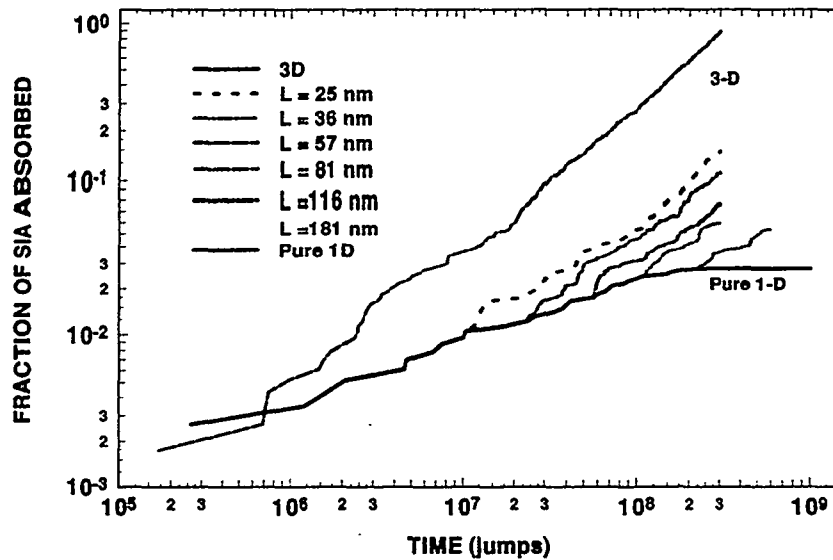
Figure 2. The fraction of 1000 initial SIAs absorbed in a random array of absorbers as a function of time (in units of defect jumps) for various values of L, the average distance between direction changes

In another example, Fig. 2 shows results of a simulation of recovery (or decay of a defect population) as a function of time. In this case 1000 mobile SIAs were placed randomly in a cell containing a random array of stationary absorbers. The SIAs did not interact with each other. Figure 2 shows the number of mobile SIAs absorbed in the absorbers as a function of time, which is measured in units of defect jumps, for runs using various values of L and the same set of random numbers. The upper curve is for 3-D migration with L=a/√2, and it shows essentially linear absorption with time. The lower curve is for pure 1-D (L=∞), and it tends toward a saturation value reflecting the finite size of the cell. In every intermediate case, there is a transition from 1-D behavior to near 3-D behavior once the defects have migrated distances comparable to the distances between direction changes. In all cases here about 3% or less of the defects are absorbed under pure 1-D kinetics; significant absorption occurs only in the regime where the defects display near 3-D kinetics.

Figure 2 illustrates that even if the distance L between direction changes is large, there is a regime in which 3-D reaction kinetics takes place. The importance of the onset of 3-D behavior is directly related to the scale, relative to L, of the microstructural features with which the SIAs can interact.

Future work will aim at further elucidating the ramifications of mixed 1-D/3-D migration on defect reaction kinetics through additional kinetic Monte Carlo simulations and incorporating them analytically into the PBM.

ACKNOWLEDGEMENTS

REFERENCES

1. B.N. Singh and J.H. Evans, J. Nucl. Mater. 226 (1995) 277.

2. S.I. Golubov, B.N. Singh and H. Trinkaus, submitted to J. Nucl. Mater.

3. Yu. N. Osetsky, V. Priego, A. Serra, B.N. Singh and S.I. Golubov, Philos. Mag. A, in press.

4. Yu. N. Osetsky, V. Priego, A. Serra, B.N. Singh and S.I. Golubov, submitted to Phil. Mag. A.

5. N. Soneda and T. Diaz de la Rubia, Philos. Mag., in press.

6. G. Gao, D.J. Bacon and Yu. N. Osetsky, submitted to J. Nucl. Mater.

7. Yu. N. Osetsky, V. Priego and A. Serra, submitted to J. Nucl. Mater.

8. U. Gösele and A. Seeger, Phil. Mag. 34 (1976) 177.

9. H.L. Heinisch and B.N. Singh, J. Nucl. Mater. 251 (1997) 77.

10. H.L. Heinisch and B.N. Singh, J. Nucl. Mater. in press.

9.0   DOSIMETRY, DAMAGE PARAMETERS, AND ACTIVATION CALCULATIONS

No contributions.

10.0 MATERIALS ENGINEERING AND DESIGN REQUIREMENTS

MATERIALS INPUT FOR THE ARIES-ST DESIGN PROGRAM*

M. C. Billone (Argonne National Laboratory)

SUMMARY

The ARIES-ST design incorporates a number of materials for which data and design criteria are required. The materials input includes the present status of the materials database, as well as progress in fabrication techniques and materials development which can be reasonably achieved over the next 25-50 years. During the past year, input was provided for the copper alloys considered for the electrically-conducting center post, the aluminum alloys proposed for the toroidal field return outer shell, the ferritic steels (low-activation and ODS) to be used as first-wall and blanket structural material, the compatibility between the slow-flowing Pb-Li breeder and the SiC thermal barrier and the ferritic steel structural material, and the tungsten selected for both the plasma-facing divertor material and the divertor coolant pipes. Some guidance was also provided with regard to fabrication and joining techniques. The level of detail provided with regard to the database and design guidelines for the various components depended on the functional importance of the component and the status of the database.

PROGRESS AND STATUS

Introduction

The ARIES Team has completed its design of the ARIES-ST spherical tokamak reactor as part of its latest power plant study. Final presentations and documentation are due at the January 28-29, 1999 ARIES Team meeting at UCSD in San Diego. Detailed information regarding design parameters, operating conditions, and material properties can be found at the public web site http://aries.ucsd.edu/PUBLIC/ by clicking sequentially on "Design Study Descriptions", "ARIES-ST", and "Engineering Design Book".

Throughout the course of the ARIES-ST design study, questions about materials performance and limits have arisen which required input from the Fusion Materials Program, as well as design criteria work performed for ITER. Documents such as the ITER Material Properties Handbook (IMPH) and the ITER Interim Structural Design Criteria (IISDC), as well as material properties summaries written for APEX have been used to resole some of these questions. On-going research efforts, such as those published in these Semiannuals, in summaries of IEA meetings and in proceedings of materials conferences (e.g., ICFRMs), have also been communicated from the Fusion Materials Program to the ARIES-ST Design Team. This author has served as the interface between the materials and design programs to facilitate communication and exchange. In particular, both material properties and materials performance evaluations have been communicated to the ARIES Design Team. In addition, design limits have been established based on the material databases.

The particular materials of interest to the ARIES-ST Design Team are: DS and PH copper alloys for the toroidal field (TF) center post, weldable aluminum alloys for the TF outer shell (which also serves as the vacuum vessel), low-activation ferritic steels (FSs) for the first-wall and blanket structural material, low-thermal-conductivity SiC or SiC/SiC composites for the thermal insulation between the FS and the hot Pb-Li breeder material, and tungsten for the divertor coolant tubes, which also serve as the plasma-facing component.

Results

The ARIES-ST Design Team selected a DS copper alloy (AL-15) as its primary candidate for the center post, with a PH alloy (Cu-Cr-Zr) as an alternate material. The operating temperature range for this water-cooled structure is 30-115°C. The selection was made early in the design process. Since then, two factors have emerged which may make Cu-Cr-Zr a better choice than Al-15. The first factor has to do with irradiation performance. Both the DS and PH copper alloys experience a significant decrease in uniform elongation with dpa in this low-temperature range. However, recent data (ICFRM-8) suggest that the fracture toughness of Cu-Cr-Zr is significantly higher than DS copper alloys both before and after low-temperature irradiation. The second factor has to do with fabrication methods planned for the construction of the center post. Mid-way though the project, a rapid-prototyping fabrication method was proposed for construction of the center post. This includes converting powder to molten material and computer-controlled deposition and shaping. This would be extremely difficult to do with DS copper as the Al2O3 particles would tend to redistribute during the melting process. However, it may be feasible with Cu-Cr-Zr if the material can be properly heat treated either during or after the deposition and shaping process.

The aluminum TF return shell also serves as the vacuum vessel for the ARIES-ST. It is water-cooled through stainless-steel coolant tubes embedded in the aluminum. The proposed fabrication includes: welding 13-mm aluminum plates to form upper, middle and lower shell segments of the vacuum vessel; using computer-controlled spray-casting of aluminum onto each shell segment to final thicknesses ranging from 0.5-0.7 m at the mid-plane to 2.5 m at the top; and assembling the three shell segments in the power core area. The top shell is built in place in the power core area. The bottom and middle shells are constructed outside the power core area. 5000 series aluminum alloys (e.g., 5002 or 5052) are considered as prime candidate materials because of their good electrical conductivity and weldability. The outer shell operates at relatively low temperature and stress. All but a very small portion of the shell experiences very low dpa rates. From a materials perspective, several questions were raised as to the homogeneity and tensile properties of the final product. For example, would the shell segments need an O-temper anneal to increase the homogeneity of the final product? Also, given the large mass ($\approx$2700 metric tons) of the final product, what external structures would be used to support the weight of the TF return shell?

The first wall is a He-cooled box-like structure constructed of low-activation ferritic steel. In the early designs, the He entered the first wall at 350°C and exited to the blanket at a temperature low enough to keep the FS maximum temperature $\leq$500°C. For thermodynamic efficiency reasons, the design was later modified to have the He enter at 300°C and exit to the blanket at 420°C, while allowing the peak FS temperature to be $\leq$600°C. Considerable effort was directed toward establishing design criteria for the ferritic steel (which is not included in the IMPH). The tensile and thermal creep data for the Japanese F-82H and the IEA heat F-82H (mod) were compared to the data for the ASME and RCC-MR code-qualified modified Fe-9Cr-1MoVNb. Even with the irradiation-induced softening of ultimate tensile and yield strengths of the F82-H above $\approx$400°C, the tensile properties of F82-H remained within the scatter band of those for Fe-9Cr-1MoVNb. Thus, the established design limit stresses and criteria for the code-qualified material could be used. The short-term tensile properties resulted in a design stress intensity of 148 MPa at 500°C, 128 MPa at 550°C and 103 MPa at 600°C. However, thermal creep for 3 full-power-years of operation limited these stresses to 110 MPa at 550°C and 61 MPa at 600°C. The design stress intensity directly limits the average (through-wall) primary stress and indirectly (though multiplicative factors) the primary bending and secondary thermal stresses. Because of the low thermal creep strength in the temperature range of 550-600°C, the decision was made to use an Oxide-Dispersion-Strengthened (ODS) ferritic steel. Because of the limited data on such steels, the tensile and creep properties of F82-H were shifted (upward) by 50°C which may be reasonably conservative. However, the change from 350°C to 300°C minimum temperature and the change to ODS FS has introduced some uncertainties into the design because of the uncertainties in the

databases for both FS and ODS-FS. The simultaneous effects of neutron damage and He transmutation on the DBTT of FS are not well established. While a minimum FS temperature of 300°C may be reasonable based on neutron irradiations without significant He production, some question remains regarding the effects of He on the DBTT of ferritic steels such as F82-H. With regard to the switch to ODS-FS, the uncertainties in the database increase significantly. Also, special joining techniques are required for ODS-FS in order to retain the creep-resistance of these alloys. Questions also remain regarding the lower temperature limit (based on DBTT) and the upper temperature limit (based on possible irradiation-induced softening).

The ARIES-ST blanket consists of a box-like structure of ODS-FS cooled internally by He exiting the first wall, a thin layer of stagnant or slow-flowing Pb-Li, a SiC thermal barrier, and slow-flowing Pb-Li breeder. The Pb-Li exits the blanket at 700°C. The database for Pb-Li/FS is reasonably well established for faster flow rates. However, the database for the compatibility of Pb-Li/SiC is quite poor (static Pb-Li with poor quality SiC). More R&D is required in this area to support the design. Also, no data were found regarding the compatibility of ODS-FS with Pb-Li.

Tungsten was chosen as the divertor material. The divertor consists of Porous Metal Heat Exchanger Tubes which are best described through the figures in the "Engineering Design Book." While the fabrication of these tubes is quite challenging, the focus of this section is the material properties of the final product. The decision to use unalloyed W rather than more-easily-fabricated W-Re alloys was based on reducing material costs. This issue will have to be revisited after a final fabrication cost estimate is made for the unalloyed W. It is specified that the W pipes will be formed by powder-metallurgy hot-isostatic-pressing, cold-worked, and stress-relieved to give optimum tensile strength and ductility. The anticipated temperature range is 250-800°C with the coolant being He. The main structural issues with the stress-relieved W are related to ductility and fracture toughness both before and after irradiation. The nominal DBTT for stress-relieved W is given as 100-200°C. However, tensile properties show very low ductility (uniform elongation, total elongation, and reduction-in-area) in the range of RT-500°C. In general, there are few data points in this range and there is considerable scatter in the data for cold-worked/stress-relieved W depending on impurities, amount of cold-work, and time-temperature of the stress relief. Whatever the DBTT of unirradiated W, the DBTT is expected to increase with neutron irradiation. It is possible that the whole divertor will eventually be in the "brittle" regime with regard to design rules. Thus, the fracture toughness and/or the critical stress intensity become extremely important design parameters. With the database for the fracture toughness of unirradiated W relatively limited, one can only expect that the database for irradiated W is even more limited. Thus, there remains a material's issue with regard to the performance of the W divertor. An additional design feature which may require optimization and demonstration is the joining of the W divertor to the FS He manifolds in the back of the divertor. Brazing has been specified with Ti-25Cr-3Be as a possible braze material.

Discussion

While a number of fabrication and materials performance issues regarding the ARIES-ST design remain unresolved, the design study concerns a power reactor with about a 50 year lead time. In evaluating the design, it is important to consider what improvements in materials performance and fabrication can be reasonably achieved over the next 25-50 years, rather than rely on the limitations of the existing database.

FUTURE WORK

The materials input to the ARIES-ST Design Team will be documented for incorporation into the final report, as well as journal articles.

11.0 IRRADIATION FACILITIES, TEST MATRICES, AND EXPERIMENTAL METHODS

ACCELERATED HELIUM PRODUCTION IN FE-54 DOPED ALLOYS – MEASUREMENTS AND CALCULATIONS FOR THE FIST (FERRITIC ISOTOPIC TAILORING) EXPERIMENT

L. R. Greenwood, B. M. Oliver, D. S. Gelles (Pacific Northwest National Laboratory)[*], S. Ohnuki (Hokkaido University), K. Shiba (JAERI), Y. Kohno (University of Tokyo), A. Kohyama (Kyoto University) and J. P. Robertson (Oak Ridge National Laboratory)

OBJECTIVE

To demonstrate and predict the production of helium in iron alloys enriched in Fe-54 to accelerate helium production for fusion irradiation simulations in mixed-spectrum reactors.

SUMMARY

Iron alloys enriched in Fe-54 were irradiated in the High Flux Isotopes Reactor (HFIR). Measurements and calculations have been performed to demonstrate and to predict the accelerated helium production due to higher fast and/or thermal neutron cross sections for helium-producing reactions on the iron isotopes of Fe-54 and Fe-55. A helium/dpa ratio of 2.3 was achieved for a 1.25-year irradiation.

PROGRESS AND STATUS

Helium analyses of natural iron samples irradiated in HFIR indicated a non-linear buildup of helium suggesting accelerated helium production due to isotopic shifts.[1] In order to study these isotopic differences in both helium and hydrogen production, iron alloys enriched up to 90% in Fe-54 were fabricated in Japan.[2] The F-82H alloy nominally consisted of 8Cr-2WVTa. Fe-54 in the alloy comprised 96% of the iron or 86% of the total alloy by weight. For comparison, similar alloys were produced both with natural iron and with natural iron doped with varying amounts of boron.

TEM (transmission electron microscopy) alloy specimens were irradiated in the JP17 and JP22 irradiations in HFIR.[3,4] Neutron dosimetry measurements and radiation damage calculations for the JP17 experiment were reported previously.[5] Dosimetry monitors have not yet been analyzed for the JP22 irradiation. The JP17 irradiation was conducted from December 31, 1991, to February 17, 1992 for an exposure of 43.5 EFPD leading to about 2.8 dpa and 1.0 appm helium in natural iron. The JP22 irradiation from December 1993 to January 1996 produced an exposure of 458.2 EFPD leading to about 29 dpa and 10.5 appm helium in natural iron. Calculations discussed in this report used the JP17 dosimetry data normalized to the JP22 exposure conditions.

Recently, four samples from these irradiations were analyzed for helium content at the Pacific Northwest National Laboratory. The composition of each specimen is listed in Table I. The helium content of each specimen was determined by isotope-dilution gas mass spectrometry following vaporization in a resistance-heated graphite crucible in one of the mass spectrometer system's high-temperature vacuum furnaces.[6] The absolute amount of ^{4}He released was measured relative to a known quantity of added ^{3}He "spike". The results of the helium analyses are given in Table II, and are listed as total atoms of ^{4}He released, and as ^{4}He concentrations in atomic parts per million (10^{-6} atom fraction). Conversion from total

helium to helium concentration was based on an average value of 1.075×10^{22} atoms/g. The conversion values were calculated using the alloy compositions. It should be noted, however, that these conversion values, and the helium concentrations obtained using them, are not very sensitive to small changes in material composition. Absolute uncertainty (1σ) in the individual helium analysis results, determined from the cumulative uncertainties in the sample mass, the isotope ratio measurement, and the spike size, is estimated to be approximately 1%.

Table 1. Composition of Fe Alloys

Sample	Irradiation	Alloy*	Iron	Boron-10
FN51	JP-17	F-82H Fe54	96% Fe-54	-
C603	JP-22	F-82H Fe54	96% Fe-54	-
C103	JP-22	F-82H B-10	Natural Iron	0.0001 %
C203	JP-22	F-82H B-10	Natural Iron	0.0058 %

*F82-H Fe-54 alloy composition: 7.1Cr-1.8W-0.55Si-0.40Mn-0.17V-0.1C-0.04Ta

Table 2. Helium Concentrations in FIST Samples

Specimen	Mass[a] (mg)	Measured ^{4}He (10^{14} atoms)	Helium Concentration (appm)[b] Measured	Average[c]
FN51-2-A	1.073	0.5278	4.550	4.52
-B	1.603	0.7765	4.481	0.05
C103-A	1.567	3.684	21.89	21.8
-B	1.892	4.407	21.69	0.1
C203-A	0.851	29.81	325.9	320
-B	1.864	63.05	314.7	8
C603-A	1.047	7.348	· 64.92	64.8
-B	1.711	11.96	64.66	0.2

[a]Mass of specimen for analysis. Mass uncertainty is ±0.002 mg.
[b]Helium concentration in atomic parts per million (10^{-6} atom fraction) with respect to the total number of atoms in the specimen.
[c]Mean and standard deviation (1σ) of duplicate analyses.

The production cross sections for helium differ for each iron isotope, as shown in Figure 1. The cross sections shown in the figure were taken from the ENDF/B-VI libraries.[7] During the course of each irradiation, the iron isotope ratios change due to (n,γ) reactions, followed by the subsequent decay of the radioactive isotopes of Fe-55 (2.73 y) and Fe-59 (44.5 d). Reference 1 demonstrated these effects using mass spectrometry to measure the altered iron isotopic ratios. As the iron isotope ratios change, the helium production will increase or decrease according to the different cross sections shown in Figure 1.

These cross sections were integrated over the HFIR neutron energy spectrum to determine the helium production rates. The calculated ratios of fast neutron helium production relative to that of natural iron are 1.85 (Fe-54), 0.93 (Fe-56), 1.89 (Fe-57), and 0.16 (Fe-58). Helium production cross sections are not available for the radioactive isotopes Fe-55 and Fe-59. New theoretical calculations would be highly useful for predicting these effects. In reference 1, the semi-empirical computer code THRESH2 was used to calculate the helium production rate ratios. These calculations predicted a ratio of 5.95 for Fe-55, although the ratios differed somewhat from the ENDF/B-VI values for the other iron isotopes.
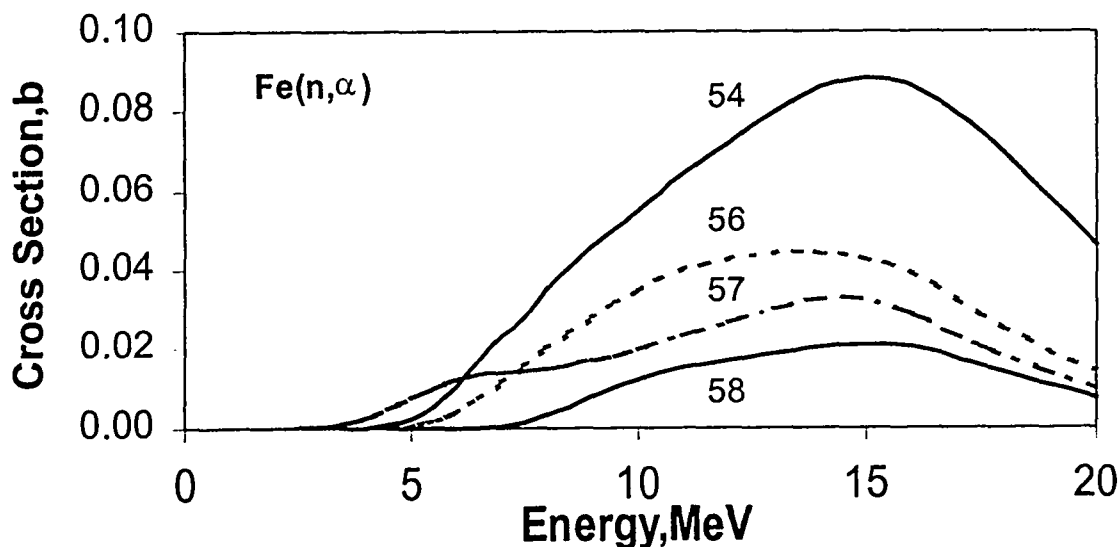
Figure 1. ENDF/B-VI neutron cross sections for the (n,α) reaction for various iron isotopes.

In order to calculate the helium production for the materials used in the present study, the measured neutron energy spectrum was used to calculate the transmutation rates for the various iron isotopes. Helium production was then integrated over short time intervals over the course of each irradiation. For the samples FN-51 and C603, which are enriched in Fe-54, the calculations using the above cross section ratios underpredict the measured helium values by about 50%. In order to fit the JP-17 helium measurement for sample FN-51, it is necessary to increase the fast neutron helium production in Fe-54 by about 86%. This cross section is not very well known at lower neutron energies, which are the most important in the HFIR neutron energy spectrum. This new measurement would thus suggest that the Fe-54 (n,α) cross section in ENDF/B-VI is too low. The higher helium level seen in the JP-22 irradiation for sample C603 further requires some adjustment of the helium production cross section in Fe-55. Mathematically, it is possible to fit the data with either a greatly elevated rate of fast neutron production in Fe-55 or a weak thermal neutron effect in Fe-55, as originally suggested in reference 1. If the effect is solely due to fast neutrons, then the ratio of helium production in Fe-55 to that of natural iron would have to be quite high at about 37:1. Looking at Figure 1, this would require a neutron cross section peaking at about 1.8 barns, which seems rather unlikely. The Q-value for the Fe-55(n,α)Cr-52 reaction is quite high at +3.584 MeV. This would suggest the possibility of a thermal neutron cross section. If the Fe-55/natural iron helium production ratio is held at the THRESH2 predicted value of 5.95, then the helium data can be very well fit using a small thermal neutron helium production cross section in Fe-55 of about 0.011 barns,

well within the range of the suggested value given in reference 1. Since we do not know either the fast or thermal helium cross sections for Fe-55, we can only give a range of values that would fit the data. The most likely answer is that there is a thermal neutron cross section in Fe-55 of about 0.01 barns and that the fast helium cross section ratio to natural iron is about 5-10. The data and calculations are compared in Figure 2. The dotted line is calculated without considering any possible helium production from Fe-55. The curve starts to bend over at high dpa due to the burnup of Fe-54. The solid line includes helium production from Fe-55 using a thermal neutron cross section of 0.01 barns and a fast helium cross section of 6 times the natural iron helium production. The calculations were extended to higher exposures to predict achievable helium/dpa ratios in HFIR for these alloys, as discussed below.
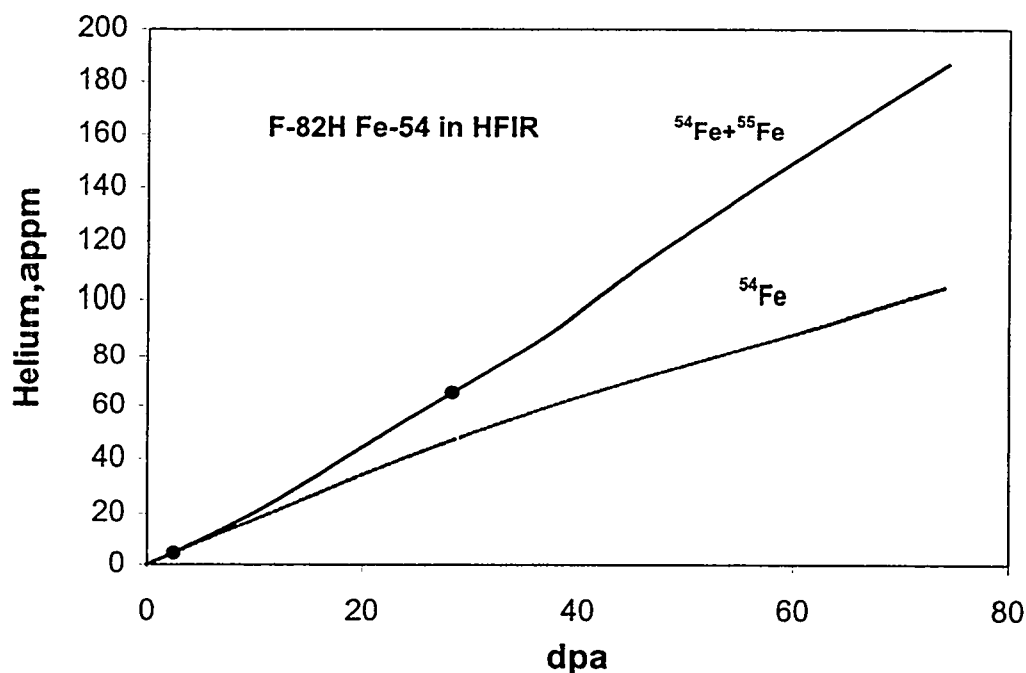
Figure 2. Measured helium production (solid circles) compared to calculations with only the modified Fe-54 cross sections (dotted line) and with both Fe-54 and Fe-55 modified cross sections (solid line).

In the case of the natural iron alloys doped with boron (C103 and C203) the high thermal neutron fluences in these HFIR experiments totally burned out the B-10 to helium. Converting from weight percent to atom percent this would predict 4 appm helium from B-10 in sample C103 and 321 appm helium from B-10 in sample C203. Using the same iron isotopic cross sections derived for the Fe-54 doped alloys, we would predict 20 appm helium from the natural iron alloys. Adding this to the B-10 values would predict 24 appm helium in sample C103 compared to the experimental value of 22 appm helium (C/E = 1.10). Similarly, the calculated value for sample C203 is 344 appm helium compared to the measured value of 321 appm helium (C/E = 1.07). This level of agreement is well within the uncertainties on the boron concentrations. Hence, the Fe-54 and Fe-55 cross sections also give good agreement for natural iron, similar to that seen previously in Reference 1.

RECOMMENDATIONS FOR FUTURE IRRADIATIONS

The present work demonstrates that elevated helium production can be achieved in iron by enriching with Fe-54 or Fe-55. Irradiations with natural iron produce a nearly constant ratio of helium (appm) to dpa of about 0.54 using the ENDF/B-VI calculated rate. It should be noted that this rate is somewhat higher than the ENDF/B-V Gas Production File value of 0.37, as quoted in reference 5, for example. The present experiment achieved a helium/dpa ratio of 2.3, an increase of a factor of 4.3 over natural iron. In order to simulate fusion reactor conditions, we would like to achieve a helium/dpa ratio of about 10. Using the present alloys, which are nearly fully-enriched in Fe-54, it would only be possible to achieve a helium/dpa ratio of about 3:1 with a similar irradiation in HFIR lasting about 4 years, as shown in Figure 2. HFIR produces about 22.7 dpa in iron per full power year of operation. If alloys were produced with an initial doping with Fe-55, then fusion-like ratios of helium/dpa could be easily achieved. Regardless of whether the Fe-55 effect is due to thermal or fast neutrons, Fe-55 will produce about 37 times more helium than natural iron in HFIR. Pure Fe-55 would thus produce a helium/dpa ratio of about 20:1. The desired fusion helium/dpa ratio of 10:1 could be achieved by doping natural iron with 50% Fe-55 or with a mix of Fe-54 and Fe-55. This production rate would, however, decrease with time as Fe-55 either decays (2.73 y) or is transmuted to Fe-56. It would be possible to offset these losses by using a mix of Fe-54 and Fe-55 so that Fe-54 would be transmuted to Fe-55 to replace these losses. Total replacement is possible if we match the initial Fe-54/Fe-55 ratio to the ratio of the decay rate of Fe-55 to the transmutation rate of Fe-54 of about 3.5:1. In this case, we could achieve a nearly constant helium/dpa ratio of about 5.9:1. Of course, one would have to allow for losses of Fe-55 due to decay from the time of production and including possible reactor down times.

Fe-55 is a low-energy x-ray emitter. Hence, it could be safely handled in relatively large quantities for production of doped alloys, although cost considerations might be a more serious problem. An alternative would be to first irradiate Fe-54 to breed Fe-55, then use this transmuted material to make the alloy for the fusion simulation experiment. For example, a two-year irradiation of Fe-54 in HFIR would breed about 8% Fe-55. The Fe-54 will decrease about 15%, the difference mostly going to Fe-56. The decay of Fe-55 produces Mn-55 which also rapidly burnsup to Fe-56. This transmuted iron would then produce an initial helium/dpa ratio of about 3.3:1 increasing to about 4:1 after a year of irradiation. In order to achieve higher helium/dpa ratios, it would be necessary to isotopically separate the Fe-55 produced from the Fe-54 irradiation (or purchased commercially) and then use the separated Fe-55 for further alloy preparation. In this way, one could produce alloys with any desired helium/dpa ratio including 20:1 (pure Fe-55), 10:1 (50:50 mix of Fe and Fe-55), or a steady-state production at 6:1 (3.5:1 ratio of Fe-54 to Fe-55).

FUTURE WORK

Work is in progress to measure and calculate hydrogen production in these samples. Additional helium measurements at higher exposure levels would be highly useful in establishing the helium production cross sections in the iron isotopes.

REFERENCES

1. L. R. Greenwood, D. G. Graczyk, and D. W. Kneff, Jou. of Nucl. Mater. 155-157, 1335 1339 (1988).

2. M. Suzuki, A. Hishinuma, N. Yamanouchi, M. Tamura, and A. F Rowcliffe, J. of Nucl. Mater. 191-194,1056-1059 (1992).

3. A. W. Longest, D. W. Heatherly,and K. Thoms, Fusion Materials Semiannual Progress Report DOE/ER-0313/12,pp. 24-28, July 1992.

4. J. P. Pawel and R. L. Senn, Fusion Materials Semiannual Progress Report DOE/ER 0313/12, pp. 15-23, July 1992.

5. L. R. Greenwood and C. A. Baldwin, Fusion Materials Semiannual Progress Report DOE/ER-0313/19,pp. 286-290, April 1996.

6. H. Farrar and B. M. Oliver, "A Mass Spectrometer System to Determine Very Low Levels of Helium in Small Solid and Liquid Samples," J. Vac. Sci. Technol. A4, 1740 (1986).

7. Evaluated Nuclear Data File, Part B, Version VI, National Nuclear Data Center, Brookhaven National Laboratory.

MODULATED-BEAM MASS SPECTOMETRY SYSTEM FOR THE DETERMINATION OF LOW LEVELS OF HYDROGEN IN IRRADIATED MATERIALS - B. M. Oliver, J. A. Abrefah, F. A. Garner (Pacific Northwest National Laboratory)*, and A. Kumar (University of Missouri, Rolla)

OBJECTIVE

To develop a hydrogen analysis system for the determination of low levels of hydrogen in irradiated materials.

SUMMARY

A high-sensitivity analysis system has been developed for the measurement of hydrogen in solid materials. The system is based on a low-volume hot crucible hydrogen extraction furnace in combination with a modulated-beam quadrupole mass spectrometer detector system. Calibration of the system is conducted using a commercially available hydrogen leak source attached to the detector volume input line. Initial tests on the system using 5 to 10 mg sized specimens cut from a hydrogen-containing steel standard of 5.2 ± 0.3 wppm gave an average concentration of 5.8 ± 0.2 wppm. The ultimate system detection limit is currently ~5 x 10^{14} atoms, or ~5 appm for a 10 mg specimen. Future work will now involve analysis of a number of irradiated materials from various fission and fusion research programs.

PROGRESS AND STATUS

Introduction

Starting in 1997, tests were carried out at Pacific Northwest National Laboratory (PNNL) for the purpose of fabricating a furnace/analysis system to measure hydrogen gas generation in 1) target and cladding materials proposed for the Accelerator Production of Tritium (APT) program, and 2) various materials of interest to the U.S. Fusion Materials Program and the U.S.-Japan JUPITER program. An initial system was developed which permitted the measurement of hydrogen in tungsten material irradiated in an 800-MeV proton beam[1]. This initial system was based on isotope-dilution static-mode gas mass spectrometry, which is the basis for an existing system at PNNL for the measurement of very low levels of helium in irradiated materials[2]. Although this system provided useful initial data to the APT program, the system could only be used for relatively high hydrogen levels (thousands of appm), and the absolute accuracy of the system was difficult to assess.

In order to improve on the accuracy and sensitivity of hydrogen measurements at PNNL, a second development effort was undertaken which involved improvements to both the sample hydrogen extraction and detector components. The hydrogen extraction system improvements involved significantly reducing the volume and type of materials in the sample furnace that were heated and in direct connection to the mass spectrometer detector. The detector improvements involved a redesign of the detector based on a technique known as modulated-beam mass spectrometry (MBMS)[3]. The MBMS technique involves chopping the

input gas flow to the mass spectrometer using a chopper blade, and then using a lock-in amplifier to detect the resulting modulated hydrogen signal from the much larger background "dc" hydrogen signal emanating from the detector volume.

Hydrogen Extraction System

A schematic diagram of the hydrogen analysis system is shown in Figure 1, with the sample extraction furnace shown on the left side, and the MBMS detector system on the right. Hydrogen is extracted from the analysis samples by heating to temperatures up to ~1200°C. The extraction furnace consists of a sample turntable assembly located above a boron nitride "test-tube" shaped crucible heated on the outside by a resistance-heated tungsten filament. Samples are loaded into the upper section of the turntable and remotely dropped through the central vertical channel into the crucible using a bellows-sealed pusher rod. The upper section can be isolated, vented, and then vacuum pumped to allow for sample loading while the crucible is maintained under vacuum heating. The top view-port section is sealed to the turntable section using a double o-ring seal with differential pumping between the o-rings. Connection to the hydrogen detector system is through a side vacuum channel located below the isolation gate valve.

The tungsten heating filament is contained inside a water-cooled copper enclosure connected to its own separate vacuum system. The upper sample/viewport section is sealed to the lower copper-block section using the same type of double o-ring seal used in the upper section. Currently, the crucible temperature range is ~750°C to ~1200°C and is determined using an optical pyrometer through the upper viewport. Temperature uncertainty is estimated to be ±50°C. A near-term improvement to the system will be the addition of direct thermocouple measurement of the temperature which will permit more accurate temperature determination, and allow for stepped-anneal or ramped hydrogen release measurement.

Hydrogen Detector System

The hydrogen detector system is shown in the right hand side of Figure 1. An isolation valve and quick-disconnect VCR-type® fitting are provided in the gas line from the extraction furnace to allow for easy access to the lower water-cooled copper chamber for crucible or heater replacement. Hydrogen gas flow from the extraction system travels through the horizontal vacuum line and is interrupted by the rotating six-blade chopper wheel, which periodically "blocks" and "unblocks" the direct movement of the hydrogen gas to the ionization region of the detector. The rotational frequency of the chopper blade is controlled by an ultra-high vacuum stepper motor and external controller. The rotational speed of the motor can be varied to provide chopping frequencies up to ~120 Hz.

The mass spectrometer detector is a standard quadrupole analyzer with both faraday cup and electron multiplier detectors. For the present application, the direct output of the electron-multiplier is fed to a lock-in amplifier which is synchronized to the chopper frequency. Synchronization is provided by a square-wave output signal from an infrared emitter-detector assembly located around the lower section of the chopper wheel. Calibration of the MBMS system is performed using an external calibrated hydrogen leak attached to the vacuum line from the extraction system. This calibrated leak has a very small trapped volume, resulting in virtually no lowering of the leak rate with time.

Initial System Tests

Initial tests have been conducted on the system to allow for optimization of the various system parameters including, chopping frequency, mass spectrometer ionizer parameters, and lock-in amplifier settings. These initial tests were conducted using small stainless steel samples cut from material[1] with a known hydrogen content of 5.2 ± 0.3 wppm (equivalent to 285 appm H) at a system crucible temperature of ~1200°C. The form of the standard material was rods, ~4 mm in diameter and ~10 mm in length. Samples for analysis were obtained from slices cut from the rods using a slow-speed Isomet® saw both with and without water cooling. From each cut slice, four or five analysis specimens were then cut using small diagonal cutters. Prior to analysis, each specimen was ultrasonically cleaned in acetone, air dried, and then weighed using a NIST traceable microbalance.

The results of the initial hydrogen analyses are given in Table 1. Column 2 in Table 1 indicates the cutting method employed for each specimen. The hydrogen release curve for Sample SS501-13 is also shown in Figure 2 as an example. Two release peaks are evident as the sample quickly heats to the crucible temperature of ~1200°C. The results of the six analyses indicate an average measured hydrogen content in the steel of 5.8 wppm, with a standard deviation in the measurements of ~3%. Compared to the stated content of the steel, the present results show an average bias of +12%, although the measured value is within the 2σ uncertainty of the standard. This possible bias is also within the stated ±15% uncertainty of the calibrated leak used to obtain the absolute sensitivity for the MBMS system. Additional analyses of different standard samples may permit an adjustment in the calibrated hydrogen leak value, resulting in improved absolute uncertainty estimates.

Hydrogen background levels in the system are currently limited by dissociation of residual water from the room-temperature parts of the system by the hot crucible. This background level drops significantly for crucible temperatures of ~1000°C, and this lower temperature may be sufficient for complete hydrogen release in steels. Addition of a water vapor cold trap to the upper sample section is also being considered. At the present hydrogen background levels, the lower sensitivity limit for the system is ~5 x 10^{14} atoms of hydrogen release. This is equivalent to ~5 appm in a 10 mg size steel sample.

FUTURE WORK

Following confirmation of system sensitivity and reproducibility, hydrogen analyses will be conducted on Inconel 718 and additional tungsten samples from the APT program, as well as a variety of samples from U.S. and U.S.-Japan JUPITER fusion materials programs, including isotopically-tailored ferritic alloys, SiC composites, vanadium alloys, and reactor steels.

REFERENCES

1. B. M. Oliver, M. L. Hamilton, F. A. Garner, W. F. Sommer, S. A. Maloy, and P. D. Ferguson, "Stepped-Anneal and Total Helium/Hydrogen Measurements in High-Energy Proton-Irradiated Tungsten", Proc. 19th Int. Symp. Effects of Radiation on Material, Seattle, WA, June 16-18, 1998.

---

[1] Part No. 501-529, Leco Corporation, St. Joseph, Michigan.

2. H. Farrar and B. M. Oliver, "A Mass Spectrometer System to Determine Very Low Levels of Helium in Small Solid and Liquid Samples," J. Vac. Sci. Technol. **A4**, 1740 (1986).

3. W. H. Miller, A. Kumar, and W. Meyer, "Techniques for Measuring Low Levels of Hydrogen or Hydrogen-Bearing Materials in Solids", J. Nondestructive Evaluation, **10**, 151 (1991).

Figure 1. Schematic Diagram of Hydrogen Analysis System
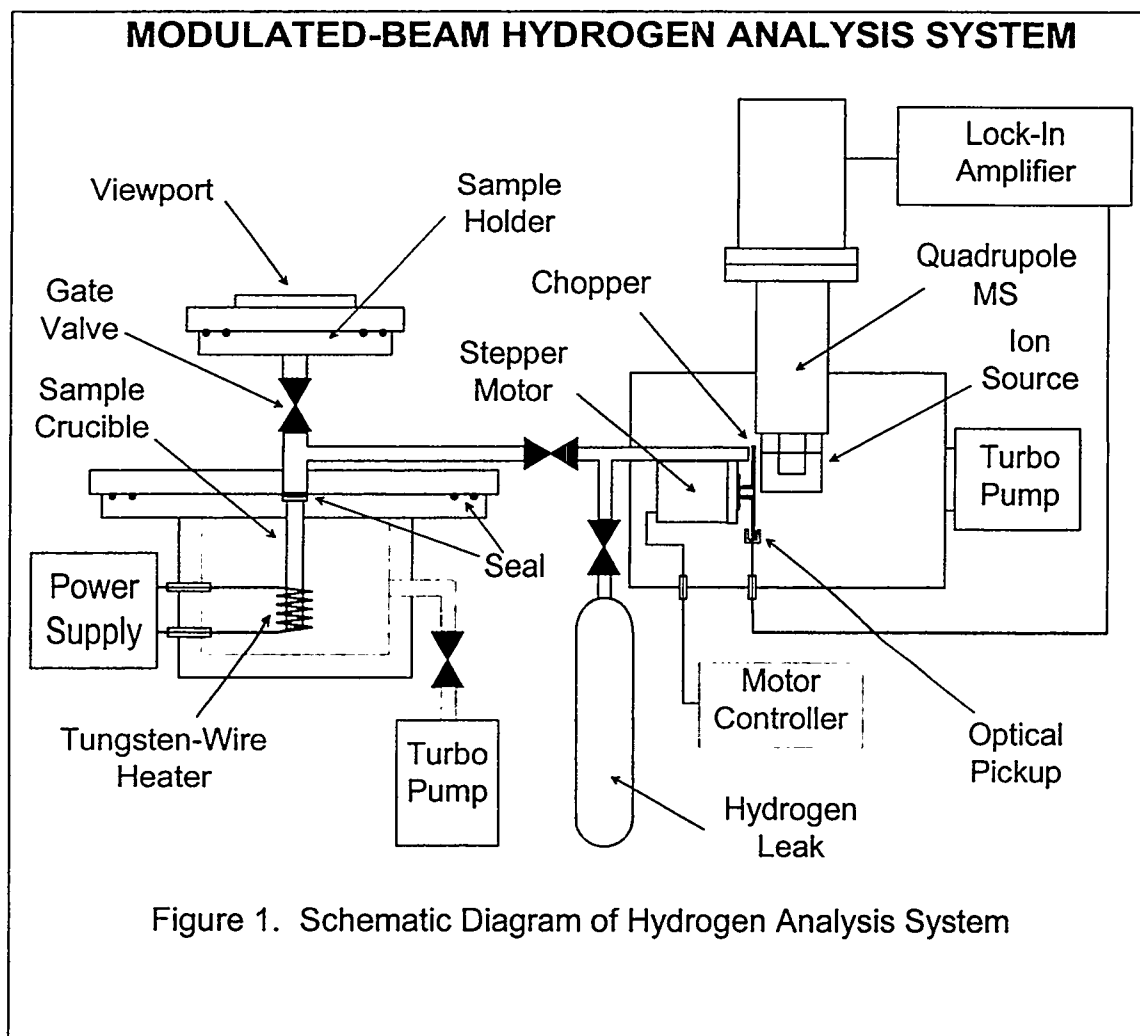
Table 1. Measured Hydrogen Contents in Test Steel Samples

Sample	Cutting Method	Mass (mg)	Measured Sensitivity (V·s/mole)	Integrated Hydrogen Release (V·s)	Calculated Hydrogen Concentration (wppm)
SS501-17	dry	6.59	1.15E-02	6.24E+05	5.66
SS501-18	dry	7.02	1.22E-02	5.98E+05	5.88
SS501-11	wet	7.34	1.19E-02	5.88E+05	5.56
SS501-12	wet	7.48	1.29E-02	5.74E+05	6.07
SS501-16	dry	5.31	9.96E-03	6.48E+05	5.83
SS501-13	wet	9.37	1.74E-02	6.45E+05	5.80
				Mean	5.8
				1σ	±3.1%
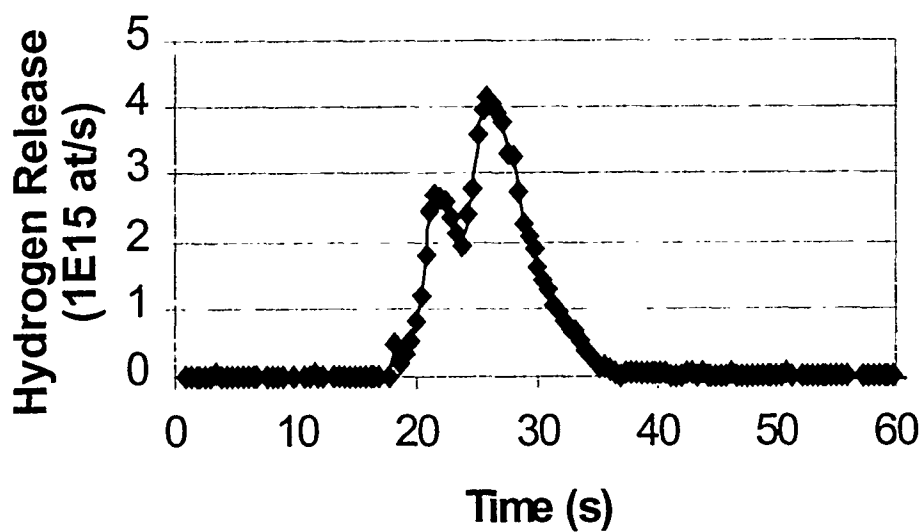
Figure 2. Hydrogen Release Curve for Sample SS501-13

CONCEPTUAL DEVELOPMENT OF THE FUSION-2 EXPERIMENT FOR IRRADIATION TESTING OF VANADIUM ALLOYS IN A LITHIUM ENVIRONMENT AT 500-700°C IN THE BOR-60 REACTOR[1]

– V. Kazakov, V. Chakin, V. Efimov, V. Petukhov, A. Tuktabiev, P. Gabiev (Research Institute of Atomic Reactors), H. Tsai, T. S. Bray, D. L. Smith (Argonne National Laboratory) and A. Rowcliffe (Oak Ridge National Laboratory)

OBJECTIVE

BOR-60 is a sodium-cooled fast reactor in Russia with a coolant inlet temperature of 300-330°C. Previous vanadium alloy experiments conducted in the BOR-60, EBR-II, HFIR, ATR, and SM reactors indicate that the threshold for low-temperature embrittlement of vanadium-base alloys is ≈400°C. The purpose of the proposed Fusion-2 experiment in BOR-60 is to study the effects of neutron damage in vanadium-base alloys in a lithium environment at the high-temperature end, i.e., 500-750°C. The objective of the present task is to develop the conceptual design of the experimental assembly based on the functional requirements of the experiment. The conceptual development focuses on the construction of the experimental assembly, methods of temperature control and measurement, thermal performance of the assembly, and the feasibility of conducting assembly and disassembly in the Research Institute of Atomic Reactors (RIAR) where BOR-60 is located.

SUMMARY

The specific requirements of this task were to complete the conceptual designs of irradiation capsules to a neutron dose of approximately 20 dpa in BOR-60. The specimen matrix will include sheet tensile, compact tension, bend bars, irradiation creep tubes, and TEM disks. The irradiation temperatures will be approximately 500, 550, 600, and 650°C; the temperature changes related to changes in reactor operating conditions are to be minimized; and all specimens are to be encapsulated in lithium. In addition, the possibility of a multi-temperature assembly and reconstitution of assemblies was assessed.

PROGRESS

Task Formulation

The Fusion-2 conceptual design effort concentrated on defining the capabilities and limitations of the experimental irradiation facility. The conclusions of the conceptual design can then be used as the basis for the detailed engineering design of the Fusion-2 experiment. The task formulation consisted of defining the requirements of the conceptual design. The requirements are outlined as follows:

- Determine the maximum irradiation temperature achievable in the BOR-60 reactor with specimens in a lithium environment. (The desired range is 450-750°C.)
- Determine the methods for specimen temperature control and measurement.
- Design a capsule assembly that allows two irradiation temperatures.
- Design a capsule with the possibility of reconstitution for achieving top radiation damage doses of ~100 dpa.
- Determine the feasibility of assembly, disassembly, and reloading of capsules in RIAR.

Capsule Construction

A conceptual design has been established and the schematic of this design is presented in Figure 1. Table 1 presents the materials of construction for the capsule; item numbers refer to components as identified in Figure 1.
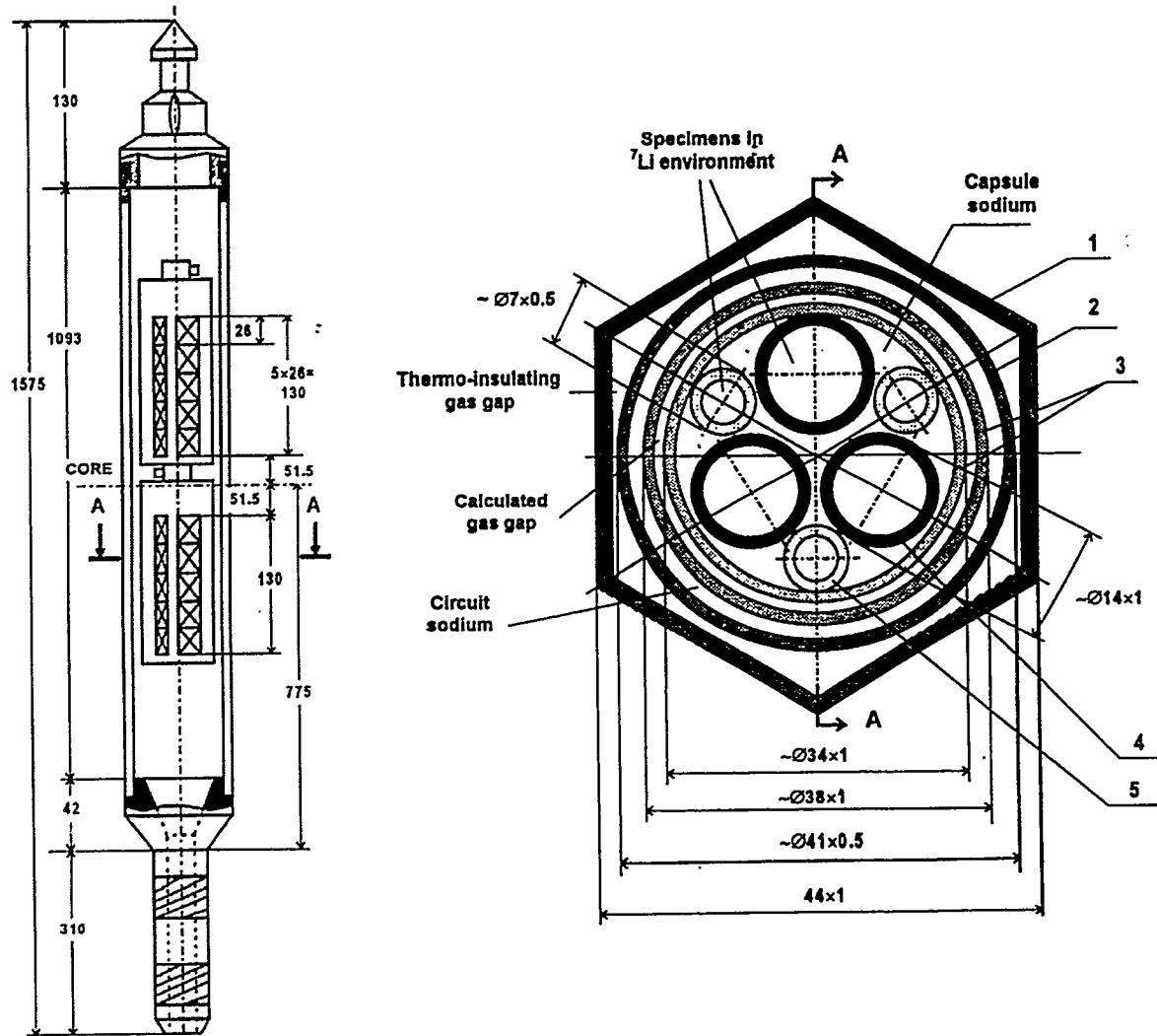
Figure 1: Two-temperature Fusion-2 capsule assembly (left) and cross-section of the capsule (right).

Table 1: Materials of construction for the Fusion-2 test assembly

Item No.	Test Temperature = 500, 550, 600°C	Test Temperature = 700°C	Fill
1	Hex Can	Hex Can	He
2	SS	SS	Sodium
3	304 SS	Inconel	He (outer) Sodium (inner)
4	Mo alloy of TZM or VM-1A type	Mo alloy of TZM or VM-1A type	Li-7, specimens
5	Mo alloy of TZM or VM-1A type	Mo alloy of TZM or VM-1A type	Li-7, specimens

Thermal Calculations

Thermal calculations were performed assuming one and two capsules in the assembly. The thermal calculations were performed in consideration of the reactor power (55 MW), the distribution of radiation heating in the elements, specimens and the coolant at the specimen height, radial and axial heat transfer in the assembly, and convective heat transfer in the capsule. Thermal gas gaps and spatial distribution of temperature were determined using helium as the gap gas. The results of the calculations are presented in Tables 2 and 3 for a one and two capsule assembly, respectively, for capsules at temperatures of 500, 550, 600, and 700°C.

Table 2.   Results of Fusion-2 basic variant thermal calculations for one capsule in the capsule assembly

Parameter	Capsule Assembly Variation			
	A	B	C	D
Capsule Temperature (°C)	500	550	600	700
Calculated Gas Gap (mm)	0.25	0.34	0.41	0.62
Axial Temperature Variation from the average (°C)*	±20	±26	±28	±42

*The axial temperature variation can be significantly reduced with the addition of masses (e.g., tungsten) at the upper and lower locations of the capsule.

Table 3.   Results of Fusion-2 basic variant thermal calculations for two capsules in the capsule assembly

Parameter	Capsule Assembly Variation			
	A		B	
	Lower Capsule	Upper Capsule	Lower Capsule	Upper Capsule
Capsule Temperature (°C)	500	600	550	700
Calculated Gas Gap (mm)	0.31	0.41	0.43	0.62
Axial Temperature Variation from the Average (°C)	±36	±45	±42	±63
Axial Temperature Variation from the average after smoothing attempts (°C)*	±20	±15	±25	±25

*The axial temperature variation can be significantly reduced with the addition of masses (e.g., tungsten) at optimum locations within the capsules.

The calculations show that without extra measures, the axial temperature variation across the capsule can be large. With the addition of mass (tungsten) into the capsule, the temperature deviation can be significantly decreased; however, the temperature variation may still be somewhat unsatisfactory.

The one capsule assembly has two drawbacks. First, only a single test temperature would be achieved in a single capsule; therefore, in order to irradiate specimens at multiple temperatures, multiple capsules would need to be constructed. If a single assembly were used, and only one capsule was irradiated at a time, the irradiation time increases. The combination of constructing multiple capsules and increased irradiation time increases the total cost of the study. The assembly irradiation time could be decreased by means of a parallel irradiation of a few capsule assemblies in analogous cells of the fifth row of the BOR-60 reactor; however, this option also has increased costs.

The two capsule assembly also has disadvantages. First, the central part of the core is unused; this does not take advantage of the temperature profile in this area. Second, the lower capsule specimens are in the lower part of the core where radiation heating uncertainty increases, and the axial temperature variation throughout the capsule is quite high.

Temperature Control

The specimen temperature will not be actively controlled. Rather, it will be determined by the preset width of the gas gap. Errors in the radiation heating calculations are ±7% and determination of the reactor power is ±2.5%. There is also some uncertainty in the accuracy of the gas gap and associated with the thermohydraulic process inside of the capsule. The uncertainty is approximately 30-40°C for a test temperature of 700°C and ~25°C for a test temperature of 500°C.

Reductions in the temperature uncertainty can be achieved through the use of a methodical capsule in an instrumented D-23 cell of the BOR-60 reactor. The methodical capsule assembly contains thermocouples in the capsule sodium (see Fig. 1), thereby allowing for the measurement of the temperature in the capsule. In addition, the D-23 cell has neutronics and temperatures similar to those found in the E-23 cell. If the D-23 reactor location is available for the entire irradiation time and the costs are not prohibitive, the capsule could remain in this location for the entire irradiation period up to a damage dose of 20 dpa. If the core location is not used throughout the irradiation period, after a short (i.e., weeks) irradiation in the D-23 cell, the assembly would be discharged and the themocouples disconnected at the top of the assembly. If possible, the assembly would then be inserted into the analogous E-23 cell to continue the irradiation. A potential complication of this approach is that if the disconnection of the thermocouples and subsequent insertion of the assembly into the E-23 location fails, the capsules would need to be removed from the D-23 assembly, the subcapsules would need to be opened, and the capsules would have to be reconstructed and placed into a new assembly.

The reactor power over the course of a year can be described in two campaigns, winter and summer, divided by 45-day outages between each campaign. In addition, another 10 day refueling outage occurs in the winter campaign. The reactor power averages 30-35 MW in the summer and ~45 MW in the winter. For a 10-MW change in the reactor power, the corresponding change in the specimen temperature is estimated to be 65-70°C for a test temperature of 700°C and 30-35°C for a test temperature of 500°C. Additionally, the reactor power fluctuates ±10-15% during normal operations. Therefore, an acceptable test temperature range must be developed.

One possible way to achieve a more steady temperature for the specimens during the entire irradiation is to irradiate the assembly only in winter campaigns. Two winters would be necessary to achieve the desired damage dose of ~20 dpa. There is, however, a potentially significant drawback of staying out of the reactor during the summer. In addition to the prolonged irradiation time, such action could potentially jeopardize the conduct of a dynamic helium charging experiment (DHCE) which may be included in Fusion-2. (In a DHCE, tritium is implanted in the capsule. During the irradiation, some of the tritium would diffuse into the specimen and decay in-situ into ^{3}He, thereby yielding the concurrent effects of helium generation and neutron damage. If, however, the assembly is out of the core during the summer, excessive helium may build up in the specimens without the concurrent neutron damage, thus degrading the experiment.) These drawbacks could be eliminated by moving the assembly to a more central core location for the summer to compensate for the lower reactor power in the summer campaign.

Reconstituted Capsule

A dose-dependent radiation creep model can be developed by collecting geometric data on specimens at varying doses. The BOR-60 reactor and associated facilities do not allow for the removal, measurement, and reinsertion of the specimens. Thus, Tables 4 and 5 propose an irradiation scheme for multiple capsules that allows for the collection of the geometric data on samples removed and replaced with fresh specimens. Table 4 allows for three capsules in the assembly; Table 5 allows for four capsules in the assembly. The maximum dose accumulation for any one capsule is 100 dpa.

Table 4: Dose Accumulation for a Reconstituted Capsule Assembly with Three Capsules.

Irradiation Time (Years)	Accumulated Dose (dpa)			
	Capsule Position 1	Capsule Position 2	Capsule Position 3	Removed Capsule
1	20*	20	20	20
2	20	40*	40	40
3	40	20	60*	60
4	60	40	20	-
5	80*	60	40	80
6	20	80	60	-
7	40*	100*	80*	100, 80, 40

*Accumulated dose of capsule removed at the end of the year

Table 5: Dose Accumulation for a Reconstituted Capsule Assembly with Four Capsules.

Irradiation Time (years)	Accumulated dose (dpa)				
	Capsule Position 1	Capsule Position 2	Capsule Position 3	Capsule Position 4	Removed capsule
1	20*	20	20	20	20
2	20	40*	40	40	40
3	40	20	60*	60	60
4	60	40	20	80*	80
5	80	60	40	20	100
6	100*	80*	60*	40*	100, 80, 60, 40

*Accumulated dose of capsule removed at the end of the year

The irradiation schemes presented in Tables 4 and 5 assume that the assemblies are at a single irradiation temperature. However, because some data points will be duplicated with the above schemes, one could insert the fresh capsules at a second temperature, thereby allowing for the collection of dose dependent data at two temperatures.

Table 6 presents the thermal calculations for a four capsule assembly assuming a two-temperature irradiation scheme. The first four capsules, variations 1 through 4, are at an assumed 700°C. The last three capsules, inserted after the removal of an original capsule, variations 5 through 7, are assumed to be inserted at 650°C.

Table 6: Thermal calculation results for a four-capsule assembly that involves the removal of one capsule per year and replacing the removed capsule with a fresh capsule.

Parameter	Capsule Variation						
	1	2	3	4	5*	6*	7*
Capsule Temperature (°C)	700	700	700	700	650	650	650
Calculated Gas Gap (mm)	0.77	0.59	0.56	0.36	0.64	0.49	0.53
Axial Temperature Variation from the average (°C)**	±32	±5	±20	±65	±35	±5	±20

*Fresh capsules reinserted after the removal of an original capsule (i.e., capsule 5 replaces capsule 1 after year one, etc.).
** The axial temperature variation can be significantly reduced with the addition of masses (e.g., tungsten) at the upper and lower locations of the capsule.

From the table, it can be seen that the highest axial temperature variation occurs in capsule 4, or bottom-most, capsule. The addition of tungsten rods does not acceptably smooth the temperature profile; therefore, a slight shift of the capsules upwards in the core should alleviate this high axial temperature variation.

CONCLUSION

The Fusion-2 conceptual design effort concentrated on defining the capabilities and limitations of the experimental irradiation facility. The conclusions of the conceptual design can be used in the engineering design of the Fusion-2 experiment. During the conceptual design effort, irradiation temperatures and corresponding thermal gas gaps for multiple capsule assemblies were determined. Calculations also showed that the test temperatures can be maintained to provide the desired irradiation damage doses up to 100 dpa; higher doses can be achieved through increased irradiation time.

REFERENCE

V. Kazakov et. al., "Conceptual Development of Fusion-2 Experiment for Radiation Test of Vanadium Alloys in BOR-60 Reactor at 500-700°C in Lithium Environment," Report on Milestone 1 of the Subcontract 28X-SZ738V of 06/08/98 with Lockheed Martin Energy Systems, Inc., USA, 1998.

PROGRESS REPORT ON THE OPERATION OF THE VARYING TEMPERATURE EXPERIMENT (HFIR-MFE-RB-13J)

A. L. Qualls (Oak Ridge National Laboratory) and T. Muroga (National Institute for Fusion Science, Japan)

OBJECTIVE

The objective of this report is to summarize the irradiation history of the DOE/MONBUSHO Varying Temperature Experiment (HFIR-MFE-RB13J).

SUMMARY

Irradiation of the HFIR-MFE-RB-13J irradiation experiment began during this reporting period. Four cycles of operation were completed and the fifth cycle began during the reporting period. While the operating temperatures of the experiment are slightly higher than anticipated, control of the experiment has worked as expected including temperature control during reactor startup.

PROGRESS AND STATUS

A detailed description of the experiment and planned operating conditions have been reported [1,2]. The operating guidelines of the experiment were changed to accommodate a higher than expected heat generation rate within the experimental facility. The temperature of holders B, C, and D are higher than expected, as shown below. Specimens in Zone B operate at approximately 530°C. The average specimen temperature in Zone C during the low temperature operation is approximately 375°C. Specimen temperatures in Zone C are increased to match and follow those of Zone B during the high temperature phase of the irradiation. The average specimen temperature during the low temperature phase of the irradiation in Zone D is approximately 230°C. Zone A operates at the design temperature and the average temperature of specimens in Zone D are controlled to match those of Zone A during the high temperature phase of operation.

	Average Specimen Temperature (°C)		
Zone	Design	First 10%	Remainder
A	350	350	350
B	500	530	530
C	300	375	530
D	200	230	350

Several new control features developed for this experiment have performed well. Electrical resistance heaters can maintain desired specimen temperatures at all reactor power levels. Changes in the control gas mixtures take only 10-15 seconds to complete, which results in only small temperature fluctuations during the reactor power increases of a startup (provided that the correct flow rates are set before a power change is initiated). Thermal isolation between zones, and from the zones to the housing is better than expected, which may partially account for high operating temperatures.

Of the 36 heater elements in the capsule, four failed during pre-irradiation checkouts due to improper wiring at an instrument cabinet and one was taken out of operation after the first cycle because of a low electrical resistance to ground. The remaining 31 heaters operated for approximately 122-full power days and show no evidence of degradation to date.

The control system can maintain specimen temperatures during ascension to full reactor power in all four zones. Figure 1 shows the reactor power level in MW and the average indicated temperature of the four specimen holders during a startup and the transition of the variable temperature zones to the higher temperatures shortly after startup. Typically the temperature transitions occur approximately 2.4 days after startup, however this startup was a mid-cycle restart and the temperatures of Zones C and D were increased to match those of B and A soon after startup.

Mid-cycle restart of Cycle 364
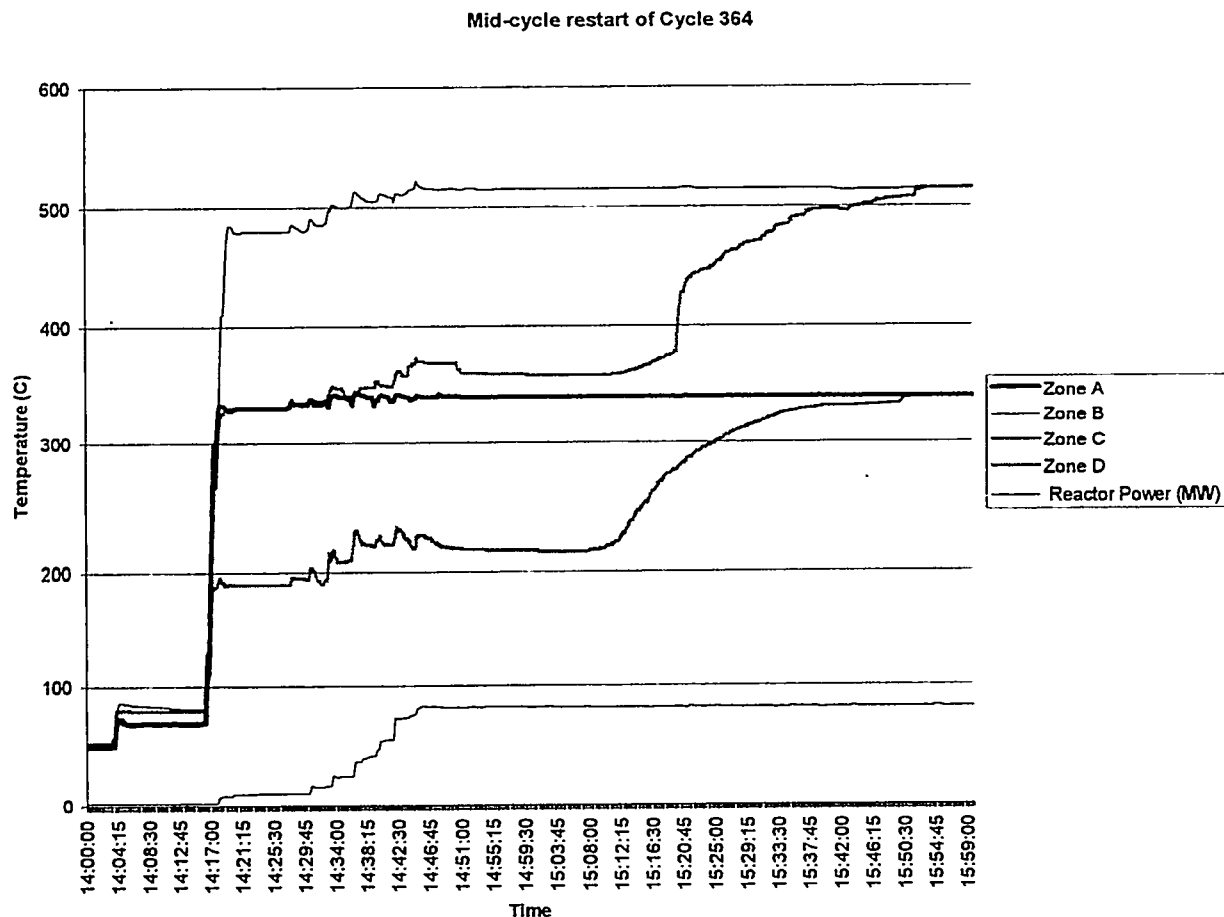
Figure 1: Average indicated temperature of each zone and the indicated reactor power during a restart of HFIR cycle 364. Soon after startup, the temperature of Zones C and D were increased to match their steady temperature counterpart.

Due to variations in each startup, reactor power changes will occasionally produce holder temperatures 10°C higher than the control system is trying to maintain. When this occurs, the safety systems of the experiment will automatically cool the holder, which results in short term irradiation of the specimens below the desired irradiation temperature. The temperatures are returned to normal within a few minutes. Figure 2 shows the average indicated temperature of each zone during a startup in which the gas flow adjustments made prior to an increase in reactor power were not sufficient to prevent automated cooling responses.

Startup of Cycle 365
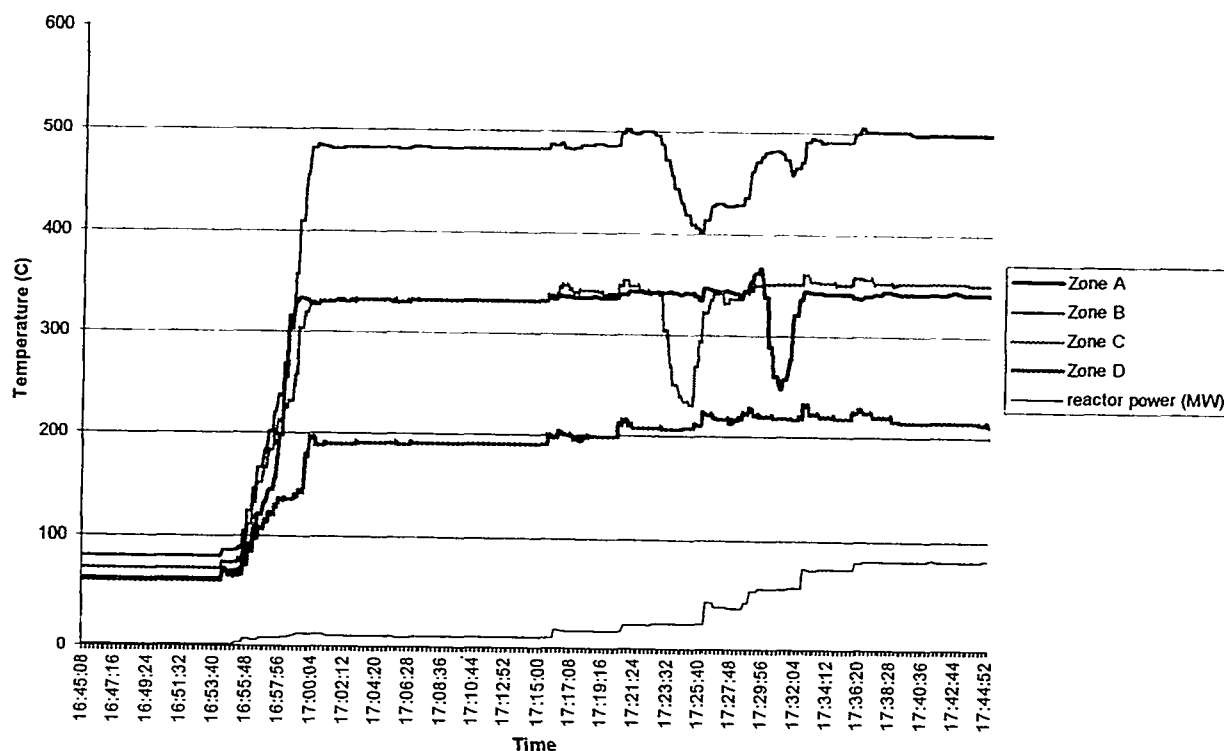
Figure 2: Average indicated temperature of each zone and the indicated reactor power during startup of cycle 365. The temperature of Zones A, B and C experienced some low temperature operation during the startup.

The heaters are rated for 10 amps, but are limited by the control system to an operational range of 6 amps. The thermal conductivity of the control gas mixture for each zone is varied independently to keep the required heater power within the operational range of the heaters at all power levels. Once the reactor reaches full power, the gas mixtures are adjusted throughout the cycle to keep current demands between 1 and 2.5 amps. Gas mixture adjustments are required every other day at the beginning of a cycle and every day near the end of a cycle.

Zones C and D operate with pure helium (the highest thermally conductive gas available) as the temperature control gas during the low temperature phase of operation. Argon is added to the helium to increase their temperature to match those of the steady temperature zones. Because Zone B operates above the design temperature, pure helium is maintained in its gas gap and little or no heater input is used in Zone B during full power operation. Because the temperature of Zone B is not actively controlled, its temperature increases approximately 5°C when the temperatures of the variable temperature zones are increased. This small temperature change implies that the gas separation seals between zones are working as planned and the thermal insulation provided by the stainless steel holder spacers is very good. Within an experimental length of 44 cm, four zones with temperature differentials as large as 300°C can be essentially independently controlled.

Another consequence of not actively controlling the temperature of Zone B is that its temperature increases approximately 15°C over the course of a 24-day cycle. This is due to increased heat generation within the holder (mostly at the end displaced from the reactor mid-plane) that occurs as the control plates are pulled from the center of the core to compensate for fuel burn-up near the mid-plane. The use of electric heaters to control temperature in the other zones allows the response time of the control system to be sufficient to accommodate minor changes in reactor

power and primary coolant conditions that can occur when control plates are moved. These operational necessities can cause short-term temperature changes on the order of 2°C to 4°C in capsules that are controlled by gas mixture adjustment alone. The use of electrical heaters for temperature control typically reduces the magnitude of the temperature excursions to 0.1°C.

The experiment is rotated 180° after each cycle to ensure that specimens receive a balanced dose over the course of the irradiation. The angular location within the experimental region designated Top-Dead-Center (TDC) is closest to the reactor centerline for cycles 2, 4, 6, 8 and 10, and is farthest from the centerline for cycles 1, 3, 5, 7 and 9. The average indicated temperature of Zone B changes from cycle-to-cycle due to the orientation of the thermocouples within the zone. The temperature of Zone C is controlled to match that of Zone B. The temperature of specimens close to TDC will, (on average), experience the largest change in temperature due to capsule rotation. The average indicated temperature of Zone C is shown in Figure 3 during cycles 3 and 4 along with the indicated temperature of a group of instrumented stainless steel CVN and TEM specimens, which are located 15° from TDC. The indicated temperatures of the specimens are approximately 530°C +/- 8°C in Zone C during the high temperature phase of irradiation of both cycles. These values are considered typical for stainless steel specimens in Zones B and C, however additional analysis is required.
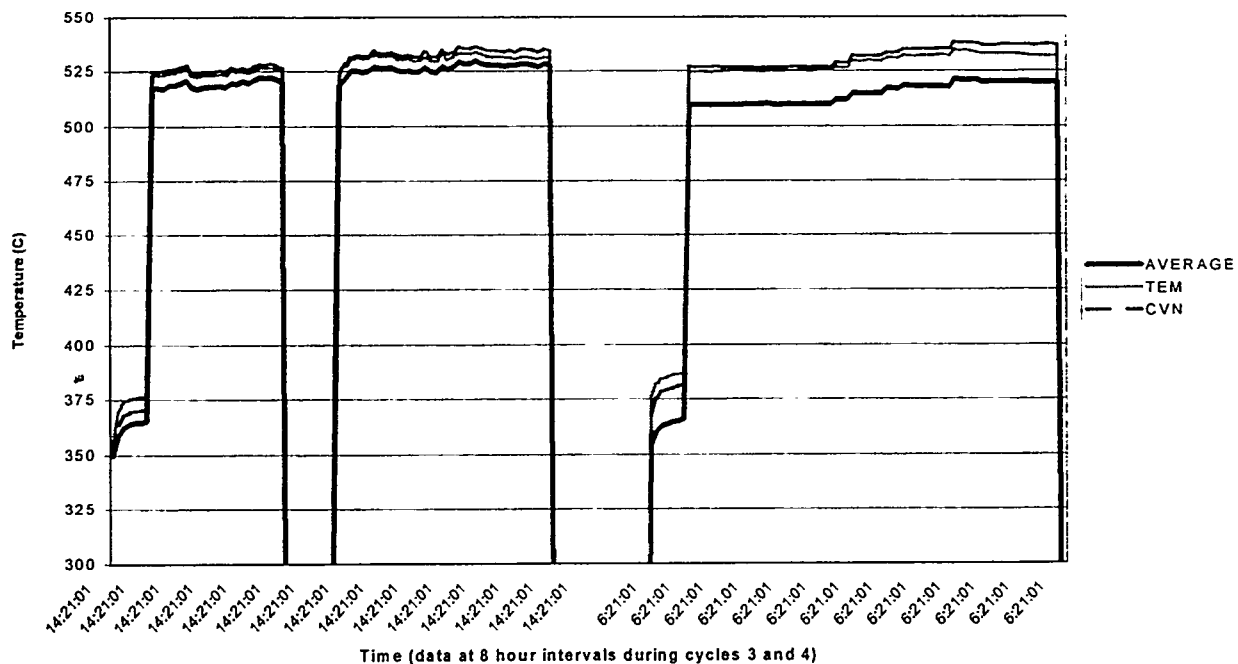
Figure 3: Average indicated temperature of Zone C and the measured temperature of stainless steel TEM and CVN specimens in Zone C for cycles 3 and 4 of a 10-cycle irradiation. The indicated temperature of the zone changes due to rotation from cycle to cycle but the indicated specimen temperatures remain the same.

One positive temperature excursion occurred in Zone B due to a control computer failure. The temperature of the zone increased to a maximum value of approximately 570°C during an

306

excursion, which lasted approximately 15 minutes. Selected individual thermocouple readings from each zone are shown in Figure 4 during the transient.

The 10-cycle irradiation of HFIR-RB-13J is projected to be complete in July 1999.

Cycle 364 temperature excursion
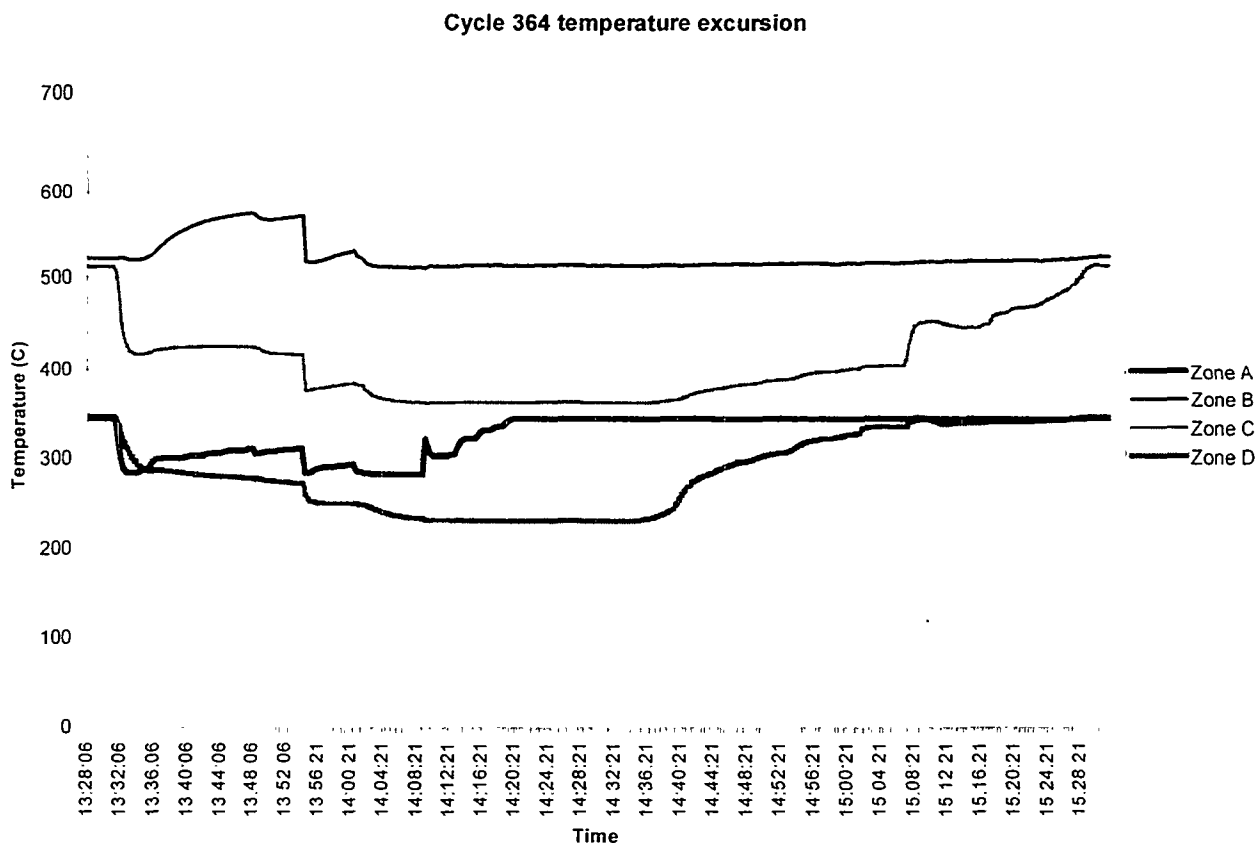
Figure 4: Temperature of an individual thermocouple from each zone during a temperature transient caused by a computer malfunction. Normally the temperature of all zones would decrease during such a failure, however the temperature of Zone B increased due to argon from the other zones mixing with the initially pure helium in the Zone B gas gap. The control system has been modified to prevent additional positive temperature excursions.

REFERENCES:

1. A. L. Qualls and T. Muroga, "Progress on the Design of a Varying Temperature Irradiation Experiment for Operation in HFIR, "Fusion Materials Semiannual Progress Report for Period Ending December 31, 1996, p. 255.

2. A. L. Qualls, M. T. Hurst, D. L. Raby, D. W. Sparks and T. Muroga, "Progress Report on the Varying Temperature, "Fusion Materials Semiannual Progress Report for Period Ending June 30, 1997, p. 243.

OPERATING HISTORY OF THE HFIR MFE-RB-11J AND -12J (P3-2 AND P3-3) EXPERIMENTS – K. E. Lenox and M. L. Grossbeck (Oak Ridge National Laboratory)

OBJECTIVE

The objective of this report is to provide information on the irradiation history of the HFIR MFE-RB-11J and -12J experiments.

SUMMARY

The HFIR MFE-RB-11J and -12J experiments are being conducted under the auspices of the Japanese Monbusho, the Japan Atomic Energy Research Institute (JAERI), and the U.S. Fusion Energy Sciences Program. The irradiation of the experiments was completed in July of 1998, and the disassembly of the experiments is scheduled to be complete in early 1999. The operating history of both experiments, including the operating temperatures of the specimens, is discussed.

PROGRESS AND STATUS

Irradiation History

Both capsules and their associated europium liners were installed into HFIR at the beginning of fuel cycle 352 which began on February 7, 1997. RB-11J occupied position RB-1A in HFIR and RB-12J occupied position RB-5B, 180° apart. The desired ten cycles of irradiation were completed for both capsules at the end of fuel cycle 361, which ended on July 17, 1998. At the end of ten cycles, both capsules had accumulated 19,034 MWD (megawatt-days) of operation for a peak dose of 4.9 dpa (in stainless steel).

After HFIR cycle 361, the capsules and liners were removed from the reactor and placed in the HFIR pool for storage. In December of 1998, the RB-11J capsule was shipped to the hot cells at Oak Ridge.National Laboratory for disassembly. The RB-12J capsule is scheduled for shipment to the hot cells in January of 1999.

Detailed descriptions of the capsules and the associated liners have been reported previously. [1]

Temperature and Irradiation Data

Tables 1 and 2 contain information on the specimens loaded into the RB-11J and -12J capsules. Each table is sorted by specimen type: Charpy (CVN) specimens in two sizes, bend bars in eight sizes (BB), tensile specimens (SS-3), TEM holders, SiC fibers, J-type tensile specimens (SS-J), thermal diffusivity specimens (TD, includes temperature monitors), disk compact tension (DCT) specimens, and pressurized creep tube specimens (PT). Under each specimen type, except for the TEM holders, a listing of individual specimens is given, grouped by their location and accumulated dpa values. The operating temperatures are also shown. The same data is given for the TEM holders, but not for individual TEM disks. The data shown for each of the TEM holders relates to the centerline of the holder itself. The location of the TEM disks in each holder and the material composition of each specimen in both capsules was reported previously. [1]

A range is given for each of the temperatures shown in Tables 1 and 2. The range does not reflect the variation in temperature of an individual specimen. Instead, the specimen temperature lies within this range, and the variation of temperature for an individual specimen is less than that for

the group of specimens. With additional analyses, the temperature range for each individual specimen could be found. The ranges shown for the groups of specimens reflect several different factors. The factors include changes in HFIR power levels during operation, the change in temperatures as the capsules are rotated 180° at the end of each cycle, the variation in temperature over the length of each cycle due to the movement of the HFIR control plates, uncertainties in the relationship between specimen temperatures and thermocouple temperatures, and any variation in individual thermocouples over the course of the 10 cycles.

The reactor operated at 85 MW for the majority of the irradiation. However, during cycles 359, 360, and 361, the reactor operated at a reduced power level for short intervals. During cycle 359, the reactor operated at 10% power for 45 minutes. During cycle 360, the reactor power dipped to approximately 83 MW and returned to 85 MW over the course of 30 minutes. During cycle 361, the reactor operated at 50% power for 47 minutes. The reduced power operation affects less than 3.5 MWD of operation, which is 0.02% of the total MWD. Temperature data was collected during these periods of low power operation and the data is included in the results shown in Tables 1 and 2, but the low power data does not have a large impact on the results due to the low displacement damage accumulated during these periods of low power.

Also included in the temperature data shown in the tables is the observable difference in the thermocouple readings from cycle to cycle as the capsule is rotated 180° at the end of each cycle. The thermocouples are oriented such that one half of them are always on the side of the capsule nearest the reactor core, and the other half are on the other side of the capsule, facing away from the core. The thermocouple readings are noticeably lower when the thermocouples are not facing the core. For example, for cycle 354 the average reading on a particular thermocouple in RB-12J was 478°C, and for cycle 355, the average reading was 491°C. The variation is apparent in all of the thermocouples in both capsules, but the variation is less for the RB-11J capsule. For RB-11J, the temperature change is 2-10°C, and for RB-12J the temperature change is 5-15°C.

Temperature data was lost for both experiments on two occasions due to the failure of the computer systems that control the experiments and collect the data. Data is missing for 18 hours or 64 MWD of operation for the RB-11J experiment, which is 0.34% of the total MWD. The data is missing from cycle 355 (16 hours) and cycle 361 (2 hours). Data is missing for 13 hours or 46 MWD of operation for the RB-12J experiment, which is 0.24% of the total MWD. The data is missing from cycle 353 (4 hours) and cycle 358 (9 hours). The control equipment for both experiments is designed to automatically go to a failsafe mode if a control computer fails. This means that the specimen temperatures during these periods are expected to be lower than the temperatures shown in the tables by approximately 50°C in RB-11J and 100°C in RB-12J.

For RB-12J, the attempts to recover from the computer failure during cycle 353 also led to three separate high temperature excursions. The total time spent at temperatures above the desired values was 4 minutes (0.24 MWD). The peak temperatures for the specimens during this time are approximately 40°C above those shown in Table 2.

REFERENCES

1. M. L. Grossbeck, K. E. Lenox, M. A. Janney, T. Muroga, D. W. Heatherly, K. R. Thoms,"The Monbusho/U.S. Shielded HFIR Irradiation Experiment: HFIR-MFE-RB-11J and 12J (P3-2 And P3-3)," *Fusion Materials Semiannual Progress Report for the Period Ending June 30, 1997*, DOE/ER-0313/22, pp. 254-283.

2. R. L. Senn and W. R. Mixon, "Experimental Measurement of Gamma Heat in the High Flux Isotope Reactor," *Nuclear Technology*, Vol. 12, pp. 235-240, October 1971.

Table 1. Operating temperature, axial location, accumulated dpa of specimens in RB-11J.

Capsule:	11J						
Type:	1.5 CVN						
Temp. (°C)	DPA	z (cm)	ID Code	Temp. (°C)	DPA	z (cm)	ID Code
263±19	4.2	-12	LBV5	283±19	4.8	-2	GF35
			LBV6				GF36*
			LDV8				LFV3
			LDV9				LFV4
		12	L1V1			2	GF31
			L1V2				GF32
			LHV1				L2V5
			LHV2				L2V6
276±10	4.7	-6	LDV2		4.9	0	GF33
			LDV3				GF34
			LFV8				LFV1
			LFV9				LFV2
	4.8	-4	GF37	Grand Total of 52			
			LDV1				
			LFV6				
			LFV7				
283±19	4.4	-10	LBV3				
			LBV4				
			LDV6				
			LDV7				
		10	L1V3				
			L1V4				
			LHV3				
			LHV4				
	4.6	-8	LBV1				
			LBV2				
			LDV4				
			LDV5				
		8	L1V5				
			L1V6				
			LHV5				
			LHV6				
	4.7	6	L2V1				
			L2V2				
			LHV7				
			LHV8				
	4.8	4	L2V3				
			L2V4				
			LFV5				
			LHV9				

*Poorly marked

Capsule:	11J		
Type:	DCT		
Temp. (°C)	DPA	z (cm)	ID Code
240±19	3.6	16.8	FA13
			LFV5
			N202
			Z106
	3.8	15.5	FA12
			LFV4
			TJ02
			FA01
	4.0	14.15	FA11
			LFV3
			TWO2
261±19	3.6	-16.8	FA00
			FA08
			N201
			Z105
	3.8	-15.5	FA09
			LFV1
			LFW1
			TJ01
	4.0	-14.2	FA10
			LFV2
			LFW2
			TWO1
Grand Total of 23			

All dpa values are calculated. Measured values will be reported upon completion of dosimetry analysis.

DPA calculation basis: 19034 MWD of operation; The peak DPA/MWD value is 0.000255 for SS, 0.000324 for V, 0.000498 for Al and 2*0.000255 for the ceramics. All DPA values have been rounded off.

DPA varies with axial location with the equation: $\cos(0.00858(z-12.7)) + 0.0000171(z-12.7)^2$, z in mm (see Ref. 2).

z (cm) is the axial distance of the midpoint of the specimen from the HFIR centerline. All distances have been rounded off. Operating temperatures are based on the thermocouple data, corrected for the specimen type and location. The given ranges represent the variation in thermocouple data.

Table 1. Operating temperature, axial location, accumulated dpa of specimens in RB-11J. (cont.)

Capsule:	11J						
Type:	1/3 CVN						
Temp. (°C)	DPA	z (cm)	ID Code	Temp. (°C)	DPA	z (cm)	ID Code
294±19	4.5	-9.29	138 Z1	274±19	4.3	-11.43	125 Z1
			A026				FA41
		9.29	FK02				FA55
			N205				TJ11
	4.5	-8.89	126 Z1			11.43	A001
			FA40				FK34
			FA54				N201
			TJ12				TW05
		8.89	A002		5.4	-11.83	QC62*
			FK33				QC63*
			N202			11.83	QC61*
			TW04				QC64*
	4.7	-6.75	142 Z1	287±10	4.7	-6.35	FA51
			A025				TJ13
		6.75	FK01			6.35	A003
			FK03				FK32
		-6.35	127 Z1		4.8	-4.21	143 Z1
			FA39			4.21	FK04
		6.35	N203			-3.81	FA50
			TW03				TJ14
	4.8	-4.21	A024			3.81	A004
		4.21	FK00				FK31
		-3.81	129 Z1	Grand Total of 60			
			FA38				
		3.81	N204				
			TW02				
	4.9	-1.67	144 Z1				
			A023				
		-1.27	130 Z1				
			A006				
			FA49				
			TJ15				
		1.27	A005				
			FA42				
			FK30				
			TW01				
		1.67	145 Z1				
			A021				

*Surrounded by Zr foil

Capsule:	11J		
Type:	PT		
Temp. (°C)	DPA	z (cm)	ID Code
257±19	4.3	-11.2	L1VA
			LHVA
		11.2	LBVF
			LFVG
270±10	4.8	-4.48	L1VF
		4.48	LFVB
277±19	4.5	-8.96	L1VB
			LHVB
		8.96	LBVD
			LFVF
	4.7	-6.72	L1VD
			LHVD
		6.72	LBVB
			LFVD
	4.8	-4.48	LHVF
		4.48	LBVA
		-2.24	L2VB
			LHVG
		2.24	L2VF
			LFVA
	4.9	0	L2VA
			L2VD
Grand Total of 22			

Capsule:	11J		
Type:	TEM holder		
Temp. (°C)	DPA	z (cm)	ID Code
273±19	4.1	12.6	1-2
	4.3	11.5	1-1**
286±10	4.7	-5.4	1-5*
293±19	4.4	9.9	1-8
	4.6	-8	1-4*
		7.3	1-9
	4.8	4.8	1-10
		-2.9	1-6*
		2.2	1-11
	4.9	-0.3	1-12
Grand Total of 10			

*Holders made of Zr
** Contains previously irradiated TEMs

All dpa values are calculated. Measured values will be reported upon completion of dosimetry analysis.

DPA calculation basis: 19034 MWD of operation; The peak DPA/MWD value is 0.000255 for SS, 0.000324 for V, 0.000498 for Al and 2*0.000255 for the ceramics. All DPA values have been rounded off.

DPA varies with axial location with the equation: $\cos(0.00858(z-12.7)) + 0.0000171(z-12.7)^2$, z in mm   (see Ref. 2).

z (cm) is the axial distance of the midpoint of the specimen from the HFIR centerline. All distances have been rounded off.

Operating temperatures are based on the thermocouple data, corrected for the specimen type and location. The given ranges represent the variation in thermocouple data.

Table 1. Operating temperature, axial location, accumulated dpa of specimens in RB-11J. (cont.)

Capsule:	11J		
Type:	B-1		
Temp. (°C)	DPA	z (cm)	ID Code
266±19	4.2	-12	Y603
			Y608*
		12	Y605*
			Y606
286±19	4.8	-3	Y602
			Y604*
		3	Y601
			Y607
	8.5	10.5	DY07
	8.7	-10.5	DY03
	8.8	-9	DY11
		9	DY08
	9.0	-7.5	DY12
		7.5	DY91
	9.2	-6	DY10
		6	DY09
		-7.5	DT05
		7.5	DT02
	9.5	-1.5	DY37
			DY40
		1.5	DY38
		-1	DY39
	9.6	-4.5	DT03
			DT06
		4.5	DT01
			DT04
	9.7	0	DY01
			DY05
Grand Total of 28			

*Poorly marked

Capsule:	11J		
Type:	B-2		
Temp. (°C)	DPA	z (cm)	ID Code
281±19	8.5	-10.5	DY18
			DY19
		10.5	DY13
	8.8	-9	DY17
		9	DY14
	9.2	-6	DY16
		6	DY15
Grand Total of 7			

Capsule:	11J		
Type:	B-3		
Temp. (°C)	DPA	z (cm)	ID Code
281±19	8.5	10.5	DY26
	8.8	-9	DY27
		9	DY25
	9.2	-6	DY23
			DY24
		6	DY21
			DY22
Grand Total of 7			

Capsule:	11J		
Type:	B-4		
Temp. (°C)	DPA	z (cm)	ID Code
281±19	8.5	10.5	DY31
			DY32
	8.8	-9	DY33
			DY34
		9	DY29
			DY30
Grand Total of 6			

Capsule:	11J		
Type:	B-5		
Temp. (°C)	DPA	z (cm)	ID Code
312±19	6.2	-2.25	FV1
		2.25	FY3
		-1.35	FV2
		1.35	FY2
		-0.45	FV3
		0.45	FY1
Grand Total of 6			

All dpa values are calculated. Measured values will be reported upon completion of dosimetry analysis.

DPA calculation basis: 19034 MWD of operation; The peak DPA/MWD value is 0.000255 for SS, 0.000324 for V, 0.000498 for Al and 2*0.000255 for the ceramics. All DPA values have been rounded off.

DPA varies with axial location with the equation: $\cos(0.00858(z-12.7)) + 0.0000171(z-12.7)^2$, z in mm   (see Ref. 2).

z (cm) is the axial distance of the midpoint of the specimen from the HFIR centerline. All distances have been rounded off.

Operating temperatures are based on the thermocouple data, corrected for the specimen type and location. The given ranges represent the variation in thermocouple data.

Table 1. Operating temperature, axial location, accumulated dpa of specimens in RB-11J. (cont.)

Capsule:	11J			Capsule:	11J		
Type:	B-7						
Temp. (°C)	DPA	z (cm)	ID Code	Temp. (°C)	DPA	z (cm)	ID Code
280±9	4.2	-12.5	I--1	312±19	4.8	-4.5	J--1
		12.5	H--5			4.5	G--5
		-12.2	A--4			-4.2	E--1
		12.2	D--5			4.2	C--2
	4.3	-11.5	I--2			-3.5	J--2
		11.5	H--4			3.5	G--4
		-11.2	A--1			-3.2	E--2
		11.2	D--4			3.2	C--1
312±19	4.4	-10.5	I--3			-2.5	J--3
		10.5	H--3			2.5	G--3
		-10.2	A--2		4.9	-1.5	J--4
		10.2	D--3			-0.5	J--5
	4.5	-9.5	I--4			0.5	G--1
		9.5	H--2			1.5	G--2
		-9.2	A--3	Grand Total of 46			
		9.2	D--2				
		-8.5	I--5				
		8.5	H--1				
	4.6	-8.2	A--5				
		8.2	D--1				
		-7.5	F--5				
		7.5	F--3*				
		-7.2	B--1				
		7.2	C--5				
	4.7	-6.5	E--3				
		6.5	F--3*				
		-6.2	B--2				
		6.2	C--4				
		-5.5	F--4				
		5.5	F--2				
		-5.2	B--3				
		5.2	C--3				

*These are labelled identically.

Capsule:	11J		
Type:	B-8		
Temp. (°C)	DPA	z (cm)	ID Code
258±19	8.6	-11.25	843 M1 919 T2
		11.25	917 T4 919 M2
271±10	9.4	6.25	942 T4 T13
	9.6	3.75	6 sticks* 917 M4
278±19	9.0	-8.75	6 sticks* 6 sticks*
		8.75	6 sticks* 6 sticks*
	9.4	-6.25	942 M3 T7
	9.6	-3.75	843 T1 919 M1
	9.7	-1.25	917 T3 T11
		1.25	843 M2 942 M4
Grand Total of 20			

*These specimens are small unmarked bend bars that take up the space of one B-8.

Capsule:	11J		
Type:	TD		
Temp. (°C)	DPA	z (cm)	ID Code
252±19	7.9	14.1	M1
Grand Total of 1			

All dpa values are calculated. Measured values will be reported upon completion of dosimetry analysis.

DPA calculation basis: 19034 MWD of operation; The peak DPA/MWD value is 0.000255 for SS, 0.000324 for V, 0.000498 for Al and 2*0.000255 for the ceramics. All DPA values have been rounded off.

DPA varies with axial location with the equation: $\cos(0.00858(z-12.7)) + 0.0000171(z-12.7)^2$, z in mm   (see Ref. 2).

z (cm) is the axial distance of the midpoint of the specimen from the HFIR centerline. All distances have been rounded off.

Operating temperatures are based on the thermocouple data, corrected for the specimen type and location. The given ranges represent the variation in thermocouple data.

Table 1. Operating temperature, axial location, accumulated dpa of specimens in RB-11J. (cont.)

Capsule:	11J		
Type:	SS-3		

Temp. (°C)	DPA	z (cm)	ID Code
274±9	4.3	-11.43	A002
			A003
			N201
			N202
		11.43	FA11
			FA12
			FK08
			FK09
			TJ03
			TJ04
	5.4	-11.43	72*
			72*
			ST01*
			ST02*
		11.43	70*
			70*
307±19	4.5	-8.89	A006
			A008
			N203
			N204
		8.89	FA09
			FA10
			FK06
			FK07
			TW03
			TW04
	4.7	-6.35	A010
			A011
			TJ01
			TJ02
		6.35	FA07
			FA08
			FK04
			FK05
			TW01
			TW02
	4.8	-3.81	A012
			A022
			N205
			TH02
			TH03

Temp. (°C)	DPA	z (cm)	ID Code
307±19	4.8	3.81	FA05
			FA06
			FK02
			FK03
			ZH40
			ZH41
	4.9	-1.27	A023
			A024
			TH04
			TH05
			Z142
			Z143
		1.27	A025
			A026
			FK00
			FK01
			Z140
			Z141
	5.7	-8.89	71*
			72*
			ST03*
			ST04*
		8.89	70*
			UC15*
	6.0	-6.35	71*
			71*
			71
			72
		6.35	ST05*
			ST06*
	6.1	-3.81	ST07
			XC13*
			XC14*
		3.81	ZC13*
			ZC14*
	6.2	-1.27	XC15*
			ZC15*
		1.27	UC13*
			UC14*
Grand Total of 80			

*Surrounded by Zr foil

All dpa values are calculated. Measured values will be reported upon completion of dosimetry analysis.

DPA calculation basis: 19034 MWD of operation; The peak DPA/MWD value is 0.000255 for SS, 0.000324 for V, 0.000498 for Al and 2*0.000255 for the ceramics. All DPA values have been rounded off.

DPA varies with axial location with the equation: $\cos(0.00858(z-12.7)) + 0.0000171(z-12.7)^2$, z in mm   (see Ref. 2).

z (cm) is the axial distance of the midpoint of the specimen from the HFIR centerline. All distances have been rounded off.

Operating temperatures are based on the thermocouple data, corrected for the specimen type and location. The given ranges represent the variation in thermocouple data.

Table 1. Operating temperature, axial location, accumulated dpa of specimens in RB-11J. (cont.)

Capsule:	11J										
Type:	SS-J										
Temp. (°C)	DPA	z (cm)	ID Code	Temp. (°C)	DPA	z (cm)	ID Code	Temp. (°C)	DPA	z (cm)	ID Code
274±9	4.2	-12	AL13**	307±19	4.5	-8.8	L2V5	307±19	4.8	4	LBV1
			AL14**				LHV2				LBV2
			GD37				LHV3				YDO4
			GD39			8.8	AF82			-2.4	AA40
			L2V1				AF85				AF77
			L2V2				LFV2				AF80
		12	AL19				LFV3				GF38
			AA47				LHV1				GF39
			GB38				LHV4				YDO3
			GB39		4.6	-7.2	AA46			2.4	AA39
			LFV6				AL18				AA45
			LFV7				GB37				AF79
	5.4	-12	F7A1*				L1V2				LDV4
			TD26*				L1V3				LDV5
			TD31*				YDO2				YD10
			TD34*			7.2	AF84		4.9	-0.8	AA36
			TD60*				AF86				AA49
			TD72*				LBV5				AL20
			TD95*				LFV1				LDV1
			TD96*				LHV5				LFV8
		12	AV46*				YDO8				YDO5
			AV52*		4.7	-5.6	AA42			0.8	AA37
			F4AR*				AF83				AF81
			F5AH*				GD38				AL16
			TA03*				L1V4				LDV2
			TD16*				L1V5				LDV3
			TD40*				YDO1				YDO6
			TD55*			5.6	AF91		5.6	-10.4	F2AF*
307±19	4.4	-10.4	AF78				AF92				F347*
			AL15				GD30				F6A2*
			GA37				LBV3				F6A4*
			GA38				LBV4				TD14*
			L2V3				YDO9				TD22*
			L2V4		4.8	-4	AA38				TD42*
		10.4	AF87				AA43				TD66*
			AL17				AA48			10.4	F2A7*
			GA30				GF30				F2AG*
			GA39				GF37				F5AK*
			LFV4				YDO7				F6A1*
			LFV5			4	AA41				TD25*
	4.5	-8.8	AF88				AA44				TD36*
			AF89				AF90^				TD84*
			L1V1								TD85*

**Bent during installation   *Surrounded by Zr foil   ^ Poorly marked

All dpa values are calculated. Measured values will be reported upon completion of dosimetry analysis.

DPA calculation basis: 19034 MWD of operation; The peak DPA/MWD value is 0.000255 for SS, 0.000324 for V, 0.000498 for Al and $2*0.000255$ for the ceramics. All DPA values have been rounded off to 2 decimal places.

DPA varies with axial location with the equation: $cos(0.00858(z-12.7)) + 0.0000171(z-12.7)^2$, z in mm   (see Ref. 2).

z (cm) is the axial distance of the midpoint of the specimen from the HFIR centerline. All distances have been rounded off.

Operating temperatures are based on the thermocouple data, corrected for the specimen type and location. The given ranges represent the variation in thermocouple data.

Table 1. Operating temperature, axial location, accumulated dpa of specimens in RB-11J. (cont.)

Capsule:	11J										
Type:	SS-J	(cont.)									
Temp. (°C)	DPA	z (cm)	ID Code*	Temp. (°C)	DPA	z (cm)	ID Code*	Temp. (°C)	DPA	z (cm)	ID Code*
307±19	5.7	-8.8	F2A1, F2A8, F5A7, F7A6, TD12, TD24, TD44, TD46	307±19	6.0	5.6	AV38, AV41, F5A6, F8A7, TD13, TD54, TD63, TD90	307±19	6.2	-0.8	AV43, AV45, F4A9, F8A0, TA05, TD32, TD53, TD80
		8.8	AV44, AV53, F8A1, F8AG, TA00, TD52, TD65, TD74		6.1	-4	AV40, AV47, F6AM, TA06, TD21, TD51, TD62, TD75			0.8	F2A2, F4A1, F8AK, TD33, TD70, TD81, TD91, TD92
	5.9	-7.2	AV42, AV54, F7B0, F8AH, TD20, TD50, TD64, TD76			4	AV48, AV50, F4AB, TA04, TD30, TD41, TD43, TD73	Grand Total of 224			
		7.2	F340, F34M, F5A0, F7A9, TD10, TD45, TD83, TD93			-2.4	F34R, F4A3, F6AH, F7D0, TA01, TD11, TD35, TD61				
	6.0	-5.6	AV37, AV39, F6A6, F7AD, TA02, TD15, TD71, TD86			2.4	AV49, AV51, F4AH, F5AL, TD23, TD56, TD82, TD94				

*All of these specimens are surrounded by Zr foil.

All dpa values are calculated. Measured values will be reported upon completion of dosimetry analysis.

DPA calculation basis: 19034 MWD of operation; The peak DPA/MWD value is 0.000255 for SS, 0.000324 for V, 0.000498 for Al and 2*0.000255 for the ceramics. All DPA values have been rounded off.

DPA varies with axial location with the equation: $\cos(0.00858(z-12.7)) + 0.0000171(z-12.7)^2$, z in mm   (see Ref. 2).

z (cm) is the axial distance of the midpoint of the specimen from the HFIR centerline. All distances have been rounded off.

Operating temperatures are based on the thermocouple data, corrected for the specimen type and location. The given ranges represent the variation in thermocouple data.

Table 2. Operating temperature, axial location, accumulated dpa of specimens in RB-12J.

Capsule:	12J		
Type:	1.5 CVN		
Temp. (°C)	DPA	z (cm)	ID Code
388±24	3.9	14.46	LDW4
			LDW5
			LDW6
			LHW2
414±23	3.9	-14.46	LDW1
			LDW2
			LDW3
			LHW1
481±22	4.4	-10.11	LHW3
490±17	4.2	-12	L1W1
			L2W1
		12	LBW6
			LFW6
501±22	4.6	-8.11	LHW4
509±22	4.4	-10	L1W2
			L2W2
		10	LBW5
			LFW5
	4.6	-8	L1W3
			L2W3
		8	LBW4
			LFW4
	4.7	-6	L1W4
			L2W4
		6	LBW3
			LFW3
	4.8	-4	L1W5
			L2W5
		-2	L1W6
			L2W6
		2	LBW1
			LFW1
		4	LBW2
			LFW2
	4.9	0	LHW5
			LHW6
Grand Total of 36			

Capsule:	12J		
Type:	PT		
Temp. (°C)	DPA	z (cm)	ID Code
399±21	4.8	3.79	LFWA
	5.96	6.18	12*
445±16	4.7	-5.18	LHWA
	4.8	-4.48	1010
476±22	4.2	-11.89	LFWG
			LHWG
	4.3	-11.2	1515
		11.2	L2WA
	5.45	11.26	3*
			5*
496±22	4.4	-9.65	LBWB
			LHWF
	4.5	-8.96	1414
		8.96	L2WB
	4.6	-7.41	L1WD
			LHWD
	4.7	-6.72	1111
		-5.18	LHWB
		6.72	L2WD
	4.8	-2.93	LBWD
			LFWF
		-2.24	X9X9
		1.55	L1WB
			LFWB
		2.24	X7X7
		3.79	L1WA
		4.48	X6X6
	4.9	-0.69	LBWA
			LFWD
		0	X8X8
	5.75	8.72	11*
			9*
	5.96	6.18	1*
Grand Total of 33			

*Sealed in a Zr tube

All dpa values are calculated. Measured values will be reported upon completion of dosimetry analysis.

DPA calculation basis: 19034 MWD of operation; The peak DPA/MWD value is 0.000255 for SS, 0.000324 for V, 0.000498 for Al and 2*0.000255 for the ceramics. All DPA values have been rounded off.

DPA varies with axial location with the equation: $\cos(0.00858(z-12.7)) + 0.0000171(z-12.7)^2$, z in mm (see Ref. 2).

z (cm) is the axial distance of the midpoint of the specimen from the HFIR centerline. All distances have been rounded off.

Operating temperatures are based on the thermocouple data, corrected for the specimen type and location. The given ranges represent the variation in thermocouple data.

Table 2. Operating temperature, axial location, accumulated dpa of specimens in RB-12J. (cont.)

Capsule:	12J		
Type:	1/3 CVN		
Temp. (°C)	DPA	z (cm)	ID Code
412±21	4.7	6.35	150 Z1
			FA46
	4.8	3.81	A027
			FA45
		4.32	135 Z1
458±16	4.7	-6.35	FA61
			FK11
			TW08
	4.8	-3.81	FA62
			FK13
			TW09
489±22	4.2	11.94	149 Z1
	4.3	-11.43	A008
			A028**
			FA58
			N206
			TW06
	5.4	11.43	QC65*
			QC66*
			QC67*
			QC68*
			QC69*
509±22	4.5	-8.89	A009
			A029
			FA59
			N207
			TW07
		8.89	151 Z1
			FA47
			FK09
			FK39
			N211
		9.4	148 Z1
	4.7	-6.35	A010
			A030
		-5.84	131 Z1
		6.35	FK06
			FK38
			N210
		6.86	147 Z1

Temp. (°C)	DPA	z (cm)	ID Code
509±22	4.8	-3.81	A011
			A031
		-3.3	132 Z1
		1.78	134 Z1
		3.81	FK05
			FK37
			N209
	4.9	-1.27	A012
			FA44
			FA64
			FK35
			TW10
		-0.76	133 Z1
		1.27	A007
			FA43
			FA48
			FK36
			N208
Grand Total of 58			

Capsule:	12J		
Type:	TEM holder		
Temp. (°C)	DPA	z (cm)	ID Code
412±21	4.8	4.6	2-9
489±22	4.2	12.2	2-12
	4.6	-7.8	2-6*
509±22	4.4	9.7	2-11
	4.6	7.1	2-10
	4.7	-5.3	2-5*
	4.8	-2	2-8
		-2.8	2-4*
	4.9	0.3	2-1**
		-0.9	2-2
Grand Total of 10			

*Holders made of Zr
** Contains previously irradiated TEMs

*Surrounded by Zr foil
**Appeared bent prior to loading

All dpa values are calculated. Measured values will be reported upon completion of dosimetry analysis.

DPA calculation basis: 19034 MWD of operation; The peak DPA/MWD value is 0.000255 for SS, 0.000324 for V, 0.000498 for Al and 2*0.000255 for the ceramics. All DPA values have been rounded off.

DPA varies with axial location with the equation: $\cos(0.00858(z-12.7)) + 0.0000171(z-12.7)^2$, z in mm (see Ref. 2).
z (cm) is the axial distance of the midpoint of the specimen from the HFIR centerline. All distances have been rounded off.
Operating temperatures are based on the thermocouple data, corrected for the specimen type and location. The given ranges represent the variation in thermocouple data.

Table 2. Operating temperature, axial location, accumulated dpa of specimens in RB-12J. (cont.)

Capsule:	12J		
Type:	B-1		

Temp. (°C)	DPA	z (cm)	ID Code
390±24	7.7	14.21	DY50
	7.9	14.21	DY41
406±21	9.5	4.5	DY02
			DY04
416±24	7.7	-14.21	DY51
	7.9	-14.21	DY42
483±22	4.21	-12	Y616
			Y616*
	8.4	12	DY06
			DY49
503±22	4.37	-10.5	Y609
		10.5	Y624
	4.5	-9	Y610*
		9	Y623
	4.61	-7.5	Y611
		7.5	Y622
	4.7	-6	Y612
		6	Y621*
	4.77	-4.5	Y613
		4.5	Y620
	4.82	-3	Y614
		3	Y619
	4.85	-1.5	Y615
		0	Y617*
		1.5	Y618
	8.7	-10.5	DY43
			DY48
		10.5	DY44
			DY45
	8.8	-9	DT13
			DT15
		9	DY80
			DY83
	9	-7.5	DY53
			DY55
		7.5	DY52
			DY54
	9.4	-6	DT08
			DT09
		-3	DY81
			DY82

Temp. (°C)	DPA	z (cm)	ID Code
503±22	9.4	3	DT14
			DT16
		6	DT07
			DT11
	9.5	-4.5	DY46
			DY47
		-1.5	DY94
			DY95
		1.5	DY93
			DY96
	9.7	0	DT10
			DT12
Grand Total of 53			

*Poorly marked

Capsule:	12J		
Type:	B-2		

Temp. (°C)	DPA	z (cm)	ID Code
390±24	7.7	14.21	DY56
			DY57
			DY58
			DY59
416±24	7.7	-14.21	DY60
			DY61
			DY62
			DY63
Grand Total of 8			

Capsule:	12J		
Type	B-3		

Temp. (°C)	DPA	z (cm)	ID Code
390±24	7.7	14.21	DY68
			DY69
			DY70
			DY71
			DY92
416±24	7.7	-14.21	DY28
			DY64
			DY65
			DY66
			DY67
Grand Total of 10			

All dpa values are calculated. Measured values will be reported upon completion of dosimetry analysis.

DPA calculation basis: 19034 MWD of operation; The peak DPA/MWD value is 0.000255 for SS, 0.000324 for V, 0.000498 for Al and 2*0.000255 for the ceramics. All DPA values have been rounded off.

DPA varies with axial location with the equation: $\cos(0.00858(z-12.7)) + 0.0000171(z-12.7)^2$, z in mm (see Ref. 2).

z (cm) is the axial distance of the midpoint of the specimen from the HFIR centerline. All distances have been rounded off.

Operating temperatures are based on the thermocouple data, corrected for the specimen type and location. The given ranges represent the variation in thermocouple data.

Table 2. Operating temperature, axial location, accumulated dpa of specimens in RB-12J. (cont.)

Capsule:	12J		
Type:	B-4		
Temp. (°C)	DPA	z (cm)	ID Code
390±24	7.7	14.21	DY35
			DY36
			DY72
			DY73
			DY78
416±24	7.7	-14.21	DY74
			DY75
			DY76
			DY77
			DY79
Grand Total of 10			

Capsule:	12J		
Type:	B-5		
Temp. (°C)	DPA	z (cm)	ID Code
484±17	5.3	12.05	FY6
	8.2	-12.05	None
503±22	5.5	-11.15	FVD
		11.15	FY5
	5.6	-10.25	FVA
		10.25	FY4
	5.7	-9.35	FZ1
		9.35	FX7
	5.8	-8.45	FZ2
		8.45	FX6
	5.9	-7.55	FZ3
		-6.65	FZ4
		6.65	FX4
		7.55	FX5
	6	-5.75	FZ5
		-4.85	FZ6
		4.85	FX2
		5.75	FX3
	6.1	-3.95	FZ7
		3.95	FX1
Grand Total of 20			

Capsule:	12J		
Type:	B-6		
Temp. (°C)	DPA	z (cm)	ID Code
355±33	7.8	14.71	D1
			D2
389±28	7.8	-14.71	D3
			D4
401±21	9.4	6.25	D7
	9.6	3.75	S7
447±16	9.4	-6.25	G1
	9.6	-3.75	H2
478±22	8.6	-11.25	P2
			S1
		11.25	P6
			S8
498±22	9	-8.75	H1
			N1
		8.75	D5
			N3
	9.4	-6.25	D6
		6.25	H3
	9.6	-3.75	H5
		3.75	G4
	9.7	-1.25	G3
			N2
		1.25	P5
			S3
Grand Total of 24			

Capsule:	12J		
Type:	B-8		
Temp. (°C)	DPA	z (cm)	ID Code
447±16	9.4	-6.25	917 T2
	9.6	-3.75	917 M2
478±22	8.6	11.25	942 M1
			T5
498±22	9	-8.75	917 T1
		8.75	T3
	9.4	6.25	942 T2
	9.6	3.75	942 M2
	9.7	-1.25	917 M1
		1.25	942 T1
Grand Total of 10			

All dpa values are calculated. Measured values will be reported upon completion of dosimetry analysis.

DPA calculation basis: 19034 MWD of operation; The peak DPA/MWD value is 0.000255 for SS, 0.000324 for V, 0.000498 for Al and 2*0.000255 for the ceramics. All DPA values have been rounded off.

DPA varies with axial location with the equation: $\cos(0.00858(z-12.7)) + 0.0000171(z-12.7)^2$, z in mm   (see Ref. 2).

z (cm) is the axial distance of the midpoint of the specimen from the HFIR centerline. All distances have been rounded off. Operating temperatures are based on the thermocouple data, corrected for the specimen type and location. The given ranges represent the variation in thermocouple data.

Table 2. Operating temperature, axial location, accumulated dpa of specimens in RB-12J. (cont.)

Capsule:	12J
Type:	B-7

Temp. (°C)	DPA	z (cm)	ID Code
486±17	4.2	-12.5	B-+5
			F-+4
		12.5	G-+5
			H-+3
505±22	4.3	-11.5	B-+2
			I-+1
		11.5	A-+5
			C-+3
	4.4	-10.5	A-+4
			E-+2
		10.5	E-+4
			I-+3
	4.5	-9.5	E-+3
			I-+5
		-8.5	J-+3
			K-+3
		8.5	H-+5
			M-+2
		9.5	D-+2
			I-+4
	4.6	-7.5	G-+4
			K-+2
		7.5	B--4
			D-+4
	4.7	-6.5	J-+4
			M-+1
		-5.5	G-+3
			J-+5
		5.5	A-+2
			G-+2
		6.5	C-+2
			H-+4
	4.8	-4.5	E-+5
			I-+2
		-3.5	B--5
			D-+3
		-3	A-+1
		-2.5	E--5
			H-+1
		-2	B-+1
		-1.5	C-+5
			K-+1

Temp. (°C)	DPA	z (cm)	ID Code
505±22	4.8	1.5	H-+2
			J-+2
		2	F-+1
		2.5	A-+3
			B-+4
		3	G-+1
		3.5	D-+5
			F-+5
		4.5	F-+ 1*
			J-+1
	4.9	-1	C-+1
		-0.5	B-+3
			F-+2
		0	D-+1
		0.5	C-+4
			E--4
		1	E-+1

Grand Total of 59

*Markings are poor.

Capsule:	12J
Type:	DCT

Temp. (°C)	DPA	z (cm)	ID Code
343±33	3.8	15.46	FA03
			N204
			TWO4
			Z108
	4	14.15	FA02*
			N203*
			TWO3*
			Z107*
377±28	3.6	-16.78	LFTA
			LFTB
			FA14
			FA17
	3.8	-15.46	LFTD
			LFTG
			FA15
			FA18
	4	-14.15	LFTF
			LFTH
			FA16
			FA19

Grand Total of 20

*2 out of 4 are actually at z=16.8 cm & 3.6 dpa

All dpa values are calculated. Measured values will be reported upon completion of dosimetry analysis.

DPA calculation basis: 19034 MWD of operation; The peak DPA/MWD value is 0.000255 for SS, 0.000324 for V, 0.000498 for Al and 2*0.000255 for the ceramics. All DPA values have been rounded off.

DPA varies with axial location with the equation: $\cos(0.00858(z-12.7)) + 0.0000171(z-12.7)^2$, z in mm (see Ref. 2).

z (cm) is the axial distance of the midpoint of the specimen from the HFIR centerline. All distances have been rounded off. Operating temperatures are based on the thermocouple data, corrected for the specimen type and location. The given ranges represent the variation in thermocouple data.

Table 2. Operating temperature, axial location, accumulated dpa of specimens in RB-12J. (cont.)

Capsule:	12J						
Type:	SS-3						
Temp. (°C)	DPA	z (cm)	ID Code	Temp. (°C)	DPA	z (cm)	ID Code
478±17	4.3	-11.43	N208	497±22	4.9	1.27	A036
			N209				FA13
			TH08				FK16
			TH09				FK17
			Z146		5.7	8.89	70*
			Z147				70*
		11.43	N206		6	6.35	UC16*
			N207				UC17*
			TH06		6.1	-3.81	XC16*
			TH07				XC17*
	5.4	11.43	71*			3.81	ZC16*
			71*				ZC17*
497±22	4.5	-8.89	FA16		6.2	-1.27	ST08*
			FA17				ST09*
			TW05			1.27	ST10*
			TW06				ST11*
			Z144	Grand Total of 60			
			Z145				
		8.89	FA14				
			FA15				
			TW07				
			TW08				
	4.7	-6.35	A029				
			A030				
			FK10				
			FK11				
			TJ07				
			TJ08				
		6.35	A055				
			A056				
			TJ05				
			TJ06				
	4.8	-3.81	A031				
			A033				
			FK12				
			FK13				
		3.81	A038				
			A039				
			FK18				
			FK19				
497±22	4.9	-1.27	A034				
			A035				
			FK14				
			FK15				

*Surrounded by Zr foil

Capsule:	12J		
Type:	SiC Tube		
Temp. (°C)	DPA	z (cm)	ID Code
499±22	8.9	-9.6	J10
			J18
		9.6	J2
			J20
	9.5	-4.8	J16
			J8
		4.8	J12
			J4
	9.7	0	J14
			J6
Grand Total of 10			

Capsule:	12J		
Type:	TD		
Temp. (°C)	DPA	z (cm)	ID Code*
355±33	7.1	16.83	B1
			D1
			D2
			P1
			P2
			M2
Grand Total of 6			

*3 out of 6 are actually at z=14.1 cm & 8 dpa

All dpa values are calculated. Measured values will be reported upon completion of dosimetry analysis.

DPA calculation basis: 19034 MWD of operation; The peak DPA/MWD value is 0.000255 for SS, 0.000324 for V, 0.000498 for Al and 2*0.000255 for the ceramics. All DPA values have been rounded off.

DPA varies with axial location with the equation: $\cos(0.00858(z-12.7)) + 0.0000171(z-12.7)^2$, z in mm   (see Ref. 2).

z (cm) is the axial distance of the midpoint of the specimen from the HFIR centerline. All distances have been rounded off.

Operating temperatures are based on the thermocouple data, corrected for the specimen type and location. The given ranges represent the variation in thermocouple data.

Table 2. Operating temperature, axial location, accumulated dpa of specimens in RB-12J. (cont.)

Capsule:	12J										
Type:	SS-J										
Temp. (°C)	DPA	z (cm)	ID Code	Temp. (°C)	DPA	z (cm)	ID Code	Temp. (°C)	DPA	z (cm)	ID Code
478±17	4.2	-12	AFK0	497±22	4.5	8.8	AFL3	497±22	4.9	-0.8	AA89
			AFK2				AFL8				AFJ0
			AFL0		4.6	-7.2	AF74				LFW3
		12	AA87^				AFJ9				LHW1
			AFJ7				AFM1				YD12
			AFL2				AFM2				YD13
			AFL7				YD15			0.8	AA96**
	5.4	-12	AV56				YD20				AF75
			AV93*			7.2	AA95				L1W2
			AV97*				AFK3				L2W1
			AV98*				AFK9		5.6	-10.4	AV55
			AV99*^				AFL9				AV94*
			AVB0		4.7	-5.6	AA88				AVB2*
			TH16*				AA91				AVC1
			TH37*				AFK7				F6AK*
			TH38				AFK8				F8A9*
			TH45*				YD11				TH15*
			TH78*				YD19				TH22*
		12	AV92*			5.6	AA92				TH52*
			AV95*^				AA99				TH67*
			F6A8*				AFL6			10.4	AVB5*
			F7F0*				LDW2				AVB6*
			TH23*		4.8	-4	AF73				F7A5*
			TH31*				AF76				F8AL*
			TH56*				LDW1				TH17*
			TH61*				LFW2				TH35*
			TH88*				YD14				TH46*
			TH92*				YD18				TH74*
497±22	4.4	-10.4	AA86			-2.4	AF67				TH84*
			AF68				AF71				TH93*
			AFK4				L1W1		5.7	-8.8	AV96*
			AFL5				LBW1				AVB8*^
		10.4	AA90				YD16				F343
			AF72				YD17				F344
			AFK5			2.4	AA94				TB01*
			AFL1				AA98				TB02*
	4.5	-8.8	AA93				LBW2				TH12*
			AF69				LHW2				TH40*
			AFK6			4	AF70				TH65*
			AFL4				AFK1^				TH81*
		8.8	AA97				L2W2				
			AFJ8				LFW1				

* Surrounded by Zr foil   ** Bent during installation   ^ Markings are poor

All dpa values are calculated. Measured values will be reported upon completion of dosimetry analysis.
DPA calculation basis: 19034 MWD of operation; The peak DPA/MWD value is 0.000255 for SS, 0.000324 for V, 0.000498 for Al and 2*0.000255 for the ceramics. All DPA values have been rounded off.
DPA varies with axial location with the equation: $\cos(0.00858(z-12.7)) + 0.0000171(z-12.7)^2$, z in mm (see Ref. 2).
z (cm) is the axial distance of the midpoint of the specimen from the HFIR centerline. All distances have been rounded off.
Operating temperatures are based on the thermocouple data, corrected for the specimen type and location. The given ranges represent the variation in thermocouple data.

Table 2. Operating temperature, axial location, accumulated dpa of specimens in RB-12J. (cont.)

Capsule:	12J										
Type:	SS-J	(cont.)									
Temp. (°C)	DPA	z (cm)	ID Code*	Temp. (°C)	DPA	z (cm)	ID Code*	Temp. (°C)	DPA	z (cm)	ID Code*
497±22	5.7	8.8	AV00	497±22	6	5.6	F2A6	497±22	6.1	4	F2A5
			AVB1				F5A4				F2AM
			F5AR				TB05				F4AM
			F6AL				TB06				F6A9
			TH33				TH26				TH24
			TH41				TH27				TH44
			TH71				TH51				TH75
			TH73				TH55				TH77
			TH87				TH91				TH86
			TH98				TH97				TH95
	5.9	-7.2	AVB4		6.1	-4	F2A3		6.2	-0.8	F349
			AVB7				F346				F4A2
			TH10				F6AD				F7AF
			TH34				F7G0				F8AM
			TH50				TB08				TH18
			TH70				TH42				TH21
		7.2	AVB3				TH48				TH53
			AVB9				TH76				TH62
			F4AF			-2.4	F2AK			0.8	F4A5
			F5AG				F4A7				F4A6
			F7A2				F6A5				TB04
			F8A4				F7AA				TB07
			TH14				TH11				TH32
			TH30				TH28				TH36
			TH58				TH47				TH64
			TH63				TH54				TH80
			TH82			2.4	F2AR				TH83
			TH96				F5AD				TH85
	6	-5.6	F5A2				TB00	Grand Total of 224			
			F5A8				TB03				
			F8AB				TH20				
			F8AD				TH25				
			TH13				TH66				
			TH43				TH72				
			TH57				TH90				
			TH60				TH94				

*All of the specimens on this page are surrounded by Zr foil.

All dpa values are calculated. Measured values will be reported upon completion of dosimetry analysis.

DPA calculation basis: 19034 MWD of operation; The peak DPA/MWD value is 0.000255 for SS, 0.000324 for V, 0.000498 for Al and 2*0.000255 for the ceramics. All DPA values have been rounded off.

DPA varies with axial location with the equation: $\cos(0.00858(z-12.7)) + 0.0000171(z-12.7)^2$, z in mm   (see Ref. 2).

z (cm) is the axial distance of the midpoint of the specimen from the HFIR centerline. All distances have been rounded off.

Operating temperatures are based on the thermocouple data, corrected for the specimen type and location. The given ranges represent the variation in thermocouple data.

AS-BUILT CONDITION AND OPERATING HISTORY OF THE U.S./JAERI HFIR MFE-RB-10J CAPSULE – K. E. Lenox and J. P. Robertson (Oak Ridge National Laboratory)

OBJECTIVE

The objective of this report is to provide information on the current status of the HFIR MFE-RB-10J experiment.

SUMMARY

The HFIR-MFE-RB-10J experiment is being conducted under the auspices of the U.S. Department of Energy (DOE)/Japan Atomic Energy Research Institute (JAERI) Collaborative Testing Program. The final specimen loading lists, operating constraints, and operating history of the experiment are discussed. The experiment has undergone approximately ten (10) days of irradiation, but has been removed from HFIR due to the development of a leak in the primary containment vessel. The associated europium liner has also been removed. Efforts are underway to apply for approval to continue the irradiation of the RB-10J experiment as soon as possible.

PROGRESS AND STATUS

Description of the RB-10J Capsule

The RB-10J capsule contains three temperature zones designed to operate at 250°C, 420°C, and 480°C. Two of the zones (420°C and 480°C) contain vanadium specimens in lithium-filled containers, or subcapsules, while the third zone (250°C) consists of steel specimens placed into cutouts in an aluminum block. The lithium-filled subcapsules are nested inside of a stainless steel primary containment vessel, which is nested inside of a stainless steel secondary containment vessel. The stainless steel specimens in the aluminum block are outside of the primary containment vessel, but inside the secondary containment vessel. The secondary containment vessel is in contact with the reactor coolant water. (See Figs. 1-2)
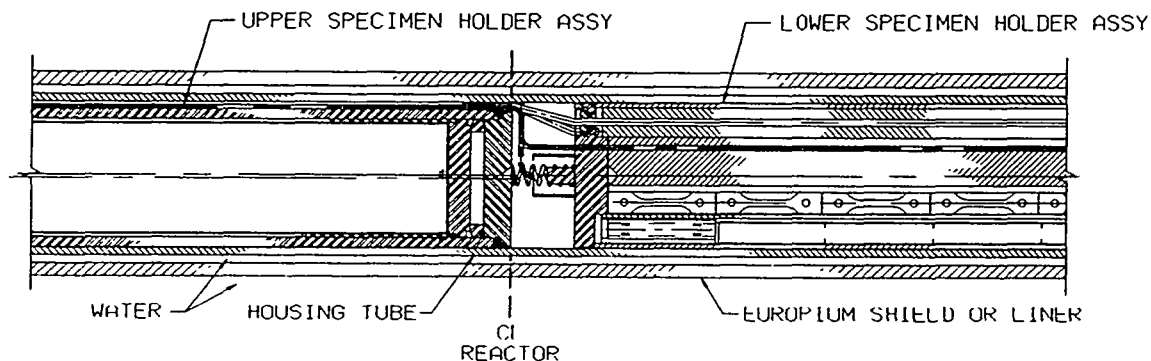
Fig. 1. The interface between the upper and lower halves of the RB-10J specimen region. The positions of the housing tube and the europium shield are also shown.
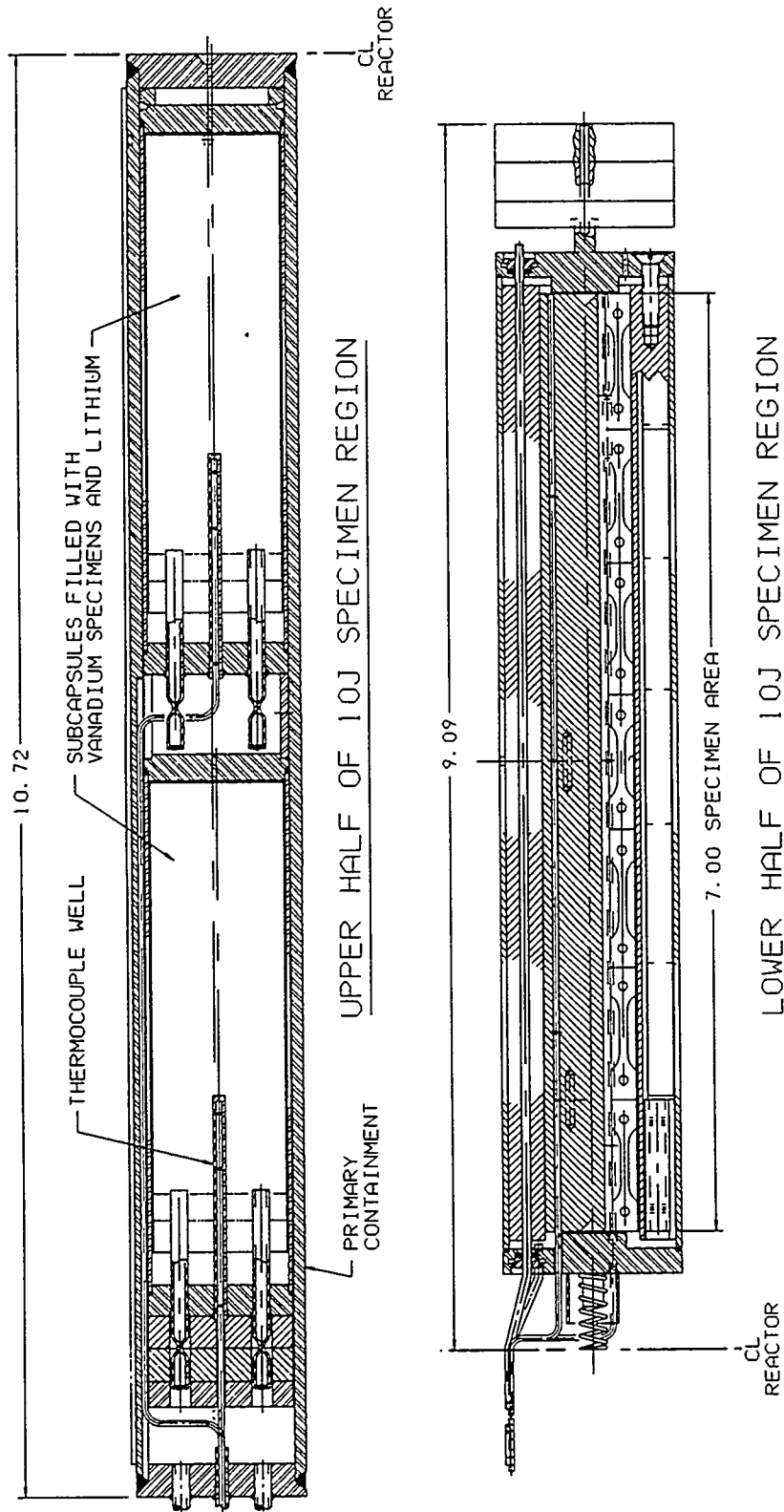
Fig. 2. Upper and lower halves of the RB-10J specimen region. The upper half contains the primary containment vessel and two lithium filled subcapsules. The lower half contains steel specimens in a cylindrical aluminum block.

Temperature control is maintained by varying the conductivity in a gas-filled gap inside of the secondary containment vessel. The conductivity is changed by varying the composition of gas in the gap. The gas composition can range from pure helium to pure neon or any mixture of the two. Additional neon can be added to the region around the lithium-filled subcapsules in order to boost the temperature of the vanadium specimens, without increasing the temperature of the steel specimens. There are thermocouples in each temperature zone, and the data from the thermocouples are used to control the gas mixture in the gap.

Additional descriptions of the capsule have been reported previously. [1,2]

Specimen Loading Lists

Table 1 contains information on the specimens loaded into the RB-10J capsule. The table is sorted into each of eight (8) specimen types: Charpy or bend bars (CVN), tensile specimens (SS-3), TEM disks, notched thin strip specimens (TS), notched strip specimens (NS), J-type tensile specimen (SS-3J), and disk compact tension (DCT) specimens, and pressurized creep tube specimens (PT). Under each specimen type, a listing of individual specimens is given, grouped by their location and accumulated DPA values. The operating temperatures are also shown.

Operating Constraints

Several operating constraints, above and beyond that of typical MFE type capsules, were placed upon the RB-10J capsule due to the presence of lithium. The constraints are intended to make the possibility of interaction between molten lithium and the reactor coolant water an incredible event. The constraints also influenced the design and physical makeup of the capsule.

The constraints include the requirement of two independent containment vessels, each with its own monitoring system to verify the integrity of the containment, along with extensive requirements on the type and amount of additional analyses and testing that had to be performed on capsule components. A probabilistic risk assessment was performed to evaluate the potential for a catastrophic failure of both containment vessels. Furnace experiments were performed using lithium to evaluate the potential for lithium to attack the capsule materials for the given conditions. A finite element stress analysis was performed on the lithium-filled subcapsules to evaluate the behavior of the subcapsules during the melting and solidification of lithium during the irradiation. In addition, internal and external pressure tests of the containment vessels and lithium-filled subcapsules were performed prior to irradiation to confirm the integrity of the as-built capsule.

Operating History

The irradiation of the RB-10J experiment began on Oct. 13, 1998. The 250°C region was brought up to the desired operating temperature within thirty (30) minutes after the reactor reached full power (84 MW). Due to unexpectedly high temperature readings in one of the three thermocouples in the 420°C region, the temperatures in the lithium filled regions were left at 30°C below the desired values until Oct. 16, 1998. At that time, because all other temperature indications showed that the lithium-filled regions were in fact below the desired operating temperature, the temperatures were brought up to the desired values. The temperature readings from the deviant thermocouple in the 420°C region stabilized after five days, most likely due to the release of a helium bubble trapped in the molten lithium. The average temperature readings in the three zones for the period from Oct. 16, 1998 to Oct. 23, 1998 were 265°C, 410°C and 475°C.

Table 1. Axial Location, Accumulated DPA, and Operating Temperatures of specimens in RB-10J.

Type: CVN

DPA	z (cm)	Operating Temp. (C)	Alloy	ID Code
0.12	-18.6	291±7	SA-316F	8HA9, 8HC1, 8HD2
0.13	-16.1	291±7	SA-316F	8HB2, 8HC5
			SA-JPCA	8NA3
0.15	-13.5	291±7	SA-316F	8HB0, 8HC6
			SA-JPCA	8NA1
0.17	-11.0	291±7	SA-316F	8HB3, 8HD0, 8HD4
	18.2	415±10	V-4Cr-4Ti	RC11, RC12, RC13, RC14, RC82, RC83, RC91, RC92
0.18	-8.4	291±7	SA-316F	8HB1, 8HC2, 8HD3
0.19	15.6	415±10	V-4Cr-4Ti	RC15, RC16, RC17, RC18, RC19, RC20, RC21, RC22, RC23, RC24, RC25, RC84, RC85, RC93, RC94

DPA	z (cm)	Operating Temp. (C)	Alloy	ID Code
0.20	-5.9	291±7	SA-316F	8HB4, 8HD1
			SA-JPCA	8NA4
0.21	-3.4	291±7	SA-316F	8HC8
			SA-JPCA	8NA0, 8NA2
0.27	5.8	479±7	V-4Cr-4Ti	RC42, RC43, RC44, RC45, RC89, RC90, RC98, RC99
0.28	3.2	479±7	V-4Cr-4Ti	RC31, RC32, RC33, RC34, RC35, RC36, RC37, RC38, RC39, RC40, RC41, RC87, RC88, RC96, RC97

Grand Total of 67

DPA calculation basis: 865 MWD of operation; The peak DPA/MWD value is 0.000255 for SS and 0.000324 for V.

DPA varies with axial location with the equation: $\cos(0.00858(z-12.7)) + 0.0000171(z-12.7)^2$, z in mm (see Ref. 3).

All DPA values have been rounded off to 2 decimal places.

z (cm) is the axial distance of the midpoint of the specimen from the HFIR centerline. All distances have been rounded off.

Operating temperatures are based on the thermocouple data, corrected for the specimen type and location. The given ranges represent the variation in thermocouple data.

Table 1. Axial Location, Accumulated DPA, and Operating Temperatures of specimens in RB-10J. (cont.)

Type: NS

DPA	z (cm)	Operating Temp. (C)	Alloy	ID Code
0.12	-18.8	285±10	SA-316F	1HA6
				4HA1
	-18.6	269±10	SA-316F	1HA2
				2HA2
				3HA0
				4HA2
			SA-JPCA	1NA0
				3NA0
0.13	-16.2	285±10	SA-316F	5HA6
			SA-JPCA	1NA3
	-16.1	269±10	SA-316F	5HA3*
				7HA2
			SA-JPCA	1PA0
				2PA0
				3PA1
				7NA0
0.15	-13.7	285±10	SA-316F	3HA6
				7HA5
	-13.5	269±10	SA-316F	1HA3
				2HA3
				3HA3
				4HA3
			SA-JPCA	1NA1
				3NA1
0.16	-11.1	285±10	SA-JPCA	3NA3
				7NA3
0.17	-11.0	269±10	SA-316F	5HA3*
				7HA3
			SA-JPCA	1PA1
				2PA1
				3PA0
	-11.0	269±10	SA-JPCA	7NA1

DPA	z (cm)	Operating Temp. (C)	Alloy	ID Code
0.18	-8.6	285±10	SA-316F	1HA7
				3HA7
	-8.4	269±10	SA-316F	1HA4
				2HA4
				3HA1
				4HA4
			SA-JPCA	1NA2
				3NA2
0.20	-6.1	285±10	SA-316F	4HA6
				5HA5
	-5.9	269±10	F82H IEA heat	NS03
				NS04
				NT07
				NT10
			SA-316F	5HA4
				7HA4
				7HA7
			SA-JPCA	7NA2
0.21	-3.5	285±10	SA-316F	7HA6
	-3.4	269±10	F82H IEA heat	NS01
				NS02
				NT04
				NT06
			SA-316F	1HA5
				3HA5
				4HA7
				5HA7
Grand Total of 59				

*One of these two entries may be in error. One may actually be 5HA2.

Type: SS-3J

DPA	z (cm)	Operating Temp. (C)	Alloy	ID Code
0.17	17.7	415±10	V-4Cr-4Ti-0.5SiAlY	LB01
		.		LB02
				LB03
0.27	5.3	479±7	V-4Cr-4Ti-0.5SiAlY	LB04
				LB05
				LB06
Grand Total of 6				

Type: DCT

DPA	z (cm)	Operating Temp. (C)	Alloy	ID Code
0.21	14.1	415±10	V-4Cr-4Ti	RC01
0.28	1.7	479±7	V-4Cr-4Ti	RC03
Grand Total of 2				

DPA calculation basis: 865 MWD of operation; The peak DPA/MWD value is 0.000255 for SS and 0.000324 for V.

DPA varies with axial location with the equation: $\cos(0.00858(z-12.7)) + 0.0000171(z-12.7)^2$, z in mm   (see Ref. 3).

All DPA values have been rounded off to 2 decimal places.

z (cm) is the axial distance of the midpoint of the specimen from the HFIR centerline. All distances have been rounded off.

Operating temperatures are based on the thermocouple data, corrected for the specimen type and location. The given ranges represent the variation in thermocouple data.

Table 1. Axial Location, Accumulated DPA, and Operating Temperatures of specimens in RB-10J. (cont.)

Type: SS-3									
DPA	z (cm)	Operating Temp. (C)	Alloy	ID Code	DPA	z (cm)	Operating Temp. (C)	Alloy	ID Code
0.12	-18.8	289±7	F82H IEA heat	A905	0.17	18.2	415±10	V-4Cr-4Ti	RC06
				A913					RC07
				A926					RC08
				A934					RC09
			JPCA	CPA0					RC10
			SA-316F	CHB4					RC21
				CHC5					RC23
				CHC6					RC30
			SA-JPCA	CNA0					RC31
				CNA7					RC32
0.13	-16.2	289±7	F82H IEA heat	A906					RC33
				A916					RC34
				A922					RC35
				A936					RC36
			JPCA	CPA1					RC37
			SA-316F	CHB5					RC38
				CHC7					RC39
				CHC8					RC94
			SA-JPCA	CNA1					RC95
				CNA8					RC97
0.15	-13.7	289±7	F82H IEA heat	A907				V-4Cr-4Ti-RF	RV05
				A918					RV06
				A927					RV07
				A937	0.18	-8.6	289±7	F82H IEA heat	A909
			JPCA	CPA2					A915
			SA-316F	CHB6					A930
				CHC9					A939
				CHD0				SA-316F	CHB8
			SA-JPCA	CNA2					CHC2
				CNA9					CHD3
0.16	-11.1	289±7	F82H IEA heat	A908					CHD4
				A919				SA-JPCA	CNA4
				A929					CNB1
				A938	0.19	15.6	415±10	V-4Cr-4Ti	RC24
			SA-316F	CHB7					RC25
				CHC1					RC40
				CHD1					RC41
				CHD2					RC42
			SA-JPCA	CNA3					RC43
				CNB0					RC44
0.17	18.2	415±10	V-4Cr-4Ti	RC03					RC45
				RC04					RC46
				RC05					RC47

DPA calculation basis: 865 MWD of operation; The peak DPA/MWD value is 0.000255 for SS and 0.000324 for V.

DPA varies with axial location with the equation: $\cos(0.00858(z-12.7)) + 0.0000171(z-12.7)^2$, z in mm   (see Ref. 3).

All DPA values have been rounded off to 2 decimal places.

z (cm) is the axial distance of the midpoint of the specimen from the HFIR centerline. All distances have been rounded off.

Operating temperatures are based on the thermocouple data, corrected for the specimen type and location. The given ranges represent the variation in thermocouple data.

330

Table 1. Axial Location, Accumulated DPA, and Operating Temperatures of specimens in RB-10J. (cont.)

Type: SS-3 (cont.)

Left section:

DPA	z (cm)	Operating Temp. (C)	Alloy	ID Code
0.19	15.6	415±10	V-4Cr-4Ti	RC48
				RC49
			V-4Cr-4Ti-0.5SiAlY	LB01
				LB02
				LB05
				LB06
				LB07
			V-4Cr-4Ti-RF	RV01
				RV02
				RV08
				RV09
				RV10
0.20	-6.1	289±7	F82H IEA heat	A910
				A923
				A932
				A942
			SA-316F	CHB9
				CHC3
				CHD5
				CHD6
			SA-JPCA	CNA5
				CNB2
0.21	-3.5	289±7	F82H IEA heat	A911
				A925
				A933
				A944
			SA-316F	CHC0
				CHC4
				CHD7
			SA-JPCA	CHD8
				CHD9
				CNA6
				CNB3
0.27	5.8	479±7	V-4Cr-4Ti	RC01
				RC02
				RC100
				RC101
				RC13
				RC14
				RC15
				RC16
				RC17
				RC18

Right section:

DPA	z (cm)	Operating Temp. (C)	Alloy	ID Code
0.27	5.8	479±7	V-4Cr-4Ti	RC26
				RC27
				RC66
				RC67
				RC68
				RC69
				RC70
				RC71
				RC72
				RC73
				RC74
				RC75
				RC98
			V-4Cr-4Ti-RF	RV20
				RV21
				RV22
0.28	3.2	479±7	V-4Cr-4Ti	RC28
				RC29
				RC56
				RC57
				RC58
				RC59
				RC60
				RC61
				RC62
				RC63
				RC64
				RC65
			V-4Cr-4Ti-0.5SiAlY	LB03
				LB04
				LB09
				LB10
				LB11
			V-4Cr-4Ti-RF	RV03
				RV04
				RV17
				RV18
				RV19

Grand Total of 167

DPA calculation basis: 865 MWD of operation; The peak DPA/MWD value is 0.000255 for SS and 0.000324 for V.

DPA varies with axial location with the equation: $\cos(0.00858(z-12.7)) + 0.0000171(z-12.7)^2$, z in mm   (see Ref. 3).

All DPA values have been rounded off to 2 decimal places.

z (cm) is the axial distance of the midpoint of the specimen from the HFIR centerline. All distances have been rounded off.

Operating temperatures are based on the thermocouple data, corrected for the specimen type and location. The given ranges represent the variation in thermocouple data.

Table 1. Axial Location, Accumulated DPA, and Operating Temperatures of specimens in RB-10J. (cont.)

Type:	TEM					Type	TEM			
DPA	z (cm)	Operating Temp. (C)	Alloy	ID Code		DPA	z (cm)	Operating Temp. (C)	Alloy	ID Code
0.21	-4.3	291±7	SA-JPCA	SN13		0.21	-3.5	291±7	F82H IEA STD	A907
	-4.2	291±7	SA-316F	SH10						A916
				SH14					SA-316F	SH12
			F82H IEA STD	A914						SH26
				A903			-3.4	291±7	F82H IEA STD	A910
	-4.1	291±7	F82H IEA STD	A922					SA-JPCA	SN03
			SA-316F	SH18						SN05
				SH25						SN07
				SH17			-3.3	291±7	SA-JPCA	SN01
	-4.0	291±7	SA-316F	SH29						SN06
			F82H IEA STD	A912						SN11
				A904					F82H IEA STD	A902
				A905			-3.2	291±7	SA-316F	SH13
	-3.9	291±7	F82H IEA STD	A915					SA-316F	SH19
				A917					F82H IEA STD	A906
			SA-316F	SH27						A911
	-3.8	291±7	F82H IEA STD	A913			-3.1	291±7	SA-316F	SH16
				A920						SH28
				A921					SA-JPCA	SN10
			SA-316F	SH21			-3.0	291±7	SA-316F	SH20
	-3.7	291±7	SA-JPCA	SN09						SH23
			SA-316F	SH11					SA-JPCA	SN08
				SH15						SN02
			F82H IEA STD	A918			-2.9	291±7	SA-316F	SH24
	-3.6	291±7	F82H IEA STD	A901						SH22
				A908					SA-JPCA	SN04
				A909						SN14
				A919			-2.8	291±7	SA-JPCA	SN00
										SN12

Type:	TS			
DPA	z (cm)	Operating Temp. (C)	Alloy	ID Code
0.12	-18.6	275±9	SA-316F	3HB5
0.13	-16.1	275±9	SA-316F	7HB1
0.15	-13.5	275±9	SA-316F	3HB3
0.17	-11.0	275±9	SA-316F	7HB4
0.18	-8.4	275±9	SA-316F	3HB2
0.20	-5.9	275±9	SA-316F	7HB5
Grand Total of 6				

DPA calculation basis: 865 MWD of operation; The peak DPA/MWD value is 0.000255 for SS and 0.000324 for V.

DPA varies with axial location with the equation: $\cos(0.00858(z-12.7)) + 0.0000171(z-12.7)^2$, z in mm   (see Ref. 3).

All DPA values have been rounded off to 2 decimal places.

z (cm) is the axial distance of the midpoint of the specimen from the HFIR centerline. All distances have been rounded off.

Operating temperatures are based on the thermocouple data, corrected for the specimen type and location. The given ranges represent the variation in thermocouple data.

Table 1. Axial Location, Accumulated DPA, and Operating Temperatures of specimens in RB-10J. (cont.)

Type:	TEM	(cont.)								
DPA	z (cm)	Operating Temp. (C)	Alloy	ID Code		DPA	z (cm)	Operating Temp. (C)	Alloy	ID Code
0.21	14.1	415±10	V-4Cr-4Ti	RC01		0.28	1.7	479±7	V-4Cr-4Ti	RC07
				RC02						RC08
				RC03						RC09
				RC04						RC10
				RC05						RC11
				RC06						RC12
				RC47						RC52
				RC48						RC53
				RC49						RC54
				RC50						RC55
				RC51						RC56
			V-4Cr-4Ti-RF	RB31*					V-4Cr-4Ti-RF	RV35
				RV32						RV36
				RV33						RV37
				RV34						RV38
				RV42						RV46
				RB43*						RV47
				RV44						RV48
				RV45						RV49
			V-4Cr-4Ti-SiAlY	LB01					V-4Cr-4Ti-SiAlY	LB03
				LB02						LB04
				LB05						LB09
				LB06						LB10
				LB07						LB11
				LB08						LB12

*May actually be RV31 and RV43   Grand Total of 107

Type.	PT			
DPA	z (cm)	Operating Temp. (C)	Alloy	ID Code
0.17	18.2	415±10	V-4Cr-4Ti	20
				21
				22
				23
				F
				G
0.27	5.8	479±7	V-4Cr-4Ti	24
				25
				26
				27
				Q
				R
Grand Total of 12				

DPA calculation basis: 865 MWD of operation; The peak DPA/MWD value is 0.000255 for SS and 0.000324 for V.

DPA varies with axial location with the equation: $\cos(0.00858(z-12.7)) + 0.0000171(z-12.7)^2$, z in mm (see Ref. 3).

All DPA values have been rounded off to 2 decimal places.

z (cm) is the axial distance of the midpoint of the specimen from the HFIR centerline. All distances have been rounded off.

Operating temperatures are based on the thermocouple data, corrected for the specimen type and location. The given ranges represent the variation in thermocouple data.

Approximately five days into the irradiation, on Oct. 18, 1998, pressure readings on the primary containment system started a slow persistent decline. The primary containment system is a static system, and therefore, a loss of pressure indicated a breach of the primary containment system. An in-reactor pressure test was performed on Oct. 23, 1998, and the test confirmed that the leak was in the in-vessel portion of the experiment, not in the associated piping and valves.

Based on the operating constraints for the experiment, HFIR was shut down on Oct. 23, 1998 and the experiment was removed. HFIR was restarted on Oct. 26, 1998 to complete the rest of the irradiation cycle. The europium liner associated with the experiment was removed after the completion of the cycle.

Current Status

The RB-10J experiment and the europium liner are currently stored in the HFIR pool. All of the instrumentation is still hooked up to the experiment and is fully operational. A variety of pressurization experiments have been performed on the capsule to determine the size of the leak, and the data have been provided to an independent researcher who is currently working on a report on the leak and its behavior. An independent review committee has evaluated the operational data, in conjunction with the design of the experiment, and has provided valuable input into possible approaches to operating the experiment with the existing leak. Several members of the staff involved in the design, construction, and operation of the experiment are currently working on these conceptual approaches from the review committee in an effort to develop a feasible plan to apply for approval to resume the irradiation of the experiment. The RB-10J capsule must be approved by the HFIR Reactor Experiment Review Committee prior to re-insertion in the reactor.

REFERENCES

1. J. P. Robertson, K. E. Lenox, M. L. Grossbeck, A. F. Rowcliffe, S. Jitsukawa and K. Shiba, "Description and Status of the U.S./JAERI HFIR-MFE-RB-10J Irradiation Capsule," *Fusion Materials Semiannual Progress Report for the Period Ending December 31, 1997*, DOE/ER-0313/23, pp. 347-351.

2. J. P. Robertson, M. Howell, and K. E. Lenox, "Status of Lithium-Filled Specimen Subcapsules for the HFIR-MFE-RB-10J Experiment," *Fusion Materials Semiannual Progress Report for the Period Ending June 30, 1998*, DOE/ER-0313/24, pp. 257-259.

3. R. L. Senn and W. R. Mixon, "Experimental Measurement of Gamma Heat in the High Flux Isotope Reactor," *Nuclear Technology*, Vol. 12, pp. 235-240, October 1971.

STATUS OF DOE/JAERI COLLABORATIVE PROGRAM PHASE II AND PHASE III CAPSULES
– J. P. Robertson, K. E. Lenox (Oak Ridge National Laboratory), and Y. Miwa (Japan Atomic Energy Research Institute)

OBJECTIVE

The objective of the High Flux Isotope Reactor (HFIR) irradiations is to determine the response of various U.S. and Japanese structural alloys with different pretreatments and alloy compositions to the combined effects of displacement damage and helium generation.

SUMMARY

Significant progress continues to be made in the post-irradiation examinations (PIE) of the specimens from the DOE ORNL/JAERI collaborative capsules and in the design and fabrication of additional capsules. This report serves as a summary of the irradiation parameters for the capsules and the Fusion Materials progress reports related to the design, loading, operation, and dosimetry.

PROGRESS AND STATUS

Tables 1 and 2 summarize the progress and status of the capsules involved in the Phase II and Phase III irradiation programs. Details of the capsule design, assembly, and operation, specimen matrices and testing, and alloy compositions can be found in previous reports in this series. The locations of some of the more detailed reports are shown in the table, but this is not intended to be an exhaustive list. The dose levels shown in the table are the peak capsule values achieved at the reactor centerline. The dpa values in the HFIR target are estimated by assuming 9.38×10^{-4} dpa/MWd. The dpa values in the hafnium-shielded HFIR RB experiments are estimated by assuming 2.55×10^{-4} dpa/MWd. While a status of "testing complete" is listed for several of the capsules, it should be noted that data analyses and microscopy examinations are still in progress.

The JP series HFIR target capsules (JP9-16, JP20-22) contain primarily transmission electron microscopy disks (TEM) and SS-3 flat tensile specimens. A wide variety of alloys and thermomechanical conditions are included. Many of the TEM disks were made from isotopically tailored alloys to produce a range of He/dpa ratios (<0.1, 10, 20, 70 appm/dpa). The specimen temperatures are 300, 400, 500, and 600°C and the dose levels are 8, 17, 34, and 60 dpa.

The JP17, 18, and 19 capsules each contained miniature fracture toughness specimens, SS-3 tensile specimens, and TEM disk specimens, in order to directly compare fracture toughness, tensile properties, and microstructure of several austenitic and ferritic steel alloys.

The CTR-62 and 63 capsules, containing low activation ferritic steel specimens, were irradiated for 7 cycles to approximately 14 dpa. The tensile, Charpy, and TEM specimens operated at either 300 or 400°C.

The HFIR-JP25 target capsule will be the last of five capsules that compose the ORNL/JAERI Phase III Task I project on low activation ferritic steels (the other capsules are RB-11J, RB-12J, CTR-62, and CTR-63). This capsule is to be irradiated to a peak dose of 20 dpa. The specimens will operate at 300 and 500°C, the same temperatures as the RB-11J and 12J capsules. The capsule will include tensile, Charpy V-notch, pre-cracked Charpy, and TEM specimens of IEA F82H base metal, nickel-doped base metal, weld metal, and weldment.

The RB-60J-1, 200J-1, 330J-1, and 400J-1 experiments are a continuation of the Oak Ridge Research Reactor (ORR) spectrally tailored experiments. The capsules operated in the RB positions of the HFIR surrounded by a hafnium shield to simulate the expected fusion helium to damage (He/dpa) ratio in steel. The doses shown in the table are in addition to the 7 dpa accumulated during the ORR irradiation, bringing the total for the two-stage irradiation to 16-19 dpa. Dosimetry and helium measurements from specimens from the 60J-1 and 330J-1 capsules indicate that this experiment was successful in producing fusion relevant helium/dpa

Table 1. Summary of Target Capsule Irradiation Parameters and Status

Capsule	Primary Research Objectives	Irradiation Start and End; Number of Cycles	Operating Parameters: MWd; dpa; temperature	Status	Most Pertinent Semiannual Report Numbers DOE/ER-0313/xx
JP10 JP11 JP13 JP16	austenitic and ferritic steels; isotopically tailored TEM disks; tensile specimens	start: 7/90 end: 9/91 11 cycles	20161 MWd 17.3 dpa 300-600°C	testing complete	Design: 0313/3 Loading: 0313/5 Operation: 0313/16 Dosimetry: 0313/19
JP14	austenitic and ferritic steels; isotopically tailored TEM disks; tensile specimens	start: 7/90 end: 9/92 21 cycles	38786 MWd 33.9 dpa* 300-600°C	testing complete	Design: 0313/3 Loading: 0313/5 Operation: 0313/16
JP9 JP12 JP15	austenitic and ferritic steels; isotopically tailored TEM disks; tensile specimens	start: 7/90 end: 4/94 35 cycles	64904 MWd 59.6 dpa 300-600°C	testing complete	Design: 0313/3 Loading: 0313/5 Operation: 0313/16 Dosimetry: 0313/23
JP17	austenitic and ferritic steels; fracture toughness, tensile, TEM specimens	start: 12/91 end: 2/92 2 cycles	3702 MWd 2.9 dpa 250-300 °C	testing complete	Design: 0313/12 Loading: 0313/12 Operation: 0313/19 Dosimetry: 0313/19
JP18 JP19	austenitic and ferritic steels; fracture toughness, tensile, TEM specimens	start: 8/91 end: 10/91 2 cycles	3575 MWd 2.9 dpa 60-125°C	testing complete	Design: 0313/11 Loading: 0313/11 Operation: 0313/19 Dosimetry: 0313/19
JP20	austenitic and ferritic steels; isotopically tailored TEM disks; tensile specimens	start: 12/93 end: 6/94 5 cycles	9367 MWd 8.4 dpa 300-600°C	testing in progress	Design: 0313/12 Loading: 0313/15 Operation: 0313/18 Dosimetry: 0313/23
JP21	austenitic and ferritic steels; isotopically tailored TEM disks; tensile specimens	start: 12/93 end: 4/95 11 cycles	21337 MWd 18.6 dpa* 300-600°C	disassembly complete	Design: 0313/12 Loading: 0313/15 Operation: 0313/18
JP22	austenitic and ferritic steels; isotopically tailored TEM disks; tensile specimens	start: 12/93 end: 1/96 19 cycles	38880 MWd 34 dpa* 300-600°C	testing in progress	Design: 0313/12 Loading: 0313/15 Operation: 0313/18
CTR-62 CTR-63	ferritic steels; tensile, CVN, and TEM specimens	start: 4/95 end: 12/95 7 cycles	14 dpa* 300, 400°C	testing in progress	Design: 0313/18 Loading: 0313/18
JP25	ferritic steels; tensile, CVN, and TEM specimens	10 cycles	20 dpa* 300, 500°C	design in progress	

*estimated

levels (approximately 11 appm He/dpa). The irradiation temperatures in these experiments were actively controlled at 60, 200, 330, and 400°C.

The RB-11J and 12J capsules are the first of the spectrally tailored capsules in the Phase III program. These capsules operated in the HFIR removable beryllium (RB) positions with a europium oxide (Eu2O3) thermal neutron shield in place. They achieved approximately 5 dpa at 300 and 500°C, respectively. The capsules contained primarily low activation ferritic steel and

vanadium alloy specimens in the form of tensile, fracture, creep, and TEM specimens. The capsules began irradiation with the start of HFIR fuel cycle 352 (February 1997) and achieved their goal fluence at the end of cycle 361 (July 1998).

The RB-10J capsule will be irradiated to 5 dpa in a Eu_2O_3-shielded RB position. It is composed of two distinct sections separated at the reactor centerline. The upper portion contains vanadium alloy specimens operating at 420 and 480°C. Bend bars, fracture toughness specimens, tensile specimens, and TEM disks are included at each temperature. The specimens are surrounded by lithium in order to prevent oxygen contamination and to provide good thermal contact to the specimens. The lower portion contains primarily austenitic stainless steels and operates at approximately 250°C. Tensile specimens, Charpy V-notch specimens, and TEM disks are included. Fabrication of this capsule was completed in August 1998 and irradiation began in October. The irradiation was suspended after 10 days due to a change in the operating conditions. More details can be found in a companion report in this volume [1].

REFERENCES

1. K. E. Lenox, "As-Built Condition and Operating History of the U.S./JAERI HFIR-MFE-RB-10J Capsule," Fusion Materials Semiannual Progress Report for the Period Ending December 31, 1998, DOE/ER-0313/25.

Table 2. Summary of RB Capsule Irradiation Parameters and Status

Capsule	Primary Research Objectives	Irradiation Start and End; Number of Cycles	Operating Parameters: MWd; dpa; temperature	Status	Most Pertinent Semiannual Report Numbers DOE/ER-0313/xx
RB-60J-1	spectrally tailored (Hf-shielded); tensile, creep, TEM specimens	start: 7/90 end: 11/92 24 cycles	44450 MWd 11.6 dpa 60°C	testing in progress	Design: 0313/3, 4 Loading: 0313/4 Operation: 0313/13 Dosimetry: 0313/17
RB-200J-1	spectrally tailored (Hf-shielded); tensile, creep, TEM specimens	start: 11/92 end: 1/95 20 cycles	37450 MWd 11.6 dpa 200°C	testing in progress	Design: 0313/3, 6 Loading: 0313/14 Operation: 0313/15, 18 Dosimetry: 0313/23
RB-330J-1	spectrally tailored (Hf-shielded); tensile, creep, TEM specimens	start: 7/90 end: 11/92 24 cycles	44450 MWd 11.6 dpa 330°C	testing in progress	Design: 0313/3, 5 Loading: 0313/5 Operation: 0313/11, 13 Dosimetry: 0313/17
RB-400J-1	spectrally tailored (Hf-shielded); tensile, creep, TEM specimens	start: 11/92 end: 1/95 20 cycles	37450 MWd 9.2 dpa* 400°C	testing in progress	Design: 0313/3, 6 Loading: 0313/14 Operation: 0313/15, 18
TRIST-ER1	alumina; in-situ measurement of electrical conductivity	start: 3/96 end: 6/96 3 cycles	3 dpa* 450°C	testing complete	Design: 0313/19, 20 Loading: 0313/19 Operation: 0313/20, 22
RB-10J	austenitic steels and V alloys; spectrally tailored (Eu_2O_3-shielded); tensile, fracture, TEM specimens	start: 10/98 end: 4/00* 10 cycles	5 dpa* steel: 250°C V: 420, 480°C	irradiation in progress	Design: 0313/23, 24 Loading: 0313/25 Operation: 0313/25
RB-11J RB-12J	ferritic steels and V alloys; spectrally tailored (Eu_2O_3-shielded); tensile, fracture, TEM specimens	start: 2/97 end: 7/98 10 cycles	5 dpa* 300, 500°C	irradiation complete; disassembly in progress	Design: 0313/22 Loading: 0313/22 Operation: 0313/22

*estimated

SCHEDULE AND STATUS OF IRRADIATION EXPERIMENTS – A. F. Rowcliffe and J. P. Robertson (Oak Ridge National Laboratory)

OBJECTIVE

To provide an updated summary of the status of irradiation experiments for the fusion materials program.
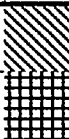
SUMMARY

The current status of reactor irradiation experiments is presented in tables summarizing the experimental objectives, conditions, and schedule.

PROGRESS AND STATUS

Currently, the program has two irradiation experiments in reactor and three experiments in the design or construction stages. Postirradiation examination and testing is in progress on eight separate experiments.

Summary of Reactor Irradiation Experiments

Experiment	Lead Lab	Collaborators	Responsible Person	Major Objectives	Materials	Temperature °C	Dose (dpa) or fluence	Irrad. Start	Irrad. Finish	Status
EBR-II, Reactor, ANL, Idaho Falls, ID										
COBRA 1A2	PNL	ORNL, ANL, MONBUSHO	M.L. Hamilton	Tensile and fatigue prop., Charpy impact, fracture toughness, TEM	Austenitic and ferritic steels, Fe-alloys, V, Be, low act. materials, Cu alloys, Ti-Al, SIC, C-C comp.	370, 400, 800	33	Nov-92	Sep-94	
X530	ANL		H. Tsai, H.M. Chung	He-effects, swelling, Charpy impact, fracture toughness, tensile prop.	V alloys	370	5	Aug-94	Sep-94	
High Flux Isotope Reactor, ORNL, Oak Ridge, TN										
HFIR-CTR-60	ORNL		S.J. Zinkle	Flexure bars, TEM, indentation disks	Isotopically tailored ceramics	100-600	2.4E+26 n/m2	Dec-94	Aug-95	
HFIR-CTR-61	ORNL		S.J. Zinkle	Similar to HFIR-CTR-60			7.20E+26	Dec-94	Aug-98	
HFIR-JP-9	ORNL	JAERI	P.J. Maziasz/ J.E. Pawel	He effects by isotopic tailoring, tensile prop., TEM	Austenitic and ferritic steels	300-600	57	Jul-90	Apr-94	
HFIR-JP-12	ORNL	JAERI	P.J. Maziasz/ J.E. Pawel	Similar to HFIR-JP-9			57	Jul-90	Apr-94	
HFIR-JP-15	ORNL	JAERI	P.J. Maziasz/ J.E. Pawel	Similar to HFIR-JP-9			57	Jul-90	Apr-94	
HFIR-JP-20	ORNL	JAERI	J.E. Pawel	Tensile Prop., TEM, He effects by isotopic tailoring	Austenitic and ferritic steels	300-600	8	Dec-93	Jun-94	
HFIR-JP-21	ORNL	JAERI	J.E. Pawel	Similar to HFIR-JP-20			18	Dec-93	Apr-95	
HFIR-JP-22	ORNL	JAERI	J.E. Pawel	Similar to HFIR -JP-20			34	Dec-93	Jan-96	
HFIR-JP-23	PNL	MONBUSHO	D.S. Gelles	TEM	Austenitic and ferritic steels, Cu, Mo, V alloys, TiAl	300-600	8	Dec-93	Jun-94	
HFIR-HT-S1, -S7	ORNL		L.L. Snead	Thermal conductivity	Various insulators	80-350	0.01-1.0	Jun-95	Aug-95	
HFIR-HT-F Series	ORNL		L. L. Snead	Fiber tensile	SiC	80-800	0.001-1.0	Jan-95	Mar-96	

Summary of Reactor Irradiation Experiments

Experiment	Lead Lab	Collaborators	Responsible Person	Major Objectives	Materials	Temperature °C	Dose (dpa) or fluence	Irrad. Start	Irrad. Finish	Status
HFIR-TRIST-ER1	ORNL	MONBUSHO/ JAERI	S.J. Zinkle	In-situ electrical conductivity	Al2O3	450	3E+25 n/m2	Apr-96	Jun-96	
HFIR-RB-10J	ORNL	JAERI	J.E. Pawel	Tensile, fracture	Vanadium, 316LN-1G, J316	200, 500	5	Oct-98	Oct-99	
HFIR-RB-11J	ORNL	MONBUSHO/ JAERI	M. L. Grossbeck	Tensile, fracture, TEM	Low activation ferritics, V alloys, SiC	300	5	Feb-97	May-98	
HFIR-RB-12J	ORNL	MONBUSHO/ JAERI	M. L. Grossbeck	Tensile, fracture, TEM	Low activation ferritics, V alloys, SiC	500	5	Feb-97	May-98	
HFIR-RB-13J	ORNL	MONBUSHO/ JAERI	S. J. Zinkle	Varying temp. experiment	Ceramics, Fe-Cr-Ni, V alloys, ferritics, copper	200, 350, 500	5	Jul-98	Jul-99	
HFIR-RB-14J	ORNL	MONBUSHO	L. L. Snead	Strength, fracture, dim. stability, diffusivity	2nd generation SiC/SiC	300, 500, 800	5	Feb-99	Feb-00	
HFIR-TRIST-TC1	ORNL	MONBUSHO/ JAERI	L. L. Snead	In-situ thermal conductivity	SiC/SiC, SiC	150-700	3	Jan-99	Dec-99	
HFIR-CTR-62	ORNL	JAERI	R.L. Klueh	Charpy impact and He effects	and conventional ferritic steels	300, 400	13	Apr-95	Dec-95	
HFIR-CTR-63	ORNL	JAERI	R.L. Klueh	Charpy impact and tensile, TEM, He effects	and conventional ferritic steels	300, 400	13	Apr-95	Dec-95	
HFIR-JP25	ORNL	JAERI	R.L. Klueh	Tensile, fracture, TEM	Low activation ferritics	300, 500	20	Feb-99	Jan-00	

High Flux Beam Reactor, Brookhaven National Laboratory

Experiment	Lead Lab	Collaborators	Responsible Person	Major Objectives	Materials	Temperature °C	Dose (dpa) or fluence	Irrad. Start	Irrad. Finish	Status
HFBR-ISEC-3	ORNL		L.L. Snead	In-situ electrical	WESGO Al2O3	450	1.5	Jul-95	Sep-95	
HFBR-V1	ORNL		L.L. Snead	Tensile, fracture	V-4Cr-4Ti	75, 150, 225	0.4	May-95	Jun-95	
HFBR-V2	ORNL		L.L. Snead	Tensile, fracture	V-4Cr-4Ti	75, 225, 300, 375	0.4	Jul-95	Aug-95	
HFBR-V3	ORNL		L.L. Snead	Tensile, fracture	V-4Cr-4Ti	160, 265, 315, 420	0.4	Aug-96	Sep-96	
HFBR-V4	ORNL		L.L. Snead	Tensile, fracture	V-4Cr-4Ti	105-505	0.1	Aug-96	Sep-96	

Summary of Reactor Irradiation Experiments

Experiment	Lead Lab	Collaborators	Responsible Person	Major Objectives	Materials	Temperature °C	Dose (dpa) or fluence	Irrad. Start	Irrad. Finish	Status
Advanced Test Reactor, Idaho Falls										
ATR-A1	ANL	MONBUSHO	D.L. Smith	Tensile, fracture toughness, TEM, creep	Vanadium alloys	200, 300	5	Dec-95	May-96	▨
BOR-60 Reactor, RIAR, Dimitrovgrad, Russia										
BOR-60-Fusion-1	ORNL, ANL	RDIPE, RIAR	A.F. Rowcliffe, D.L. Smith	Mechanical and microstructural properties	V alloys	350-380	10	Jul-95	Mar-96	▨
SM-2 Reactor, RIAR, Dimitrovgrad, Russia										
SM-2.1	ORNL, PNL	RIAR	S.J. Zinkle	Tensile, electrical, microstructural, and creep properties	Cu alloys	100, 200, 330	1, 5	Dec-93	Feb-94	▨
SM-2.2	PNL	SRIAR	D.J. Edwards	Mechanical behavior of bonded materials	Cu alloys/SS, Cu/Be	120, 300	0.2	Mar-96	May-96	▨
SM-2.3	PNL	SRIAR	D.J. Edwards	Mechanical behavior of bonded materials	Cu alloys/SS, Cu/Be	150, 300 200	0.4 2.0	Sep-97 Jul-98	Dec-97 Oct-98	▨

▨ Irradiation complete

▦ Irradiation in progress

Irradiation planned

340

Experiment Schedule

	FY 1996	FY 1997	FY 1998	FY 1999	FY 2000

Months: May-95, Jun-95, Jul-95, Aug-95, Sep-95, Oct-95, Nov-95, Dec-95, Jan-96, Feb-96, Mar-96, Apr-96, May-96, Jun-96, Jul-96, Aug-96, Sep-96, Oct-96, Nov-96, Dec-96, Jan-97, Feb-97, Mar-97, Apr-97, May-97, Jun-97, Jul-97, Aug-97, Sep-97, Oct-97, Nov-97, Dec-97, Jan-98, Feb-98, Mar-98, Apr-98, May-98, Jun-98, Jul-98, Aug-98, Sep-98, Oct-98, Nov-98, Dec-98, Jan-99, Feb-99, Mar-99, Apr-99, May-99, Jun-99, Jul-99, Aug-99, Sep-99, Oct-99, Nov-99, Dec-99, Jan-00, Feb-00, Mar-00, Apr-00

EBR-II Reactor, Idaho Falls

COBRA 1A2
4 Mark B7A capsules
P.I.E.

X530
2 Mark B7 capsules
Disassembly
P.I.E.

High Flux Isotope Reactor, ORNL

JP 9-16
8 Ph. 2 Target capsules
P.I.E.

JP-20
Ph. 2 Target capsule
P.I.E.

JP-21
Ph. 2 Target
Disassembly
P.I.E.

JP-22
Ph. 2 Target capsule
Disassembly
P.I.E.

CTR-60
Target capsule
Disassembly
P.I.E.

CTR-61
Target capsule
Irradiation
Disassembly

HT-S Series
10 rabbits
Irradiation
P.I.E.

Experiment Schedule

Experiment	FY 1996	FY 1997	FY 1998	FY 1999	FY 2000

HT-F Series
6 rabbits
- Irradiation
- P.I.E.

HFIR-TRIST-ER1
RB In-situ experiment
- Irradiation
- Disassembly
- P.I.E.

HFIR-MFE-RB-10J
RB Spectrally tailored
- Design/assembly
- Irradiation
- Disassembly
- P.I.E.

HFIR-MFE-RB-11J, 12J
2 RB spectrally tailored
- Design/assembly
- Irradiation
- Disassembly
- P.I.E.

HFIR-RB-13J
RB varying temperature
- Design/Assembly
- Irradiation
- Disassembly
- P.I.E.

HFIR-RB-14J
Unshielded
- Irradiation
- Disassembly
- P.I.E.

342

Experiment Schedule

	FY 1996	FY 1997	FY 1998	FY 1999	FY 2000
Experiment	May-95 Jun-95 Jul-95 Aug-95 Sep-95 Oct-95 Nov-95 Dec-95 Jan-96 Feb-96 Mar-96 Apr-96 May-96 Jun-96 Jul-96 Aug-96 Sep-96	Oct-96 Nov-96 Dec-96 Jan-97 Feb-97 Mar-97 Apr-97 May-97 Jun-97 Jul-97 Aug-97 Sep-97	Oct-97 Nov-97 Dec-97 Jan-98 Feb-98 Mar-98 Apr-98 May-98 Jun-98 Jul-98 Aug-98 Sep-98	Oct-98 Nov-98 Dec-98 Jan-99 Feb-99 Mar-99 Apr-99 May-99 Jun-99 Jul-99 Aug-99 Sep-99	Oct-99 Nov-99 Dec-99 Jan-00 Feb-00 Mar-00 Apr-00

HFIR-TRIST-TC1
In-situ
- Irradiation — (FY 1999)
- Disassembly — (FY 2000)
- P.I.E.

HFIR-CTR-62, 63
2 Target capsules
- Irradiation — (FY 1996, May-95–Dec-95)
- Disassembly — (FY 1996, Apr-96–Jun-96)
- P.I.E. — (FY 1998)

HFIR-JP-25
Target capsule
- Design/Assembly — (FY 1998)
- Irradiation — (FY 1999)
- Disassembly — (FY 2000)
- P.I.E.

High Flux Beam Reactor, Brookhaven

HFBR-V1, V2
8 rabbits
- Irradiation — (FY 1996, May-95–Aug-95)
- Disassembly — (FY 1996, Dec-95–Feb-96)
- P.I.E. — (FY 1996, Feb-96–Jun-96)

HFBR-V3, V4
- Irradiation — (FY 1996, Jul-96)
- Disassembly — (FY 1996–97, Sep-96–Dec-96)
- P.I.E. — (FY 1997, Jan-97–Apr-97)

Advanced Test Reactor, Idaho Falls

ATR-A1
Drop-in
- Irradiation — (FY 1996, May-95–Sep-96)
- Disassembly — (FY 1997, Feb-97–Apr-97)
- P.I.E. — (FY 1997–98, Apr-97–Mar-98)

343

Experiment Schedule

BOR-60 Reactor, Dimitrovgrad
SM-2 Reactor, Dimitrovgrad

Experiment	FY 1995	FY 1996	FY 1997	FY 1998	FY 1999	FY 2000

Fusion-1
1 Capsule, Row 5
- Irradiation
- Disassembly/shipping
- P.I.E.

SM-2.1
1 Channel capsule
4 Core capsules
- Disassembly/shipping
- P.I.E.

SM-2.2
2 Core capsules
- Specimen preparation
- Irradiation
- Disassembly/shipping
- P.I.E.

SM-2.3
3 Core capsules
- Specimen preparation
- Irradiation
- Disassembly/shipping
- P.I.E.

PROGRESS REPORT ON THE TRIST-TC1 EXPERIMENT – A. L. Qualls,

L. L. Snead, S. J. Zinkle, W. S. Eatherly, R.G. Sitterson, and D.W. Sparks (Oak Ridge National Laboratory), R. Yamada (Japan Atomic Energy Research Institute), and Y. Katoh (Kyoto University, Institute of Advanced Energy)

OBJECTIVE

The objective of this report is to summarize the progress of the TRIST-TC1 Experiment.

SUMMARY

Fabrication of the experiment began during this reporting period. Forty specimens, in addition to eight heat generation measurement standards, were cut to size and brazed into twenty-four specimen pads. The specimen pads were assembled into three temperature zones comprising the experimental region of the capsule.

PROGRESS AND STATUS

Figure 1 shows a typical specimen pad assembly used in the TRIST-TC1 experiment. Specimen pads are made of a vanadium alloy (V4Cr4Ti). The specimens are right circular cylinders. Holes are drilled into the face of the specimens and .023" OD Type N thermocouples are brazed into the holes. One end of each specimen is brazed into a counterbored hole on the two outside surfaces (of the three flat, inner surfaces) of a specimen pad. The specimens are displaced axially so they will not intersect as they extend toward the center of the capsule. The outer radius of the specimen pad fits precisely against the inside diameter of a specimen pad holder, and each pad is secured to the holder with eight stainless steel screws, as shown in Figure 2.

Nuclear interactions produce heat in the specimens, specimen pads and specimen pad holder during reactor operation. The temperature of a holder, and therefore the specimens, is controlled by varying the thermal conductivity of a gas mixture in the annular region between the outer diameter of the holder and the inner diameter of the capsule housing tube, which is cooled to approximately 60°C by the reactor primary coolant.

During operation, the capsule has a constant purge of helium flowing into the central portion of the experimental region. The helium flows into plenums below each specimen holder and then upwards through the temperature control gas gaps and into exhaust plenums at the top of the holders. To control the temperature of an individual holder, neon or argon is mixed into the helium as it enters a lower plenum and forms a gas mixture with a thermal conductivity between that of the gases used (helium and neon or argon). The flow rate of the neon or argon is adjusted to achieve and maintain the desired operating temperature.

Nuclear heating within a specimen will produce a temperature drop as the heat is lost along its length to the specimen pad. The temperature difference from the base to the tip of a specimen is a function of the specimen length, thermal conductivity and the internal volumetric heat generation rate. The heat generation rates within capsule components are relatively constant near the reactor mid-plane, but increase substantially in the upper and lower portions of the experimental region as a reactor cycle progresses. The lengths of specimens are set to produce a 40°C drop across the specimen based on the expected thermal conductivity of the irradiated material and the End-of-Cycle heat generation profile.
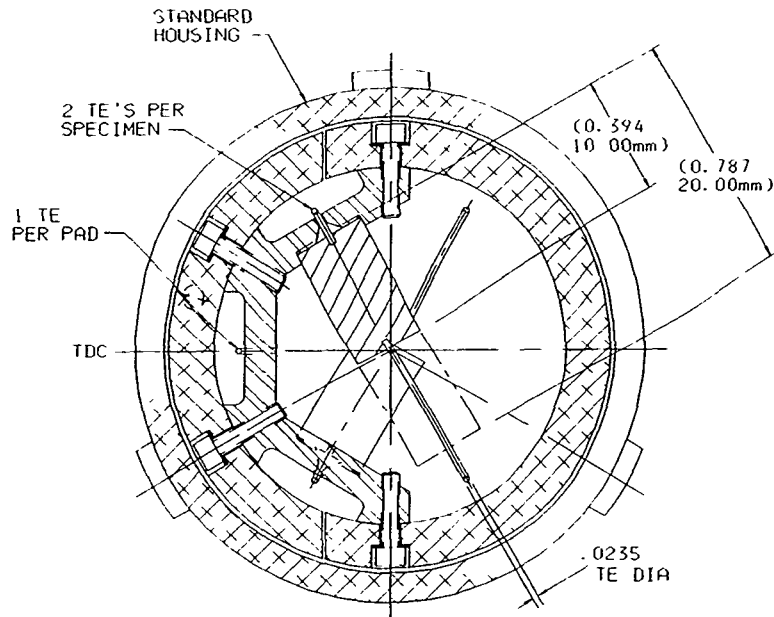
Figure 1. Specimen pad assembly for the TRIST-TC 1 experiment.

The experimental matrix for the TRIST-TC1 capsule is summarized in Table 1. A total of 17 different types of ceramic specimens are contained in 3 different temperature zones. The specimen matrix includes both monolithic ceramics and current state-of-the-art ceramic composites (C/C and SiC/SiC).

The experiment contains eight steel measurement standards displaced over the length of the experimental region. The standards are in positions 1, 6, 16, 21, 27, 33, 40, and 46, numbered from the top specimen location. The thermal conductivity of the steel will not change due to irradiation damage, and the temperature drop across the standards will provide a direct measurement of the heat generation at different axial locations within an unshielded RB* position of HFIR. The interpolated (and for two specimens, extrapolated) data will allow those temperature changes resulting from changes in specimen thermal conductivity to be distinguished from those that are a result of a changing heat generation profile.

Average specimen temperatures are to be 400°C in Zone A, 700°C in Zone B, and 200°C in Zone C. Temperature control and thermal isolation of the three zones is based on concepts tested in the Varying Temperature Experiment (RB-13J) [1]. Temperature zones with temperature differences of 150°C are separated by approximately 1.9 cm in that experiment, and a temperature increase of 150°C in a zone results in only a 5°C increase in the temperature of adjacent temperature zones. To accommodate larger temperature differences between zones in the TRIST-TC1 experiment, the spacing between zones has been increased to 2.5 cm. Figure 3 shows the assembled experimental region of the irradiation capsule.

Table 1. Experimental matrix for TRIST-TC1 capsule. Position #1 is located at the top of the irradiation capsule and #48 is located at the bottom of the capsule. Samples 1-20 are in the 400°C irradiation zone (Zone A), Samples 21-40 are in the 700°C irradiation zone (Zone B), and Samples 41-48 are in the 200°C irradiation zone (Zone C).

Material	Position	Temperature (°C)			Vendor and Grade
		200	400	700	
F82H F/M steel (standard)	2,5,12,15,28,34,39,45	1	3	4	NKK (IEA heat)
CVD SiC (Hi TC)	11,20,21,42	1	2	1	Morton CVD (K_{th}^{rt}~400 W/m-K)
CVD SiC (Lo TC)	17,30,41	1	1	1	CVD SiC (K_{th}^{rt}~110 W/m-K)
Single X SiC	19		1		Cree Systems 6H-Alpha
3D SiC Composite	6,33		1	1	Kawasaki PIP 3-D, Hi-Nicalon fiber
Felt SiC Composite	8,31		1	1	Mitsui CVI/PIP, Hi-Nicalon-S fiber
2-D SiC/SiC, in-plane	7,9*,29		2	1	ORNL FCVI, Satin Weave Hi-Nicalon-S
2-D SiC/SiC, cross plane	10,27		1	1	ORNL FCVI, Satin Weave Hi-Nicalon-S
2-D SiC Composite	16,25		1	1	MER CVR, T-300 PAN Fiber
SiC Doped CFC	13,32		1	1	Tonen, (K_{th}^{rt}~410 W/m-K)
1D CFC	12		1		Mitsubishi MKC-1PH (K_{th}^{rt}~560 W/m-K)
1D CFC	18,26		1	1	Tonen, (K_{th}^{rt}~495 W/m-K)
2D-CFC	1,23		1	1	FMI-222 (K_{th}^{rt}~200 W/m-K)
Graphite	14,24		1	1	Segri-Great Lakes H451
Sapphire	4,37,48	1	1	1	Crystal Systems Hemlux Ultra (VUV)
Silicon Nitride	38,46	1		1	Kyocera SN235P
Beryllium Oxide	3,36,44	1	1	1	Brush Wellman 995
Aluminum Nitride	35,43	1		1	Tokoyama SH15
Spinel	40,47	1		1	Commercial Crystal Systems

*Sample oxidized for 24 hr. at 600°C.

347
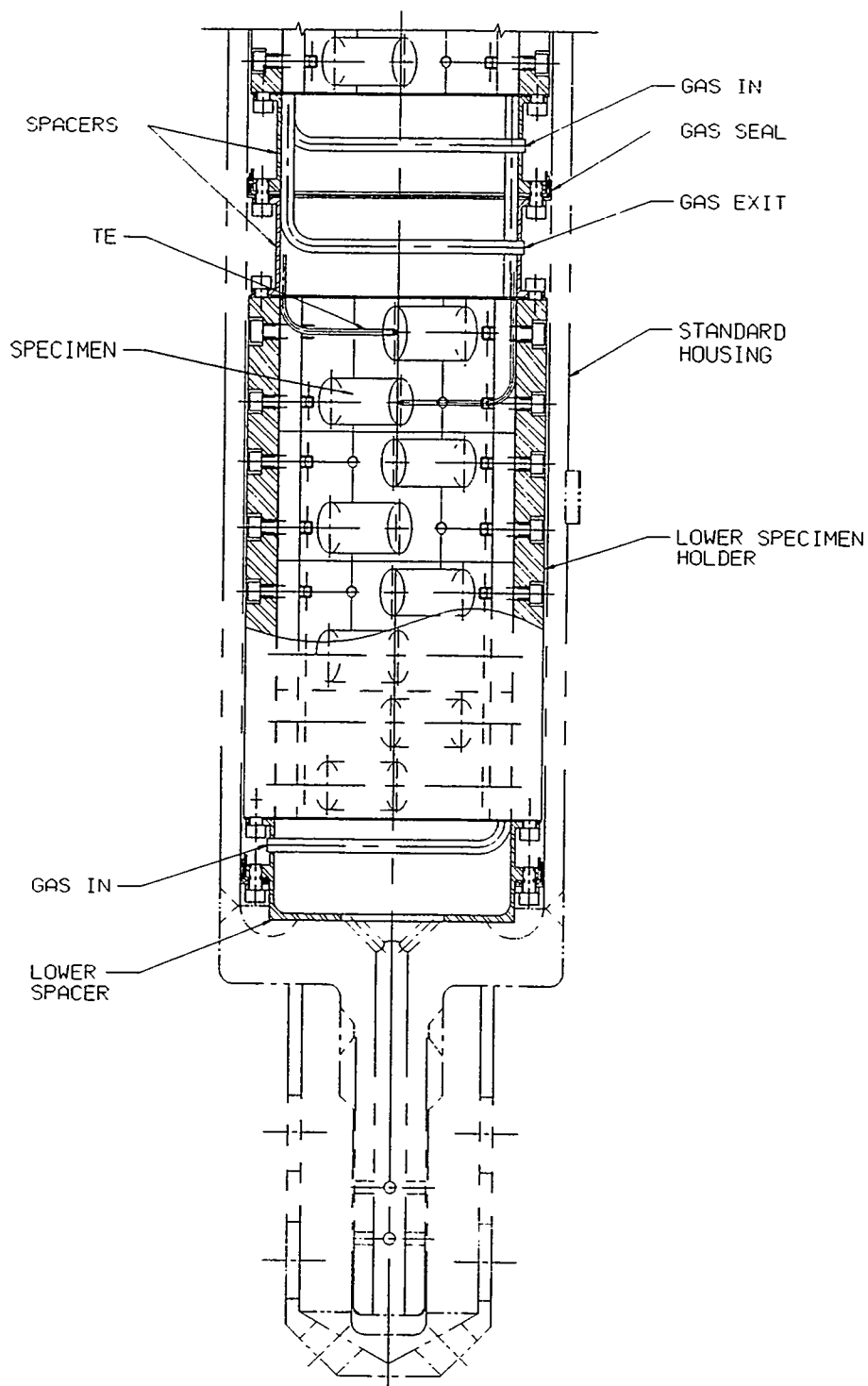
Figure 2. Cross sectional view of the 200°C temperature zone of the TRIST-TC1 experiment.
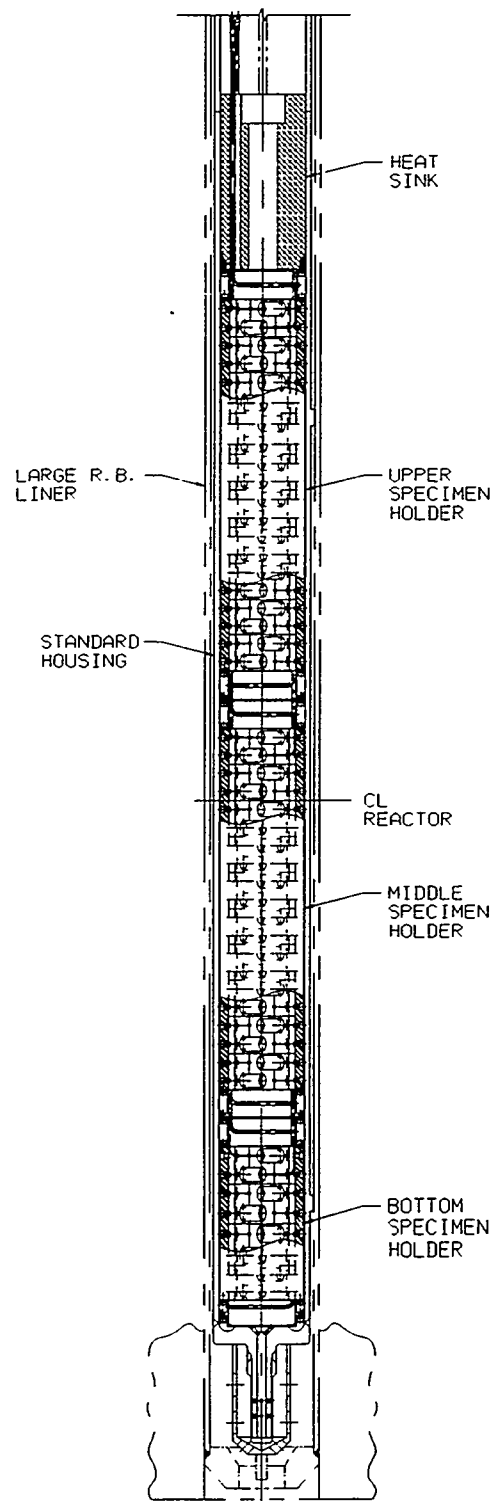
Figure 3. View of the experimental region of the TRIST-TC1 experiment.

Typically, experiments are rotated 180° after each cycle to ensure that specimens receive a balanced dose during irradiation. However, since this rotation would change the nuclear heating rate of individual specimens (and thereby produce difficulties in interpreting the data), it is currently planned to maintain the same capsule orientation for all three irradiation cycles. Dosimetry packets are positioned such that the accumulated dose of all specimens can be determined.

The three-cycle irradiation is projected to begin near the first of March and end in June 1999.

REFERENCES:

A. L. Qualls and T. Muroga, "Progress on the Design of a Varying Temperature Irradiation Experiment for Operation in HFIR, "Fusion Materials Semiannual Progress Report for Period Ending December 31, 1996, p. 255.

Distribution

1. Advanced Micro Devices, Inc., 5204 E. Ben White Blvd., MS-613, PCAL-Analytical TEM Section, Austin TX 78741
   J. Gazda

2-14. Argonne National Laboratory, 9700 South Cass Avenue, Argonne, IL 60439

M. C. Billone	A. B. Hull	K. Nateson
T. S. Bray	C. E. Johnson	J. H. Park
O. K. Chopra	J. P. Kopasz	D. L. Smith
H. M. Chung	R. F. Mattas	H. C. Tsai
D. R. Diercks		

15-16. Argonne National Laboratory, EBR-II Division, P.O. Box 2528, Idaho Falls, ID 83403-2528
   H. P. Planchon   D. L. Porter

17. Auburn University, Department of Mechanical Engineering, 201 Ross Hall, Auburn, AL 36849
   B. A. Chin

18-19. Boeing, Mail Code S 106 7220, P.O. Box 516, St. Louis, MO 63166-0516
   J. W. Davis   G. W. Wille

20. Carnegie Institute of Technology, Carnegie-Mellon University, Schenley Park, Pittsburgh, PA 15213
   W. M. Garrison, Jr.

21. Commissariat à l'Energie Atomique, Direction des Technologies Advancées, M2R1/DECM Cen-Saclay, Gif Sur Yvette, Cedex, France
   F. Tavassoli

22. Dow Corning Corporation, 3901 S. Saginaw Rd., MS-500, Midland, MI 48686-0995
   R. E. Jones

23-25. General Atomics, P.O. Box 85608, San Diego, CA 92138
   W. R. Johnson   K. R. Schultz   C. Wong

26. Georgia Institute of Technology, Fusion Research Center, 0225, Atlanta, GA 30332
   W. M. Stacey

27. Grand Canyon University, Department of Natural Science, 3300 W. Camelback Rd., Phoenix, AZ 85017
   W. A. Coghlan

28-30. Idaho National Engineering Laboratory, Fusion Safety Program, P.O. Box 1625, Idaho Falls, ID 83415-3523
   G. Longhurst   K. McCarthy   D. Petti

31. Knolls Atomic Power Laboratory, P.O. Box 1072, Schenectady, NY 12301
   G. Newsome

32-34. Lawrence Livermore National Laboratory, P.O. Box 808, Livermore, CA 94550
   T. Diaz de la Rubia   W. G. Wolfer   J. Perkins

35-41. Los Alamos National Laboratory, Los Alamos, NM 87545
J. L. Anderson E. H. Farnum W. F. Sommer
R. G. Castro R. E. Siemon K. E. Sickafus
D. W. Cooke

42-44. Massachusetts Institute of Technology, Department of Metallurgy and Materials Science, Cambridge, MA 02139
L. W. Hobbs N. J. Grant K. C. Russell

45. Massachusette Institute of Technology, Plasma Fusion Center Headquarters, Cambridge, MA 02139
D. B. Montgomery

46. McMaster University, Engineering Physics, Hamilton, Ontario, Canada L8S 4L7
D. P. Jackson

47. MER Corp., 7960 South Kolb Rd., Tucson, AZ 85706
W. Kowbel

48. Merrimack College, Dept. of Physics, 315 Turnpike Street, North Andover, MA 01845
D. P. White

49. M. J. Schiff & Associates, 1291 N. Indian Hill Blvd., Claremont, CA 91711-3897
G.E.C. Bell

50. NASA Lewis Research Center, MS-106-5, Cleveland, OH 44135
G. Morscher

51-53. National Institute of Standards and Technology, Boulder, CO 80302
F. R. Fickett H. I. McHenry R. P. Reed

54-55. Naval Research Laboratory, Code 6506, Washington, DC 20375
D. L. Griscom J. A. Sprague

56-97. Oak Ridge National Laboratory, P.O. Box 2008, Oak Ridge, TN 37831
Central Research Library M. L. Grossbeck T. C. Reuther
Document Reference Section N. Hashimoto J. P. Robertson
Laboratory Records-OSTI (2) J. F. King A. F. Rowcliffe (10)
Laboratory Records-RC E. A. Kenik J. Sheffield
Patent Section R. L. Klueh L. L. Snead
J. Bentley E. H. Lee R. E. Stoller
E. E. Bloom L. K. Mansur K. R. Thoms
T. D. Burchell P. J. Maziasz S. J. Zinkle
S. D. Connery S. Milora
J. R. DiStefano Y. Miwa
G. M. Goodwin B. A. Pint
R. H. Goulding L. Qualls

98-111. Pacific Northwest National Laboratory, P.O. Box 999, Richland, WA 99352
D. J. Edwards M. L. Hamilton R. H. Jones
F. A. Garner (5) H. L. Heinisch R. J. Kurtz
D. S. Gelles G. W. Hollenberg J. Youngblood
L. R. Greenwood

112. Oregon Graduate Institute, Dept. of Materials Science & Engineering, 19600 N.W. Von Neumann Drive, Beaverton, OR 97006
    J. M. McCarthy

113-115. Princeton University, Princeton Plasma Physics Laboratory, P.O. Box 451, Princeton, NJ 08540
    R. Goldston   Long-Poe Ku   D. M. Meade

116-117. Rensselaer Polytechnic Institute, Troy, NY 12181
    D. Duquette   D. Steiner

118-120. Sandia National Laboratories, Fusion Technology Dept., Dept. No 6531, P.O. Box 5800, Albuquerque, NM 87185-5800
    M. J. Davis   M. Ulrickson   R. D. Watson

121-122. Sandia National Laboratories, Livermore Division 8316, Livermore, CA 94550
    W. Bauer   K. Wilson

123. San Diego State University, Mechanical Engineering Dept., San Diego, CA 92182-0191
    L. D. Thompson

124. Texas A&M University, Box 397, Prairie View, TX 77446
    D. Baker

125. TSI Research, 225 Stevens Ave., #110, Solana Beach, CA 92075
    E. T. Cheng

126. University of California at San Diego, U.S. ITER Project Office, 9500 Gilman Drive, Bldg. 302, La Jolla, CA 92093-0035
    C. C. Baker

127. University of California at San Diego, Fusion Energy Research Program, 9500 Gilman Drive, MC0417, La Jolla, CA 92093-0417
    M. Tillack

128-129. University of California at Santa Barbara, Dept. of Mechanical and Environmental Engineering, Engineering II, Room 2355, Santa Barbara, CA 93106-5070
    G. E. Lucas   G. R. Odette

130-132. University of California at Los Angeles, Dept. of Chemical, Nuclear, and Thermal Engineering, Los Angeles, CA 90024
    M. A. Abdou   N. M. Ghoniem   S. Sharafat

133. University of Illinois, Dept. of Nuclear Engineering, Urbana, IL 61801
    J. Stubbins

134. University of Michigan, Dept. of Nuclear Engineering, Ann Arbor, MI 48109
    T. Kammash

135. University of Missouri, Department of Nuclear Engineering, Rolla, MO 65401
    A. Kumar

136-137. University of Tennessee, Dept. of Materials Science and Engineering, 427-B Dougherty Bldg., Knoxville, TN 37996-2200
    P. K. Liaw   C. J. McHargue

170. Teikyo University, 359 Otsuka, Hachioji, Tokyo 192-0395, Japan
     Akira Miyahara

171. Tohoku University, Institute for Materials Research, Katahira 2-2-1, Aoba-ku, Sendai 980-8577, Japan
     Hideki Matsui

172-173. Tohoku University, Institute for Materials Research, Oarai Branch, Oarai-machi, Ibaraki 311-13, Japan
     Hiroaki Kurishita   Tatsuo Shikama

174-176. Tohoku University, Dept. of Quantum Science & Energy Engineering, Aoba, Aramaki, Sendai 980-8579, Japan
     Katsunori Abe   Akira Hasegawa   Manabu Satou

177. Tokai University, Dept. of Nuclear Engineering, 1117 Kitakaname, Hiratsuka-shi, Kanagawa-ken 259-1292, Japan
     Shiori Ishino

178. University of Tokyo, Dept. of Nuclear Engineering, 3-1, Hongo 7-Chome, Bunkyo-Ku, Tokyo 113-8654, Japan
     Naoto Sekimura

179. University of Tokyo, Dept. of Materials Science, 3-1, Hongo 7-Chome, Bunkyo-ku, Tokyo 113-8654, Japan
     Yutaka Kohno

180. VTT Manufacturing Technology, P.O. Box 1704, FIN-02044 VTT, Finland
     P. Aaltonen

181. Commission of European Communities, Directorate-General for Research Science and Education, Fusion Programme RUE De La Loi 200, B-1049 Brussels, Belgium
     F. Cozzani

182. Southwestern Institute of Physics, P.O. Box 432, Chenedu 610041, Sichuan, P.R. China
     Zeng Yu Xu

183-184. Institute of Atomic Energy, Academia Sinica, P.O. Box 275-51, Beijing 102413, P.R. China
     J. P. Qian   J. Yu

185. Riso National Laboratory, Materials Dept., P.O. Box 49, DK-4000, Roskilde, Denmark
     B. N. Singh

186. Centre d'Etudes Nucleaires, Saclay, DLPC/SMCM, Commissariat a l'Energie Atomique, 91191 Gif-Sur-Yvette, Cedex, France
     N. Roux

187. Commission for European Communities, Joint Research Centre, I.A.M. Ispra Establishment, 21020 Ispra (Varese), Italy
     P. Fenici

188. EURATOM/CIEMAT Fusion Association, Avenida Complutense 22, 28040, Madrid, Spain
     E. R. Hodgson

189. Netherlands Energy Research Foundation ECN, Westerduinweg 3, P.O. Box 1, NI 1755 LE Petten, Netherlands
    B. Van der Schaaf

190. Paul Scherrer Institute, CH-5232 Villigen, Wuerenlingen PSI, Switzerland
    M. Victoria

191. Harwell Laboratory, B393, Radiation Damage Dept., Oxfordshire, OX11 ORA, United Kingdom
    C. A. English

192. Metallurgical and Nuclear Consultant, 9A Cumnor Rise Road, Cumnor Hill, Oxford OX2 9HD, United Kingdom
    D. R. Harries

193. Hahn-Mietner-Institut fur Kernforschung Berlin, Postfach 390128, Glienicker Str. 100, D-14109, Germany
    H. Wollenberger

194. Institut fur Festkorperforschung Forschungszentrum Jülich, Postfach 1913, D-52425 Jülich, Germany
    H. Ullmaier

195-196. ITER Garching Joint Work Site, Max-Planck-Institute für Plasmaphysik, Boltzmannstrasse 2, D-85748 Garching bei München, Germany
    V. Barabash   G. Kalinin

197-198. ITER Naka Joint Work Site, 801-1 Mukouyama, Naka-machi, Naka-gun, Ibaraki-Ken, 311-01, Japan
    M. Huguet (2)

199-201. Kernforschungszentrum Karlsruhe, Postfach 3640, 75 Karlsruhe 1, Germany
    M. Dalle-Donne (INR)   A. Moeslang
    K. Ehrlich (IMF-II)

202. Max-Planck-Institut für Plasmaphysik, Boltzmannstrasse 2, D-85748 Garching bei München, Germany
    Patrick Lorenzetto

203. A. A. Baikov Institute of Metallurgy, USSR Academy of Sciences, Leninsky Prospect 49, Moscow, Russia
    L. I. Ivanov

204. CRISM "Prometey," Naberezhnava r. Monastyrick 1, 193167, St. Petersburg, Russia
    V. V. Rybin

205. D. V. Efremov Institute of Electro-Physical Apparatus, Scientific Technical Center "Sintez,"189631, St. Petersburg, Russia
    S. A. Fabritsiev

206. Kharkov Institute of Physics & Technology, Radiation Damage and Materials Dept., Akademicheskaya 1, 310108 Kharkov, Ukraine
    I. M. Neckludov

207-209.   V. I. Lenin Research Institute of Atomic Reactors, 433510 Dimitrovgrad-10, Ulyanovsk Region, Russia
       V. Kazakov   A. S. Pokrovsky   V. K. Shamardin

210.   Korea Advanced Institute of Science and Technology, Department of Nuclear Engineering, DaeDukDanji, Taejon, 305-701, Korea
       I-S. Kim

211-212.   Korean Atomic Energy Research Institute, P.O. Box 105, Yusung, Taejon, 305-600, Korea
       Thak-Sang Byun   Jun Hwa Hong

213.   Seoul National University, Dept. of Nuclear Engineering, 56-1 Shinrim-Dong, Kwanak-Ku Seoul, 151-742, Korea
       K. H. Chung

214.   Sung Kyun Kwan University, Dept. of Metallurgical Engineering, 300 Chunchun-dong, Jangan-gu, Suwon, 440-746, Korea
       J. G. Han

215.   Department of Energy, DOE Oak Ridge Field Office, P.O. Box 2008, Oak Ridge, TN 37831-6269
       Assistant Manager for Energy Research and Development

216.   Department of Energy, DOE Oak Ridge Field Office, P.O. Box 2008, Oak Ridge, TN 37831-6269
       S. D. Frey

217.   Department of Energy, Office of Basic Energy Sciences, Washington, D.C. 20585
       R. J. Gottschall

218-222.   Department of Energy, Office of Fusion Energy, Germantown, MD 20874
       S. E. Berk   W. Marton   F. W. Wiffen
       N. A. Davies   R. McKnight

222.   Department of Energy, Richland Operations Office, P.O. Box 550, MS-K850, Richland, WA 99352
       J. Turner